Universidad de Salamanca
Instituto de Biología Molecular y Celular del Cáncer

Functional analysis of a truncating variant of RAD51B and two ultraconserved genomic elements in gametogenesis

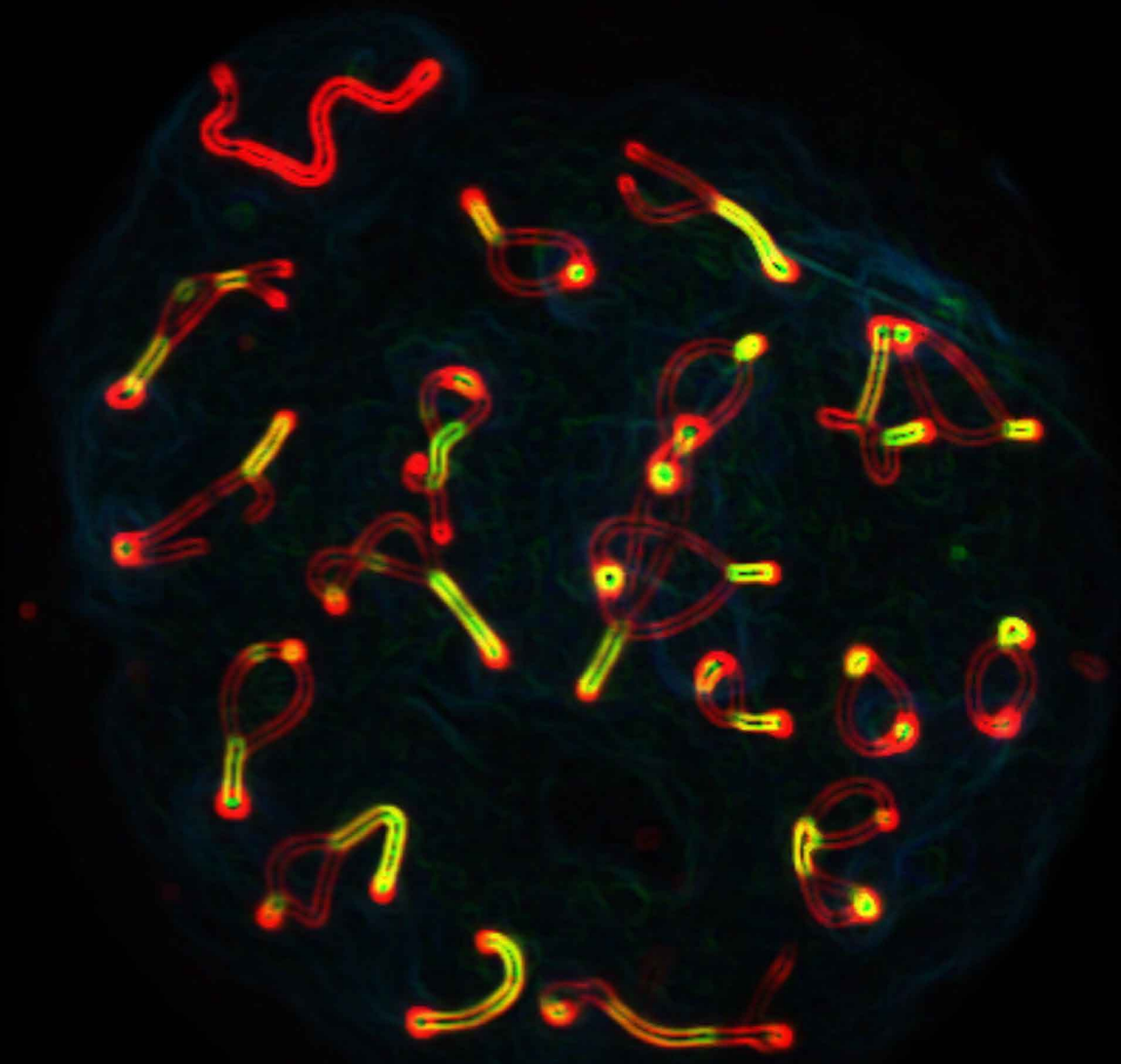

Tesis Doctoral
Yazmine Bejarano Condezo
Salamanca, 2022

Functional analysis of a truncating variant of RAD51B and two ultraconserved genomic elements in gametogenesis

Tesis Doctoral

Yazmine Bejarano Condezo

Director: Dr. Alberto Martín Pendás

Codirectora: Dra. Elena Llano Cuadra

Universidad de Salamanca

Instituto de Biología Molecular y Celular del Cáncer

Salamanca, 2022

El Dr. Alberto Martín Pendás, Investigador principal del Instituto de Biología Molecular y Célular del Cáncer (IBMCC) y la Dra. Elena Llano Cuadra, Profesora Titular del Departamento de Fisiología y Farmacología de la Universidad de Salamanca,

Certifican que Yazmine Bejarano Condezo ha realizado bajo su dirección el trabajo de tesis doctoral titulado:

Functional analysis of a truncating variant of RAD51B and two ultraconserved genomic elements in gametogenesis

Revisado el presente trabajo, consideran que reúne todos los méritos necesarios para su presentación y defensa, con el fin de optar al grado de Doctor por el programa "Biociencias: Biología y Clínica del Cáncer y Medicina Traslacional" de la Universidad de Salamanca.

Y para que así conste firman el presente certificado en Salamanca a 27 de Junio de 2022

Dr. Alberto Martín Pendás

Dra. Elena Llano Cuadra

INDEX

ABSTRACT

ABSTRACT

Mammalian gametogenesis, whose ultimate aim is to generate haploid gametes from diploid cells, represents one of the most complex differentiation processes in developmental biology and requires an accurate regulation of gene expression. Although a vast knowledge has been generated in this field throughout decades, several aspects regarding its regulation are still to be thoroughly understood.

In the present thesis, we have carried out functional analysis of a family with hereditary infertility and two mammalian ultraconserved elements, HS205 and HS1442, potentially involved in gametogenesis.

Primary ovarian insufficiency (POI) causes female infertility by abolishing normal ovarian function. Although the genetic etiology of this disorder has been extensively investigated, most POI cases remain unexplained. RAD51B is a member of the RAD51 family of recombinases. Results of whole-exome sequencing of a family with POI identified a homozygous truncating variant in RAD51B-(c.92delT) in two affected sisters. *In vitro* studies revealed that this variant leads to translation reinitiation at AUG codon 64. Here, we show that this is a pathogenic hypomorphic variant in a mouse model. *Rad51b*$^{c.92delT/c.92delT}$ mice exhibited meiotic DNA repair defects due to γH2AX, RAD51 and HSF2BP/BMRE1 accumulation in the chromosome axes leading to a reduction in the number of crossovers. Interestingly, the interaction of RAD51B-c.92delT with RAD51C and with its newly identified interactors RAD51 and HELQ was abrogated or diminished. Repair of Mitomycin-C-induced chromosomal aberrations was impaired in RAD51B/*Rad51b*-c.92delT human and mouse somatic cells *in vitro* and in explanted mouse bone marrow cells. Accordingly, RAD51B-c.92delT variant reduced pluripotent reprogramming efficiency of primary mouse embryonic fibroblasts. Finally, *Rad51b*$^{c.92delT/c.92delT}$ mice displayed increased incidence of pituitary gland hyperplasia. These results provide new mechanistic insights into the role of RAD51B not only in meiosis but in the maintenance of somatic genome stability.

Ultraconserved elements are genomic sequences showing extremely high levels of similarity across distant species. To date, no compelling functional explanation has been proposed which would result in such high level of conservation. However, the distribution of these elements within and across vertebrate genomes suggest that they could have many roles as transcriptional regulatory elements during the differentiation associated with development. To directly explore a functional role of these ultraconserved elements in the regulation of spermatogenesis, we have selected two ultraconserved elements, HS205 and HS1442, potentially involved in germ cell biology according to its restricted enhancer activity during mouse development to the genital tubercle. In order to analyze their role, we have further characterized its enhancer activity either *in vitro* different cell types, and *in vivo* by testis electroporation. In addition, we have deleted both *hs205* and *hs1442* in the mouse using CRISPR/Cas9 system and analyzed its consequences during spermatogenesis. Our results provide *in vivo* evidence that HS205 and HS1442 are not essential for male gametogenesis and thus, fertility in the mouse.

ABBREVIATIONS

ACTH: Adrenocorticotropic Hormone

AEs: Axial Elements

APC/C: Anaphase Promoting Complex/Cyclosome

ATP: Adenosine triphosphate

cDNA: complementary DNA

CE: Central Element

CNG: Conserved Non-genic

CO: Crossover

CRISPR: Clustered Regularly Interspaced Short Palindromic Repeats

DAPI: 4',6-diamidino-2-phenylindole

dHJ: double Holliday Junction

DMEM: Dulbecco's Modified Eagle Medium

DMSO: Dimethyl sulfoxide

DNA: Deoxyribonucleic Acid

dpc: days post coitum

dpp: days post-partum

DSBs: Double Strand Breaks

DTT: 1,4- dithiothreitol

EDTA: Ethylenediamine tetraacetic acid

EGTA: Ethyleneglycol tetraacetic acid

ES cells: Embryonic Stem cells

FA: Fanconi Anemia

FBS: Foetal Bovine Serum

FITC: Fluorescein Isothiocyanate

FSH: Follicle Stimulating Hormone

GFP: Green Fluorescent Protein

GH: Growth Hormone

HR: Homologous Recombination

ICL: Interstrand Crosslink

IF: Immunofluorescence

IP: Immunoprecipitation

iPSC: induced Pluripotent Stem Cell

LE: Lateral Element

LH: Luteinizing Hormone

MEFs: Mouse Embryonic Fibroblasts

MMC: Mitomycin C

mRNA: messenger RNA

NCO: Non-Crossover

NOA: Non-Obstructive Azoospermia

OA: Obstructive Azoospermia

ORF: Open Reading Frame

OSC: Oogonial Stem Cell

PAR: Pseudoautosomic Region

PAS: Periodic Acid–Schiff

PBS: Phosphate Buffered Saline

PCR: Polymerase Chain Reaction

PGC: Primordial Germ Cell

PCOS: Polycystic Ovary Syndrome

POI: Primary Ovarian Insufficiency

PRL: Prolactin

PSG: Penicillin Streptomycin Glutamine

PTC: Premature Termination Codon

RN: Recombination Nodule

RNA: Ribonucleic Acid

RT-PCR: Reverse Transcription PCR

SAC: Spindle Assembly Checkpoint

SC: Synaptonemal Complex

SMS: SUMO-Modification System

SNV: Single Nucleotide Variant

SNP: Single Nucleotide Polymorphism

SSC: Spermatogonial Stem Cell

ssDNA: single-stranded DNA

ssODN: single-stranded Oligodeoxynucleotide

SUMO: Small Ubiquitin-like Modifier

TE: Tris-EDTA

TF: Transverse Filament

TRITC: Tetramethyl Rhodamine Isothiocyanate

Ub: Ubiquitin

UCE: Ultraconserved Element

UTR: Untranslated Region

WES: Whole-Exome Sequencing

INTRODUCTION

1. Gametogenesis

Mammalian sexual reproduction involves a complex life cycle in which two haploid gamete (egg cell or sperm) fuse to generate a zygote that develops into an organism composed of diploid cells. The essential biological process by which these diploid cells produce haploid gametes is called **gametogenesis**. These gametes, in mammals referred as oocyte and spermatozoa, are highly specialized haploid cells capable to fuse generating a totipotent zygote, from which all somatic lineages and the next generation of gametes will later arise, giving rise to a new individual.

In mammals, gametogenesis begins very early in development with the extragonadal emergence of the primary undifferentiated stem cell type called the primordial germ cells (PGCs). These first layer of cells are the embryonic precursor of the gametes and represent the founder cells of the germline. PGCs precursors emerge as a cluster of about 20 cells at the embryonic (E) day 18-19 in humans (E7.25 in mice). PGCs localize near the extra-embryonic yolk sac wall, close to the allantois. Between E28-36 (E10.5 in mice) these germ cells migrate through the hindgut to the developing genital ridges (gonads). These migratory PGCs undergo genome-wide epigenetic reprogramming, including global DNA demethylation (erasing imprints and other somatic epigenetic memories), X-chromosome reactivation, and chromatin remodelling in order to supress differentiation programmes of somatic cells and acquire pluripotency (Sekl et al., 2007; Surani, 2001). Finally, from E44 to 49 (E10.5 to E.11.5 in mice), PGCs colonize the emerging gonads, lose their migratory potential and initiate either male or female differentiation pathways.

1.1 Oogenesis

In female embryos, the colonization of the gonadal ridges by PGCs is followed by sex determination and subsequent differentiation into oogonia in the developing ovary. These oogonias divide by mitosis (approximately 20 divisions) with incomplete cytokinesis, whereby they remained joined by intercellular bridges generating the germ cell cysts. Between week 10 and 20 of embryonic development (E13.5-17.5 in mice), the whole pool of oogonias enter in meiotic prophase I (through leptotene, zygotene and pachytene stages) to become primary oocytes that arrest at the end of meiosis I in a stage called dictyate (corresponding to diplotene or diakinesis stages) also referred as germinal vesicle (GV) stage. Concurrently, the germ cell cyst disaggregates into single oocytes surrounded by pre-granulosa cells generating the primordial follicles. During the disaggregation of the germ cell cyst several oocytes are removed through apoptosis (atresia) helping in the individualization of surviving oocytes and selecting the highest quality oocyte. Oocytes will remain arrested until the preovulatory surge of luteinizing hormone (LH) stimulates meiotic resumption which occurs not before puberty (X. Wang & Pepling, 2021; Wassarman & Litscher, 2021).

In mammalian females, regulation of the meiotic progression in the ovaries is carried out by retinoic acid (RA) signalling. RA is synthetized by the Aldehyde dehydrogenase 1 family (ALDH1A2/3) enzymes, together with ALDH1A1 which is transcribed by the foetal gonads (Bowles et al., 2016). Upon the expression of the RNA binding protein, *DAZL,* germ cells achieve the capacity to respond to RA as a meiosis-stimulating signal (Bowles et al., 2006). RA induce the expression of the transcription factor *Stra8,* and of the meiotic cohesin *Rec8*, among other essential players for meiotic progression (**Figure I**). *Stra8* expression starts at E12.5 in mouse

foetal ovaries and progresses in a subsequent anterior-posterior (A-P) wave in a way that the expression of *Stra8* and other meiotic markers (i.e., *Sycp3*, *Dmc1*) are heterogeneous through the population of germ cells (Menke et al., 2003). It is known that *Stra8*-null mice do not undergo meiotic DNA replication and do not enter into meiotic prophase I, suggesting that *Stra8* is an initiator of meiosis in mice (Baltus et al., 2006). Recently, it has been suggested that MEIOSIN and STRA8 act in the same transcriptional complex for the initiation of meiosis under RA (Ishiguro et al., 2020). Together, these proteins bind and activate important meiotic genes that are essential for establishing the meiosis-specific chromosome structures.

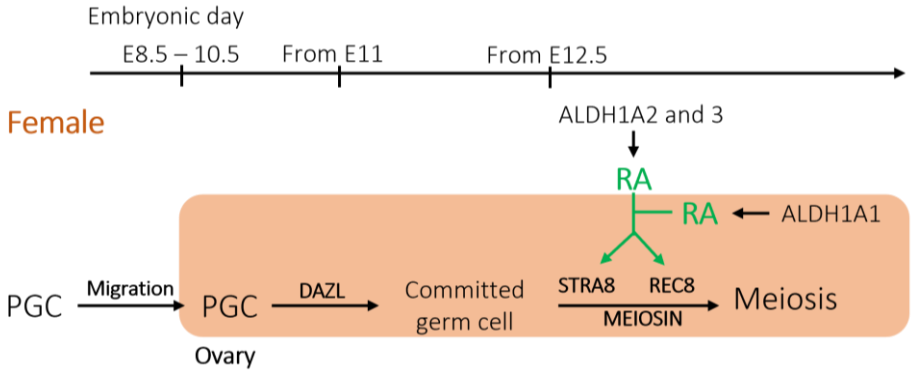

Figure I. RA signalling regulates meiosis progression in foetal ovaries. In females, STRA8 and MEIOSIN drives the initiation of meiosis in response to RA. Modified from (Endo et al., 2019).

In the course of embryonic development, a pool of **primordial follicles** is obtained each containing an oocyte arrested at the end of prophase I. This pool represents the whole ovarian reserve of oocytes that will be available during the entire reproductive lifespan of females. Humans and mice carry out oogenesis in a similar way, except that in mice the process is accelerated probably due to their shorter lifespan.

On the onset of puberty, oocytes grow and differentiate from primordial follicles to **preovulatory follicles** in response to hormonal stimulation in a process called folliculogenesis. The follicle stimulating hormone (FSH) stimulates the proliferation of the supporting somatic cells, called granulosa cells, and consequently there is an increase in the size of the oocytes. FSH also stimulates estradiol production, inducing the luteinizing hormone (LH) which drives meiosis progression from prophase I to metaphase II (McGee & Hsueh, 2000). Subsequently, the metaphase II arrested oocyte is released (ovulation) after the LH secretion, generating the secondary oocyte and the first polar body. The second meiotic division will only progress if fertilization occurs, generating the mature egg together with a second polar body (**Figure IV**).

1.2 Spermatogenesis

In male embryos, the colonization of the gonadal ridges by PGCs is followed by sex determination and subsequent differentiation into spermatogonia in the developing testes. In XY gonads, the sex determining and Y-linked transcription factor SRY induces SOX9 upregulation and subsequent FGF9 expression, leading to the differentiation of Sertoli cells. The expression of these and other male specifying factors such as the Cytochrome P450 26B oxygenase (CYP26B1), TCF21, NTF3 and CBLN4 promote testis formation in XY gonads by actively suppressing the ovarian developmental pathway that would occur otherwise (Bowles et al., 2018; H. Suzuki et al., 2015).

In developing foetal testes, under the influence of the transcription factor *Sox9*, a set of primitive testicular cords shape in the genital ridge, and the PGCs migrate into these primitive cords. Once the sex cords have formed, these germ cells present in the cord are referred as gonocytes, which differ morphologically from migratory PGCs. Gonocytes proliferate mitotically in order to increase their number and then they become arrested in G0/G1 phase, called prospermatogonia stage. For this arrest to take place in the mouse gonads, the CYP26B1 degrades RA avoiding the induction of *Stra8*, and thus preventing the initiation of meiosis (Bowles et al., 2006; McLaren & Southee et al., 1997). In *Cyp26b1*-deficient XY embryos, testis determination is compromised, resulting in the formation of a mild ovotestis (Bowles et al., 2018). The expression levels of CYP26B1 together with NANOS2, which repress the expression of DAZL within germ cells (**Figure II**), prevent the male germ line from entering meiosis and maintain the arrest in G0/G1 phase, where they will remain until birth (A. Suzuki & Saga, 2008).

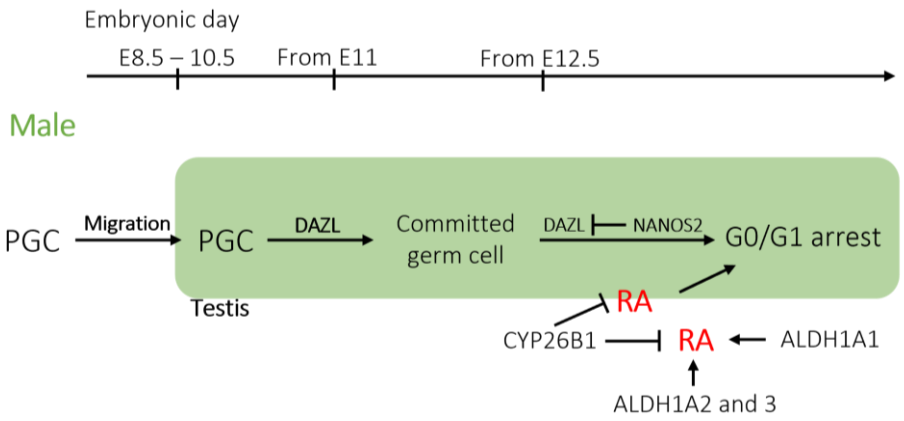

Figure II. Germ cell development in mouse foetal testis before birth. The expression levels of CYP26B1 together with NANOS2 prevent the male germ line entering in meiosis. Modified from (Endo et al., 2019).

After birth, the prospermatogonia arrested in G0/G1 phase, resume mitosis and migrate to the basement of the testis cords generating the undifferentiated type A spermatogonia. These cells have self-renewal features perpetuating the stem cell pool throughout reproductive life. Several models have been proposed to explain the relationship between spermatogonial stem cells (SSCs) and progenitors (de Rooij, 2017).

In the "clone fragmentation model", all SSCs, that have stem cell potential and renewal, are generated by fragmentation of the intercellular bridges that keep them connected by incomplete cytokinesis (syncytia). It has been hypothesized that in this model, clones of undifferentiated spermatogonia can transform providing responses in how the A single (A_s) spermatogonias pool is maintained (Hara et al., 2014). These A_s spermatogonia divide into paired A (A_{pr}) spermatogonia that either complete cytokinesis to produce two new A_s spermatogonia (self-renewal) or remain connected by intercellular bridges (Weber & Russell, 1987). The A_{pr} spermatogonia then, divide into extended networks of 4, 8 or 16 cells, known as aligned (A_{al}) spermatogonia. The transition to differentiating type A spermatogonia can occur from A_s, A_{pr} or A_{al4} clones, but most frequently occurs from A_{al8} or A_{al16} clones. Eight successive divisions from A1 spermatogonia lead to differentiating spermatogonial types A2, A3, A4, and finally, to B spermatogonia. During this course of differentiation, spermatogonia lose stemness (de Rooij, 2017; Fayomi et al., 2018; La & Hobbs, 2019; Nakagawa et al., 2010). At puberty, these B spermatogonia initiate meiosis leading to four haploid round spermatids that will elongate giving rise to elongated spermatids. Finally,

these elongated spermatids release into the seminiferous tubule lumen where they mature to spermatozoa (O'Donnell et al., 2011).

Spermatogenesis in mammals occurs within the seminiferous tubules, which are highly organised cytologically. In this regard, Sertoli cells, that act as supporting epithelial cells of the seminiferous tubules, are located at the base of the tubules, joined by tight junctions, generating the blood-testis barrier (BTB) (Cheng & Mruk, 2002).

The BTB subdivides the epithelium into basal and adluminal regions, thus separating the germ cells into two anatomically and functionally distinct compartments: the basal compartment and the adluminal compartment. Surrounding the seminiferous tubules, in the interstitial, there are the Leydig cells, peritubular myoid cells and macrophages (**Figure III**). The basal compartment contains the earlier germ cell types including spermatogonia and pre-leptotene spermatocytes. This compartment is thought to be essential for excluding meiotic germ cells from immune system, maintaining the basal stem cell niche, and allowing selective exposure of basal germ cells to regulatory factors produced by Leydig cells and peritubular myoid cells, which are located in the interstitium. On the other hand, the adluminal compartment contain post-leptotene spermatocytes and spermatids (round and elongated). Thus, germ cells are in continuous differentiation coupled to migration from the basal surface to the lumen of tubules (Yan Cheng & Mruk, 2015).

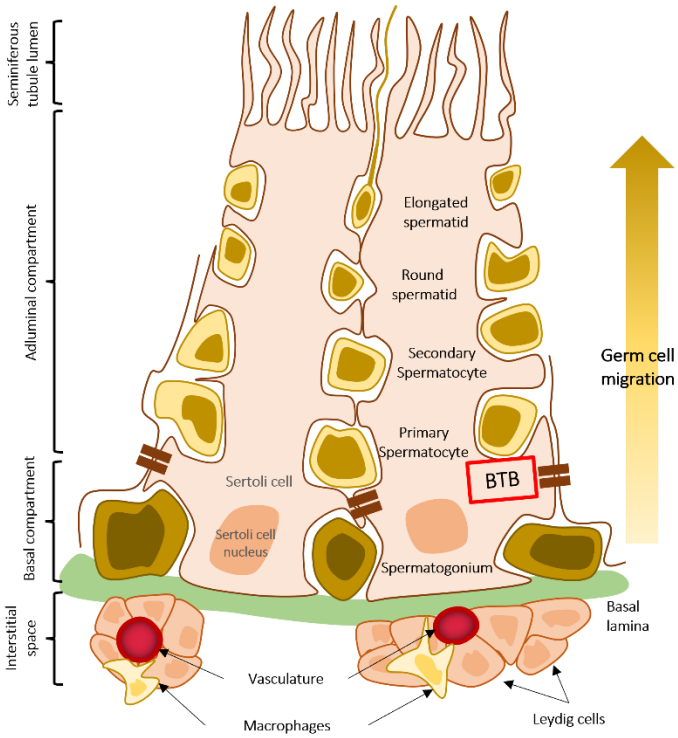

Figure III. Blood-testis barrier. Cellular composition showing the intimate relationship between Sertoli cells and germ cells, as well as the relative location of the BTB. The contribution of surrounding cells to barrier function and homeostasis is also shown. Leydig cells and peritubular myoid cells are located in the interstitium.

Accordingly, the seminiferous epithelium contains a mixture of germ cells at various developmental stages. The **seminiferous cycle** refers to all cellular interaction that occur between the Sertoli cells and the developing germ cells. This cycle takes 72 days (35 days in mice) to complete from undifferentiated spermatogonia to mature sperm, being this process initiate

cyclically every 16 days (8.6 days in mice). In the mouse, the seminiferous cycle is divided into 12 different cellular associations, known as seminiferous stages I to XII (Russell et al., 1993). This classification is useful to determine the stage at which meiosis is arrested in mouse mutants. During stages VII and VIII four important phases of germ cell development take place: i) the differentiation of spermatogonia, ii) the initiation of meiosis, iii) spermatid elongation, and iv) the release of elongated spermatids (Clermont, 1972; Oakberg, 1956). The intimate proximity of each of these transitions is largely conserved in other mammals including humans (Muciaccia et al., 2013), rats (Huckins, 1971), hamsters, and rams (Lok et al., 1982). Definitely, the final goal of spermatogenesis is to ensure that spermatozoa are produced at a constant rate throughout male reproductive life (**Figure IV**) (de Kretser et al., 2016).

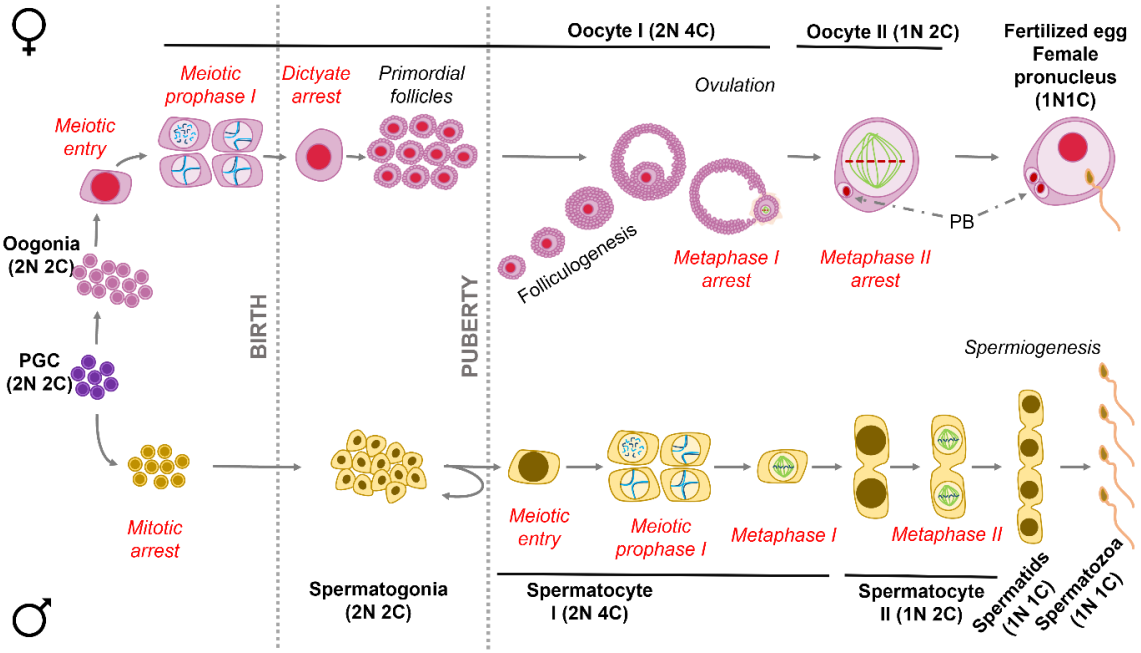

Figure IV. Schematic representation of sexually dimorphic progressive events of gametogenesis and meiosis in female and male germline. This figure shows both DNA content (C value) and the ploidy (N value) in germ cells at the different stages of differentiation. PGCs are initially sexually undifferentiated and the sex-specific differentiation programs begin after PGCs colonize the foetal gonads. In **females**, after a limited period of mitotic proliferation, oogonia enter meiotic prophase I during foetal development. Diploid oocytes complete meiotic recombination around birth, and arrest at the dictyate stage. Shortly after birth, somatic pre-granulosa cells surround arrested oocytes to form primordial follicles. At puberty, when a primordial follicle is activated, it grows in size through both granulosa cell proliferation and increase in oocyte size (arrested at dictyate). Prior to ovulation, the oocyte resumes meiosis and arrests at metaphase I. Upon ovulation, first meiotic division is completed, and the first polar body is extruded into the space under the zona pellucida. The ovulated oocyte re-arrests at metaphase II, until fertilization which triggers the second meiotic division and extrusion of the second polar body. Oocytes are never truly haploid because at the time of their second meiotic division, they already contain the male haploid genome. In **males**, germ cells undergo mitotic proliferation and then arrest forming quiescent gonocytes. Gonocytes remain in an arrested state until after birth, when they resume mitotic divisions and establish SSC. Type A spermatogonia either self-renew or differentiate to type B spermatogonia, which are committed to enter meiosis, thus initiating the spermatocyte stage. The diploid spermatocytes progress through prophase I, completing meiotic recombination, and, without interruption, undergo the first and second meiotic divisions. The haploid spermatids thus formed undergo spermiogenesis to form mature sperm. Modified from (Bolcun-Filas & Handel, 2018).

2. Meiosis

Meiosis es a crucial cellular process that underlies sexual reproduction and halved the genome generating haploid cells (n) from diploid cells (2n). To achieve this reduction of the diploid somatic chromosomal complement to haploid state, one round of DNA replication is followed by two rounds of segregation. During the first division (meiosis I, MI), the segregation of the maternal and paternal homologous chromosomes occurs, undergoing a reductional division. During the second division (meiosis II, MII), the sister chromatids segregate, generating a highly specialized haploid cell called the gamete.

It is thought that meiosis evolved from mitosis, acquiring different characteristics, including pairing of homologous chromosomes, recombination between non-sister chromatids, and the absence of DNA replication prior the second meiotic division, which is essential for reducing the ploidy (Wilkins & Holliday, 2009). The reduction of the paternal genetic material is crucial to restore ploidy after fertilization thus allowing the stability of genome size between generations. The new individual resulting from the fusion of female and male gametes will have a combination of the two parents generating a new chromosomal combination.

2.1 Meiotic prophase I

Prophase I is the longest and most relevant event of meiosis. During this phase, chromosomes are organized into axis-loop structures, which provide the structural framework for several meiotic specific events such as i) the generation of programmed double-strand breaks (DSBs), repair of the DSBs by homologous recombination (HR), ii) pairing and synapsis of the homologues chromosomes to give rise to bivalents chromosomes as well as, iii) recombination and iv) segregation of the homologues. The main objective and consequence of the meiotic recombination, using as DNA template in the repair of the homologous chromosome instead of the sister chromatid, is the formation of physical connections between the homologues, the chiasmata. These junctions are essential for the proper alignment and segregation of the homologues during the first meiotic division (Handel & Schimenti, 2010; Zickler & Kleckner, 2015).

Prophase I is subdivided in five well defined stages: leptotene, zygotene, pachytene, diplotene, and diakinesis. This classification is based on the behaviour of the homologues chromosomes when they pair and synapse through the formation of the synaptonemal complex (SC) (Handel & Schimenti, 2010). The SC is a zipper-like protein scaffold that is assembled between the homologues and hold them along their entire chromosome length. This tripartite proteinaceous structure is formed by two axial elements (AEs), and a central region that contains the transverse filaments (TFs) and the central element (CE). Currently, in mammals, eight meiosis-specific proteins have been identified as structural components of the SC: the AE proteins SYCP3 (Lammers et al., 1994) and SYCP2 (Offenberg et al., 1998), the TF protein SYCP1 (Meuwissen et al., 1992), and the CE proteins SYCE1, SYCE2, SYCE3, TEX12 and SIX6OS1 (Costa et al., 2005; Gómez-H et al., 2016; Hamer et al., 2006; Schramm et al., 2011). By double immunolabelling of gametocytes with SYCP3 and any of these CE proteins, it is feasible to evaluate the degree of synapsis of the AEs, and thus to assign their corresponding stage of prophase I (**Figure V**).

At the beginning of prophase I, at **leptotene**, chromosomes start to condense organizing chromatin into loop-axis structure and the AEs begin to assembly onto the cohesins threads, constituting the chromosome axes. At this time, the chromosomes search for their homologue to

pair and the AEs and cohesins complexes assemble into small fragments that elongate reaching the stage of **zygotene** (Ishiguro, 2019). One of the most distinctive features of meiosis is chromosome pairing, which requires telomere attachment and rotation in the nuclear envelope via microtubules, driving the search for chromosome homology. The telomere pulling to the centrosome forms the meiotic bouquet (Kim et al., 2022; Lee et al., 2015). A recent study identified the "zygotene cilium" in oocytes. This cilium provides a cable system for the bouquet machinery, extending throughout the germline cyst demonstrating that the cilium anchors the centrosome to counterbalance telomere pulling. The cilium is essential for bouquet and SC formation (Mytlis et al., 2022). At this zygotene stage the homologue chromosomes align even closer through the assembly of the TFs and CE acting as a zipper. This process is referred as synapsis. Then, at **pachytene**, the SC is completely assembled along the chromosome hence, fully synapsis is achieved. The synapsed AEs are now called as lateral elements (LEs) (**Figure V**). In males the synapsis is incomplete, and the X and Y sex chromosomes only show homology in a small region known as the pseudo-autosomal region (PAR) (Simmler et al., 1985). It is in this region where the formation of the chiasmata occurs, ensuring the correct segregation of the sex chromosomes (Acquaviva et al., 2020). The asynapsis of most of the sex chromosomes results in their transcriptional inactivation. This process is called the meiotic sex chromosome inactivation (MSCI) and plays an important role in the prophase I checkpoint response to asynapsis (Turner et al., 2015). Finally, homologue chromosomes desynapse and the SC starts to disassemble from **diplotene** to diakineses. During this process, DNA achieves the maximum condensation before metaphase I.

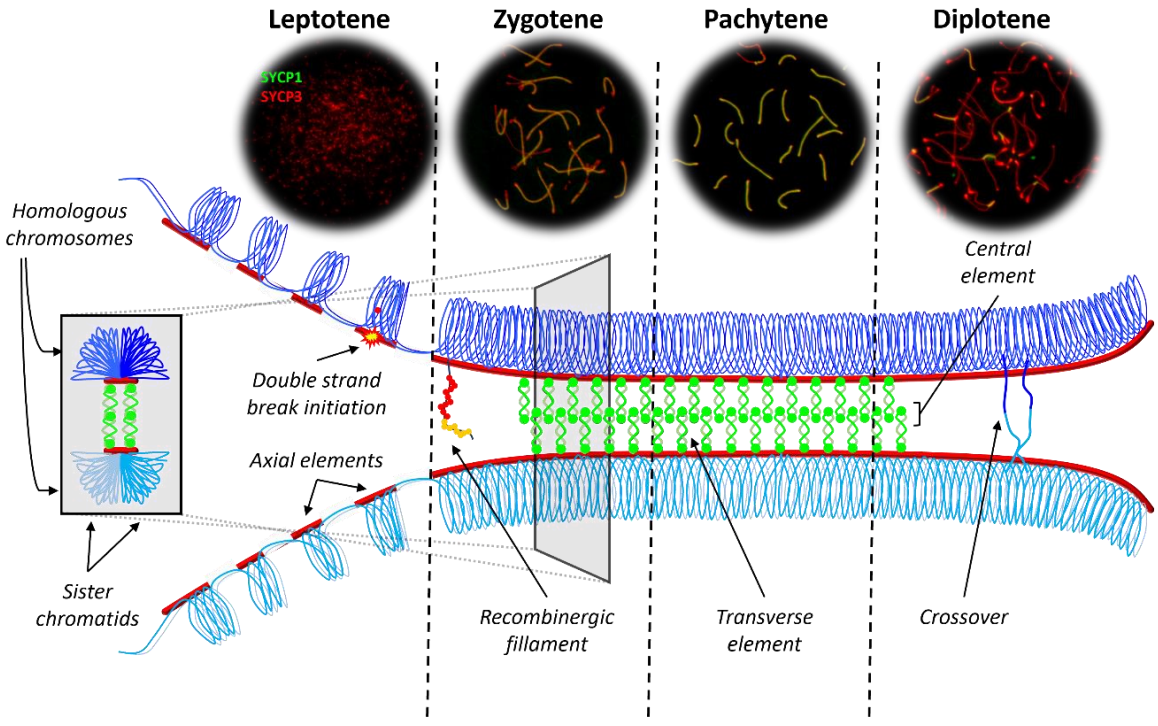

Figure V. The synaptonemal complex. Schematic representation of the most relevant the events of prophase I in the SC. During leptotene the AE formation, the cohesion loading and the DSBs formation are produced. At zygotene, the homologues start to synapse, and the meiotic recombination take place. During pachytene, the crossover are formed and at diplotene the SC disassemble.

2.1.1 Meiotic recombination

Meiosis is responsible for genomic diversity since enable independent chromosome assortment of homologues chromosomes and the generation of new chromosomes by shuffling genomic segments between parental genomes. The law of independent assortment, formulated by Gregor Mendel is based on the random orientation of homologous chromosome pairs during metaphase I which allows the production of gametes with many different random assortments of maternal and paternal chromosomes. Meiotic recombination, on the other hand, refers to a phenomenon that takes place during prophase I at the early-leptotene. Through meiotic recombination homologous chromosomes join together to form tetrads and also leads to the reciprocal exchange of chromosome segments (crossovers) between homologous chromosomes resulting in a new combination of alleles.

Initiation of recombination

In molecular terms, meiotic recombination begins with the programmed formation of DSBs, which are generated by the meiotic-topoisomerase-like protein SPO11 (Baudat et al., 2000; Keeney et al., 1997) and by the meiotic topoisomerase VIB–like TOPO6BL (Robert et al., 2016; Vrielynck et al., 2016). These DSBs are concentrated on short chromosomal regions of the genome called hotspots. PRDM9, a histone-lysin methyltransferase, is responsible for specifying recombination hotspots in mice and humans. Genome-wide mapping of DSBs led to the identification of ~20,000 hotspots in mouse (Brick et al., 2012; Smagulova et al., 2011). PRDM9, which is expressed in meiocytes, contains a zinc finger binding domain that binds to specific DNA sequences and catalyse the trimethylation of histone H3 at lysine 4 and 36 (H3K4me3 and H3K36me3) at recombination hotspots (Baudat et al., 2010; Myers et al., 2010). These epigenetic marks promote the recruitment of SPO11 that together with MEI4, REC114 and IHO1 catalyze the endonucleolytic cleavage of the DNA generating the DSBs (Kumar et al., 2010, 2015; Stanzione et al., 2016) (**Figure VI**). The next step is the removal of SPO11 from the DSBs by the MRN complex (MRE11-RAD50-NBS1) through endonucleolytic cleavage (Neale et al., 2005).

Processing ends to promote strand invasion

One of the first events after the DSBs formation is the ATM-dependent phosphorylation of histone H2AX at serine 139 (γH2AX) which activated the DSB repair response (Bellani et al., 2005). H2AX phosphorylation regulates the formation and repair of programmed DSBs, as well as meiotic silencing of unrepaired chromosomes, so that the dynamics of γH2AX distribution is mainly used as a marker for meiotic progression (Jiang et al., 2018). Once H2AX is phosphorylated at the DSBs, 5' overhangs are resected by the exonuclease EXO1 and ssDNA (single-stranded DNA) 3' overhangs ends are thus generated (Zakharyevich et al., 2010). After that, the ssDNA binding protein RPA together with SPATA22 (la Salle et al., 2012) and MEIOB (Luo et al., 2013; Xu et al., 2017) are recruited to the 3' ends, protecting them from nuclease degradation and avoiding the formation of secondary structures (Chen et al., 2013). Thereafter, RPA is replaced from the ssDNA by RAD51 and DMC1 recombinases, generating the early recombination nodules (RNs) (**Figure VI**). The resulting recombinase-coated ssDNA filaments can invade the homologous chromosome dsDNA, searching for a complementary sequence (chromosome pairing), which will foster genetic material exchange. During the strand invasion, the structure known as D-loop is generated and fosters the exchange of genetic material. This process is mediated in mammals by the multidomain hub protein BRCA2 together with the DSBs recruiter PALB2 (Xia et al., 2006) and the

heterodimer HSF2BP/BRME1 which has been recently identified in our laboratory (Felipe-Medina et al., 2020).

RAD51 and DMC1 share ~50% protein identity, being higher in the C-terminal regions (Sheridan et al., 2008). However, the meiotic analysis of *Rad51* and *Dmc1* knockdown mice shown no interdependent foci formation, leading to different phenotypes. These results support the idea that DMC1 have a non-essential role in synapsis and homology search, while RAD51 would have a role in crossover (CO) and synapsis of the sex chromosomes (Dai et al., 2017). As prophase I proceeds, the early RNs mature into intermediate nodules, and it is in this step where RPA, SPATA22 and MEIOB are loaded again into the ssDNA generated in the D-loops (**Figure VI**). These proteins play important roles in the protection of ssDNA and in the capture of the second end by the homologue chromosome, which is essential for the formation of double Holliday junctions (dHJ) and the resolution of COs (Xu et al., 2017).

Hence, BRCA2 govern most of the steps of meiotic recombination including the initial binding of RPA to the resected DNA, the exchange of RPA by RAD51/DMC1 and the loading of MEIOB/SPATA22 complex to the RPA complexes (Martinez et al., 2016; W. Zhao et al., 2015).

Resolution of recombination intermediates

In mammals most of the recombination intermediates are resolved as non-crossovers (NCOs) and only 10% of them are resolved as COs (Baudat & de Massy, 2007; Hunter, 2015). When the D-loop is not properly stablished, the repair of the DSB does not produce reciprocal exchange of DNA between homologues, producing a NCO (**Figure VI**). Conversely, when a dHJ is generated, it will be resolved as a CO or NCO depending on whether two of four DNA strands are cleaved (Allers & Lichten, 2001; Hunter & Kleckner, 2001).

Therefore, as prophase I progresses, the intermediates nodules also progress and matures. In addition to the afore mentioned RPA, SPATA22 and MEIOB, there are a large number of proteins involved in this processing for the final fate of DSBs. These include BLM, TEX11, CNTD1, RNF212, HEI10 and the MSH4/MSH5 complex, which are firstly loaded at zygonema and show partial colocalization with RAD51/DMC1 on synapsed axes, and their levels decrease by the end of pachynema. These proteins seems to play a role in stabilizing and processing the recombination intermediates (Baudat et al., 2013). It has been recently hypothesized that sumoylation and ubiquitination antagonistic activities are essential in the regulation/maturations of meiotic intermediate. Thus, it has been proposed that the balance between the posttranslational modifications SUMO/ubiquitination regulate the recombination rate (Qiao et al., 2014). In this regard, RNF212 (E3 SUMO-ligase) and HEI10 (E3 ubiquitin-ligase) would act by regulating the turnover of the ZMM proteins (MutS, MSH4 or TEX11) (Rao et al., 2017; Reynolds et al., 2013; Ward et al., 2007). Accordingly, RNF212 would promote DSBs resolution into CO by stabilizing the RNs, whereas HEI10 would promote DSBs resolution into NCOs by destabilizing the RNs.

The final resolution of the recombination intermediates should occur at pachytene, to ensure the existence of at least one CO per bivalent. This process is manly mediated by the mismatch repair proteins MLH1/MLH3 (MutLγ complex) and EXO1 (Baker et al., 1996; Wei et al., 2003). In many organisms, most COs are regulated by a phenomenon known as interference, a process by with the presence of a CO on a chromosome decrease the chances of a second CO occurring nearby the same chromosome. In yeast, the majority of COs are processed by the Msh4-Msh5

and Mlh1-Mlh3 interference-dependent pathway (Class I CO), whereas a second class of interference-independent COs (Class II CO) are thought to be processed by the alternative Mus81-Mms4 pathway. In mice, both *Mhl1* and *Mlh3* KOs present a subset of persistent normal COs suggesting that independent-MLH1/MLH3 pathway also exists in mammals. (Holloway et al., 2008). Recently, by comparative analysis of different mutants in yeast, MLH1-3 was revealed to promote both asymmetric maturation and biased resolution of COs intermediates (Marsolier-Kergoat et al., 2018). The correct regulation of this pathway is essential for CO homeostasis by ensuring the proper segregation of the homologue chromosomes in metaphase I.

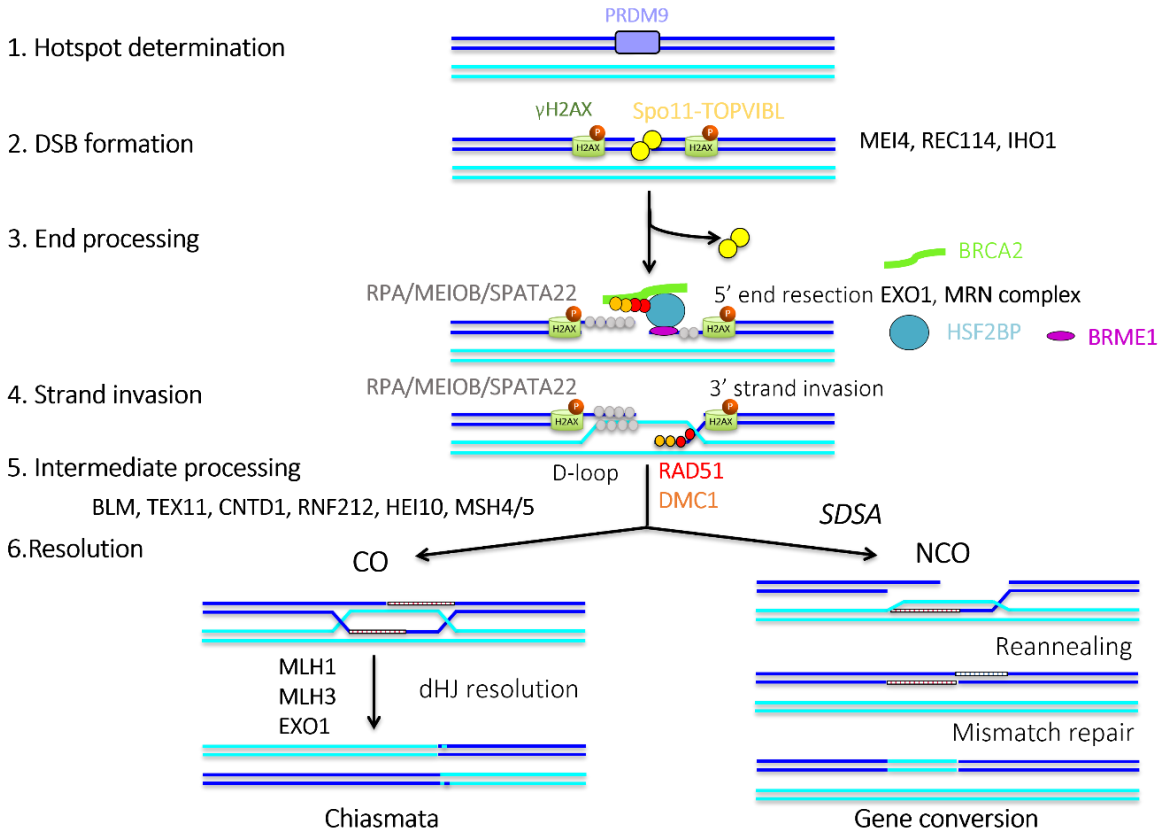

Figure VI. Model of meiotic recombination. Schematic representation of meiotic recombination highlighting the key steps, beginning with the hotspot determination and DSB formation by SPO11-TOPVIBL. Next, end processing and strand invasion by RAD51/DMC1. Early RNs are formed, become intermediate RNs, and finally being resolved as CO or NCO.

2.2 Metaphase-anaphase I transition

At the end of meiosis, two consecutive cell divisions will have taken place, generating the haploid gametes. The first division is reductional in which the homologue chromosomes segregate. The second is an equational division, similar to mitosis, where sister chromatids are the ones that segregate. These consecutive segregations occur by the differential release of the cohesins complexes from the chromosome arms and from the centromeres. At the metaphase-anaphase I transition, only the chromosome arm cohesin complexes will be removed and centromere cohesins will be protected, allowing the segregation of the homologues chromosomes.

The two homologous chromosomes of each metaphase I bivalent are physically connected by chiasmata, which is stabilized by cohesion distal to the CO. These physical junctions, counteract the opposing force generated by the spindle and promote biorientation of bivalents (Gutiérrez-Caballero et al., 2012). At the onset anaphase I, bivalent segregation is achieved by the removal of cohesins from the chromosome arms by a proteolytic-dependent Separase cleavage of the α-kleisin subunit of the cohesin complexes (**REC8** or RAD21L) (Hauf et al., 2001; Kitajima et al., 2003; Kudo et al., 2009; Llano et al., 2008; Uhlmann et al., 2000). Separase activation is highly regulated through a double inhibitory mechanism mediated by Securin and CDK1/Cyclin B1 complex (Hellmuth et al., 2015; Stemmann et al., 2001). Briefly, once the homologues are bioriented at the metaphase I plate, the spindle assemble checkpoint (SAC) is satisfied, the anaphase-promoting complex/cyclosome (APC/C) complexed to Cdc20 is activated, and Securin and Cyclin B are targeted by APC-dependent ubiquitination, Separase is activated (Hagting et al., 2002; Vorlaufer & Peters, 1998).

The simultaneous Separase cleavage of centromeric and chromosome arm cohesins does not abolish or interfere with bivalent monorientation but abrogated the sister chromatid cohesion that is essential for sister segregation during the second meiotic division (Llano et al., 2008).

The protection of the centromeric cohesins is essential for the proper segregation of sister chromatids. Shugoshins, a family of highly conserved proteins, are responsible of this protection (Kerrebrock et al., 1995). In mammals, SGOL2 is the only responsible of the protection of centromeric REC8-containing cohesin complexes against Separase in meiosis (Llano et al., 2008). The Shugoshins' mechanism of protection is based on a complex with PP2A phosphatase which counteracts cohesins phosphorylation avoiding Separase cleavage. *Sgol2* deficient mice present infertility due to premature separation of sister chromatids during anaphase I, resulting in aneuploid gametes (J. Lee et al., 2008; Llano et al., 2008). SGOL2 localization at centromeres in MI is stabilized by MEIKIN, a protein that is required for mono-orientation of kinetochores on sister chromosomes. It is also required to protect centromeric cohesin from Separase-mediated cleavage during MI, possibly acting as a regulator of the shugoshin-dependent protection pathway. These functions are mainly mediated by Polo-like kinase (PLK1) activity, which is enriched to kinetochores in a MEIKIN-dependent manner. Spermatocytes lacking MEIKIN result in a decrease of SGOL2 levels, leading to similar but milder defects in cohesion than in the *Sgol2* deficient mice (Kim et al., 2014; Ma et al., 2021).

2.3 Second meiotic division

REC8-containing cohesins keep physically joined the centromeres of the sister chromatids until the second meiotic division when they will be released by a second wave of Separase activation, resulting in the segregation of sister chromatids (Clift et al., 2018). So, at the metaphase-anaphase II transition, the chromosomes congress at the metaphase plate with each sister kinetochore oriented towards one pole.

It is unclear how the mechanism of protection of centromeric cohesion is modified/remove at MII to allow the cleavage of centromeric cohesion to enable the segregation of sister chromatids. Differents hypothesis have been proposed to shed light to this open issue. The most classical defends that the tension across the centromeres results in a redistribution of SGOL2 from the inner centromeres towards the kinetochores leaving the centromeric cohesins accessible to the cleavage of Separase in anaphase II, leading to the generation of haploid gametes (Gómez et al.,

2007; J. Lee et al., 2008). The second proposes that the histone chaperone I2PP2A/Set, a putative PP2A inhibitor, specifically counteracts Rec8 protection in MII in a tension-independent manner (Chambon et al., 2013). The third hypothesis proposes that yeast Sgo1 (similar to mammalian *Sgo2*) and Msp1 are degraded at the onset of anaphase II in an APC/C-dependent manner to ensure deprotection in budding yeast (Argüello-Miranda et al., 2017).

Recently, it has been hypothesized that kinetochores individualization, before entering MII, is the key event that allow the removal of centromeric cohesion and the proper separation of sister chromatids (Gryaznova et al., 2021). It has been proposed that Separase activity before entering in MII is required for kinetochore individualization, as the absence of separase in MI and its presence only in MII leads to the removal of cohesin from the arm and segregation of bivalents into dyads instead of sister chromatids (Gryaznova et al., 2021; Mengoli et al., 2021). Another recent study has proposed the existence of a third fraction of Rec8 in the centromere region that confers loss of sister kinetochore co-orientation and cohesin protection of the MII when cleaved by separase after MI (Ogushi et al., 2021).

On balance, meiosis is a very complex process and must be strictly regulated. Missegregation of chromosomes either in MI/II results in the generation aneuploidy or aberrant numbers of chromosomes which occur in at least 5% of all clinically diagnosed pregnancies (Hassold & Hunt, 2001). It is believed that women over 35 have higher possibilities of aneuploidy, which leads to miscarriage, birth abnormalities and infertility (Herbert et al., 2015).

3. Human infertility

The World Health Organization (WHO) defines infertility as a disease of the reproductive system caused by the failure to achieve a pregnancy after 12 months or more of regular unprotected sexual intercourse. If no pregnancy has ever happened, it is classified as primary infertility, whereas if there has been a conception it is known as secondary infertility. Infertility is a complex and heterogenous disorder, which can affect the male, female or both partners, affecting approximately 10-15% of the couples at reproductive age, with 25-30% of the cases classified as idiopathic (Jose-Miller et al., 2007; Mallepaly et al., 2017).

Female infertility can be caused by genetic, hormonal, or environmental factors in most cases affecting ovulation. In this regard, polycystic ovarian syndrome (PCOS) is a hormone imbalance condition that can interfere with regular ovulation and affects 7% of women at reproductive age (Zorrilla & Yatsenko, 2013). Less common causes of women infertility include pelvic inflammatory disease, endometriosis, uterine fibroids, or chemotherapy/radiation treatments (Venkatesh et al., 2014). In women, the interruption of the ovarian function occurs physiologically as a consequence of age, with the onset of menopause. However, primary ovarian insufficiency (POI) is characterized by a loss of normal ovarian function well before the natural age of menopause, and is one of the leading causes of infertility in young women. Clinically, POI is characterized by the loss of ovarian function under the age of 40 years with decrease in ovarian follicles, oligo/amenorrhoea for at least 4 months, and FSH levels as in menopausal range (>25IU/L) (Nelson, 2009). A recent meta-analysis estimated that 3.7% of women worldwide are affected by POI (Golezar et al., 2019), although 5-10% of these women are able to conceive after an early diagnosis with assisted reproductive techniques (Huang et al., 2022).

In men, infertility is caused mostly due to any condition that affects sperm quantity and/or quality such as impaired spermatogenesis, hypogonadism, testicular maldescent, structural abnormalities in the genital tract, infection, impotence, chronic illness, chemotherapy, or immunological disorders (Jose-Miller et al., 2007). Among the sperm quantity and/or quality-abnormalities, the most frequent ones are reduced sperm concentration (oligospermia), motility (asthenospermia), increased percentage of aberrant sperm (teratospermia), and total absence of spermatozoa in the ejaculate (azoospermia). Within this last group, we can distinguish between obstructive and non-obstructive azoospermia (OA and NOA, respectively). In OA, the sperm produced cannot be secreted due an obstruction in the seminal ducts and affects 1% of the male population, while in NOA spermatozoa are not produced due to a failure in spermatogenesis being the most frequent in comparison with OA (Lindsay & Vitrikas, 2015).

3.1 Genetics bases of female and male infertility

It is challenging to estimate the contribution of genetic factors to infertility although a considerable number of human infertilities have a genetic component. As mentioned before, while a considerable proportion of infertility cases are classified as idiopathic, genetic causes are likely to underlie about 50% of these cases (Shah et al., 2003). A variety of factors including i) chromosomal abnormalities, such as aneuploidy or structural defects, ii) monogenic disorders, iii) polygenic alterations, iv) epigenetic dysregulation, and v) phenotypes with multifactorial inheritance have been linked to human infertility. Many of these genetic factors have been assigned specifically in females or in males, whereas others affect both sexes (Zorrilla & Yatsenko, 2013).

The chromosomal aberration best documented of causing female infertility is the Turner syndrome (45, X0), which is characterized by hypergonadotropic hypogonadism in most patients, leading to amenorrhoea and thus infertility (Abir et al., 2001; Sybert & McCauley, 2004). During the last two decades, several genes have been discovered to cause female infertility, at least 107 genes have been implicated in the etiology of POI (França & Mendonca, 2022). The most frequent are mutations in X-linked genes including FMR1 (causing Fragile X syndrome) and BMP15 located at the Xp11.2 region (Di Pasquale et al., 2004; Pastore & Johnson, 2014). There are also autosomal gene mutations such as in FOXL2 (Harris et al., 2002), GDF9 (H. Zhao et al., 2007), FIGLA(H. Zhao et al., 2008) or NOBOX (Bouilly et al., 2011).

Genetic causes of spermatogenic impairment account for 10-15% of male infertility including chromosomal abnormalities and monogenic mutations (Ferlin et al., 2007). The most frequent sex chromosome aneuploidy in males correspond to the Klinefelter syndrome (47, XXY) which accounts for 0.1-0.2% of new-borns. Patients with this syndrome have defective spermatogenesis, having more than 90% of them have azoospermia (Krausz & Riera-Escamilla, 2018; Martin, 2008). Structural chromosomal alterations that include deletions, duplications, translocations or inversions also contribute to infertility. In this regard, microdeletions on the Y chromosome, that represent the 13% of cases of idiopathic NOA, affect the azoospermia factor (AZF) region Yq11, which contains genes essential for spermatogenesis (Reijo et al., 1995, 1996). Mutations in a single gene are also a frequent cause of male infertility. This is the case of alterations in cystic fibrosis transmembrane conductance regulator (*CFTR)* gene, an ion channel that when mutated causes the development of bilateral congenital aplasia of the vas deferens leading to OA (Grangeia et al., 2007; O'Flynn O'Brien et al., 2010).

In the last decade, recent advances in next-generation sequencing (NGS) technologies have shed light on several human disorders. Whole-exome sequencing (WES) of infertile families has made possible the identification of several genes with a direct causal relationship with this disease. In this regard, hundreds of candidates have been identified, the POI genes are listed in the **Supplementary Table 1.** Some examples of identified candidates are the meiotic genes SYCE1 (de Vries et al., 2014), STAG3 (Caburet et al., 2014; Llano et al., 2014), SPO11 (Tran & Schimenti, 2019), MSH4 (Carlosama et al., 2017), MSH5 (Guo et al., 2017), DMC1 (He et al., 2018), BRCA2 (Caburet et al., 2020), MEIOB (Caburet et al., 2019; Y. Wu et al., 2021), SPATA22 (Y. Wu et al., 2021; C. Yao et al., 2022) and HSF2BP (Felipe-Medina et al., 2020). In very near future, it is expected that this technology allows the identification of all the variants in an individual genome enabling personalized medicine for each patient.

4. Genome instability

Cell division involves several mechanisms that must be finely regulated in order to preserve the genome integrity and ensure its faithful propagation to offspring. Efficient regulation of DNA replication, DNA damage detection and repair, and regulation of the cell cycle progression ensures genome maintenance during cell divisions (Aguilera & Gómez-González, 2008).

Genome instability (GIN) refers to a range of genetic alterations ranging from nucleotides mutations to chromosome rearrangements. There are two types of elements that play a fundamental role in GIN, those that act in *trans* to prevent instability such as DNA replication, DNA repair, and S-phase checkpoint factors, and chromosome sites that act in *cis* as hotspots of instability including fragile sites, and highly transcribed regions (Aguilera & Gómez-González, 2008). GIN is usually associated with pathological disorders such as premature ageing, tumorigenesis, neurodegenerative diseases, immunodeficiencies, miscarriage and infertility (Aguilera & García-Muse, 2013). However, GIN also happens during development under physiological conditions such as in in immunoglobulin gene diversification in T and B cells (Maizels, 2005) and during DSBs repair in meiotic recombination which is essential for independent assortment of chromosomes (random segregation of chromosomes at meiosis) and of genes (exchange of genetic material between parental genomes).

Considering the type of instability generated, GIN can be divided into different classes:

I) **Mutations** (point mutations, microinsertions and microdeletions) which can be caused by endogenous/exogenous mutagens associated with replication errors, impaired base excision repair (BER) and impaired mismatch repair (MMR) or failure in translesion synthesis (TLS) (Aguilera & García-Muse, 2013).
II) **Micro and minisatellite** (MIN) that results in expansions and contractions of repetitive DNA which can be caused by replication slippage, impaired MMR or HR (Cherri et al., 2022).
III) **Chromosomal instability** (CIN) which refers to changes in the chromosome number leading to a chromosome gain or loss. It usually occurs through several mechanisms including dysregulation of genes that govern mitosis (cyclins and cyclin-dependent kinases), aberrant centrosome duplication, defects in microtubule attachments to chromosomes, pre-mitotic replication stress, and DNA damage (Bakhoum & Landau, 2017; Neuse et al., 2020).
IV) **Chromosomal rearrangements**, which involve a fusion of two or more chromosomal segments that are not normally attached. These events can result from recombination of

misaligned sequences, unequal sister chromatid exchange (SCE), ectopic HR between non-allelic repeat fragments, an increase in end-joining between non-homologous DNA fragments or in presence of multiple DSBs where incorrect end ligation can occur leading to deletions, duplications, inversions, and translocations (Tsai & Lieber, 2010).

All these genetic alterations can be initiated as a result of failures in different steps of the DNA cycle, from replication to segregation. In this sense, the most common causes of GIN are failures in DNA replication and repair.

4.1 DNA damage response

Cells are constantly suffering genotoxic stress produced by exogenous or endogenous agents that affect the integrity for our genetic material as blocking DNA replication, altering transcription, and if they are not repaired or incorrectly repaired, they lead to mutations or wide-scale genome aberrations (Campos & Clemente-Blanco, 2020). In order to detect, signal, and promote the repair genetic damage, cells have evolved a complex network of DNA-damage response (DDR) mechanisms (Giglia-Mari et al., 2011). The complexity of genome maintenance underscores the relevance of preserving genome integrity.

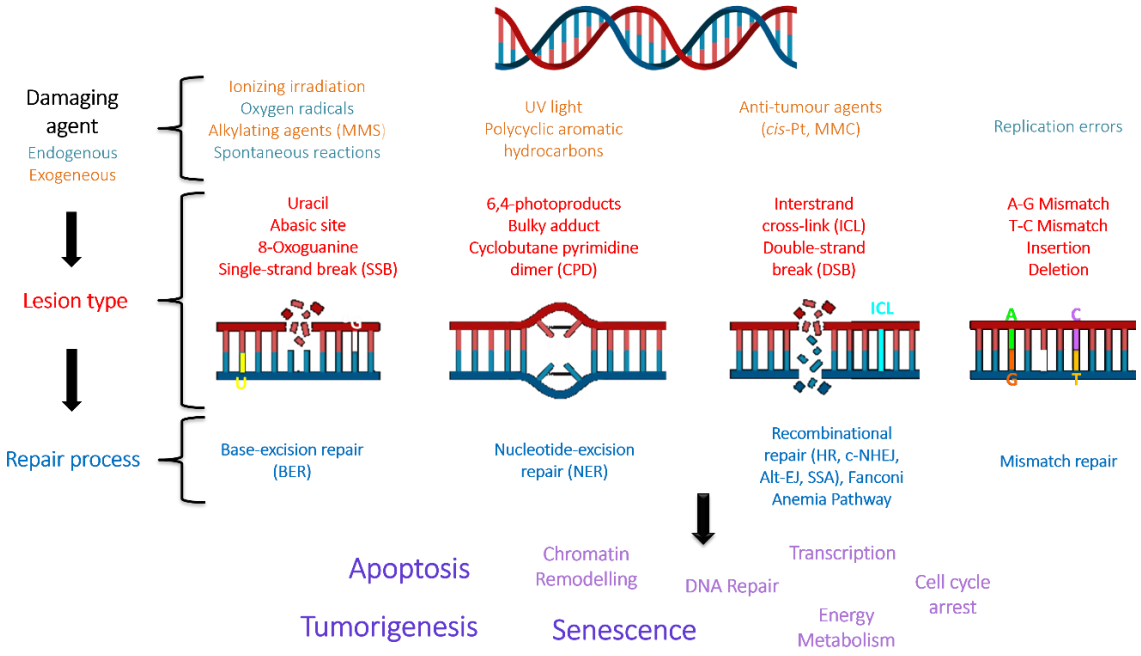

Figure VII. The DDR pathway. Schematic representation of the responses upon DNA damage. Endogenous or exogenous DNA damage agents provoke a wide variety alterations in DNA, depending on the specific lesion type cell evolve specific mechanism of repair inducing different cell response.

DDR pathway can be activated by a wide variety of physical and chemical damaging agents which involve specific lesions and activate different repair processes (**Figure VII**). To ensure proper repair, DNA can be restored by several mechanism such as: base excision (BER) repair that reverses oxidative base modifications, nucleotide excision (NER) repair that removes DNA-distorting lesions, the Fanconi anemia (FA) pathway responsible for the repair DNA interstrand crosslinks (ICLs), non-homologous end joining (NHEJ) repair and HR both of which remove DSBs, and the mismatch repair (MMR) that reestablish errors that occurred during DNA replication (Caldecott, 2008; D'Andrea & Grompe, 2003; Hoeijmakers, 2009; Jiricny, 2006; Lindahl & Barnes, 2000; West, 2003).

4.1.1 Double-strand break repair

DSBs are one of the most toxic forms of DNA damage, which, if left unrepaired, leads to cell death. Cells repair DSBs through two main mechanisms: **NHEJ and HR**.

NHEJ is a fast end joining process that brings together two broken ends without requiring extensive resection, thus providing the means to rapidly repair DNA breaks. During NHEJ, DSBs are recognized by the Ku protein, which binds and activates the DNA-PKcs protein kinase, leading to the recruitment and activation of end-processing enzymes, polymerases, and DNA ligase IV. Even though NHEJ is error-prone, this mechanism can operate at any stage of the cell cycle (Chang et al., 2017; Lieber, 2008). By contrast, **HR** requires the presence of an intact homologous DNA template, thus it is mainly only active in S/G2 phase when the sister chromatid is present (Jasin & Rothstein, 2013), being the centromeric heterochromatin repair at G1 by HR the only known exception (Yilmaz et al., 2021). Similar to meiotic recombination, during HR, the MRN complex is recruited to the DSBs and promote DNA resection together with CtIP, EXO1, DNA2, BLM and WRN (Sartori et al., 2007). This complex generates the 3' ssDNA ends, essential for homology searching and strand invasion. The ssDNA is rapidly coated by RPA, which also stimulates resection and prevent ssDNA degradation (Chen et al., 2013). RPA-coated DNA is required for the binding of RAD51, which is loaded into the DNA by BRCA2. RAD51 nucleofilaments starts the homology search and strand invasion, this process is also regulated by the RAD51 paralogues (M. Takata et al., 2000). RAD51 nucleofilaments displace one strand of the sister chromatid to form the D-loop. Then the polymerases copy the missing information from the homologous sister chromatid in order to restore nucleotides at the break site (Krejci et al., 2012). Once DNA synthesis is initiated, there are mainly two routes that can take place allowing proper chromosome segregation. In the first one, the second end of the DSB can be engaged to stabilize the D-loop structure (second-end capture), resulting in the generation of a dHJ. Resolution of dHJ can occur either to generate CO or NCO products. In the second route, the extended nascent strand is displaced, followed by pairing with the other 3' ssDNA tail, and DNA synthesis completes repair, generating a NCO product (Krejci et al., 2012; San Filippo et al., 2008).

Furthermore, HR is also required for the restart of broken replication forks and, in the absence of post-replicative repair, as an alternative pathway to avoid lesions that block DNA synthesis (Heyer et al., 2010), as well as to repair DNA ICLs, in which the FA pathway is deeply involved (Godin et al., 2016).

4.1.2 Repair of interstrand crosslinks: Fanconi Anemia Pathway

ICLs are extremely toxic DNA lesions that prevent DNA unwinding properly leading to replication and transcription failure. ICLs are induced from chemical compounds like cis-platin, mitomycin C (MMC) (Paz et al., 2004) and alkylating agents. However, potential sources of ICLs can also become from lipid peroxidation subproducts such as acrolein and β-unsaturated aldehydes, whose concentrations may increase with a high-fat diet or alcoholism (Balbo & Brooks, 2015; Folmer et al., 2003; Stonez et al., 2008).

The cell has evolved the FA pathway to deal with ICLs. The main function of this pathways is the coordination of DNA repair in order to remove crosslinks. ICLs are recognized by the **FA core complex** composed by FANCA, FANCB, FANCC, FANCE, FANCF, FANCG (XRCC9), FANCL, FAAP100 and the FANCM ubiquitin ligase protein (Peake & Noguchi, 2022). The FA core complex then monoubiquitinates two DNA-associated proteins, FANCI and FANCD2, leading to their retention

in the chromatin (**Figure VIII**). This ubiquitination is essential for the activation of the FA pathway, in the absence of one of the components of the FA core complex ubiquitination does not occur (Matsushita et al., 2005). This activation recruits BRCA1 (FANCS) which, together with BARD1, exhibit the ubiquitin ligase activity required for proper RAD51 localization (Bhattacharyya et al., 2000; Wu-Baer et al., 2003). BRCA2 (FANCD1) also belongs to the FA pathway promoting the specific targeting of RAD51 to sites where recombination is initiated (Thorslund et al., 2010) and proceed to the DNA repair as explained in the *section 4.1.1*. Once repaired by HR, the dHJ is dissolved by the BTR complex, composed by BLM, TOPOIIIα, RMI1 and, RMI2, in a way that this complex prevents SCEs (L. Wu & Hickson, 2003). In this regard, the BTR complex associates with the FA core complex, providing a direct link between signalling of ICL damage recognition and resolution of HR products (Meetei et al., 2003).

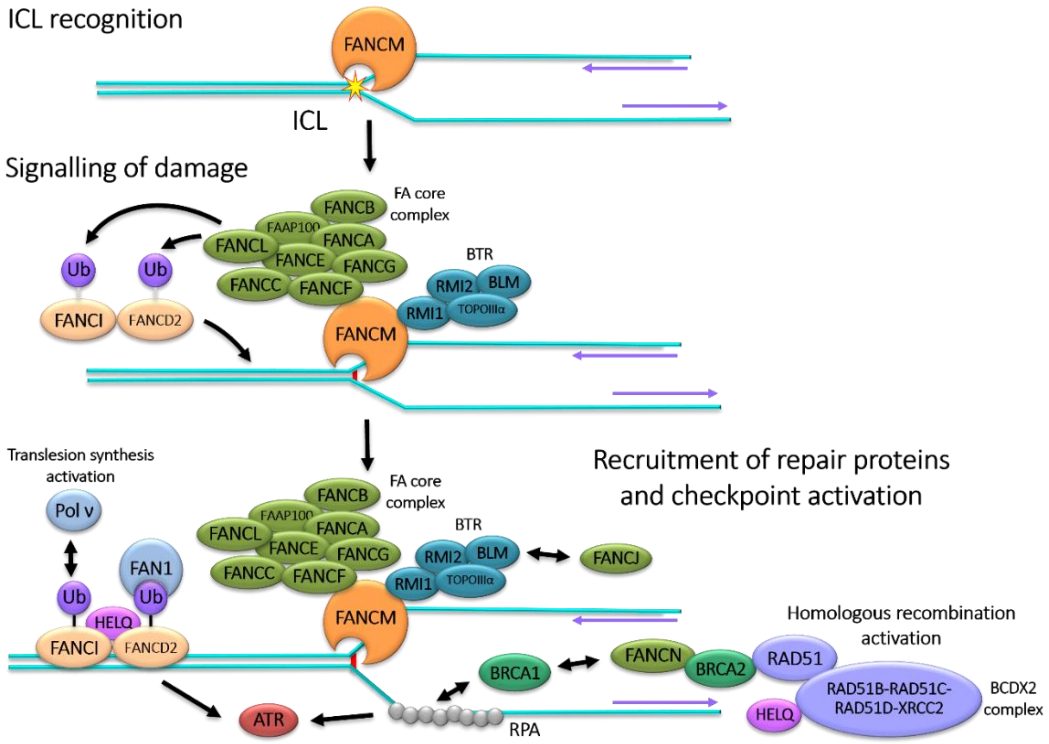

Figure VIII. Activation of the FA pathway. ICL recognition by FANCM and associated proteins, afterwards the FA core complex monoubiquitinates FANCI and FANCD2 stating the signalizing pathway. This signalling of damage recruits nucleases and polymerases for the repair process. Modified from Deans & West, 2011.

The incapacity to repair ICLs leads to replication fork collapse, especially in actively dividing cells, such as the hematopoietic system. Consequently, individuals with alterations in this pathway suffer, as the name indicated, from FA which is characterized by hypersensitivity to ICL-inducing agents (used for diagnosis), chromosomal aberrations in the bone marrow and infertility as well as predisposition to hematopoietic and non-hematopoietic cancers (L. C. Wang & Gautier, 2010).

Therefore, the FANC genes are essential in the repair of ICLs and thus, in the maintenance of the genome stability. Currently, 22 FA genes have been identified, including RAD51 (FANCR), RAD51C (FANCO) and XRCC2 (FANCU) (Nalepa & Clapp, 2018; Peake & Noguchi, 2022). Mutations in both alleles of RAD51, RAD51C or XRCC2 result in FA or an FA-like syndrome (Shamseldin et al., 2012; Vaz et al., 2010).

4.1.3 RAD51 paralogues

RAD51 is a DNA-dependent ATPase that binds to single-stranded DNA and promotes strand invasion and exchange between homologous DNA molecules. The *Rad51* gene is an ortholog of the well-studied *Escherichia coli* recombinase RecA. In vertebrates, there are seven different RAD51 paralogues: RAD51, RAD51B, RAD51C, RAD51D, DMC1, XRCC2 and XRCC3 which emerged from ancient RAD51 gene duplications. The RAD51 paralogues play a relevant role in homologous recombination and in maintaining chromosomal integrity in mitotic and meiotic cells. Defects in RAD51 paralogues genes are associated with tumorigenesis and diseases such as FA (Sullivan & Bernstein, 2018).

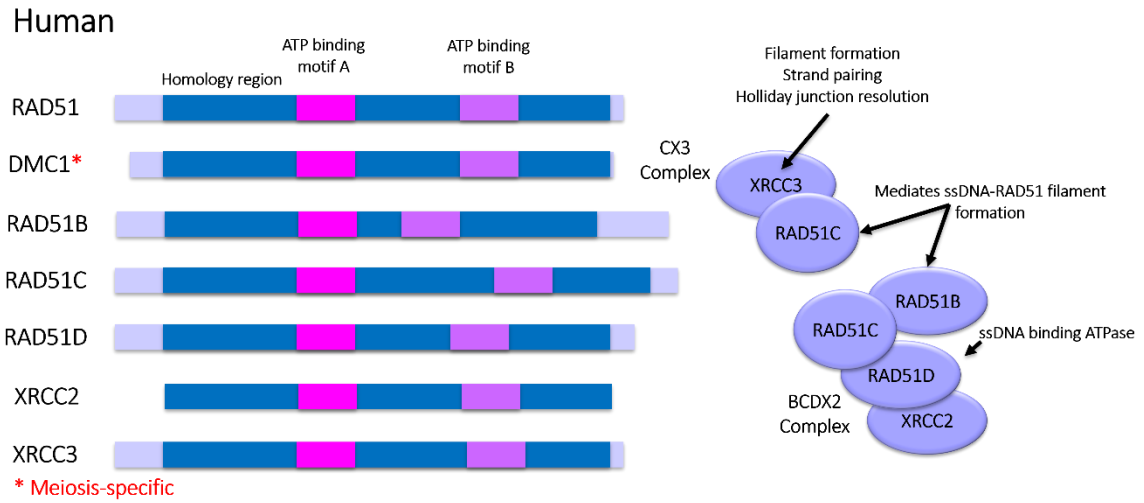

Figure IX. Human RAD51 family of paralogues. Schematic representation of domain structures of representative RAD51 paralogues, drawn to scale. Domain names are indicated in the figure containing the ATP binding motif A and B (also called Walker motif A and B). Protein complex CX3 (RAD51C and XRCC3) and BCDX2 (RAD51B, RAD51C, RAD51D, XRCC2) are represented with their described functions.

The RecA/RAD51 superfamily of recombinases are present almost in all domains of life which originated from an ancient common ancestor that predates the emerge of Archaea and Eukarya.

RAD51 paralogues are proposed to form two biochemically and functionally distinct complexes, the RAD51B-RAD51C-RAD51D-XRCC2 complex (BCDX2) and the RAD51C-XRCC3 complex (CX3) (**Figure IX**) (Bonilla et al., 2020). These paralogues play essential roles in preserving genomic integrity during development, as well as during physiological cell proliferation. In addition to these paralogues, another member of this family, *Dmc1*, shows 50% sequence identity to *Rad51* and functions exclusively in meiotic recombination. The conserved RAD51 paralogues assist RAD51's function in DSB repair, meiosis, and DNA replication (Godin et al., 2016). However, the mechanism underlying how they promote and contribute to HR remain unclear (Bonilla et al., 2020). The functional study of the RAD51 paralogues has been difficult because they tend to form insoluble aggregates *in vitro*, beside their low cellular abundance, and because the fact that knock-out (KO) mutants show embryonic lethality in mice (B. Deans et al., 2000; S. Kuznetsov et al., 2007; Pittman et al., 1998; Prakash et al., 2021; Shu et al., 1999). This lethality indicated that each of the paralogues are essential and non-redundant during development. RAD51 paralogues have been shown to also play a role in replication fork homeostasis. The CX3 complex mediate the efficient restart of reversed forks and has additional functions such as in mitochondrial DNA replication and genomic maintenance (Mishra et al., 2018) as well as in ICL DNA repair (Sasaki et

al., 2004). The BCDX2 complex limits the fork speed upon DNA damage and mediates stalled fork degradation in BRCA2-deficient cells assisting RAD51 functions (Berti et al., 2020).

It has been shown that the disruption of each RAD51 paralog in U2OS and HEK293 cells leads to a reduction in RAD51 foci, cell growth defects, DNA damage sensitivity and impaired HR (Garcin et al., 2019). These observations were similar to those made with mutant RAD51 paralogues in chicken B-lymphocyte DT40 cell line. All mutant cell lines exhibit similar phenotypes such as spontaneous chromosomal aberrations, high sensitivity to crosslinking agents, mild gamma sensitivity and partial correction of DNA damage resistance by overexpression of RAD51 (M. Takata et al., 2000, 2001). Overall, these observations suggest that the paralogues are also required as mediators for the formation of active RAD51 nucleofilaments. Despite their overlapped functions, each RAD51 paralogue mutant gives rise to a distinct phenotype, suggesting they have a unique and specific functions. Indeed, RAD51D has been shown to play a dual cellular function in both DSB repair and telomere protection (Tarsounas et al., 2004). RAD51C and XRCC3 have been shown to play a role in meiotic recombination and Holliday junction (HJ) resolution by playing an essential function in the resolution of recombination intermediates prior to chromosome segregation (Liu et al., 2007).

5.Conserved non-genic sequences

The genomes of large multicellular eukaryotes are mostly comprised of non-protein coding DNA sequences (98-99%). However, although some non-coding DNA sequences are known to serve relevant roles, such as in the regulation of gene expression, the functional importance of most of these regions is largely unknown.

The genome sequencing of multitude of species has allowed, through their genome alignment and comparison, the identification of regions preferably intolerant to genetic variation. Several highly conserved sequences have been identified not only in the protein-coding sequences, but also in the non-coding fraction of the genome. In this regard, the overall similarity between human and mouse genomes was estimated to be 66.7% (Waterston et al., 2002). It has been estimated from the mouse genome sequence publications: “the proportion of small (50-100 bp) segments in the mammalian genome that is under (purifying) selection can be estimated to be ∼5%” that is referred to ancestral repeats that are under an evolutionary pressure to remove deleterious sequence variants from the population. Only a small part of this sequence is due to protein coding regions (1.5%), indicating that the genome contains large fraction of functional conserved non-coding regions that are under selection and whose biological function remains unknown (Waterston et al., 2002).

One of the first chromosome-wide analysis was carried out focusing on chromosome 21, in which 2262 conserved non-genic sequences (CNGs) were found. These CNGs consisted in sequences of more than 100bp with more than 70% of identical sequences between human and mouse chromosome 21. In this study they further analysed 220 CNGs without evidence of transcriptional potential and found that CNGs are more conserved than protein-coding sequences and non-coding RNA (Dermitzakis et al., 2005). In fact, a similarity of about 80% in protein-coding genomic sequences is enough to maintain 100% of the aminoacid sequence identity due to the degeneracy of the genetic code. Therefore, to have a high percentage of homology in any two sequences, there must be some underlying mechanism different to the

mechanism that maintain the protein function. The existence of these sequences with high levels of conservation in the genome indicate that CNGs might be essential for genome function.

5.1 Ultraconserved elements

Ultraconserved elements (UCEs) are highly conserved regions of organismal genomes shared among evolutionary distant taxa. UCEs were identified using a more stringent condition on these CNGs. This screening consisting in searching sequences >200 bp in length with 100% identity in human, mouse, and rat whole genomes. From this selection, 481 UCEs were found, most of them also conserved in many vertebrate species. For example, 477, 467 and 324 UCEs exhibited averages of 99.2, 95.7 and 76.8% identities in dog, chicken, and fugu fish genomes, respectively. These 481 UCEs were classified according to their genomic neighbourhood. From this classification, 111 and 256 UCEs were found in exons and in no-coding regions, respectively. The remaining 114 were unknown in terms of this classification. The no-coding UCEs were further classified into 100 intronic UCEs and 156 intergenic UCEs (Bejerano et al., 2004).

5.1.1 Potential functional roles of UCEs

There is barely information about the functions of UCEs, and so far, only experimental efforts have been made to identify them. The heterogeneity of UCEs' features and the recent experimental approaches have determined that a fraction of the UCEs act functionally as *cis*-transcriptional regulators such as enhancers or silencers. It has also been postulated that UCEs may play a structural role (Dermitzakis et al., 2005) and that up to 10% of UCEs might be matrix-binding regions. These regions might regulate chromatin conformation through specific binding of certain proteins (Glazko et al., 2003).

Further analysis of UCEs suggested that exonic UCEs (which can be translated or not) are enriched in genes associated with RNA processing, including regulation of RNA splicing (Bejerano et al., 2004). It is presumed that the ultraconserved elements in 5' untranslated regions (UTRs) of coding genes could regulate the cell type-specific translation of the resulting protein (Byeon et al., 2021). In addition, some ultraconserved exons are alternatively spliced as poison exons resulting in messenger RNAs degradation. These ultraconserved poison exons are proposed to be crucial for the growth of cultured cells, and some of them exhibit tumour suppressor activity (J. D. Thomas et al., 2020). In regard to non-exonic UCEs, these are often clustered and enriched in the neighbourhood of developmental transcription factors, suggesting a role in regulating the expression of specific genes during development (**Figure X).**

It has also been postulated that these conserved elements might be involved in interchromosomal interactions that are mediated by protein bridges and bring together chromosomes in the nucleus. Chromosomes have been shown to occupy a tissue-specific position in the nucleus (Dermitzakis et al., 2005). This nuclear organization could be relevant for specific functional interactions between chromosomes that are mediated by protein interactions that could involve UCEs (Croft et al., 1999; Tanabe et al., 2002). If such interchromosomal interactions occur, it is possible that UCEs may also be functioning as regulatory regions in *trans* to the gene they regulate, similar to transvection in *Drosophila melanogaster*, a phenomenon where homologous chromosomes synapse in somatic cells (Müller & Schaffner, 1990). Therefore, it has been proposed that UCEs might also play a similar role in meiotic recombination (Bishop et al., 2000).

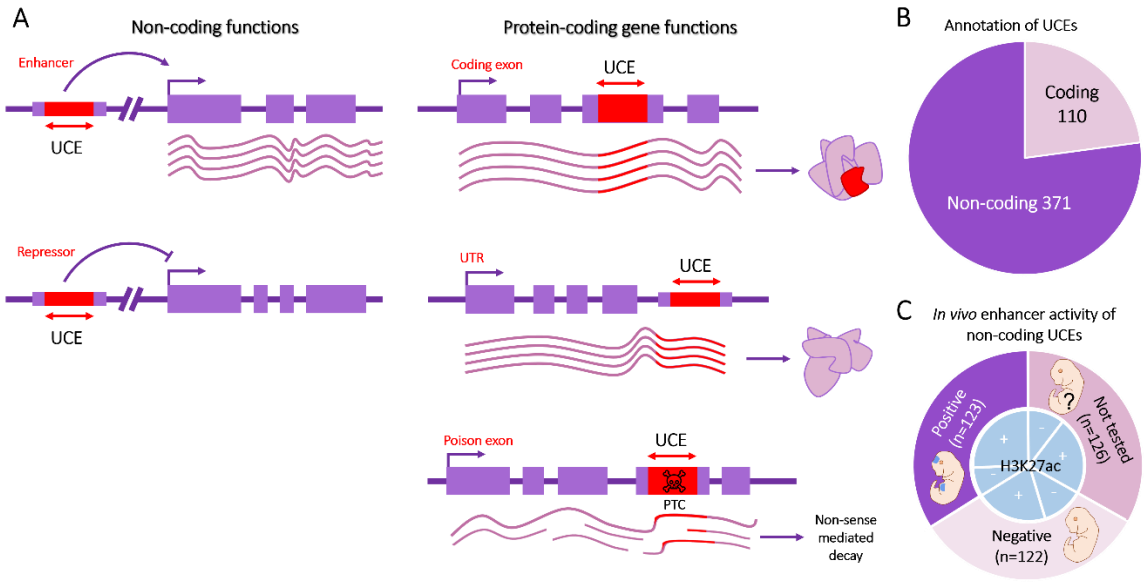

Fig X. Functions attributed to UCEs. A) UCEs could be classified by its functions, in non-coding regions or in exonic regions. **B)** Pie chart showing the functional classification of UCEs using current human RefSeq genome annotations. "Coding" includes all types of exons for protein-coding genes and UTRs. **C)** *In vivo* enhancer activity for the 371 non-coding sequences. Outer circle: transgenic mouse enhancer assay results for each element (positive, negative, or not tested). These results were obtained from the VISTA Enhancer Browser (https://enhancer.lbl.gov/). Inner circle: fraction of UCEs in each category with (+) or without (-) histone H3 acetylated at lysine 27 (H3K27ac), a strong predictor of enhancer activity. Modified from (Snetkova et al., 2022).

Mice transgenic assays have been widely used to characterize enhancer functions in non-coding UCEs. The methodology involved the cloning of a candidate regulatory elements of interest in front of a minimal promoter (*Hsp68* or *β-globin*) and a reporter gene (*lacZ* or *GFP*). The resulting linearized DNA plasmid is microinjected into the pronucleus of fertilized eggs where it will randomly integrate into the genome. With this method, the expression of the gene reporter, which is an indicator of the activity of the candidate enhancer, can be visualized by staining (Kvon et al., 2020; Pennacchio et al., 2006). From these assays, 123 out of 254 non-coding UCEs were reproducibly positive for enhancer activity, with the 50% of them in neural tissues. However, these assays are made at a single developmental time point (E11.5), so those negative for enhancer activity could be active at a different stage of development. Indeed, 58% of those "negative" sites are marked by histone H3 acetylated at lysine 27 (H3K27ac) which is a strong predictor of enhancer activity (Snetkova et al., 2022). By using these reporter constructs some functional studies suggest that UCEs are likely to be regulatory regions of gene expression (Boffelli et al., 2003; Frazer et al., 2004; Nobrega et al., 2003), but the full functionality of UCEs has yet to be revealed.

OBJECTIVES

OBJETIVES

Mammalian gametogenesis is a biological process involving tightly regulated processes by which diploid cells undergo cell division and differentiation to form haploid gametes. Finding out the causes of human infertility is of great importance given that a high fraction of its diagnoses is idiopathic with a yet unknown genetic basis. Due to the complexity of studying gametogenesis in humans, the best approach to deepen in this specialized cell division process is to use the mouse as an experimental model.

For this purpose, we decided to functionally analyze and characterize a family with hereditary POI and two mammalian ultraconserved elements potentially involved in gametogenesis using the mouse as a model. This approach not only enables the establishment of direct causal relationship between the gene variant/elements and gametogenesis, but it also to gain further mechanistic insights into their functions.

The specific objectives of this thesis were the following:

1. Identification of the underlying genetic cause of primary ovarian insufficiency in a consanguineous family.

    A. Functional characterization and validation of the *c.92delT* variant in RAD51B as the cause of familial infertility using the mouse as a model.

    B. Dissection of molecular mechanism of action of RAD51B-c.92delT.

2. Functional analysis of two ultraconserved elements, HS205 and HS1442, in mouse gametogenesis and its relationship to male infertility.

METHODS & MATERIAL

1. Case report

Written informed consent were obtained from all subjects before sample collection for DNA analysis. This study was approved by the Ethics Committee of Hospital das Clínicas, Sao Paulo University School of Medicine, Brazil (protocol number 2015/12837/1.015.223). The patient (II-1) and her younger sister (II-4) were born from first-degree cousins (**Figure 1A**). On examination at 23 and 21 years of age respectively, they were diagnosed with POI presenting with primary amenorrhea. These siblings had no menarche and physical examination revealed Tanner stage I for breast development (II-1 and II-4) and Tanner stage IV pubic hair. Consistent with the diagnosis of hypergonadotropic hypogonadism, basal gonadotropin levels were elevated in the proband and her affected sister (FSH = 44 and 31 $U \cdot L^{-1}$, LH = 21 and 17 $U \cdot L^{-1}$, respectively) while estradiol levels were undetectable. At first appointments, physical examination showed normal height (149 and 156 cm respectively), and body weight (60 and 47 Kg, respectively). Pelvic ultrasound scans showed infantile uterus, and the ovaries could not be visualized. Thyroid, adrenal or ovarian autoimmune disorders had been excluded in these patients. On karyotyping analysis performed in 30 metaphases, both sisters were 46,XX. Treatment with conjugated estrogens followed by progesterone replacement resulted in complete breast development and menstrual bleeding. However, these affected patients developed hypertension, insulin resistance, primary hypothyroidism with absence of thyroid antibodies, and obesity over the years, being current BMI = 41 and 34 $Kg \cdot m^{-2}$, respectively. During the course of this investigation, the affected sister (II-1) was also diagnosed with a duodenal tubulovillous adenoma with high-grade dysplasia and underwent surgery. Thereafter, she was found to have an indeterminate hepatic nodules and hepatic steatosis. She has been followed and no additional radiotherapy or chemotherapy has been done and has not been diagnosed with any neoplasia.

1.1 Genetic Analysis

DNA extraction: Genomic DNA was extracted from peripheral blood leukocytes from all patients using standard procedures (S. A. Miller et al., 1988). *Whole-exome sequencing:* Libraries were prepared on both sisters (II-1 and II-4) and her unaffected sister (II-2). Briefly, genomic DNA was sheared to 200-300 bp using the Covaris acoustic adaptor. Exons were captured using Sure Select Human All exons kit (Agilent Technologies) and sequenced by Illumina platform (HiSeq2500, Illumina). Alignment of raw data and variant calling were performed following the steps described by Franca and collaborators (França et al., 2017). Briefly, the reads were aligned to the human reference genome GRCh37/hg19 using Burrows-Wheeler aligner (H. Li & Durbin, 2010). Variant calling was performed with Freebeys and annotated ANNOVAR (Garrison & Marth, 2012). SNVs were run through independent protein pathogenicity predictors: Polyphen-2, SIFT, Mutation Taster, Mutation Assessor, FATHMM, Radial SVN, and LRT. Sanger sequencing: Sanger sequencing was done to validate only the primary variant of interest in all subjects. Primers flanking the RAD51B variant (ENSG00000182185/NM_133509: exon3:c.92delT:p.Leu31Tyrfs*9) were used for PCR amplification. Sanger sequencing was performed to validate only the primary variant of interest in all family subjects for whom DNA was available. Primers flanking the RAD51B variant (ENSG00000182185/NM_133509:exon3:c.92delT:p.Leu31Tyrfs*9) were used for PCR amplification. Moreover, Sanger sequencing was used to screen 235 fertile Brazilian control women for the presence of the putative damaging variant. All PCR products were sequencing using BigDye terminator v1.1 followed by automated sequencing at the ABI PRISM 310 (Applied Biosystems, Foster City, CA).

2. Mouse models

2.1 Animal welfare

Mice were housed in a temperature-controlled facility (specific pathogen free, spf) using individually ventilated cages, standard diet and a 12h light-dark cycle, according to European Union regulations at the *"Servicio de Experimentación Animal, SEA"*. Mouse protocols were approved by the Ethics Committee for Animal Experimentation of the University of Salamanca (USAL). We made every effort to minimize suffering and to improve animal welfare. Blinded experiments were applied when possible. No randomization methods were applied since the animals were not divided in groups/treatments. The minimum size used for each analysis was at least two animals/genotype. The mice analyzed were between 2 and 4 months of age, except in those experiments where is indicated.

2.2 CRISPR/Cas9 genome editing

CRISPR/Cas9 technology has emerged as a powerful alternative to classical methods of generating genetically modified mice such as gene targeting. This genome editing technology has two main components: on the one hand, an endonuclease (Cas9), responsible for generating targeted DNA breaks. The other component is the guide RNAs (guide or sgRNAs) responsible for directing Cas9 specifically to its target in the genome. Once generated, these breaks can be repaired by non-homologous end joining (NHEJ). This is a highly error-prone mechanism that can generate non-specific insertions or deletions that give rise to mutant alleles. Alternatively, if we add a repair template to the system, we can generate very specific insertions, deletions or point mutations. This template usually consists of a single-stranded donor DNA (single-stranded donor oligonucleotide-ssODN) containing the mutations to be introduced flanked by homology arms adjacent to the target site to favour repair by homologous recombination, a high-fidelity repair mechanism (H. Yang et al., 2014).

2.2.1 Design of sgRNAs

The sgRNAs or RNAs guide are made of two components, both of which are essential: the CRISPR RNAs (crRNAs) and trans-activating crRNAs (tracrRNAs). The crRNAs are responsible for the specificity and the tracrRNAs participate in the processing of the crRNAs by acting as a scaffold for the binding of both RNAs to the Cas9 protein and this complex to the DNA to produce the targeted excision (H. Wang et al., 2016). Therefore, the designed part in each model will be the crRNA while the sequence of the tracrRNA will always be the same. From the first description of the CRISPR/Cas9 system as a molecular biology tool (Jinek et al., 2012) to the present day, the system has undergone a great evolution, with the appearance of different design tools that have improved the existing ones.

In this sense, for the design of our crRNAs, we have used two tools:

- The crispr.mit.edu server developed by the Zhang Lab (Massachusetts Institute of Technology, MIT).
- IDT server (https://eu.idtdna.com/site/order/designtool/index/CRISPR_CUSTOM).

The crRNAs used for the different models are grouped in **Table 1**.

Mouse model	crRNAs	Sequence (5'-3')	Target region
Rad51b$^{KI/KI}$	sgRNA1	CTAGAACTTATGAAAGTGAC	Exon 3
	sgRNA2	GAGACTTAAAAAGTGCTAAA	
hs205$^{-/-}$	sgRNA5	AACACATAGTCTAAGTGCTC	Intergenic
	sgRNA6	CGTTCAGAATGTTGCCATTT	
Hs1442$^{-/-}$	sgRNA7	GAAACGGCACTGCCCCAGTG	Intragenic
	sgRNA8	ACCATACTGGTGTCGATGTC	

Table 1. crRNAs used for mouse genome editing through CRISPR/Cas9.

2.2.2 Obtention of sgRNAs, Cas9 and ssODNs

In our laboratory, sgRNAs were initially produced by annealing complementary oligonucleotides coding for crRNAs. These annealed oligonucleotides were then cloned into the vector pX330 (#42230; Addgene) digested with the enzyme BbsI. This vector carries the tracrRNA sequence after the BbsI site. From this vector PCR products, containing the T7 promoter region followed by the cr and the tracrRNA, were amplified. The primers used are:

- T7-sgRNA-S: TAATACGACGACTCACTATAGGNNNNNNNNNNNNNNNNNNN where the underlined area corresponds to the T7 promoter (common to all the designs) and the N's the sequence corresponding to each crRNA.
- T7-sgRNA-AS: AAAAGCACCGACTCGGTGCC.

These products were purified on column (NZYGelpure, MB011, NZYtech) and *in vitro* transcribed using the MEGAshortscript™ T7 Transcription Kit (AM1354, Invitrogen). To obtain the Cas9 mRNA, the plasmid pST1374-NLS-flag-linker-Cas9 (#44758, Addgene), linearised with AgeI, was used. *In vitro* transcription and capping were carried out using the mMESSAGE mMACHINE T7 Transcription Kit (AM1345, Invitrogen). The products were purified using the RNeasy Mini Kit (74106, Qiagen). The ssODNs used were produced by chemical synthesis by IDT.

Since 2017, all components of the CRISPR/Cas9 system (crRNAs, tracrRNAs, ssODNs and the Cas9 protein) are manufactured by chemical synthesis by IDT. In this case the crRNA and tracrRNA are synthesised separately and must be complementary annealed before use. For this purpose, equimolar amounts of both molecules are boiled for 5 min at 95°C and then ramped down to RT.

The ssODNs used for the different models are listed below in Table 2.

Mouse model	ssODN sequence (5'-3')
Rad51b$^{KI/KI}$	TAATTATTATATCTTTGCTACACATGCATGTTAAACTATTTTTCTTTACTTTTTTTTTCCT TTTAGCACTTTTATGTCTCTCCCCACTGGAGCTTATGAAGGTGACTGGCCTGAGTTAC AGAGGTGTCCACGAGCTTCTTCATACAGTAAGCAAGGCCTGTGCCCCGCAGATGCAA ACGGTTCGTGT
hs205$^{-/-}$	CAAATGAAGGAAAGAAAGAGTCACTCTATGGCCTGCTCAATAACCTCGAGGTTTTGA GCCATTGACCTGATTAGGCTGCTGAGGTCAACCTTTCCTTAGGTCAGCATGGAGGGC CCAGTGACCCCCAGATGGAAGTCCAT
hs1442$^{-/-}$	GAAAGCTATTTTCAGTTATTTCCTTTCCTTTCACAGTTAGAAGCACGAGAGCTTGGCA GTGGATGGCCCTTCTGGCCATTGTAACCTTTCTGACTGGAGTGTTTAGAAGGCTACTC CATTAATGGTTTCTAGTCTGTCTG

Table 2. ssODNs used as template for mouse genome editing through CRISPR/Cas9.

2.2.3 CRISPR/Cas9 system microinjection into mice zygotes

For microinjection, a mixture of different components was prepared in the following concentrations:

- Microinjection of RNAs from *in vitro* transcription: 50-100 ng/µL of Cas9, 30 ng/µL of each sgRNA (cr + tracrRNA synthesised as a single molecule) and 30 ng/µL of ssODN when required.
- Microinjection of synthetic RNAs and protein: 30 ng/µL of recombinant Cas9, 20 ng/µL of each annealed sgRNA and 10 ng/µL of ssODN when required.

This mixture was microinjected into B6/CBA F2 zygotes (hybrids between C57BL/6J and CBA/J strains) as previously described (Singh et al., 2015). This procedure was carried out by the Transgenic Facility of the University of Salamanca.

2.2.4 Characterisation of the founders and mice lines establishment

Edited founders were identified by PCR amplification (Taq polymerase, NZYtech) with primers flanking the edited region (**Table 3**). PCR products were sequenced directly or subcloned into pBlueScript (Stratagene) followed by Sanger sequencing. Selected founders, carrying the desired alleles, were crossed with wild-type C57BL/6J to eliminate possible unwanted off-targets. Heterozygous mice were re-sequenced and crossed to generate the edited homozygotes. Genotyping was performed by agarose gels analysis or Sanger sequencing (in *Rad51b* humanized mutant) of PCR products from genomic DNA extracted from tail biopsies (*section 3.1*).

Mouse model	Primers	Sequence (5'-3')	Allele	Amplicon size (bp)
Rad51b$^{KI/KI}$	F1	GCCCACGATGAACATTTCTTTTT	WT	320
	R1	TGTGTTTGCCTGTCTCCCCTATT	KI	320
hs205$^{-/-}$	F3	ATGGGGGTGTGCATAGAAGGA	WT	383
	R3	AGAGCTATCGCCGCACCATAA		
	F4	TCCCTTTCTTCCCTCTCACTC	KO	446
	R4	CTATTCCTCCCCAGAGATGCT		
hs1442$^{-/-}$	F5	GCCTGTGGCTTTGATCTTGCT	WT	358
	R5	GCAAATCCACCACCTCTCTGC		
	F6	CCTCCACTGCTTGGACACTAA	KO	421
	R6	TGAGTCTCTGGATAGGCTGGA		

Table 3. Primers used for genotyping of genetically modified mice.

3. Molecular Biology techniques

3.1 Genomic DNA extraction

3.1.1 Extraction by alkaline lysis

Pieces of mouse tails of 2 mm long were cut between 15 to 21 dpp (days postpartum) and incubated in 600 µl of 50 mM NaOH for 30 minutes at 95°C. After that, the tails were broken up through vortex and the NaOH was neutralized with 50 µl of 1M Tris-HCl pH 8.8. This DNA was used as a template for mice genotyping by PCRs.

3.1.2 Extraction with phenol/chloroform

The fragments of mice tails were incubated with 500 µl of lysis buffer (0.1 M Tris-HCl pH 7.4, 0.1 M EDTA, 0.5% SDS) and 0.6 mg/ml proteinase K at 55°C during 12-20 h. The solubilized DNA was extracted in 1 volume of phenol/chloroform:isoamyl alcohol (24:1) and separated by centrifugation for 5 minutes at 13000 rpm. Next, the upper aqueous phase containing the DNA was carefully collected and precipitated by adding 200 µl 7.5 M of ammonium acetate and 700 µl of isopropanol (0.4 volumes of ammonium acetate, 1.4 volumes isopropanol). Then, the DNA was washed with 70% ethanol. Once the ethanol was evaporated, the DNA was resuspended in 1x TE.

3.2 PCR for genotyping

Mice genotyping was performed by PCR amplification (Polymerase Chain Reaction). Primers were designed flanking the edited region of the gene of interest. The optimization of the reaction conditions was performed according to the manufacturer protocol of the Taq DNA polymerase (NZYtech). 1.5 µl of DNA (< 0.1µg) isolated from tail biopsies was used as a template, in a mix containing 0.4 µM of each oligo, 200 µM of dNTPs, 1x polymerase buffer and 0.75 U of Taq polymerase (NZYTaq II DNA polymerase), in a total volume of 25 µl. The reaction was carried out in a thermocycler Veriti Thermal Cycler (Thermo Fisher). The PCR conditions vary depending on the size of the amplified DNA fragment and the primers used (see **Table 3**), being the standard PCR conditions: initial denaturation for 2 minutes at 94°C, 35 cycles of i) denaturation for 20 sec at 94°C, ii) annealing for 20 sec 55-68°C according to the primers used, iii) elongation at 72°C 1 minute per kb, and a final elongation time of 5 minutes at 72°C. The PCR product was analysed through electrophoresis in agarose gel.

3.3 Generation of expression vectors

3.3.1 RNA extraction

100 mg of tissue or cell pellet was placed in a 2 ml eppendorf tube containing 750 µl of GIT (4 M guanidinium thiocyanate, 25 mM sodium citrate, 0.5% (w/v) sodium lauryl sarcosiante and 0.1 M β-mercaptoethanol). The tissue was broken up with a polytron homogenizer (IKA T10 basic, UltraTurrax). Subsequently, 0.1 volumes of 2 M sodium acetate pH 4.0, 1 volume of phenol-water, 0.4 volumes of chloroform:isoamyl alcohol (24:1) were added, mixed thoroughly by vortexing, and incubated for 15 minutes at room temperature (RT). The samples were subsequently centrifuged at 13000 rpm for 15 minutes at 4°C. The aqueous phase containing the RNA was transferred to a new tube and the RNA was precipitated by adding 1 volume of isopropanol, centrifuging it during 15 minutes at 13000 rpm and 4°C. The RNA pellet was washed twice with 70% ethanol, resuspended with MQ-H_2O and quantified measuring the absorbance at 260 nm.

3.3.2 Reverse transcription- PCR (RT-PCR)

cDNA was synthesized through retrotranscription of 5 µg RNA using oligo(dT) and the commercial kit SuperScript® IV Reverse Transcriptase (Invitrogen, Life Technologies). Subsequently, cDNA of interest was amplified by PCR using specific oligos and 2 µl of the cDNA amplified. In detail, the full-length cDNAs of the proteins of interest were RT-PCR amplified from murine testis cDNA, as most of them are meiotic recombination proteins (i.e., RAD51B, RAD51C RAD51, DMC1, HELQ), using specific primers for each of them (**Table 4**). The polymerase used for that purpose was Phusion High-Fidelity (ThermoFisher) or Expand Long polymerase (Roche) for long sized amplicons. To do that, 2 µl of total cDNA was added to a PCR mix containing 0.4 µM of

each primer, 200 µM dNTPs, 1x polymerase buffer and the suitable polymerase (0.8 U Phusion, 3.5 U Expand Long), in a total volume of 50 µl. The standard PCR conditions were the following: 2 minutes at 94°C, 35 cycles: i) 20 sec at 94°C, ii) 20 sec at 55-68°C, iii) 1 minute per kb at 72°C (Phusion polymerase) or 68°C (Expand Long polymerase); and a final elongation cycle of 5 minutes at 72°C or at 68°C.

RT-PCR	Primers	Sequence (5'-3')	Size (bp)
Rad51b	F7	CATGAGCAGCAAGAAACTAAGAC	WT allele: 1053
	R7	ATGGTCTTTCGTGGCCTTGAAG	KI allele: 1052
RAD51B	F8	CATGGGTAGCAAGAAACTAAAACGAG	WT allele: 1157
	R8	GAAAAATTAGCTGGGTATGGTGGC	KI allele: 1156
Rad21	F9	AATGTTCTACGCACATTTTGTCCTC	WT allele: 1908
	R9	GAACACATCTAGCTCCTCAGATA	
Rad51	F10	CATGGCTATGCAAATGCAGCTTG	WT allele: 1032
	R10	GCCTAAGGAGTCAGTCTTTGGC	
Rad51c	F11	AAAAATGCAGCGGGAGTTGGT	WT allele: 1104
	R11	AGCATTCTTCCTCTGGTTCTC	
Helq	F12	GGTCACCTGCTGTCTCCAGAAC	WT allele: 3389
	R12	CTCACCACTGGGCAGTTTACAAC	
Dmc1	F13	CATGAAGGAGGATCAAGTTGTGCA	WT allele: 1029
	R13	ATCGGGGATGCCAAGGAGTAGGT	
Brca2-N	F14	GAAAATGCCCGTTGAATACAAAAG	WT allele: 2978
	R14	AGCTGTTCTGAAGCTACCTCCAA	
Brca2-M	F15	TGGAGGTAGCTTCAGAACAGCTT	WT allele: 3113
	R15	AACTGTGACCAGTTTTCCACCTG	
Brca2-C	F16	AGGTGGAAAACTGGTCACAGTTT	WT allele: 3959
	R16	ACCGGGAGGCTAAGACTCAACA	
Meiob	F17	AAGCATGGCAAAGTTCTTTGCAT	WT allele: 1418
	R17	TTTAAGTATGTCCTTGTCTAGCC	
Brme1	F18	AGATAAAATGAATAAGAAGAAACAGC	WT allele: 1828
	R18	CTACAGGCTGCAGCAGATTACAA	
Hsf2bp	F19	GGCTATGGCCGCAACCGTGGG	WT allele: 1023
	R19	TCTAAACATTACAGTCCAGGGCGC	
Rpa	F20	AGCCATGGTGGGACACCTGAG	WT allele: 1957
	R20	AGTGGTACTTGCTCCCATCACAT	

Table 4. Primers employed in the amplification of the cDNAs.

3.3.3 Insert preparation and cloning

The PCR product was purified through a column (NZYGelpure, NZYtech). The amplified cDNA and genomic elements were phosphorylated by a T4 polynucleotide kinase (Takara), repaired with a T4 DNA polymerase (Takara) when using Expand Long polymerase. Then, it was cloned into different mammalian expression vectors (pcDNA3, pcDNA3 2xFlag, pcDNA3 2xHA, pEGFP) through ligation with the T4 ligase enzyme (Takara) during 3 h at RT.

In the case of the cloning of the plasmid UCE-Hsp68-EGFP first, with restriction digestion we eliminate the CMV of pEGFP-N1 using BglII and AgeI, then we insert Hsp68 previous amplified by PCR using genomic murine DNA (primers listed in **Table 5**). On the other side, we amplified UCEs (HS205 and HS1442) from genomic DNA and inserted to the plasmid generated before pHsp68-EGFP opened with SmaI.

The ligation reaction was transformed in *E. coli* competent cells (DH5α). In frame cloning was verified by Sanger sequencing.

PCR	Primers	Sequence (5'-3')	Size (bp)
Hsp68	F21	GCGCCGCGCTCTGCTTCTGGA	856
	R21	GAGCTCCAGGAACATCCAAACTGA	
hs205	F22	CCACCATGCTGGTATTTCATTCACA	1644
	R22	CTTTGTCCTAAGAGTGTCTTGCTATT	
hs1442	F23	CTACAAGTAAAATAATAGAACTGAATC	2598
	R23	GATTGAGATTTTTTCTTTCACTTCC	

Table 5. Primers employed for the generation of UCE-Hsp68-EGFP plasmid.

3.3.4 Transformation of DH5α competent E. coli cells

The propagation of the plasmid obtained as a ligation product was performed in DH5α *E. coli* competent cells, through heat shock. For this, one vial of competent cells was thawed on ice and 2-4 µL of the ligation was added. Then, the vial was incubated for 30 minutes on ice, followed by 33 seconds in a bath at 42°C (heat-shock) and 5 minutes in ice. The bacteria were allowed to recover for 1 h (Ampicillin resistance) or 3 h (Kanamycin resistance) in 1 mL of liquid media LB without antibiotic at 37°C in agitation to let them develop the expression of antibiotic resistance gene. Finally, the bacteria were seeded on an LB agar plate containing the correspondent selection antibiotic and incubated at 37°C for at least 15 hours. In the case of transformation of pure plasmids, not from ligation, 30 µL of competent cells were incubated with 1 µL of plasmid for 15-20 minutes on ice, followed by 33 seconds in a 42°C bath and 1 minute on ice. After this, when resistance was to Ampicillin, the bacteria were seeded directly onto an LB agar plate. But in cases where the plasmid carries resistance to Kanamycin, they were recovered for 1 hour in 1 ml of liquid LB medium at 37°C under agitation, before being plated.

3.3.5 Extraction of plasmid DNA from E. coli by alkaline lysis

The *E. coli* colonies obtained on the LB plate were inoculated in 1.5 ml of liquid LB with the selection antibiotic and incubated at 37°C overnight with shaking. The culture was centrifuged for 2 minutes at 13000 rpm and the bacterial pellet obtained was resuspended in 200 µL of P1 buffer (50 mM Tris-HCl pH 8, 10 mM EDTA and 100 µg/ml of RNAse). Then the cells were lysed by adding 200 µL of P2 buffer (0.2 M NaOH, 1% SDS), mixing by inversion and incubating for 5 minutes at RT. After 5 minutes, 200 µL of P3 buffer (3 M of potassium acetate and 11.5% of glacial acetic acid) was added to neutralise the lysis mixture and precipitate the bacterial DNA and proteins. After centrifugation for 10 minutes at 13000 rpm, the supernatant (containing plasmid DNA) was collected and precipitated by adding 0.7 volumes of isopropanol, mixing vigorously, and centrifuging for 5 minutes at 13000 rpm. The DNA pellet was washed with 70% ethanol and resuspended in 1x TE (10 mM Tris-HCl pH 8, 1mM EDTA).

3.3.6 Restriction analysis

In order to check which colonies contained the correct recombinant plasmid, an enzymatic digestion analysis was performed. For this, DNA (1 µL) was digested with 0.2 µL of each of the required restriction enzymes and the corresponding buffer (1x) in a final volume of 10 µL. This mixture was incubated for 1 hour at the temperature indicated for each enzyme. Finally, the restriction fragments obtained were analysed by electrophoresis in agarose gel and, in the correct cases, it was also validated through Sanger sequencing.

3.3.7 Purification of plasmid DNA by alkaline lysis followed by affinity column

Once the cloning was validated by sequencing, plasmidic DNA was obtained with a high degree of purity using an anion exchange column. For this, one of the colonies of *E. coli* transformed with the plasmid of interest was previously cultured in 200 ml of LB supplemented with the appropriate antibiotic according to the resistance of the plasmid and incubated at 37°C under agitation until a saturated culture was obtained. This culture was centrifuged at 7000 rpm for 15 minutes and the pellet obtained was resuspended in 10 ml of P1 buffer. Cells were then lysed with 10 ml of P2 buffer, incubated for 5 minutes at RT therefore neutralised with 10 ml of P3 buffer and centrifuged at 14000 rpm for 10 minutes, leaving the plasmidic DNA in the supernatant. On the other side, a column (JETSTAR Column) was equilibrated with 30 ml of E4 buffer (600 mM NaCl, 100 mM sodium acetate, 0.15% Triton X-100 and acetic acid to pH 5). After equilibration, the supernatant of the cell lysate, previously filtered in a syringe with glass wool, was passed through the column. The column was then washed twice with 60 ml of E5 buffer (800 mM NaCl, 100 mM sodium acetate and adjust with NaOH to pH 5). DNA was eluted with 15 ml of E6 buffer (1.5 M NaCl, 100 mM sodium acetate and acetic acid to pH 5), and precipitated with 0.7 volumes of isopropanol by centrifugation at 14500 rpm for 30 minutes at 4°C. The pellet was washed with 70% ethanol and centrifuged for 10 minutes at 14500 rpm. The pellet was allowed to dry and finally resuspended in 200 µL of TE 1x. To determine the concentration of DNA, its absorbance was measured in the NanoDrop spectrophotometer.

3.4 Site-directed mutagenesis

Point-mutations were introduced to hRAD51B cloned in pEGFP-N1 using primers listed in Table 6 (with the desired mutation) in which the three secondary methionine codons were PCR replaced by CGX encoding alanine codons (individual and double Met to Ala substitutions). The parent template was removed using a methylation-dependent endonuclease DpnI incubation at 37°C overnight. Then, plasmids were isolated from the resulting colonies and screened for the desired modification by restriction analysis. Positive clones are verified by Sanger sequencing.

Primer	Sequence (5'-3')
hRAD51B-2nd Met-F	GCTAAGGTGACTGGTCTGAGTTATC
hRAD51B-2nd Met-R	AAGCTCCAGTGGGGAAAGACA
hRAD51B-3rd Met-F	GCGGTCAGCAGGGCCTGTGCCCCAA
hRAD51B-3rd Met-R	ACATAGAAGTTCATGGACACCTCG

hRAD51B-4th Met-F	GCGCAAACGGCTTATGGGATAAAAG
hRAD51B-4th Met-R	CTTTGGGGCACAGGCCCTGCT

Table 6. Primers used to generate the site-directed mutagenesis analysis.

3.5 Protein analysis

3.5.1 Protein extraction from mouse tissues

Testis were detunicated, homogenized in RIPA lysis buffer (50 mM Tris-HCl pH 7.5, 150 mM NaCl, 1% NP40, 0.5% sodium deoxycholate, 0.1% SDS) supplemented with protease inhibitors (Complete EDTA-free, ROCHE) (1 ml per testis) with a polytron homogenizer and incubated for 15 minutes on ice to allow the protein extraction. After that, the sample was centrifuged at 13000 rpm for 30 minutes at 4°C and the protein concentration of the supernatant was quantified through absorbance carrying out a Bradford assay with the DC Protein Assay kit (BioRad).

3.5.2 Immunoprecipitation from overexpressed proteins

HEK 293T cells were transiently transfected with at least two expression plasmids encoding for the candidate proteins with Jet Pei (Polyplus). 48 hours after the transfection, the whole cell protein extracts were prepared by lysing the cells with DEBANANDA buffer (50 mM Tris-HCl pH 7.4, 150 mM NaCl, 1 mM EDTA, 1% Triton X-100) supplemented with protease inhibitors (Complete EDTA-free, ROCHE).

The protein concentration was determined through absorbance with the DC Protein Assay kit (BioRad). 0.5-1 mg of protein was cleared with protein G Sepharose beads (GammaBindTM G SepharoseTM, GE Healthcare) for 1 hour at 4°C under rotation. The blocked extract was incubated with the corresponding antibody (3-4 µg) for at least 2 h at 4°C under rotation. As negative control, the protein extract was incubated with IgG (2-3 µg/1mg protein) from the same species as the antibody. The immunocomplexes were isolated by adsorption to protein G-Sepharose beads overnight at 4°C. After 4 washing steps with DEBANANDA buffer, the proteins were eluted from the beads with 20 µL of 2x Laemmli buffer (100 mM Tris-HCl pH 7, 4% SDS, 0.2% bromophenol blue, 200 mM β-mercaptoethanol and 20% glycerol) boiled at 95°C for 5 minutes and loaded onto reducing polyacrylamide SDS gels.

The proteins were detected by western blotting with the indicated antibodies in **Table 7**. The IgGs used were ChromPure mouse IgG (2 µg/1 mg prot; 015-000-003), ChomPure rabbit IgG (3.4 µg/1 mg prot; 011-000-003, Jackson ImmunoResearch).

3.5.3 Western Blot

Protein extracts were resolved in denaturing SDS-polyacrylamide gels following the protocol described by Laemmli (Laemmli, 1970). The proteins were separated in 8 – 12% polyacrylamide gels, running on 1x SDS-Page (250 mM Tris-HCl, 200 mM glycine, 0.05% SDS) at 200 V. Proteins were transferred to nitrocellulose membranes (GE Healthcare Amersham) in transfer buffer (25 mM Tris-HCl, 200 mM glycine, 20% methanol) at 70 V for 1 hour. The blot was blocked for 1 hour in 5% non-fat milk in TBST (TBS-Tween-20: 50 mM Tris-HCl pH 7.5, 150 mM NaCl, 0.1% Tween 20). After that, the blot was incubated with the primary antibody in 5% milk-TBST for 1 hour under

rotation, washed three times with TBST shacking for 5 minutes and incubated for 1 hour with the secondary antibody conjugated to a fluorochrome at 1:10000 dilution and incubated at dark (α-mouse DyLight™ 680 (35518, Thermo Scientific), α-rabbit DyLight™ 800 (35571, Thermo Scientific)). The fluorescent signal of the antibodies was obtained through Odyssey Infrared Imaging system.

For retesting the blots, the primary and secondary antibodies were removed from the blot by stripping. To do that, the blot was incubated twice for 10 minutes in a mild stripping buffer (0.2M glycine, 1% SDS, 0.01% Tween 20, pH 2.2) shacking at RT. After that, the blot was washed twice in PBS for 10 min, and two more times in TBST for 5 min. Then, the blot was blocked and blotted as normal. The blot can be retested without stripping, by inactivating the peroxidase activity of the secondary antibody with an excess of hydrogen peroxide. To do that, the blot was incubated with 15% H_2O_2 in PBS for 15 min gently shacking and rinsed twice in TBST.

3.5.4 Immunoprecipitation coupled to mass spectrometry analysis

Testis and human lymphoblastoid cells were lysed in CO-IP lysis buffer (50 mM Tris-HCl pH 8, 500 mM NaCl, 1mM EDTA, 1% Triton-X100, proteases inhibitors). 10 mg of protein extracts were incubated 2 h with 30 µg of antibody against mouse RAD51B (residues 122 to 350, ProteintechTM) or IgG from rabbit. The corresponding immunocomplexes were incubated with 60 µl of sepharose beads overnight. After washing, beads were eluted in 100 mM Glycine pH 2.5-3 and analysed by Lc-MS/MS shotgun in LTQ Velos Orbitrap at the Proteomics facility of Centro de Investigación del Cáncer (CISC/University of Salamanca).

Raw data were analysed using MaxQuant v 1.6.2.6 (Cox & Mann, 2008) against SwissProt Mouse database (UP000000589, Oct 2019) and MaxQuant contaminants. All FDRs were of 1%. Variable modifications considered were oxidation of M and acetylation of the N-terminal, while fixed modifications included considered only carbamidomethylation of C. The maximum number of modifications allowed per peptide was of 5. The proteins related with DNA repair were quantified using iBAQ (Schwanhäusser et al., 2013).

4. Cytological techniques

4.1 Histological analysis

To perform the histological analysis of mouse tissues, after the necropsy the organs were removed and fixed in 10% formol during 24 hours at RT, except for testes that were preserved in Bouin fixative. They were embedded in paraffin and were cut into serial sections of 5 µm. The sections were stained with haematoxylin-eosin or PAS (Periodic Acid-Schiff)-haematoxylin following standard protocols. These techniques were developed in collaboration with the service of “Patología Molecular Comparada” of the Centro de Investigación del Cáncer (Salamanca). The samples were analysed using a microscope OLYMPUS BX51 and images were taken with a digital camera OLYMPUS DP70.

4.2 Dry down spreading of spermatocytes

The study of the mouse spermatocytes was carried out by performing this fixation technique of the meiotic cells over slides, with some modifications of the protocol developed by Peters et al (Peters et al., 1997).Testis were detunicated and placed in a Petri dish with a drop of 1x PBS.

The seminiferous tubules were ground with the aid of 2 scalpels, and the extracted cells were collected with PBS 1X into a tube to a total volume of 6 ml of PBS 1X. The cells were spin down for 7 min at 1200 rpm and rinsed once with 6 ml of 1x PBS. The pellet of cells was resuspended in 75 - 350 µL of 100 mM sucrose pH 8.4 for 5 min to bring the cells under a hypotonic shock. A clean glass slide was covered with 400 µL of the fixative solution (1% paraformaldehyde (PFA), 0.15% Triton X-100, 0.05% PBS, 2.5 mM sodium tetraborate, pH 9.2) and it was placed 20 µL of the cell suspension in the upper corner of the slide, slowly dispersing them. The slides were kept for 2 to 3 h in a closed box to allow the fixation of the cells, and then they were left to air dry almost completely. To remove the fixative, the slides were washed with 0.08% Photo-Flo (Kodak) and dried at RT. The quality of the spreads was checked in an inverted phase contrast microscope Nikon Eclipse TS100. The slides were stored in 0.05% azide in PBS 1X at 4ºC.

4.3 Squash of seminiferous tubules

The method developed by Parra et al (Parra et al., 2002) allows obtaining a monolayer of seminiferous tubule cells keeping their 3D conformation. Testis were detunicated and the seminiferous tubules were fixed for 10 min (2% formaldehyde, 0.1% Triton X-100 in 1x PBS). A small fraction of the tubules was placed in pre-treated poly-L-lysine (1 mg/ml, Sigma-Aldrich) slide with a drop of fixative and coated. Tubules were crushed with a pencil over the coverslip and squashed to get a monolayer of cells. After immersing the slides in liquid nitrogen for a few seconds, the coverslip was immediately removed with the help of a scalpel and the slides were put 1x PBS. The slides were stored in 0.05% azide in 1x PBS at 4ºC until needed.

4.4 Ovary drying-down chromosome spread

Prophase oocytes were obtained from female embryos, from 17.5 to 18.5 dpc (days post coitum) depending on the stage of interest (from 14.5 to 19.5 meiosis take place). Pregnant females were sacrificed, and the embryos were extracted from the uterus and placed into PBS. The ovaries were taken out from the embryo and put into a well (24-wells plate) containing 200 µL of M2 medium (Sigma-Aldrich). 10 µL of 50 mg/ml collagenase/M2 was added and incubated for 20 – 30 min at 37ºC to allow the release of the ovaries. Then, the ovaries were transferred to 200 µL of hypotonic buffer (30 mM Tris-HCl pH 8.2, 50mM sucrose, 17 mM sodium citrate, 5 mM EDTA, 0.5 mM DTT) and incubated for 45 min at RT. In the meanwhile, the slides (6 slides per pair of ovaries) were labelled, and it was drawn a circle in the middle of the slides with Rubbercement adhesive to delimit a small area. After hypotonic treatment, the ovaries were transferred into 60 µL of 100 mM sucrose pH 8.2 and the cells were dispersed pipetting up-down. It was checked if single cells were thoroughly suspended under a microscope (oocytes appeared bigger and round). Afterwards, 40 µL of fixative buffer (1% (w/v) PFA, 5 mM sodium borate, 0.15% Triton X-100, 3 mM DTT, pH 9.2) were placed in the slide inside the circle, and it was added 10 µL of cell suspension to the centre of the fixative drop. The slide was tilted in a zig-zag movement to spread the cell suspension within the circle. It was incubated inside a closed chamber for 2 to 3 h and then, the slides were air-dried almost completely. Finally, they were washed with 0.08% Photo-Flo (Kodak) to remove the fixative and dried at RT. The spreads preparations were stored in 0.05% azide in 1x PBS at 4ºC.

4.5 Immunofluorescence

The slides were incubated with the primary antibody (**Table 7**) diluted in 1x PBS for 1 h or overnight at RT in a wet chamber and then they were washed three times in 1x PBS for 5 min.

Thereupon, the slides were incubated during 1 h with the secondary antibody conjugated to a fluorochrome diluted in 1x PBS or ADB (**Table 8**) and washed three times in 1x PBS for 5 min. Finally, the slides were mounted with Vectashield® mounting media (Vector Laboratories) and DAPI (4',6-Diamidino-2-Phenylindole, 10 µg/ml) to counterstain the DNA. Alternatively, and in order to reduce the background, the slides can be initially blocked for 15 min with 10% ADB buffer (10% serum, 3% BSA and 0.05% Triton X-100 in 1x PBS) and the antibodies diluted in 10% ADB. In this case, the washing was done with PBST (0.05% Triton X-100 in 1x PBS).

To carry out immunofluorescence of cultured cells, cells were seeded in 3.5 cm dishes with a gelatine-coated coverslip inside (0.5% gelatine, Sigma-Aldrich) to enhance cellular adhesion. The cells were fixed with 4% paraformaldehyde in 1x PBS for 7 min at 4°C and washed 3 times in 1x PBS for 5 min. After that, the cells were permeabilized with 0.2% Triton X-100 in KB buffer (0.1 M NaCl, 20 mM Tris-HCl pH 7.5, 0.1% BSA) for 4 min and washed in 1x PBS. The blockage of cells was carried out with 7% FBS in 1x PBS for 30 min at RT. Next, the cells were incubated with the primary antibody diluted in 7% FBS in 1x PBS for 1 h in a wet chamber at RT. Following 3 washes in 1x PBS for 5 min, the slides were incubated with the secondary antibody conjugated with a fluorochrome diluted 1:100 in 7% FBS in 1x PBS for 1 h. They were washed 3 times in PBS, and finally they were mounted with Vectashield® and DAPI.

Target Protein	Antibody	Host	Type	Dilution			Supplier
				IF	WB	IP	
ACA	15-235	Human	IgG	1:15			Antibodies Incorporated
BRME1	R1	Rabbit	IgG	1:100	1:2000		Proteogenix
	R2	Rabbit	IgG	1:200	1:2000		Proteogenix
DMC1	R1	Rabbit	IgG	1:500			Proteogenix
	R2	Rabbit	IgG	1:500			Proteogenix
	ab11054	Mouse	IgG	1:50			Abcam
Flag	F1804	Mouse	IgG	1:300	1:2000	3.6 µg	Sigma-Aldrich
	F7425	Rabbit	IgG	1:300	1:2000	3.2 µg	Sigma-Aldrich
GFP	CSB-MA000051M0m	Mouse	IgG			3.8 µg	Cusabio
	A-11122	Rabbit	IgG	1:50*	1:3000	3 µg	Life Technologies
HA	αHA.11 101R	Mouse	IgG		1:2000	3 µg	Covance
	H6908	Rabbit	IgG		1:2000	3 µg	Sigma-Aldrich
HSF2BP	R1	Rabbit	IgG	1:30	1:2000		Proteogenix
	R2	Rabbit	IgG	1:20	1:2000		Proteogenix
H1t		Guinea pig	IgG	1:100			MA Handel
MLH1	51-1327GR	Mouse	IgG	1:20			BD Biosciences
RAD51	sc-8349	Rabbit	IgG	1:50			Santa-Cruz
	PC130	Rabbit	IgG	1:50			Calbiochem
RAD51B	R1	Rabbit	IgG		1:1000		Proteogenix
	R2	Rabbit	IgG		1:2000	3 µg	Proteogenix
	AP20559PU-N	Rabbit	IgG		1:200		OriGene
RAD51C	Sc-56214	Mouse	IgG		1:200		Santa Cruz
RFN212		Goat	IgG	1:150			Dr. N. Hunter
RPA	Molly-RPA1	Rabbit	IgG	1:30			Dr. E. Marcon
	RPA2-2208S	Rat	IgG	1:150	1:1000		Cell Signalling
SPATA22	16989-1-AP	Rabbit	IgG	1:60			Proteintech
SYCP1	K919	Rabbit	Serum	1:60			Dr. J.L. Barbero
SYCP3	sc-74569	Mouse	IgG	1:1000			Santa Cruz

	K921/K1037	Rabbit	Serum	1:500		Dr. J.L. Barbero
αTubulin	T9026	Mouse	IgG	1:100	1:10000	Sigma
β-Actin	Clone AC-15; A5441	Mouse	IgG		1:10000	Sigma-Aldrich
γH2AX (Ser139)	#05-636	Mouse	IgG	1:500		Millipore
	#07-164	Rabbit	IgG	1:500*		Millipore
53BP1	H-300; sc-22760	Rabbit	IgG	1:150*		Santa Cruz

Table 7. Primary antibodies. IF: Immunofluorescence; **WB**: Western Blot; **IP**: Immunoprecipitation (µg of antibody for 1 mg protein extract); *: Immunofluorescences in cultured cells (the rest are concentrations for IF in spreads or squash of meiocytes).

Target	Fluorochrome	Antibody	Host	Dilution	Supplier
α-goat	TRITC	703-025-155	Donkey	1:100	Jackson Immunoresearch
	FITC	703-095-155	Donkey	1:100	Jackson Immunoresearch
α-guinea pig	TRITC	706-025-148	Donkey	1:100	Jackson Immunoresearch
	FITC	706-095-148	Donkey	1:100	Jackson Immunoresearch
α-human	Texas Red	709-075-149	Donkey	1:100	Jackson Immunoresearch
α- mouse	TRITC	115-095-146	Goat	1:100	Jackson Immunoresearch
	TRITC	715-025-150	Donkey	1:100	Jackson Immunoresearch
	Alexa 555	A-32727	Goat	1:200	ThermoFisher
	FITC	115-095-146	Goat	1:100	Jackson Immunoresearch
	Alexa 488	A-11001	Goat	1:200	ThermoFisher
α-rabbit	TRITC	711-025-152	Donkey	1:100	Jackson Immunoresearch
	Alexa 555	A-31572	Donkey	1:200	ThermoFisher
	FITC	711-095-152	Donkey	1:100	Jackson Immunoresearch
	Alexa 488	A-32731	Goat	1:200	ThermoFisher
	Alexa 488 - Fab	111-547-003	Goat	1:100	Jackson Immunoresearch
α-rat	Alexa 488	A-11006	Goat	1:200	ThermoFisher

Table 8. Secondary antibodies. FITC: Fluorescein, TRITC: Rhodamine.

4.6 Fluorescence microscopy

The spreads preparations were visualized at RT using a microscope Leica DM6000 B with a 63x objectives. Images were taken with a digital camera Hamamatsu ORCA-ER C4742-80. Squashed immunofluorescences were visualized with a Delta Vision microscope station with 100x objectives. The images were processed using Leica LAS X Life Science Software and Adobe Photoshop CS6 2020. Quantification of fluorescence signals, as well as the measurement of lengths and distribution profiles, were performed using Fiji (Image J) software.

4.7 Mitotic chromosome preparations from mouse cells

Mice between 6-12 weeks old were injected intraperitoneally with a single dose of 4 mg of MMC (Mitomycin C) per kilogram of body weight. After 24 hours were injected with 0.1 ml of 0.5% colchicine solution intraperitoneally and the karyotyping derived from bone marrow was realized following standard procedures protocol (Akeson & Davisson, 2000). Metaphase spreads were stained with 5% Giemsa in 10 mM phosphate buffer pH 6.8 and analyzed for microscopically visible chromosomal aberrations. Chromatid gap, chromatid break and triradial/quatriradial chromosomes were classified as previously described (N. Li et al., 2018). At least 100 metaphases were counted from three independent mice of each genotype.

4.8 *In vivo* testis electroporation

This technique developed by Dr. Muramatsu (Muramatsu, 2000) allows to transitorily express cDNAs cloned in expression vectors in testis cells after minor surgery. To get higher efficiency, the electroporation (EP) was carried out in 16 dpp ICR mice or 20-30 dpp B6 mice. After anaesthetising the mice with isoflurane, the testes were pulled out from the abdominal cavity. 10 µL of DNA solution was injected to the rete testis (region surrounded by the white dotty line) using a glass capillary. The DNA solution contained 5 µg/µL of expression vector diluted in 1x HBS (HEPES buffered saline: 20 mM HEPES, 140 mM NaCl, 5 mM KCl, 0.1% glucose, 0.7 mM Na2HPO4·12H2O) stained with 1µl of 0.1% FastGreen (Sigma-Aldrich). After a period of 1 h to let the DNA to penetrate the seminiferous tubules, the testis, wet with PBS, was held between a pair of electrodes, applying 4 electric pulses of 35 V for 50 ms in each direction using a CUY21 BEX electroporator (BEX Ltd). Finally, the testes were returned into the abdominal cavity and the incision was closed with sutures. The spermatocytes were squashed or spread after 24 – 72 h and analysed by immunofluorescence.

5. Cellular cultures

5.1 Cell types and culture conditions

During the development of this study, *in vitro* experiments have been carried out with several cell lines and primary cultures of fibroblast obtained from mouse. All of them were cultured in culture dishes (BD Falcon), in incubators with a wet atmosphere at 37ºC and 7% CO2. The cells used were the following:

- HEK 293T: Human embryonic kidney cell line.
- COS7: African green monkey kidney fibroblast-like cell line.
- Primary and immortalized MEFs: Mouse Embryonic Fibroblasts.
- Immortalized lymphoblastoid cells derived from patients.
- GC-1spg: Mouse spermatogonia cell line.
- GC-2spd: Mouse spermatocyte cell line.
- TM3: Mouse Leydig cell line.
- TM4: Mouse Sertoli cell line.

HEK 293T, COS7, GC-1spg, GC-2spd and MEFs were cultured in DMEM (Dulbecco's Modified Eagle Medium, GIBCO) supplemented with 10% FBS (foetal bovine serum, Gibco) and 1% PSG (Penicillin-Streptomycin-Glutamine; Gibco). Lymphoblastoid cells were cultured in RPMI medium (GIBCO) supplemented with 10% inactivated FBS and 2mM Glutamine. TM3 and TM4 cell lines were cultured in DMEM: Ham's F12 medium (1:1, Gibco) with 1.2 g/l sodium bicarbonate, 15 mM HEPES, 5% horse serum and 2.5% FBS.

Once cells achieved the desired confluence or in order to seed them, the adherent cells were trypsinized with 0.25% Trypsin-EDTA (Gibco) for 5 min at 37ºC. Trypsin was neutralized by adding media with FBS. The cells were mechanically unicellularized by gently pipetting and seeded at the suitable confluence. For long term preservation, the cells were maintained in liquid nitrogen (-180ºC). The cells were frozen in culture medium supplemented with 20% FBS and 10% DMSO (dimethylsulfoxide, Sigma-Aldrich), were slowly frozen at -70ºC in isopropanol containers (MrFrosty™, Thermo Scientific™) and finally transferred to liquid nitrogen tank (-180°C).

5.2 Isolation of MEFs

To obtain primary cultures of MEFs, embryos were extracted from pregnant females at 13.5 dpc. The uterus was placed in a Petri dish with PBS and the embryos were extracted by cutting the wall of the uterus. Then, the head and the viscera (red tissue: heart and liver) were tear out, and the rest of the embryo was transferred to a tube with 1 ml of 0.25% trypsin-EDTA. The embryos were chopped up with scissors and incubated overnight at 4ºC. After 24 h, the cell suspension was pipetted up and down to mince the cells and was transferred to a 10 cm culture dish with DMEM, incubating them at 37ºC. When the MEFs reached 100% confluence, proximately after 24 h, they were trypsinized and transferred to a 15 cm dish. After reaching newly 100% confluence, the MEFs were frozen in DMEM supplemented with 20% FBS and 10% DMSO, in 5 cryovials per embryo, considered as passage 0.

5.3 Transfection of cell lines

For transfection of HEK 293T, 4x 10^6 cells were plated in a 10 cm dish the day before the transfection. A mix containing 20 µL of jetPEI (Polyplus-Transfection) diluted in 250 µL 150 mM NaCl was added to the DNA solution (10 µg DNA in 250 µL 150 mM NaCl), gently vortexed and incubated for 15-30 min at RT. The culture media of the cells was replaced by fresh media. Next, the transfection mix was added dropwise to the cells and homogenized by swirling the plate. The media was replaced after 24 h.

5.4 Retroviral/Lentiviral transduction

To perform the survival assay based on colony formation, it is necessary to immortalize MEFs so that they can proliferate and form colonies when seeded at low density. For that purpose, MEFs were infected with viral particles previously produced by HEK 293T transfected with retroviral or lentiviral vectors. 4x 10^6 HEK 293T cells were seeded in a 10 cm dish the day before the transfection. The HEK 293T were transfected as described above with the plasmid of interest, together with a packaging vector that encodes the capsid, the reverse transcriptase and the ecotropic envelope of the virus, in the following proportions (10 µg total DNA):

- Retroviral plasmids: 40% pCL-ECO (packaging plasmid) + 60% expression vector
- Lentiviral plasmids: 12.5% pMD2G (envelope) + 37.5% pSPAX2/pCMV dR8.91 (packaging) + 50% expression vector.

The day before the infection 2.6x 10^5 MEFs were plated in a 6 cm dish. The media of the HEK 293T cells containing the viral particles was collected at 48, 60 and 72 h after the transfection, and centrifuged at 4000 rpm for 8 min to pellet any remaining packaging cells. The MEFs were cultured with this media, containing 4-8 µg/ml polybrene. Finally, the transduced MEFs were selected with a suitable antibiotic, commonly 2 µg/ml puromycin (Sigma-Aldrich) for 2-3 days or 75 µg/ml hygromycin for 6 days.

5.5 Cell proliferation assay

2.5× 10^4 MEFs cells/well were seeded in 12-well plates in duplicates in complete DMEM media. After 19 h, MEFs were incubated in presence of a continuous treatment with MMC (0, 5, 10, 20 and 30 ng/ml), Ultraviolet irradiation (UV) (0, 10, 20 and 30 J/m^2), Methyl methanesulfonate (MMS) (0.25, 0.5, 1 and 1.5 mM), Ionizing irradiation (0, 2, 4 and 6 Gy), Hydroxyurea (HU) (0, 5, 10, and 20 µM) and Aphidicolin (0, 50, 100 and 500 nM).Cells from one plate were trypsinized and counted as a “before treatment” day 1 reference. Three days later (4th day after seeding)

the remaining cells were counted the same way. Day 1 reference numbers were subtracted from day 3 cell numbers to evaluate growth of each cell line. The resulting cell counts were expressed as percentages from the untreated wells.

5.6 Clonogenic survival assay

Clonogenic survival following an exposure to MMC, HU and Aphidicolin was assessed in immortalized wild-type and mutant *Rad51b* MEFs. 700 cells were plated per well in 60 mm plates. The day after plating, cells were treated with: 0, 50, 100, 150 and 300 nM of MMC for 2h; 0, 25, 50, 100, 200 μM of HU for 24h and 0, 0.2, 0.5, 1 μM of Aphidicolin for 24h. After drug treatment, media was removed, cells were washed twice with 1x PBS and fresh media was added. Once colonies were detectable by the naked eye (7–12 days), media was removed, and cells were washed with 1x PBS and incubated for 30 min at RT in a fixation solution (8% paraformaldehyde in cell media). The fixation solution was removed, and colonies were stained with Giemsa (0.02% Giemsa solution in PBS) for 30 min at RT. Plates were then rinsed with water and allowed to dry for 24 h. Colonies were counted by hand.

5.7 DNA damage recuperation

In order to analyse the DNA damage repair capacity of mutant *Rad51b* cells, the formation of DSBs was induced by MMC treatment. The day before treatment, 1.4x 10^4 MEFs (passage 2-3) were seeded on 3.5 cm plates. Cells were incubated for 1 hour in the presence of MMC at a concentration of 1 μg/ml or γ irradiated with 5 Gy. Then MEFs were washed twice with PBS 1X and incubated at 37 °C in medium without MMC until recovery. Cells were fixed at 0, 6, 12, 48 and 72h in the case of MMC and fixed at 0, 2, 4, 6, 8, 12, 24h with 4% paraformaldehyde in PBS 1X for 7 minutes at 4°C and immunofluorescence against γH2AX was performed. The assay was performed using 3 lines of wild-type and mutant MEFs, each representing independent replicates of the experiment.

5.8 Karyotyping

Metaphases were obtained after MMC treatment, 150 nM for MEFs at passage 2-5 and 200 nM for lymphoblastoid cells by standard procedures. Active growing cultures were arrested using colcemide (1 μg/mL, Sigma-Aldrich) for 4 h for MEFs and 3 h for lymphoblastoid cells, trypsinized, treated with hypotonic solution (0.75 mM KCl), and fixed with Methanol/Acetic 3:1. Metaphase spreads were stained with 5% Giemsa in 10 mM phosphate buffer pH 6.8 and analyzed for microscopically visible chromosomal aberrations. Chromatid gap, chromatid break and triradial/quatriradial chromosomes were classified as previously described (N. Li et al., 2018). At least 100 metaphases were counted from three independent experiments.

5.9 Sister chromatid exchange analysis

Exponentially growing lymphoblastoid cells were inoculated at a density of 3 x 10^5 and were treated with 10 μM of BrdU (5-bromodeoxyuridine, Sigma) for 48 h (approximately two cell divisions). 5 and 10 ng/ml of MMC was added 24h after BrdU treatment followed by a 3 h incubation with 1 μg/ml of colcemide. Metaphase spreads were stained with 0.1 mg/ml of acridine orange (ThermoFisher) in dH_2O for 5 min at RT. Slides were washed for 2 min under running dH2O tap water, incubated 1 min in Sorenson Buffer (0.1 M Na2HPO4, 0.1 M NaH2PO4, pH 6.8) and mounted in Sorenson Buffer. Slides were immediately visualized under FITC filter and at least 30 reciprocal exchange events were counted of each genotype.

5.10 Induced pluripotent stem cells (iPSC) generation

For iPSC generation, 2.5 x 10^5 MEFs were infected with retroviral particles produced by HEK293T transfected with constitutive retroviral expression vectors pMXs KLF4, OCT4 and SOX2 (as described in *section 5.4*). The iPSC media (DMEM, GIBCO; 15% KSR, Invitrogen; 1% Non-essential aminoacids, MEM NEE 100X GIBCO; 1% PSG; 0,002% β-mercaptoethanol 50 mM, GIBCO; 1000 units/mL LIF, Merck) was changed every 24 h until iPS cell colonies appeared (after ~14 days of treatment). Three weeks after plating the MEFs, reprogramming plates were stained for alkaline phosphatase activity (AP detection kit, MERCK).

6. Statistical analysis

The data presented along this work are indicated as mean ± standard deviation. In order to compare counts between several genotypes at different stages, we used the Welch's t-test (unequal variances t-test), which was appropriate as the count data were not highly skewed (that is, were reasonably approximated by a normal distribution) and in most cases showed unequal variance. We applied a two-sided test in all the cases. Asterisks denote statistical significance: *P value <0.05, **P value <0.01, ***P value <0.001, ****P value <0.0001 and P value > 0.01 indicate no significant differences. The software employed to perform the analysis was GraphPad Prism 8.

RESULTS

1. Functional analysis of *Rad51b-c.92delT* variant

1.1 A variant in RAD51B as the best candidate of the POI phenotype

Human infertility is a major health issue affecting 10-15% of the couples at reproductive age with 25% of the cases classified as idiopathic (Mallepaly et al., 2017). The majority of these infertilities are thought to be caused by genetic factors however, only a small subset of genes have been associated with infertility issues such as POI or NOA. Some examples are the synaptonemal complex components, SYCP3 (Yuan et al., 2000), SYCE1 (de Vries et al., 2014) and SIX6OS1 (Ali et al., 2022; Fan et al., 2021; Gómez-H et al., 2016), the cohesin STAG3 (Caburet et al., 2014; Llano et al., 2014) and, recombination proteins like SPO11 (Tran & Schimenti, 2019), BRCA2 (Caburet et al., 2020; Zhang et al., 2019), DMC1 (Bannister et al., 2007), MEIOB (Caburet et al., 2019), and HSF2BP (Felipe-Medina et al., 2020). These data highlight the need for further research about meiosis and human infertility.

Given that our group have experience in determining the underlying genetic causes of infertility in humans we address, in collaboration with the group of Dr. Reiner A. Veitia (Institut Jacques Monod, Université de Paris, France) and the group of Dra. Berenice B. Mendonca (Unidade de Endocrinologia do Desenvolvimento, Faculdade de Medicina da Universidade de São Paulo, Brasil), the study of a consanguineous Brazilian family affected by POI.

The parents of this POI family are first-degree cousins and have two daughters affected by POI with primary amenorrhea (**Figure 1A**). In order to identify the genetic basis of this POI, whole-exome sequencing was performed in these two affected sisters (II-1 and II-4) and in one unaffected sister (II-2). The mean coverage of the capture regions was ≥150x in all samples with at least 99.38% of the targeted positions being sequenced at ≥10x (**Supplementary Table 2**). Consistent with an autosomal recessive inheritance, homozygous candidate variants were selected in both affected sisters and a minor allele frequency cut-off of 0.01% was applied. After an in-depth assessment of coding variants (missense, nonsense, and frameshift) and splice sites, a homozygous frameshift pathogenic variant in the *RAD51B* gene was identified in the two affected sisters as the best genetic candidate (**Supplementary Table 3**).

RAD51B gene is located in chromosome 14, position 14q23-q24.2, and the c.92delT variant is located in exon 3. As predicted by Mutalyzer, the *RAD51B*-c.92delT variant creates a premature termination codon (PTC) at aminoacid #39 (predicted alteration:p.Leu31Tyrfs*9). The variant c.92delT (i.e., 14-68292183-CT-C) is reported in gnomAD with extremely low allele frequency of 4.05×10^{-6}, which represents one allele count of 1 in 247,159 alleles and has not been reported to exist in the homozygous state (Lerario et al., 2020; Naslavsky et al., 2017). The presence of this variant was screened by Sanger sequencing in other members of this family. As expected from the exome sequencing results, the father (I-1) and unaffected siblings (II-2, II-3, II-6, and II-8) were heterozygous for this variant (**Figure 1B**). Moreover, the *RAD51B*-c.92delT variant was not found in 235 fertile Brazilian women controls screened by Sanger sequencing. No other clearly pathogenic variant, which could underlie the phenotype, could be identified in this family.

These analyses, carried out in collaboration with Dra. Mendonca, suggest that c.92delT variant in RAD51B could be responsible for the development of POI in this family.

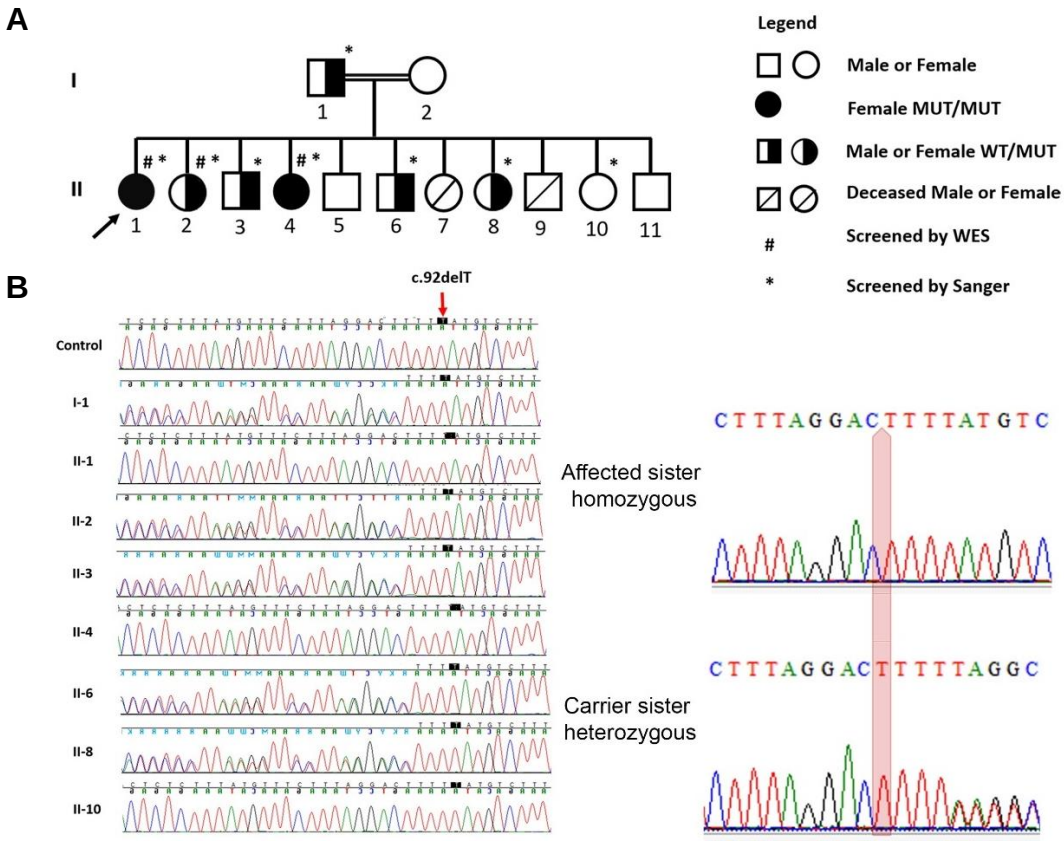

Figure 1. Identification of the variant c.92delT of *RAD51B*. **(A)** Family Pedigree. A homozygous recessive variant in *RAD51B* was shown to be present in two sisters from Brazil affected with POI. The black arrow indicates proband (II-1). Pedigree numbers of individuals are indicated below the symbols. Samples sent for WES are indicated by a hash (#). Sanger electropherograms confirmed the presence of the homozygous variant in both affected sisters II-1 and II-4. **(B)** The affected sister was confirmed to be homozygous for the *RAD51B* c.92delT variant whereas her sisters were heterozygous. Examples of chromatogram are displayed in the right panel.

1.2. RAD51B-c.92delT leads to translation re-initiation

RAD51 is a member of the RAD51 protein family. RAD51 paralogues are essential for DNA repair by HR. RAD51B has been shown to form a complex with the paralogues RAD51C, RAD51D and XRCC2 (BCDX2 complex) (Bonilla et al., 2020).

In silico analysis predicts that the c.92delT variant in RAD51B would provoke the appearance of a PTC potentially leading to the production of a very short, truncated protein. This short form of RAD51B with only 39 aminoacids out of a total of 350 aminoacids would lack most of the protein including the two Walker motifs essential for its ATPase activity (Wiese et al., 2006) (Figure 2A). Given that the constitutive KO of *Rad51b* in mouse is embryonic lethal (Shu et al., 1999), we hypothesized that the translation might restart in one of the three in-frame AUG codons (AUG39, AUG55, and AUG64) that exist downstream. In order to check this hypothesis and have a somatic cell model of the disease, we generated lymphoblastoid cells derived from the affected and unaffected sister making use of the classical infection of human B cells with the Epstein Bar Virus in vitro (Kieff & Rickinson, 2001). Lymphoblastoid cells were grown, and total RNA was extracted to amplify RAD5B cDNA from the lymphoblastoid cells derived from the affected and unaffected sister. The RAD51B ORFs were cloned in a mammalian expression vector. HEK293T cells were transfected with these constructs encoding RAD51B WT and RAD551B-c.92delT, and protein expression was analyzed by Western blot. This experiment showed the

production of a smaller band in the c.92delT construct than the main product resulting from the overexpression of the WT construct indicating that indeed the translation reinitiation is taking place (**Figure 2B**).

Considering the existence of three closed and in frame downstream AUG codons (AUG39, AUG55, AUG64) to the PTC, we decided to identify which AUG codon is responsible for the translation restart. To do that, we replaced by directed mutagenesis, the three secondary AUG codons (shown in red in the **Figure 2A**) with Alanines (individual and double Met to Ala substitutions) and protein expression was analyzed by Western blot. We observed that the band corresponding to the c.92delT translation only disappeared when replacing the codons underlying M64 to A64 but not when M39 or M55 were replaced by alanines (**Figure 2B**). These results showed that the RAD51B-c.92delT leads to translation reinitiation at Methionine 64.

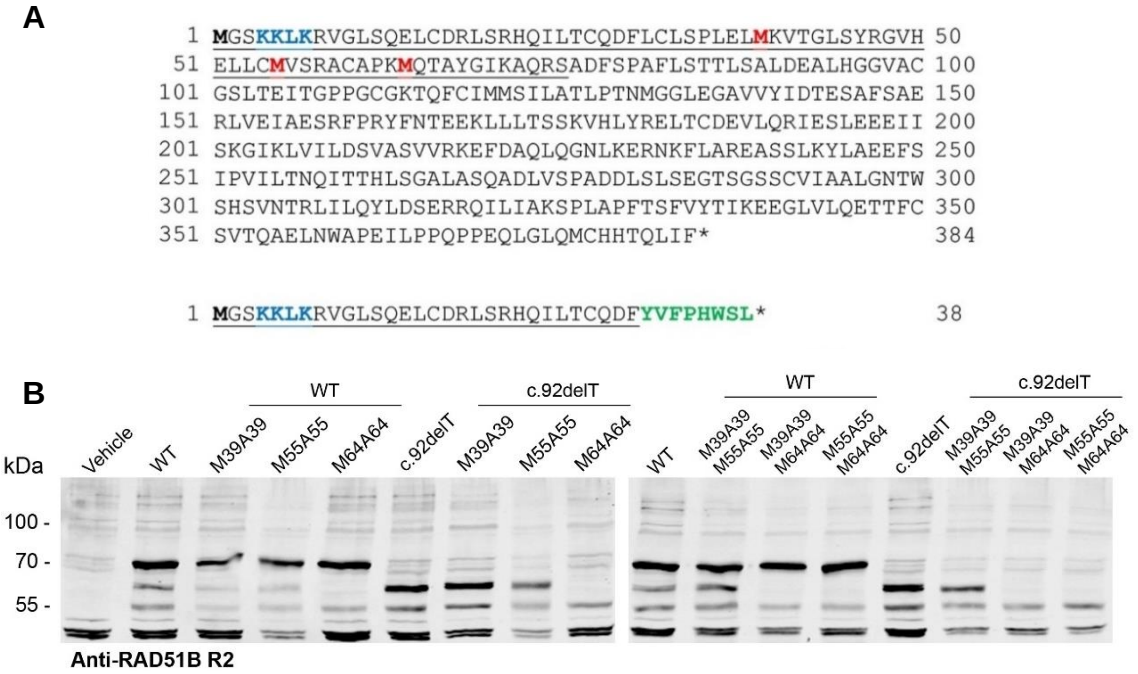

Figure 2. The variant *c.92delT* leads to translation re-initiation at Methionine 64. (A) The WT human RAD51B protein is 384 aa long. The known N-terminal part of the protein involved in protein-protein interaction with RAD51C is underlined. The nuclear localization sequence (NLS) is marked in blue. The downstream methionines (M39, M55, M64) are in red. The putative c.92delT mutant protein sequence without re-initiation of the translation is shown below (38 residues long). **(B)** HEK293T cells were transfected with the different variants of RAD51B: the WT form (WT), the c.92delT form and both the WT and c.92delT forms in which the three secondary Methionines were mutated into Alanines (individual Methionine to Alanine substituting the M39 to A39, the M55 to A55 and the M64 to A64; double Met to Ala substitutions following the above argument, both M39A39 and M55A55, both M39A39 and M64A64 and both M55A55 and M64A64. Of note, the bigger size of the RAD51B products is due to the presence of GFP tag (27 kDa).

In order to demonstrate the translation of the RAD51B-c.92delT endogenous protein and considering that we failed to detect by Western blot and immunofluorescence (IF) endogenous RAD51B protein with commercial or even home-made antibodies (see *Methods and Material 4.5 section*), we analyzed by IP-coupled with Mass spectrometry (MS) human lymphoblastoid cells extracts from c.92delT and WT/c.92delT *RAD51B*. Our results clearly showed the presence of peptides corresponding to the C-terminal of RAD51B-c,92delT protein, demonstrating that *in vivo* translation in the presence of the PTC is taking place (**Table 1**).

RAD51B peptides Sequence	Position	LFQ intensity RAD51B-WT/c.92delT	LFQ intensity RAD51B-c.92delT
KEFDAQLQGNLK	218-229	5442.3	16019
LILQYLDSERR	308-318	25023	86063
LVILDSVASVVR	206-217	0	15087
SPLAPFTSFVYTIK	325-338	56743	62268

Table 1. RAD51B peptide identification in human extracts. Protein extracts from *RAD51B*$^{WT/c.92delT}$ and *RAD51B*$^{c.92delT/c.92delT}$ lymphoblastoid cells (human extracts) were immunoprecipitated with home-made anti-RAD51B R2. The LFQ (label-free quantitation) intensity values of RAD51B-WT vs RAD51B-KI are shown.

Given that c.92delT translation is reinitiated at Methionine 64, the mutant RAD51B would lack the first 63 aminoacids including a NLS located at the N-terminal (**Figure 1A**, (K. A. Miller et al., 2005)). Thus, we decided to assess if the subcellular localization of the RAD51B-c.92delT variant was altered. For this purpose, the human (**Figure 3A**) and murine (**Figure 3B**) RAD51B variant and the WT forms (fused to GFP and untagged) were expressed in Cos7 cells and their corresponding subcellular localization was analyzed in detail. RAD51B-c.92delT displayed lower ratio of nuclear to cytoplasmic labelling in comparison to the WT, indicating that the absence of the NLS in the RAD51B-c.92delT variant partially delocalized RAD51B from the nucleus to the cytoplasm.

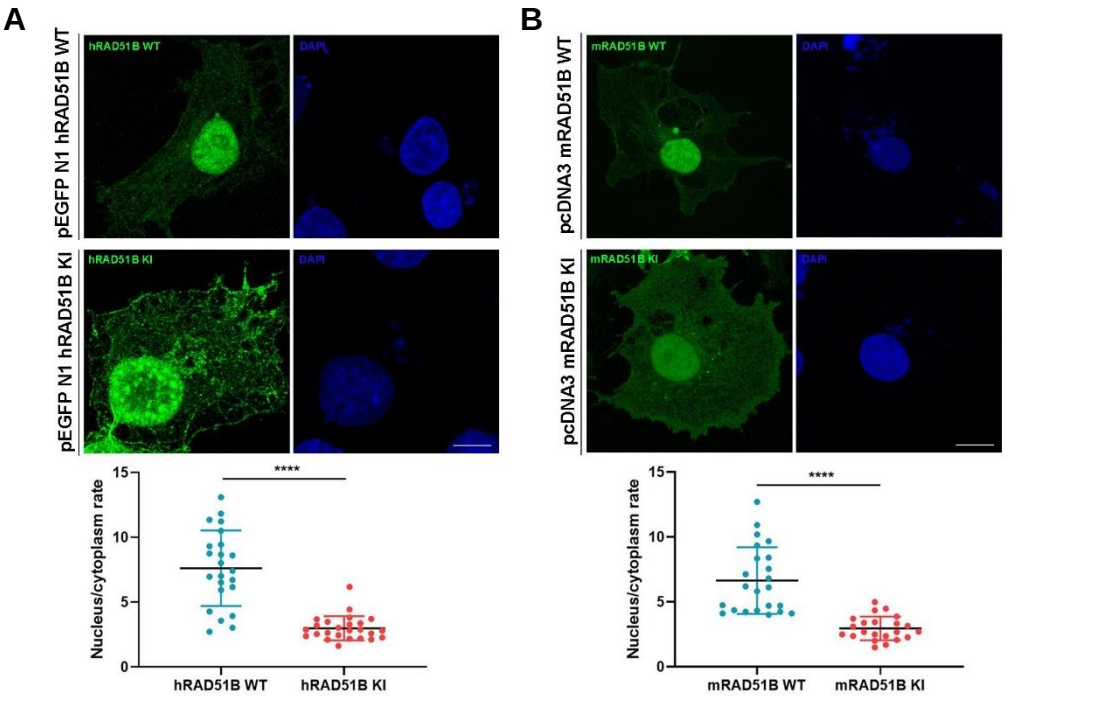

Figure 3. The variant c.92delT leads to altered nuclear localization. COS7 cells were transfected to express human **(A)** and murine **(B)** WT or mutant RAD51B fused to GFP tag. The WT construct showed a robust nuclear signal in addition to a faint cytoplasmic pattern. In contrast, the mutant variant displayed a strong delocalization of the nuclear signal to the cytoplasm. Quantification of the nucleus/cytoplasm signal rate is shown in the lower plot. Scale bars: 20 µm. hRAD51B-c.92delT variant is referred as hRAD51B-KI for simplicity. Welch´s t-test analysis: ns, non-significant differences; ****p<0.0001.

1.3. *Rad51b-c.92delT* mice were viable and fertile

Considering the observed results from human lymphoblastoid cells and in order to evaluate if the RAD51B-c.92delT variant was the cause of the POI phenotype in the two affected sisters we generated a humanized KI mouse *Rad51b*$^{c.92delT/c.92delT}$ by CRISPR/Cas9 editing (**Figure 4A**). For this

purpose, two sgRNAs were designed targeting exon 3 of *Rad51b* in combination with a single-stranded oligodeoxynucleotide (ssODN) containing humanized residue to study the human variant identified in the consanguineous family (for further details go to *Methods and Material 2.2 section*).

Although RAD51B is essential for mouse development (Shu et al., 1999), humanized KI mice were viable, showed no early somatic phenotype, and were born with the expected Mendelian ratios (**Supplementary Table 4**). These results strongly suggests that the reinitiation of the translation using a secondary downstream AUG codon is also operating in this mutant mouse model. In order to validate that the mutant allele was being transcribed after edition, we carried our RT-PCR amplification using testicular cDNA derived from *Rad51b*$^{c.92delT/c.92delT}$ and WT mice (**Figure 4B**).

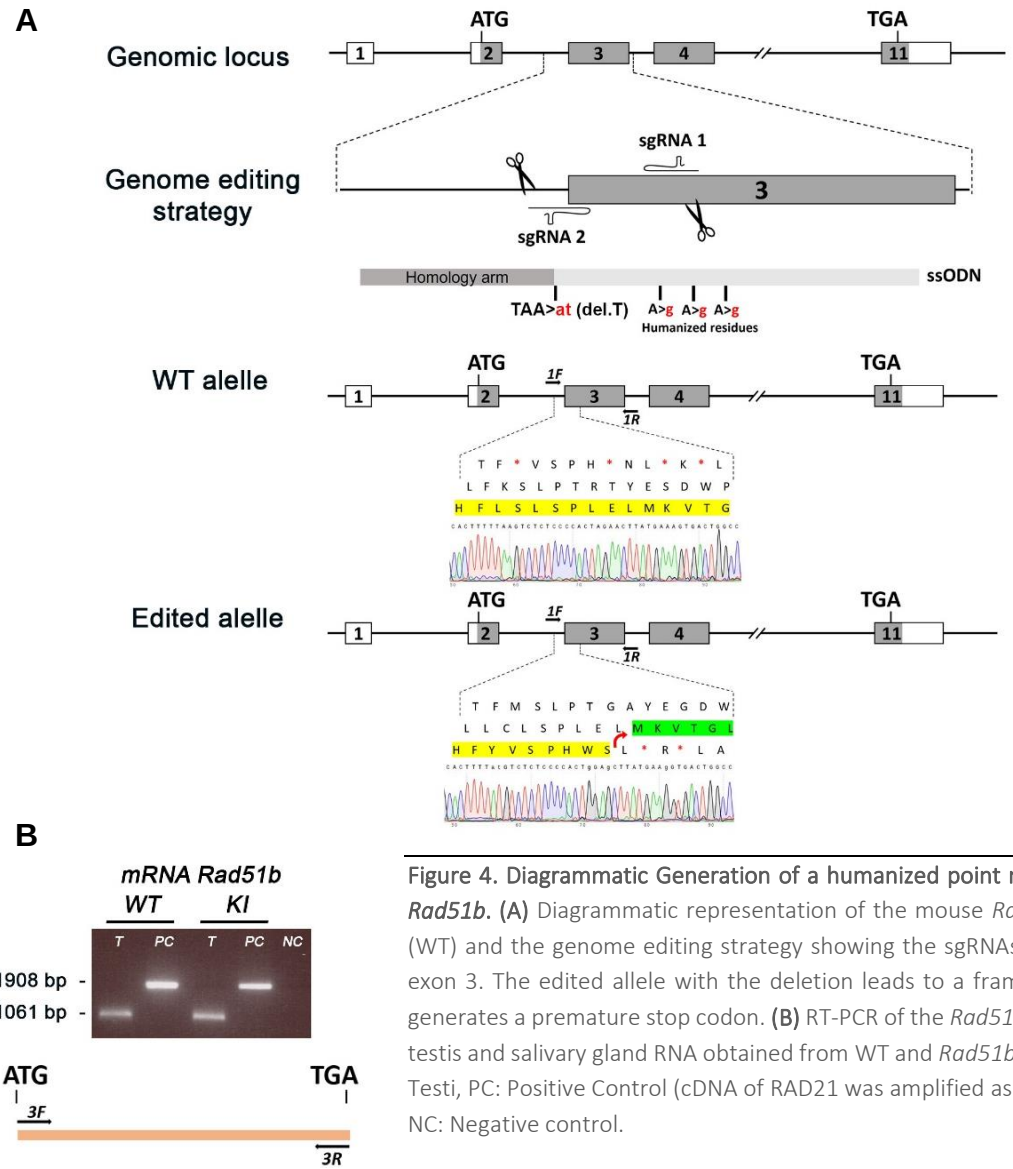

Figure 4. Diagrammatic Generation of a humanized point mutation in *Rad51b*. (A) Diagrammatic representation of the mouse *Rad51b* locus (WT) and the genome editing strategy showing the sgRNAs located in exon 3. The edited allele with the deletion leads to a frameshift that generates a premature stop codon. (B) RT-PCR of the *Rad51b* ORF from testis and salivary gland RNA obtained from WT and *Rad51b*$^{KI/KI}$ mice. T: Testi, PC: Positive Control (cDNA of RAD21 was amplified as a control) , NC: Negative control.

As shown in **Figure 4**, the expected band was similarly obtained in RNAs from both mutant and wild type mice confirming the transcription of the RAD51B-c.92delT variant.

Next, we attempted to evaluate the impact of the c.92delT variant in mouse fertility. For this purpose, we established mattings of *Rad51b*$^{c.92delT/c.92delT}$ males and females with *Rad51b*$^{WT/WT}$ females and males, respectively. The presence of vaginal plug was monitored daily, and the litters obtained together with the number of the pups of each litter was recorded. *Rad51b*$^{c.92delT/c.92delT}$ male and female mice were able to reproduce, but the fertility assessment in females showed a trend towards a reduction in the number of pups per litter (though not statistically significant) (Figure 5A). The histological analysis of adult mutant *Rad51b* testes revealed no apparent differences in the seminiferous tubules or in their epididymis in comparison to WT mice. Moreover, no morphological abnormalities of spermatogonia, spermatocytes, Sertoli, and Leydig cells were observed in *Rad51b*$^{c.92delT/c.92delT}$ mice (Figure 5B). In females, hematoxylin-eosin staining patters of ovaries were similar between mutant and wild-type mice (both at 5 dpp, in which primordial follicles are expected to be found, and at 3-months when the female ovary is fully mature). The quantification of the primordial follicles pool was also similar between genotypes (Figure 5C). Furthermore, the mutant ovaries also showed no difference in the number and maturation of follicles compared to WT mice at 4 months (Figure 5C). These results suggest that the c.92delT variant in *Rad51b* has some impact on mice fertility but not as severe as the POI phenotype (primary amenorrhea) observed in humans.

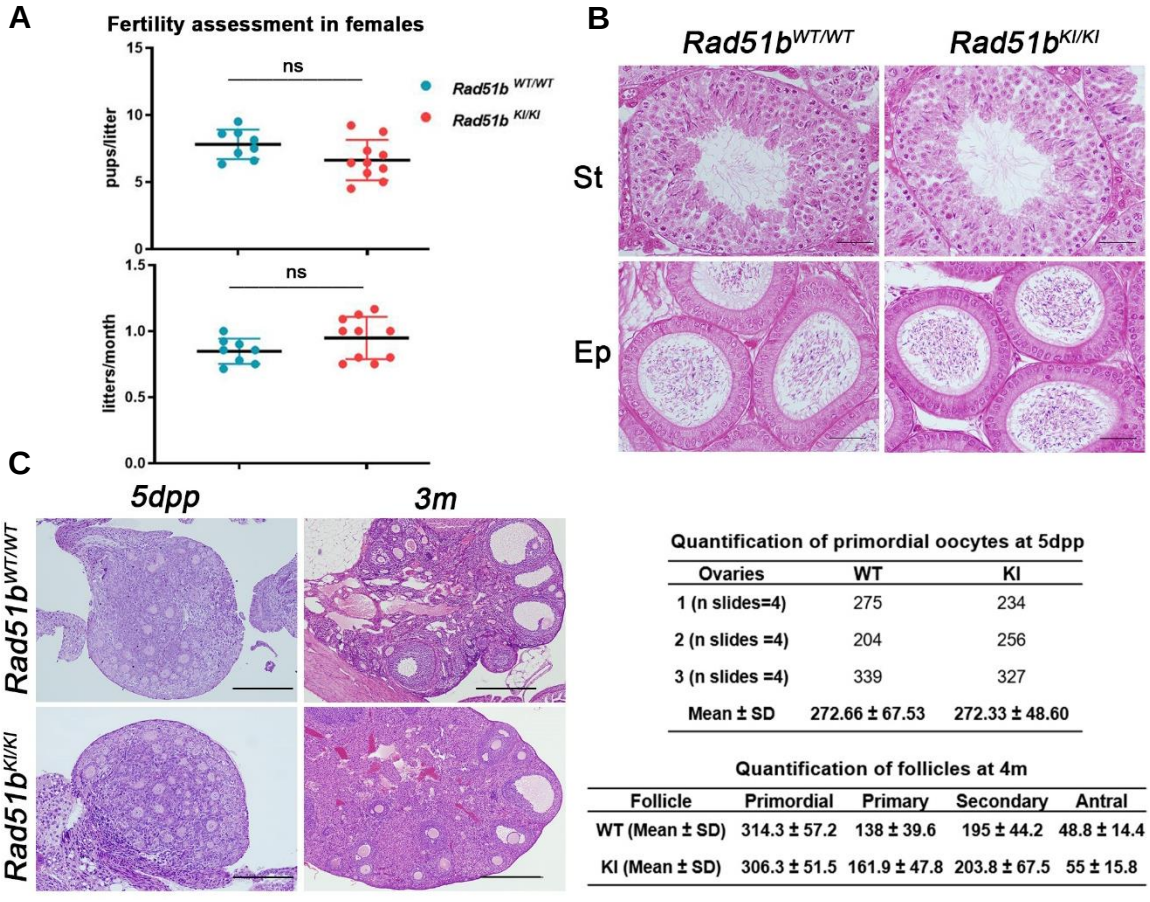

Quantification of primordial oocytes at 5dpp

Ovaries	WT	KI
1 (n slides=4)	275	234
2 (n slides =4)	204	256
3 (n slides =4)	339	327
Mean ± SD	272.66 ± 67.53	272.33 ± 48.60

Quantification of follicles at 4m

Follicle	Primordial	Primary	Secondary	Antral
WT (Mean ± SD)	314.3 ± 57.2	138 ± 39.6	195 ± 44.2	48.8 ± 14.4
KI (Mean ± SD)	306.3 ± 51.5	161.9 ± 47.8	203.8 ± 67.5	55 ± 15.8

Figure 5. Histologies of *Rad51b* mutant mice and fertility assessment of females. (A) Fertility assessment in female mice of WT and mutant *Rad51b*. Upper plot shows the number of pups per litter and the lower plot shows the litters per month. (B) *Rad51b* mutant male mice do not show alterations in PAS + Haematoxylin-stained testis sections. (St) Seminiferous tubules, (Ep) Epididymides. Bars in panels 20 µm. (C) Haematoxylin-eosin (HE) stained of mouse ovaries at 5 dpp and 3 months. Right panel: quantification of primordial oocytes at 5 dpp and quantification of follicles at 4 months old are described. Bars in panels 100 µm. *Rad51b*$^{c.92delT/c.92delT}$ variant is referred as *Rad51b*$^{KI/KI}$ for simplicity. Welch´s t-test analysis: ns, non-significant differences.

1.4. Humanized *Rad51b* mice show defects in the meiotic DNA repair process

Rad51b is expressed in somatic and reproductive tissues including meiocytes (see www.uniprot.org) but, unlike other members of the RAD51B family, a meiotic function has not been assigned to RAD51B yet. To further characterize the meiotic process in detail, we first analyzed *Rad1b*$^{c.92delT/c.92delT}$ meiocytes for the assembly and disassembly of the SC by monitoring the distribution of SYCP1 (central element) and SYCP3 (lateral element) labelling.

Our results showed no defects in synapsis and desynapsis from leptotene to diakinesis in spermatocytes and from zygotene to diplotene in oocytes (**Figure 6A and B**). However, when we perform the quantification of the stages of prophase I, we observed a reduced number of pachynemas accompanied by an elevated number of diplonemas in *Rad51b*$^{c.92delT/c.92delT}$ male and female meiocytes (**Figure 6C and D**). These results could indicate a subtle alteration of normal prophase I progression.

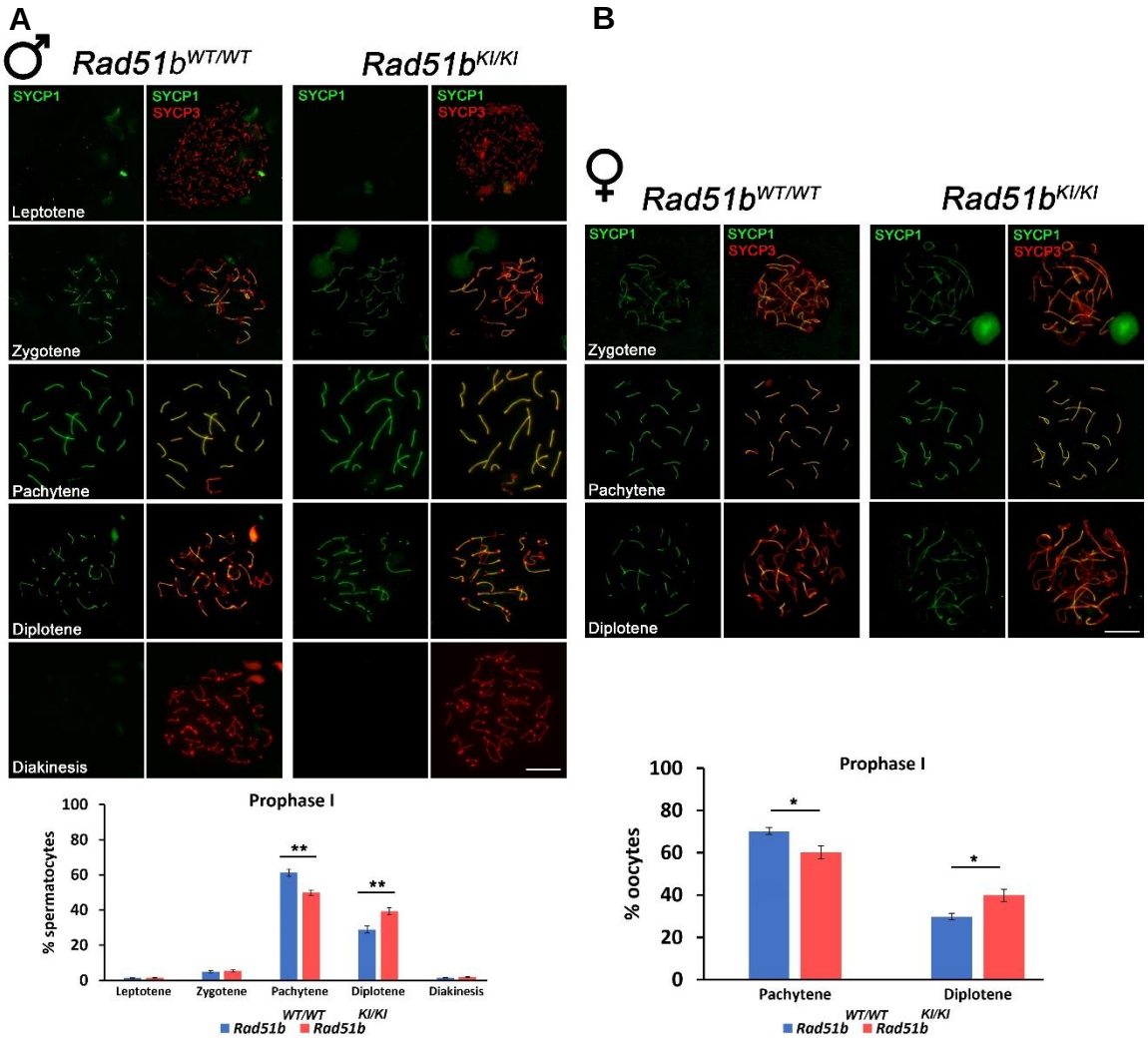

Figure 6. *Rad51b*$^{KI/KI}$ mice do not show synapsis defects but exhibit a delay in prophase I with accumulation of diplotenes. **(A)** and **(B)** Double immunolabelling of meiocyte spread preparations with SYCP1 (green) and SYCP3 (red), showing that meiotic prophase proceeds with no defects in synapsis/desynapsis in *Rad51b*$^{KI/KI}$ mutants. Plots below show the quantification of the different stages of the prophase I in spermatocytes and the quantification of the different stages of the prophase I in oocytes. *Rad51b*$^{KI/KI}$ mutant mice show a reduction of pachytenes and an accumulation of diplotenes. n=3. *Rad51b*$^{c.92delT/c.92delT}$ variant is referred as *Rad51b*$^{KI/KI}$ for simplicity. Welch´s t-test analysis: *p<0.05, **p<0.01. Bar in panels, 10 µm.

Considering that RAD51B is expressed during prophase I in both spermatocytes and oocytes (da Cruz et al., 2016; Niu & Spradling, 2020) and that in somatic cells the RAD51 paralogues play an important role in HR-mediated DNA repair (Suwaki et al., 2011), we decided to analyze the kinetics of DSB repair during meiotic recombination in the *Rad51b*$^{c.92delT/c.92delT}$ mice.

One of the first events of meiotic recombination is the generation of DSBs by the SPO11-TOPOVIBL complex at leptotene stage. An indirect way to measure DSB generation at this stage is by detecting phosphorylated histone H2AX (γH2AX) labelling. We observed similar labelling of γH2AX from leptotene to zygotene in mutant and WT spermatocytes (**Figure 7A**) indicating that DSBs are generated to a similar extent. However, γH2AX immuno-detection not only enables to mark DSBs formation but also their repair as well as synapsis and meiotic silencing of unpaired chromosomes. In this sense, we observed increased levels of labelling in both male and female c.92delT meiocytes at pachytene. This γH2AX accumulation was also observed in mutant oocytes at diplotene (**Figure 7B**). Altogether, these results could indicate the accumulation at the end of prophase I of DSBs that have not been repaired in both meiocytes.

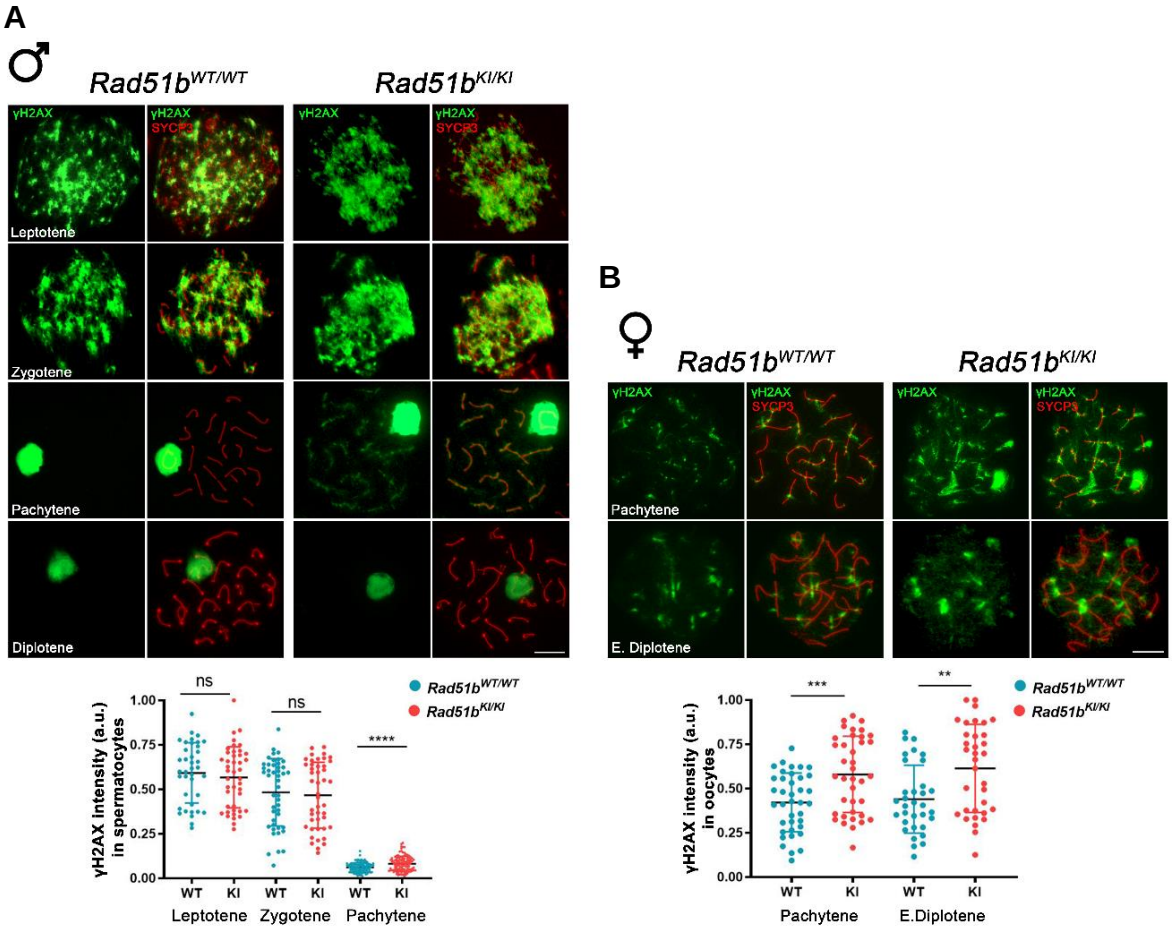

Figure 7. DSBs dynamics of *Rad51 c.92delT* mice in meiotic prophase I. Double immunolabelling of γH2AX (green) and SYCP3 (red) of **(A)** spermatocyte and **(B)** oocyte spreads from WT and mutant mice showing the accumulation of γH2AX in the mutant pachynemas. Plots below the panels show the quantification of γH2AX intensity in meiocytes. *Rad51b*$^{c.92delT/c.92delT}$ variant is referred as *Rad51b*$^{KI/KI}$ for simplicity. Welch´s t-test analysis: ns, non-significant differences; **p<0.01; ***p<0.001. Bar in panels, 10 µm. Quantifications at **Supplementary Table 5**.

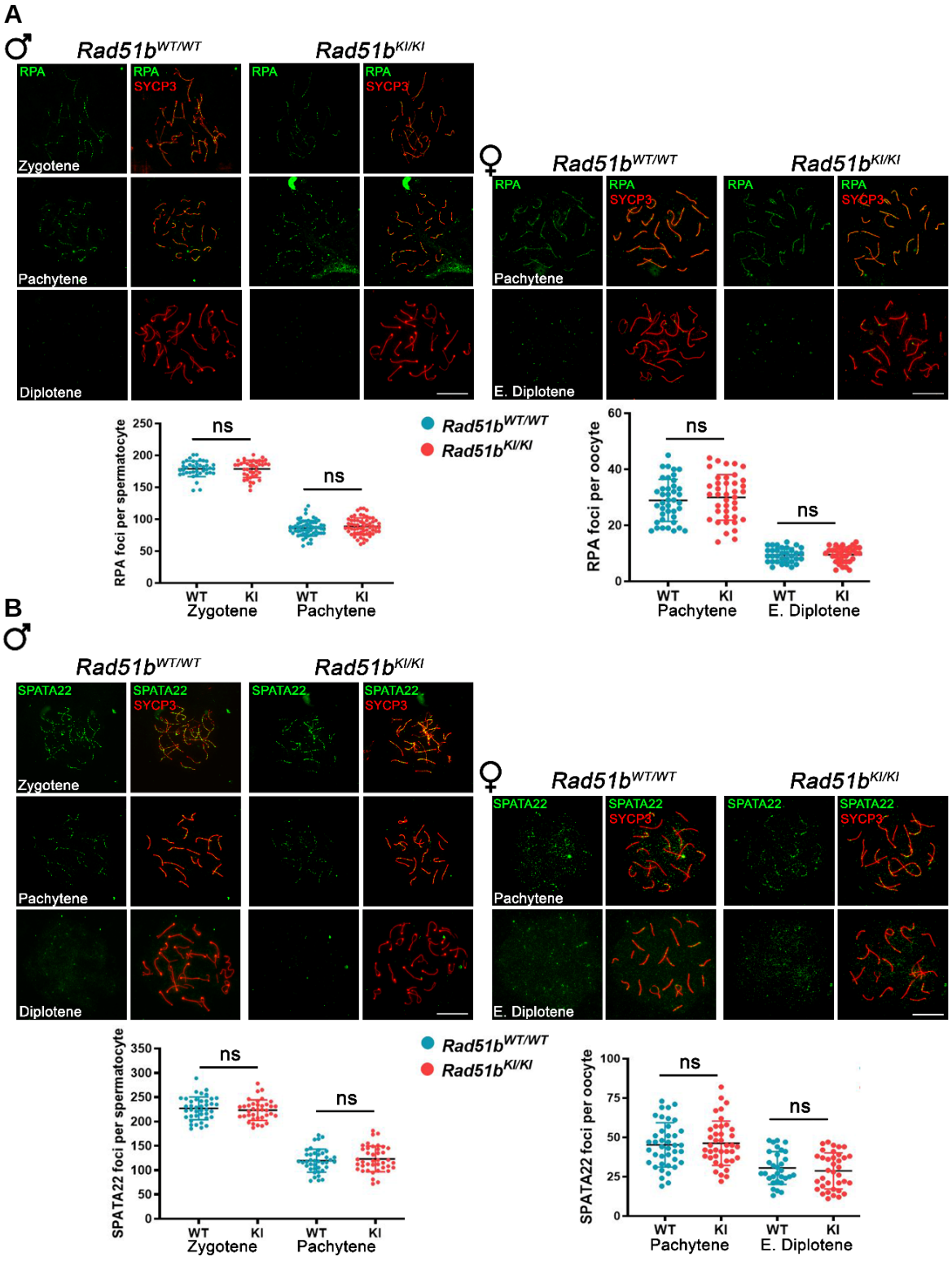

Figure 8. *Rad51b*$^{c.92delT/c.92delT}$ mice do not show no alterations in the labelling of RPA and SPATA22. (A) Double immunolabelling of RPA (green) and SYCP3 (red) in meiocyte spreads from mutant *Rad51b* and WT mice. (B) Double immunolabelling of SPATA22 (green) and SYCP3 (red) in meiocyte spreads from WT and KI mice. No significant differences between *Rad51b*$^{WT/WT}$ and *Rad51b*$^{KI/KI}$ were observed in meiocytes. Plots below each panel show the foci quantification of the labelling. *Rad51b*$^{c.92delT/c.92delT}$ variant is referred as *Rad51b*$^{KI/KI}$ for simplicity. Welch´s t-test analysis: ns, no significant differences. Bar in panels, 10 µm.

Repair of SPO11-induced DSBs by HR is orchestrated by BRCA2. By forming a central proteinaceous complex, BRCA2 governs the sequential recruitment of repair proteins to the DSBs, such as the initial binding of the single strand binding protein RPA for end resection, the exchange of RPA by RAD51/DMC1, and the loading of the complex MEIOB-SPATA22 to the RPA complexes with the interplay of HSF2BP and its interactor/stabilizer BRME1 (meiotic double-stranded break BRCA2/HSF2BP complex associated protein) (Brandsma et al., 2019; Felipe-Medina et al., 2020; Martinez et al., 2016; Zhang et al., 2019; W. Zhao et al., 2015). To study this process, we first analyzed the distribution of RPA and its associated protein SPATA22. Our results showed a normal distribution of RPA and SPATA22 labelling in *c.92delT* spermatocytes and oocytes suggesting that DSBs resection and ssDNA protection remain unaffected (Figure 8A and B).

Given the impossibility to detect the endogenous BRCA2 protein in the mice and thus also in our *Rad51b* mutant meiocytes, we analyzed by immunofluorescence the recombination proteins BRME1 and HSF2BP as an indirect readout. We observed that the labelling of both proteins was not affected in zygotene in WT and c.92delT spermatocytes, but they were accumulated at late pachytene in mutant mice meiocytes and persisted at diplotene as cloudy axes (Figure 9A and B).

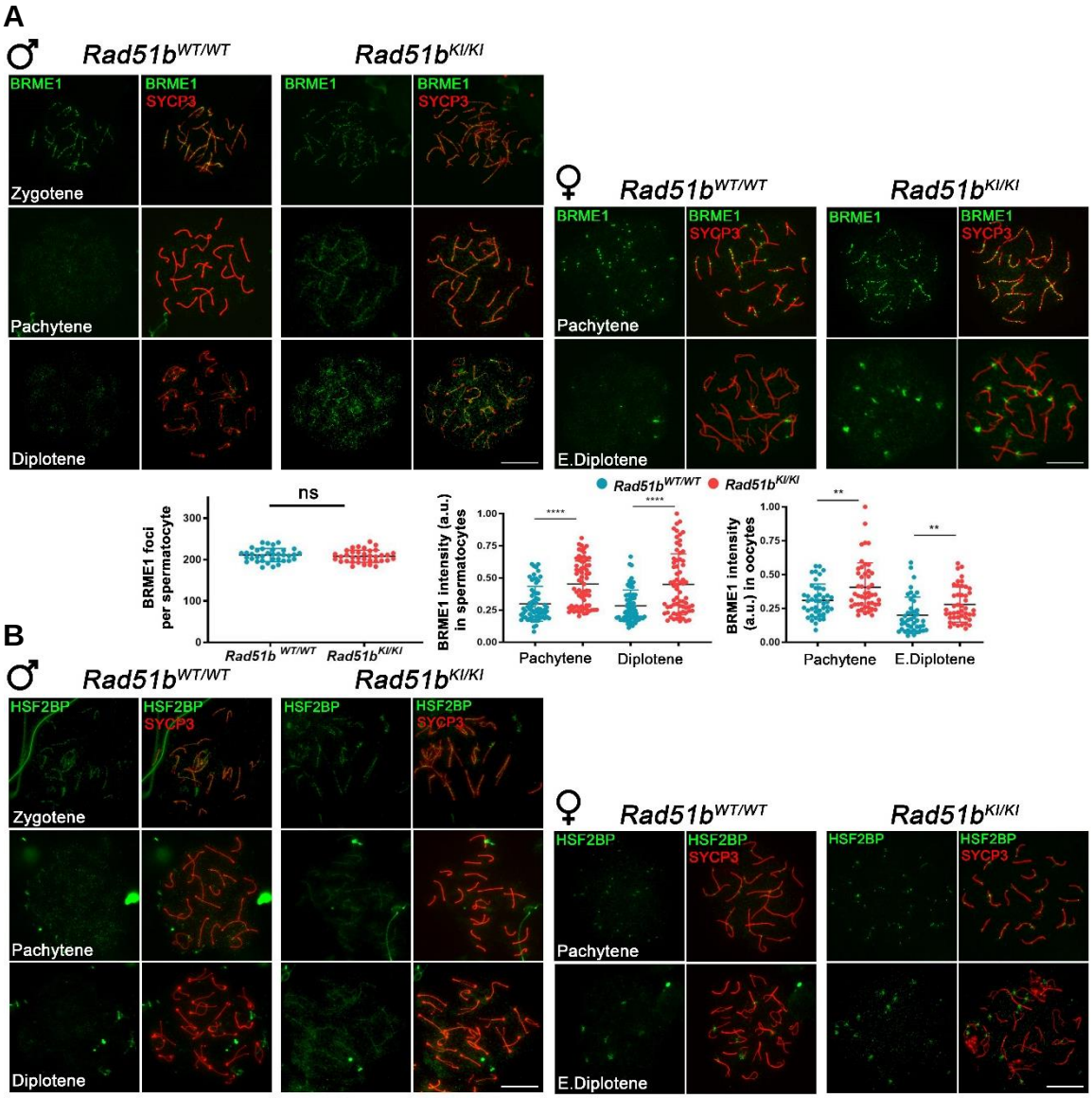

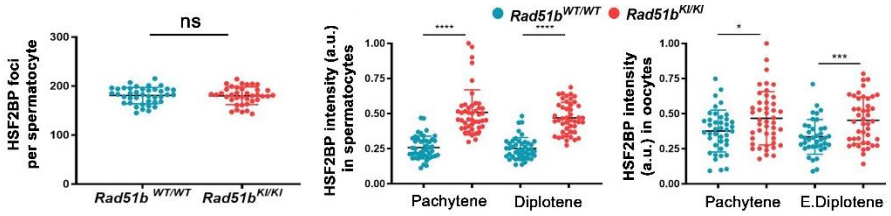

Figure 9. *Rad51b* mutant mice show an accumulation of BRME1 and HSF2BP. (A) Double labelling of BRME1 (green) and SYCP3 (red) of spermatocytes and oocyte spreads from WT and KI mice . **(B)** Double labelling of HSF2BP (green) and SYCP3 (red) of meiocyte spreads from WT and mutant mice. There is an accumulation of BRME1 and HSF2BP in mutant late pachynemas and diplonemas. Plots below the panels represent the quantification of both BRME1 and HSF2BP. *Rad51b*$^{c.92delT/c.92delT}$ variant is referred as *Rad51b*$^{KI/KI}$ for simplicity. Welch´s t-test analysis: ns, no significant differences; *p<0.05; **p<0.01 ***p<0.001; ****p<0.0001. Bar in panels, 10 µm.

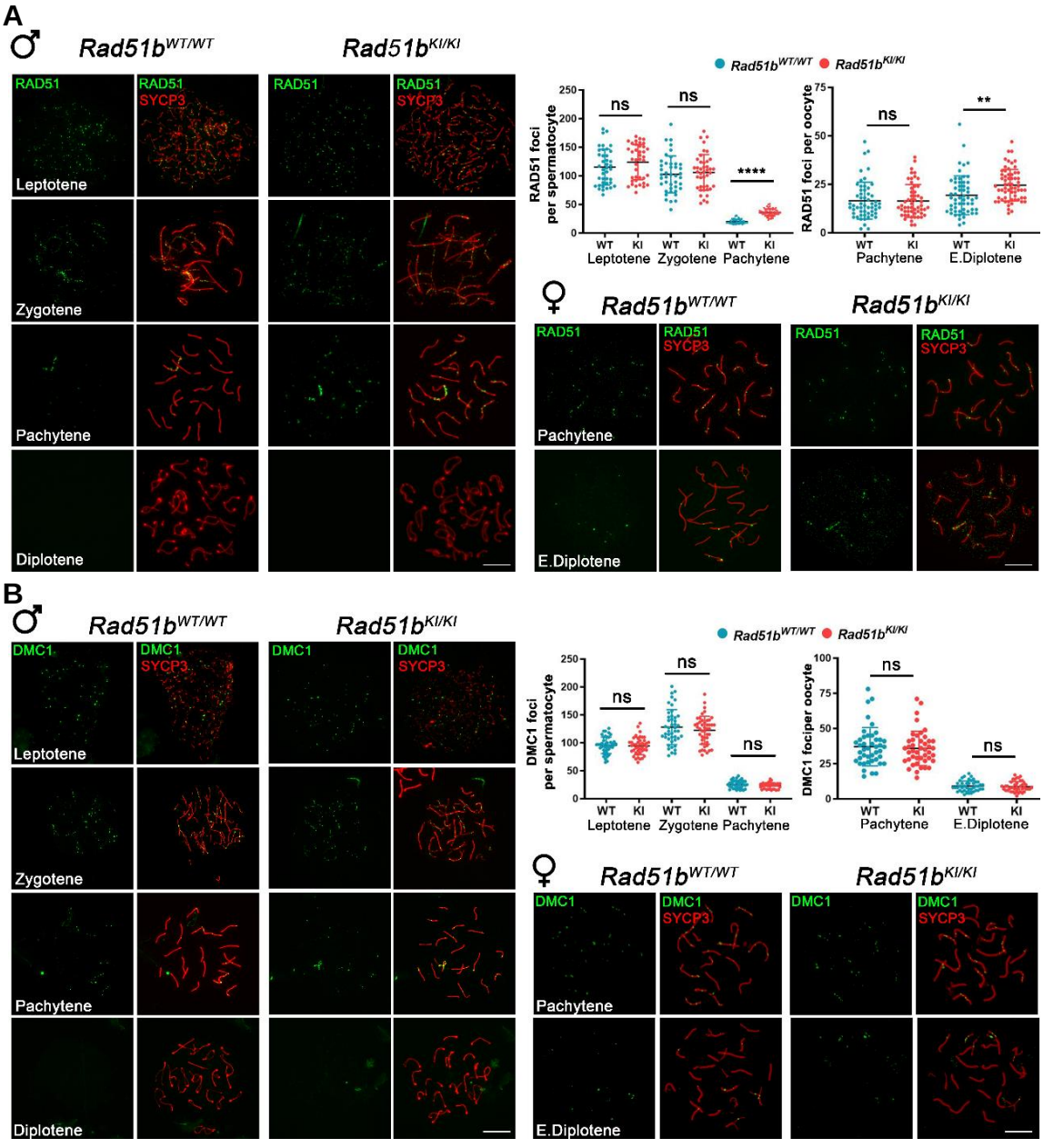

Figure 10. Kinetics of the recombinases RAD51 and DMC1 in *Rad51b*$^{c.92delT/c.92delT}$ mice. (A) Double immunolabeling of RAD51 (green) and SYCP3 (red) of spermatocyte and oocyte spreads from *Rad51*$^{WT/WT}$ and *Rad51b*$^{KI/KI}$. The

labelling of RAD51 foci at leptotene and zygotene is not altered, however RAD51 foci accumulate at pachytene in KI spermatocytes and at diplotene in KI oocytes. Plots above the panels represents the quantification of RAD51 foci. **(B)** Double immunolabeling of DMC1 (green) and SYCP3 (red) in spermatocyte and oocyte spreads from WT and mutant mice. The plots above the panel represent the quantification of DMC1 foci. *Rad51b*$^{c.92delT/c.92delT}$ variant is referred as *Rad51b*$^{KI/KI}$ for simplicity. Welch´s t-test analysis: ns, no significant differences; **p<0.01; ****p<0.0001. Bar in panels, 10 µm.

Then, we analyzed the recombinases RAD51 and DMC1 to assess the strand invasion process in our *Rad51b* mutant model. RAD51 foci formation was similar at leptotene and zygotene in WT and c.92delT meiocytes but foci persisted in pachytene nuclei in mutant spermatocytes and in diplotene nuclei in mutant oocytes, indicating a defect in DSBs repair (Figure 10A). By contrast, the meiotic recombinase DMC1, was not affected in mutant *Rad51b* meiocytes (Figure 10B). The accumulation of RAD51 but not DMC1 suggest that there could be an activation of a somatic-like HR DNA repair pathway at late-pachytene involving RAD51 but not DMC1 (Enguita-Marruedo et al., 2019), as described for other mouse mutants (i.e., HSF2BP and BRME1 (Takemoto et al., 2020; Zhang et al., 2019)).

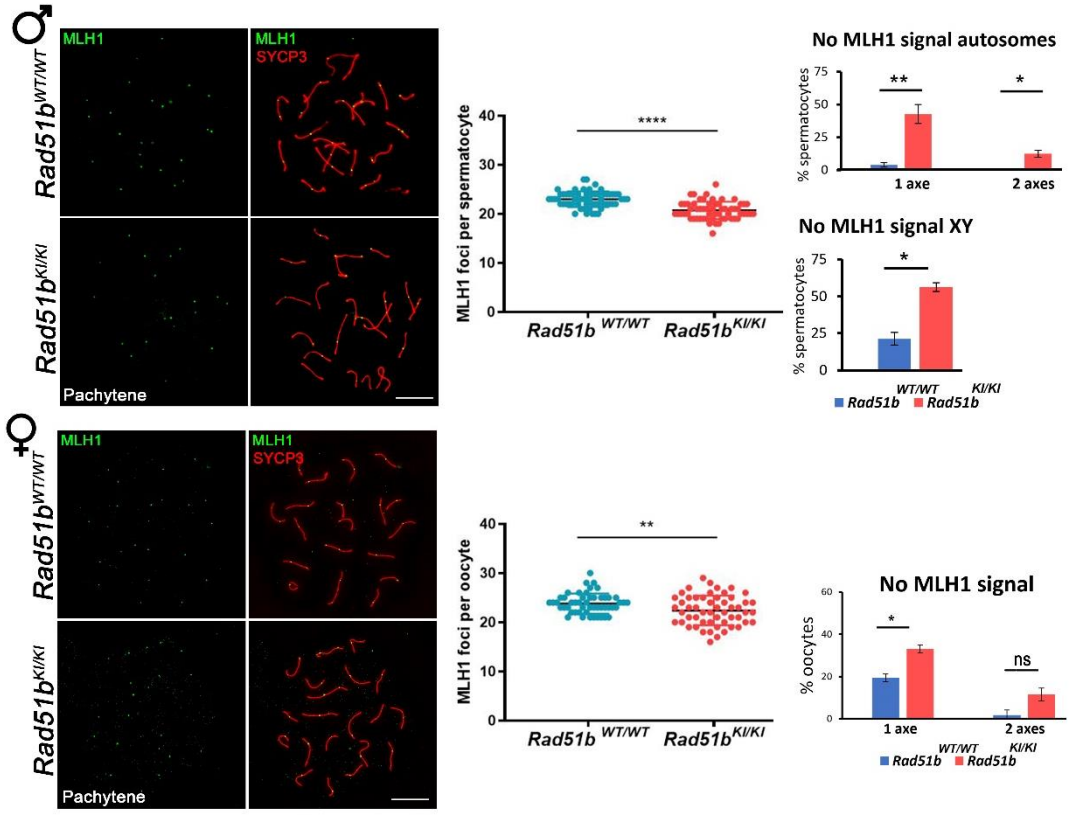

Figure 11. *Rad51b* mutant mice show an abnormal CO formation. Double labelling of MLH1 (green) and SYCP3 (red) of spermatocyte and oocyte spreads from *Rad51b*$^{WT/WT}$ and *Rad51b*$^{KI/KI}$. MLH1 foci are significant reduced in mutant *Rad51b* meiocytes. The plots on the right of the panels represent the quantification of MLH1 foci at pachytene in both male and female meiocytes. As well, the quantification of the % of spermatocytes and % of oocytes with any autosome or the sexual bivalent (males) without MLH1 signal. *Rad51b*$^{c.92delT/c.92delT}$ variant is referred as *Rad51b*$^{KI/KI}$ for simplicity. Welch´s t-test analysis: ns, no significant differences; *p<0.05; **p<0.01; ****p<0.0001. Bar in panels, 10 µm.

Meiotic recombination culminates with the formation of at least one CO per bivalent, thereby establishing the physical bonds (chiasmata) between homologous chromosomes necessary for proper segregation during the first meiotic division. To further elucidate the fate of the excess of

unrepaired DSBs in our mutant mice, we decided to analyze the distribution of MLH1 foci, a mismatch repair protein that marks future COs. We found a reduction on CO events in humanized mice compared to WTs in spermatocytes (KI: 20.70 ± 1.79 vs WT: 22.98 ± 1.61) and oocytes (KI:22.39 ± 3.01 vs WT: 23.82 ±2.02). We also evaluated the functional relevance of this reduction of COs by measuring the number of bivalents without MLH1 foci that would lead to univalents during metaphase I. Our results revealed an increased number of bivalents that did not show MLH1 foci in both mutant meiocytes (both sexual and autosomal bivalents) (**Figure 11**). Altogether, these results suggest that *Rad51b-c.92delT* causes an increase of DSBs that are not effectively repaired as COs in both spermatocytes and oocytes.

1.5. RAD51B interacts with the meiotic recombination machinery

To identify RAD51B interactors, we decided to immuno-precipitate RAD51B from mouse testis extracts coupled with MS (**Supplementary Table 6**) making use of our own developed antibodies. We identified RAD51C, in addition to RAD51B itself, a well-known interactor of RAD51B essential for meiotic recombination (S. G. Kuznetsov et al., 2009; K. A. Miller et al., 2004). Next, we adopted a complementary assay (candidate gene approach) to identify additional putative interactors of RAD51B. Thus, we decided to co-transfected in HEK293T the WT and c.92delT RAD51B with cDNAs encoding proteins involved in meiotic recombination: RAD51, HELQ, DMC1, BRCA2, PALB2, MEIOB, BRME1, HSF2BP, RPA and the MS identified protein RAD51C (**Figure 12**).

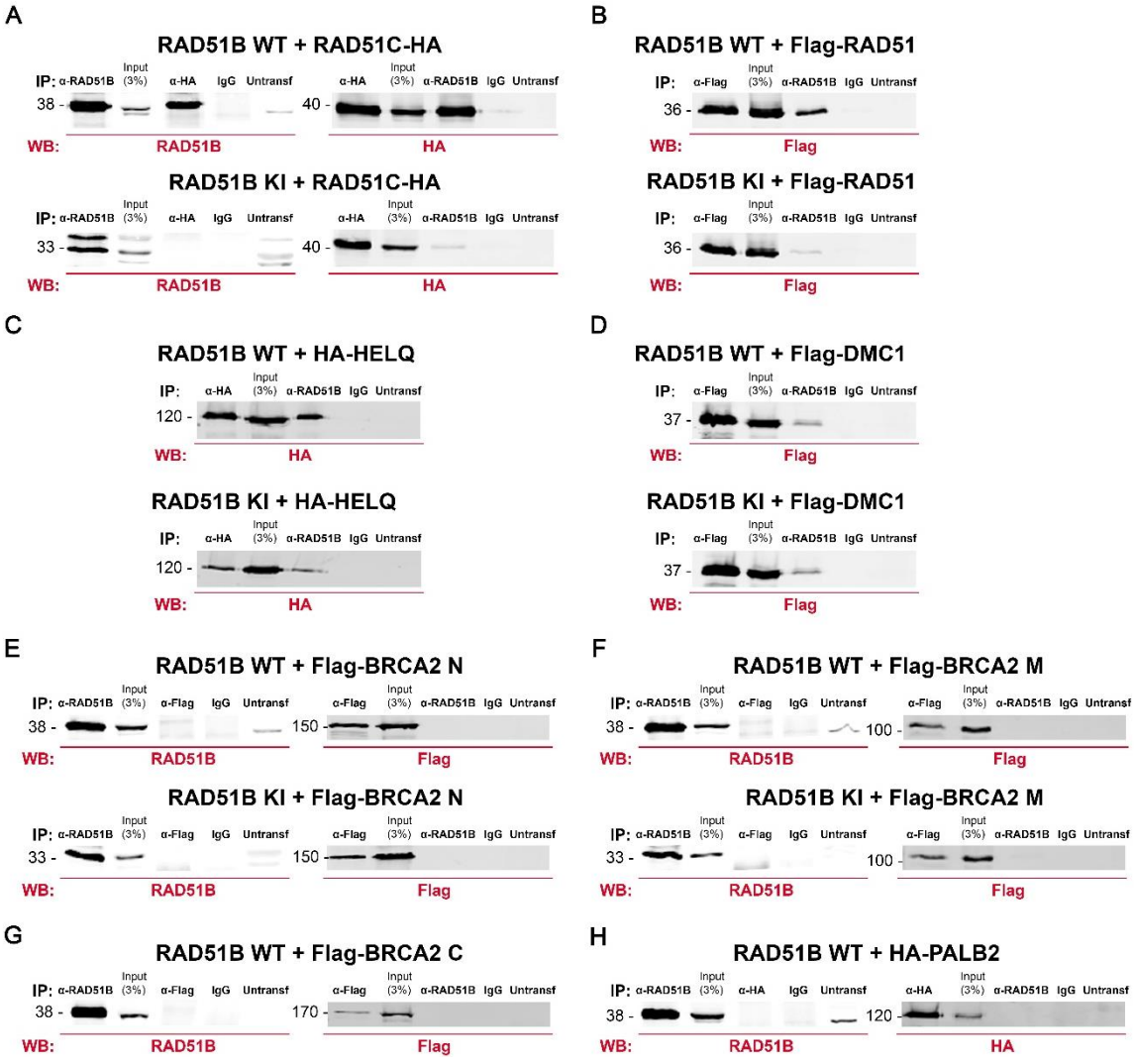

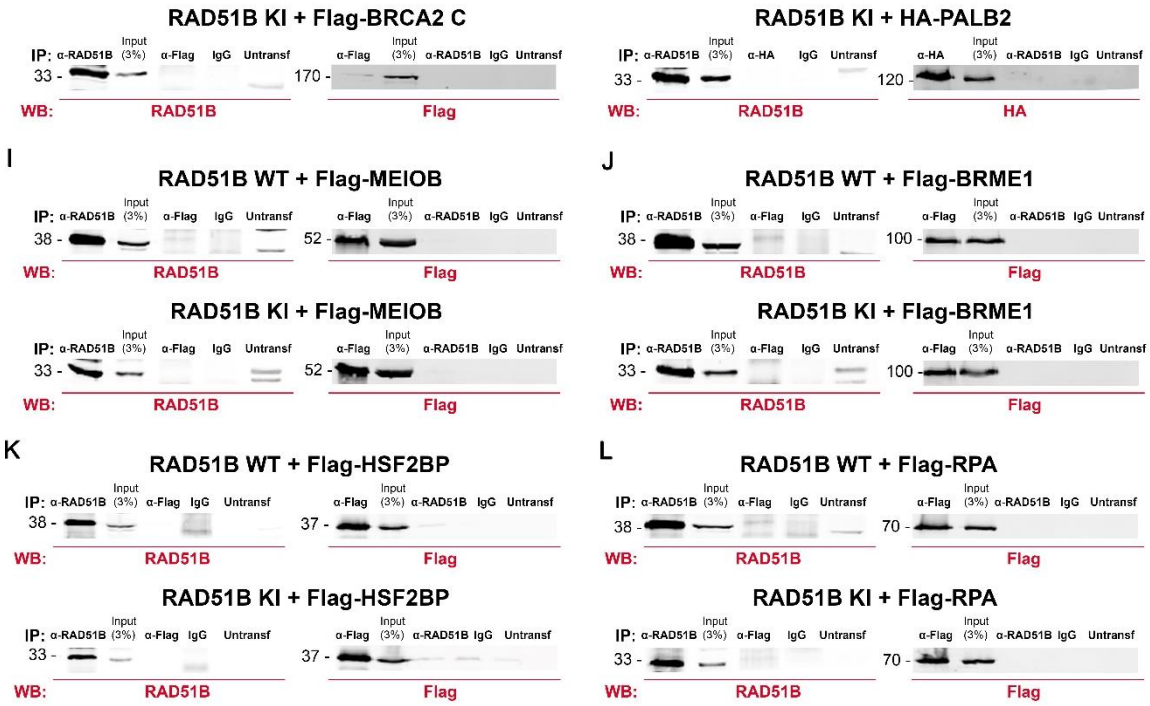

Figure 12. Interaction between RAD51B-c.92delT and RAD51C is lost and the interaction between RAD51-c.92delT and HR-specific interactors is reduced. HEK293T cells were co-transfected with either RAD51B-WT or RAD51B-c.92delT and different tagged-ORFs expressing potential interactors: **(A)** RAD51C-HA, **(B)** Flag-RAD51, **(C)** HA-HELQ, **(D)** Flag-DMC1, **(E-G)** Flag-BRCA2, **(H)** HA-PALB2, **(I)** Flag-MEIOB, **(J)** Flag-BRME1, **(K)** Flag-HS2BP and **(L)** Flag-RPA. Protein complexes were immunoprecipitated overnight with an anti-RAD51B, anti-Flag, anti-HA or IgGs (negative control), and analyzed by immunoblotting with the indicated antibodies. RAD51B-c.92delT variant is referred as RAD51B KI for simplicity.

As shown in **Figure 12**, we detected positive co-immunoprecipitations between RAD51B and RAD51C, RAD51, HELQ and DMC1. Given that the N-terminal part of RAD51B (residues 1-75) interacts with RAD51C (K. A. Miller et al., 2004), we analyzed the ability of mutant RAD51B to maintain this interaction. RAD51C immunoprecipitated WT RAD51B but not mutant RAD51B indicating that the c.92delT variant drastically diminishes or abrogates their interaction (**Figure 12A**). Similarly, RAD51B-c.92delT interaction was weaker with RAD51 and with the helicase HELQ (**Figure 12B and C**), but not with DMC1 (**Figure 12D**). This result is consistent with the normal distribution of DMC1 labelling in meiocytes, supporting the hypothesis of the activation of a somatic-like HR DNA repair pathway at prophase I involving RAD51 but not DMC1. We did not find co-immunoprecipitation with BRCA2, PALB2, MEIOB, BRME1, HSF2BP nor RPA (**Figure 12E-L**). Altogether, these results suggest that RAD51B acts in concert with DMC1/RAD51/RAD51C recombinases to mediate meiotic recombination.

1.6. RAD51B-c.92delT mouse and human cells are sensitive to MMC

Once we characterized the meiotic alterations produced by the presence of the c.92delT variant of *Rad51b* in mice and given that RAD51B is also expressed in somatic tissues, we decided to examine the possibility that RAD51B-c.92delT could alter somatic DNA repair. For that purpose, we test different DNA damaging compounds which might have a different DNA damage response in mutant MEFs. The results showed that mutant MEFs treated with ultraviolet light (UV) **(Figure 13A)**, Methyl methanesulfonate (MMS) **(Figure 13B)** or ionizing radiation (IR) **(Figure 13C)** have

no alterations in their growth rates in comparison with the WTs. Next, and in order to evaluate the repair of radiation-induced DNA damage, we irradiated MEFs with 5 Gy and followed the dynamics of DNA repair by labelling of γH2AX foci. The results show similar kinetics of γH2AX foci disappearance between mutant and WT MEFs **(Figure 13D)**. These results indicate that DNA damage induced by, UV, MMS and IR was repaired in the *Rad51b* mutant MEFs similarly to the wild-type controls.

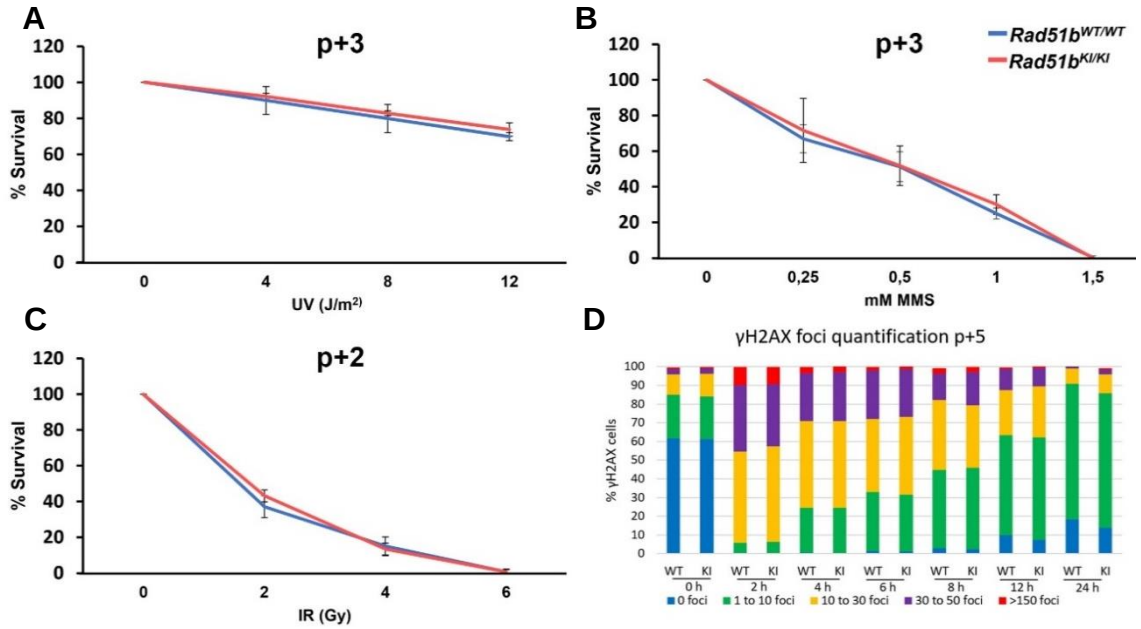

Figure 13. Primary *Rad51b* mutant MEFs did not show susceptibility to UV, MMS nor IR. (A) Cell proliferation assay of WT and mutant *Rad51b* primary MEFs at earlier passages 2 and 3 (p+2, p+3) incubated in presence of a continuous treatment with: **(A)** Ultraviolet irradiation (UV), **(B)** Methyl methanesulfonate (MMS) and **(C)** Ionizing radiation (IR) at the indicated doses. The results are expressed as a percentage relative to the control (untreated). Each point on the graphs represents the mean ± SD. **(D)** Quantification of γH2AX foci in WT and mutant *Rad51b* MEFs upon γ irradiation and performed at different time points: 0 hours: 0 h, 2 hours: 2 h, 4 hours: 4 h, 6 hours: 6 h, 8 hours: 8h, 12 hours: 12 h and 24 hours: 24 h. Cells were classified in 5 groups: 0 foci, 1 to 10 foci, 10 to 30 foci, 30 to 150 foci and >150 foci. n=3. *Rad51b*$^{c.92delT/c.92delT}$ variant is referred as *Rad51b*$^{KI/KI}$ for simplicity. Welch´s t-test analysis: no significant differences.

Defects in RAD51 and its paralogues RAD51C and XRCC2 have been associated with cancer predisposition and FA, which is a genetic disorder defined by cellular hypersensitivity to DNA crosslinking agents such as cisplatin or MMC (Ameziane et al., 2015; Park et al., 2016; Schlacher et al., 2012; Vaz et al., 2010). Other studies corroborate that RAD51 paralogues-deficient cells are hypersensitive to MMC (Chun et al., 2013; Garcin et al., 2019). Given this background, we decided to examine if the mutated *Rad51b* MEFs could be sensitive to this compound.

To do that, we decided to monitor the percentage of survival primary MEFs in presence of MMC. Our results show that primary *Rad51b*$^{c.92delT/c.92delT}$ MEFs have a relative lower growth rate in the presence of MMC in comparison with WT MEFs (**Figure 14A**). Then, we decided to carry out a clonogenic assay because this approach is widely used to test for the effects of drugs on the growth and proliferative features of cells. To this end, first, we immortalized MEFs with Simian Virus 40 (SV40) by retroviral infection. The resulting MEFs are able to surpass senescence, proliferate and form colonies when seeded at low density. Accordingly, mutant MEFs showed a reduced number of colonies when compared to WT MEFs (**Figure 14B**). In the light of these

results, we decided to evaluate if MMC sensitivity was caused by defects in DNA damage repair. To do that, we monitored the dynamics of disappearance of γH2AX foci after MMC treatment. As mentioned before, γH2AX is a marker of DSBs and in somatic cells is also a marker for DNA damage. The results of this experiment showed a delay in the disappearance pf γH2AX foci event at 72 hours after MMC treatment, indicating the presence of unrepaired DNA (**Figure 14C**).

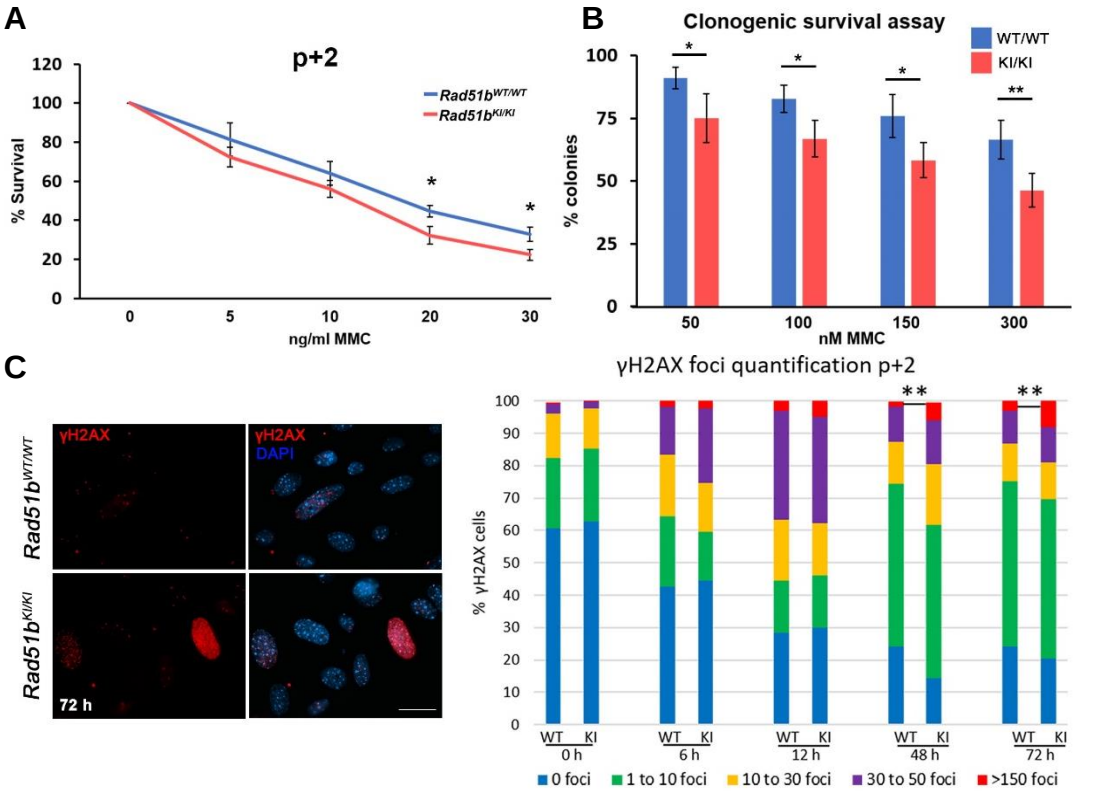

Figure 14. *Rad51b* mutant MEFs show susceptibility to MMC. (A) Cell proliferation assay of WT and mutant *Rad51b* primary MEFs at passage 2(p+2) incubated in presence of a continuous treatment with Mitomycin C (MMC) at the indicated doses. The results are expressed as a percentage relative to the control (untreated). Each point on the graphs represents the mean ± SD. *Rad51b*$^{c.92delT/c.92delT}$ variant is referred as *Rad51b*$^{KI/KI}$ for simplicity. Welch´s t-test analysis: *p<0.05. **(B)** Percentage of colonies obtained by clonogenic cell survival assays after treatment with MMC. The results are expressed as a percentage relative to the control (untreated) of *Rad51b*$^{WT/WT}$ and *Rad51b*$^{KI/KI}$ immortalized cells. **(C)** Representative γH2AX immunolabelling of WT and mutant *Rad51b* at 72 hours. Plot at the right indicates the quantification of γH2AX foci in *Rad51b* WT and mutant MEFs which was performed at different time points: 0 hours: 0 h, 6 hours: 6 h, 24 hours: 24 h, 48 hours: 48 h and 72 hours: 72 h. Cells were classified in 5 groups: 0 foci, 1 to 10 foci, 10 to 30 foci, 30 to 150 foci and >150 foci. n=3. *Rad51b*$^{c.92delT/c.92delT}$ variant is referred as *Rad51b*$^{KI/KI}$ for simplicity. Welch´s t-test analysis: *p<0.05; **p<0.01. Bar in panel, 10 µm.

Defects in DNA repair mechanism is a hallmark of a type of genetic disorders known as chromosomal breakage syndromes which are usually transmitted in an autosomal recessive mode of inheritance (Kaseb et al., 2022). We wanted to check if our POI family could also be included in this group of genetic disorders.

Given the observed persistence of DNA damage *Rad51-c.92delT* MEFs and the recessive inheritance of the RAD51B variant in the POI family, we decided to evaluate chromosomal breakage events in mutant MEFs and in patient-derived lymphoblastoid cells in the presence of MMC. Our results show that MMC treated MEFs from *Rad51b*$^{c.92delT/c.92delT}$ have more chromosome break events (passage 2 and passage 4) and confirms that the mutant MEFs are

unable to repair efficiently the MMC-induced DNA damage (**Figure 15A**). These results were also mirrored in the *RAD51B*$^{c.92delT/c.92delT}$ immortalized lymphoblastoid cells from the affected patient (II-4) which also displayed more chromosome break events in comparison with the heterozygous cells (unaffected sister (II-2)) in the presence of MMC and even in its absence (**Figure 15B**).

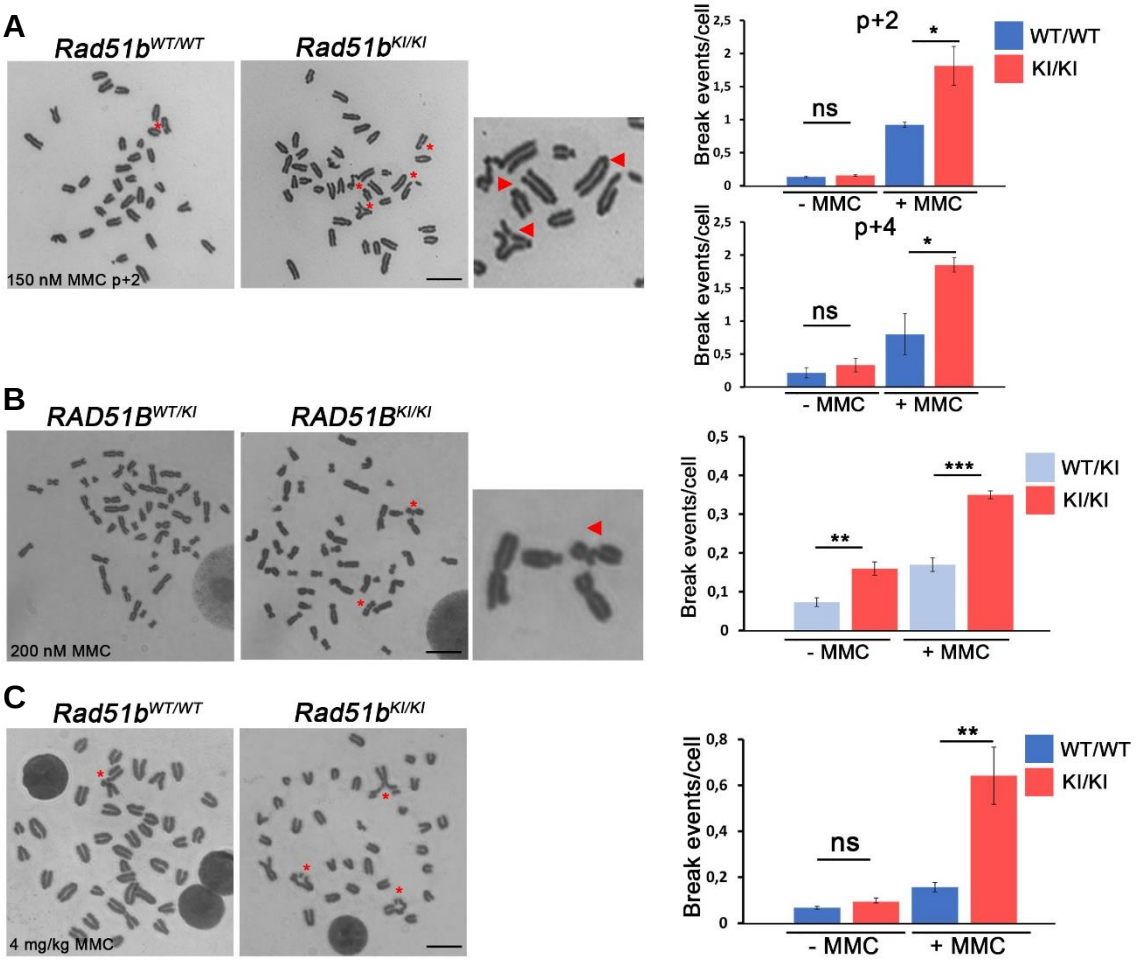

Figure 15. MMC-induced CIN in *RAD51B-c.92delT* cells and in explanted bone marrow. (A) Evaluation of metaphase chromosome breaks/gaps from primary *Rad51*$^{WT/WT}$ and *Rad51b*$^{KI/KI}$ MEFs after MMC treatment (150nM). Red triangles mark chromosomes abnormalities in the magnification of the mutant *Rad51b*. Right panels show the quantification of breaks/gaps at passage 2 and 4 (p+2, p+4). **(B)** Homozygous *RAD51B-c.92delT* human-derived lymphoblastoid cells showed more chromosome alterations with and without MMC treatment (200nM) in comparison with the corresponding heterozygous sister (II-2). n=3. **(C)** Evaluation of metaphase chromosome aberrations from explanted bone marrow cells from *Rad51b*$^{WT/WT}$ and *Rad51b*$^{KI/KI}$ after intraperitoneal injection of MMC. In addition, to breaks/gaps, triradial chromosomes were observed only in the mutant mice (shown by red asterisks). n=3. *Rad51b*$^{c.92delT/c.92delT}$ variant is referred as *Rad51b*$^{KI/KI}$ for simplicity. Welch´s t-test analysis: ns, no significant differences; *p<0.05; **p<0.01; ***p<0.001. Bar in panel, 10 µm.

Considering these results, we next evaluated whether the c.92delT variant also affects genome stability *in vivo*. For this purpose, WT and mutant *Rad51b* mice were intraperitoneally injected with MMC, and metaphases preparations were directly prepared from bone marrow following standard procedures protocol (Akeson & Davisson, 2000). Our results show a significant increase in the number of chromosome break events per cell from *Rad51b*$^{c.92delT/c.92delT}$ MMC-treated mice in comparison with the WT mice (**Figure 15C**). Overall, these results confirm that the homozygous *RAD51B*-c.92delT variant leads to an impaired repair of MMC-induced DNA damage and as a consequence an increase level of chromosomal instability *in vitro* and *in vivo*.

As stated above, the covalent linkage between opposite strands of DNA or ICLs are induced by MMC stress. This type of DNA lesion can block the progression of replicative DNA helicases (Q. Li et al., 2021). To further assess the involvement of *Rad51b-c.92delT* in replication fork homeostasis, we analyzed its susceptibility to hydroxyurea (HU) and the specific DNA polymerase inhibitor Aphidicolin, two inducers of replication fork DNA damage (Howlett et al., 2005).

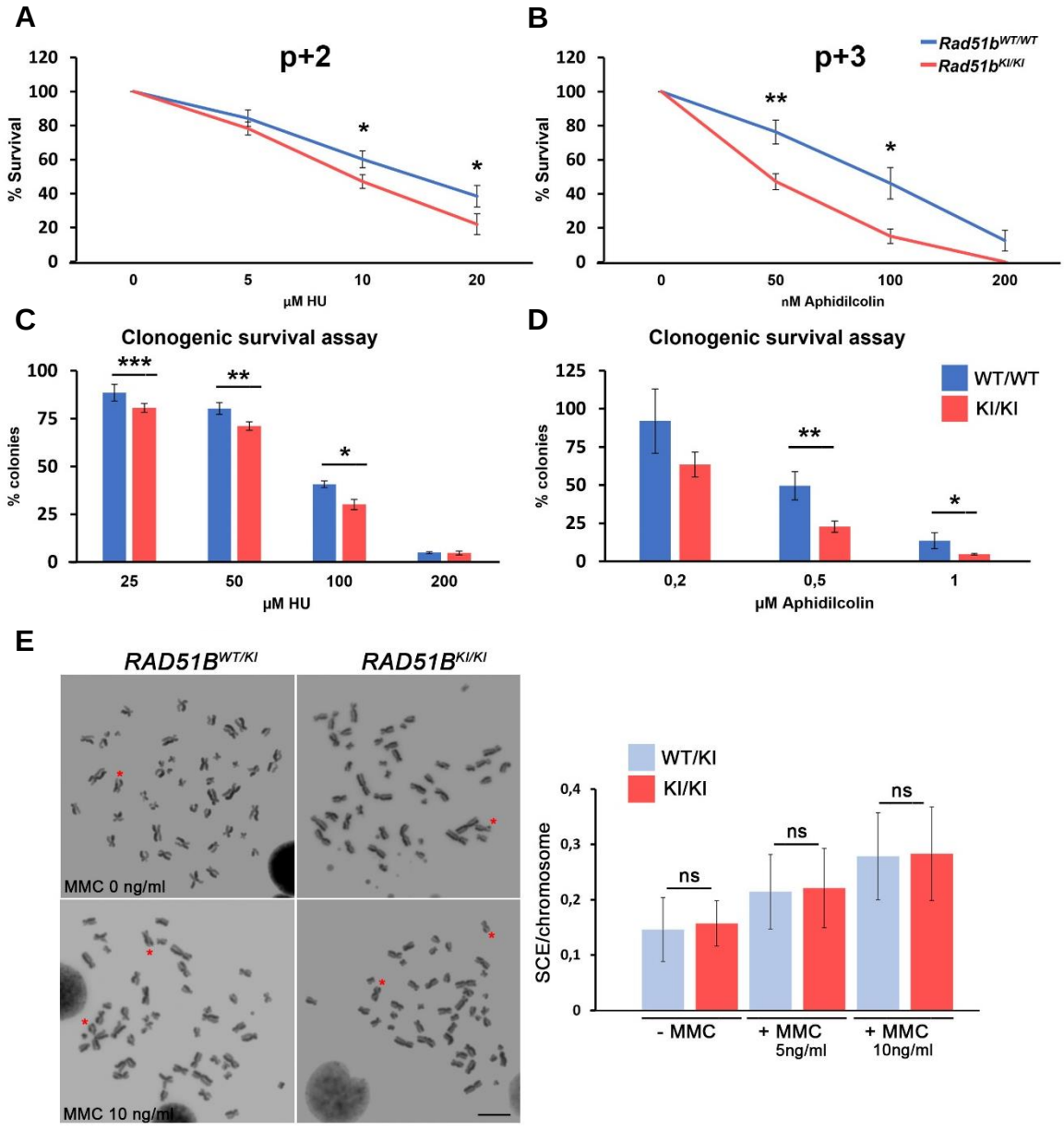

Figure 16. *Rad51b-c.92delT* MEFs are sensitive to inducers of replication fork DNA damage. Cell proliferation assay of WT and mutant *Rad51b* primary MEFs at passage 2 and 3 (p+2, p+3) incubated in presence of a continuous treatment with **(A)** hydroxyurea (HU) and **(B)** Aphidicolin. The results are expressed as a percentage relative to the control (not treated). Each point on the graph represents the mean ± SD. Percentage of colonies obtained by clonogenic cell survival assays after treatment with **(C)** HU and **(D)** Aphidicolin at the indicated doses. The results are expressed as a percentage relative to the control (untreated) of *Rad51b*$^{WT/WT}$ and *Rad51b*$^{KI/KI}$ immortalized MEFs. **(E)** Sister chromatid exchange (SCE) per chromosome after treatment with MMC. Orange acridine staining were visualized under FITC filter and images are shown in black and white. SCE are marked by red asterisks (*). Right plot show SCE per chromosome. *Rad51b*$^{c.92delT/c.92delT}$ variant is referred to as *Rad51b*$^{KI/KI}$ for simplicity. Welch´s t-test analysis: ns, non-significant differences; *p<0.5; **p<0.01, ***p<0.001. Bar in panel, 10 µm.

Our results show that both drugs produce a lower percentage of survival in the c.92delT MEFs (**Figure 16A and B**) as well as a reduced number of colonies in a clonogenic survival assay (**Figure 16C and D**). These results are consistent with RAD51B playing a role in replication fork homeostasis.

It is accepted that RAD51 interacts with HR proteins to protect stalled replication forks from nucleolytic attacks (Cortez, 2019; Schlacher et al., 2012). This function in replication stress is genetically uncoupled from their canonical role in DSB repair (Schlacher et al., 2011; A. T. Wang et al., 2015). Given the involvement of the RAD51 paralogues in the canonical pathway of HR between sister chromatids (Takata et al., 2001) we assessed SCE in RAD51B-c.92delT lymphoblastoid cells in presence or not of MMC treatment. We observed no differences between the WT and RAD51B-c.92delT cells even in presence of MMC (**Figure 16E**).

1.7. Reprogramming efficiency is decreased in mutant *Rad51b-c.92delT* MEFs

The exogenous expression of the Yamanaka reprogramming factors (Takahashi & Yamanaka, 2006) induce genomic instability in part by generating DSBs. This fact can explain why low replication stress and an intact HR pathway are needed for an efficient reprogramming process (González et al., 2013; Ruiz et al., 2015). Having regard to these observations, we decided to evaluate the role of *Rad51b* during reprogramming. To do this, we retroviral infected the Yamanaka factors to primary MEFs and after 2-3 weeks we evaluate the number of iPSC colonies with alkaline phosphatase staining which is a marker of pluripotency. We observed a ~2-fold reduction in the number of alkaline phosphatase positive colonies in in *Rad51b-c.92delT* MEFs in comparison with the WT primary MEFs (**Figure 17**). We decided to pick colonies with iPS-like morphology (3D shape, defined borders and refringence) and we were able to establish *Rad51b*-c.92delT mutant iPS cell lines with comparable efficiency to WT controls, suggesting that they are similarly functional *bona fide* iPS clones. These results showed that the reprogramming efficiency is decreased in *c.92delT* MEFs providing a finding in the genome instability surrounding the c.92delT variant in RAD51B.

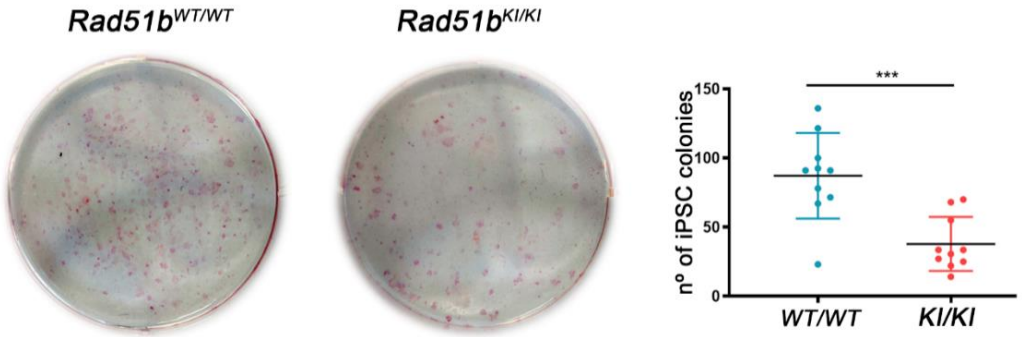

Figure 17. *Rad51b-c.92delT* leads to a reduced reprogramming efficiency of MEFs. MEFs from the indicated genotypes were infected with the 3 reprogramming factors (KLF4, OCT4 and SOX2) and the numbers of alkaline phosphatase positive colonies were counted showing a significantly reduction (up to ~2 fold) in *RAD51B-c.92delT* homozygous mutant MEFs in comparison with the wild-type. n=9. $Rad51b^{c.92delT/c.92delT}$ variant is referred as $Rad51b^{KI/KI}$ for simplicity. Welch´s t-test analysis: ***p<0.001.

1.8. *Rad51b-c.92delT* mice show increased incidence of pituitary hyperplasia

All the somatic phenotypes observed in the mutant mouse and human cells such as MMC hypersensitivity, DNA repair delay, chromosomal instability, replication stress and low reprogramming efficiency are all hallmarks of genome instability. These defects in the

maintenance of genome stability can lead to malignant transformation (Y. Yao & Dai, 2014). In addition, and considering that one affected sister developed duodenal adenoma, we evaluated the incidence of spontaneous neoplasia in aged mice (from 18-22 months).

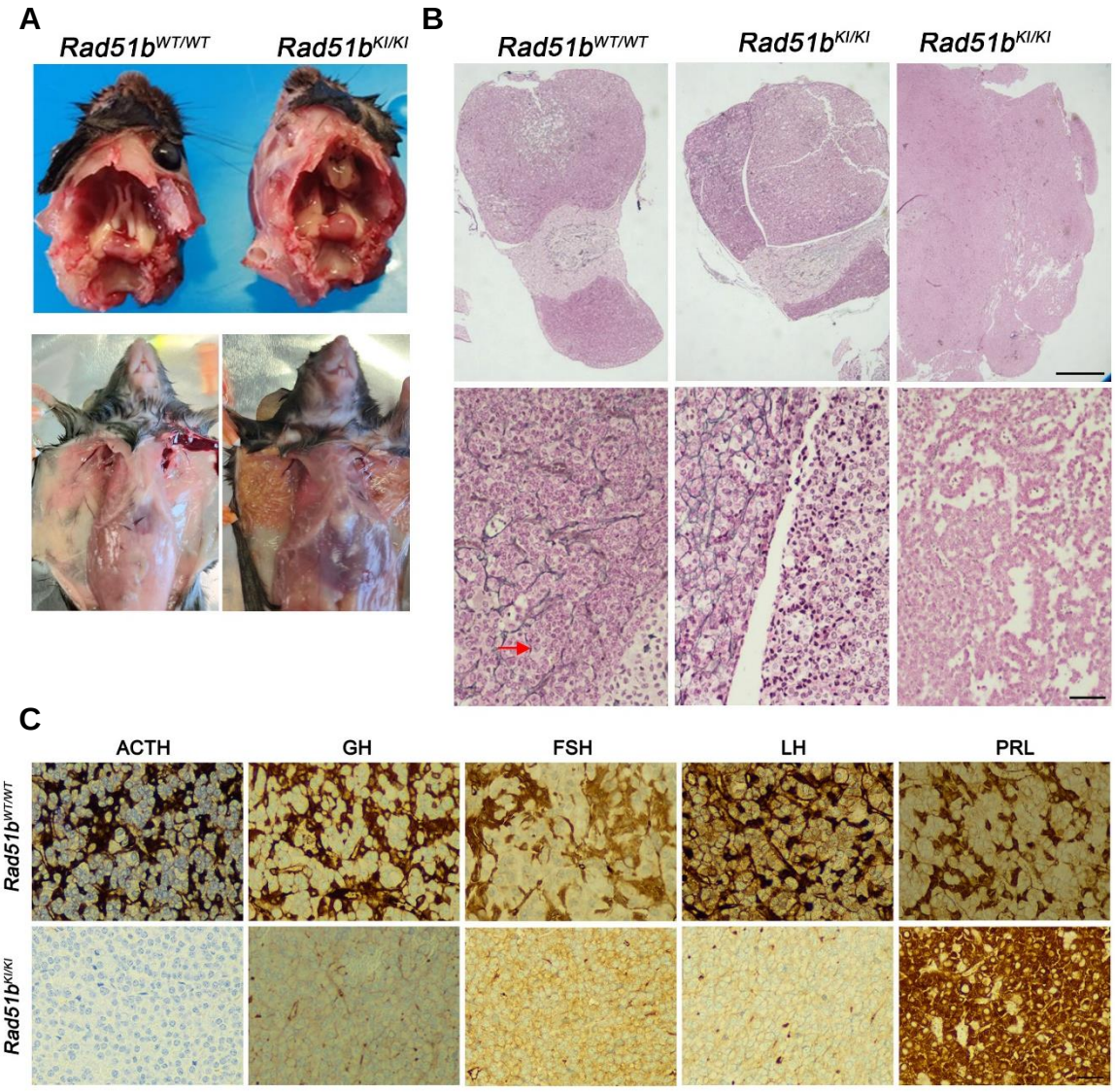

Figure 18. Humanized *Rad51b*$^{KI/KI}$ mice show an increased incidence of hyperplasia of the pituitary gland. **(A)** Macroscopic images of adenohypophysis from *Rad51b*$^{WT/WT}$ and *Rad51b*$^{KI/KI}$ mice. Below panel showing mammary tubules formation in KI mice when compared to WT at the same age. **(B)** Reticulin staining of pituitary adenohypophysis from WT and mutant *Rad51b*. Bar in upper panels 250 µm and in lower panels 50 µm. **(C)** Immunohistochemical detection of pituitary ACTH, GH, FSH, LH and prolactin hormones of WT and *Rad51b* mutant mice. *Rad51b*$^{c.92delT/c.92delT}$ variant is referred as *Rad51b*$^{KI/KI}$ for simplicity. Scale bar corresponds to 25 µm for all sections.

The results show the presence of pituitary hyperplasia and frequent adenomas of the pituitary gland in mutant homozygous mice (9 out of 14 in mutant mice vs 1 out of 12 in wild type). The *c.92delT* mice also developed mammary tubules when compared with WT mice at the same age (Figure 18A), suggesting hormonal alterations. These benign tumors ranged from micro to macroadenomas as shown by the reticulin staining pattern (Figure 18B). Reticulin staining of normal adenohypophysis outlines the supporting stroma around the blood vessels and shows regular meshwork interconnecting the capillaries. In contrast, reticulin staining of adenomatous

tissue shows a loss of meshwork or fragmentation (Noh et al., 2015). In the infrequent pituitary tumours from WT mice, reticulin pattern showed a partially loss of staining in zones of hyperplasia, where the cell size is increased (red arrow in Figure 18B). In contrast, microadenomas and macroadenomas from c.92delT mice showed a complete loss of reticulin staining pattern (right panel in Figure 18B).

As the pituitary gland is responsible of the secretion of several hormones such as Adrenocorticotropic hormone (ACTH), Growth hormone (GH), FSH, LH and prolactin (PRL), and given the development of mammary tubules in mutant mice, we undertook the characterization of the adenomas following a clinical diagnosis criterion. We observed normal staining for ACTH, GH, FSH and LH in c.92delT and WT mice. However, for PRL we observed that normal pituitary showed isolated positive cells unevenly distributed whereas c.92delT pituitary adenomas are predominantly composed of prolactin expressing cells (Figure 18C). Therefore, mutant mice developed pituitary hyperplasia and frequent adenomas, with typical features of prolactinomas. Interestingly, a germline RAD51B truncating mutation in a family with cutaneous melanoma also led to the development of a pituitary tumour (Wadt et al., 2015) and more recently a spontaneous genetic variant in human *RAD51B* has been recently associated with an increased risk of development of pituitary tumors (Juknytė et al., 2021).

2. Functional analysis of UCEs

UCEs are defined as highly conserved regions of the genome that are shared between evolutionary distant taxa, for example regions conserved between humans and fish. These conserved sequences were described for the first time by Gil Bejerano (Bejerano et al., 2004). These genetic elements are commonly located in overlapping exons in genes involved in RNA processing, or neighbouring non-coding regions of genes involved in transcription and development control.

For a genome region to be considered as a UCE it must have the following features:

- High degree of conservation.
- Not being a transcript (coding or non-coding) with functional properties at the RNA or protein level.
- Clustered around developmental genes.

As mentioned in the introduction, UCEs could have a functional role in chromatin remodelling, transcriptional regulation, interchromosomal interactions and in homologous recombination (Dermitzakis et al., 2005; Snetkova et al., 2022).

2.1. HS205 and HS1442 as potential candidates involved in fertility

There is a huge availability of information regarding human coding sequences (Craig Venter et al., 2001), whereas the availability of non-coding sequences is by far less abundant. For these reasons there is a need to validate potential regulatory elements that may be involved in physiological or pathological pathways.

Nowadays it is possible to predict the localization of candidate regulatory elements (i.e., enhancers) on a genome-wide scale thanks to the availability of whole genomes sequences and the advance comparative genomic tools (Abascal et al., 2020). Therefore, using these already developed methods it is possible to predict an enhancer function.

Few years ago, VISTA Enhancer Browser (https://enhancer.lbl.gov/) emerged as a powerful database on which non-coding fragments were validated for enhancer activity. The core data set of the VISTA Enhancer Browser consist in the identification of elements that are highly conserved among mammals and non-mammalian vertebrates (chicken, frog, and zebrafish). The enhancer validation consists in transgenic mouse assays. In these assays, the candidates' elements are amplified from genomic human DNA and cloned upstream of a heat shock protein 68 (Hsp68) which is a promoter that drives reporter gene expression when coupled with tissue-specific enhancers, and a *LacZ* reporter gene. This construct is then injected into mouse zygotes and the resulting embryos are collected at E11.5 and stained to visualize *LacZ* gene activity is evaluated (Pennacchio et al., 2006). Positive LacZ staining correlates with reporter gene expression indicating enhancers, which are then annotated with the standardized nomenclature for mouse development anatomy (Bard et al., 1998).

Making use of the advanced search of the VISTA Enhancer Browser, we found 13 positive enhancers with a restricted pattern to the genital tubercle, with HS205 and HS1442 being the ones with a higher *LacZ* activity. We decided to select these two regions in order to functionally analyze their role in gametogenesis and fertility. HS205 is located at chromosome 2 in humans

and chromosome 11 in mice and is flanked by the SPRED2 and MIR4778 genes. In the case of HS1442 it was found to be intragenic of KIFAP3 gene and located in chromosome 1 in both humans and mice.

2.1. HS205 and HS1442 show low enhancer activity

In order to validate the enhancer activity of HS205 and HS1442 we decided to create a construct containing the UCE (HS205 or HS1442) upstream coupled to Hsp68 and EGFP (**Figure 19**) mimicking the *LacZ* assays in mouse embryos mentioned above. We evaluate the enhancer activity of the UCE by measuring the EGFP intensity obtained by overexpressing the construct in the HEK293T and U2OS cell lines.

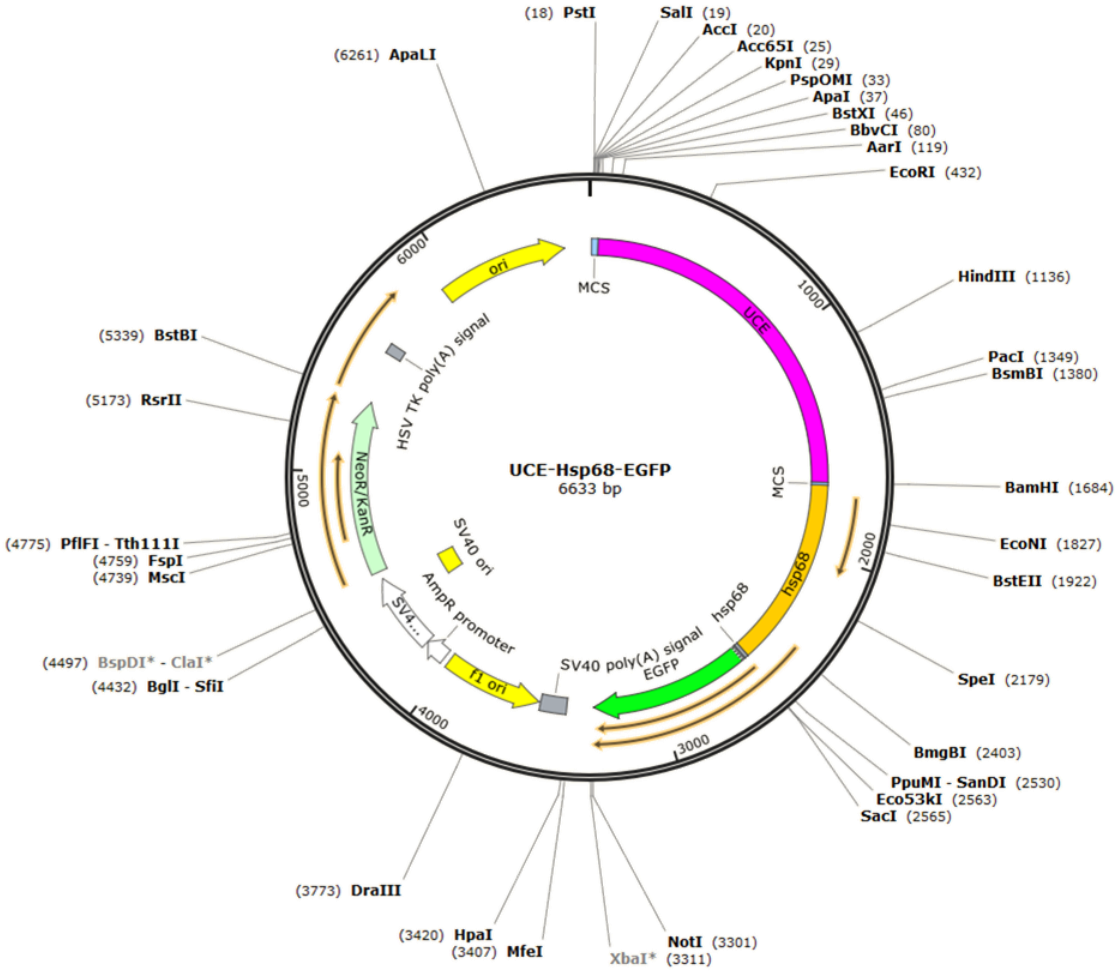

Figure 19. Map of the UCE-Hsp68-EGFP vector. Schematic representation of the plasmid UCE-Hsp68-EGFP map in which first the CMV of pEGFP-N1 was eliminate and insert the Hsp68 and the UCE (HS205 or HS1442) previously amplified by PCR from genomic mouse DNA (see *Methods 3.3.3*). In silico map made with SnapGene.

Our results showed that in presence of HS205 and HS1442 there was some enhancer activity (**Figure 20**), but the levels were very low when compared to the Empty vector (EV) used as a negative control. These results indicate that the GFP signal corresponding to enhancer activity is not promiscuous and could have some specificity.

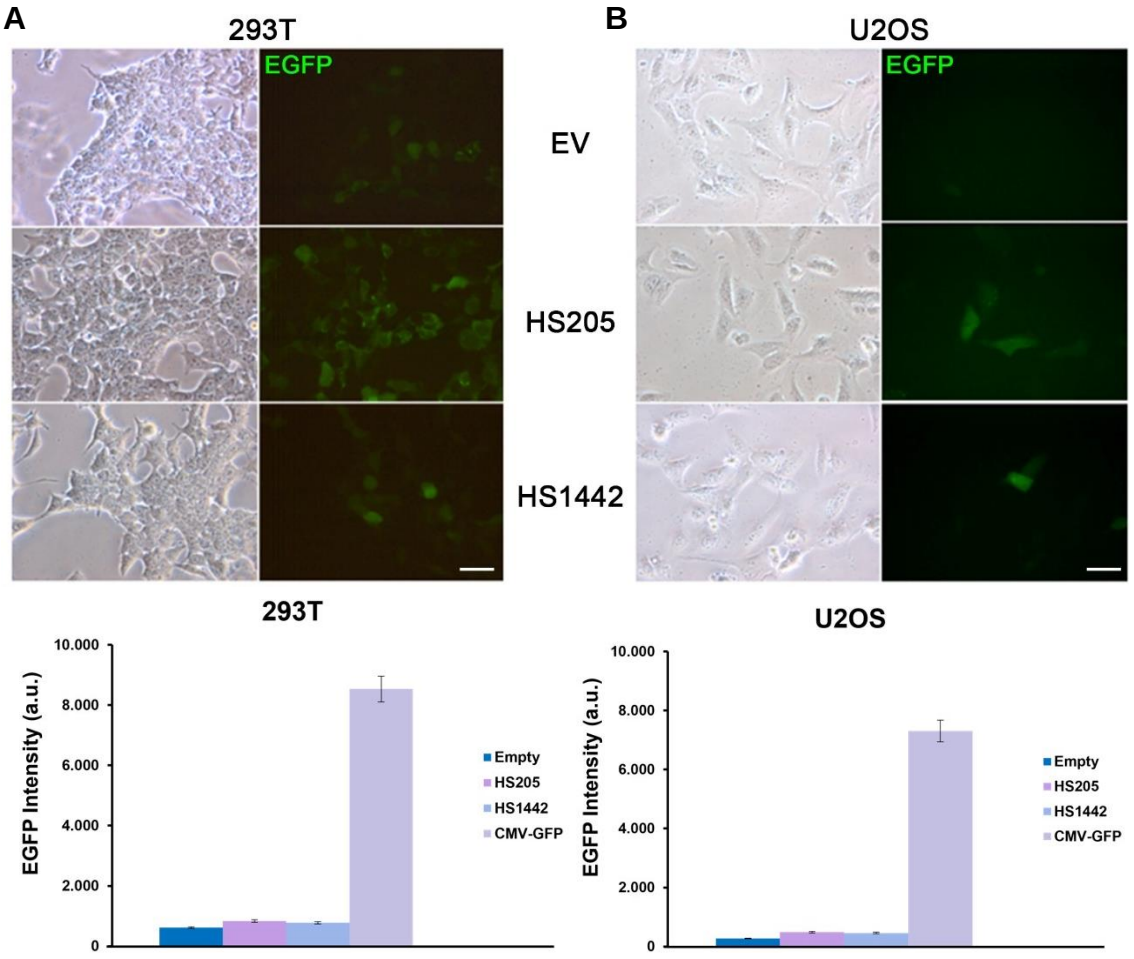

Figure 20. Low enhancer activity in HEK293T and U2OS cells. Overexpression of the empty vector (EV) and the construct UCE-Hsp68-EGFP in **(A)** HEK293T and in **(B)** U2OS. Plot below showed the relative quantification of EGFP intensity showing discrete enhancer activity in both cell lines. Bar in panel, 10 µm.

Considering that HS205 and HS1442 showed some enhancer activity in the genital tubercule we decided to check enhancer activity in testis-derived cell lines (GC-1spg, GC-2spd, TM3 and TM4). Our results showed a slightly labelling of GFP in these cells when compared with the EV with the exception of GC-2spd (cell line of spermatocytes) where the GFP signal was totally absent (**Figure 21**).

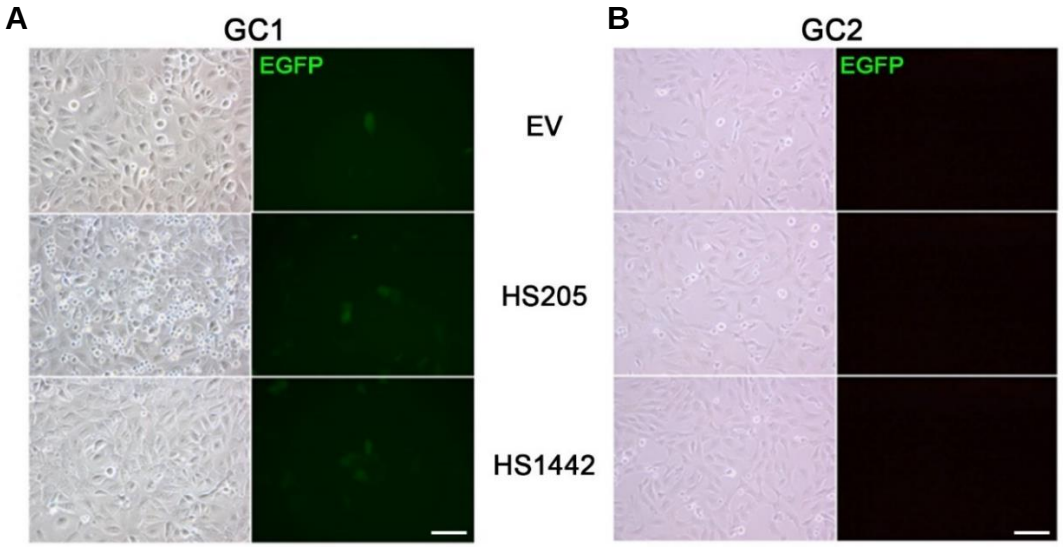

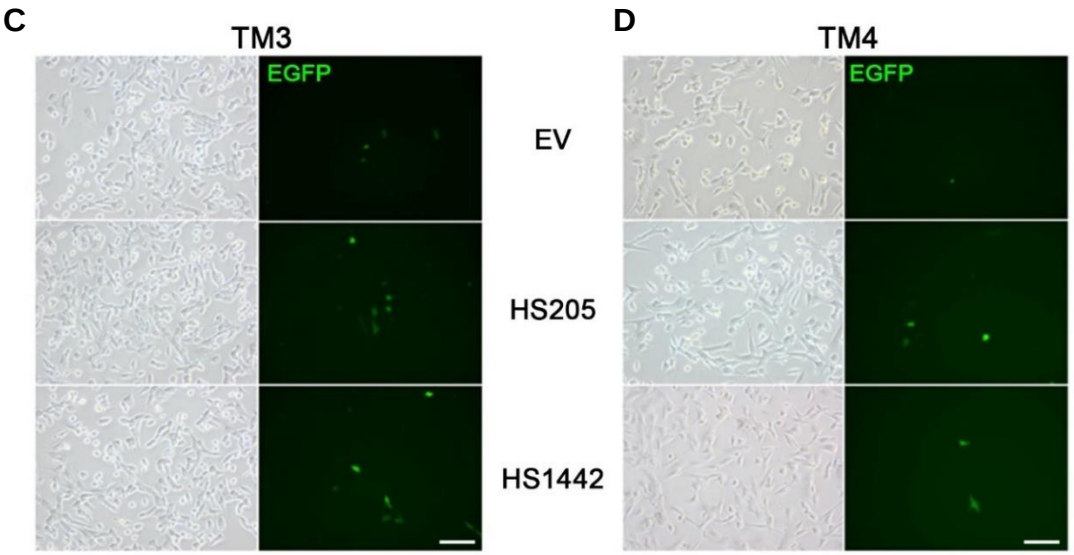

Figure 21. Low enhancer activity in testis cell lines. Overexpression of the empty vector (EV) and the construct UCE-Hsp68-EGFP in **(A)** GC-1spg, in **(B)** GC-2spd in which no signal of EGFP was recorded, in **(C)** TM3 and in **(D)** TM4. Bar in panel, 10 µm.

2.1.1. In vivo Electroporation of the construct UCE-Hsp68-EGFP

Once validate the enhancer activity *in vitro*, we decide to check the enhancer activity also *in vivo*. To this end we carried out the *in vivo* EP of the plasmid encoding for EGFP with the minimal promoter downstream of the UCEs in mouse testis. After EP, the immunolabelling of EGFP was detected in a 19% of cells in case of HS205 and a 7% of cells for HS1442 which shows specifically enhancer activity when compared to the EP of the EV which only showed a 5% of labelled cells (Figure 22). All together, these results show that in fact there is some activity of the UCEs, but these levels are low when compared to the EV.

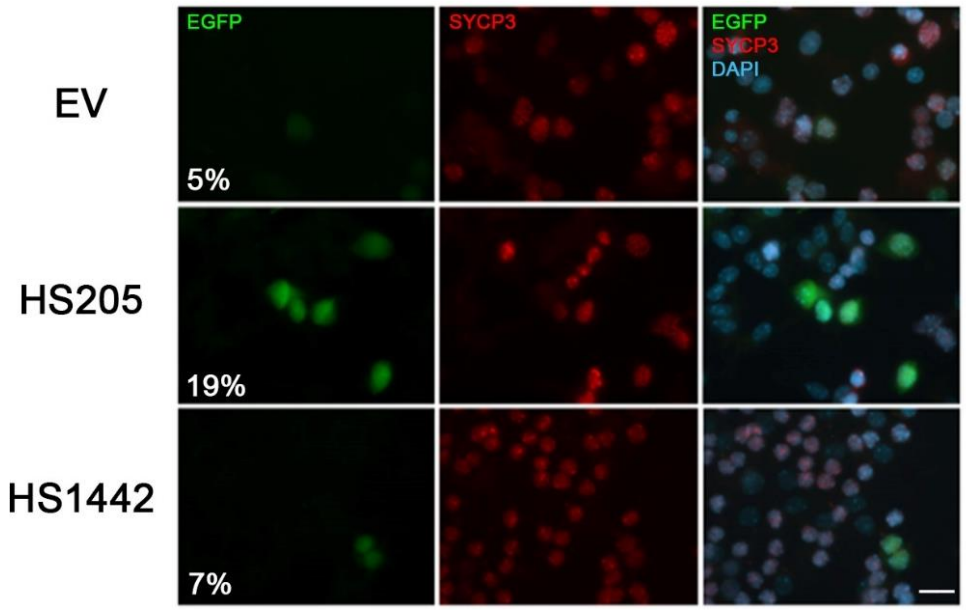

Figure 22. ***In vivo*** **electroporation of UCE-Hsp68-EGFP in mice.** Double immunolabelling of EGFP (green) and SYCP3 (red) in spermatocytes after in vivo EP in testis of UCE-Hsp68-EGFP showing a cytoplasmic pattern. Bar in panel, 100 µm.

2.2. HS205 and HS1442 are not essential for mouse spermatogenesis

Considering these results, we decided to functionally analyze the role of these genomic elements in the mouse. For this purpose, we developed a genome editing strategy to generate a deletion of the *hs205* and of the *hs1442* conserved element (**Figure 23A**). To this end, two sgRNAs were designed surrounding the targeting conserved sequences and a ssODN as a template. Zygotes were microinjected with recombinant Cas9, each annealed sgRNA and the ssODN. This procedure was carried out by the Transgenic Facility of the University of Salamanca.

The selected mouse founder bearing the corresponding deletions were crossed with a wild-type and the corresponding heterozygous were interbred to produce the *hs205*$^{\Delta/\Delta}$ following mendelian ratios. Both homozygous mutant mice were viable and did not show any somatic phenotype. In addition, mice show normal testis size and were fertile (**Figure 23B**). These results suggest that apparently HS205 and HS1442 are not essential for mouse development and fertility.

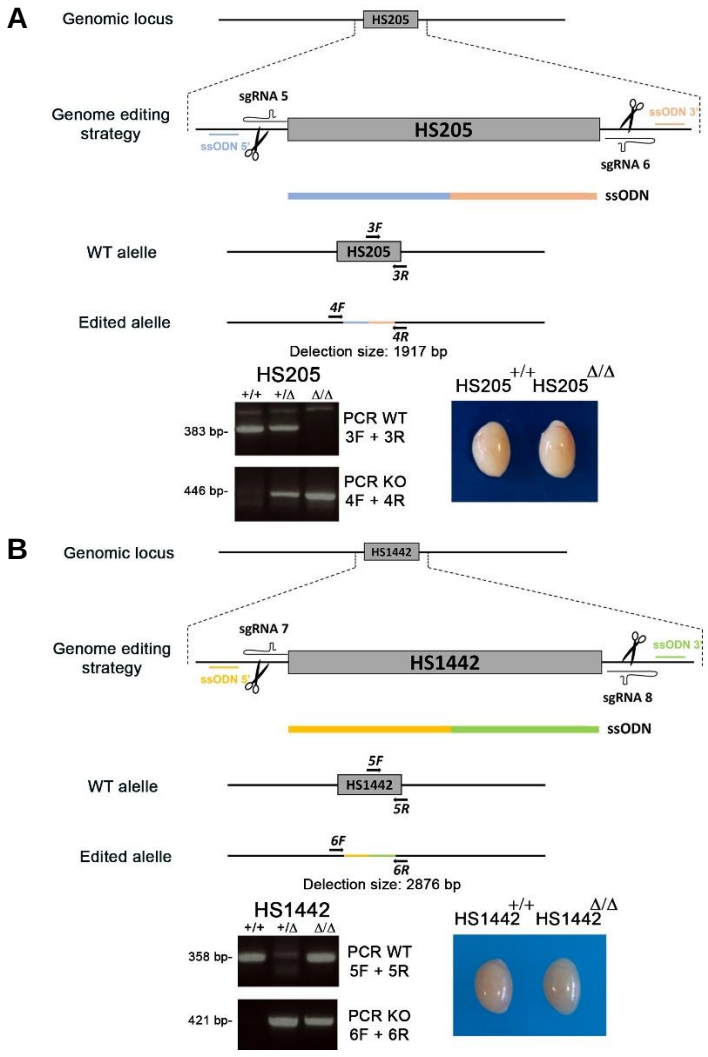

Figure 23. Generation of *hs205*$^{\Delta/\Delta}$ and *hs1442*$^{\Delta/\Delta}$ mice by CRISPR/Cas9 editing. Diagrammatic representation of the mouse genomic elements **A)** HS205 and **B)** HS1442. Genome editing strategy showing the sgRNAs located at the beginning and at the end of the enhancers. The ssODN was used in order to promote the HR. Below each diagram: PCR analysis from littermate progeny of *hs205*$^{+/\Delta}$ and *hs1442*$^{+/\Delta}$. Two PCR strategies were performed for genotyping the mice, one amplifying a small fragment inside the genomic elements which correspond to the WT and another one only amplifying when the enhancers are absent (null). Ablation of *hs205* and *hs1442* leads to a normal size of the testis in mutant mice, right panel.

Bearing in mind that HS205 and HS1442 showed a restricted pattern to the genital tubercle at E11.5 and had some enhancer activity *in vitro* and *in vivo*, we decided to evaluate the meiosis process. We analyzed mutant meiocytes for the assembly and disassembly of the SC by checking the distribution of SYCP1/SYCP3 labelling. Our results showed no defects in synapsis from leptotene to diplotene in mouse spermatocytes.

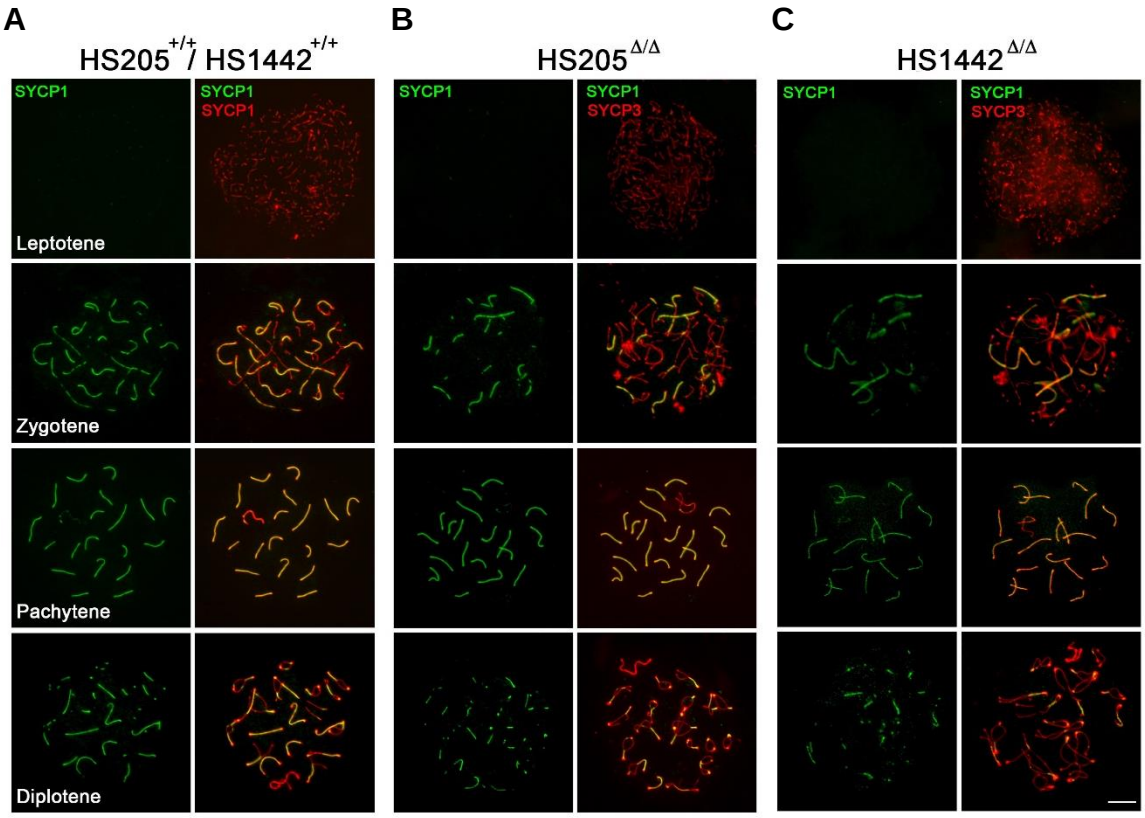

Figure 24. Normal progression of prophase I in spermatocytes lacking *hs205* and *hs1442*. Double immunolabeling of SYCP3 (red) and SYCP1 (green) showing normal synapsis and desynapsis from leptotene to diplotene in spermatocytes in **(A)** WT, **(B)** hs205 and **(C)** hs1442 deficient mice. Bar in panels, 10 µm.

To assess synapse progression in our mutants, we analyzed the distribution of SYCP3 and SYCP1 in spermatocyte spreads from *hs205*$^{\Delta/\Delta}$ and *hs1442*$^{\Delta/\Delta}$. The formation of the AEs was normal, starting to assemble in leptotene as small fragments which became longer as the zygotene stage progressed. In pachytene, correct synapsis spanning the full length of the homologues was detected and no defects were observed in the desynapsis from diplotene to diakinesis (Figure 24A-C). In addition, metaphases I and II of the mutants showed completely normal morphology and develop normal elongated spermatids (Figure 25A-C).

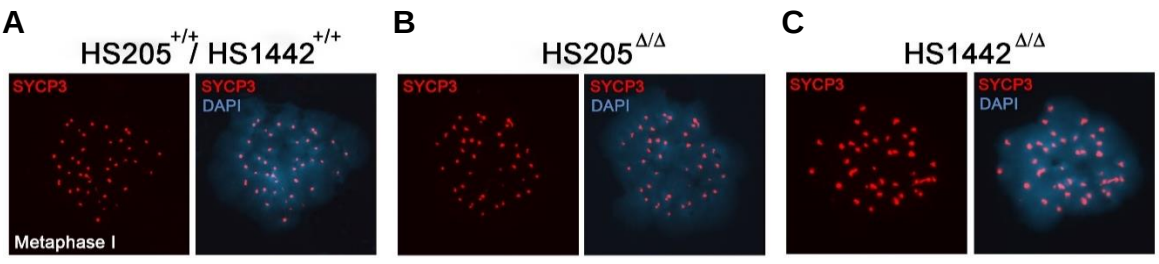

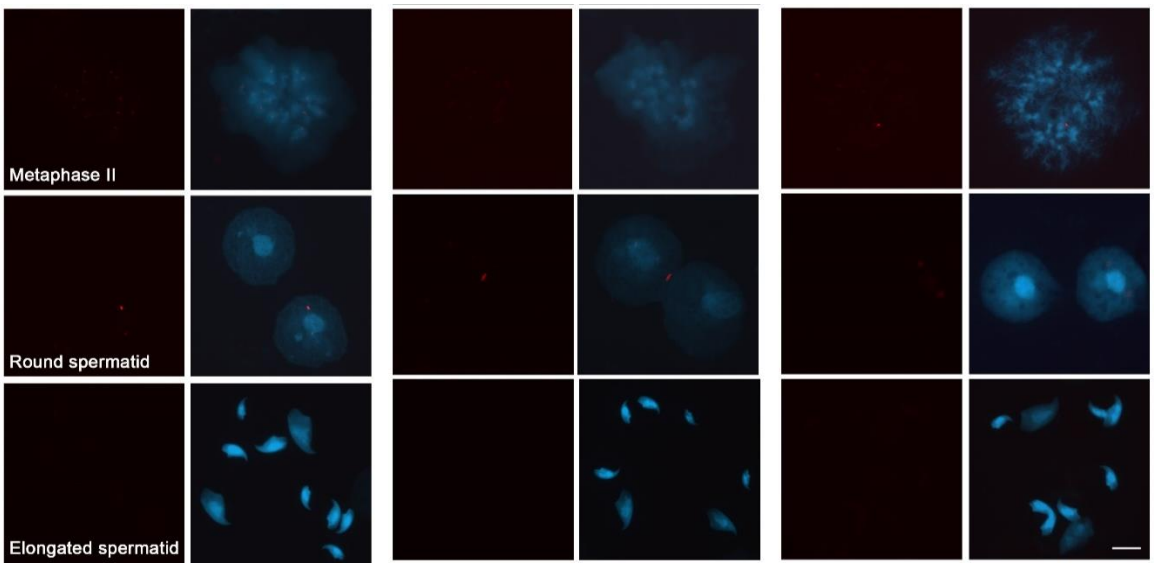

Figure 25. Second meiotic division remains unaffected in *hs205*$^{\Delta/\Delta}$ and in *hs1442*$^{\Delta/\Delta}$ mice. (A-B) Immunolabelling of SYCP3 (red) and DNA stained with DAPI showing normal progression of meiosis in both mutant mice. Bar in panels, 10 µm.

Despite seeing no phenotype in the single mutant mice, we decided to cross the HS205 and HS1442 null mice to generate a double null mice line. These mutant mice were also viable, fertile showing normal testis size and with a normal distribution of SYCP1/SYCP3 (data non-shown).

Therefore, these observations suggest that HS205 and HS1442 play no role in synapse establishment and chromosomal dynamics. Taken together, these results suggest that in mice the absence of these UCEs do not affect the fundamental events of male meiotic prophase I, indicating that HS205 and HS1442 are not essential for mouse spermatogenesis.

DISCUSSION

1.The truncated variant of RAD51B leads to meiotic and somatic DNA repair defects

1.1 RAD51B-c.92delT affects fertility in two sisters of a consanguineous family

In this work, by WES of two sisters with an isolated POI phenotype from a consanguineous family, we identified a variant of RAD51B as the best causal candidate for infertility. This variant consists of a deletion of a thymine at the position 92 (c.92delT). In this family all affected sisters are homozygous for the mutation while healthy members are heterozygous carriers. This evidence, together with the fact that RAD51B is a paralogue of RAD51 which has not been assigned a meiotic role, although it may assist RAD51 in the strand invasion process (Berti et al., 2020), would support the causality of the RAD51B-c.92delT variant in this familial POI. This causality was corroborated by the meiotic phenotype of the humanized *Rad51b* mutant mice such as the accumulation of γH2AX, RAD51, HSF2BP and BRME1 at the chromosome axes and the consequent reduction in the number of COs in the mutant meiocytes.

The tendency for female subfertility represents a less severe phenotype than the observed in the affected sisters, and it is quite unexpected considering a recent study carried out by our laboratory evaluating a POI-inducing variant in the gene *HSF2BP* (Felipe-Medina et al., 2020). In this study, the humanized *Hsf2bp-S167L* mice displayed a similar reduction in the number of COs with a reduced female fertility. This trend in the reduction of litter sizes in the humanized females could support the slight impact on fertility. The differences between the human and mice phenotype could be due to the biological differences in the meiotic pathway such as oocyte spindle formation, the SAC, and CO maturation (Namgoong et al., 2018; S. Wang et al., 2017). In this context, is has been recently reported that human oocytes show some inefficiency in CO maturation, in which approximately 25% of the intermediates never become actual COs and this has not been observed in mouse. In this same study, it has been hypothesized that this maturation inefficiency could occur while the DSB/partner interaction at the leading DSB end is extended to allow a single-end invasion, or while the lagging DSB end is incorporate into the developing recombination complex to give a dHJ, which precedes MLH1 loading (S. Wang et al., 2017). We speculate that this would be consistent with the timing of RAD51B recruitment given its meiotic interactors (i.e., RAD51, DMC1) and the meiotic phenotype of *Rad51b-c.92delT* mice. Moreover, several endocrine disorders that lead to delayed puberty and infertility, such as hypogonadotropic hypogonadism or hypopituitarism, also have a variable phenotypic spectrum in humans and mice. In the case of pituitary hormone deficiency phenotype, mice homozygous for a loss-of-function variant in either *Prop1* or *Pouf1* display quite different phenotypes on different genetic backgrounds, even when environmental parameters are invariant (Fang et al., 2016). In this same regard, mutant mice lacking the infertility associated gene *Usp26* do have defective meiosis or normal strictly depending on the genetic background (Kauppi, 2021). All these observations could explain the more severe phenotype of POI patients compared to females in the *Rad51b-c.92delT* mice model.

The identification of *RAD51B* as a new gene causing POI due to alterations in meiotic recombination makes it candidate of the growing but reduced list of genes responsible for POI (included in the **Supplementary Table 1**). Some examples of them are: BRCA2 (Caburet et al., 2020), FANCL (Yang et al., 2020), MEIOB (Caburet et al., 2019; Y. Wu et al., 2021), SPATA22 (Y.

Wu et al., 2021; C. Yao et al., 2022), SYCE1 (de Vries et al., 2014), MSH4 (Carlosama et al., 2017), DMC1 (He et al., 2018) or HSF2BP (Felipe-Medina et al., 2020).

In the case of males, the absence of male siblings in the family carrying the mutation in homozygosis prevents direct comparison between the phenotype observed in male RAD51B-c.92delT mice and humans. However, extrapolation of our mouse results to humans suggests that the presence of the c.92delT variant in homozygosis would cause fertility defects in males.

1.2 The RAD51B-c.92delT variant causes a loss of interaction with its partners

In silico analysis predicted that this variant would provoke the appearance of PTC potentially leading to the production of a highly truncated protein of 39 aminoacids. This truncated RAD51B would lack most of the protein including the two Walker motifs essential for its ATPase activity (Wiese et al., 2006), which would result in a loss of function allele that has been shown to be lethal in the mouse (Shu et al., 1999). On the other hand, and beyond the absence of functional domains in the truncated protein, this PTC might also generate a null allele by activating the non-sense mediated decay (NMD), a surveillance pathway that reduces the production of truncated proteins by targeting mRNA encoding PTCs for decay (Y. F. Chang et al., 2007). The location of the PTC in the RAD51B-c.92delT variant could trigger the NMD fulfilling the rule that this pathway is triggered if a PTC is located ~50 nucleotides upstream of the last exon-junction (Thermann et al., 1998).

When replicating the human variant mutation in the mice using CRISPR/Cas9 methodology, we observed that mice were viable without any early somatic phenotype which strongly suggest that the reinitiation of the translation using a secondary downstream AUG codon is operating in this mutant mouse model. This observation was sustained with *Rad51b* mRNA expression in *Rad51b*$^{c.92delT/c.92delT}$ mice, indicating that NMD is not operating, probably abrogated by the restart of the translation. On the other hand, the presence of peptides corresponding to the C-terminal of the protein *RAD51B-c.92delT* from human-derived lymphoblastoid cells support direct evidence that translation is indeed taking place (**Table 1**). Accordingly, these observations agree with a genome-wide analysis of naturally occurring PTCs in human tumors, which demonstrated that transcripts bearing 5'-proximal PTCs can bypass NMD by downstream reinitiation of translation (Lindeboom et al., 2016). This model would explain the absence of NMD in the *RAD51B-c.92delT* variant due to translation reinitiation at AUG64 and consequently, allow the expression of an N-terminally truncated RAD51B protein in both human and mouse genes. The domain present at the N-terminal domain of RAD51B is involved in protein-protein interactions with its paralogues, such as RAD51C and in nuclear localization through a NLS (K. A. Miller et al., 2004, 2005). This is consistent with the observed altered nuclear localization of the truncated variant of RAD51B in comparison to the WT in transfected Cos7 cells and would suggest a similar dysfunction of the endogenous protein *in vivo*.

As mentioned before and similar to other RAD51 paralogues (B. Deans et al., 2000; S. Kuznetsov et al., 2007; Pittman et al., 1998; Prakash et al., 2021), the disruption of *Rad51b* in mice has shown to be embryonic lethal (Shu et al., 1999). We observed that *Rad51b* hypomorphic allele caused a loss of RAD51B-c.92delT interaction with RAD51C. In this regard, *Rad51c* hypomorphic mice have an essential role in meiotic recombination, mutant *Rad51c* spermatocytes displayed a reduction in the RAD51 loading at leptotene and a precocious meiotic arrest at mid-zygotene, whereas mutant *Rad51c* oocytes progressed to aberrant metaphase I

with unrepaired DSB (S. Kuznetsov et al., 2007). We also observed a partial loss of interaction between RAD51B-c.92delT with its novel interactors RAD51 and the helicase POLQ-like (HELQ). Concerning HELQ, this helicase promotes efficient HR at damaged replication forks by interacting directly with the RAD51-containing BCDX2 complex. BCDX2 complex and HELQ act together in the resolution of DNA-ICLs upon exposure to MMC (Adelman et al., 2013). The diminished interaction between the mutant *RAD51B*-c.92delT and HELQ sheds light into the presence of unrepaired DNA in MEFs, bone marrow and human lymphoblastoid cells, increased incidence of pituitary adenomas but also into the persistence of unrepaired meiotic DSBs and reduced number of COs. Interestingly, disruption of HELQ in mice exhibit MMC sensitivity, increase susceptibility to ovarian and pituitary tumors as well as germ cell attrition with subfertility (Adelman et al., 2013; Luebben et al., 2013) and *C. elegans* lacking both HELQ and the RAD51 paralogue RFS1 results in a block to meiotic DSB repair after strand invasion (J. D. Ward et al., 2010). At the cellular level, defects in HELQ result in hypersensitivity to cisplatin and MMC, and persistence of RAD51 foci after damage (Takata et al., 2013). These observations in *Rad51b*$^{c.92delT/c.92delT}$ and HELQ-deficient mice suggest a common pathological mechanism of action. A recent study has shown that HELQ helicase activity is differentially regulated by RPA and RAD51. RPA inhibits DNA unwinding by HELQ but strongly stimulates DNA strand annealing, whereas RAD51 forms a complex with HELQ and strongly stimulates it upon translocation during DNA unwinding (Anand et al., 2022).

Altogether, these inefficient interactions between RAD51B-c.92delT and their interactors RAD51C, RAD51 and HELQ, as a consequence of the deletion of the residues of the RAD51B N-terminal, synergistically lead to a reduction in the number of COs observed in both *Rad51b-c.92delT* spermatocytes and oocytes.

In vivo, *Rad51b-c.92delT* mice meiocytes did not show any effect on DMC1 loading, as well as the interaction between RAD51B-c.92delT and DMC1 was maintained invariable in comparison with the RAD51B-WT. In this context, DMC1 is the meiotic paralogue of RAD51 and both proteins share 53% of overall protein identity, which is even higher in their C-terminal regions (80%; (Slotman et al., 2020)). However, the meiotic analysis of *Rad51* and *Dmc1* knockdown mice have shown no interdependent foci formation and lead to distinct phenotypes (Dai et al., 2017). The disruption of RAD51 depletes late prophase I spermatocytes, probably through a p53-dependent apoptotic pathway and the few cells escaping apoptosis present sex chromosome asynapsis and COs reduction. These spermatocytes were blocked at metaphase I probably due to the presence of univalents. On the other hand, DMC1 depletion leads to an increased zygotene-like arrest and loss of pachynemas (p53-independent). These observations suggest differentiated and independent functions of both paralogues (Dai et al., 2017). Based on these conclusions, DMC1 would have a non-essential role in homology search and synapsis, whereas RAD51 would play a role in CO and synapsis of sex chromosomes.

Despite mutant *Rad51b* present no defects in DMC1, humanized meiocytes of *Rad51b* revealed accumulation of foci containing γH2AX, RAD51 and the BRCA2-associated proteins HSF2BP/BRME1 on the chromosome axes from pachytene onward leading to a reduction in COs, as described for other mouse mutants (Brandsma et al., 2019; Felipe-Medina et al., 2020; Takemoto et al., 2020; Zhang et al., 2019). The accumulation of these non-meiotic specific repair proteins could be explained by the reactivation of a somatic-like HR DNA-repair pathway at

pachytene involving RAD51, but not DMC1, as a consequence of the persistence of unrepaired meiotic DSBs (Enguita-Marruedo et al., 2019).

1.3 RAD51B-c.92delT somatic cells induce genome instability

Several repair pathways are essential for the elimination of DNA lesions introduced by the action of damaging compounds (Helleday et al., 2008). Considering that RAD15B is also expressed in somatic tissues we tested different DNA damaging that could alter somatic DNA repair in *Rad51b-c.92delT* MEFs. Our results showed that mutant MEFs were not sensitive to UV, MMS nor IR, each of these drugs induce different DNA repair pathways. From these results we can extrapolate in the case of UV that the NER pathway is unaffected because this pathway is essential for repair of UV-induced damage such as cyclobutene pyrimidine dimers, or pyrimidine-pyrimidone (6-4) photoproducts (D'Souza et al., 2022), in the case of MMS and IR the BER pathway would be unaffected because is the pathway responsible to remove and replace single base damage or ssDNA break (Caldecott, 2008).

Interestingly the observed sensitivity of *Rad51b-c.92delT* MEFs to MMC in cell proliferation and clonogenic survival assay and the presence of unrepaired DNA strongly suggested that ICL pathway is affected. MMC has been shown to produce DNA ICLs that are specifically repaired by the FA pathway. Consistently, *RAD51B-c.92delT* somatic human-derived lymphoblastoid cells, as well as MEFs and uncultured bone marrow cells from humanized mutant mouse are sensitive to MMC-induced CIN. It has been also reported that mutations in RAD51 and its paralogues have been also associated with cancer predisposition and FA, in particular RAD51C (FANCO) and XRCC2 (FANCU) (Ameziane et al., 2015; Park et al., 2016; Schlacher et al., 2012; Vaz et al., 2010). Specifically, RAD51B has been involved cancer such as breast cancer, ovary cancer, prostate cancer, uterus leiomyoma, nasopharyngeal carcinoma, retinoblastoma, melanoma, and aneuploidy (Date et al., 2006; Mehine et al., 2013; Nowacka-Zawisza et al., 2015; Orr et al., 2012; Qin et al., 2011; Song et al., 2015; G. Thomas et al., 2009; Wadt et al., 2015). In addition, the RAD51B-rs8017304 polymorphism has been implicated in pituitary adenoma (Juknytė et al., 2021) in agreement with our results in which mutant mice showed increased incidence of pituitary hyperplasia. It is worth mentioning that one of the affected sisters (II-4) was diagnosed with a duodenal tubulovillous adenoma with high-grade dysplasia and she underwent to surgery with no additional treatment. Altogether, these data provide evidence for a critical role of RAD51B in somatic genome instability and tumorigenesis.

Previous studies have been shown that efficient reprogramming of MEFs to a pluripotent stage requires a proficient pathway to repair by HR the inherent genome instability occurring during reprogramming. Accordingly, efficient reprogramming requires key HR genes, including *Brca1*, *Brca2* and *Rad51* in a p53-dependent manner (González et al., 2013). Consistently, *Rad51* overexpression in primary MEFs enhances reprogramming efficiency, possibly by regulating a DNA damage repair pathway during the early phase of the reprogramming process (J.-Y. Lee et al., 2016). Interestingly, the expression of reprogramming factors in MEFs induces replication stress, and genetic reduction of stress, such as overexpressing *Chk1*, increases the efficiency of iPSC generation (Ruiz et al., 2015). This is compatible with the reduction of the iPSC colonies derived from *Rad51b-c.92delT* MEFs that was observed, again suggesting that RAD51B has a role in genome stability and integrity.

Furthermore, it is well known that replication forks are stalled on either side of the ICL, such as those generated by cellular metabolism (aldehydes) or DNA damaging agents like MMC and cisplatin, when are detected by the Replisome (Cortez, 2019). One pathway to resolve them during S-phase is by promoting fork remodeling. Recently it has been proposed that RAD51 paralogues sequentially orchestrate molecular transactions at replication forks, cooperatively promoting fork remodeling and restart (Berti et al., 2020). In this regard, the sensitivity to HU and Aphidicolin of the RAD51B-c.92delT cells in the cell proliferation and clonogenic assays points towards a direct effect of the RAD51B variant on this pathway. It is well established that these compounds do not damage the DNA structure directly but interfere with replication-related enzymes. In particular, HU inhibits the ribonucleotide reductase, which causes and alteration in the metabolism of dNTPs, thus blocking the progression of the replication fork and, on the other hand, Aphidicolin is an inhibitor of replicative DNA polymerase, which causes replication uncoupling (Muñoz & Méndez, 2017; Vesela et al., 2017). SCE is the reciprocal exchange of genomic fragments between two identical sister chromatids. S phase-dependent agents like MMC and UV light are among the stronger inducers of SCEs (Mourelatos, 2016). The observed invariable rate of SCE in RAD51-c.92delT lymphoblastoid cells untreated (spontaneous) or treated with MMC (induced) strongly indicates that the canonical HR pathway remains unaffected by the RAD51B variant. This result is consistent with the absence of impaired sister chromatid recombination in RAD51B-deficient U2OS cells (Garcin et al., 2019). In addition, experiments carried out by the Méndez's lab during the reviewing process of our MS within a collaboration effort (Franca et al., 2022), indicated a direct involvement of the RAD51B genetic variant in replication fork restart as shown by the stretched DNA-fibers' experiments in which they observed a delay in fork speed in cells treated with MMC. These results, together with MMC-induced chromosomal breakage both *in vitro* and *in vivo*, support a somatic function of RAD51B in assisting fork progression through certain DNA lesions, as part of the DNA damage tolerance response.

In summary, in this work we describe for the first time two sisters where an isolated POI phenotype is caused by the c.92delT variant in RAD51B. By analysis of humanized mice, we have shown that this variant behaves as a hypomorphic allele that evades NMD probably owing to the reinitiation of the translation at a secondary downstream AUG codon. The resulting truncated protein lacks most of the N-terminal domain involved in protein-protein interactions and proper nuclear localization. As a result, *Rad51b*$^{c.92delT/c.92delT}$ mice shows meiotic DNA repair defects with γH2AX, RAD51, and HSF2BP/BRME1 accumulation in the chromosome axes which leads to a significant reduction in CO. In addition, *RAD51B-c.92delT* human-derived lymphoblastoid cells and mutant MEFs are sensitive to MMC-induced CIN and revealed a reduced reprogramming efficiency to iPSCs. Also, humanized mice exhibit a higher incidence of pituitary hyperplasia, which is probably attributable to the *RAD51B-c.92delT*-induced genome instability.

2. HS205 and H1442 enhancers are not essential for mouse spermatogenesis

In the present study, we have generated *hs205*$^{\Delta/\Delta}$ and *hs1442*$^{\Delta/\Delta}$ mice by CRISPR/Cas9 editing, as well as double *hs205*$^{\Delta/\Delta}$/*hs1442*$^{\Delta/\Delta}$ mutants by crossing mutant homozygous mice. Although *in silico* analysis showed that these two UCEs have a restricted pattern on the genital tubercle, we were unable to demonstrate that the absence of these genetic elements could be essential for mouse spermatogenesis.

The existing functional studies of conserved elements suggest that UCEs are most likely to be regulatory regions of gene expression (Dermitzakis et al., 2005). However, there is a lot of controversy in the functional/genetic role of UCEs. There is one study that suggest the existence of disposable DNA in mammalian genomes, in this same study, they perform a deletion of 1 Mb long on mouse chromosomes 3 and 19, these segments contain a total of 1243 sequences that are >100 bp long and >70% identical between human and mouse. These deletions did not show any overt phenotype effects, homozygous mice were viable, supporting the possibility that mammalian genomes are not densely coded and that there are significant reductions that can be tolerated (Nóbrega et al., 2004). Contrary to these results, other studies have shown apathogenic mutations in CNGs pathogenic mutations, one example is the case of single nucleotide pathogenic mutations in a conserved regulatory element named ZRS. This genetic element regulates the expression of the limb-specific signalling protein Sonic hedgehog (*Shh*), and is located 1 Mb far away from the coding gene. Accordingly, point mutations within ZRS causes preaxial polydactyly in humans and hemimelic extra toes (*Hx*) in mice (Gurnett et al., 2007; Lettice et al., 2003).

In this regard, another study selected four UCEs, which had been shown to act as enhancers *in vivo* and were located in the surrounding of genes that are essential for development (such as *Dmrt1/2/3*, *Pax6*, *Arx* and *Sox3*), were individually deleted from the mouse genome (Ahituv et al., 2007). Mice that were homozygous-null for these UCEs were fully viable and lived well into adulthood. Further assessment of pathology, growth and gene expression did not reveal obvious harmful phenotypes as a consequence of the genetic deletion of these enhancers/UCEs (Ahituv et al., 2007).

These results are consistent with our findings, in which we show that HS205 and HS1442 have *in vivo* enhancer activity and that depleting HS205, HS1442 or both give rise to fully viable and fertile mice. In the case of HS205 we show for the first time that this regulatory element, which is conserved in vertebrates, has no role in mouse spermatogenesis. In the case of HS1442, this UCE is intragenic to *Kifap3* which is ubiquitously expressed. This gene is involved in the tethering the chromosomes to the spindle pole and in chromosome movement. In addition, a previous study also disrupted this element by gene targeting, and the results showed that HS1442 is not important for limb development in the mouse, showing algo normal phenotype. However, there were significant transcriptional differences in genes proximal to this UCE such as in *Kifap3*, *Gorab*, *Syc13* and *Nme7* (Nolte et al., 2014).

Given the high sequence conservation of these loci, the lack of apparent phenotypes was surprising and has led to several hypotheses as to the reason for these observations. Amon the possible explanations these include the presence of other enhancers with partially redundant

functions relative to the UCEs (Ahituv et al., 2007; McLean & Bejerano, 2008; Visel et al., 2008), and the presence of subtle phenotypes or not readily apparent under optimal laboratory conditions (Ahituv et al., 2007; McLean & Bejerano, 2008). So far, a total of eleven UCEs have been individually deleted from the mouse genome (Snetkova et al., 2022). All homozygous-null mice were viable and fertile (Ahituv et al., 2007; Dickel et al., 2018; Gaynor et al., 2020; Nolte et al., 2014), but more exhaustive examinations revealed the presence of subtle developmental phenotypes in some of the null UCEs mouse lines. These are the cases of HS119 and HS280, in which individual loss of these two UCEs with different tissue-restricted pattern, in the case of HS119 in the forebrain (near *Arx*) and in the case of HS280 in the limb (near *Tmem53*), both results in body mass reduction (Dickel et al., 2018; Nolte et al., 2014).

In essence, we found two plausible candidates of ultraconserved elements, HS205 and HS1442, which have a restricted pattern in the genital tubercle and could be essential for mouse gametogenesis. However, our findings provide *in vivo* evidence that these UCEs are not essential for gametogenesis and fertility in mice, providing new data to the great controversy surrounding this conserved regions. Our results and those of others suggest that the UCEs are not essential in the mouse since its genetic depletion does not lead to the predicted phenotypes according to its conserved sequence through long evolutionary times. It might be possible that ultraconserved elements have additional roles in the genome beyond their regulatory capacities.

3. Significance of the study

Human infertility is a public health problem affecting 10-15% of couples at reproductive age with 25% of these cases of unknown etiology. One of the main causes of female infertility is POI which affects about 1% of women under 40 years of age. The genetic etiology of POI is very heterogenous and the genetic cause of a high fraction of patients is still unknown. In the last decade, the development of massive genomic sequencing techniques of the coding genome has made possible to identify several genes involved in meiosis as causative agents of the disease in families with hereditary POI. This is the case of the meiotic genes SYCE1, STAG3, SPO11, MSH4, DMC1, BRCA2, MEIOB or HSF2BP, in addition to others POI genes (Supplementary Table 1).

In this study and in collaboration with Dr. Veitia's group and Dra. Berenice Mendonca, we have identified by WES of three sisters (two affected and one unaffected) belonging to a consanguineous Brazilian family with hereditary POI. The results revealed the presence of a homozygous variant in RAD51B-(c.92delT) in two sisters affected by POI that leads to a PTC. Using genome editing techniques, we have replicated this mutation in the mouse, demonstrating that this variant in RAD51B leads to the reinitiation of translation generating a N-terminally truncated protein. As a result, *Rad51b*$^{c.92delT/c.92delT}$ mice showed meiotic defects due to the accumulation of γH2AX RAD51 and HSF2BP/BMRE1 in the chromosomal axes of spermatocytes and oocytes, leading to a reduction in the number of COs. Moreover, MEFs derived from mutant mice and patient-derived lymphoblastoid cells showed an increase in chromosomal aberrations, as well as a delay in the proper repair of DNA damage. This variant also showed reduced DNA replication fork progression and reduced efficiency of reprogramming to pluripotent stem cells. The truncated protein compromises RAD51B interaction with other proteins and thus hinders its proper function in meiotic recombination and DNA damage repair in somatic cells. Finally, *Rad51b*$^{c.92delT/c.92delT}$ mice showed an increased incidence of pituitary hyperplasia, probably as a

consequence of increased genomic instability in this tissue. These results provide new insights into the role of RAD51B repair protein not only in meiosis, but also in the maintenance of genome stability. These finding could have clinical implications for the genetic counselling of couples in whom genetic variants in RAD51B are identified.

It has been more than 18 years since the first description of UCEs, since then and up to present these genetic elements still remained as an "obscure matter" from the functional/genetic point of view. These elements, originally defined as 481 sequences with perfect sequence conservation among three available mammalian reference genomes, have grown into a larger group of thousands of extremely conserved sites in the human genome (Snetkova et al., 2022). In this work, we describe two UCEs which have a restricted pattern in the genital tubercle making them good candidates to address the role of UCEs in gametogenesis and thus, infertility. However the disruption of HS205, HS1442 or both of them yield viable and fertile mice. This is consistent with the fact that to date, half of the ultraconserved enhancers removed in mice have not directly shown to lead to reduced viability or fertility. However, evolution acts over generations, and selection against even small fitness defects will easily remove deleterious variants from the population. Therefore, the effects on these mutant mice may be very subtle or unobservable under typical laboratory conditions. To explore whether the loss of UCEs affects viability and reproductive success across generations, it would be useful to conduct population-based field experiments, such as those that have been used to study selection in wild mouse populations (Barrett et al., 2019).

The results obtained in this doctoral thesis allow us to expand our knowledge in the collection of genes that are essential for human fertility and for the maintenance of genome stability. These work, provide important new insights into the molecular mechanisms that govern meiotic recombination, demonstrating its complexity and the need to continue studying these processes in depth, since, despite the current knowledge of the elements involved in this pathway, there are elements that have not yet been identified and whose functions are still unknown. On the other hand, this doctoral thesis also addresses the potential role of ultraconserved sequences in mouse gametogenesis, whose functions to date remain a puzzle to be completed.

CONCLUSIONS

CONCLUSIONS

1. RAD51B-c.92delT leads to translation reinitiation at the downstream AUG codon 64 which generates an N-terminal truncated protein.

2. RAD51B-c.92delT showed altered nuclear localization in transfected cells suggesting a similar dysfunction of the endogenous protein *in vivo*.

3. *Rad51b*$^{c.92delT/c.92delT}$ mice were viable but displayed accumulated DNA repair proteins in the chromosome axes, and consequently a significant reduction in COs of the meiocytes.

4. This reduction in the number of COs in the mutant meiocytes could be due to the altered interactions between RAD51B-c.92delT and RAD51, RAD51C, and HELQ.

5. RAD51B-c.92delT variant is thus responsible of the POI phenotype in a consanguineous family from Brazil.

6. RAD51B-c.92delT human and mouse cells are sensitive to MMC-induced DNA damage supporting a somatic function of this variant in DNA repair.

7. *Rad51b-c.92delT* MEFs challenged with DNA polymerase inhibitors showed a reduced survival and colony formation pointing to a function in protecting replication fork DNA damage.

8. Reprogramming efficiency is diminished in *Rad51b-c.92delT* MEFs, supporting a somatic function of RAD51B in genome stability and integrity.

9. *Rad51b*$^{c.92delT/c.92delT}$ mice showed elevated incidence of spontaneous pituitary gland hyperplasia with features of prolactinomas suggesting that RAD51B have a critical role in tumorigenesis.

10. HS205 and HS1442 show a relative enhancer activity *in vitro* and *in vivo*.

11. Single and double mutants of HS205 and HS1442 present normal testis size, normal meiotic progressions and normal production of spermatozoa.

12. HS205 and HS1442 are not essential for mouse spermatogenesis.

SUPPLEMENTARY MATERIAL

Supplementary Table 1. Premature ovarian insufficiency genes. Modified from (Ruth et al., 2021)

Gene	Publication (First author, year)
AARS2	Zhou et al (2019)
AIRE	Krohn et al. (1992)
ALOX12B	Alavi et al. (2020)
AMH	Alvaro Mercadal et al. (2015)
AR	Chatterjee et al. (2009); Panda et al. (2011)
ATG7	Delcour et al. (2019); Patiño et al. (2017)
ATG9A	Delcour et al. (2019)
ATM	Christin-Maitre et al. (1998)
BMP15	Fonseca et al. (2014)
BMPR1B	Demirhan et al. (2005)
BNC1	Tšuiko et al. (2016); Zhang et al. (2018)
BRCA2	Miao et al. (2019); Caburet et al. (2020)
CDKN1B	Ojeda et al. (2011) ; Chasseloup et al. (2020)
CLPP	Pyun et al. (2012) ; Ahmed et al. (2015); Dursun et al. (2016)
CPEB1	Tšuiko et al. (2016); Jiao et al. (2020)
CSB-PGBD3	Qin et al. (2015)
DACH2	Bione et al. (2004)
DIAPH2	Marozzi et al. (2000)
DMC1	He et al. (2018)
EIF4ENIF1	Zhao et al. (2019)
ESR1	M'Rabet et al. (2012)
FANCA	Yang et al. (2019)
FANCL	Yang et al. (2020)
FANCM	Fouquet et al. (2017)
FIGLA	Chen et al. (2018)
FMR1	Wang et al. (2018)
FOXL2	Georges et al. (2013); Uda et al (2004)
FSHR	Liu et al. (2017)
GDF9	Simpson et al. (2014)
HARS2	Pierce et al. (2011)
HFM1	Qin et al. (2015); Pu et al. (2016)
HSD17B4	Pyun et al. (2012); Ahmed et al. (2015); Dursun et al. (2016)
HSF2BP	Felipe-Medina et al. (2020)
IGSF10	Jolly et al. (2019)
INHA	Harris et al. (2005)
KHDRBS1	Wang et al. (2017)
LARS2	Pierce et al. (2013)
LHCGR	Latronico et al. (1996)
LHX8	Simpson (2008)
LRPPRC	Ghaddhab et al. (2017)
MCM8	Desai et al. (2017); Bouali et al. (2017); Wood-Trageser et al. (2014); Yang et al. (2019)
MCM9	Desai et al. (2017); Alvarez-Mora et al. (2020)
MEIOB	Caburet et al. (2019); Y. Wu et al. (2021)
MND1	Jolly et al. (2019)
MRPS22	Chen et al. (2018); Jolly et al. (2019)
MSH4	Carlosama et al. (2017)
MSH5	Guo et al. (2017)
NANOS3	Qin et al. (2007)
NOBOX	Ferrari et al. (2016)

NOTCH2	Li et al. (2020)
NR5A1	Bashamboo et al. (2009); Jiao et al. (2013)
NUP107	Weinberg-Shukron et al. (2015)
PGRMC1	Mansouri et al. (2008)
PMM2	Yang et al. (2019)
POF1B	Lacombe et al. (2006)
POLG	Pagnamenta et al. (2006)
POLR2C	Moriwaki et al. (2017)
POLR3H	Franca et al. (2019)
PSMC3IP	Al-Agha et al. (2018)
PTHB1	Kang et al. (2008)
RAD51B	(Franca et al., 2022)
SALL4	Wang et al. (2019)
SF1	Lakhal et al. (2012)
SGOL2	Tšuiko et al. (2016); Faridi et al. (2017)
SIX6OS1	Fan et al. (2021)
SMC1β	Bouilly et al. (2016)
SOHLH2	Qin et al. (2014)
SPATA22	Y. Wu et al. (2021); C. Yao et al. (2022)
SPIDR	Smirin-Yosef et al. (2017)
STAG3	Caburet et al. (2014)
SYCE1	Vries et al. (2014)
TGFBR3	Qin et al. (2011)
TP63	Tucker et al. (2019); Mathorne et al. (2020)
TRIM37	Karlberg et al. (2018)
TWNK	Morino et al. (2014)
WDR62	Zhou et al. (2018)
WT1	Wang et al. (2015)
WWTR1	Zhang et al. (2020)

Supplementary Table2. Whole Exome Sequencing Alignment Information.

Sample	Number of reads	Number of Mapped reads	Mean coverage	Mean coverage ±SD	Coverage data ≥10x
Proband (II-1)	118,566,928	118,500,310 (99.94%)	188.16x	110.25	99,55%
Affected sister (II-3)	104,994,635	104,925,163 (99.93%)	168.74x	97.62	99.56%
Unaffected sister (II-2)	95,072,780	95,023,928 (99.95%)	154.08x	90.85	99.38%

Supplementary Table 3. Whole-Exome Sequencing Workflow.

Data Filtering Criteria	Members of Family (II-1, II-2, and II-3)
Total variants called in the family	73178
Homozygous in both affected sisters	431
Heterozygous in unaffected sister	246
Minor allele frequency <0.01% *	10
Coding/Splicing variants **	6
Frameshift insertion/deletion	1

* Based on 1000Genomes, 6500ESP and ExAC database.

** Nonsense, frameshift, codon insertion/deletion, splicing and missense.

Supplementary Table 4. Observed and expected number of offspring of various genotypes obtained from *Rad51b*$^{WT/c.92delT}$ intercross.

	Rad51b$^{WT/WT}$	*Rad51b*$^{WT/c.92delT}$	*Rad51b*$^{c.92delT/c.92delT}$
Expected	53	106	53
Observed	51	105	56
χ2 p-value		0.8804	

Supplementary Table 5. Quantification of γH2AX levels, RAD51 foci, BRME foci and levels, HSF2BP foci and levels, MLH1 foci, DMC1 foci, RPA foci and SPATA22 foci.

γH2AX spermatocytes		Mean (intensity)	SD	n
Leptotene	WT	0.5921	0.169	38
	KI	0.5674	0.171	43
Zygotene	WT	0.4829	0.189	46
	KI	0.4668	0.185	45
Pachytene	WT	0.0609	0.026	119
	KI	0.0815	0.041	119

γH2AX oocytes		Mean (intensity)	SD	n
Pachytene	WT	0.4216	0.166	39
	KI	0.5800	0.215	39
Diplotene	WT	0.4398	0.191	33
	KI	0.6137	0.249	34

RAD51 spermatocytes		Nº foci	SD	n
Leptotene	WT	115.2	31.28	40
	KI	123.9	30.69	40
Zygotene	WT	102.5	32.22	42
	KI	105.9	31.29	42
Pachytene	WT	20.18	3.88	60
	KI	35.97	6.23	60

RAD51 oocytes		Nº foci	SD	n
Pachytene	WT	16.55	9.54	55
	KI	16.42	8.48	55
Diplotene	WT	19.33	9.99	57
	KI	24.55	8.16	62

BRME1 spermatocytes		Nº foci	SD	n
Zygotene	WT	210.60	15.84	37
	KI	207.90	14.84	37
		Mean (intensity)	SD	n
Pachytene	WT	0.2984	0.1356	65
	KI	0.4532	0.1784	70
Diplotene	WT	0.2829	0.1232	70
	KI	0.4497	0.2373	69

BRME1 oocytes		Mean (intensity)	SD	n
Pachytene	WT	0.3090	0.1204	44
	KI	0.4058	0.1806	49
Diplotene	WT	0.1993	0.1343	43
	KI	0.2787	0.1302	45

HSF2BP spermatocytes		Nº foci	SD	n
Zygotene	WT	180.5	16.70	40
	KI	180.1	18.08	38
		Mean (intensity)	SD	n
Pachytene	WT	0.2579	0.0820	45
	KI	0.5086	0.1602	45
Diplotene	WT	0.2514	0.0777	45
	KI	0.4694	0.1103	45

HSF2BP oocytes		Mean (intensity)	SD	n
Pachytene	WT	0.3763	0.1490	41
	KI	0.4670	0.1899	45
Diplotene	WT	0.3353	0.1237	39
	KI	0.4528	0.1655	44

MLH1 spermatocytes		Nº foci	SD	n
Pachytene	WT	22.98	1.61	60
	KI	20.72	1.79	60

MLH1 oocytes		Nº foci	SD	n
Pachytene	WT	23.82	2.02	51
	KI	22.39	3.01	54

DMC1 spermatocytes		Nº foci	SD	n
Leptotene	WT	95.53	14.76	43
	KI	94.42	15.47	43
Zygotene	WT	128.10	31.33	45
	KI	122.50	25.06	45
Pachytene	WT	25.51	7.03	37
	KI	23.17	5.30	29

DMC1 oocytes		Nº foci	SD	n
Pachytene	WT	37.09	13.61	43
	KI	35.86	12.14	44
Diplotene	WT	9.14	3.67	42
	KI	8.67	3.63	42

RPA spermatocytes		Nº foci	SD	n
Zygotene	WT	178.90	12.24	40
	KI	178.70	13.56	40
Pachytene	WT	85.92	12.17	60
	KI	88.63	13.27	60

RPA oocytes		Nº foci	SD	n
Pachytene	WT	28.90	7.52	40
	KI	29.95	8.12	40
Diplotene	WT	9.39	2.56	33
	KI	9.54	2.73	35

SPATA22 spermatocytes		Nº foci	SD	n
Zygotene	WT	226.90	23.52	40
	KI	223.20	21.05	37
Pachytene	WT	119.50	23.73	40
	KI	123.00	26.22	40

SPATA22 oocytes		Nº foci	SD	n
Pachytene	WT	45.18	14.09	40
	KI	46.30	14.05	40
Diplotene	WT	30.55	10.39	31
	KI	28.67	11.44	36

n = numbers of analysed cells from at least two animals.

Supplementary Table 6. Mass spectrometry.

Protein extracts from wild-type testis were immunoprecipitated with anti-RAD51B. The IBAQ values corresponding to RAD51C and RAD51B (positive control) are shown.

Protein	IBAQ anti-RAD51B	IBAQ IgG
RAD51C	261220	0
RAD51B	227510	0

REFERENCES

REFERENCES

Abascal, F., Acosta, R., Addleman, N. J., Adrian, J., Afzal, V., Aken, B., Akiyama, J. A., Jammal, O. al, Amrhein, H., Anderson, S. M., Andrews, G. R., Antoshechkin, I., Ardlie, K. G., Armstrong, J., Astley, M., Banerjee, B., Barkal, A. A., Barnes, I. H. A., Barozzi, I., … Myers, R. M. (2020). Perspectives on ENCODE. *Nature 2020 583:7818*, *583*(7818), 693–698. https://doi.org/10.1038/s41586-020-2449-8

Abir, R., Fisch, B., Nahum, R., Orvieto, R., Nitke, S., & Rafael, Z. ben. (2001). Turner's syndrome and fertility: current status and possible putative prospects. *Human Reproduction Update*, *7*(6), 603–610. https://doi.org/10.1093/HUMUPD/7.6.603

Adelman, C. A., Lolo, R. L., Birkbak, N. J., Murina, O., Matsuzaki, K., Horejsi, Z., Parmar, K., Borel, V., Skehel, J. M., Stamp, G., D'Andrea, A., Sartori, A. A., Swanton, C., & Boulton, S. J. (2013). HELQ promotes RAD51 paralog-dependent repair to avert germ cell attrition and tumourigenesis. *Nature*, *502*(7471), 381–384. https://doi.org/10.1038/NATURE12565

Aguilera, A., & García-Muse, T. (2013). Causes of genome instability. *Annual Review of Genetics*, *47*, 1–32. https://doi.org/10.1146/ANNUREV-GENET-111212-133232

Aguilera, A., & Gómez-González, B. (2008). Genome instability: A mechanistic view of its causes and consequences. In *Nature Reviews Genetics* (Vol. 9, Issue 3, pp. 204–217). https://doi.org/10.1038/nrg2268

Ahituv, N., Zhu, Y., Visel, A., Holt, A., Afzal, V., Pennacchio, L. A., & Rubin, E. M. (2007). Deletion of Ultraconserved Elements Yields Viable Mice. *PLOS Biology*, *5*(9), e234. https://doi.org/10.1371/JOURNAL.PBIO.0050234

Akeson, E. C., & Davisson, M. T. (2000). Mitotic Chromosome Preparations from Mouse Cells for Karyotyping. *Current Protocols in Human Genetics*, *25*(1), 4.10.1-4.10.19. https://doi.org/10.1002/0471142905.HG0410S25

Ali, H., Unar, A., Zubair, M., Dil, S., Ullah, F., Khan, I., Hussain, A., & Shi, Q. (2022). In silico analysis of a novel pathogenic variant c.7G > A in C14orf39 gene identified by WES in a Pakistani family with azoospermia. *Molecular Genetics and Genomics : MGG*, *297*(3), 719–730. https://doi.org/10.1007/S00438-022-01876-4

Allers, T., & Lichten, M. (2001). Differential timing and control of noncrossover and crossover recombination during meiosis. *Cell*, *106*(1), 47–57. https://doi.org/10.1016/S0092-8674(01)00416-0

Ameziane, N., May, P., Haitjema, A., van de Vrugt, H. J., van Rossum-Fikkert, S. E., Ristic, D., Williams, G. J., Balk, J., Rockx, D., Li, H., Rooimans, M. A., Oostra, A. B., Velleuer, E., Dietrich, R., Bleijerveld, O. B., Maarten Altelaar, A. F., Meijers-Heijboer, H., Joenje, H., Glusman, G., … Dorsman, J. C. (2015). A novel Fanconi anaemia subtype associated with a dominant-negative mutation in RAD51. *Nature Communications*, *6*. https://doi.org/10.1038/NCOMMS9829

Anand, R., Buechelmaier, E., Belan, O., Newton, M., Vancevska, A., Kaczmarczyk, A., Takaki, T., Rueda, D. S., Powell, S. N., & Boulton, S. J. (2022). HELQ is a dual-function DSB repair enzyme modulated by RPA and RAD51. *Nature*, *601*(7892), 268–273. https://doi.org/10.1038/S41586-021-04261-0

Argüello-Miranda, O., Zagoriy, I., Mengoli, V., Rojas, J., Jonak, K., Oz, T., Graf, P., & Zachariae, W. (2017). Casein Kinase 1 Coordinates Cohesin Cleavage, Gametogenesis, and Exit from M Phase in Meiosis II. *Developmental Cell*, *40*(1), 37–52. https://doi.org/10.1016/J.DEVCEL.2016.11.021

Baker, S. M., Plug, A. W., Prolla, T. A., Bronner, C. E., Harris, A. C., Yao, X., Christie, D. M., Monell, C., Arnheim, N., Bradley, A., Ashley, T., & Liskay, R. M. (1996). Involvement of mouse Mlh1 in DNA mismatch repair and meiotic crossing over. *Nature Genetics*, *13*(3), 336–342. https://doi.org/10.1038/NG0796-336

Bakhoum, S. F., & Landau, D. A. (2017). Chromosomal Instability as a Driver of Tumor Heterogeneity and Evolution. *Cold Spring Harbor Perspectives in Medicine*, *7*(6). https://doi.org/10.1101/cshperspect.a029611

Balbo, S., & Brooks, P. J. (2015). Implications of acetaldehyde-derived DNA adducts for understanding alcohol-related carcinogenesis. *Advances in Experimental Medicine and Biology*, *815*, 71–88. https://doi.org/10.1007/978-3-319-09614-8_5

Baltus, A. E., Menke, D. B., Hu, Y. C., Goodheart, M. L., Carpenter, A. E., de Rooij, D. G., & Page, D. C. (2006). In germ cells of mouse embryonic ovaries, the decision to enter meiosis precedes premeiotic DNA replication. *Nature Genetics*, *38*(12), 1430–1434. https://doi.org/10.1038/NG1919

Bannister, L. A., Pezza, R. J., Donaldson, J. R., de Rooij, D. G., Schimenti, K. J., Camerini-Otero, R. D., & Schimenti, J. C. (2007). A dominant, recombination-defective allele of Dmc1 causing male-specific sterility. *PLoS Biology*, *5*(5), 1016–1025. https://doi.org/10.1371/JOURNAL.PBIO.0050105

Bard, J. B. l., Kaufman, M. H., Dubreuil, C., Brune, R. M., Burger, A., Baldock, R. A., & Davidson, D. R. (1998). An internet-accessible database of mouse developmental anatomy based on a systematic nomenclature. *Mechanisms of Development*, *74*(1–2), 111–120. https://doi.org/10.1016/S0925-4773(98)00069-0

Barrett, R. D. H., Laurent, S., Mallarino, R., Pfeifer, S. P., Xu, C. C. Y., Foll, M., Wakamatsu, K., Duke-Cohan, J. S., Jensen, J. D., & Hoekstra, H. E. (2019). Linking a mutation to survival in wild mice. *Science (New York, N.Y.)*, *363*(6426), 499–504. https://doi.org/10.1126/SCIENCE.AAV3824

Baudat, F., Buard, J., Grey, C., Fledel-Alon, A., Ober, C., Przeworski, M., Coop, G., & de Massy, B. (2010). PRDM9 is a major determinant of meiotic recombination hotspots in humans and mice. *Science (New York, N.Y.)*, *327*(5967), 836–840. https://doi.org/10.1126/SCIENCE.1183439

Baudat, F., & de Massy, B. (2007). Regulating double-stranded DNA break repair towards crossover or non-crossover during mammalian meiosis. *Chromosome Research : An International Journal on the Molecular, Supramolecular and Evolutionary Aspects of Chromosome Biology*, *15*(5), 565–577. https://doi.org/10.1007/S10577-007-1140-3

Baudat, F., Imai, Y., & de Massy, B. (2013). Meiotic recombination in mammals: localization and regulation. *Nature Publishing Group*. https://doi.org/10.1038/nrg3573

Baudat, F., Manova, K., Yuen, J. P., Jasin, M., & Keeney, S. (2000). Chromosome synapsis defects and sexually dimorphic meiotic progression in mice lacking Spo11. *Molecular Cell*, *6*(5), 989–998. https://doi.org/10.1016/S1097-2765(00)00098-8

Bejerano, G., Pheasant, M., Makunin, I., Stephen, S., Kent, W. J., Mattick, J. S., & Haussler, D. (2004). Ultraconserved elements in the human genome. *Science (New York, N.Y.)*, *304*(5675), 1321–1325. https://doi.org/10.1126/science.1098119

Bellani, M. A., Romanienko, P. J., Cairatti, D. A., & Camerini-Otero, R. D. (2005). SPO11 is required for sex-body formation, and Spo11 heterozygosity rescues the prophase arrest of Atm-/- spermatocytes. *Journal of Cell Science*, *118*(Pt 15), 3233–3245. https://doi.org/10.1242/JCS.02466

Berti, M., Teloni, F., Mijic, S., Ursich, S., Fuchs, J., Palumbieri, M. D., Krietsch, J., Schmid, J. A., Garcin, E. B., Gon, S., Modesti, M., Altmeyer, M., & Lopes, M. (2020). Sequential role of RAD51 paralog complexes in replication fork remodeling and restart. *Nature Communications*, *11*(1). https://doi.org/10.1038/S41467-020-17324-Z

Bhattacharyya, A., Ear, U. S., Koller, B. H., Weichselbaum, R. R., & Bishop, D. K. (2000). The breast cancer susceptibility gene BRCA1 is required for subnuclear assembly of Rad51 and survival following treatment with the DNA cross-linking agent cisplatin. *The Journal of Biological Chemistry*, *275*(31), 23899–23903. https://doi.org/10.1074/JBC.C000276200

Bishop, C. E., Whitworth, D. J., Qin, Y., Agoulnik, A. I., Agoulnik, I. U., Harrison, W. R., Behringer, R. R., & Overbeek, P. A. (2000). A transgenic insertion upstream of sox9 is associated with dominant XX sex reversal in the mouse. *Nature Genetics*, *26*(4), 490–494. https://doi.org/10.1038/82652

Boffelli, D., McAuliffe, J., Ovcharenko, D., Lewis, K. D., Ovcharenko, I., Pachter, L., & Rubin, E. M. (2003). Phylogenetic shadowing of primate sequences to find functional regions of the human genome. *Science (New York, N.Y.)*, *299*(5611), 1391–1394. https://doi.org/10.1126/SCIENCE.1081331

Bolcun-Filas, E., & Handel, M. A. (2018). Meiosis: the chromosomal foundation of reproduction. *Biology of Reproduction*, *99*(1), 112–126. https://doi.org/10.1093/BIOLRE/IOY021

Bonilla, B., Hengel, S. R., Grundy, M. K., & Bernstein, K. A. (2020). RAD51 Gene Family Structure and Function. *Annual Review of Genetics*, *54*, 25–46. https://doi.org/10.1146/ANNUREV-GENET-021920-092410

Bouilly, J., Bachelot, A., Broutin, I., Touraine, P., & Binart, N. (2011). Novel NOBOX loss-of-function mutations account for 6.2% of cases in a large primary ovarian insufficiency cohort. *Human Mutation*, *32*(10), 1108–1113. https://doi.org/10.1002/HUMU.21543

Bowles, J., Feng, C. W., Ineson, J., Miles, K., Spiller, C. M., Harley, V. R., Sinclair, A. H., & Koopman, P. (2018). Retinoic Acid Antagonizes Testis Development in Mice. *Cell Reports*, *24*(5), 1330–1341. https://doi.org/10.1016/J.CELREP.2018.06.111

Bowles, J., Feng, C. W., Miles, K., Ineson, J., Spiller, C., & Koopman, P. (2016). ALDH1A1 provides a source of meiosis-inducing retinoic acid in mouse fetal ovaries. *Nature Communications*, *7*. https://doi.org/10.1038/NCOMMS10845

Bowles, J., Knight, D., Smith, C., Wilhelm, D., Richman, J., Mamiya, S., Yashiro, K., Chawengsaksophak, K., Wilson, M. J., Rossant, J., Hamada, H., & Koopman, P. (2006). Retinoid signaling determines germ cell fate in mice. *Science (New York, N.Y.)*, *312*(5773), 596–600. https://doi.org/10.1126/SCIENCE.1125691

Brandsma, I., Sato, K., van Rossum-Fikkert, S. E., van Vliet, N., Sleddens, E., Reuter, M., Odijk, H., van den Tempel, N., Dekkers, D. H. W., Bezstarosti, K., Demmers, J. A. A., Maas, A., Lebbink, J., Wyman, C., Essers, J., van Gent, D. C., Baarends, W. M., Knipscheer, P., Kanaar, R., & Zelensky, A. N. (2019). HSF2BP Interacts with a Conserved Domain of BRCA2 and Is Required for Mouse Spermatogenesis. *Cell Reports*, *27*(13), 3790-3798.e7. https://doi.org/10.1016/J.CELREP.2019.05.096

Brick, K., Smagulova, F., Khil, P., Camerini-Otero, R. D., & Petukhova, G. v. (2012). Genetic recombination is directed away from functional genomic elements in mice. *Nature*, *485*(7400), 642–645. https://doi.org/10.1038/NATURE11089

Byeon, G. W., Cenik, E. S., Jiang, L., Tang, H., Das, R., & Barna, M. (2021). Functional and structural basis of extreme conservation in vertebrate 5' untranslated regions. *Nature Genetics*, *53*(5), 729–741. https://doi.org/10.1038/S41588-021-00830-1

Caburet, S., Arboleda, V. A., Llano, E., Overbeek, P. A., Barbero, J. L., Oka, K., Harrison, W., Vaiman, D., Ben-Neriah, Z., García-Tuñón, I., Fellous, M., Pendás, A. M., Veitia, R. A., & Vilain, E. (2014). Mutant cohesin in premature ovarian failure. *The New England Journal of Medicine*, *370*(10), 943–949. https://doi.org/10.1056/NEJMOA1309635

Caburet, S., Heddar, A., Dardillac, E., Creux, H., Lambert, M., Messiaen, S., Tourpin, S., Livera, G., Lopez, B. S., & Misrahi, M. (2020). Homozygous hypomorphic BRCA2 variant in primary ovarian insufficiency without cancer or Fanconi anaemia trait. *Journal of Medical Genetics*, *58*(2), 125–134. https://doi.org/10.1136/JMEDGENET-2019-106672

Caburet, S., Todeschini, A. L., Petrillo, C., Martini, E., Farran, N. D., Legois, B., Livera, G., Younis, J. S., Shalev, S., & Veitia, R. A. (2019). A truncating MEIOB mutation responsible for familial primary ovarian insufficiency abolishes its interaction with its partner SPATA22 and their recruitment to DNA double-strand breaks. *EBioMedicine*, *42*, 524–531. https://doi.org/10.1016/J.EBIOM.2019.03.075

Caldecott, K. W. (2008). Single-strand break repair and genetic disease. *Nature Reviews. Genetics*, *9*(8), 619–631. https://doi.org/10.1038/NRG2380

Campos, A., & Clemente-Blanco, A. (2020). Cell Cycle and DNA Repair Regulation in the Damage Response: Protein Phosphatases Take Over the Reins. *International Journal of Molecular Sciences*, *21*(2). https://doi.org/10.3390/IJMS21020446

Carlosama, C., Elzaiat, M., Patiño, L. C., Mateus, H. E., Veitia, R. A., & Laissue, P. (2017). A homozygous donor splice-site mutation in the meiotic gene MSH4 causes primary ovarian insufficiency. *Human Molecular Genetics*, *26*(16), 3161–3166. https://doi.org/10.1093/HMG/DDX199

Chambon, J. P., Touati, S. A., Berneau, S., Cladière, D., Hebras, C., Groeme, R., McDougall, A., & Wassmann, K. (2013). The PP2A inhibitor I2PP2A is essential for sister chromatid segregation in oocyte meiosis II. *Current Biology : CB*, *23*(6), 485–490. https://doi.org/10.1016/J.CUB.2013.02.004

Chang, H. H. Y., Pannunzio, N. R., Adachi, N., & Lieber, M. R. (2017). Non-homologous DNA end joining and alternative pathways to double-strand break repair. *Nature Reviews. Molecular Cell Biology*, *18*(8), 495–506. https://doi.org/10.1038/nrm.2017.48

Chang, Y. F., Imam, J. S., & Wilkinson, M. F. (2007). The nonsense-mediated decay RNA surveillance pathway. *Annual Review of Biochemistry*, *76*, 51–74. https://doi.org/10.1146/ANNUREV.BIOCHEM.76.050106.093909

Chen, H., Lisby, M., & Symington, L. S. (2013). RPA coordinates DNA end resection and prevents formation of DNA hairpins. *Molecular Cell*, *50*(4), 589–600. https://doi.org/10.1016/J.MOLCEL.2013.04.032

Cheng, C. Y., & Mruk, D. D. (2002). Cell junction dynamics in the testis: Sertoli-germ cell interactions and male contraceptive development. *Physiological Reviews*, *82*(4), 825–874. https://doi.org/10.1152/PHYSREV.00009.2002

Cherri, S., Oneda, E., Noventa, S., Melocchi, L., & Zaniboni, A. (2022). Microsatellite instability and chemosensitivity in solid tumours. *Therapeutic Advances in Medical Oncology*, *14*, 17588359221099348. https://doi.org/10.1177/17588359221099347

Chun, J., Buechelmaier, E. S., & Powell, S. N. (2013). Rad51 paralog complexes BCDX2 and CX3 act at different stages in the BRCA1-BRCA2-dependent homologous recombination pathway. *Molecular and Cellular Biology*, *33*(2), 387–395. https://doi.org/10.1128/MCB.00465-12

Clermont, Y. (1972). Kinetics of spermatogenesis in mammals: seminiferous epithelium cycle and spermatogonial renewal. *Physiological Reviews*, *52*(1), 198–236. https://doi.org/10.1152/PHYSREV.1972.52.1.198

Clift, D., So, C., McEwan, W. A., James, L. C., & Schuh, M. (2018). Acute and rapid degradation of endogenous proteins by Trim-Away. *Nature Protocols*, *13*(10), 2149–2175. https://doi.org/10.1038/S41596-018-0028-3

Cortez, D. (2019). Replication-Coupled DNA Repair. *Molecular Cell*, *74*(5), 866–876. https://doi.org/10.1016/J.MOLCEL.2019.04.027

Costa, Y., Speed, R., Öllinger, R., Aisheimer, M., Semple, C. A., Gautier, P., Maratou, K., Novak, I., Höög, C., Benavente, R., & Cooke, H. J. (2005). Two novel proteins recruited by synaptonemal complex protein 1 (SYCP1) are at the centre of meiosis. *Journal of Cell Science*, *118*(Pt 12), 2755–2762. https://doi.org/10.1242/JCS.02402

Cox, J., & Mann, M. (2008). MaxQuant enables high peptide identification rates, individualized p.p.b.-range mass accuracies and proteome-wide protein quantification. *Nature Biotechnology*, *26*(12), 1367–1372. https://doi.org/10.1038/nbt.1511

Craig Venter, J., Adams, M. D., Myers, E. W., Li, P. W., Mural, R. J., Sutton, G. G., Smith, H. O., Yandell, M., Evans, C. A., Holt, R. A., Gocayne, J. D., Amanatides, P., Ballew, R. M., Huson, D. H., Wortman, J. R., Zhang, Q., Kodira, C. D., Zheng, X. H., Chen, L., … Zhu, X. (2001). The sequence of the human genome. *Science (New York, N.Y.)*, *291*(5507), 1304–1351. https://doi.org/10.1126/SCIENCE.1058040

Croft, J. A., Bridger, J. M., Boyle, S., Perry, P., Teague, P., & Bickmore, W. A. (1999). Differences in the localization and morphology of chromosomes in the human nucleus. *The Journal of Cell Biology*, *145*(6), 1119–1131. https://doi.org/10.1083/JCB.145.6.1119

da Cruz, I., Rodríguez-Casuriaga, R., Santiñaque, F. F., Farías, J., Curti, G., Capoano, C. A., Folle, G. A., Benavente, R., Sotelo-Silveira, J. R., & Geisinger, A. (2016). Transcriptome analysis of highly purified mouse spermatogenic cell populations: gene expression signatures switch from meiotic-to postmeiotic-related processes at pachytene stage. *BMC Genomics*, *17*(1). https://doi.org/10.1186/S12864-016-2618-1

Dai, J., Voloshin, O., Potapova, S., & Camerini-Otero, R. D. (2017). Meiotic Knockdown and Complementation Reveals Essential Role of RAD51 in Mouse Spermatogenesis. *Cell Reports*, *18*(6), 1383–1394. https://doi.org/10.1016/J.CELREP.2017.01.024

D'Andrea, A. D., & Grompe, M. (2003). The Fanconi anaemia/BRCA pathway. *Nature Reviews. Cancer*, *3*(1), 23–34. https://doi.org/10.1038/NRC970

Date, O., Katsura, M., Ishida, M., Yoshihara, T., Kinomura, A., Sueda, T., & Miyagawa, K. (2006). Haploinsufficiency of RAD51B causes centrosome fragmentation and aneuploidy in human cells. *Cancer Research*, *66*(12), 6018–6024. https://doi.org/10.1158/0008-5472.CAN-05-2803

de Kretser, D. M., Loveland, K., & O'Bryan, M. (2016). Spermatogenesis. *Endocrinology: Adult and Pediatric*, *2–2*, 2325-2353.e9. https://doi.org/10.1016/B978-0-323-18907-1.00136-0

de Rooij, D. G. (2017). The nature and dynamics of spermatogonial stem cells. *Development (Cambridge, England)*, *144*(17), 3022–3030. https://doi.org/10.1242/DEV.146571

de Vries, L., Behar, D. M., Smirin-Yosef, P., Lagovsky, I., Tzur, S., & Basel-Vanagaite, L. (2014). Exome sequencing reveals SYCE1 mutation associated with autosomal recessive primary ovarian insufficiency. *The Journal of Clinical Endocrinology and Metabolism*, *99*(10), E2129–E2132. https://doi.org/10.1210/JC.2014-1268

Deans, A. J., & West, S. C. (2011). DNA interstrand crosslink repair and cancer. *Nature Reviews. Cancer*, *11*(7), 467–480. https://doi.org/10.1038/NRC3088

Deans, B., Griffin, C. S., Maconochie, M., & Thacker, J. (2000). Xrcc2 is required for genetic stability, embryonic neurogenesis and viability in mice. *The EMBO Journal*, *19*(24), 6675–6685. https://doi.org/10.1093/EMBOJ/19.24.6675

Dermitzakis, E. T., Reymond, A., & Antonarakis, S. E. (2005). Conserved non-genic sequences — an unexpected feature of mammalian genomes. *Nature Reviews Genetics 2005 6:2*, *6*(2), 151–157. https://doi.org/10.1038/nrg1527

di Pasquale, E., Beck-Peccoz, P., & Persani, L. (2004). Hypergonadotropic ovarian failure associated with an inherited mutation of human bone morphogenetic protein-15 (BMP15) gene. *American Journal of Human Genetics*, *75*(1), 106–111. https://doi.org/10.1086/422103

Dickel, D. E., Ypsilanti, A. R., Pla, R., Zhu, Y., Barozzi, I., Mannion, B. J., Khin, Y. S., Fukuda-Yuzawa, Y., Plajzer-Frick, I., Pickle, C. S., Lee, E. A., Harrington, A. N., Pham, Q. T., Garvin, T. H., Kato, M., Osterwalder, M., Akiyama, J. A., Afzal, V., Rubenstein, J. L. R., … Visel, A. (2018). Ultraconserved Enhancers Are Required for Normal Development. *Cell*, *172*(3), 491. https://doi.org/10.1016/J.CELL.2017.12.017

D'Souza, A., Blee, A. M., & Chazin, W. J. (2022). Mechanism of action of nucleotide excision repair machinery. *Biochemical Society Transactions*, *50*(1), 375–386. https://doi.org/10.1042/BST20210246

Endo, T., Mikedis, M. M., Nicholls, P. K., Page, D. C., & de Rooij, D. G. (2019). Retinoic Acid and Germ Cell Development in the Ovary and Testis. *Biomolecules*, *9*(12). https://doi.org/10.3390/BIOM9120775

Enguita-Marruedo, A., Martín-Ruiz, M., García, E., Gil-Fernández, A., Parra, M. T., Viera, A., Rufas, J. S., & Page, J. (2019). Transition from a meiotic to a somatic-like DNA damage response during the pachytene stage in mouse meiosis. *PLoS Genetics*, *15*(1). https://doi.org/10.1371/JOURNAL.PGEN.1007439

Fang, Q., George, A. S., Brinkmeier, M. L., Mortensen, A. H., Gergics, P., Cheung, L. Y. M., Daly, A. Z., Ajmal, A., Millán, M. I. P., Bilge Ozel, A., Kitzman, J. O., Mills, R. E., Li, J. Z., & Camper, S. A. (2016). Genetics of Combined Pituitary Hormone Deficiency: Roadmap into the Genome Era. *Endocrine Reviews*, *37*(6), 636–675. https://doi.org/10.1210/ER.2016-1101

Fayomi, A., David, S., Doungkamchan, C., & Orwig, K. E. (2018). Spermatogonia. *Encyclopedia of Reproduction*, 24–35. https://doi.org/10.1016/B978-0-12-801238-3.64424-0

Felipe-Medina, N., Caburet, S., Sánchez-Sáez, F., Condezo, Y. B., de Rooij, D., Gómez-H, L., García-Valiente, R., Todeschini, A. L., Duque, P., Sánchez-Martín, M., Shalev, S. A., Llano, E., Veitia, R. A., & Pendás, A. M. (2020). A missense in HSF2BP causing primary ovarian insufficiency affects meiotic recombination by its novel interactor C19ORF57/BRME1. *ELife*, *9*, 1–93. https://doi.org/10.7554/ELIFE.56996

Ferlin, A., Raicu, F., Gatta, V., Zuccarello, D., Palka, G., & Foresta, C. (2007). Male infertility: role of genetic background. *Reproductive Biomedicine Online*, *14*(6), 734–745. https://doi.org/10.1016/S1472-6483(10)60677-3

Folmer, V., Soares, J. C. M., Gabriel, D., & Rocha, J. B. T. (2003). A high fat diet inhibits delta-aminolevulinate dehydratase and increases lipid peroxidation in mice (Mus musculus). *The Journal of Nutrition*, *133*(7), 2165–2170. https://doi.org/10.1093/JN/133.7.2165

Franca, M. M., Condezo, Y. B., Elzaiat, M., Felipe-Medina, N., Sánchez-Sáez, F., Muñoz, S., Sainz-Urruela, R., Martín-Hervás, M. R., García-Valiente, R., Sánchez-Martín, M. A., Astudillo, A., Mendez, J., Llano, E., Veitia, R. A., Mendonca, B. B., & Pendás, A. M. (2022). A truncating variant of RAD51B associated with primary ovarian insufficiency provides insights into its meiotic and somatic functions. *Cell Death and Differentiation*. https://doi.org/10.1038/S41418-022-01021-Z

França, M. M., Lerario, A. M., Funari, M. F. A., Nishi, M. Y., Narcizo, A. M., Mello, M. P. de, Guerra-Junior, G., Maciel-Guerra, A. T., & Mendonça, B. B. (2017). A Novel Homozygous Missense FSHR Variant Associated with Hypergonadotropic Hypogonadism in Two Siblings from a Brazilian Family. *Sexual Development*, *11*(3), 137–142. https://doi.org/10.1159/000477193

França, M. M., & Mendonca, B. B. (2022). Genetics of ovarian insufficiency and defects of folliculogenesis. *Best Practice & Research. Clinical Endocrinology & Metabolism*, *36*(1). https://doi.org/10.1016/J.BEEM.2021.101594

Frazer, K. A., Tao, H., Osoegawa, K., de Jong, P. J., Chen, X., Doherty, M. F., & Cox, D. R. (2004). Noncoding sequences conserved in a limited number of mammals in the SIM2 interval are frequently functional. *Genome Research*, *14*(3), 367–372. https://doi.org/10.1101/GR.1961204

Garcin, E. B., Gon, S., Sullivan, M. R., Brunette, G. J., de Cian, A., Concordet, J. P., Giovannangeli, C., Dirks, W. G., Eberth, S., Bernstein, K. A., Prakash, R., Jasin, M., & Modesti, M. (2019). Differential Requirements for the RAD51 Paralogs in Genome Repair and Maintenance in Human Cells. *PLoS Genetics*, *15*(10). https://doi.org/10.1371/JOURNAL.PGEN.1008355

Garrison, E., & Marth, G. (2012). *Haplotype-based variant detection from short-read sequencing*.

Gaynor, K. U., Grigorieva, I. v., Mirczuk, S. M., Piret, S. E., Kooblall, K. G., Stevenson, M., Rizzoti, K., Bowl, M. R., Nesbit, M. A., Christie, P. T., Fraser, W. D., Hough, T., Whyte, M. P., Lovell-Badge, R., & Thakker, R. v. (2020). Studies of mice deleted for Sox3 and uc482: relevance to X-linked hypoparathyroidism. *Endocrine Connections*, *9*(2), 173–186. https://doi.org/10.1530/EC-19-0478

Giglia-Mari, G., Zotter, A., & Vermeulen, W. (2011). DNA damage response. *Cold Spring Harbor Perspectives in Biology*, *3*(1), 1–19. https://doi.org/10.1101/CSHPERSPECT.A000745

Glazko, G. v., Koonin, E. v., Rogozin, I. B., & Shabalina, S. A. (2003). A significant fraction of conserved noncoding DNA in human and mouse consists of predicted matrix attachment regions. *Trends in Genetics : TIG*, *19*(3), 119–124. https://doi.org/10.1016/S0168-9525(03)00016-7

Godin, S. K., Sullivan, M. R., & Bernstein, K. A. (2016). Novel insights into RAD51 activity and regulation during homologous recombination and DNA replication. *Biochemistry and Cell Biology = Biochimie et Biologie Cellulaire*, *94*(5), 407–418. https://doi.org/10.1139/BCB-2016-0012

Golezar, S., Ramezani Tehrani, F., Khazaei, S., Ebadi, A., & Keshavarz, Z. (2019). The global prevalence of primary ovarian insufficiency and early menopause: a meta-analysis. *Climacteric : The Journal of the International Menopause Society*, *22*(4), 403–411. https://doi.org/10.1080/13697137.2019.1574738

Gómez, R., Valdeolmillos, A., Parra, M. T., Viera, A., Carreiro, C., Roncal, F., Rufas, J. S., Barbero, J. L., & Suja, J. A. (2007). Mammalian SGO2 appears at the inner centromere domain and redistributes depending on tension across centromeres during meiosis II and mitosis. *EMBO Reports*, *8*(2), 173–180. https://doi.org/10.1038/SJ.EMBOR.7400877

Gómez-H, L., Felipe-Medina, N., Sánchez-Martín, M., Davies, O. R., Ramos, I., García-Tuñón, I., de Rooij, D. G., Dereli, I., Tóth, A., Barbero, J. L., Benavente, R., Llano, E., & Pendas, A. M. (2016). C14ORF39/SIX6OS1 is a constituent of the synaptonemal complex and is essential for mouse fertility. *Nature Communications*, *7*. https://doi.org/10.1038/NCOMMS13298

González, F., Georgieva, D., Vanoli, F., Shi, Z.-D., Stadtfeld, M., Ludwig, T., Jasin, M., & Huangfu, D. (2013). Homologous Recombination DNA Repair Genes Play a Critical Role in Reprogramming to a Pluripotent State. *Cell Reports*, *3*(3), 651–660. https://doi.org/10.1016/J.CELREP.2013.02.005

Grangeia, A., Sá, R., Carvalho, F., Martin, J., Girodon, E., Silva, J., Ferráz, L., Barros, A., & Sousa, M. (2007). Molecular characterization of the cystic fibrosis transmembrane conductance regulator gene in congenital absence of the vas deferens. *Genetics in Medicine : Official Journal of the American College of Medical Genetics*, *9*(3), 163–172. https://doi.org/10.1097/GIM.0B013E3180318AAF

Gryaznova, Y., Keating, L., Touati, S. A., Cladière, D., Yakoubi, W. el, Buffin, E., & Wassmann, K. (2021). Kinetochore individualization in meiosis I is required for centromeric cohesin removal in meiosis II. *The EMBO Journal*, *40*(7). https://doi.org/10.15252/EMBJ.2020106797

Guo, T., Zhao, S., Zhao, S., Chen, M., Li, G., Jiao, X., Wang, Z., Zhao, Y., Qin, Y., Gao, F., & Chen, Z. J. (2017). Mutations in MSH5 in primary ovarian insufficiency. *Human Molecular Genetics*, *26*(8), 1452–1457. https://doi.org/10.1093/HMG/DDX044

Gurnett, C. A., Bowcock, A. M., Dietz, F. R., Morcuende, J. A., Murray, J. C., & Dobbs, M. B. (2007). Two novel point mutations in the long-range SHH enhancer in three families with triphalangeal thumb and preaxial polydactyly. *American Journal of Medical Genetics. Part A*, *143A*(1), 27–32. https://doi.org/10.1002/AJMG.A.31563

Gutiérrez-Caballero, C., Cebollero, L. R., & Pendás, A. M. (2012). Shugoshins: from protectors of cohesion to versatile adaptors at the centromere. *Trends in Genetics : TIG*, *28*(7), 351–360. https://doi.org/10.1016/J.TIG.2012.03.003

Hagting, A., den Elzen, N., Vodermaier, H. C., Waizenegger, I. C., Peters, J. M., & Pines, J. (2002). Human securin proteolysis is controlled by the spindle checkpoint and reveals when the APC/C switches from activation by Cdc20 to Cdh1. *The Journal of Cell Biology*, *157*(7), 1125–1137. https://doi.org/10.1083/JCB.200111001

Hamer, G., Gell, K., Kouznetsova, A., Novak, I., Benavente, R., & Höög, C. (2006). Characterization of a novel meiosis-specific protein within the central element of the synaptonemal complex. *Journal of Cell Science*, *119*(Pt 19), 4025–4032. https://doi.org/10.1242/JCS.03182

Handel, M. A., & Schimenti, J. C. (2010). Genetics of mammalian meiosis: regulation, dynamics and impact on fertility. *Nature Reviews Genetics 2010 11:2*, *11*(2), 124–136. https://doi.org/10.1038/nrg2723

Hara, K., Nakagawa, T., Enomoto, H., Suzuki, M., Yamamoto, M., Simons, B. D., & Yoshida, S. (2014). Mouse spermatogenic stem cells continually interconvert between equipotent singly isolated and syncytial states. *Cell Stem Cell*, *14*(5), 658–672. https://doi.org/10.1016/j.stem.2014.01.019

Harris, S. E., Chand, A. L., Winship, I. M., Gersak, K., Aittomäki, K., & Shelling, A. N. (2002). Identification of novel mutations in FOXL2 associated with premature ovarian failure. *Molecular Human Reproduction*, *8*(8), 729–733. https://doi.org/10.1093/MOLEHR/8.8.729

Hassold, T., & Hunt, P. (2001). To err (meiotically) is human: the genesis of human aneuploidy. *Nature Reviews. Genetics*, *2*(4), 280–291. https://doi.org/10.1038/35066065

Hauf, S., Waizenegger, I. C., & Peters, J. M. (2001). Cohesin cleavage by separase required for anaphase and cytokinesis in human cells. *Science (New York, N.Y.)*, *293*(5533), 1320–1323. https://doi.org/10.1126/SCIENCE.1061376

He, W. bin, Tu, C. F., Liu, Q., Meng, L. L., Yuan, S. M., Luo, A. X., He, F. S., Shen, J., Li, W., Du, J., Zhong, C. G., Lu, G. X., Lin, G., Fan, L. Q., & Tan, Y. Q. (2018). DMC1 mutation that causes human non-obstructive azoospermia and premature ovarian insufficiency identified by whole-exome sequencing. *Journal of Medical Genetics*, *55*(3), 198–204. https://doi.org/10.1136/JMEDGENET-2017-104992

Helleday, T., Petermann, E., Lundin, C., Hodgson, B., & Sharma, R. A. (2008). DNA repair pathways as targets for cancer therapy. *Nature Reviews. Cancer*, *8*(3), 193–204. https://doi.org/10.1038/NRC2342

Hellmuth, S., Pöhlmann, C., Brown, A., Böttger, F., Sprinzl, M., & Stemmann, O. (2015). Positive and negative regulation of vertebrate separase by Cdk1-cyclin B1 may explain why securin is dispensable. *The Journal of Biological Chemistry*, *290*(12), 8002–8010. https://doi.org/10.1074/JBC.M114.615310

Herbert, M., Kalleas, D., Cooney, D., Lamb, M., & Lister, L. (2015). Meiosis and maternal aging: insights from aneuploid oocytes and trisomy births. *Cold Spring Harbor Perspectives in Biology*, *7*(4). https://doi.org/10.1101/CSHPERSPECT.A017970

Heyer, W. D., Ehmsen, K. T., & Liu, J. (2010). Regulation of homologous recombination in eukaryotes. *Annual Review of Genetics*, *44*, 113–139. https://doi.org/10.1146/ANNUREV-GENET-051710-150955

Hoeijmakers, J. H. J. (2009). DNA damage, aging, and cancer. *The New England Journal of Medicine*, *361*(15), 1475–1485. https://doi.org/10.1056/NEJMRA0804615

Holloway, J. K., Booth, J., Edelmann, W., McGowan, C. H., & Cohen, P. E. (2008). MUS81 Generates a Subset of MLH1-MLH3–Independent Crossovers in Mammalian Meiosis. *PLoS Genetics*, *4*(9), 1000186. https://doi.org/10.1371/JOURNAL.PGEN.1000186

Howlett, N. G., Taniguchi, T., Durkin, S. G., D'Andrea, A. D., & Glover, T. W. (2005). The Fanconi anemia pathway is required for the DNA replication stress response and for the regulation of common fragile site stability. *Human Molecular Genetics*, *14*(5), 693–701. https://doi.org/10.1093/HMG/DDI065

Huang, Q. yi, Chen, S. rong, Chen, J. ming, Shi, Q. yang, & Lin, S. (2022). Therapeutic options for premature ovarian insufficiency: an updated review. *Reproductive Biology and Endocrinology : RB&E*, *20*(1). https://doi.org/10.1186/S12958-022-00892-8

Huckins, C. (1971). The spermatogonial stem cell population in adult rats. I. Their morphology, proliferation and maturation. *The Anatomical Record*, *169*(3), 533–557. https://doi.org/10.1002/AR.1091690306

Hunter, N. (2015). Meiotic Recombination: The Essence of Heredity. *Cold Spring Harbor Perspectives in Biology*, *7*(12). https://doi.org/10.1101/CSHPERSPECT.A016618

Hunter, N., & Kleckner, N. (2001). The single-end invasion: an asymmetric intermediate at the double-strand break to double-holliday junction transition of meiotic recombination. *Cell*, *106*(1), 59–70. https://doi.org/10.1016/S0092-8674(01)00430-5

Ishiguro, K. ichiro. (2019). The cohesin complex in mammalian meiosis. *Genes to Cells : Devoted to Molecular & Cellular Mechanisms*, *24*(1), 6–30. https://doi.org/10.1111/GTC.12652

Ishiguro, K. ichiro, Matsuura, K., Tani, N., Takeda, N., Usuki, S., Yamane, M., Sugimoto, M., Fujimura, S., Hosokawa, M., Chuma, S., Ko, M. S. H., Araki, K., & Niwa, H. (2020). MEIOSIN Directs the Switch from Mitosis to Meiosis in Mammalian Germ Cells. *Developmental Cell*, *52*(4), 429-445.e10. https://doi.org/10.1016/J.DEVCEL.2020.01.010

Jasin, M., & Rothstein, R. (2013). Repair of strand breaks by homologous recombination. *Cold Spring Harbor Perspectives in Biology*, *5*(11). https://doi.org/10.1101/CSHPERSPECT.A012740

Jiang, H., Gao, Q., Zheng, W., Yin, S., Wang, L., Zhong, L., Ali, A., Khan, T., Hao, Q., Fang, H., Sun, X., Xu, P., Pandita, T. K., Jiang, X., & Shi, Q. (2018). MOF influences meiotic expansion of H2AX phosphorylation and spermatogenesis in mice. *PLoS Genetics*, *14*(5). https://doi.org/10.1371/JOURNAL.PGEN.1007300

Jinek, M., Chylinski, K., Fonfara, I., Hauer, M., Doudna, J. A., & Charpentier, E. (2012). A programmable dual RNA-guided DNA endonuclease in adaptive bacterial immunity. *Science (New York, N.Y.)*, *337*(6096), 816. https://doi.org/10.1126/SCIENCE.1225829

Jiricny, J. (2006). The multifaceted mismatch-repair system. *Nature Reviews. Molecular Cell Biology*, *7*(5), 335–346. https://doi.org/10.1038/NRM1907

Jose-Miller, A. B., Boyden, J., & Fry, K. (2007). Infertility. *American Family Physician*, *75*(6), 849–856. www.aafp.org/afp.

Juknytė, G., Laurinaitytė, I., Vilkevičiūtė, A., Gedvilaitė, G., Glebauskienė, B., Kriaučiūnienė, L., & Liutkevičienė, R. (2021). TBX15 rs98422, DNM3 rs1011731, RAD51B rs8017304, and rs2588809 Gene Polymorphisms and Associations With Pituitary Adenoma. *In Vivo (Athens, Greece)*, *35*(2), 815–826. https://doi.org/10.21873/INVIVO.12322

Kaseb, H., Rayi, A., & Hozayen, S. (2022). Chromosome Instability Syndromes. *StatPearls*. https://pubmed.ncbi.nlm.nih.gov/30725883/

Kauppi, L. (2021). USP26: a genetic risk factor for sperm X-Y aneuploidy. *The EMBO Journal*, *40*(13). https://doi.org/10.15252/EMBJ.2021108552

Kauppi, L., Barchi, M., Baudat, F., Romanienko, P. J., Keeney, S., & Jasin, M. (2011). Distinct properties of the XY pseudoautosomal region crucial for male meiosis. *Science (New York, N.Y.)*, *331*(6019), 916–920. https://doi.org/10.1126/SCIENCE.1195774

Keeney, S., Giroux, C. N., & Kleckner, N. (1997). Meiosis-specific DNA double-strand breaks are catalyzed by Spo11, a member of a widely conserved protein family. *Cell*, *88*(3), 375–384. https://doi.org/10.1016/S0092-8674(00)81876-0

Kerrebrock, A. W., Moore, D. P., Wu, J. S., & Orr-Weaver, T. L. (1995). Mei-S332, a Drosophila protein required for sister-chromatid cohesion, can localize to meiotic centromere regions. *Cell*, *83*(2), 247–256. https://doi.org/10.1016/0092-8674(95)90166-3

Kieff, E. and Rickinson, A.B. (2001) In Knipe, D.M., Howley, P.M. and Griffin, D.E., Eds., Fields Virology, Lippincott Williams & Wilkins, Philadelphia, 2511-2573. - References - Scientific Research Publishing. (n.d.). Retrieved June 22, 2022, from https://www.scirp.org/(S(351jmbntvnsjt1aadkozje))/reference/referencespapers.aspx?referenceid=1732968

Kim, H. J., Liu, C., & Dernburg, A. F. (2022). How and Why Chromosomes Interact with the Cytoskeleton during Meiosis. *Genes*, *13*(5). https://doi.org/10.3390/GENES13050901

Kim, J., Ishiguro, K., Nambu, A., Akiyoshi, B., Yokobayashi, S., Kagami, A., Ishiguro, T., Pendas, A. M., Takeda, N., Sakakibara, Y., Kitajima, T. S., Tanno, Y., Sakuno, T., & Watanabe, Y. (2014). *Meikin is a conserved regulator of meiosis-I-specific kinetochore function*. https://doi.org/10.1038/nature14097

Kitajima, T. S., Miyazaki, Y., Yamamoto, M., & Watanabe, Y. (2003). Rec8 cleavage by separase is required for meiotic nuclear divisions in fission yeast. *The EMBO Journal*, *22*(20), 5643–5653. https://doi.org/10.1093/EMBOJ/CDG527

Krausz, C., & Riera-Escamilla, A. (2018). Genetics of male infertility. *Nature Reviews Urology 2018 15:6*, *15*(6), 369–384. https://doi.org/10.1038/s41585-018-0003-3

Krejci, L., Altmannova, V., Spirek, M., & Zhao, X. (2012). Homologous recombination and its regulation. *Nucleic Acids Research*, *40*(13), 5795–5818. https://doi.org/10.1093/NAR/GKS270

Kudo, N. R., Anger, M., Peters, A. H. F. M., Stemmann, O., Theussl, H. C., Helmhart, W., Kudo, H., Heyting, C., & Nasmyth, K. (2009). Role of cleavage by separase of the Rec8 kleisin subunit of cohesin during mammalian meiosis I. *Journal of Cell Science*, *122*(Pt 15), 2686–2698. https://doi.org/10.1242/JCS.035287

Kumar, R., Bourbon, H. M., & de Massy, B. (2010). Functional conservation of Mei4 for meiotic DNA double-strand break formation from yeasts to mice. *Genes & Development*, *24*(12), 1266–1280. https://doi.org/10.1101/GAD.571710

Kumar, R., Ghyselinck, N., Ishiguro, K. ichiro, Watanabe, Y., Kouznetsova, A., Höög, C., Strong, E., Schimenti, J., Daniel, K., Toth, A., & de Massy, B. (2015). MEI4 – a central player in the regulation of meiotic DNA double-strand break formation in the mouse. *Journal of Cell Science*, *128*(9), 1800–1811. https://doi.org/10.1242/JCS.165464

Kuznetsov, S. G., Haines, D. C., Martin, B. K., & Sharan, S. K. (2009). Loss of Rad51c leads to embryonic lethality and modulation of Trp53-dependent tumorigenesis in mice. *Cancer Research*, *69*(3), 863–872. https://doi.org/10.1158/0008-5472.CAN-08-3057

Kuznetsov, S., Pellegrini, M., Shuda, K., Fernandez-Capetillo, O., Liu, Y., Martin, B. K., Burkett, S., Southon, E., Pati, D., Tessarollo, L., West, S. C., Donovan, P. J., Nussenzweig, A., & Sharan, S. K. (2007). RAD51C deficiency in mice results in early prophase I arrest in males and sister chromatid separation at metaphase II in females. *The Journal of Cell Biology*, *176*(5), 581–592. https://doi.org/10.1083/JCB.200608130

Kvon, E. Z., Zhu, Y., Kelman, G., Novak, C. S., Plajzer-Frick, I., Kato, M., Garvin, T. H., Pham, Q., Harrington, A. N., Hunter, R. D., Godoy, J., Meky, E. M., Akiyama, J. A., Afzal, V., Tran, S., Escande, F., Gilbert-Dussardier, B., Jean-Marçais, N., Hudaiberdiev, S., … Pennacchio, L. A. (2020). Comprehensive In Vivo Interrogation Reveals Phenotypic Impact of Human Enhancer Variants. *Cell*, *180*(6), 1262-1271.e15. https://doi.org/10.1016/J.CELL.2020.02.031

La, H. M., & Hobbs, R. M. (2019). Mechanisms regulating mammalian spermatogenesis and fertility recovery following germ cell depletion. *Cellular and Molecular Life Sciences : CMLS*, *76*(20), 4071–4102. https://doi.org/10.1007/s00018-019-03201-6

la Salle, S., Palmer, K., O'Brien, M., Schimenti, J. C., Eppig, J., & Handel, M. A. (2012). Spata22, a novel vertebrate-specific gene, is required for meiotic progress in mouse germ cells. *Biology of Reproduction*, *86*(2). https://doi.org/10.1095/BIOLREPROD.111.095752

Laemmli, U. K. (1970). Cleavage of structural proteins during the assembly of the head of bacteriophage T4. *Nature*, *227*(5259), 680–685. https://doi.org/10.1038/227680A0

Lammers, J. H., Offenberg, H. H., van Aalderen, M., Vink, A. C., Dietrich, A. J., & Heyting, C. (1994). The gene encoding a major component of the lateral elements of synaptonemal complexes of the rat is related to X-linked lymphocyte-regulated genes. *Molecular and Cellular Biology*, *14*(2), 1137–1146. https://doi.org/10.1128/MCB.14.2.1137-1146.1994

Lee, C. Y., Horn, H. F., Stewart, C. L., Burke, B., Bolcun-Filas, E., Schimenti, J. C., Dresser, M. E., & Pezza, R. J. (2015). Mechanism and regulation of rapid telomere prophase movements in mouse meiotic chromosomes. *Cell Reports*, *11*(4), 551–563. https://doi.org/10.1016/J.CELREP.2015.03.045

Lee, J., Kitajima, T. S., Tanno, Y., Yoshida, K., Morita, T., Miyano, T., Miyake, M., & Watanabe, Y. (2008). Unified mode of centromeric protection by shugoshin in mammalian oocytes and somatic cells. *Nature Cell Biology*, *10*(1), 42–52. https://doi.org/10.1038/NCB1667

Lee, J.-Y., Kim, D.-K., Ko, J.-J., Kim, K. P., & Park, K. (2016). Rad51 Regulates Reprogramming Efficiency through DNA Repair Pathway. *Development & Reproduction*, *20*(2), 163–169. https://doi.org/10.12717/DR.2016.20.2.163

Lerario, A. M., Mohan, D. R., Montenegro, L. R., Funari, M. F. de A., Nishi, M. Y., Narcizo, A. de M., Benedetti, A. F. F., Oba-Shinjo, S. M., Vitorino, A. J., Santos, R. A. S. X. dos, Jorge, A. A. de L., Onuchic, L. F., Marie, S. K. N., & Mendonca, B. B. (2020). SELAdb: A database of exonic variants in a Brazilian population referred to a quaternary medical center in São Paulo. *Clinics*, *75*, 1–9. https://doi.org/10.6061/CLINICS/2020/E1913

Lettice, L. A., Heaney, S. J. H., Purdie, L. A., Li, L., de Beer, P., Oostra, B. A., Goode, D., Elgar, G., Hill, R. E., & de Graaff, E. (2003). A long-range Shh enhancer regulates expression in the developing limb and fin and is associated with preaxial polydactyly. *Human Molecular Genetics*, *12*(14), 1725–1735. https://doi.org/10.1093/HMG/DDG180

Li, H., & Durbin, R. (2010). Fast and accurate long-read alignment with Burrows–Wheeler transform. *Bioinformatics*, *26*(5), 589. https://doi.org/10.1093/BIOINFORMATICS/BTP698

Li, N., Ding, L., Li, B., Wang, J., D'Andrea, A. D., & Chen, J. (2018). Functional analysis of Fanconi anemia mutations in China. *Experimental Hematology*, *66*, 32-41.e8. https://doi.org/10.1016/J.EXPHEM.2018.07.003

Li, Q., Dudás, K., Tick, G., & Haracska, L. (2021). Coordinated Cut and Bypass: Replication of Interstrand Crosslink-Containing DNA. *Frontiers in Cell and Developmental Biology*, *9*. https://doi.org/10.3389/FCELL.2021.699966

Lieber, M. R. (2008). The mechanism of human nonhomologous DNA end joining. *The Journal of Biological Chemistry*, *283*(1), 1–5. https://doi.org/10.1074/JBC.R700039200

Lindahl, T., & Barnes, D. E. (2000). Repair of endogenous DNA damage. *Cold Spring Harbor Symposia on Quantitative Biology*, *65*, 127–133. https://doi.org/10.1101/SQB.2000.65.127

Lindeboom, R. G. H., Supek, F., & Lehner, B. (2016). The rules and impact of nonsense-mediated mRNA decay in human cancers. *Nature Genetics*, *48*(10), 1112–1118. https://doi.org/10.1038/NG.3664

Lindsay, T. J., & Vitrikas, K. R. (2015). Evaluation and treatment of infertility. *American Family Physician*, *91*(5), 308–314. https://pubmed.ncbi.nlm.nih.gov/25822387/

Liu, Y., Tarsounas, M., O'Regan, P., & West, S. C. (2007). Role of RAD51C and XRCC3 in genetic recombination and DNA repair. *The Journal of Biological Chemistry*, *282*(3), 1973–1979. https://doi.org/10.1074/JBC.M609066200

Llano, E., Gómez, R., Gutiéerrez-Caballero, C., Herrán, Y., Sánchez-Martín, M., Vázquez-Quiñones, L., Hernández, T., de Álava, E., Cuadrado, A., Barbero, J. L., Suja, J. A., & Pendás, A. M. (2008). Shugoshin-2 is essential for the completion of meiosis but not for mitotic cell division in mice. *Genes & Development*, *22*(17), 2400–2413. https://doi.org/10.1101/GAD.475308

Llano, E., Gomez-H, L., García-Tuñón, I., Sánchez-Martín, M., Caburet, S., Barbero, J. L., Schimenti, J. C., Veitia, R. A., & Pendas, A. M. (2014). STAG3 is a strong candidate gene for male infertility. *Human Molecular Genetics*, *23*(13), 3421–3431. https://doi.org/10.1093/HMG/DDU051

Lok, D., Weenk, D., & de Rooij, D. G. (1982). Morphology, proliferation, and differentiation of undifferentiated spermatogonia in the Chinese hamster and the ram. *The Anatomical Record*, *203*(1), 83–99. https://doi.org/10.1002/AR.1092030109

Luebben, S. W., Kawabata, T., Akre, M. K., Lee, W. L., Johnson, C. S., O'Sullivan, M. G., & Shima, N. (2013). Helq acts in parallel to Fancc to suppress replication-associated genome instability. *Nucleic Acids Research*, *41*(22), 10283–10297. https://doi.org/10.1093/NAR/GKT676

Luo, M., Yang, F., Leu, N. A., Landaiche, J., Handel, M. A., Benavente, R., la Salle, S., & Wang, P. J. (2013). MEIOB exhibits single-stranded DNA-binding and exonuclease activities and is essential for meiotic recombination. *Nature Communications*, *4*. https://doi.org/10.1038/NCOMMS3788

Ma, W., Zhou, J., Chen, J., Carr, A. M., & Watanabe, Y. (2021). Meikin synergizes with shugoshin to protect cohesin Rec8 during meiosis I. *Genes & Development*, *35*(9–10), 692–697. https://doi.org/10.1101/GAD.348052.120

Maizels, N. (2005). Immunoglobulin gene diversification. *Annual Review of Genetics*, *39*, 23–46. https://doi.org/10.1146/ANNUREV.GENET.39.073003.110544

Mallepaly, R., Butler, P. R., Herati, A. S., & Lamb, D. J. (2017). Genetic Basis of Male and Female Infertility. *Monographs in Human Genetics*, *21*, 1–16. https://doi.org/10.1159/000477275

Marsolier-Kergoat, M.-C., Khan, M. M., Schott, J., Zhu, X., & Llorente, B. (2018). Mechanistic View and Genetic Control of DNA Recombination during Meiosis. *Molecular Cell*, *70*(1), 9-20.e6. https://doi.org/10.1016/j.molcel.2018.02.032

Martin, R. H. (2008). Cytogenetic determinants of male fertility. *Human Reproduction Update*, *14*(4), 379–390. https://doi.org/10.1093/HUMUPD/DMN017

Martinez, J. S., von Nicolai, C., Kim, T., Ehlén, Å., Mazin, A. v., Kowalczykowski, S. C., & Carreira, A. (2016). BRCA2 regulates DMC1-mediated recombination through the BRC repeats. *Proceedings of the National Academy of Sciences of the United States of America*, *113*(13), 3515–3520. https://doi.org/10.1073/PNAS.1601691113

Matsushita, N., Kitao, H., Ishiai, M., Nagashima, N., Hirano, S., Okawa, K., Ohta, T., Yu, D. S., McHugh, P. J., Hickson, I. D., Venkitaraman, A. R., Kurumizaka, H., & Takata, M. (2005). A FancD2-monoubiquitin fusion reveals hidden functions of Fanconi anemia core complex in DNA repair. *Molecular Cell*, *19*(6), 841–847. https://doi.org/10.1016/J.MOLCEL.2005.08.018

McGee, E. A., & Hsueh, A. J. W. (2000). Initial and cyclic recruitment of ovarian follicles. *Endocrine Reviews*, *21*(2), 200–214. https://doi.org/10.1210/EDRV.21.2.0394

McLaren, A., & Southee, D. (1997). Entry of mouse embryonic germ cells into meiosis. *Developmental Biology*, *187*(1), 107–113. https://doi.org/10.1006/dbio.1997.8584

McLean, C., & Bejerano, G. (2008). Dispensability of mammalian DNA. *Genome Research*, *18*(11), 1743–1751. https://doi.org/10.1101/GR.080184.108

Meetei, A. R., Sechi, S., Wallisch, M., Yang, D., Young, M. K., Joenje, H., Hoatlin, M. E., & Wang, W. (2003). A multiprotein nuclear complex connects Fanconi anemia and Bloom syndrome. *Molecular and Cellular Biology*, *23*(10), 3417–3426. https://doi.org/10.1128/MCB.23.10.3417-3426.2003

Mehine, M., Kaasinen, E., Mäkinen, N., Katainen, R., Kämpjärvi, K., Pitkänen, E., Heinonen, H.-R., Bützow, R., Kilpivaara, O., Kuosmanen, A., Ristolainen, H., Gentile, M., Sjöberg, J., Vahteristo, P., & Aaltonen, L. A. (2013). Characterization of uterine leiomyomas by whole-genome sequencing. *The New England Journal of Medicine*, *369*(1), 43–53. https://doi.org/10.1056/NEJMOA1302736

Mengoli, V., Jonak, K., Lyzak, O., Lamb, M., Lister, L. M., Lodge, C., Rojas, J., Zagoriy, I., Herbert, M., & Zachariae, W. (2021). Deprotection of centromeric cohesin at meiosis II requires APC/C activity but not kinetochore tension. *The EMBO Journal*, *40*(7). https://doi.org/10.15252/EMBJ.2020106812

Menke, D. B., Koubova, J., & Page, D. C. (2003). Sexual differentiation of germ cells in XX mouse gonads occurs in an anterior-to-posterior wave. *Developmental Biology*, *262*(2), 303–312. https://doi.org/10.1016/S0012-1606(03)00391-9

Meuwissen, R. L. J., Offenberg, H. H., Dietrich, A. J. J., Riesewijk, A., van Iersel, M., & Heyting, C. (1992). A coiled-coil related protein specific for synapsed regions of meiotic prophase chromosomes. *The EMBO Journal*, *11*(13), 5091. https://doi.org/10.1002/j.1460-2075.1992.tb05616.x

Miller, K. A., Hinz, J. M., Yamada, N. A., Thompson, L. H., & Albala, J. S. (2005). Nuclear localization of Rad51B is independent of Rad51C and BRCA2. *Mutagenesis*, *20*(1), 57–63. https://doi.org/10.1093/MUTAGE/GEI011

Miller, K. A., Sawicka, D., Barsky, D., & Albala, J. S. (2004). Domain mapping of the Rad51 paralog protein complexes. *Nucleic Acids Research*, *32*(1), 169–178. https://doi.org/10.1093/NAR/GKG925

Miller, S. A., Dykes, D. D., & Polesky, H. F. (1988). A simple salting out procedure for extracting DNA from human nucleated cells. *Nucleic Acids Research*, *16*(3), 1215. https://doi.org/10.1093/NAR/16.3.1215

Mishra, A., Saxena, S., Kaushal, A., & Nagaraju, G. (2018). RAD51C/XRCC3 Facilitates Mitochondrial DNA Replication and Maintains Integrity of the Mitochondrial Genome. *Molecular and Cellular Biology*, *38*(3). https://doi.org/10.1128/MCB.00489-17

Mourelatos, D. (2016). Sister chromatid exchange assay as a predictor of tumor chemoresponse. *Mutation Research. Genetic Toxicology and Environmental Mutagenesis*, *803–804*, 1–12. https://doi.org/10.1016/J.MRGENTOX.2016.03.011

Muciaccia, B., Boitani, C., Berloco, B. P., Nudo, F., Spadetta, G., Stefanini, M., de Rooij, D. G., & Vicini, E. (2013). Novel stage classification of human spermatogenesis based on acrosome development. *Biology of Reproduction*, *89*(3). https://doi.org/10.1095/BIOLREPROD.113.111682

Müller, H. P., & Schaffner, W. (1990). Transcriptional enhancers can act in trans. *Trends in Genetics : TIG*, *6*(9), 300–304. https://doi.org/10.1016/0168-9525(90)90236-Y

Muñoz, S., & Méndez, J. (2017). DNA replication stress: from molecular mechanisms to human disease. *Chromosoma*, *126*(1). https://doi.org/10.1007/S00412-016-0573-X

Muramatsu, T. (2000). In Vivo Gene Electroporation in the Mouse Testis. *Electrochemotherapy, Electrogenetherapy, and Transdermal Drug Delivery*, 349–357. https://doi.org/10.1385/1-59259-080-2:349

Myers, S., Bowden, R., Tumian, A., Bontrop, R. E., Freeman, C., MacFie, T. S., McVean, G., & Donnelly, P. (2010). Drive against hotspot motifs in primates implicates the PRDM9 gene in meiotic recombination. *Science (New York, N.Y.)*, *327*(5967), 876–879. https://doi.org/10.1126/SCIENCE.1182363

Mytlis, A., Kumar, V., Qiu, T., Deis, R., Hart, N., Levy, K., Masek, M., Shawahny, A., Ahmad, A., Eitan, H., Nather, F., Adar-Levor, S., Birnbaum, R. Y., Elia, N., Bachmann-Gagescu, R., Roy, S., & Elkouby, Y. M. (2022). Control of meiotic chromosomal bouquet and germ cell morphogenesis by the zygotene cilium. *Science (New York, N.Y.)*, eabh3104. https://doi.org/10.1126/science.abh3104

Nakagawa, T., Sharma, M., Nabeshima, Y. I., Braun, R. E., & Yoshida, S. (2010). Functional Hierarchy and Reversibility within the Murine Spermatogenic Stem Cell Compartment. *Science (New York, N.Y.)*, *328*(5974), 62. https://doi.org/10.1126/SCIENCE.1182868

Nalepa, G., & Clapp, D. W. (2018). Fanconi anaemia and cancer: an intricate relationship. *Nature Reviews. Cancer*, *18*(3), 168–185. https://doi.org/10.1038/NRC.2017.116

Namgoong, S., Kim, N. H., & Christenson, L. K. (2018). Meiotic spindle formation in mammalian oocytes: implications for human infertility. *Biology of Reproduction*, *98*(2), 153–161. https://doi.org/10.1093/BIOLRE/IOX145

Naslavsky, M. S., Yamamoto, G. L., Almeida, T. F. de, Ezquina, S. A. M., Sunaga, D. Y., Pho, N., Bozoklian, D., Sandberg, T. O. M., Brito, L. A., Lazar, M., Bernardo, D. V., Amaro, E., Duarte, Y. A. O., Lebrão, M. L., Passos-Bueno, M. R., & Zatz, M. (2017). Exomic variants of an elderly cohort of Brazilians in the ABraOM database. *Human Mutation*, *38*(7), 751–763. https://doi.org/10.1002/HUMU.23220

Neale, M. J., Pan, J., & Keeney, S. (2005). Endonucleolytic processing of covalent protein-linked DNA double-strand breaks. *Nature*, *436*(7053), 1053–1057. https://doi.org/10.1038/NATURE03872

Nelson, L. M. (2009). Clinical practice. Primary ovarian insufficiency. *The New England Journal of Medicine*, *360*(6), 606–614. https://doi.org/10.1056/NEJMCP0808697

Neuse, C. J., Lomas, O. C., Schliemann, C., Shen, Y. J., Manier, S., Bustoros, M., & Ghobrial, I. M. (2020). Genome instability in multiple myeloma. *Leukemia*, *34*(11), 2887–2897. https://doi.org/10.1038/s41375-020-0921-y

Niu, W., & Spradling, A. C. (2020). Two distinct pathways of pregranulosa cell differentiation support follicle formation in the mouse ovary. *Proceedings of the National Academy of Sciences of the United States of America*, *117*(33), 20015–20026. https://doi.org/10.1073/PNAS.2005570117

Nobrega, M. A., Ovcharenko, I., Afzal, V., & Rubin, E. M. (2003). Scanning human gene deserts for long-range enhancers. *Science (New York, N.Y.)*, *302*(5644), 413. https://doi.org/10.1126/SCIENCE.1088328

Nóbrega, M. A., Zhu, Y., Plajer-Frick, I., Afzal, Y., & Rubin, E. M. (2004). Megabase deletions of gene deserts result in viable mice. *Nature*, *431*(7011), 988–993. https://doi.org/10.1038/NATURE03022

Noh, S., Kim, S. H., Cho, N. H., & Kim, S. H. (2015). Rapid Reticulin Fiber Staining Method is Helpful for the Diagnosis of Pituitary Adenoma in Frozen Section. *Endocrine Pathology*, *26*(2), 178–184. https://doi.org/10.1007/S12022-015-9370-Y

Nolte, M. J., Wang, Y., Deng, J. M., Swinton, P. G., Wei, C., Guindani, M., Schwartz, R. J., & Behringer, R. R. (2014). Functional analysis of limb transcriptional enhancers in the mouse. *Evolution & Development*, *16*(4), 207–223. https://doi.org/10.1111/EDE.12084

Nowacka-Zawisza, M., Wiśnik, E., Wasilewski, A., Skowrońska, M., Forma, E., Bryś, M., Rózański, W., & Krajewska, W. M. (2015). Polymorphisms of homologous recombination RAD51, RAD51B, XRCC2, and XRCC3 genes and the risk of prostate cancer. *Analytical Cellular Pathology (Amsterdam)*, *2015*. https://doi.org/10.1155/2015/828646

Oakberg, E. F. (1956). A description of spermiogenesis in the mouse and its use in analysis of the cycle of the seminiferous epithelium and germ cell renewal. *The American Journal of Anatomy*, *99*(3), 391–413. https://doi.org/10.1002/AJA.1000990303

O'Donnell, L., Nicholls, P. K., O'Bryan, M. K., McLachlan, R. I., & Stanton, P. G. (2011). Spermiation: The process of sperm release. *Spermatogenesis*, *1*(1), 14–35. https://doi.org/10.4161/SPMG.1.1.14525

Offenberg, H. H., Schalk, J. A. C., Meuwissen, R. L. J., van Aalderen, M., Kester, H. A., Dietrich, A. J. J., & Heyting, C. (1998). SCP2: a major protein component of the axial elements of synaptonemal complexes of the rat. *Nucleic Acids Research*, *26*(11), 2572–2579. https://doi.org/10.1093/NAR/26.11.2572

O'Flynn O'Brien, K. L., Varghese, A. C., & Agarwal, A. (2010). The genetic causes of male factor infertility: a review. *Fertility and Sterility*, *93*(1), 1–12. https://doi.org/10.1016/J.FERTNSTERT.2009.10.045

Ogushi, S., Rattani, A., Godwin, J., Metson, J., Schermelleh, L., & Nasmyth, K. (2021). Loss of sister kinetochore co-orientation and peri-centromeric cohesin protection after meiosis I depends on cleavage of centromeric REC8. *Developmental Cell*, *56*(22), 3100-3114.e4. https://doi.org/10.1016/J.DEVCEL.2021.10.017

Orr, N., Lemnrau, A., Cooke, R., Fletcher, O., Tomczyk, K., Jones, M., Johnson, N., Lord, C. J., Mitsopoulos, C., Zvelebil, M., McDade, S. S., Buck, G., Blancher, C., Trainer, A. H., James, P. A., Bojesen, S. E., Bokmand, S., Nevanlinna, H., Mattson, J., … Swerdlow, A. J. (2012). Genome-wide association study identifies a common variant in RAD51B associated with male breast cancer risk. *Nature Genetics*, *44*(11), 1182–1184. https://doi.org/10.1038/NG.2417

Park, J. Y., Virts, E. L., Jankowska, A., Wiek, C., Othman, M., Chakraborty, S. C., Vance, G. H., Alkuraya, F. S., Hanenberg, H., & Andreassen, P. R. (2016). Complementation of hypersensitivity to DNA interstrand crosslinking agents demonstrates that XRCC2 is a Fanconi anaemia gene. *Journal of Medical Genetics*, *53*(10), 672–680. https://doi.org/10.1136/JMEDGENET-2016-103847

Parra, M. T., Page, J., Yen, T. J., He, D., Valdeolmillos, A., Rufas, J. S., & Suja, J. A. (2002). Expression and behaviour of CENP-E at kinetochores during mouse spermatogenesis. *Chromosoma*, *111*(1), 53–61. https://doi.org/10.1007/S00412-002-0185-5

Pastore, L. M., & Johnson, J. (2014). The FMR1 gene, infertility, and reproductive decision-making: a review. *Frontiers in Genetics*, *5*(JUL). https://doi.org/10.3389/FGENE.2014.00195

Paz, M. M., Kumar, G. S., Glover, M., Waring, M. J., & Tomasz, M. (2004). Mitomycin dimers: Polyfunctional cross-linkers of DNA. *Journal of Medicinal Chemistry*, *47*(12), 3308–3319. https://doi.org/10.1021/jm049863j

Peake, J. D., & Noguchi, E. (2022). Fanconi anemia: current insights regarding epidemiology, cancer, and DNA repair. *Human Genetics 2022*, 1–26. https://doi.org/10.1007/S00439-022-02462-9

Pennacchio, L. A., Ahituv, N., Moses, A. M., Prabhakar, S., Nobrega, M. A., Shoukry, M., Minovitsky, S., Dubchak, I., Holt, A., Lewis, K. D., Plajzer-Frick, I., Akiyama, J., de Val, S., Afzal, V., Black, B. L., Couronne, O., Eisen, M. B., Visel, A., & Rubin, E. M. (2006). In vivo enhancer analysis of human conserved non-coding sequences. *Nature*, *444*(7118), 499–502. https://doi.org/10.1038/NATURE05295

Peters, A. H. F. M., Plug, A. W., van Vugt, M. J., & de Boer, P. (1997). A drying-down technique for the spreading of mammalian melocytes from the male and female germline. *Chromosome Research*, *5*(1), 66–68. https://doi.org/10.1023/A:1018445520117

Pittman, D. L., Weinberg, L. R., & Schimenti, J. C. (1998). Identification, characterization, and genetic mapping of Rad51d, a new mouse and human RAD51/RecA-related gene. *Genomics*, *49*(1), 103–111. https://doi.org/10.1006/geno.1998.5226

Prakash, R., Freyer, L., Saiz, N., Gavrilov, S., Wang, R. Q., Romanienko, P. J., Lacy, E., Hadjantonakis, A. K., & Jasin, M. (2021). XRCC3 loss leads to midgestational embryonic lethality in mice. *DNA Repair*, *108*. https://doi.org/10.1016/J.DNAREP.2021.103227

Prasada Rao, H. B. D., Qiao, H., Bhatt, S. K., Bailey, L. R. J., Tran, H. D., Bourne, S. L., Qiu, W., Deshpande, A., Sharma, A. N., Beebout, C. J., Pezza, R. J., & Hunter, N. (2017). A SUMO-ubiquitin relay recruits proteasomes to chromosome axes to regulate meiotic recombination. *Science (New York, N.Y.)*, *355*(6323), 403–407. https://doi.org/10.1126/SCIENCE.AAF6407

Qiao, H., Prasada Rao, H. B. D., Yang, Y., Fong, J. H., Cloutier, J. M., Deacon, D. C., Nagel, K. E., Swartz, R. K., Strong, E., Holloway, J. K., Cohen, P. E., Schimenti, J., Ward, J., & Hunter, N. (2014). Antagonistic roles of ubiquitin ligase HEI10 and SUMO ligase RNF212 regulate meiotic recombination. *Nature Genetics*, *46*(2), 194–199. https://doi.org/10.1038/NG.2858

Qin, H. de, Shugart, Y. Y., Bei, J. X., Pan, Q. H., Chen, L., Feng, Q. S., Chen, L. Z., Huang, W., Liu, J. J., Jorgensen, T. J., Zeng, Y. X., & Jia, W. H. (2011). Comprehensive pathway-based association study of DNA repair gene variants and the risk of nasopharyngeal carcinoma. *Cancer Research*, *71*(8), 3000–3008. https://doi.org/10.1158/0008-5472.CAN-10-0469

Reijo, R., Alagappan, R. K., Patrizio, P., & Page, D. C. (1996). Severe oligozoospermia resulting from deletions of azoospermia factor gene on Y chromosome. *Lancet (London, England)*, *347*(9011), 1290–1293. https://doi.org/10.1016/S0140-6736(96)90938-1

Reijo, R., Lee, T. Y., Salo, P., Alagappan, R., Brown, L. G., Rosenberg, M., Rozen, S., Jaffe, T., Straus, D., Hovatta, O., de la Chapelle, A., Silber, S., & Page, D. C. (1995). Diverse spermatogenic defects in humans caused by Y chromosome deletions encompassing a novel RNA-binding protein gene. *Nature Genetics*, *10*(4), 383–393. https://doi.org/10.1038/NG0895-383

Reynolds, A., Qiao, H., Yang, Y., Chen, J. K., Jackson, N., Biswas, K., Holloway, J. K., Baudat, F., de Massy, B., Wang, J., Höög, C., Cohen, P. E., & Hunter, N. (2013). RNF212 is a dosage-sensitive regulator of crossing-over during mammalian meiosis. *Nature Genetics*, *45*(3), 269–278. https://doi.org/10.1038/NG.2541

Robert, T., Nore, A., Brun, C., Maffre, C., Crimi, B., Bourbon, H.-M., & de Massy, B. (2016). The TopoVIB-Like protein family is required for meiotic DNA double-strand break formation. *Science (New York, N.Y.)*, *351*(6276), 943–949. https://doi.org/10.1126/science.aad5309

Ruiz, S., Lopez-Contreras, A. J., Gabut, M., Marion, R. M., Gutierrez-Martinez, P., Bua, S., Ramirez, O., Olalde, I., Rodrigo-Perez, S., Li, H., Marques-Bonet, T., Serrano, M., Blasco, M. A., Batada, N. N., & Fernandez-Capetillo, O. (2015). Limiting replication stress during somatic cell reprogramming reduces genomic instability in induced pluripotent stem cells. *Nature Communications*, *6*. https://doi.org/10.1038/NCOMMS9036

Russell, L. D., Ettlin, R. A., Hikim, A. P. S., & Clegg, E. D. (1993). Histological and Histopathological Evaluation of the Testis. *International Journal of Andrology*, *16*(1), 83–83. https://doi.org/10.1111/J.1365-2605.1993.TB01156.X

Ruth, K. S., Day, F. R., Hussain, J., Martínez-Marchal, A., Aiken, C. E., Azad, A., Thompson, D. J., Knoblochova, L., Abe, H., Tarry-Adkins, J. L., Gonzalez, J. M., Fontanillas, P., Claringbould, A., Bakker, O. B., Sulem, P., Walters, R. G., Terao, C., Turon, S., Horikoshi, M., … Perry, J. R. B. (2021). Genetic insights into biological mechanisms governing human ovarian ageing. *Nature 2021 596:7872*, *596*(7872), 393–397. https://doi.org/10.1038/s41586-021-03779-7

San Filippo, J., Sung, P., & Klein, H. (2008). Mechanism of eukaryotic homologous recombination. *Annual Review of Biochemistry*, *77*, 229–257. https://doi.org/10.1146/ANNUREV.BIOCHEM.77.061306.125255

Sartori, A. A., Lukas, C., Coates, J., Mistrik, M., Fu, S., Bartek, J., Baer, R., Lukas, J., & Jackson, S. P. (2007). Human CtIP promotes DNA end resection. *Nature*, *450*(7169), 509–514. https://doi.org/10.1038/NATURE06337

Sasaki, M. S., Takata, M., Sonoda, E., Tachibana, A., & Takeda, S. (2004). Recombination repair pathway in the maintenance of chromosomal integrity against DNA interstrand crosslinks. *Cytogenetic and Genome Research*, *104*(1–4), 28–34. https://doi.org/10.1159/000077463

Schlacher, K., Christ, N., Siaud, N., Egashira, A., Wu, H., & Jasin, M. (2011). Double-strand break repair-independent role for BRCA2 in blocking stalled replication fork degradation by MRE11. *Cell*, *145*(4), 529–542. https://doi.org/10.1016/J.CELL.2011.03.041

Schlacher, K., Wu, H., & Jasin, M. (2012). A distinct replication fork protection pathway connects Fanconi anemia tumor suppressors to RAD51-BRCA1/2. *Cancer Cell*, *22*(1), 106–116. https://doi.org/10.1016/J.CCR.2012.05.015

Schramm, S., Fraune, J., Naumann, R., Hernandez-Hernandez, A., Höög, C., Cooke, H. J., Alsheimer, M., & Benavente, R. (2011). A novel mouse synaptonemal complex protein is essential for loading of central element proteins, recombination, and fertility. *PLoS Genetics*, *7*(5). https://doi.org/10.1371/JOURNAL.PGEN.1002088

Schwanhäusser, B., Busse, D., Li, N., Dittmar, G., Schuchhardt, J., Wolf, J., Chen, W., & Selbach, M. (2013). *Global quantification of mammalian gene expression control*. https://doi.org/10.1038/nature10098

Sekl, Y., Yamaji, M., Yabuta, Y., Sano, M., Shigeta, M., Matsui, Y., Saga, Y., Tachibana, M., Shinkai, Y., & Saitou, M. (2007). Cellular dynamics associated with the genome-wide epigenetic reprogramming in migrating primordial germ cells in mice. *Development (Cambridge, England)*, *134*(14), 2627–2638. https://doi.org/10.1242/DEV.005611

Shah, K., Sivapalan, G., Gibbons, N., Tempest, H., & Griffin, D. K. (2003). The genetic basis of infertility. *Reproduction (Cambridge, England)*, *126*(1), 13–25. https://doi.org/10.1530/REP.0.1260013

Shamseldin, H. E., Elfaki, M., & Alkuraya, F. S. (2012). Exome sequencing reveals a novel Fanconi group defined by XRCC2 mutation. *Journal of Medical Genetics*, *49*(3), 184–186. https://doi.org/10.1136/JMEDGENET-2011-100585

Sheridan, S. D., Yu, X., Roth, R., Heuser, J. E., Sehorn, M. G., Sung, P., Egelman, E. H., & Bishop, D. K. (2008). A comparative analysis of Dmc1 and Rad51 nucleoprotein filaments. *Nucleic Acids Research*, *36*(12), 4057–4066. https://doi.org/10.1093/NAR/GKN352

Shu, Z., Smith, S., Wang, L., Rice, M. C., & Kmiec, E. B. (1999). Disruption of muREC2/RAD51L1 in Mice Results in Early Embryonic Lethality Which Can Be Partially Rescued in a p53−/− Background. *Molecular and Cellular Biology*, *19*(12), 8686. https://doi.org/10.1128/MCB.19.12.8686

Simmler, M. C., Rouyer, F., Vergnaud, G., Nyström-Lahti, M., Ngo, K. Y., de La Chapelle, A., & Weissenbach, J. (1985). Pseudoautosomal DNA sequences in the pairing region of the human sex chromosomes. *Nature 1985 317:6039*, *317*(6039), 692–697. https://doi.org/10.1038/317692a0

Singh, P., Schimenti, J. C., & Bolcun-Filas, E. (2015). A Mouse Geneticist's Practical Guide to CRISPR Applications. *Genetics*, *199*(1), 1. https://doi.org/10.1534/GENETICS.114.169771

Slotman, J. A., Paul, M. W., Carofiglio, F., Gruiter, H. M. de, Vergroesen, T., Koornneef, L., Cappellen, W. A. V., Houtsmuller, A. B., & Baarends, W. M. (2020). Super-resolution imaging of RAD51 and DMC1 in DNA repair foci

reveals dynamic distribution patterns in meiotic prophase. *PLoS Genetics*, *16*(6). https://doi.org/10.1371/JOURNAL.PGEN.1008595

Smagulova, F., Gregoretti, I. v., Brick, K., Khil, P., Camerini-Otero, R. D., & Petukhova, G. v. (2011). Genome-wide analysis reveals novel molecular features of mouse recombination hotspots. *Nature*, *472*(7343), 375–378. https://doi.org/10.1038/NATURE09869

Snetkova, V., Pennacchio, L. A., Visel, A., & Dickel, D. E. (2022). Perfect and imperfect views of ultraconserved sequences. *Nature Reviews. Genetics*, *23*(3), 182–194. https://doi.org/10.1038/S41576-021-00424-X

Song, H., Dicks, E., Ramus, S. J., Tyrer, J. P., Intermaggio, M. P., Hayward, J., Edlund, C. K., Conti, D., Harrington, P., Fraser, L., Philpott, S., Anderson, C., Rosenthal, A., Gentry-Maharaj, A., Bowtell, D. D., Alsop, K., Cicek, M. S., Cunningham, J. M., Fridley, B. L., … Pharoah, P. D. P. (2015). Contribution of Germline Mutations in the RAD51B, RAD51C, and RAD51D Genes to Ovarian Cancer in the Population. *Journal of Clinical Oncology : Official Journal of the American Society of Clinical Oncology*, *33*(26), 2901–2907. https://doi.org/10.1200/JCO.2015.61.2408

Stanzione, M., Baumann, M., Papanikos, F., Dereli, I., Lange, J., Ramlal, A., Tränkner, D., Shibuya, H., de Massy, B., Watanabe, Y., Jasin, M., Keeney, S., & Tóth, A. (2016). Meiotic DNA break formation requires the unsynapsed chromosome axis-binding protein IHO1 (CCDC36) in mice. *Nature Cell Biology*, *18*(11), 1208–1220. https://doi.org/10.1038/NCB3417

Stemmann, O., Zou, H., Gerber, S. A., Gygi, S. P., & Kirschner, M. W. (2001). Dual inhibition of sister chromatid separation at metaphase. *Cell*, *107*(6), 715–726. https://doi.org/10.1016/S0092-8674(01)00603-1

Stonez, M. P., Cho, Y. J., Huang, H., Kim, H. Y., Kozekov, I. D., Kozekova, A., Wang, H., Minko, I. G., Lloyd, R. S., Harris, T. M., & Rizzo, C. J. (2008). Interstrand DNA cross-links induced by alpha,beta-unsaturated aldehydes derived from lipid peroxidation and environmental sources. *Accounts of Chemical Research*, *41*(7), 793–804. https://doi.org/10.1021/AR700246X

Sullivan, M. R., & Bernstein, K. A. (2018). RAD-ical New Insights into RAD51 Regulation. *Genes*, *9*(12). https://doi.org/10.3390/GENES9120629

Surani, M. A. (2001). Reprogramming of genome function through epigenetic inheritance. *Nature*, *414*(6859), 122–128. https://doi.org/10.1038/35102186

Suwaki, N., Klare, K., & Tarsounas, M. (2011). RAD51 paralogs: roles in DNA damage signalling, recombinational repair and tumorigenesis. *Seminars in Cell & Developmental Biology*, *22*(8), 898–905. https://doi.org/10.1016/J.SEMCDB.2011.07.019

Suzuki, A., & Saga, Y. (2008). Nanos2 suppresses meiosis and promotes male germ cell differentiation. *Genes & Development*, *22*(4), 430–435. https://doi.org/10.1101/GAD.1612708

Suzuki, H., Kanai-Azuma, M., & Kanai, Y. (2015). From Sex Determination to Initial Folliculogenesis in Mammalian Ovaries: Morphogenetic Waves along the Anteroposterior and Dorsoventral Axes. *Sexual Development*, *9*(4), 190–204. https://doi.org/10.1159/000440689

Sybert, V. P., & McCauley, E. (2004). Turner's syndrome. *The New England Journal of Medicine*, *351*(12), 1227–1238. https://doi.org/10.1056/NEJMRA030360

Takahashi, K., & Yamanaka, S. (2006). Induction of Pluripotent Stem Cells from Mouse Embryonic and Adult Fibroblast Cultures by Defined Factors. *Cell*, *126*(4), 663–676. https://doi.org/10.1016/J.CELL.2006.07.024

Takata, K. I., Reh, S., Tomida, J., Person, M. D., & Wood, R. D. (2013). Human DNA helicase HELQ participates in DNA interstrand crosslink tolerance with ATR and RAD51 paralogs. *Nature Communications*, *4*. https://doi.org/10.1038/NCOMMS3338

Takata, M., Sasaki, M. S., Sonoda, E., Fukushima, T., Morrison, C., Albala, J. S., Swagemakers, S. M. A., Kanaar, R., Thompson, L. H., & Takeda, S. (2000). The Rad51 paralog Rad51B promotes homologous recombinational repair. *Molecular and Cellular Biology*, *20*(17), 6476–6482. https://doi.org/10.1128/MCB.20.17.6476-6482.2000

Takata, M., Sasaki, M. S., Tachiiri, S., Fukushima, T., Sonoda, E., Schild, D., Thompson, L. H., & Takeda, S. (2001). Chromosome instability and defective recombinational repair in knockout mutants of the five Rad51 paralogs. *Molecular and Cellular Biology*, *21*(8), 2858–2866. https://doi.org/10.1128/MCB.21.8.2858-2866.2001

Takemoto, K., Tani, N., Takada-Horisawa, Y., Fujimura, S., Tanno, N., Yamane, M., Okamura, K., Sugimoto, M., Araki, K., & Ishiguro, K. ichiro. (2020). Meiosis-Specific C19orf57/4930432K21Rik/BRME1 Modulates Localization of

RAD51 and DMC1 to DSBs in Mouse Meiotic Recombination. *Cell Reports*, *31*(8). https://doi.org/10.1016/J.CELREP.2020.107686

Tanabe, H., Müller, S., Neusser, M., von Hase, J., Calcagno, E., Cremer, M., Solovei, I., Cremer, C., & Cremer, T. (2002). Evolutionary conservation of chromosome territory arrangements in cell nuclei from higher primates. *Proceedings of the National Academy of Sciences of the United States of America*, *99*(7), 4424–4429. https://doi.org/10.1073/PNAS.072618599

Tarsounas, M., Muñoz, P., Claas, A., Smiraldo, P. G., Pittman, D. L., Blasco, M. A., & West, S. C. (2004). Telomere maintenance requires the RAD51D recombination/repair protein. *Cell*, *117*(3), 337–347. https://doi.org/10.1016/S0092-8674(04)00337-X

Thermann, R., Neu-Yilik, G., Deters, A., Frede, U., Wehr, K., Hagemeier, C., Hentze, M. W., & Kulozik, A. E. (1998). Binary specification of nonsense codons by splicing and cytoplasmic translation. *The EMBO Journal*, *17*(12), 3484–3494. https://doi.org/10.1093/EMBOJ/17.12.3484

Thomas, G., Jacobs, K. B., Kraft, P., Yeager, M., Wacholder, S., Cox, D. G., Hankinson, S. E., Hutchinson, A., Wang, Z., Yu, K., Chatterjee, N., Garcia-Closas, M., Gonzalez-Bosquet, J., Prokunina-Olsson, L., Orr, N., Willett, W. C., Colditz, G. A., Ziegler, R. G., Berg, C. D., … Hunter, D. J. (2009). A multistage genome-wide association study in breast cancer identifies two new risk alleles at 1p11.2 and 14q24.1 (RAD51L1). *Nature Genetics*, *41*(5), 579–584. https://doi.org/10.1038/NG.353

Thomas, J. D., Polaski, J. T., Feng, Q., de Neef, E. J., Hoppe, E. R., McSharry, M. v., Pangallo, J., Gabel, A. M., Belleville, A. E., Watson, J., Nkinsi, N. T., Berger, A. H., & Bradley, R. K. (2020). RNA isoform screens uncover the essentiality and tumor-suppressor activity of ultraconserved poison exons. *Nature Genetics*, *52*(1), 84–94. https://doi.org/10.1038/S41588-019-0555-Z

Thorslund, T., McIlwraith, M. J., Compton, S. A., Lekomtsev, S., Petronczki, M., Griffith, J. D., & West, S. C. (2010). The breast cancer tumor suppressor BRCA2 promotes the specific targeting of RAD51 to single-stranded DNA. *Nature Structural & Molecular Biology*, *17*(10), 1263–1265. https://doi.org/10.1038/NSMB.1905

Tran, T. N., & Schimenti, J. C. (2019). A segregating human allele of SPO11 modeled in mice disrupts timing and amounts of meiotic recombination, causing oligospermia and a decreased ovarian reserve†. *Biology of Reproduction*, *101*(2), 347–359. https://doi.org/10.1093/BIOLRE/IOZ089

Tsai, A. G., & Lieber, M. R. (2010). Mechanisms of chromosomal rearrangement in the human genome. *BMC Genomics*, *11 Suppl 1*, S1. https://doi.org/10.1186/1471-2164-11-S1-S1

Turner, J. M. A. (2015). Meiotic Silencing in Mammals. *Annual Review of Genetics*, *49*, 395–412. https://doi.org/10.1146/ANNUREV-GENET-112414-055145

Uhlmann, F., Wernic, D., Poupart, M. A., Koonin, E. v., & Nasmyth, K. (2000). Cleavage of cohesin by the CD clan protease separin triggers anaphase in yeast. *Cell*, *103*(3), 375–386. https://doi.org/10.1016/S0092-8674(00)00130-6

Vaz, F., Hanenberg, H., Schuster, B., Barker, K., Wiek, C., Erven, V., Neveling, K., Endt, D., Kesterton, I., Autore, F., Fraternali, F., Freund, M., Hartmann, L., Grimwade, D., Roberts, R. G., Schaal, H., Mohammed, S., Rahman, N., Schindler, D., & Mathew, C. G. (2010). Mutation of the RAD51C gene in a Fanconi anemia-like disorder. *Nature Genetics*, *42*(5), 406–409. https://doi.org/10.1038/NG.570

Venkatesh, T., Suresh, P. S., & Tsutsumi, R. (2014). New insights into the genetic basis of infertility. *The Application of Clinical Genetics*, *7*, 235. https://doi.org/10.2147/TACG.S40809

Vesela, E., Chroma, K., Turi, Z., & Mistrik, M. (2017). Common Chemical Inductors of Replication Stress: Focus on Cell-Based Studies. *Biomolecules*, *7*(1). https://doi.org/10.3390/BIOM7010019

Visel, A., Prabhakar, S., Akiyama, J. A., Shoukry, M., Lewis, K. D., Holt, A., Plajzer-Frick, I., Afzal, V., Rubin, E. M., & Pennacchio, L. A. (2008). Ultraconservation identifies a small subset of extremely constrained developmental enhancers. *Nature Genetics*, *40*(2), 158. https://doi.org/10.1038/NG.2007.55

Vorlaufer, E., & Peters, J. M. (1998). Regulation of the cyclin B degradation system by an inhibitor of mitotic proteolysis. *Molecular Biology of the Cell*, *9*(7), 1817–1831. https://doi.org/10.1091/MBC.9.7.1817

Vrielynck, N., Chambon, A., Vezon, D., Pereira, L., Chelysheva, L., de Muyt, A., Mézard, C., Mayer, C., & Grelon, M. (2016). A DNA topoisomerase VI-like complex initiates meiotic recombination. *Science (New York, N.Y.)*, *351*(6276), 939–943. https://doi.org/10.1126/science.aad5196

Wadt, K. A. W., Aoude, L. G., Golmard, L., Hansen, T. V. O., Sastre-Garau, X., Hayward, N. K., & Gerdes, A. M. (2015). Germline RAD51B truncating mutation in a family with cutaneous melanoma. *Familial Cancer*, *14*(2), 337–340. https://doi.org/10.1007/S10689-015-9781-4

Wang, A. T., Kim, T., Wagner, J. E., Conti, B. A., Lach, F. P., Huang, A. L., Molina, H., Sanborn, E. M., Zierhut, H., Cornes, B. K., Abhyankar, A., Sougnez, C., Gabriel, S. B., Auerbach, A. D., Kowalczykowski, S. C., & Smogorzewska, A. (2015). A Dominant Mutation in Human RAD51 Reveals Its Function in DNA Interstrand Crosslink Repair Independent of Homologous Recombination. *Molecular Cell*, *59*(3), 478–490. https://doi.org/10.1016/J.MOLCEL.2015.07.009

Wang, H., Russa, M. la, & Qi, L. S. (2016). CRISPR/Cas9 in Genome Editing and Beyond. *Http://Dx.Doi.Org/10.1146/Annurev-Biochem-060815-014607*, *85*, 227–264. https://doi.org/10.1146/ANNUREV-BIOCHEM-060815-014607

Wang, L. C., & Gautier, J. (2010). The Fanconi anemia pathway and ICL repair: implications for cancer therapy. *Critical Reviews in Biochemistry and Molecular Biology*, *45*(5), 424. https://doi.org/10.3109/10409238.2010.502166

Wang, S., Hassold, T., Hunt, P., White, M. A., Zickler, D., Kleckner, N., & Zhang, L. (2017). Inefficient Crossover Maturation Underlies Elevated Aneuploidy in Human Female Meiosis. *Cell*, *168*(6), 977-989.e17. https://doi.org/10.1016/J.CELL.2017.02.002

Wang, X., & Pepling, M. E. (2021). Regulation of Meiotic Prophase One in Mammalian Oocytes. *Frontiers in Cell and Developmental Biology*, *9*. https://doi.org/10.3389/FCELL.2021.667306

Ward, J. D., Muzzini, D. M., Petalcorin, M. I. R., Martinez-Perez, E., Martin, J. S., Plevani, P., Cassata, G., Marini, F., & Boulton, S. J. (2010). Overlapping mechanisms promote postsynaptic RAD-51 filament disassembly during meiotic double-strand break repair. *Molecular Cell*, *37*(2), 259–272. https://doi.org/10.1016/J.MOLCEL.2009.12.026

Ward, J. O., Reinholdt, L. G., Motley, W. W., Niswander, L. M., Deacon, D. C., Griffin, L. B., Langlais, K. K., Backus, V. L., Schimenti, K. J., O'Brien, M. J., Eppig, J. J., & Schimenti, J. C. (2007). Mutation in mouse hei10, an e3 ubiquitin ligase, disrupts meiotic crossing over. *PLoS Genetics*, *3*(8), 1550–1563. https://doi.org/10.1371/JOURNAL.PGEN.0030139

Wassarman, P. M., & Litscher, E. S. (2021). Zona Pellucida Genes and Proteins: Essential Players in Mammalian Oogenesis and Fertility. *Genes*, *12*(8), 1266. https://doi.org/10.3390/GENES12081266

Waterston, R. H., Lindblad-Toh, K., Birney, E., Rogers, J., Abril, J. F., Agarwal, P., Agarwala, R., Ainscough, R., Alexandersson, M., An, P., Antonarakis, S. E., Attwood, J., Baertsch, R., Bailey, J., Barlow, K., Beck, S., Berry, E., Birren, B., Bloom, T., … Lander, E. S. (2002). Initial sequencing and comparative analysis of the mouse genome. *Nature*, *420*(6915), 520–562. https://doi.org/10.1038/NATURE01262

Weber, J. E., & Russell, L. D. (1987). A study of intercellular bridges during spermatogenesis in the rat. *The American Journal of Anatomy*, *180*(1), 1–24. https://doi.org/10.1002/AJA.1001800102

Wei, K., Clark, A. B., Wong, E., Kane, M. F., Mazur, D. J., Parris, T., Kolas, N. K., Russell, R., Hou, H., Kneitz, B., Yang, G., Kunkel, T. A., Kolodner, R. D., Cohen, P. E., & Edelmann, W. (2003). Inactivation of Exonuclease 1 in mice results in DNA mismatch repair defects, increased cancer susceptibility, and male and female sterility. *Genes & Development*, *17*(5), 603–614. https://doi.org/10.1101/GAD.1060603

West, S. C. (2003). Molecular views of recombination proteins and their control. *Nature Reviews. Molecular Cell Biology*, *4*(6), 435–445. https://doi.org/10.1038/NRM1127

Wiese, C., Hinz, J. M., Tebbs, R. S., Nham, P. B., Urbin, S. S., Collins, D. W., Thompson, L. H., & Schild, D. (2006). Disparate requirements for the Walker A and B ATPase motifs of human RAD51D in homologous recombination. *Nucleic Acids Research*, *34*(9), 2833. https://doi.org/10.1093/NAR/GKL366

Wilkins, A. S., & Holliday, R. (2009). The evolution of meiosis from mitosis. *Genetics*, *181*(1), 3–12. https://doi.org/10.1534/GENETICS.108.099762

Wu, L., & Hickson, I. O. (2003). The Bloom's syndrome helicase suppresses crossing over during homologous recombination. *Nature*, *426*(6968), 870–874. https://doi.org/10.1038/NATURE02253

Wu, Y., Li, Y., Murtaza, G., Zhou, J., Jiao, Y., Gong, C., Hu, C., Han, Q., Zhang, H., Zhang, Y., Shi, B., Ma, H., Jiang, X., & Shi, Q. (2021). Whole-exome sequencing of consanguineous families with infertile men and women identifies homologous mutations in SPATA22 and MEIOB. *Human Reproduction (Oxford, England)*, *36*(10), 2793–2804. https://doi.org/10.1093/HUMREP/DEAB185

Wu-Baer, F., Lagrazon, K., Yuan, W., & Baer, R. (2003). The BRCA1/BARD1 heterodimer assembles polyubiquitin chains through an unconventional linkage involving lysine residue K6 of ubiquitin. *The Journal of Biological Chemistry*, *278*(37), 34743–34746. https://doi.org/10.1074/JBC.C300249200

Xia, B., Sheng, Q., Nakanishi, K., Ohashi, A., Wu, J., Christ, N., Liu, X., Jasin, M., Couch, F. J., & Livingston, D. M. (2006). Control of BRCA2 cellular and clinical functions by a nuclear partner, PALB2. *Molecular Cell*, *22*(6), 719–729. https://doi.org/10.1016/J.MOLCEL.2006.05.022

Xu, Y., Greenberg, R. A., Schonbrunn, E., & Jeremy Wang, P. (2017). Meiosis-specific proteins MEIOB and SPATA22 cooperatively associate with the single-stranded DNA-binding replication protein A complex and DNA double-strand breaks. *Biology of Reproduction*, *96*(5), 1096–1104. https://doi.org/10.1093/BIOLRE/IOX040

Yan Cheng, C., & Mruk, D. D. (2015). Biochemistry of Sertoli cell/germ cell junctions, germ cell transport, and spermiation in the seminiferous epithelium. *Sertoli Cell Biology*, 333–383. https://doi.org/10.1016/B978-0-12-417047-6.00012-0

Yang, H., Wang, H., & Jaenisch, R. (2014). Generating genetically modified mice using CRISPR/Cas-mediated genome engineering. *Nature Protocols 2014 9:8*, *9*(8), 1956–1968. https://doi.org/10.1038/nprot.2014.134

Yang, Y., Guo, T., Liu, R., Ke, H., Xu, W., Zhao, S., & Qin, Y. (2020). FANCL gene mutations in premature ovarian insufficiency. *Human Mutation*, *41*(5), 1033–1041. https://doi.org/10.1002/HUMU.23997

Yao, C., Hou, D., Ji, Z., Pang, D., Li, P., Tian, R., Zhang, Y., Ou, N., Bai, H., Zhi, E., Huang, Y., Qin, Y., Zhao, J., Wang, C., Zhou, Z., Guo, T., & Li, Z. (2022). Bi-allelic SPATA22 variants cause premature ovarian insufficiency and nonobstructive azoospermia due to meiotic arrest. *Clinical Genetics*, *101*(5–6). https://doi.org/10.1111/CGE.14129

Yao, Y., & Dai, W. (2014). Genomic Instability and Cancer. *Journal of Carcinogenesis & Mutagenesis*, *5*(02). https://doi.org/10.4172/2157-2518.1000165

Yilmaz, D., Furst, A., Meaburn, K., Lezaja, A., Wen, Y., Altmeyer, M., Reina-San-Martin, B., & Soutoglou, E. (2021). Activation of homologous recombination in G1 preserves centromeric integrity. *Nature*, *600*(7890), 748–753. https://doi.org/10.1038/S41586-021-04200-Z

Yuan, L., Liu, J. G., Zhao, J., Brundell, E., Daneholt, B., & Höög, C. (2000). The murine SCP3 gene is required for synaptonemal complex assembly, chromosome synapsis, and male fertility. *Molecular Cell*, *5*(1), 73–83. https://doi.org/10.1016/S1097-2765(00)80404-9

Zakharyevich, K., Ma, Y., Tang, S., Hwang, P. Y. H., Boiteux, S., & Hunter, N. (2010). Temporally and biochemically distinct activities of Exo1 during meiosis: double-strand break resection and resolution of double Holliday junctions. *Molecular Cell*, *40*(6), 1001–1015. https://doi.org/10.1016/J.MOLCEL.2010.11.032

Zhang, J., Fujiwara, Y., Yamamoto, S., & Shibuya, H. (2019). A meiosis-specific BRCA2 binding protein recruits recombinases to DNA double-strand breaks to ensure homologous recombination. *Nature Communications*, *10*(1). https://doi.org/10.1038/S41467-019-08676-2

Zhao, H., Chen, Z. J., Qin, Y., Shi, Y., Wang, S., Choi, Y., Simpson, J. L., & Rajkovic, A. (2008). Transcription factor FIGLA is mutated in patients with premature ovarian failure. *American Journal of Human Genetics*, *82*(6), 1342–1348. https://doi.org/10.1016/J.AJHG.2008.04.018

Zhao, H., Qin, Y., Kovanci, E., Simpson, J. L., Chen, Z. J., & Rajkovic, A. (2007). Analyses of GDF9 mutation in 100 Chinese women with premature ovarian failure. *Fertility and Sterility*, *88*(5), 1474–1476. https://doi.org/10.1016/J.FERTNSTERT.2007.01.021

Zhao, W., Vaithiyalingam, S., San Filippo, J., Maranon, D. G., Jimenez-Sainz, J., Fontenay, G. v., Kwon, Y., Leung, S. G., Lu, L., Jensen, R. B., Chazin, W. J., Wiese, C., & Sung, P. (2015). Promotion of BRCA2-Dependent Homologous Recombination by DSS1 via RPA Targeting and DNA Mimicry. *Molecular Cell*, *59*(2), 176–187. https://doi.org/10.1016/J.MOLCEL.2015.05.032

Zickler, D., & Kleckner, N. (2015). Recombination, Pairing, and Synapsis of Homologs during Meiosis. *Cold Spring Harbor Perspectives in Biology*, *7*(6). https://doi.org/10.1101/cshperspect.a016626

Zorrilla, M., & Yatsenko, A. N. (2013). The Genetics of Infertility: Current Status of the Field. *Current Genetic Medicine Reports*, *1*(4), 247–260. https://doi.org/10.1007/S40142-013-0027-1

APPENDIX

Análisis funcional de una variante truncada de RAD51B y de dos elementos genómicos ultraconservados en la gametogénesis

Tesis Doctoral

Yazmine Bejarano Condezo

Director: Dr. Alberto Martín Pendás

Codirectora: Dra. Elena Llano Cuadra

Universidad de Salamanca

Instituto de Biología Molecular y Celular del Cáncer

Salamanca, 2022

ÍNDICE

Introducción

1.Gametogénesis

La reproducción sexual de los mamíferos implica un complejo ciclo vital en el que dos gametos haploides (óvulo o espermatozoide) se fusionan para generar un cigoto que se convierte en un organismo compuesto por células diploides. El proceso biológico esencial por el que estas células diploides producen gametos haploides se denomina **gametogénesis**.

En los mamíferos, la gametogénesis comienza muy temprano en el desarrollo con la aparición extra gonadal de las células germinales primordiales (PGCs, *primordial germ cells*). Esta primera capa de células es la precursora embrionaria de los gametos y representa las células fundadoras de la línea germinal. Las PGCs precursoras surgen durante la embriogénesis y migran a través del intestino posterior hacia las crestas genitales en desarrollo (gónadas). Es en las gónadas donde se someten a una reprogramación epigenética de todo el genoma, que incluye la desmetilación global del ADN, la reactivación del cromosoma X y la remodelación de la cromatina, con el fin de suprimir los programas de diferenciación de las células somáticas y adquirir pluripotencia (Sekl et al., 2007; Surani, 2001). Finalmente, las PGCs colonizan las gónadas emergentes, pierden su potencial migratorio e inician las vías de diferenciación sexual.

1.1 Oogénesis

En los embriones femeninos, la colonización de las crestas gonadales por parte de las PGC va seguida de la determinación del sexo y la posterior diferenciación en oogonias en el ovario en desarrollo. Estas oogonias se dividen por mitosis (aproximadamente 20 divisiones) con citocinesis incompleta, por lo que quedan unidas por puentes intercelulares generando los quistes de células germinales. Entre la semana 10 y la 20 del desarrollo embrionario (E13.5-17.5 en ratones), todo el conjunto de oogonias entra en la profase meiótica I (a través de los estadios de leptoteno, zigoteno y paquiteno) para convertirse en oocitos primarios que se detienen al final de la meiosis I en un estadio de quiescencia conocido como dictiata (correspondiente a los estadios de diploteno o diacinesis). Al mismo tiempo, el quiste de células germinales se desagrega en oocitos individuales rodeados de células de la pregranulosa que generan los folículos primordiales. Durante la desagregación del quiste de células germinales se eliminan varios oocitos por apoptosis (atresia), lo que ayuda a la individualización de los oocitos supervivientes y a la selección del oocito de mayor calidad. Los oocitos permanecerán detenidos hasta que la oleada preovulatoria de la hormona luteinizante (LH, *luteinizing hormone*) estimule la reanudación meiótica, lo que ocurre no antes de la pubertad (X. Wang & Pepling, 2021; Wassarman & Litscher, 2021).

Al inicio de la pubertad, los oocitos crecen y se diferencian de folículos primordiales a folículos preovulatorios en respuesta a la estimulación hormonal en un proceso denominado foliculogénesis. La hormona estimulante del folículo (FSH, *follicle stimulating hormone*), estimula la proliferación de las células somáticas de soporte, llamadas células de la granulosa, y en consecuencia se produce un aumento en tamaño de los oocitos. La FSH también estimula la producción de estradiol, induciendo la LH que impulsa la progresión de la meiosis desde la profase I hasta la metafase II (McGee & Hsueh, 2000). Posteriormente, el oocito detenido en metafase II

es liberado (ovulación) tras la secreción de la LH, generando el oocito secundario y el primer corpúsculo polar. La segunda división meiótica solo progresará si se produce la fecundación, generando el óvulo maduro junto con un segundo corpúsculo polar.

1.2 Espermatogénesis

En los embriones masculinos, la colonización de las crestas gonadales por parte de las PGCs va seguida de la determinación del sexo y la posterior diferenciación en espermatogonias en los testículos en desarrollo. En las gónadas XY, el factor de transcripción SRY induce la regulación al alza de SOX9 y la posterior expresión de FGF9, lo que conduce a la diferenciación de las células de Sertoli. La expresión de estos y otros factores especificadores masculinos como el citocromo P450 26B oxigenasa (CYP26B1), TCF21, NTF3 y CBLN4 promueven la formación de testículos en las gónadas XY (Bowles et al., 2018; H. Suzuki et al., 2015).

En los testículos fetales, bajo la influencia del factor de transcripción *Sox9*, se forma un conjunto de cordones testiculares primitivos en la cresta genital. Una vez formados los cordones, las PGCs presentes en el cordón se denominan gonocitos que difieren morfológicamente de los PGC migratorios. Estos gonocitos proliferan mitóticamente para aumentar su número y luego se detienen en la fase G0/G1, llamada etapa de prospermatogonia. Tras el nacimiento, las prospermatogonias reanudan la mitosis y migran a la base de los cordones testiculares generando las espermatogonias indiferenciadas de tipo A. Estas células tienen características de autorrenovación que perpetúan el conjunto de células madre a lo largo de la vida reproductiva.

Se han propuesto varios modelos para explicar la relación entre las células madre espermatogoniales (SSCs, *spermatogonial stem cells*) y los progenitores (de Rooij, 2017). En el "modelo de fragmentación de clones", todas las SSCs, que tienen potencial de células madre y de renovación, se generan por fragmentación de los puentes intercelulares que las mantienen conectadas por citocinesis incompleta (sincitios). Se ha planteado la hipótesis de que, en este modelo, los clones de espermatogonias indiferenciadas pueden transformarse proporcionando respuestas en la forma de mantener el conjunto de espermatogonias A (A_s) (Hara et al., 2014). Estas espermatogonias A_s se dividen en espermatogonias A emparejadas (A_{pr}) que, o bien completan la citocinesis para producir dos nuevas espermatogonias A_s (autorrenovación), o bien permanecen conectadas por puentes intercelulares (Weber & Russell, 1987). Las espermatogonias A_{pr} se dividen entonces en redes extendidas de 4, 8 o 16 células, conocidas como espermatogonias alineadas (A_{al}). La transición a espermatogonias diferenciadas de tipo A puede producirse a partir de clones A_s, A_{pr} o A_{al4}, pero lo más frecuente es que se produzca a partir de clones A_{al8} o A_{al16}. Ocho divisiones sucesivas a partir de espermatogonias A1 conducen a espermatogonias diferenciadoras de tipo A2, A3, A4 y, finalmente, a espermatogonias B. Durante este curso de diferenciación, las espermatogonias pierden la capacidad autorenovadora (de Rooij, 2017; Fayomi et al., 2018; La & Hobbs, 2019; Nakagawa et al., 2010).

En la pubertad, estas espermatogonias B inician la meiosis dando lugar a cuatro espermátidas redondas haploides que se alargarán dando lugar a espermátidas alargadas. Finalmente, estas espermátidas alargadas se liberan en el lumen del túbulo seminífero donde maduran hasta convertirse en espermatozoides (O'Donnell et al., 2011).

2. Meiosis

La **meiosis** es un proceso celular esencial que reduce el genoma a la mitad generando células haploides (n) a partir de células diploides (2n). Para lograr esta reducción la célula sufre a una ronda de replicación del ADN seguida de dos rondas de segregación. Durante la primera división (meiosis I), se produce la segregación de los cromosomas homólogos maternos y paternos, sufriendo una división reduccional. Durante la segunda división (meiosis II), las cromátidas hermanas se segregan, generando una célula haploide altamente especializada llamada gameto.

Se cree que la meiosis evolucionó a partir de la mitosis, adquiriendo diferentes características, como el emparejamiento de cromosomas homólogos, la recombinación entre cromátidas no hermanas y la ausencia de replicación del ADN antes de la segunda división meiótica, que es esencial para reducir la ploidía (Wilkins & Holliday, 2009). La reducción del material genético paterno es crucial para restaurar la ploidía tras la fecundación, permitiendo así la estabilidad del genoma entre generaciones.

2.1 Profase I

La **profase I** es el evento más largo y complejo de la meiosis. Durante esta fase, los cromosomas se organizan en estructuras de eje, que proporcionan el andamiaje estructural para los diversos eventos específicos de la meiosis, como son i) la generación de roturas de doble cadena (DSBs, *double-strand breaks*) programados, ii) la reparación de los DSBs mediante recombinación homóloga (HR, *homologous recombination*), iii) el emparejamiento y la sinapsis de los cromosomas homólogos para dar lugar a cromosomas bivalentes, así como, iv) la recombinación y v) la segregación de los homólogos. El principal objetivo y consecuencia de la recombinación meiótica es la formación de uniones físicas entre los homólogos, los quiasmas. Estas uniones son esenciales para la correcta alineación y segregación de los homólogos durante la primera división meiótica (Handel & Schimenti, 2010; Zickler & Kleckner, 2015).

La profase I se subdivide en cinco etapas bien definidas: leptoteno, cigoto, paquiteno, diploteno y diacinesis. Esta clasificación se basa en el comportamiento de los cromosomas homólogos cuando se emparejan y sinapsan mediante la formación del complejo sinaptonémico (SC, *synaptonemal complex*) (Handel & Schimenti, 2010). El SC es una estructura proteica en forma de cremallera que se ensambla entre los cromosomas homólogos y los mantiene unidos. Esta estructura tripartita está formada por dos elementos axiales, y una región central que contiene los filamentos transversales y el elemento central. Actualmente, en mamíferos, se han identificado ocho proteínas específicas de la meiosis como componentes estructurales del SC: las proteínas del elemento axial: SYCP3 (Lammers et al., 1994) y SYCP2 (Offenberg et al., 1998), la proteína del filamento transversal: SYCP1 (Meuwissen et al., 1992), y las proteínas del elemento central: SYCE1, SYCE2, SYCE3, TEX12 y SIX6OS1 (Costa et al., 2005; Gómez-H et al., 2016; Hamer et al., 2006; Schramm et al., 2011). Mediante doble inmunofluorescencia de los meiocitos con SYCP3/SYCP1, es factible evaluar el grado de sinapsis de los elementos axiales pudiendo asignar así su correspondiente etapa de la profase I.

Al comienzo de la profase I, en el **leptoteno**, los cromosomas comienzan a condensarse organizando la cromatina y los elementos axiales comienzan a ensamblarse junto con las cohesinas, constituyendo los ejes cromosómicos. En este momento, los cromosomas buscan a su homólogo para emparejarse y los ejes cromosómicos se ensamblan en pequeños fragmentos que se alargan alcanzando el estadio de **zigoteno** (Ishiguro, 2019). Una de las características más distintivas de la meiosis es el emparejamiento de los cromosomas, que requiere la fijación y rotación de los telómeros en la envoltura nuclear a través de los microtúbulos, lo que impulsa la búsqueda de la homología cromosómica (Kim et al., 2022; Lee et al., 2015). En esta etapa los cromosomas homólogos se alinean aún más a través del ensamblaje de los filamentos transversales y el elemento central que actúan como una cremallera. Este proceso se denomina sinapsis. Luego, en el **paquiteno**, el elemento central está completamente ensamblado a lo largo del cromosoma, por lo que se logra la sinapsis completa. Los elementos axiales sinapsados se denominan ahora elementos laterales. En los machos la sinapsis es incompleta ya que los cromosomas sexuales X e Y solo muestran homología en una pequeña región conocida como región pseudoautosómica (PAR) (Simmler et al., 1985). Es en esta región donde se produce la formación de los quiasmas, que aseguran la correcta segregación de los cromosomas sexuales (Acquaviva et al., 2020). La asinapsis de la mayoría de los cromosomas sexuales provoca su inactivación transcripcional, este proceso se denomina inactivación del cromosoma sexual meiótico (MSCI, *meiotic sex chromosome inactivation*) y desempeña un papel importante en la respuesta del punto de control de la profase I a la asinapsis (Turner et al., 2015). Finalmente, los cromosomas homólogos desinapsan y el SC comienza a desensamblarse de **diploteno** a **diacinesis**. Durante este proceso, el ADN alcanza la máxima condensación antes de la metafase I.

2.2 Transición Metafase-Anafase I

Al final de la meiosis, se habrán producido dos divisiones celulares consecutivas que generarán los gametos haploides. La primera división es reduccional, en la que los cromosomas homólogos se segregan, mientras que la segunda es una división ecuacional, similar a la mitosis, en la que las cromátidas hermanas son las que se segregan. Estas segregaciones consecutivas se producen por la liberación de los complejos de cohesinas de los brazos cromosómicos y de los centrómeros. En la transición metafase-anafase I, solo se eliminarán los complejos de cohesinas de los brazos cromosómicos y se protegerán las cohesinas de los centrómeros, permitiendo la segregación de los cromosomas homólogos.

Los dos cromosomas homólogos de cada bivalente de la metafase I están conectados físicamente por quiasmas, que se estabilizan por cohesión distal al CO. Estas uniones físicas, contrarrestan la fuerza generada por el huso y promueven la orientación de los bivalentes (Gutiérrez-Caballero et al., 2012). Al inicio de la anafase I, la segregación de los bivalentes se consigue mediante la eliminación de las cohesinas de los brazos cromosómicos por una escisión proteolítica de la subunidad α-kleisina de los complejos de cohesinas (**REC8** o RAD21L) por parte de Separasa (Hauf et al., 2001; Kitajima et al., 2003; Kudo et al., 2009; Llano et al., 2008; Uhlmann et al., 2000). La activación de Separasa está altamente regulada a través de un doble mecanismo inhibitorio mediado por Securina y el complejo CDK1/Ciclina B1 (Hellmuth et al., 2015; Stemmann et al., 2001). Brevemente, una vez que los homólogos se orientan en la placa metafásica, el punto de control de ensamblaje del huso (SAC, *spindle assembly checkpoint*) se satisface, y el complejo APC/C acomplejado a Cdc20 se activa, por lo que Securina y Ciclina B1 son el objetivo de la

ubiquitinación dependiente de APC, se degradan por el proteasoma y es entonces cuando Separasa se activa (Hagting et al., 2002; Vorlaufer & Peters, 1998).

La protección de las cohesinas centroméricas es esencial para la correcta segregación de las cromátidas hermanas, esta protección se lleva a cabo por las shugoshinas (Kerrebrock et al., 1995). El mecanismo de protección de las shugoshinas se basa en un complejo que junto con la fosfatasa PP2A contrarresta la fosforilación de las cohesinas evitando así la escisión de la Separasa. Los ratones deficientes en *Sgol2* son infértiles debido a la separación prematura de las cromátidas hermanas durante la anafase I, dando lugar a gametos aneuploides (J. Lee et al., 2008; Llano et al., 2008). La localización de SGOL2 en los centrómeros está estabilizada por MEIKIN, una proteína que se requiere para la mono-orientación de los cinetocoros en los cromosomas hermanos. En espermatocitos deficientes de MEIKIN se produce una disminución de los niveles de SGOL2, lo que conduce a defectos de cohesión similares, pero más leves que en los ratones deficientes en *Sgol2* (Kim et al., 2014; Ma et al., 2021).

2.3 Segunda división meiótica

Las cohesinas se mantienen físicamente unidas a los centrómeros de las cromátidas hermanas hasta la segunda división meiótica, cuando serán liberadas por una segunda oleada de activación de la Separasa, dando lugar a la segregación de las cromátidas hermanas (Clift et al., 2018). Así, en la transición metafase-anafase II, los cromosomas se congregan en la placa metafásica con cada cinetocoro hermano orientado hacia un polo.

No está claro cómo se modifica/elimina el mecanismo de protección de la cohesión centromérica en meiosis II para permitir la ruptura de la cohesión centromérica y permitir la segregación de las cromátidas hermanas. Se han propuesto diferentes hipótesis que podrían arrojar luz a esta cuestión todavía sin resolver. La más clásica defiende que la tensión a través de los centrómeros resulta en una redistribución de SGOL2 desde los centrómeros internos hacia los cinetocoros dejando las cohesinas centroméricas accesibles a la escisión de la Separasa en anafase II, lo que conduce a la generación de gametos haploides (Gómez et al., 2007; J. Lee et al., 2008). Una segunda hipótesis propone que la chaperona de histonas I2PP2A/Set, un inhibidor de PP2A, contrarresta específicamente la protección de Rec8 en la meiosis II de forma independiente a la tensión (Chambon et al., 2013). La tercera hipótesis propone que en levaduras, Sgo1 (similar al *Sgo2* de los mamíferos) y Msp1 se degradan al inicio de la anafase II de manera dependiente de APC/C para asegurar la desprotección (Argüello-Miranda et al., 2017). Recientemente, se ha planteado la hipótesis de que la individualización de los cinetocoros, antes de entrar en meiosis II, es el evento clave que permite la eliminación de la cohesión centromérica y la correcta separación de las cromátidas hermanas (Gryaznova et al., 2021).

En definitiva, la meiosis es un proceso muy complejo y debe estar altamente regulado. La segregación errónea de cromosomas en la meiosis I o II da lugar a la generación de aneuploidía o aberraciones cromosómicas que se producen en al menos el 5% de todos los embarazos (Hassold & Hunt, 2001). Se cree que las mujeres mayores de 35 años tienen mayor probabilidad de aneuploidía, lo que conduce a abortos espontáneos, anomalías congénitas o infertilidad (Herbert et al., 2015).

3. Infertilidad humana

La Organización Mundial de la Salud (OMS) define la infertilidad como una enfermedad del sistema reproductivo masculino o femenino consistente en la imposibilidad de conseguir un embarazo después de 12 meses o más de relaciones sexuales habituales sin protección. La infertilidad primaria es la incapacidad de lograr un embarazo, mientras que la infertilidad secundaria se refiere a no poder conseguir un embarazo después de una concepción previa. La infertilidad es un trastorno complejo y heterogéneo, que puede afectar al hombre, a la mujer o a ambos, y que afecta aproximadamente al 10-15% de las parejas en edad reproductiva, con un 25-30% de los casos clasificados como idiopáticos (Jose-Miller et al., 2007; Mallepaly et al., 2017).

La **infertilidad femenina** puede estar causada por factores genéticos, hormonales o ambientales que, en la mayoría de los casos, afectan a la ovulación. En este sentido, el síndrome de ovario poliquístico es una condición de desequilibrio hormonal que puede interferir con la ovulación regular y afecta al 7% de las mujeres en edad reproductiva **(Zorrilla & Yatsenko, 2013)**. Entre las causas menos comunes de infertilidad femenina se encuentran la enfermedad inflamatoria pélvica, la endometriosis, los fibromas uterinos o los tratamientos de quimioterapia/radioterapia (Venkatesh et al., 2014). En las mujeres, la interrupción de la función ovárica se produce fisiológicamente como consecuencia de la edad, con el inicio de la menopausia. Sin embargo, la insuficiencia ovárica primaria (POI, *Primary ovarian insufficiency*) se caracteriza por una pérdida de la función ovárica normal mucho antes de la edad natural de la menopausia, y es una de las principales causas de infertilidad en mujeres jóvenes. Clínicamente, la POI se caracteriza por la pérdida de la función ovárica por debajo de los 40 años con disminución de los folículos ováricos, oligo/amenorrea durante al menos 4 meses y niveles de FSH como en el rango menopáusico (>25IU/L) (Nelson, 2009). Un meta-análisis reciente estimó que el 3,7% de las mujeres de todo el mundo están afectadas por POI (Golezar et al., 2019), aunque el 5-10% de estas mujeres son capaces de concebir tras un diagnóstico temprano con técnicas de reproducción asistida (Huang et al., 2022).

La **infertilidad masculina** se debe principalmente a cualquier condición que afecte a la cantidad y/o calidad de los espermatozoides. Algunas de estas condiciones pueden ser debidas a la alteración de la espermatogénesis, el hipogonadismo, la malformación testicular, las anomalías estructurales del tracto genital masculino, las infecciones, la impotencia, las enfermedades crónicas, la quimioterapia o los trastornos inmunológicos (Jose-Miller et al., 2007). Entre las anomalías relacionadas con la cantidad y/o calidad de los espermatozoides, las más frecuentes son la reducción de la concentración de espermatozoides (oligospermia), de la motilidad (astenospermia), el aumento del porcentaje de espermatozoides aberrantes (teratospermia) y la ausencia total de espermatozoides en el eyaculado (azoospermia). Dentro de este último grupo, podemos distinguir entre azoospermia obstructiva y no obstructiva. En la azoospermia obstructiva, los espermatozoides producidos no pueden ser secretados debido a una obstrucción en los conductos seminales y afecta al 1% de la población masculina, mientras que en la azoospermia no obstructiva no se producen espermatozoides debido a un fallo en la espermatogénesis siendo la más frecuente en comparación con la azoospermia obstructiva (Lindsay & Vitrikas, 2015).

En la última década, los recientes avances en las tecnologías de secuenciación de nueva generación han arrojado luz sobre varios trastornos humanos. La secuenciación del exoma completo (WES, *Whole Exome Sequencing*) de familias infértiles ha hecho posible la identificación de varios genes con una relación causal directa con esta enfermedad. En este sentido, se han identificado cientos de genes candidatos, los genes causantes de POI se enumeran en la ***Supplementary Table 1***. Algunos ejemplos de candidatos identificados son los genes meióticos SYCE1 (de Vries et al., 2014), STAG3 (Caburet et al., 2014; Llano et al., 2014), SPO11 **(Tran & Schimenti, 2019)**, MSH4 (Carlosama et al., 2017), MSH5 (Guo et al., 2017), DMC1 (He et al., 2018), BRCA2 (Caburet et al., 2020), MEIOB (Caburet et al., 2019; Y. Wu et al., 2021), SPATA22 (Y. Wu et al., 2021; C. Yao et al., 2022) y HSF2BP (Felipe-Medina et al., 2020). En un futuro muy cercano, se espera que esta tecnología permita identificar todas las variantes de un genoma individual permitiendo una medicina personalizada para cada paciente.

4. Inestabilidad genómica

La división celular implica varios mecanismos que deben estar finamente regulados para preservar la integridad del genoma y asegurar su propagación a la descendencia fielmente. La regulación eficiente de la replicación del ADN, la detección y reparación de daños en el ADN, así como la regulación del ciclo celular garantizan el mantenimiento del genoma durante las divisiones celulares (Aguilera & Gómez-González, 2008).

La **inestabilidad genómica** se refiere a una serie de alteraciones genéticas que van desde mutaciones de nucleótidos hasta reordenamientos cromosómicos. Hay dos tipos de elementos que juegan un papel fundamental en la inestabilidad genómica, los que actúan en *trans* para prevenir la inestabilidad, como la replicación del ADN, la reparación del ADN y los factores de punto de control de la fase S, y los sitios cromosómicos que actúan en *cis* como puntos calientes de inestabilidad, incluyendo los sitios frágiles, y las regiones altamente transcritas (Aguilera & Gómez-González, 2008). La inestabilidad genómica suele estar asociada a trastornos patológicos como el envejecimiento prematuro, la tumorigénesis, las enfermedades neurodegenerativas, las inmunodeficiencias y la infertilidad (Aguilera & García-Muse, 2013). Sin embargo, la inestabilidad genómica también ocurre en condiciones fisiológicas, como en la diversificación de genes de inmunoglobulinas en células T y B (Maizels, 2005), y durante la reparación de DSBs en la recombinación meiótica, que es esencial para el surtido independiente de cromosomas (segregación aleatoria de cromosomas en la meiosis) y de genes (intercambio de material genético entre genomas parentales).

Teniendo en cuenta el tipo de inestabilidad generada, la inestabilidad genómica puede dividirse en diferentes clases:

I) **Mutaciones** (mutaciones puntuales, microinserciones y microdeleciones) que pueden ser causadas por mutágenos endógenos/exógenos.
II) **Micro y minisatélites** que dan lugar a expansiones y contracciones de ADN repetitivo.
III) **Inestabilidad cromosómica** que se refiere a cambios en el número de cromosomas que conducen a una ganancia o pérdida de cromosomas.
IV) **Reordenamientos cromosómicos**, que implican una fusión de dos o más segmentos cromosómicos que no están normalmente unidos.

Todas estas alteraciones genéticas pueden iniciarse como resultado de fallos en diferentes pasos del ciclo del ADN, desde la replicación hasta la segregación. En este sentido, las causas más comunes de inestabilidad genómica son fallos en la replicación y reparación del ADN.

4.1 Respuesta al daño al ADN

Las células sufren constantemente estrés genotóxico producido por agentes exógenos o endógenos que afectan a la integridad de nuestro material genético como el bloqueo de la replicación del ADN, la alteración de la transcripción, y si no se reparan o se reparan incorrectamente, dan lugar a mutaciones o aberraciones genómicas (Campos & Clemente-Blanco, 2020). Para detectar, señalar y promover la reparación del daño genético, las células han desarrollado una compleja red de mecanismos de respuesta al daño del ADN (DDR, *DNA damage response*) (Giglia-Mari et al., 2011).

La vía DDR puede ser activada por agentes dañinos físicos y químicos que implican lesiones específicas y activan diferentes procesos de reparación. Para asegurar una reparación adecuada, el ADN puede ser restaurado por varios mecanismos como la reparación por escisión de bases (BER, *base excision repair*) que revierte las modificaciones oxidativas de las bases, la reparación por escisión de nucleótidos (NER, *nucleotide excision repair*) que elimina las lesiones que distorsionan el ADN, la vía de la anemia de Fanconi responsable de la reparación de los enlaces cruzados entre cadenas del ADN (ICLs, *interstrand crosslinks*), la reparación de la unión de extremos no homólogos (NHEJ, *non-homologous end joining*) y la HR, que eliminan los DSB, y finalmente, la reparación de malapareamiento (MMR, *mismatch repair*) que restablece los errores que se producen durante la replicación del ADN (Caldecott, 2008; D'Andrea & Grompe, 2003; Hoeijmakers, 2009; Jiricny, 2006; Lindahl & Barnes, 2000; West, 2003).

Los ICLs son lesiones del ADN extremadamente tóxicas que impiden que el ADN se desenrolle correctamente, lo que provoca fallos de replicación y transcripción. Los ICLs son inducidos por compuestos químicos como el cis-platino, la Mitomicina C (MMC) (Paz et al., 2004), así como agentes alquilantes. Sin embargo, otras fuentes potenciales de ICLs son los subproductos de la peroxidación lipídica como la acroleína y los aldehídos β-insaturados, cuyas concentraciones pueden aumentar con una dieta alta en grasas o al alcoholismo (Balbo & Brooks, 2015; Folmer et al., 2003; Stonez et al., 2008).

La célula utiliza la vía de la Anemia de Fanconi para hacer frente a los ICL. La incapacidad de reparar este tipo de lesión conduce al colapso de la horquilla de replicación, especialmente en las células que se dividen activamente, como en el sistema hematopoyético. En consecuencia, los individuos con alteraciones en esta vía sufren, como su nombre indica, de Anemia de Fanconi, que se caracteriza por hipersensibilidad a los agentes inductores de ICL (utilizados para el diagnóstico), aberraciones cromosómicas en la médula ósea e infertilidad, así como predisposición al cáncer (L. C. Wang & Gautier, 2010). Por lo tanto, los genes FANC son esenciales en la reparación de ICLs y, por lo tanto, en el mantenimiento de la estabilidad del genoma. En la actualidad, se han identificado 22 genes FANC, entre los que se encuentran RAD51 (FANCR), RAD51C (FANCO) y XRCC2 (FANCU) (Nalepa & Clapp, 2018; Peake & Noguchi, 2022). Las mutaciones en ambos alelos de RAD51, RAD51C o XRCC2 dan lugar a Anemia de Fanconi o a un síndrome similar (Shamseldin et al., 2012; Vaz et al., 2010).

4.2 Parálogos de RAD51

RAD51 es una ATPasa dependiente del ADN que se une al ADN monocatenario y promueve la invasión de la cadena y el intercambio entre moléculas de ADN homólogas. El gen *RAD51* es un ortólogo de la recombinasa RecA de *Escherichia coli*. En los vertebrados, existen siete parálogos diferentes de RAD51: RAD51, RAD51B, RAD51C, RAD51D, DMC1, XRCC2 y XRCC3 que surgieron de antiguas duplicaciones del gen RAD51. Los parálogos del RAD51 desempeñan un papel relevante en la HR y en el mantenimiento de la integridad cromosómica en las células mitóticas y meióticas. Los defectos en los genes parálogos de RAD51 se asocian a la tumorigénesis y a enfermedades como la Anemia de Fanconi (Sullivan & Bernstein, 2018).

Se ha propuesto que los parálogos de RAD51 forman dos complejos bioquímicos funcionalmente distintos, el complejo RAD51B-RAD51C-RAD51D-XRCC2 (BCDX2) y el complejo RAD51C-XRCC3 (CX3) (Bonilla et al., 2020). Estos parálogos juegan papeles esenciales en la preservación de la integridad genómica durante el desarrollo, así como durante la proliferación celular fisiológica. Además de estos parálogos, otro miembro de esta familia, *DMC1* que muestra un 50% de identidad de secuencia con *RAD51* y funciona exclusivamente en la recombinación meiótica. Los parálogos de RAD51 asisten a la función de RAD51 en la reparación de DSBs, la meiosis y en la replicación del ADN (Godin et al., 2016). Sin embargo, el mecanismo subyacente a cómo promueven y contribuyen la HR sigue siendo un enigma (Bonilla et al., 2020). El estudio funcional de los parálogos de RAD51 ha sido difícil porque tienden a formar agregados insolubles *in vitro*, además de su baja abundancia celular, y porque el hecho de que los ratones deficientes de los mismos muestran letalidad embrionaria en ratones (B. Deans et al., 2000; S. Kuznetsov et al., 2007; Pittman et al., 1998; Prakash et al., 2021; Shu et al., 1999). Esta letalidad indica que cada uno de los parálogos es esencial y no redundante durante el desarrollo. Se ha demostrado que los parálogos de RAD51 también desempeñan un papel en la homeostasis de la horquilla de replicación. El complejo CX3 media el reinicio eficiente de las horquillas invertidas y tiene funciones adicionales como en la replicación del ADN mitocondrial y el mantenimiento genómico (Mishra et al., 2018), así como en la reparación del ADN ICL (Sasaki et al., 2004). El complejo BCDX2 limita la velocidad de la horquilla ante el daño en el ADN y media en la degradación de la horquilla estancada en las células deficientes en BRCA2 ayudando a las funciones de RAD51 (Berti et al., 2020).

5. Elementos ultraconservados

Los genomas de los grandes eucariotas multicelulares están compuestos en su mayoría por secuencias de ADN no codificantes de proteínas (98-99%). Sin embargo, aunque se sabe que algunas secuencias de ADN no codificante desempeñan papeles relevantes, como la regulación de la expresión génica, se desconoce en gran medida la importancia funcional de la mayoría de estas regiones.

La secuenciación del genoma de multitud de especies ha permitido, mediante su alineación y comparación, la identificación de regiones codificantes como no codificantes. Se han identificado varias secuencias altamente conservadas no sólo en las secuencias codificantes, sino también en la fracción no codificante del genoma. Se estima que la similitud global entre los genomas humano y de ratón es del 66,7% (Waterston et al., 2002). A partir de la publicación de la secuencia

del genoma del ratón se ha estimado que "la proporción de segmentos pequeños (50-100 pb) en el genoma de los mamíferos que está bajo selección negativa puede estimarse aproximadamente del 5%". Esto se refiere a repeticiones ancestrales que están bajo una presión evolutiva para eliminar variantes de secuencia deletéreas de la población. Solo una pequeña parte de esta secuencia se debe a regiones codificantes de proteínas (1,5%), lo que indica que el genoma contiene una gran fracción de regiones funcionales conservadas no codificantes que están bajo selección negativa y cuya función biológica sigue siendo desconocida (Waterston et al., 2002).

Uno de los primeros análisis del cromosoma se llevó a cabo centrándose en el cromosoma 21, en el que se encontraron 2262 secuencias no génicas conservadas (CNG, *non-genic sequences*). Estas CNGs consistían en secuencias de más de 100bp con más del 70% de secuencias idénticas entre el cromosoma 21 humano y el del ratón (Dermitzakis et al., 2005).

Los **elementos ultraconservados** (**UCEs**, *Ultraconserved elements*) son regiones altamente conservadas de los genomas de los organismos entre taxones evolutivamente distantes. Los UCEs se identificaron utilizando una condición más estricta en las CNGs. Esta selección consistió en buscar secuencias de más de 200 pares de bases de longitud con un 100% de identidad en genomas completos de humanos, ratones y ratas. A partir de esta selección, se encontraron 481 UCEs, la mayoría de ellos también conservados en muchas especies de vertebrados (Bejerano et al., 2004). La heterogeneidad de las características de los UCEs y los recientes enfoques experimentales han determinado que una fracción de los UCEs actúan funcionalmente como reguladores *cis*-transcripcionales, como potenciadores (*enhancers*) o silenciadores. También se ha hipotetizado que los UCEs podrían desempeñar un papel estructural (Dermitzakis et al., 2005) y, que hasta un 10% de los UCEs podrían ser regiones de unión a la matriz. Estas regiones podrían regular la conformación de la cromatina mediante la unión específica de determinadas proteínas (Glazko et al., 2003).

Los ensayos en ratones transgénicos se han utilizado ampliamente para caracterizar las funciones potenciadoras de los UCEs no codificantes. Esta metodología implica la clonación de un elemento regulador candidato de interés frente a un promotor mínimo (*Hsp68* o *β-globina*) y un gen reportero (*lacZ* o *GFP*). El plásmido de ADN linealizado se microinyecta en el pronúcleo de los óvulos fecundados, donde se integrará al azar en el genoma. Con este método, la expresión del gen reportero, que es un indicador de la actividad del elemento regulador candidato, puede visualizarse mediante tinción (Pennacchio et al., 2006). Mediante el uso de estos constructos reporteros, algunos estudios funcionales sugieren que es probable que los UCEs sean regiones reguladoras de la expresión génica expresión (Boffelli et al., 2003; Frazer et al., 2004; Nobrega et al., 2003), sin embargo, función de los UCEs aún no ha sido revelada.

Resumen significativo

1. La variante truncada de RAD51B provoca defectos de reparación del ADN meiótico y somático

En este trabajo, mediante la secuenciación del exoma completo de dos hermanas con un fenotipo aislado de POI, identificamos una variante en el gen RAD51B como el mejor candidato causal de esta infertilidad. Esta variante consiste en una deleción de una timina en la posición 92 (c.92delT). En esta familia, todas las hermanas afectadas son homocigotas para la mutación, mientras que los miembros sanos son portadores heterocigotos. Esta evidencia, junto con el hecho de que RAD51B es un parálogo de RAD51 al que no se le ha asignado un papel meiótico, apoyaría la causalidad de la variante RAD51B-c.92delT como responsable de la POI familiar.

Para estudiar esta variante de RAD51B decidimos usar el ratón como modelo, para ello mediante CRISPR/Cas9 replicamos la mutación humana en el ratón. Las hembras con la variante de *Rad51b* en homocigosis mostraron una tendencia a la subfertilidad, presentando un fenotipo mucho menos severo que el observado en las hermanas afectadas de la familia en estudio. Este resultado fue bastante sorprendente, teniendo en cuenta un estudio reciente realizado por nuestro laboratorio en el cual se evaluó una variante inductora de POI en el gen *HSF2BP* (Felipe-Medina et al., 2020). En este estudio, los ratones humanizados *Hsf2bp-S167L* mostraron una relación directa entre la reducción en el número de COs y una disminución en la fertilidad femenina. Esta tendencia en la reducción del tamaño de las camadas en las hembras *Rad51b-c.92delT* podría apoyar la teoría de un impacto de la mutación de *Rad51b* en la fertilidad femenina. Las diferencias existentes entre el fenotipo humano y el de ratón podrían deberse a las diferencias biológicas en la vía meiótica, como en el SAC o en la maduración de los COs (Namgoong et al., 2018; S. Wang et al., 2017). Además, varios trastornos endocrinos que conducen a un retraso de la pubertad y a infertilidad, como el hipogonadismo hipogonadotrópico o el hipopituitarismo, también tienen un espectro fenotípico variable en humanos y ratones. En el caso del fenotipo de deficiencia hormonal hipofisaria, los ratones homocigotos para una variante de pérdida de función en *Prop1* o *Pouf1* muestran fenotipos muy diferentes en distintos fondos genéticos, incluso cuando los parámetros ambientales son invariables (Fang et al., 2016). Además, ratones mutantes que carecen del gen *Usp26*, el cual está asociado a infertilidad presentan una meiosis defectuosa o normal dependiendo del fondo genético (Kauppi, 2021). Todos estos datos previos podrían dar una explicación del motivo por el cual observamos un fenotipo más severo en aquellas pacientes con POI en comparación con las ratonas *Rad51b-c.92delT*.

La identificación de *RAD51B* como un nuevo gen causante de POI debido a alteraciones en la recombinación meiótica lo convierte en candidato para la creciente, pero aún reducida, lista de genes responsables de POI. Algunos ejemplos de ellos son: BRCA2 (Caburet et al., 2020), FANCL (Yang et al., 2020), MEIOB (Caburet et al., 2019; Y. Wu et al., 2021), SPATA22 (Y. Wu et al., 2021; C. Yao et al., 2022), SYCE1 (de Vries et al., 2014), MSH4 (Carlosama et al., 2017), DMC1 (He et al., 2018) o HSF2BP (Felipe-Medina et al., 2020).

El análisis *in silico* predijo que esta variante provocaría la aparición de un codón de terminación prematuro (PTC, *premature termination codon*) lo que podría conducir a la producción de una proteína altamente truncada de 39 aminoácidos. Esta proteína RAD51B truncada carecería de la mayor parte de la proteína, incluyendo los dos dominios Walker esenciales para su actividad ATPasa (Wiese et al., 2006), lo que daría lugar a un alelo de pérdida de función que ha demostrado ser letal en el ratón (Shu et al., 1999). Por otro lado, y más allá de la ausencia de dominios funcionales en la proteína truncada, esta PTC también podría generar un alelo nulo mediante la activación del mecanismo celular de supervisión de degradación del ARN mensajero (ARNm) mediada por mutaciones terminadoras (NMD, *non-sense mediated decay*), que evita la expresión de proteínas truncadas (Y. F. Chang et al., 2007). La localización del PTC en la variante RAD51B-c.92delT podría desencadenar el NMD, ya que esta vía se desencadena si un PTC está localizado aproximadamente 50 nucleótidos aguas arriba de la última unión de exones (Thermann et al., 1998).

Al replicar la variante humana de la mutación en ratones observamos que los ratones son viables, lo que sugiere que la reiniciación de la traducción utilizando un codón AUG secundario aguas abajo está operando en este modelo de ratón. Esta observación se mantuvo con la expresión del ARNm de *Rad51b* en los ratones *Rad51b*$^{c.92delT/c.92delT}$, lo que indica que la NMD no está activa, probablemente por ese reinicio de la traducción. Por otra parte, la presencia de péptidos correspondientes al C-terminal de la proteína RAD51B-c.92delT procedentes de células linfoblastoides derivadas de humanos apoya la evidencia directa de que el reinicio de la traducción está teniendo lugar. Estas observaciones concuerdan con un análisis de todo el genoma de los PTCs, que se producen de forma natural en tumores humanos, en el cual se demostró que los transcritos que llevan PTCs 5'-proximales pueden eludir la NMD mediante la reiniciación de la traducción (Lindeboom et al., 2016). Este modelo explicaría la ausencia de NMD en la variante RAD51B-c.92delT debido a la reiniciación de la traducción en el codón AUG64 y, en consecuencia, permitiría la expresión de una proteína RAD51B truncada en el N-terminal en humanos y ratones. El dominio N-terminal de RAD51B está implicado en las interacciones proteína-proteína con sus parálogos, como RAD51C, y en la localización nuclear a través de una señal de localización nuclear (K. A. Miller et al., 2004, 2005). Esto concuerda con la localización nuclear alterada observada de la variante truncada de RAD51B en comparación con el tipo salvaje (WT, *wild-type*) en células Cos7 transfectadas, sugiriendo una disfunción similar de la proteína endógena *in vivo*.

Observamos que el alelo hipomorfo de *Rad51b* causa una pérdida de la interacción de RAD51B-c.92delT con RAD51C. También observamos una pérdida parcial de la interacción entre RAD51B-c.92delT con sus nuevos interactores RAD51 y la helicasa POLQ-like (HELQ). En cuanto a HELQ, esta helicasa promueve la eficiencia de la HR en las horquillas de replicación dañadas al interactuar directamente con el complejo BCDX2. El complejo BCDX2 y HELQ actúan conjuntamente en la resolución de los entrecruzamientos entre cadenas de ADN tras la exposición a MMC (Adelman et al., 2013). La disrupción de HELQ en ratones muestra sensibilidad a la MMC, aumento de la susceptibilidad a los tumores de ovario e hipofisarios, así como subfertilidad (Adelman et al., 2013; Luebben et al., 2013). A nivel celular, defectos en HELQ dan lugar a hipersensibilidad al cisplatino y a la MMC, así como a la persistencia de RAD51 tras el daño (Takata et al., 2013). Estas observaciones en ratones *Rad51b*$^{c.92delT/c.92delT}$ y ratones deficientes de HELQ sugieren un mecanismo de acción patológico común.

En conjunto, las interacciones ineficientes entre RAD51B-c.92delT y sus interactores RAD51C, RAD51 y HELQ como consecuencia de la supresión de los residuos del N-terminal de RAD51B, conducen sinérgicamente a una reducción del número de COs observada tanto en los espermatocitos como en los oocitos de *Rad51b-c.92delT*.

Se han descrito varias vías de reparación esenciales para la eliminación de las lesiones del ADN introducidas por la acción de compuestos dañinos (Helleday et al., 2008). Teniendo en cuenta que RAD15B también se expresa en los tejidos somáticos, probamos diferentes tipos de compuestos que causan daño en el ADN y los cuales podrían alterar la reparación somática del ADN en fibroblastos embrionarios de ratón (MEFs, *mouse embryonic fibroblasts*) de *Rad51b-c.92delT*. Nuestros resultados mostraron que los MEFs mutantes no eran sensibles a los rayos ultravioletas (UV), al metil-metano sulfonato (MMS) o a la radiación ionizante, siendo cada uno de estos fármacos inductores de diferentes vías de reparación del ADN. A partir de estos resultados podemos extrapolar que, en el caso de la UV, la vía de reparación por escisión de nucleótidos no se ve afectada, ya que esta vía es esencial para la reparación del daño inducido por la luz UV, como los dímeros de pirimidina de ciclobuteno, o los fotoproductos de pirimidina-pirimidona (6-4) (D'Souza et al., 2022). En el caso de MMS y la radiación ionizante, la vía de reparación por escisión de bases no se vería afectada, ya que ésta es la vía responsable de eliminar y reemplazar el daño de una sola base o la rotura de hebra simple del ADN (Caldecott, 2008).

La sensibilidad observada de los MEFs *Rad51b-c.92delT* a la MMC en el ensayo de proliferación celular y clonogénico, así como la presencia de ADN no reparado sugieren que la vía de reparación de ICLs sí está afectada. Se ha demostrado que la MMC produce ICLs que son reparados específicamente por la vía de la Anemia de Fanconi. De forma consistente, las células linfoblastoides somáticas derivadas de humanos RAD51B-c.92delT, así como las MEFs y las células de médula ósea no cultivadas del ratón *Rad51b*$^{c.92delT/c.92delT}$ muestran inestabilidad cromosómica inducida por la sensibilidad a la MMC. También se ha descrito una asociación entre las mutaciones en RAD51 y sus parálogos con una mayor predisposición al cáncer y a la Anemia de Fanconi, en particular RAD51C (FANCO) y XRCC2 (FANCU) (Ameziane et al., 2015; Park et al., 2016; Schlacher et al., 2012; Vaz et al., 2010). En concreto, RAD51B se ha visto implicado en cánceres como el de mama, ovario, próstata, el leiomioma de útero, carcinoma nasofaríngeo, retinoblastoma, melanoma y aneuploidía (Date et al., 2006; Mehine et al., 2013; Nowacka-Zawisza et al., 2015; Orr et al., 2012; Qin et al., 2011; Song et al., 2015; G. Thomas et al., 2009; Wadt et al., 2015). Además, también se ha descrito que el polimorfismo RAD51B-rs8017304 está implicado en el adenoma hipofisario (Juknytė et al., 2021), lo cual se encuentra en concordancia con nuestras observaciones en las que los ratones mutantes mostraron una mayor incidencia de hiperplasia hipofisaria. Cabe mencionar que a una de las hermanas afectadas (II-4) se le diagnosticó un adenoma tubulovelloso duodenal con displasia de alto grado y fue operada sin tratamiento adicional. En conjunto, estos datos proporcionan pruebas de un papel crítico de RAD51B en la inestabilidad del genoma somático y la tumorigénesis.

En estudios anteriores se ha demostrado que la reprogramación eficiente de las MEFs a un estadio pluripotente requiere una vía competente para reparar mediante HR la inestabilidad inherente del genoma que se produce durante la reprogramación. En consecuencia, la reprogramación eficiente requiere genes clave de HR, incluyendo *Brca1*, *Brca2* y *Rad51* de

manera dependiente de p53 (González et al., 2013). De forma consistente, la sobreexpresión de *Rad51* en MEFs primarias mejora la eficiencia de la reprogramación, posiblemente regulando una vía de reparación de daños en el ADN durante la fase inicial del proceso de reprogramación (J.-Y. Lee et al., 2016). La expresión de los factores de Yamanaka en MEFs induce estrés de replicación, mientras que la reducción genética del estrés, como la sobreexpresión de *Chk1*, aumenta la eficiencia de la generación de células madre pluripotentes inducidas (iPSCs, *induced pluripotent stem cells*) (Ruiz et al., 2015). Esto es compatible con la reducción de las colonias de iPSCs derivadas de MEFs *Rad51b-c.92delT* que se observó, sugiriendo de nuevo que RAD51B tiene un papel en la estabilidad e integridad del genoma.

Se sabe que las horquillas de replicación se estancan a ambos lados del ICL, como las generadas por el metabolismo celular (aldehídos) o agentes dañinos para el ADN como la MMC y el cisplatino, cuando son detectadas por el Replisoma (Cortez, 2019). Una vía para resolverlos durante la fase S es promoviendo la remodelación de la horquilla. Recientemente, se ha propuesto que los parálogos de RAD51 orquestan secuencialmente transacciones moleculares en las horquillas de replicación, promoviendo la remodelación de la horquilla y el reinicio de la replicación (Berti et al., 2020). En este sentido, la sensibilidad a la Hidroxiurea (HU) y Afidicolina de las células RAD51B-c.92delT en los ensayos de proliferación celular y ensayos clonogénicos apuntan hacia un efecto directo de la variante RAD51B en esta vía. Estos compuestos no dañan la estructura del ADN directamente, sino que interfieren con aquellas las enzimas relacionadas con la replicación. En concreto, la HU inhibe la ribonucleótido reductasa, lo que provoca una alteración en el metabolismo de los dNTPs, bloqueando así la progresión de la horquilla de replicación. Por otro lado, la Afidicolina es un inhibidor de la ADN polimerasa replicativa, lo que provoca el desacoplamiento de la replicación (Muñoz & Méndez, 2017; Vesela et al., 2017). El intercambio de cromátidas hermanas (SCE, *sister chromatid exchange*) es el cambio recíproco de fragmentos genómicos entre dos cromátidas hermanas idénticas. La tasa invariable de SCE observada en las células linfoblastoides RAD51-c.92delT no tratadas (espontáneas) o tratadas con MMC (inducidas) indica que la vía canónica de HR no se ve afectada por la variante en RAD51B. Este resultado es coherente con la ausencia de alteración de la recombinación de cromátidas hermanas en las células U2OS deficientes en RAD51B (Garcin et al., 2019). Además, los experimentos llevados a cabo en el laboratorio de Juan Méndez (CNIO, Madrid) indican una implicación directa de la variante genética RAD51B en el reinicio de la horquilla de replicación, tal y como mostraron los experimentos de fibras de ADN en los que observaron un retraso en la velocidad de la horquilla en las células tratadas con MMC (Franca et al., 2022). Estos resultados, junto con la rotura cromosómica inducida por MMC tanto *in vitro* como *in vivo*, apoyan una función somática de RAD51B en la asistencia a la progresión de la horquilla a través de ciertas lesiones del ADN, como parte de la respuesta de tolerancia al daño del ADN.

En resumen, en este trabajo describimos por primera vez la variante RAD51B como la causante de un caso aislado de POI en dos hermanas. Mediante el análisis de ratones humanizados, hemos demostrado que esta variante se comporta como un alelo hipomorfo que evade la NMD, probablemente debido a la reiniciación de la traducción en un codón de reinicio secundario. La proteína truncada resultante carece de la mayor parte del dominio N-terminal, implicado en las interacciones proteína-proteína y en la correcta localización nuclear. Como resultado, los ratones *Rad51b*$^{c.92delT/c.92delT}$ muestran defectos de reparación meiótica del ADN con acumulación de γH2AX, RAD51 y HSF2BP/BRME1 en los ejes cromosómicos, lo que conduce a una reducción

significativa de COs. Además, las células linfoblastoides derivadas de humanos RAD51B-c.92delT y las MEFs mutantes son sensibles a la MMC e inducen inestabilidad cromosómica, así como una menor eficiencia de reprogramación a iPSCs. Además, los ratones humanizados presentan una mayor incidencia de hiperplasia hipofisaria, probablemente atribuible a la inestabilidad del genoma inducida por RAD51B-c.92delT.

2. Los elementos ultraconservados H205 y HS1442 no son esenciales para la espermatogénesis del ratón

En el presente estudio, hemos generado ratones *hs205*$^{\Delta/\Delta}$ y *hs1442*$^{\Delta/\Delta}$ mediante edición génica por CRISPR/Cas9, así como mutantes dobles *hs205*$^{\Delta/\Delta}$*/hs1442*$^{\Delta/\Delta}$ cruzando ratones homocigotos mutantes simples. A pesar de que el análisis *in silico* mostró que estos dos UCEs tienen un patrón restringido en el tubérculo genital, no pudimos demostrar que la ausencia de estos elementos genéticos pudiera ser esenciales para la espermatogénesis del ratón.

Estudios funcionales sobre UCEs sugieren que es muy probable que los UCEs sean regiones reguladoras de la expresión génica (Dermitzakis et al., 2005). Sin embargo, existe controversia sobre su papel funcional. Hay un estudio que sugiere la existencia de ADN desechable en los genomas de los mamíferos. En este mismo estudio, realizan una deleción de 1 Mb de longitud en los cromosomas 3 y 19 del ratón, segmentos que contienen un total de 1243 secuencias que son >100 pb de longitud y >70% idénticas entre el humano y el ratón. Estas deleciones no mostraron ningún efecto fenotípico, con ratones homocigotos viables, apoyando la posibilidad de que los genomas de los mamíferos no estén densamente codificados y que hay reducciones significativas que puedan ser toleradas (Nóbrega et al., 2004). En contraposición a estos resultados, otros estudios han mostrado mutaciones no patógenas en secuencias CNGs. Un ejemplo es el caso de mutaciones de un solo nucleótido en un elemento regulador conservado denominado ZRS. Este elemento genético regula la expresión de la proteína de señalización específica de las extremidades Sonic Hedgehog (*Shh*) y está situado a 1 Mb del gen codificador. Se han observado que las mutaciones puntuales dentro de ZRS causan polidactilia preaxial en humanos y falanges extra en ratones (Gurnett et al., 2007; Lettice et al., 2003).

En otro estudio se seleccionaron cuatro UCEs que habían demostrado actuar como *enhancers in vivo*, y estaban localizados en el entorno de genes esenciales para el desarrollo (como *Dmrt1/2/3*, *Pax6*, *Arx* y *Sox3*), y se eliminaron individualmente del genoma del ratón (Ahituv et al., 2007). Los ratones homocigotos-nulos para estas UCEs eran totalmente viables y vivían con normalidad hasta la edad adulta. La evaluación posterior de la patología, el crecimiento y la expresión génica no reveló fenotipos perjudiciales evidentes como consecuencia de la eliminación genética de estos *enhancers*/UCEs (Ahituv et al., 2007).

Estos resultados son consistentes con nuestros hallazgos, en los que demostramos que HS205 y HS1442 tienen actividad *enhancer in vivo* y que la depleción de HS205, HS1442 o ambos, da lugar a ratones totalmente viables y fértiles. En el caso de HS205, demostramos por primera vez que este elemento regulador no tiene ningún papel en la espermatogénesis del ratón. En el caso de HS1442, este UCE es intragénico a *Kifap3* que se expresa de forma ubicua. *Kifap3* está implicado en la fijación de los cromosomas al polo del huso y en el movimiento cromosómico. Además, en un estudio anterior en el que también se eliminó HS1442 mediante *gene targeting*,

se demostró que HS1442 no es importante para el desarrollo de las extremidades en el ratón, los cuales muestran un fenotipo normal. Sin embargo, hubo diferencias transcripcionales significativas en genes proximales a HS1442, como en *Kifap3*, *Gorab*, *Syc13* y *Nme7* (Nolte et al., 2014).

Dada la alta conservación de la secuencia de estos loci, la falta de fenotipos aparentes fue sorprendente y ha llevado a varias hipótesis sobre la razón de estas observaciones. Entre las posibles explicaciones se encuentra la presencia de otros *enhancers* con funciones parcialmente redundantes respecto a los UCEs (Ahituv et al., 2007; McLean & Bejerano, 2008; Visel et al., 2008) y la presencia de fenotipos sutiles o no fácilmente aparentes en condiciones de laboratorio (Ahituv et al., 2007; McLean & Bejerano, 2008). Hasta ahora, se han eliminado individualmente del genoma del ratón un total de once UCEs (Snetkova et al., 2022). Todos los ratones homocigotos-nulos eran viables y fértiles (Ahituv et al., 2007; Dickel et al., 2018; Gaynor et al., 2020; Nolte et al., 2014), pero exámenes más exhaustivos revelaron la presencia de fenotipos sutiles en el desarrollo embrionario en algunas de las líneas de ratones UCEs nulos. Es el caso de HS119 y HS280, en el que la pérdida individual de estas dos UCEs con diferente patrón de restricción tisular, HS119 en el cerebro anterior (cerca de *Arx*) y HS280 en la extremidad (cerca de *Tmem53*), resulta en ambos casos en una reducción de la masa corporal (Dickel et al., 2018; Nolte et al., 2014).

En resumen, analizamos dos posibles UCEs candidatos, HS205 y HS1442, que tienen un patrón restringido en el tubérculo genital y, por tanto, podrían ser esenciales para la gametogénesis del ratón. Sin embargo, nuestros hallazgos proporcionan pruebas *in vivo* de que estos UCEs no son esenciales para la gametogénesis y la fertilidad del ratón, aportando nuevos datos a la gran controversia que rodea a estas regiones conservadas. Nuestros resultados junto a otros trabajos sugieren que las UCEs no son esenciales en el ratón, ya que su depleción genética no conduce a los fenotipos que esperaríamos debido a tratarse de secuencias altamente conservadas a lo largo de la evolución. Es posible que los UCEs tengan funciones adicionales en el genoma más allá de sus capacidades reguladoras.

Los resultados obtenidos en esta tesis doctoral permiten ampliar nuestro conocimiento en el conjunto de genes esenciales para la fertilidad humana y para el mantenimiento de la estabilidad del genoma. Estos estudios aportan nuevos e importantes conocimientos sobre los mecanismos moleculares que gobiernan la recombinación meiótica, demostrando su complejidad y la necesidad de seguir estudiando estos procesos en profundidad, ya que, a pesar del conocimiento actual de los elementos implicados en esta vía, existen elementos que aún no han sido identificados y cuyas funciones son todavía desconocidas. Por otro lado, esta tesis doctoral también aborda el posible papel de las secuencias ultraconservadas en la gametogénesis del ratón, cuyas funciones siguen siendo hasta la fecha un rompecabezas por resolver.

Conclusiones

1. RAD51B-c.92delT conduce a la reiniciación de la traducción en el codón AUG 64, lo que genera una proteína truncada N-terminal.

2. RAD51B-c.92delT muestra una localización nuclear alterada en células transfectadas, lo que sugiere una disfunción similar de la proteína endógena *in vivo*.

3. Los ratones *Rad51b*$^{c.92delT/c.92delT}$ son viables, pero muestran una acumulación de proteínas de reparación en los ejes cromosómicos y, en consecuencia, una reducción significativa de los COs.

4. Esta reducción del número de COs en los meiocitos mutantes podría deberse a las interacciones ineficientes entre RA5D1B-c.92delT y RAD51, RAD51C y HELQ.

5. La variante RAD51B-c.92delT es, por tanto, la responsable del POI en la familia consanguínea analizada en este estudio.

6. Las células humanas y las de ratón RAD51B-c.92delT son sensibles al daño del ADN inducido por MMC, lo que apoya una función somática de esta variante en la reparación del ADN.

7. MEFs derivados de *Rad51b-c.92delT* tratados con inhibidores de la ADN polimerasa muestran una menor supervivencia y formación de colonias, lo que apunta a una función de protección del daño en las horquillas de replicación.

8. La eficiencia de la reprogramación está disminuida en los MEFs *Rad51-c.92delT*, apoyando una función somática de RAD51B en la estabilidad e integridad del genoma.

9. Los ratones *Rad51b*$^{c.92delT/c.92delT}$ muestran una elevada incidencia de hiperplasia espontánea de la glándula pituitaria con características de prolactinomas, lo que sugiere que RAD51B tiene un papel crítico en la tumorigénesis.

10. HS205 y HS1442 muestran una actividad *enhancer* relativa *in vitro* e *in vivo*.

11. Los mutantes simples y dobles de HS205 y HS1442 presentan un tamaño testicular normal, una progresión meiótica normal y una producción normal de espermatozoides.

12. HS205 y HS1442 no son esenciales para la espermatogénesis del ratón.

PUBLICATIONS

CDDpress

www.nature.com/cdd

ARTICLE

Check for updates

A truncating variant of RAD51B associated with primary ovarian insufficiency provides insights into its meiotic and somatic functions

Monica M. Franca[1,2,11], Yazmine B. Condezo[3,11], Maëva Elzaiat[4,11], Natalia Felipe-Medina[3], Fernando Sánchez-Sáez[3], Sergio Muñoz[5], Raquel Sainz-Urruela[3], M. Rosario Martín-Hervás[3], Rodrigo García-Valiente[3], Manuel A. Sánchez-Martín[6,7], Aurora Astudillo[8], Juan Mendez[5], Elena Llano[3,9], Reiner A. Veitia[4,10]✉, Berenice B. Mendonca[1]✉ and Alberto M. Pendás[3]✉

Primary ovarian insufficiency (POI) causes female infertility by abolishing normal ovarian function. Although its genetic etiology has been extensively investigated, most POI cases remain unexplained. Using whole-exome sequencing, we identified a homozygous variant in RAD51B –(c.92delT) in two sisters with POI. In vitro studies revealed that this variant leads to translation reinitiation at methionine 64. Here, we show that this is a pathogenic hypomorphic variant in a mouse model. *Rad51b*$^{c.92delT/c.92delT}$ mice exhibited meiotic DNA repair defects due to RAD51 and HSF2BP/BMRE1 accumulation in the chromosome axes leading to a reduction in the number of crossovers. Interestingly, the interaction of RAD51B-c.92delT with RAD51C and with its newly identified interactors RAD51 and HELQ was abrogated or diminished. Repair of mitomycin-C-induced chromosomal aberrations was impaired in RAD51B/Rad51b-c.92delT human and mouse somatic cells in vitro and in explanted mouse bone marrow cells. Accordingly, Rad51b-c.92delT variant reduced replication fork progression of patient-derived lymphoblastoid cell lines and pluripotent reprogramming efficiency of primary mouse embryonic fibroblasts. Finally, *Rad51b*$^{c.92delT/c.92delT}$ mice displayed increased incidence of pituitary gland hyperplasia. These results provide new mechanistic insights into the role of RAD51B not only in meiosis but in the maintenance of somatic genome stability.

Cell Death & Differentiation; https://doi.org/10.1038/s41418-022-01021-z

INTRODUCTION

Meiosis is a sexual division that halves the diploid somatic chromosomal complement to a haploid state. During this process, each chromosome associates with its corresponding homologue (pairing) whose ultimate physical hallmark is a chiasma. In mammals, this process relies on the repair of DNA double-strand breaks (DSBs) by homologous recombination (HR) that generates crossover recombination events (COs) [1].

In molecular terms, the nuclease SPO11 generates DSBs throughout the genome. After DNA resection of 5´termini [2], the generated 3′ssDNA ends recruit the recombinases RAD51 and DMC1. The resulting recombinase-coated ssDNA filaments can invade the homologous chromosome dsDNA, searching for a complementary sequence (chromosome pairing), which will foster genetic material exchange. The nucleation of RAD51 is mediated by its direct interaction with BRCA2. This supramolecular complex promotes the initial binding of RPA to the resected DNA and, importantly, fosters the displacement of RPA from ssDNA by RAD51 nucleofilaments [3, 4]. However, the presence of many paralogues of RAD51 in most taxa including vertebrates (RAD51B, RAD51C, XRCC3, XRCC2, RAD51D, and the meiotic factor DMC1) and the lethality of the constitutional mutant mice has hampered the study of the physiological role of each RAD51 paralogue to somatic and meiotic HR [5–10].

In mammals, functional analysis of the individual RAD51 paralogues in cell lines has shown similar but non-redundant contributions in DNA repair processes such as HR efficiency, RAD51 nuclear focus formation, sensitization to mitomycin C (MMC) and protection of perturbed replications forks [11]. Accordingly, mutations in genes on this pathway can lead to genome instability, which can result in both cancer- and infertility-associated genetic syndromes [12, 13].

Infertility is defined as a failure of a couple to conceive and affects 10–15% of couples [14]. POI is a disorder associated with

[1]Unidade de Endocrinologia do Desenvolvimento, Laboratório de Hormônios e Genética Molecular/LIM42 and SELA, Hospital das Clínicas, Faculdade de Medicina da Universidade de São Paulo (FMUSP), São Paulo, Brasil. [2]Section of Endocrinology Diabetes and Metabolism, Department of Medicine, The University of Chicago, Chicago, IL, USA. [3]Molecular Mechanisms Program, Centro de Investigación del Cáncer and Instituto de Biología Molecular y Celular del Cáncer (CSIC-Universidad de Salamanca), Salamanca, Spain. [4]Université Paris Cité, CNRS, Institut Jacques Monod, F-75013 Paris, France. [5]DNA Replication Group, Molecular Oncology Programme, Spanish National Cancer Research Centre (CNIO), Melchor Fernández Almagro 3, E-28029 Madrid, Spain. [6]Departamento de Medicina, Universidad de Salamanca, Salamanca, Spain. [7]Transgenic Facility, Nucleus platform, Universidad de Salamanca, Salamanca, Spain. [8]Biobanco del principado de Asturias, 33011 Oviedo, Spain. [9]Departamento de Fisiología y Farmacología, Universidad de Salamanca, Salamanca, Spain. [10]Université Paris-Saclay and Institut François Jacob, Comissariat à l'Energie Atomique, Gif-sur-Yvette, France. [11]These authors contributed equally: Monica M. Franca, Yazmine B. Condezo, Maëva Elzaiat. ✉email: reiner.veitia@ijm.fr; beremen@usp.br; amp@usal.es

Edited by D. Aberdam

Received: 28 October 2021 Revised: 12 May 2022 Accepted: 13 May 2022
Published online: 27 May 2022

female infertility that affects about 1% of women before the age of 40 years. The genetic etiology of isolated POI is highly heterogeneous. In fact, over 75 genes associated with POI have been implicated in ovarian development and meiosis [15]. Particularly, pathogenic variants in genes involved in meiotic recombination, such as *STAG3, SYCE1, HFM1, MSH4, MSH5, DMC1, MEIOB, BRCA2* and *HSF2BP*, have been associated with this disorder [15–24]. Nevertheless, the presence of genetic defects in the majority of POI patients remains to be established [15].

Here, we report the identification of a homozygous variant in *RAD51B*- (c.92delT) in two sisters with POI. This *RAD51B* variant leads to a premature termination codon (PTC) resulting in translation reinitiation at codon AUG in position 64. The "humanized" knock-in (KI; *Rad51b*$^{c.92delT/c.92delT}$) mouse shows meiotic DNA repair defects due to RAD51 and HSF2BP/BRME1 accumulation in the meiotic chromosome axes leading to a significant reduction in the number of COs. Interestingly, RAD51, RAD51C and HELQ interaction with RAD51B was diminished with the N-terminally truncated RAD51B protein. Moreover, *RAD51B-c.92delT* human lymphoblastoid cells, humanized MEFs and explanted bone marrow cells from mutant mice displayed an increased sensitivity to MMC-induced chromosome instability (CIN). The *RAD51b-c.92delT* variant was also found to decrease replication fork progression of lymphoblastoid cell lines and the reprogramming efficiency of primary mouse embryonic fibroblasts (MEFs) to produce induced pluripotent stem cells (iPSCs). Finally, *Rad51b*$^{c.92delT/c.92delT}$ mice exhibited an increased incidence of hyperplasia of the pituitary gland. These results provide new mechanistic insights into RAD51B role in human ovarian insufficiency and in the maintenance of genome stability in the soma.

RESULTS

Genetic analysis

Whole-exome sequencing was performed in two sisters presenting with POI (II-1 and II-4) and in one unaffected sister (II-2). The mean coverage of the capture regions was ≥150× in all samples with at least 99.38% of the targeted positions being sequenced at ≥10× (Supplementary Table 1). Consistent with an autosomal recessive inheritance, homozygous candidate variants were selected in both affected sisters and a minor allele frequency cut-off of 0.01% was applied. After an in-depth assessment of coding (missense, nonsense and frameshift) and splice-site variants, a homozygous frameshift pathogenic variant in the *RAD51B* gene was identified in the two affected sisters and retained as the best candidate (Supplementary Table 2). *RAD51B* is located in chromosome 14, position 14q23-q24.2, and the c.92delT variant is located in exon 3. As predicted by Mutalyzer, the *RAD51B*-c.92delT variant creates a PTC at amino acid #39 (predicted alteration: p.Leu31Tyrfs*9). The variant c.92delT (i.e., 14-68292183-CT-C) is reported in gnomAD with an extremely low allele frequency of 4.05×10^{-6}, which represents one allele count of 1 in 247,158 alleles and has not been reported to exist in a homozygous state [25, 26]. The presence of this variant was screened by Sanger sequencing in other members of this family (Fig. 1A). The father (I-1) and unaffected siblings (II-2, II-3, II-6, and II-8) were heterozygous. DNA of mother (I-2) and one brother (II-5) were unavailable (Fig. S1A). Furthermore, the *RAD51B*-c.92delT variant was not found in 235 fertile Brazilian women controls screened by Sanger sequencing. In order to rule out any additional pathogenic variants, we evaluated 107 genes already associated with POI [27]. No other clearly pathogenic variant, which could underlie the phenotype, could be identified in this family (Supplementary Table 9).

The c.92delT variant in *RAD51B* leads to translation re-initiation at AUG64

In silico analyses predict that the c.92delT variant would provoke the appearance of a PTC leading to a truncated protein of 39 residues lacking functional motifs (Fig. S1B) [28]. Given that the depletion of *Rad51b* in the mice is embryonic lethal [8] and that three close downstream in-frame AUG codons (AUG39, AUG55 and AUG64) exist, we hypothesized that the translation might restart at one of them. To test this, HEK293 cells were transfected with constructs encoding *RAD51B*: wild-type (WT), c.92delT and a mutant or WT *RAD51B* in which the three secondary Methionine codons were replaced by GCN encoding Alanines (individual and double Met to Ala substitutions) and protein expression was analyzed by Western blot (Fig. 1B). This experiment showed the production of a band in the c.92delT that was smaller than the main product resulting from the expression of the WT construct. This band disappeared only when replacing the codons underlying M64 to A64 but not when the M39 or M55 were replaced by Alanines (individually or double mutated; Fig. 1B). To demonstrate the translation of the RAD51B-c.92delT endogenous protein and given that we failed to detect by Western blot and immunofluorescence (IF) endogenous RAD51B protein with commercial or even home-made antibodies, we analyzed by IP-coupled with Mass spectrometry (MS) human lymphoblastoid cell extracts from *RAD51B*$^{WT/c.92delT}$ and *RAD51B*$^{c.92delT\ /c.92delT}$. Our results clearly show the presence of peptides corresponding to the C-Term of the protein, demonstrating that translation is indeed taking place (Supplementary Table 3). Altogether, these results reveal that the variant c.92delT leads translation re-initiation at M64. To assess the impact of the *RAD51B*-c.92delT variant on its subcellular localization, the human and murine RAD51B variant and the WT forms (fused to GFP and untagged) were expressed in Cos7 cells. *RAD51B*-c.92delT displayed lower ratio of nuclear to cytoplasmic labelling in comparison to the WT (Figs. 1C and S1C).

Rad51b$^{c.92delT/c.92delT}$ mice have no obvious ovarian and testis morphological abnormalities

In order to evaluate the physiological relevance of the *RAD51B*-c.92delT variant, we generated a humanized KI mouse *Rad51b*$^{c.92delT/c.92delT}$ by CRISPR/Cas9 editing (Fig. S2A). Although RAD51B is essential for mouse development [8], humanized KI mice showed no somatic phenotype and were born with the expected Mendelian ratios (Supplementary Table 4), which strongly suggests that the reinitiation of the translation is also operating in the mouse model. RT-PCR analysis using testis cDNA derived from *Rad51b*$^{c.92delT/c.92delT}$ mice confirmed transcription of the mutated and WT alleles (Fig. S2B).

Rad51b$^{c.92delT/c.92delT}$ male and female mice were able to reproduce. Accordingly, the histological analysis of adult *Rad51b*$^{c.92delT/c.92delT}$ testes revealed no apparent abnormalities in the seminiferous tubules (Fig. S2C). Ovaries from *Rad51b*$^{c.92delT/c.92delT}$ exhibited no differences in the number of follicles in comparison to WT mice (Fig. S2D). Haematoxylin-eosin staining patterns of mouse ovaries were similar at two time-points explored (5 dpp, in which primordial oocytes are expected to be found, and 3-months). The quantification of the primordial oocyte pool was also similar between genotypes (Fig. S2D). Fertility assessment in females also showed no statistical differences in litters per month and in pups per litter between mutant and WT mice, though a trend towards a reduction in the number of pups per litter is observed in the former (Fig. 1D).

Rad51b$^{c.92delT/c.92delT}$ mice show several defects in the DNA repair process

RAD51B is ubiquitously expressed (see www.uniprotorg) in somatic and reproductive tissues including meiocytes, though its meiotic function has not been established. To further characterize the involvement of RAD51B in meiosis, we analyzed *Rad51b*$^{c.92delT/c.92delT}$ meiocytes for the assembly of the synaptonemal complex by monitoring the distribution of SYCP1 and SYCP3. Even though, no defects in synapsis and desynapsis from leptotene to diakinesis were observed (Fig. S3A, B), a reduced number of pachynemas accompanied by an elevated number of diplonemas were found in both *Rad51b*$^{c.92delT/c.92delT}$ males and females. These results

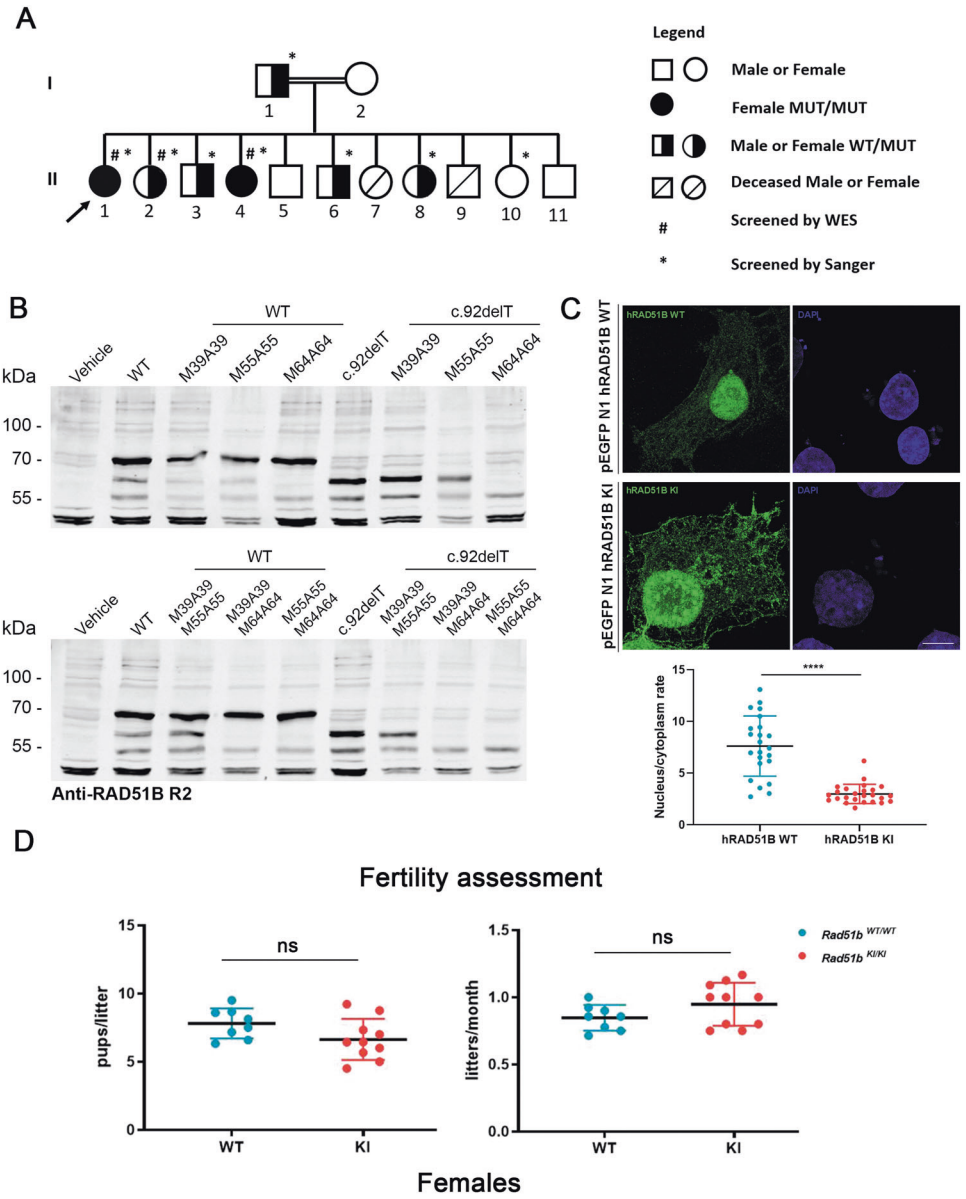

Fig. 1 The variant c.92delT leads to translation re-initiation at AUG 64 and to altered nuclear localization. A Family Pedigree. A homozygous recessive variant in *RAD51B* was shown to be present in two sisters from Brazil affected with POI. The black arrow indicates proband (II-1). Pedigree numbers of individuals are indicated below the symbols. Samples sent for whole-exome sequencing (WES) are indicated by a hash and samples sent for Sanger sequencing are indicated by an asterisk. Sanger electropherograms confirmed the presence of the homozygous variant in both affected sisters II-1 and II-4. **B** HEK293T cells were transfected or not (Vehicle) with the different variants of RAD51B: the WT form (WT), the c.92delT form and both the WT and c.92delT forms in which the three secondary Methionines were mutated into Alanines (individual Met to Ala substituting the M39 to A39, the M55 to A55 and the M64 to A64; double Met to Ala substitutions following the above argument, both M39A39 and M55A55, both M39A39 and M64A64 and both M55A55 and M64A64. Of note, the bigger size of the RAD51B products is due to the presence of GFP tag (27 kDa). **C** COS7 cells were transfected to express human WT or mutant RAD51B fused to GFP tag. The WT construct showed a robust nuclear signal in addition to a faint cytoplasmic pattern. In contrast, the mutant variant displayed a partial delocalization of the nuclear signal to the cytoplasm. Quantification of the nucleus/cytoplasm signal rate is shown in the lower plot. Scale bars: 20 µm. **D** Fertility assessment in female mice of WT and mutant *Rad51b*. The plots show the number of pups per litter and the litters per month. *Rad51b*$^{c.92delT/c.92delT}$ variant is referred as *Rad51b*$^{KI/KI}$ for simplicity. Welch´s *t*-test analysis: ns, non-significant differences; ****$p < 0.0001$.

display subtle alteration of normal prophase I progression (Fig. S3C, D).

We assessed DSBs generation and repair by detecting phosphorylated histone γH2AX in *Rad51b*$^{c.92delT/c.92delT}$ meiocytes (Quantifications at Supplementary Table 5) [29, 30]. We observed similar labelling of γH2AX from leptotene to zygotene spermatocytes (Fig. S4A), but increased levels of labelling were detected in meiocytes at pachytene. This accumulation was also observed in oocytes at diplotene (Fig. 2A).

Meiotic DSB repair is orchestrated by a BRCA2-containing supramolecular complex that dictates the sequential recruitment of proteins to the DSBs, such as the binding of RPA for end resection, exchange of RPA by RAD51/DMC1 and loading of the complex MEIOB-SPATA22 to the RPA complexes with the interplay

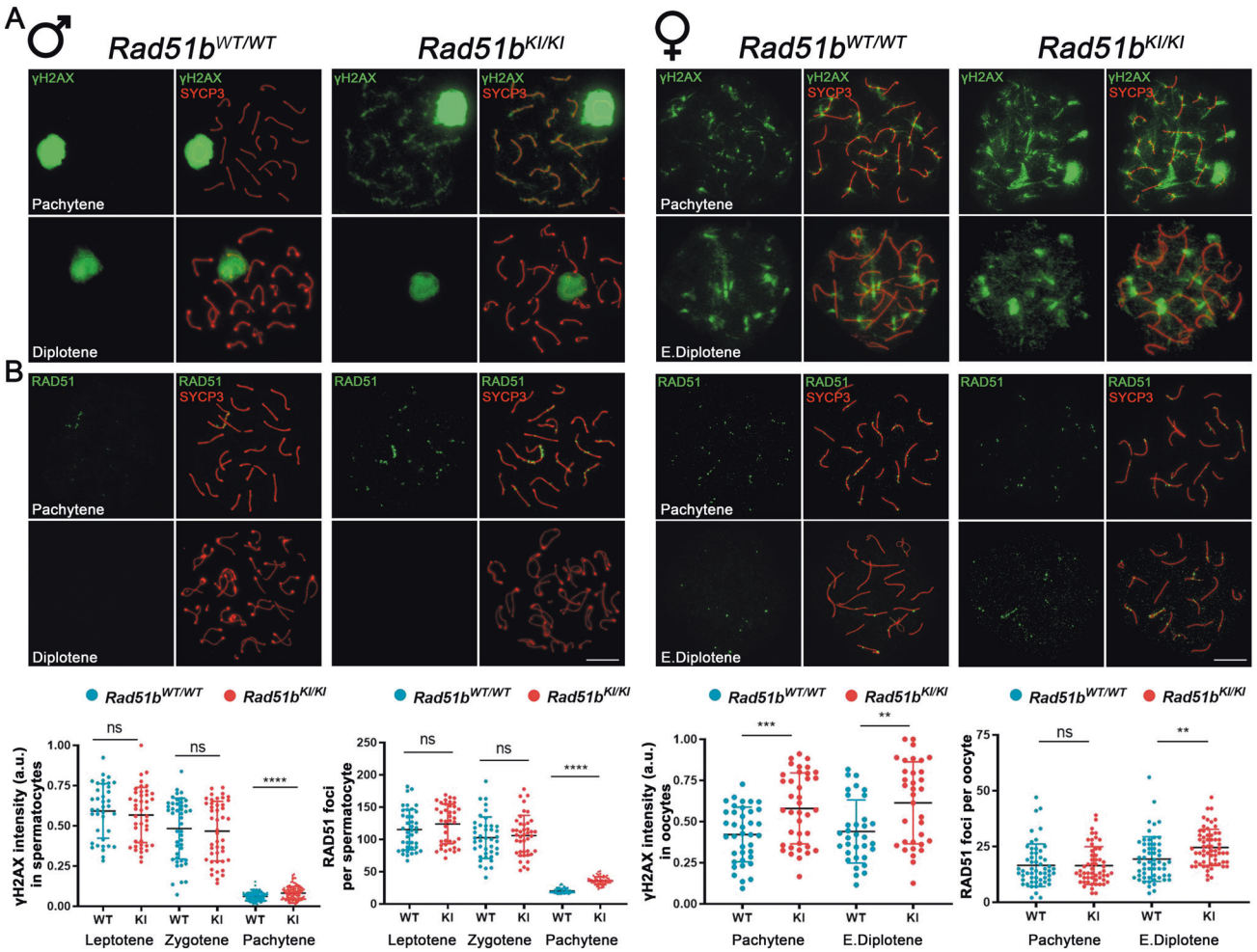

Fig. 2 ***Rad51b*$^{KI/KI}$ mice show defects in DNA repair. A** Double immunolabelling of γH2AX (green) and SYCP3 (red) of spermatocyte and oocyte spreads from WT and KI mice showing the accumulation of γH2AX patches in the mutant pachynemas. Plots below the panels show the quantification of γH2AX intensity. **B** Double immunolabelling of RAD51 (green) and SYCP3 (red) of spermatocyte and oocyte spreads from *Rad51*$^{WT/WT}$ and *Rad51b*$^{KI/KI}$. RAD51 foci accumulate at pachytene in KI spermatocytes and at diplotene in KI oocytes (small green dots). Plots below the panels represents the quantification of RAD51 foci on each genotype. *Rad51b*$^{c.92delT/c.92delT}$ variant is referred to as *Rad51b*$^{KI/KI}$ for simplicity. Welch´s *t*-test analysis: ns, non-significant differences; $^{**}p < 0.01$; $^{***}p < 0.001$; $^{****}p < 0.0001$. Bar in panels, 10 μm. See Supplementary Table 5 for raw data quantification.

of HSF2BP and its interactor/stabilizer BRME1 (meiotic double-stranded break BRCA2/HSF2BP complex associated protein) [3, 4, 24, 31]. We first analyzed the initial loading of RPA. Our results showed that the recruitment of RPA and its associated protein SPATA22 was unaltered in mutant RAD51B meiocytes (Fig. S4B, C), suggesting that DSBs resection is unaffected. Then, we analyzed the recombinases RAD51 and DMC1 to assess the strand invasion process in our *Rad51b* mutant model. RAD51 foci formation was similar at leptotene and zygotene (Fig. S5A) but foci persisted in pachytene nuclei in spermatocytes and in diplotene nuclei in oocytes, indicating a slight defect in DSB repair (Fig. 2B). By contrast, labelling of DMC1 foci was not affected (Fig. S5B). This fact could reflect the activation of a somatic-like HR DNA repair pathway at late-pachytene involving RAD51 but not DMC1 [32], as described for other mouse mutants (i.e., HSF2BP and BRME1 [33]). We next analyzed by IF these essential meiotic recombination proteins in *Rad51b*$^{c.92delT/c.92delT}$ mice (Fig. S5C). BRME1 and HSF2BP labelling accumulated at late pachytene in *Rad51b*$^{c.92delT/c.92delT}$ mice meiocytes and persisted at diplotene (Fig. 3A). DNA repair can eventually culminate with the formation of COs; therefore, we analyzed the distribution of MLH1 foci as a direct measure of CO formation. A statistically significant difference in the number of CO events was found in *Rad51b*$^{c.92delT/c.92delT}$ mice compared to WTs in both spermatocytes (KI: 20.70 ± 1.79 vs WT: 22.98 ± 1.61) and oocytes (KI:22.39 ± 3.01 vs WT: 23.82 ± 2.02) (Fig. 3B). We also evaluated the functional relevance of this reduction of COs by measuring the number of bivalents without MLH1 foci that would lead to univalents. Our results revealed an increased number of bivalents that did not show MLH1 foci in both *Rad51b*$^{c.92delT/c.92delT}$ oocytes and spermatocytes (both sexual and autosomal bivalents) (Fig. 3B). Taken altogether, these results suggest that RAD51B variant provokes an increase of DSBs that are not effectively repaired as COs in both oocytes and spermatocytes.

RAD51B interacts with the meiotic recombination machinery

We next immuno-precipitate RAD51B from mouse testis extracts coupled with MS. We identified in addition to RAD51B itself, RAD51C, a well-known interactor of RAD51B (Supplementary Table 6) [34], which is essential for meiotic recombination [35]. Next, we adopted a candidate approach to identify additional putative interactors of RAD51B. Thus, we co-transfected RAD51B with cDNAs encoding BRCA2, PALB2, DMC1, RAD51, MEIOB, BRME1, HSF2BP, HELQ, and RPA (Fig. S6) and also the MS-

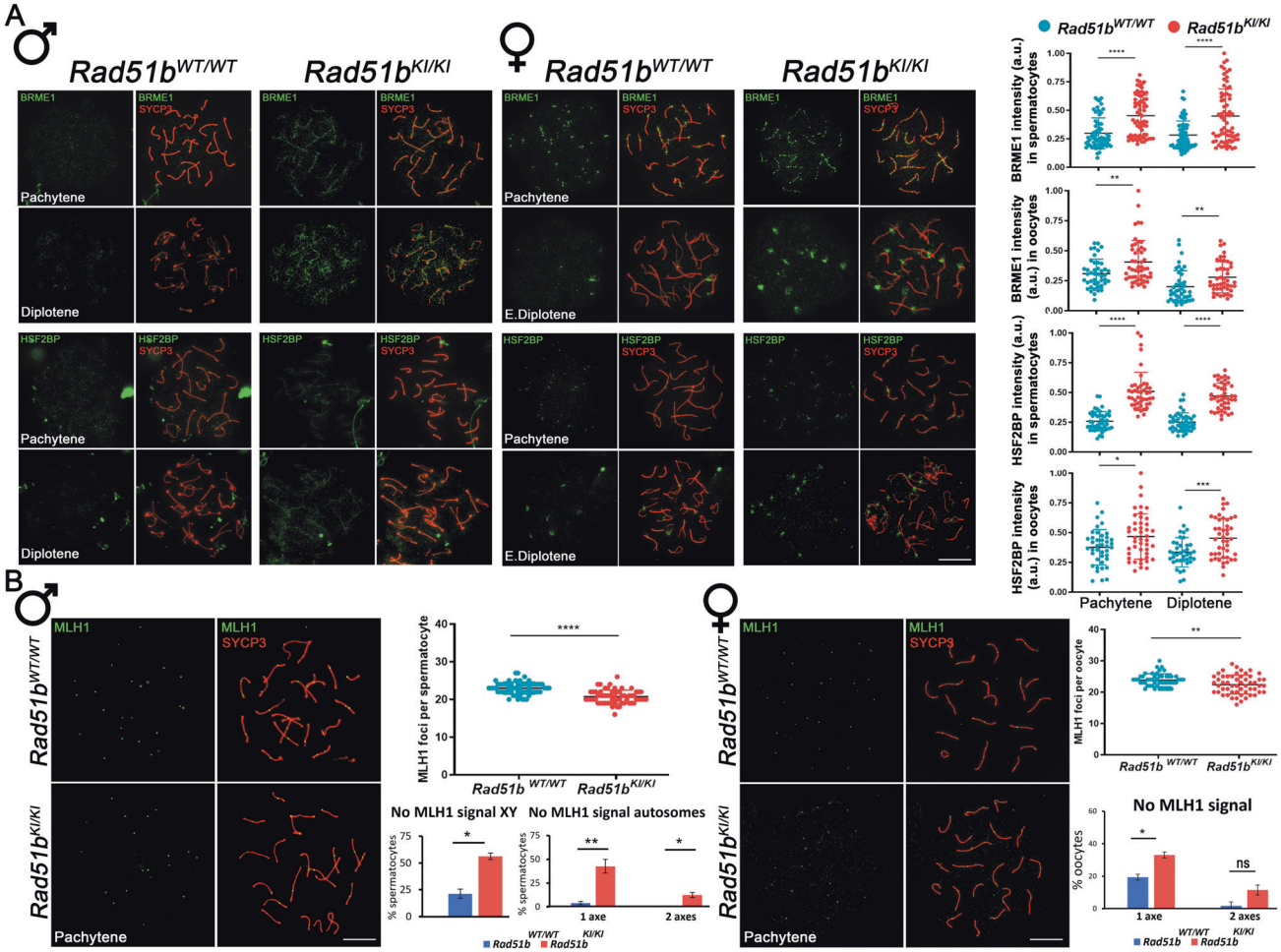

Fig. 3 ***Rad51b*** **mutant mice show an accumulation of BRME1 and HSF2BP and an abnormal CO formation. A** Double labelling of BRME1 (green) and SYCP3 (red) of spermatocyte and oocyte spreads from WT and KI mice showing the accumulation of BRME1 in mutant late pachynemas and diplonemas. Double labelling of HSF2BP (green) and SYCP3 (red) of meiocyte spreads from *Rad51b*$^{WT/WT}$ and *Rad51b*$^{KI/KI}$ mice showing the accumulation of HSF2BP in mutant late pachynemas and diplonemas. Plots on the right side of the panels represent the quantification of BRME1 and HSF2BP foci and intensity. **B** Double immunolabelling of MLH1 (green) and SYCP3 (red) of spermatocyte and oocyte spreads from *Rad51b*$^{WT/WT}$ and *Rad51b*$^{KI/KI}$. MLH1 foci are significant reduced in mutant *Rad51b* meiocytes. The plots on the right of the panels represent the quantification of MLH1 foci at pachytene in both male and female meiocytes. Quantification of the % of spermatocytes with any autosome or the sexual bivalent without MLH1 foci. $n = 108–114$ (autosomes), $n = 66–96$ (X-Y bivalent). Quantification of the % of oocytes with any autosome without MLH1 foci. $n = 51–54$ (autosomes). *Rad51b*$^{c.92delT/c.92delT}$ variant is referred as *Rad51b*$^{KI/KI}$ for simplicity. Welch´s *t*-test analysis: ns, non-significant differences; *$p < 0.05$; **$p < 0.01$; ***$p < 0.001$; ****$p < 0.0001$. Bar in panels, 10 μm. See Supplementary Table 5 for raw data quantification.

identified protein RAD51C. We detected positive co-immunoprecipitations between RAD51B and the paralogues, RAD51C, RAD51, HELQ and DMC1 (Fig. 4A–D).

Given that the N-term part of RAD51B (residues 1–75) interacts with RAD51C [34], we analyzed the ability of mutant RAD51B to maintain its interaction with the identified partners. RAD51C immunoprecipitated WT RAD51B but not mutant RAD51B indicating that the c.92delT variant drastically diminishes or abrogates their interaction (Fig. 4A). This loss of interaction was also verified by Co-IP coupled with MS of *RAD51B*$^{c.92delT/c.92delT}$ lymphoblastoid cells (Supplementary Table 3). Similarly, RAD51B-c.92delT interaction was weaker with RAD51 and with the helicase HELQ, but not with DMC1 (Fig. 4B–D). These results suggest that RAD51B acts in concert with DMC1/RAD51/RAD51C recombinases to promote/mediate meiotic recombination.

RAD51B-c.92delT human and mouse cells are sensitive to MMC-induced DNA damage

Typically, RAD51-deficient cells are hyper-sensitive to DNA interstrand crosslinking (ICL) agents such as MMC. Accordingly, *Rad51b*$^{c.92delT/c.92delT}$ MEFs showed a relatively lower growth rate in the presence of MMC (Fig. 5A). Clonogenic survival assays of MMC-treated MEFs$^{c.92delT/c.92delT}$ also showed a reduced number of colonies (Fig. 5B). We next monitored the efficiency of DNA repair. MEFs were treated with MMC and analyzed at different time points. The results of this experiment showed a delay in the disappearance of γH2AX foci even at 72 h after MMC treatment, indicating the presence of unrepaired DNA (Fig. 5C). In addition, MMC-treated MEFs from *Rad51b*$^{c.92delT/c.92delT}$ showed more chromosome break events (passage 2 and passage 4) (Fig. 6A). The assessment of the impact of the variant affected on genome stability in vivo showed that bone marrow-derived metaphase plates from *Rad51b*$^{c.92delT/c.92delT}$ MMC-treated mice had a significantly increased number of chromosomal breaks events per cell compared to WT mice (Fig. 6B).

RAD51B$^{c.92delT/c.92delT}$ immortalized lymphoblastoid cells from the affected patient (II-4) also displayed more chromosome breaks events in comparison with the heterozygous RAD51B$^{WT/c.92delT}$ cells from the unaffected sister (II-2) in the presence of MMC and even in their absence (Fig. 6C). Taken together, these results

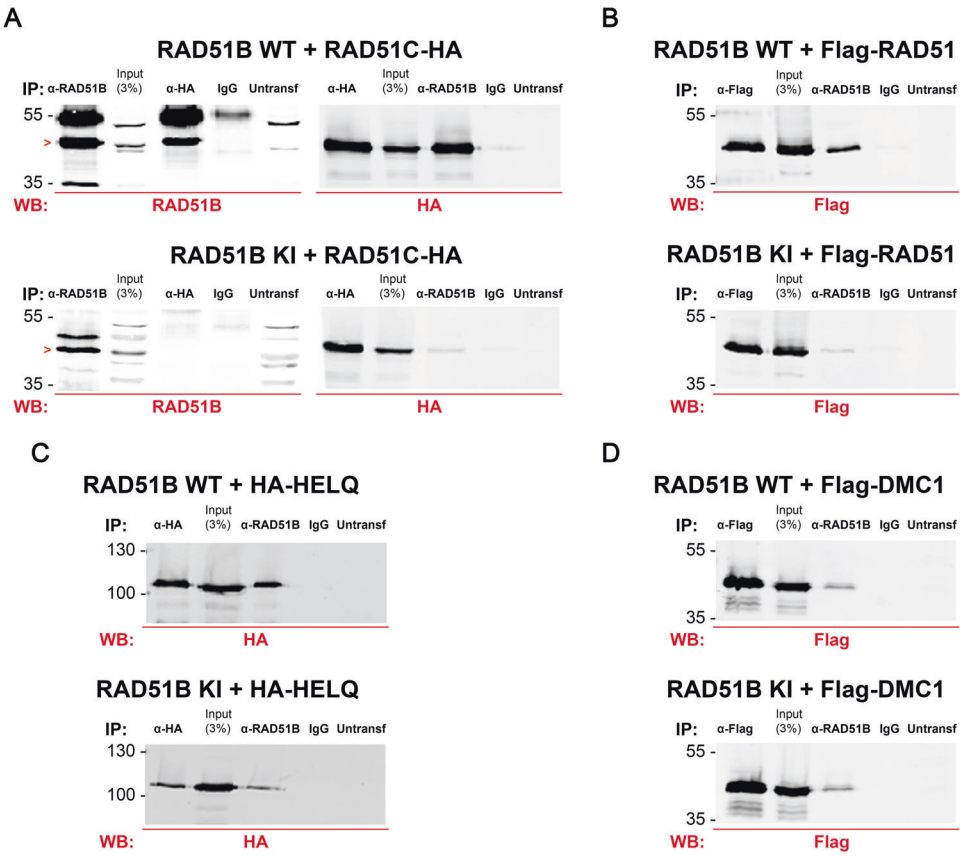

Fig. 4 Loss of interaction between RAD51B-c.92delT and RAD51C as well as a reduction of the interaction between RAD51B-c.92delT and HR-specific interactors as revealed by co-immunoprecipitation. HEK293T cells were co-transfected with either RAD51B-WT or RAD51B-c.92delT and **A** RAD51C-HA, **B** Flag-RAD51, **C** HA-HELQ or **D** Flag-DMC1. Protein complexes were immunoprecipitated with either an anti-RAD51B, anti-Flag, anti-HA or IgGs (negative control), and analyzed by immunoblotting with the indicated antibody. The red > indicates the band corresponding to RAD51B.

confirm that the homozygous *RAD51B*-c.92delT variant leads to an impaired repair of MMC-induced DNA damage and as a consequence increase the levels of CIN in vitro and in vivo.

MMC stress leads to ICL lesions that inhibits the unwinding of DNA strands and blocks the progression of replicative DNA helicases. To further assess the involvement of *Rad51b-c.92delT* in this phenotype, we also analyzed its susceptibility to hydroxyurea (HU) and the specific DNA polymerase inhibitor Aphidicolin, two inducers of replication fork DNA damage [36]. Our results show that both drugs produce a lower percentage of surveillance in the c.92delT MEFs (Fig. 7A).

Given these observations and that RAD51 paralogues participate in the response to replication stress [37, 38], we used stretched DNA fibers to monitor fork speed in $RAD51B^{c.92delT/c.92delT}$ and $RAD51B^{WT/c.92delT}$ in immortalized lymphoblastoid cells treated with MMC. In these conditions, cells derived from the affected patient displayed shorter tracks and reduced fork progression rate (Fig. 7B), which likely reflect a high frequency of fork stalling events and/or impaired fork restart [38, 39]. This observation suggests that *Rad51b-c.92delT* mutant protein is defective in the DNA damage tolerance pathways that restart DNA synthesis at stalled forks, impairing their subsequent repair and potentially increasing the frequency of DNA breaks.

Given the involvement of the Rad51 family of paralogues in the canonical pathway of HR between sister chromatids [40], we analyzed this parameter in *RAD51B-c.92delT* lymphoblastoid cells by the classical 5BrdU incorporation procedure. We observed no differences between the WT and mutant *RAD51B* even in presence of MMC indicating that the canonical HR pathway remains unaffected (Fig. 7C).

Rad51b-c.92delT decreases reprogramming efficiency in mouse embryonic fibroblasts

The expression of the Yamanaka factors [41] induce genome instability providing a plausible explanation for the requirement of an intact HR pathway and low replication stress to achieve efficient reprogramming [42, 43]. In the light of this, we evaluated the role of RAD51B during reprogramming using homozygous $Rad51b^{c92delT\text{-}c.92delT}$ MEFs. The numbers of alkaline phosphatase positive colonies were significantly reduced (up to ~2 fold) in *Rad51b*-c.92delT homozygous mutant MEFs in comparison with the WT (Fig. 8A). By picking colonies with iPS-like morphology (3D shape, defined borders and refringence), we were able to establish *Rad51b*-c.92delT mutant iPS cell lines with comparable efficiency (~30%) to WT controls, suggesting they are similarly functional bona fide iPS clones.

$Rad51b^{c.92delT/c.92delT}$ mice show increased incidence of pituitary hyperplasia

The somatic phenotypes observed are all hallmarks of genome instability. Thus, we evaluated the incidence of spontaneous neoplasia in aged mice (from 18 to 22 months). We observed a pituitary hyperplasia and frequent adenomas of the pituitary gland in mutant homozygous mice (9 out of 14 $Rad51b^{c.92delT/c.92delT}$ mice vs 1 out of 12 in wild type controls) (Fig. 8B). These benign tumors ranged from micro- to macroadenomas (Fig. 8C–H) and showed

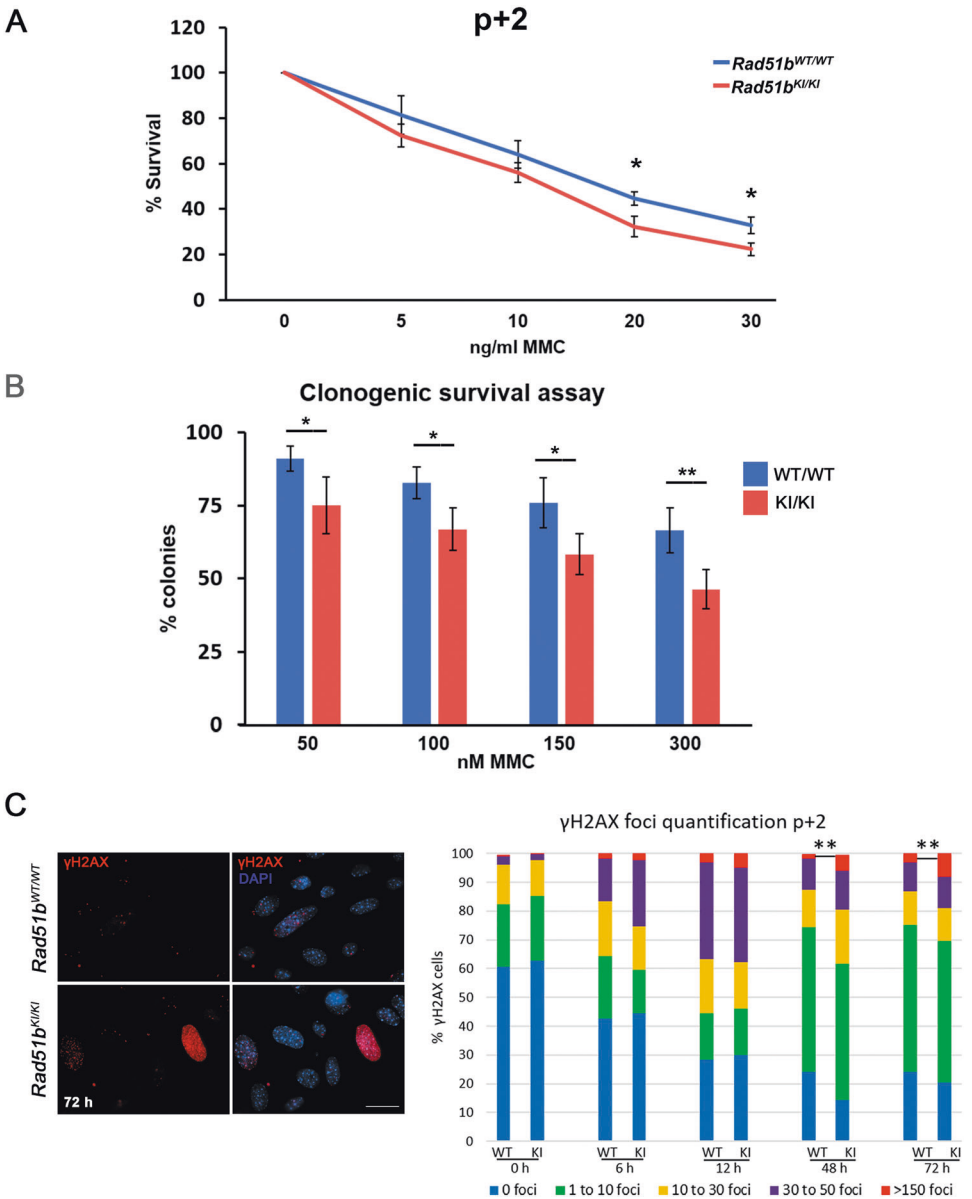

Fig. 5 ***Rad51b*** **mutant MEFs show an increased susceptibility to MMC-induced DNA damage. A** Cell proliferation assay of WT and mutant Rad51b primary MEFs at passage 2 (p + 2) incubated in presence of a continuous treatment with MMC. The results are expressed as a percentage relative to the control (not treated with MMC). Each point on the graph represents the mean ± SD. **B** Percentage of colonies obtained by clonogenic cell survival assays after treatment with MMC. The results are expressed as a percentage relative to the control (untreated) of *Rad51b*$^{WT/WT}$ and *Rad51b*$^{KI/KI}$ immortalized cells. **C** Representative γH2AX immunolabelling of WT and mutant *Rad51b* at 72 h. Quantification of γH2AX foci in *Rad51b* WT and mutant MEFs. *Rad51b*$^{WT/WT}$ and *Rad51b*$^{KI/KI}$ MEFs at p + 2 were incubated in presence of MMC at 1 µg/ml for 1 h and then supplemented with fresh medium without MMC. The quantification was performed at different time points: 0 h: 0 h, 6 h: 6 h, 24 h: 24 h, 48 h; 48 h and 72 h: 72 h. Cells were classified in 5 groups: 0 foci, 1 to 10 foci, 10 to 30 foci, 30 to 150 foci and >150 foci. $n = 3$. *Rad51b*$^{c.92delT/c.92delT}$ variant is referred as *Rad51b*$^{KI/KI}$ for simplicity. Welch´s *t*-test analysis: $*p < 0.05$; $**p < 0.01$. Bar in panel, 10 µm.

immuno-histochemical overexpression of prolactin (Fig. 8I, J) in the cytoplasm of tumor cells (but not of ACTH, GH, FSH and LH shown in Fig. S7). Overall, the mice developed pituitary hyperplasia and frequent adenomas, with typical features of prolactinomas. Interestingly, a genetic variant in human RAD51B has been recently associated with pituitary tumors [44].

DISCUSSION

We describe for the first time a homozygous variant in *RAD51B* (c.92delT) found in two sisters affected with isolated POI. RAD51B seems to be involved in the assembly of RAD51 nucleoprotein filaments during HR and in replication fork remodeling and restart [10, 38, 45]. Thus, RAD51B has been associated with CIN and cancer predisposition [44, 46, 47]. However, its role on female fertility and meiotic DSB repair has not been reported yet. Herein, a perfect segregation of *RAD51B-c.92delT* and female infertility was found in a family. Specifically, all affected subjects were homozygous for the variant, while heterozygosity or absence of this variant was observed in unaffected members.

The variant was predicted to lead to a PTC leading to the expression of a short N-term protein of only 39 residues lacking the two walker motifs essential for its ATPase activity [28], which would result in null allele known to be lethal in the mouse [8]. Such a PTC

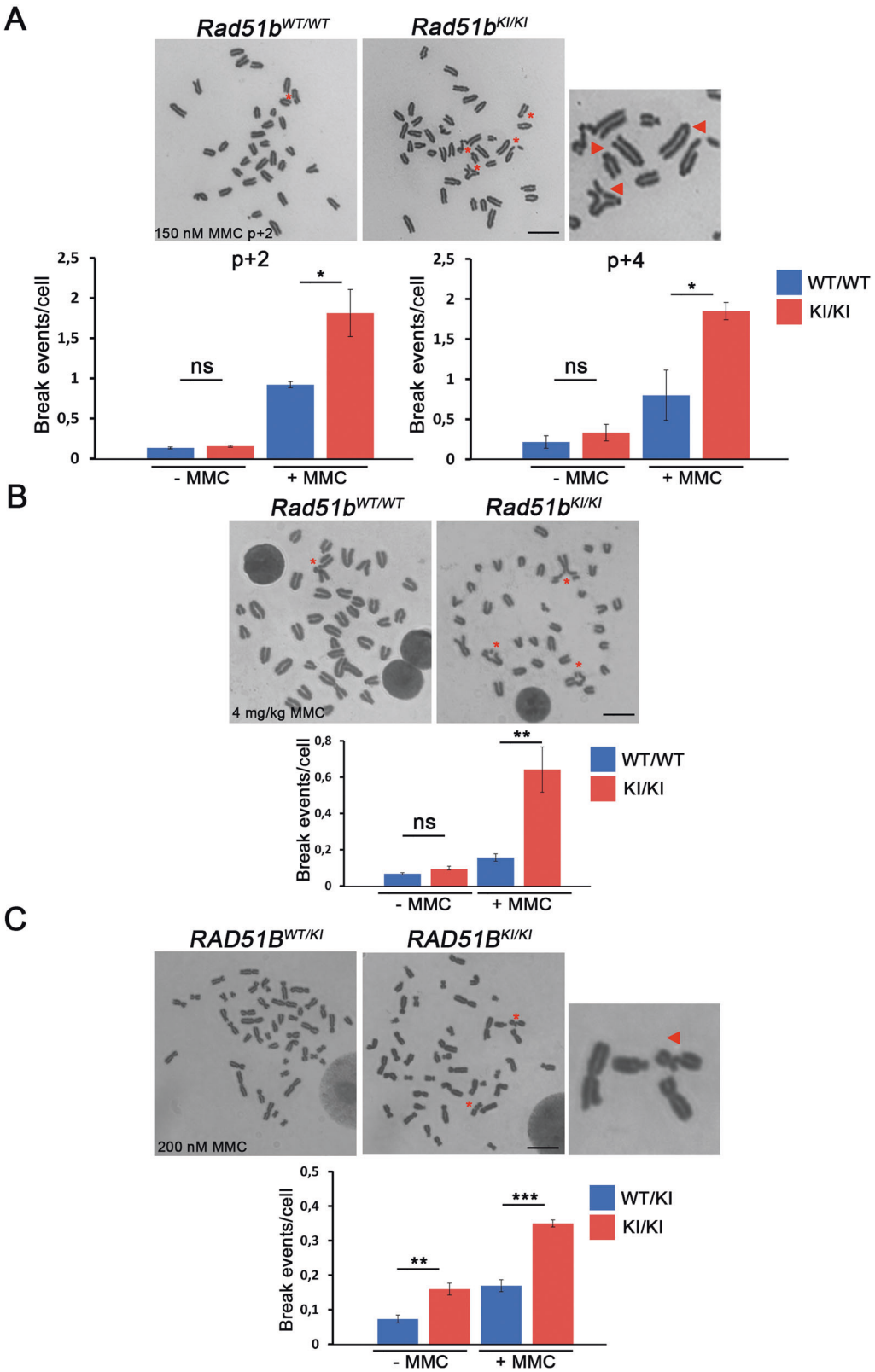

Fig. 6 MMC-induced CIN in mouse and human *RAD51B-c.92delT* cells. A Evaluation of metaphase chromosome breaks/gaps from *Rad51*$^{WT/WT}$ and *Rad51b*$^{KI/KI}$ MEFs after MMC treatment (150 nM). Lower panel (graphs) shows the quantification of breaks/gaps at passage 2 (p + 2) and passage 4 (p + 4). **B** Evaluation of metaphase chromosome aberrations from bone marrow of *Rad51b*$^{WT/WT}$ and *Rad51b*$^{KI/KI}$ after intraperitoneal injection of MMC (4 mg/kg). In addition, to breaks/gaps, triradial chromosomes were observed only in the mutant mice (shown by red asterisks). **C** Homozygous *RAD51B-c.92delT* human-derived lymphoblastoid cells showed more chromosome alterations with and without MMC treatment (200 nM) in comparison with the corresponding heterozygous sister. $n = 3$. *Rad51b*$^{c.92delT/c.92delT}$ variant is referred to as *Rad51b*$^{KI/KI}$ for simplicity. Welch´s *t*-test analysis: ns, non-significant differences; *$p < 0.5$; **$p < 0.01$; ***$p < 0.001$. Bar in panels, 10 μm.

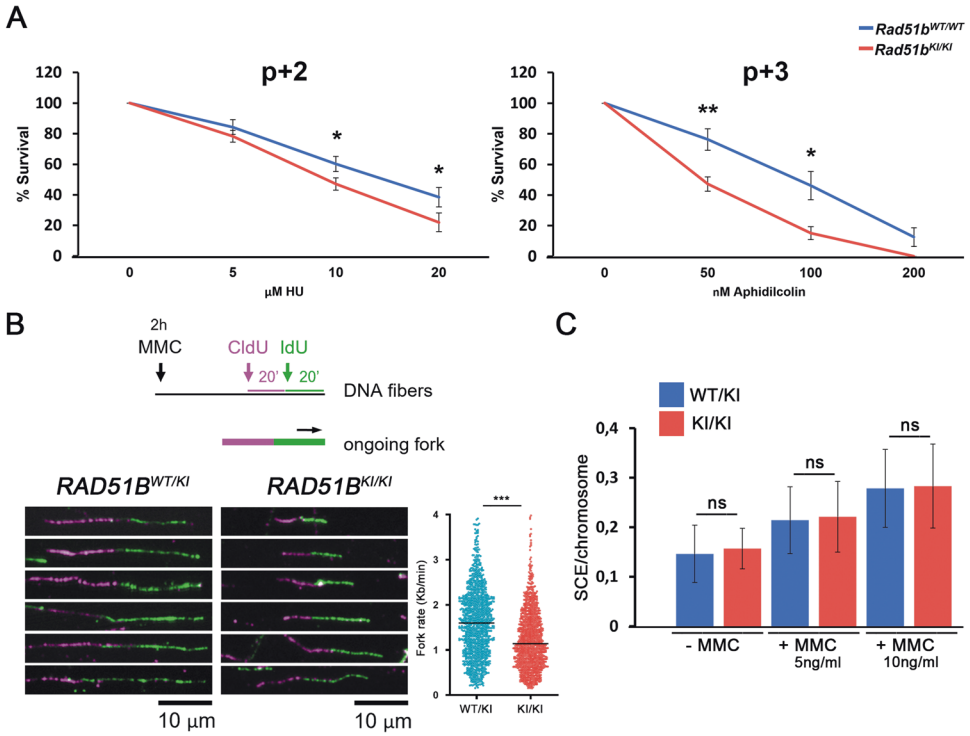

Fig. 7 ***RAD51B-c.92delT* have a role in replication fork homeostasis but not in SCE. A** Cell proliferation assay of WT and mutant *Rad51b* primary MEFs at passage 2 (p + 2) and 3 (p + 3) incubated in presence of a continuous treatment with hydroxyurea (HU) and in presence of a continuous treatment with Aphidicolin. The results are expressed as a percentage relative to the control (not treated). Each point on the graph represents the mean ± SD. **B** Top: Schematic of the stretched DNA fiber assay. Bottom: Examples of DNA fiber images from the indicated cells. Bar in panels, 10 µM. Histogram shows the fork progression rate (median and distribution) in each experimental condition. $n = 3$ experimental replicates (data pooled together). >400 structures scored per condition and replica. ***$p < 0.001$; in Mann-Whitney test. **C** Sister chromatid exchange (SCE) per chromosome after treatment with MMC. *RAD51B*$^{WT/c.92delT}$ and *RAD51B*$^{c.92delT/c.92delT}$ variants are referred to as *RAD51B*$^{WT/KI}$ and *RAD51B*$^{KI/KI}$ for simplicity. Welch's *t*-test analysis: ns, non-significant differences, *$p < 0.5$; **$p < 0.01$.

might also generate a null allele by activating the nonsense mediated decay (NMD), a surveillance pathway that reduces the production of truncated proteins translated from mRNAs bearing PTCs. NMD is more likely to be triggered when a PTC is located at least 50 nucleotides upstream of the last exon-junction [48]. This rule fits well for the location of the *RAD51B-c.92delT* variant. However, the observed expression of the RAD51B mRNA in *Rad51b*$^{c.92delT/c.92delT}$ mice and *RAD51B-c.92delT* human-derived lymphoblastoid cells indicates that NMD is not operating, probably abrogated by the restart of translation according to a recent model based on truncating mutations in tumors [49]. This model would explain the absence of NMD in the *RAD51B-c.92delT* variant because translation reinitiation at AUG64 would abrogate NMD and consequently allow the expression of a truncated RAD51B protein lacking its N-terminal domain. This domain is involved in protein-protein interactions with its paralogues, such as RAD51C and in nuclear localization through a NLS [34]. This is consistent with the observed altered nuclear localization of the RAD51B-c.92delT in comparison to the WT in transfected cells and would suggest a similar dysfunction of the endogenous protein in vivo.

The pathogenicity of the human RAD51B variant is supported by the observed meiotic DNA repair defects during mouse prophase I, the increased incidence of pituitary adenomas, and the defects of MMC-induced damage repair in *c.92delT* human and mouse cells. In addition, *RAD51B*-c.92delT variant reduced the reprogramming efficiency of primary MEFs into iPSCs.

Similar to its Rad51 paralogues [6, 35], the disruption of *Rad51b* in mice has shown early embryonic lethality [8]. The *Rad51b* hypomorphic allele analyzed in this study causes a loss of *RAD51B*-c.92delT interaction with RAD51C and a partial loss of interaction with RAD51 and HELQ. In vivo, *Rad51b-c.92delT* mice did not show any effect on DMC1 loading, but revealed accumulation of foci containing γH2AX, RAD51 and the BRCA2-associated proteins HSF2BP/BRME1 on the chromosome axes from pachytene onward [24, 31, 33, 35]. The accumulation of these non-meiotic specific repair proteins could be explained by the reactivation of a somatic-like HR DNA-repair pathway at pachytene as a consequence of the persistence of unrepaired meiotic DSBs [32]. Regarding HELQ, this helicase promotes efficient HR at damaged replication forks by interacting directly with the RAD51-containing BCDX2 complex. This complex and HELQ act together in the resolution of DNA ICLs upon exposure to MMC [50]. The diminished interaction between the mutant *RAD51B*-c.92delT variant and HELQ sheds light into the presence of unrepaired DNA in MEFs, bone marrow and human lymphoblastoid cells but also into the persistence of unrepaired meiotic DSBs and reduced number of COs. Interestingly, mice lacking HELQ exhibit MMC sensitivity, pituitary adenomas as well as germ cell attrition with subfertility [50] and worms lacking both HELQ and the RAD51 paralogue RFS1 results in a block to meiotic DSB repair after strand invasion [51]. These inefficient interactions of RAD51B-c.92delT together with the altered nuclear localization of the RAD51B variant synergistically lead to a reduction of COs in both spermatocytes and oocytes.

A recent study carried by our laboratory evaluating a POI-inducing variant in the gene *HSF2BP* showed a comparable reduction in the number of COs in comparison with the *Rad51b*-c.92delT mice, which led to a very slight reduced female fertility [24]. This trend of the reduction of litter size in the RAD51B-c.92delT, albeit not statistically significant, could be due to non-identical genetic backgrounds between both mouse models and would support the idea of a slight impact on fertility.

RAD51 and its paralogues have been also associated with cancer predisposition and Fanconi anemia [52]. RAD51B has been involved

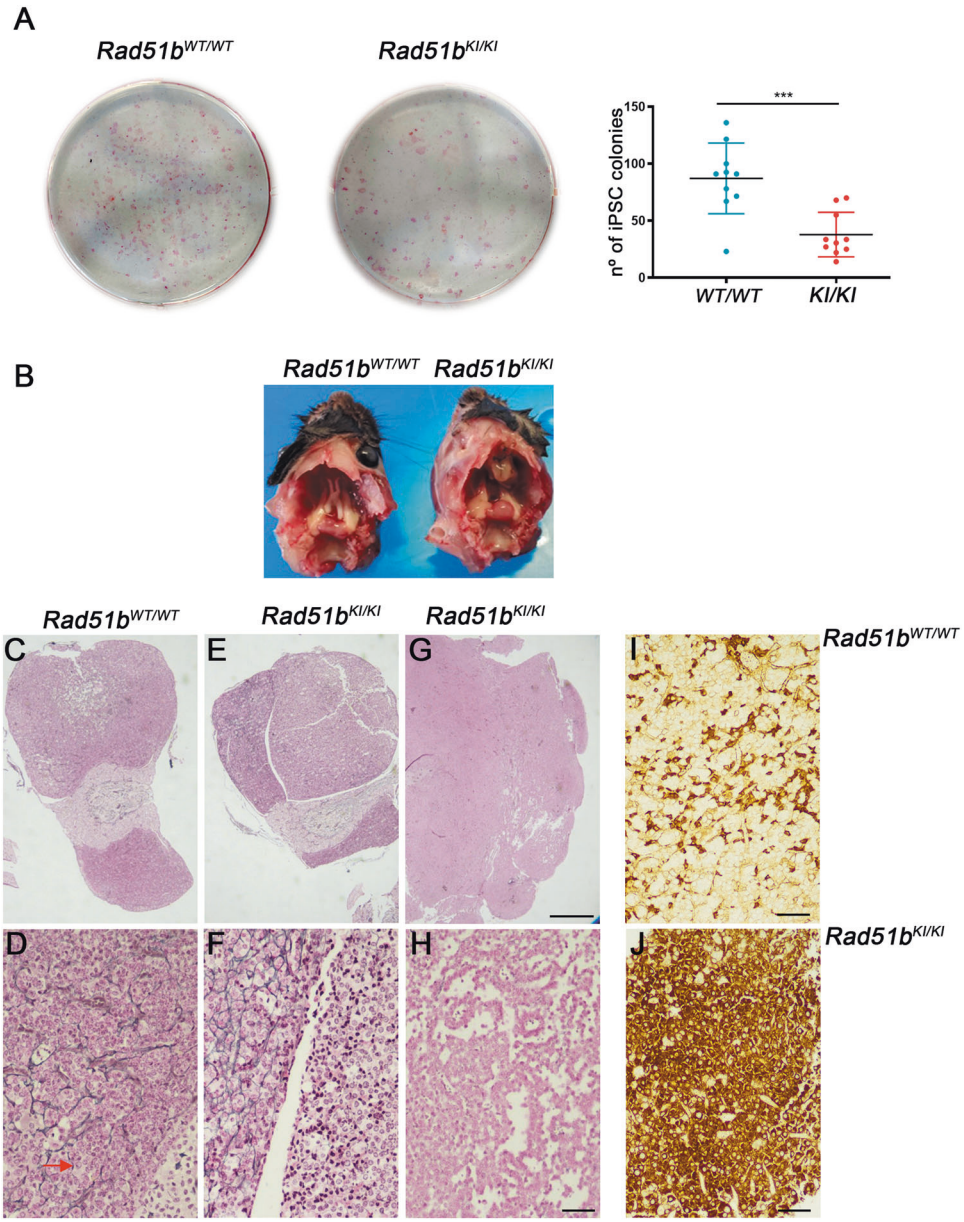

Fig. 8 ***RAD51B-c.92delT* leads to a reduced reprogramming efficiency of MEFs and humanized *Rad51b*$^{KI/KI}$ mice show an increased incidence of hyperplasia of the pituitary gland. A** MEFs from the indicated genotypes were infected with the 3 reprogramming factors and the numbers of alkaline phosphatase positive colonies were counted showing a significantly reduction (up to ~2 fold) in *Rad51b-c.92delT* homozygous mutant MEFs in comparison with the wild-type control. $n = 9$. Welch´s *t*-test analysis: $^{***}p < 0.001$. **B** Macroscopic image of adenohypophysis from *Rad51b*$^{WT/WT}$ and adenohypophysis rom *Rad51b*$^{KI/KI}$ mice. Reticulin staining (**C**–**H**) and Prolactin IHQ (**I**, **J**) of pituitary adenohypophysis from *Rad51b*$^{WT/WT}$ and *Rad51b*$^{KI/KI}$. **C**, **D** Normal adenohypophysis from *Rad51b*$^{WT/WT}$ show a reticulin staining pattern that is partially lost in zones of hyperplasia where the cell size is increased (magnified in **D**, indicated by an arrow). **E**, **F** Microadenoma from a *Rad51b*$^{KI/KI}$ showing a complete loss of reticulin staining pattern that is still persistent in the neighbor misplaced adenohypophysis (magnified in **F**). **G**, **H** Macroadenoma from a *Rad51b*$^{KI/KI}$ showing total loss of reticulin staining pattern and complete absence of normal adenohypophysis tissue. The neoplasm shows different adenoid and pseudopapillary growing patterns (magnified in **H**). **I**, **J** IHQ of prolactin in normal pituitary glands from *Rad51b*$^{WT/WT}$ showing labelled cells unevenly distributed whereas adenomas from *Rad51b*$^{KI/KI}$ revealed a high density of prolactin expressing cells. Bar in panels, 250 μm (**C**, **E**, **G**) and 50 μm (**D**, **F**, **H**, **I**, **J**). *Rad51b*$^{c.92delT/c.92delT}$ variant is referred as *Rad51b*$^{KI/KI}$ for simplicity.

in male and female breast cancer, ovary cancer, prostate cancer, and pituitary adenoma [44, 46, 47, 53–57]. Consistently, *RAD51B-c.92delT* somatic human-derived lymphoblastoid cells, as well as MEFs and explanted bone marrow cells from humanized mice are sensitive to MMC-induced CIN. Moreover, *Rad51b*$^{c.92delT/c.92delT}$ and HELQ-deficient mice display an increased incidence of pituitary hyperplasia suggesting a common pathological mechanism of action. Of note, patient II-4 was diagnosed with a duodenal tubulovillous adenoma with high-grade dysplasia (details in case report section). Altogether, these data provide evidence for a critical role of RAD51B in somatic genome instability and tumorigenesis.

Previous studies have shown that efficient reprogramming of MEFs to a pluripotent stage requires a proficient HR pathway. Accordingly, efficient reprogramming requires key HR genes [42]. Interestingly, the expression of the 3 F reprogramming factors in MEFs induces replication stress, and genetic reduction of stress (overexpressing *Chk1*) increases the efficiency of iPSC generation

[43]. Besides, it is known that replication forks may be stalled at DNA lesions generated by cellular metabolism (aldehydes) or DNA damaging agents including MMC [58]. One pathway to resume DNA synthesis involves fork remodeling events mediated in part by RAD51 paralogues [38]. Our in vivo and in vitro observations of the effects caused by *Rad51b-c.92delT* in reprogramming, fork progression, chromosomal breakage and clonogenic survival suggest also a somatic function of this paralogue in assisting fork progression through certain DNA lesions, as part of the DNA damage tolerance response.

In summary, we describe for the first time two sisters with an isolated POI phenotype caused by a novel homozygous variant in RAD51B (c.92delT). Humanized mice reveal that the RAD51B pathogenic variant evades NMD probably owing to the reinitiation of the translation at a secondary downstream AUG. The resulting truncated protein lacks most of the N-term domain involved in protein-protein interactions and proper nuclear localization. As a result, homozygous *Rad51b-c.92delT* mice shows meiotic DNA repair defects with RAD51 and HSF2BP/BRME1 accumulation in the chromosome axes which leads to a significant reduction in COs. In addition, *RAD51B-c.92delT* human-derived lymphoblastoid cells and mutant MEFs are sensitive to MMC-induced CIN and revealed a reduced reprogramming efficiency to iPSCs as well as a decrease in replication fork progression. Of interest, humanized mice exhibit an increased incidence of hyperplasia of the pituitary gland likely as a consequence of the *RAD51B-c.92delT*-induced genome instability.

METHODS

Case report

Written informed consent was obtained from all subjects before sample collection for DNA analysis. This study was approved by the Ethics Committee of Hospital das Clínicas, Sao Paulo University School of Medicine, Brazil (protocol number 2015/12837/1.015.223). The proposita (II-1) and her younger sister (II-4) were born from first-degree cousins from Northeastern of Brazil (Fig. 1A). On examination at 23 and 21 years of age respectively, they were diagnosed with POI presenting with primary amenorrhea. These siblings had no menarche and physical examination revealed Tanner stage 1 for breast development (II-1 and II-4) and Tanner stage IV pubic hair. Consistent with the diagnosis of hypergonadotropic hypogonadism, basal gonadotropin levels were elevated in the proband and her affected sister (FSH = 44 and 31 U/L, LH = 21 and 17 U/L, respectively) while estradiol levels were undetectable. At first appointments, physical examination showed normal height (149 and 156 cm respectively), and body weight (60 and 47 Kg, respectively). Pelvic ultrasound scans showed an infantile uterus, and the ovaries could not be visualized. Thyroid, adrenal or ovarian autoimmune disorders had been excluded in these patients. On karyotyping analysis performed in 30 metaphases, both sisters were 46,XX. Treatment with conjugated estrogens followed by progesterone replacement resulted in complete breast development and menstrual bleeding. However, the proband and her affected sister developed hypertension, insulin resistance, primary hypothyroidism with absence of thyroid antibodies, and obesity over the years, being current BMI = 41 and 34 kg/m^2, respectively. During the course of this investigation, the affected sister was also diagnosed with a duodenal tubulovillous adenoma with high-grade dysplasia and underwent surgery. Thereafter, she was found to have an indeterminate hepatic nodule and hepatic steatosis. She has been followed and no additional radiotherapy or chemotherapy has been done. The proband has not been diagnosed with any neoplasia. Regarding their family's history, one first-degree cousin and three-second degree cousins were found to have 46,XY DSD due to 5-alpha-reductase type 2 deficiency.

Genetic analysis

DNA extraction: Genomic DNA was extracted from peripheral blood leukocytes from all patients using standard procedures. *Whole-exome sequencing*: Libraries were prepared on both sisters (II-1 and II-4) and her unaffected sister (II-2, as shown in Fig. 1A). Briefly, genomic DNA was sheared to 200–300 bp using the Covaris acoustic adaptor. Exons were captured using SureSelect Human All exons kit (Agilent Technologies) and sequenced by Illumina platform (HiSeq2500, Illumina). Alignment of raw data and variant calling were performed following the steps described by Franca and collaborators [59]). Briefly, the reads were aligned to the human reference genome GRCh37/hg19 using Burrows-Wheeler aligner [60]. Variant calling was performed with Freebeys and annotated ANNOVAR. SNVs were run through independent protein pathogenicity predictors: Polyphen-2, SIFT, Mutation Taster, Mutation Assessor, FATHMM, Radial SVN, and LRT. *Sanger sequencing*: Sanger sequencing was done to validate only the primary variant of interest in all subjects. Primers flanking the *RAD51B* variant (ENSG00000182185/NM_133509: exon3:c.92delT:p.Leu31Tyrfs*9) were used for PCR amplification. Sanger sequencing was performed to validate only the primary variant of interest in all family subjects for whom DNA was available. Primers flanking the RAD51B variant (ENSG00000182185/NM_133509: exon3:c.92delT:p.Leu31Tyrfs*9) were used for PCR amplification. Moreover, Sanger sequencing was used to screen 235 fertile Brazilian control women for the presence of the putative damaging variant. All PCR products were sequencing using BigDye terminator v1.1 followed by automated sequencing at the ABI PRISM 310 (Applied Biosystems, Foster City, CA).

RNA extraction from patient blood samples

Blood samples were centrifuged at 400 × *g* for 10 min at room temperature with the brake off for leukocyte isolation. The buffy coats were removed, and RNA extractions were performed by adding TRI-reagent according to the manufacturer's recommendation (Sigma). Total RNA was reverse-transcribed using MMLV RT enzyme (Takara) and standard procedures. The expression and integrity of patients *RAD51B* transcript were studied by RT-PCR using the high-fidelity Herculase II fusion DNA polymerase (Agilent) and the couple of primers RAD51B-Fext: 5′-GCATGGGTAGCAAGAAACT AAAA-3′ and RAD51B-Rext: 5′-GATCCACAAGCCACACCAC-3′ encompassing the c.92delT variant. The oligo RAD51B-Fint: 5′-GAGCTGTGTGACCGTCTG AG-3′ was used to verify the PCR product by Sanger sequencing (Eurofins genomics).

Generation of CRISPR/Cas9-edited mice

For developing the *Rad51b*$^{KI/KI}$ model, Rad51b-sgRNA1 5′-CTAGAACT-TATGAAAGTGAC-3′ and sgRNA2 5′-GAGACTTAAAAAGTGCTAAA-3′ targeting the exon 3 were predicted at https://eu.idtdna.com/site/order/designtool/index/CRISPR_SEQUENCE. The designed ssODN contains the muted base (c.92delT) and mutations that humanize the locus (TTTTAAGTCTCTCCCCACTAGAACTTATGAAA > TTTATGTCTCTCCCCACTG-GAGCTTATGAAG). The crRNAs, the tracrRNAs and the ssODNs (Supplementary Table 7) were produced by chemical synthesis by IDT. The crRNA and tracrRNA were annealed to obtain the mature sgRNA. A mixture containing the sgRNAs (20 ng/µl of each annealed sgRNA), 30 ng/µl of recombinant Cas9 protein (IDT) and 10 ng/µl of the ssODN were microinjected into B6/CBA F2 zygotes (hybrids between strains C57BL/6 J and CBA/J) [61] at the Transgenic Facility of the University of Salamanca. Edited founders were identified by PCR amplification (Taq polymerase, NZYtech) with primers flanking the edited region (Supplementary Table 7). PCR products were directly sequenced or subcloned into pBlueScript (Stratagene) followed by Sanger sequencing. Selected founders, carrying the desired alleles, were crossed with wild-type C57BL/6 J to eliminate possible unwanted off-targets. Heterozygous mice were re-sequenced and crossed to generate the edited homozygotes. Genotyping was performed by agarose gels analysis or Sanger sequencing (in *Rad51b* humanized mutant) of PCR products from genomic DNA extracted from tail biopsies.

Histology

For histological analysis, after the necropsy of the mice their testes were fixed in Bouin's fixative, ovaries and pituitary glands were fixed in 10% formol. Tissues were processed into serial paraffin sections and stained with haematoxylin-eosin (ovaries) or Periodic acid–Schiff (PAS) and haematoxylin (testes). Jones' reticulin staining was performed automatically on the Artisan^{TM} Link Pro Special Staining System (Dako). Prolactin and ACTH detection by IHC was carried out in an Artisan Link Pro (DAKO) at pH6 using a polyclonal rabbit against prolactin (A0569) and a mouse monoclonal against ACTH (clone 02A3; 1:100), respectively. GH, FSH, and LH detection was carried out in an ultra-view BenchMark (Roche) using a rabbit polyclonal antibody against ACTH (206A-74), a rabbit polyclonal against GH (208A-74), a rabbit polyclonal against SH (EP257), and a rabbit polyclonal against LH (209A-14). All the immunohistochemical stainings for

pituitary hormones ACTH, TSH, GH, LH, FSH were negative, using normal pituitary as a control. The samples were analyzed using a microscope OLYMPUS BX51 and images were taken with a digital camera OLYMPUS DP70. Primordial cell evaluation was carried out by serially slicing into 5 µ thick sections the inner third of each ovary.

Fertility assessment

Rad51b$^{WT/WT}$ and *Rad51b*$^{KI/KI}$ females (8 weeks old) were mated with wild type males, respectively, over the course of 4–12 months. 8 mice per the wild type and 10 mice in the case of *Rad51b*$^{KI/KI}$ were crossed. The presence of copulatory plug was examined daily and the number of pups per litter was recorded.

RAD51B localization in Cos7 cells

Localization of RAD51B variants was studied in COS7 cells transfected with Jetpei (PolyPlus) according to the manufacturer's protocol. 5×10^4 cells were plated on 0.5% fish gelatin-treated (Sigma-Aldrich) 35 mm culture dishes and were subsequently transfected the day after with 0.2 µg of GFP-fused expression vectors. The culture media was replaced after 24 h. COS7 cells were fixed 48 h post-transfection with 4% formaldehyde solution (ThermoFisher) for 7 min at 4 °C. They were washed three times in 1X PBS before a permeabilization with 0.2% Triton X-100 in KB buffer (0.1 M NaCl, 20 mM Tris-HCl pH 7.5, 0.1% BSA). Cells were then washed again and blocked in 7% FBS-supplemented 1X PBS for 30 min at RT. After that, they were incubated with a rabbit anti-GFP antibody (Invitrogen) 1:300-diluted in 7% FBS in PBS for 1 h in a wet chamber at RT. After three washes in 1X PBS, the cells were incubated with a secondary FITC anti-rabbit antibody (Jackson Immunoresearch) diluted 1:100 in 7% FBS in PBS for 1 h. The slides were rinsed 3 times in PBS and finally mounted with Vectashield® and DAPI. Images were taken at 63X magnification with the Laser Scan Confocal Microscopy Leica SP8 (Leica).

Immunocytology and antibodies

Testes were detunicated and processed for spreading using a conventional "dry-down" technique. Oocytes from fetal ovaries (E18 and E18.5 embryos) were digested with collagenase, incubated in a hypotonic buffer, disaggregated, and fixed in paraformaldehyde. Rabbit polyclonal antibodies (R1 and R2 generated from two different host rabbits) against HSF2BP and BRME1 were developed by ProteintechTM against a fusion protein of poly-His with full length HSF2BP or BRME1 (pUC57 vector) of mouse origin. Rabbit polyclonal antibody against DMC1 was developed by ProteintechTM against a DMC1 peptide (EESGFQDDEESLFQDIDLLQKHGIN-MADIKKLKSVGICTIKG). Both meiocytes were incubated with the following primary antibodies for IF: rabbit anti-γH2AX (ser139) IgG #07–164 (1:500, Millipore), mouse anti-γH2AX (ser139) IgG #05–636 (1:400, Millipore), rabbit αRAD51 PC130 (1:100, Calbiochem), rabbit αBRME1 R2 (1:200, ProteintechTM), rabbit αHSF2BP R2 (1:30, ProteintechTM), mouse αMLH1 51-1327GR (1:30, BD Biosciences), rabbit αRPA serum ¨Molly¨ (1:30, provided by Dr. Edyta Marcon, Medical Research University of Toronto, Canada), rat RPA2 2208 S (1:100, Cell Signaling), rabbit αSPATA22 16989-1-AP (1:60, Proteintech), rabbit αDMC1 (1:500, ProteintechTM), mouse αSYCP3 IgG sc-74569 (1:1000, Santa Cruz), rabbit serum αSYCP3 K921 (1:500), rabbit αSYCP1 IgG ab15090 (1:200, Abcam). We could not find any reliable antibody that detect endogenous mouse HELQ in chromosome spreads, squashes or cytospin preps. The secondary antibodies used were goat Alexa 555 α-mouse A-32727, goat Alexa 488 α-mouse A-11001, donkey Alexa 555 α-rabbit A-31572, goat Alexa 488 α-rat A-11006 (1:200, ThermoFisher), goat Alexa 488- Fab α-rabbit 111-547-003 (1:100, Jackson Immunoresearch). Slides were mounted with DAPI and visualized at room temperature using a microscope (Axioplan2; Carl Zeiss, Inc.) with 63x objectives with an aperture of 1.4 (Carl Zeiss, Inc.). Images were taken with a digital camera (ORCA-ER C4742-80; Hamamatsu) and processed with Leica LAS X Life Science Software and Adobe Photoshop CS6 (Adobe). Quantification of fluorescence signals was performed using Fiji (ImageJ) software.

Generation of plasmids

The cDNAs encoding RAD51B (full length and truncated constructs) were RT-PCR amplified from lymphoblastoid cells (derived from patients) RNA. Full-length cDNAs encoding RAD51B (WT and mutant constructs), RPA1, BRCA2 (N, M and C constructs), PALB2, RAD51, BRME1, RAD21, DMC1, HELQ, RAD51C, MEIOB and HSF2BP were RT-PCR amplified from murine testis RNA using the primers listed in Supplementary Table 7. The cDNAs were cloned into the EcoRV pcDNA3, EcoRV pcDNA3-2XFlag, SmaI pcDNA3-2XHA, SmaI pEGFP-C1 or SmaI pEGFP-N1 expression vectors under the CMV promoter. In frame cloning was verified by Sanger sequencing.

Site-directed mutagenesis analysis

Point-mutations were introduced to hRAD51B cloned in pEGFP-N1 using primers listed in Supplementary Table 8 (with the desired mutation) in which the three secondary methionine codons were PCR replaced by CGN encoding alanine codons (individual and double Met to Ala substitutions). The parent template was removed using a methylation-dependent endonuclease DpnI. Plasmids are isolated from the resulting colonies and screened for the desired modification. Positive clones are verified by Sanger sequencing.

Immunoprecipitation

HEK293T cells were transiently transfected with WT or KI constructs of RAD51B in combination with full-length cDNAs encoding RPA1, BRCA2 (N, M and C constructs), PALB2, RAD51, BRME1, RAD21, DMC1, HELQ, RAD51C, MEIOB and HSF2BP. Whole cell extracts were prepared in a 50 mM Tris-HCl pH 7.4, 150 mM NaCl, 1 mM EDTA, 1% Triton X-100 buffer supplemented with protease inhibitors. Those extracts were cleared with protein G Sepharose beads (GE Healthcare) for 1 h. Immunoprecipitations were performed using rabbit αFlag IgG (3.2 µg; F7425, Sigma-Aldrich), rabbit αRad51b R2 IgG (3 µg; ProteintechTM), ChromPure rabbit IgG (3.4 µg/1 mg prot; 011-000-003). These were incubated with the extracts for 2 h and immunocomplexes were isolated by adsorption to protein G-Sepharose beads overnight. After washing, the proteins were eluted from the beads with 2xSDS gel-loading buffer 100 mM Tris-HCl (pH 7.0), 4% SDS, 0.2% bromophenol blue, 200 mM β-mercaptoethanol and 20% glycerol, and loaded onto reducing polyacrylamide SDS gels.

Western blot

HEK293T cells were transfected with WT and mutated constructs encoding human RAD51B generated with the site-directed mutagenesis. They were cultured for 48 h before lysis in RIPA buffer (50 mM Tris HCl pH 7.4. 150 mM NaCl, 1 mM EDTA, 1% Triton X-100) supplemented with protease inhibitors. Cell lysates were sonicated to disrupt cell membranes and shear DNA. After total protein quantification using Bradford assay, 5 µg of protein extracts were loaded onto reducing polyacrylamide SDS gels. Primary antibodies used for western blotting were mouse αFlag IgG (1:3000; F1804, Sigma-Aldrich), mouse αHA IgG (1:3000; 11 101 R, Covance), rabbit αRAD51B R2 (1:2000, ProteintechTM), rabbit αGFP IgG (1:3000; A11122, Invitrogen), rabbit αHSF2BP R2 (1:2000, ProteintechTM). Secondary fluorochrome-conjugated α-mouse DyLight™ 680 (35518, ThermoFisher), α-rabbit DyLight™ 800 (35571, ThermoFisher) antibodies were used at 1:10000 dilution and incubated in dark. The fluorescent signal of the antibodies was obtained through Odyssey Infrared Imaging system. Full length original western blots for these results are provided in Supplementary information.

Immunoprecipitation coupled to Mass spectrometry analysis

Testis extracts and human lymphoblastoid cells were prepared in 50 mM Tris-HCL (pH8), 500 mM NaCl, 1 mM EDTA, 1% Triton-X100 and 10 mg of extracts were incubated 2 h with 30 µg of antibody against mouse RAD51B (residues 122 to 350, ProteintechTM) or IgG from rabbit. The corresponding immunocomplexes were incubated with 60 µl of sepharose beads overnight. After washing, beads were eluted in 100 mM glycine pH 2.5–3 and analyzed by Lc-MS/MS shotgun in LTQ Velos Orbitrap at the Proteomics facility of Centro de Investigación del Cáncer (CSIC/University of Salamanca). Raw data were analyzed using MaxQuant v 1.6.2.6 (Cox and Mann, 2008) against SwissProt Mouse database (UP000000589, Oct, 2019) and MaxQuant contaminants. All FDRs were of 1%. Variable modifications considered were oxidation of M and acetylation of the N-term, while fixed modifications included only carbamidomethylation of C. The maximum number of modifications allowed per peptide was 5. The proteins related with DNA repair were quantified using iBAQ [62].

Cell culture

Primary MEFs were derived from embryonic day 13.5 (E13.5) embryos following standard procedures. MEFs, HEK 293 T and Cos7 cell lines were

cultured at atmospheric oxygen pressure in Dulbecco's modified Eagle's medium (GIBCO) supplemented with 10% fetal bovine serum (GIBCO), and 2 mM Glutamine. MEFs were immortalized at passage 2 using SV40 and hTERT for clonogenical survival assay. Lymphoblast cell lines were derived from donor B-lymphocytes by Epstein Bar virus transformation according to standard procedures and cultured in RPMI medium (GIBCO) supplemented with 10% inactivated fetal bovine serum (GIBCO), and 2 mM Glutamine. Cell lines were tested for mycoplasma contamination using the Mycoplasma PCR ELISA (Sigma).

Cell proliferation assay and DNA damage recuperation

For cell proliferation assays, 2.5×10^4 cells/well were seeded in 12-well plates in duplicates in complete media. Continuous treatment was started in 18 h at the following doses: 0, 5, 10, 20, and 30 ng/ml for MMC; 0, 5, 10 and 20 µM for HU; 0, 50, 100, 500 nM for Aphidicolin. Cells from one plate were trypsinized and counted as a "before treatment" day1 reference. Three days later (4th day after seeding) the remaining cells were counted the same way. Day1 reference numbers were subtracted from day 3 cell numbers to evaluate growth of each cell line. The resulting cell counts were expressed as percentages from the untreated wells. For monitoring the efficiency of DNA repair, 1.4×10^4 MEFs cells/well were treated with 1 µg/ml for one hour and the recuperation of the DNA was measured by quantification of γH2AX foci at 0, 6, 12, 48 and 72 h.

Clonogenic survival assay

Clonogenic survival following an exposure to MMC was assessed in immortalized wild-type and mutant *Rad51b* MEFs. 700 cells were plated per well in 60 mm plates. The day after plating, cells were treated with 0, 50, 100, 150 and 300 nM of MMC and allowed to incubate for 2 h. After drug treatment, media was removed, cells were washed several times with phosphate buffered saline (PBS), and fresh media was added. Once colonies were detectable by the naked eye (7–12 days), media was removed, and cells were washed with PBS and incubated for 30 min at room temperature in a fixation solution (8% paraformaldehyde in cell media). The fixation solution was removed, and colonies were stained with Giemsa (0.02% Giemsa solution in PBS) for 30 min at room temperature. Plates were then rinsed with water and allowed to dry. Colonies were counted by hand.

Karyotyping of mice bone marrow, lymphoblastoid cells and MEFs

Mice between 6–12 weeks old were injected intraperitoneally with a single dose of 4 mg of MMC per kilogram of body weight. After 24 h were injected with 0.1 ml of 0.5% colchicine solution intraperitoneally and the karyotyping derived from bone marrow was realized following standard procedures protocol [63]. Metaphases were obtained after MMC treatment, 150 nM for MEFs at passage 2–5 and 200 nM for lymphoblastoid cells by standard procedures. Active growing cultures were arrested using colcemide (1 µg/mL) for 4 h for MEFs and 3 h for lymphoblastoid cells, trypsinized, treated with hypotonic solution (0.75 mM KCl), and fixed with Methanol/Acetic. Metaphase spreads were Giemsa-stained and analyzed for microscopically visible chromosomal aberrations. Chromatid gap, chromatid break and triradial/quatriradial chromosomes were classified as previously described [64]. At least 100 metaphases were counted from three independent mice and embryos of each genotype.

Single-molecule analysis of DNA replication

Lymphoblastoid cells were treated with 1 µg/ml MMC for 2 h. In the last 40 min, cells were pulse-labelled sequentially with 50 µM CldU (20 min) and 250 µM IdU (20 min). Labelled cells were resuspended in PBS and lysed in 0.2 M Tris pH 7.4, 50 mM EDTA, 0.5% SDS (6 min/ RT). DNA fibers were prepared and stained as described [65] with the following modification: slides were incubated in stringency buffer (10 mM Tris-HCl pH 7.4; 0.1 M NaCl; 0.2% Triton X-100) for 6 min at RT, washed and incubated in blocking solution for 15 min at RT prior to secondary antibodies incubation. Images were obtained in a DM6000 B Leica microscope with an HCX PL APO 40x, 0.75 NA objective. Conversion factor 1 µm = 2.59 kb was used [66]. Fork rate values were obtained by dividing the length of green tracks in ongoing forks by the time of the IdU pulse. Primary antibodies and dilutions used: CldU (rat monoclonal anti-BrdU, 1:100, ab6326, Abcam), IdU (mouse monoclonal anti-BrdU, 1:100, BD 347580), ssDNA (1:100, MAB3034, Millipore). Secondary antibodies and dilutions used: goat anti-rat IgG AF-594 (1:300, A11007, Molecular Probes); goat anti-mouse IgG AF-488 (1:300, A121121, Molecular Probes), goat anti-mouse IgG2a AF-647 (1:300, A21241, Molecular Probes).

Sister chromatid exchange analysis

Exponentially growing lymphoblastoid cells were inoculated at a density of 3×10^5 and were treated with 10 µM of BrdU (5-bromodeoxyuridine, Sigma) for 48 h (approximately two cell divisions). 5 and 10 ng/ml of MMC was added 24 h after BrdU treatment followed by a 3 h incubation with 1 µg/ml of colcemide. Metaphase spreads were stained with 0.1 mg/ml of acridine orange (ThermoFisher) in dH_2O for 5 min at RT. Slides were washed for 2 min under running dH_2O tap water, incubated 1 min in Sorenson Buffer (0.1 M Na_2HPO_4, 0.1 M NaH_2PO_4, pH 6.8) and mounted in Sorenson Buffer. Slides were immediately visualized under FITC filter and at least 30 reciprocal exchange events were counted of each genotype.

iPSC generation from MEFs

For iPSC generation, 2.5×10^5 MEFs were infected with retroviral particles produced by HEK293T transfected with constitutive retroviral expression vectors pMXs KLF4, OCT4 and SOX2. The iPSC media (DMEM, GIBCO; 15% KSR, Invitrogen; 1% Non-essential aminoacids, MEM NEE 100X GIBCO; 1% PSG; 0,002% β-mercaptoethanol 50 mM, GIBCO; 1000 units/mL LIF, Merck) was changed every 24 h until iPS cell colonies appeared (after ~14 days of treatment). Three weeks after plating the MEFs, reprogramming plates were stained for alkaline phosphatase activity (AP detection kit, MERCK).

Statistics

In order to compare counts between genotypes, we used the Welch´s *t*-test (unequal variances *t*-test), which was appropriate as the count data were not highly skewed (i.e., were reasonably approximated by a normal distribution) and in most cases showed unequal variance. We applied a two-sided test in all the cases. Asterisks denote statistical significance: **p*-value < 0.05, ***p*-value < 0.01, ****p*-value < 0.001 and *****p*-value < 0.0001.

Reporting summary

Further information on research design is available in the Nature Research Reporting Summary linked to this article.

DATA AVAILABILITY

Genomic DNA sequences of *H. sapiens* (human, 317761), *M. musculus* (mouse, 75801) are available on GenBank (https://www.ncbi.nlm.nih.gov/genbank/). Amino acid sequences of *H. sapiens* (Q8N1H7), *M. musculus* (NP_083381) were obtained from the UniProt database (http://www.uniprot.org/). All remaining data generated during this study are included in this Article and its Supplementary Information files or available from the authors upon request from the authors.

REFERENCES

1. Handel MA, Schimenti JC. Genetics of mammalian meiosis: regulation, dynamics and impact on fertility. Nat Rev Genet. 2010;11:124–36.
2. Paiano J, Wu W, Yamada S, Sciascia N, Callen E, Paola Cotrim A, et al. ATM and PRDM9 regulate SPO11-bound recombination intermediates during meiosis. Nat Commun. 2020;11:857.
3. Zhao W, Vaithiyalingam S, San Filippo J, Maranon DG, Jimenez-Sainz J, Fontenay GV, et al. Promotion of BRCA2-Dependent Homologous Recombination by DSS1 via RPA Targeting and DNA Mimicry. Mol Cell. 2015;59:176–87.
4. Martinez JS, von Nicolai C, Kim T, Ehlen A, Mazin AV, Kowalczykowski SC, et al. BRCA2 regulates DMC1-mediated recombination through the BRC repeats. Proc Natl Acad Sci USA. 2016;113:3515–20.
5. Chun J, Buechelmaier ES, Powell SN. Rad51 paralog complexes BCDX2 and CX3 act at different stages in the BRCA1-BRCA2-dependent homologous recombination pathway. Mol Cell Biol. 2013;33:387–95.
6. Dai J, Voloshin O, Potapova S, Camerini-Otero RD. Meiotic Knockdown and Complementation Reveals Essential Role of RAD51 in Mouse Spermatogenesis. Cell Rep. 2017;18:1383–94.
7. Pittman DL, Schimenti JC. Midgestation lethality in mice deficient for the RecA-related gene, Rad51d/Rad51l3. Genesis 2000;26:167–73.
8. Shu Z, Smith S, Wang L, Rice MC, Kmiec EB. Disruption of muREC2/RAD51L1 in mice results in early embryonic lethality which can Be partially rescued in a p53 (-/-) background. Mol Cell Biol. 1999;19:8686–93.

9. Sullivan MR, Bernstein KA. RAD-ical New Insights into RAD51 Regulation. Genes (Basel). 2018;9:629. https://doi.org/10.3390/genes9120629.
10. Takata M, Sasaki MS, Sonoda E, Fukushima T, Morrison C, Albala JS, et al. The Rad51 paralog Rad51B promotes homologous recombinational repair. Mol Cell Biol. 2000;20:6476–82.
11. Garcin EB, Gon S, Sullivan MR, Brunette GJ, Cian A, Concordet JP, et al. Differential Requirements for the RAD51 Paralogs in Genome Repair and Maintenance in Human Cells. PLoS Genet. 2019;15:e1008355.
12. Huhtaniemi I, Hovatta O, La Marca A, Livera G, Monniaux D, Persani L, et al. Advances in the Molecular Pathophysiology, Genetics, and Treatment of Primary Ovarian Insufficiency. Trends Endocrinol Metab. 2018;29:400–19.
13. Tsui V, Crismani W. The Fanconi Anemia Pathway and Fertility. Trends Genet. 2019;35:199–214.
14. Thonneau P, Marchand S, Tallec A, Ferial ML, Ducot B, Lansac J, et al. Incidence and main causes of infertility in a resident population (1,850,000) of three French regions (1988-1989). Hum Reprod. 1991;6:811–6.
15. Franca MM, Mendonca BB. Genetics of Primary Ovarian Insufficiency in the Next-Generation Sequencing Era. J Endocr Soc. 2020;4:bvz037.
16. Caburet S, Todeschini AL, Petrillo C, Martini E, Farran ND, Legois B, et al. A truncating MEIOB mutation responsible for familial primary ovarian insufficiency abolishes its interaction with its partner SPATA22 and their recruitment to DNA double-strand breaks. EBioMedicine 2019;42:524–31.
17. de Vries L, Behar DM, Smirin-Yosef P, Lagovsky I, Tzur S, Basel-Vanagaite L. Exome sequencing reveals SYCE1 mutation associated with autosomal recessive primary ovarian insufficiency. J Clin Endocrinol Metab. 2014;99:E2129–32.
18. Wang J, Zhang W, Jiang H, Wu BL, Primary Ovarian Insufficiency C. Mutations in HFM1 in recessive primary ovarian insufficiency. N. Engl J Med. 2014;370:972–4.
19. Guo T, Zhao S, Zhao S, Chen M, Li G, Jiao X, et al. Mutations in MSH5 in primary ovarian insufficiency. Hum Mol Genet. 2017;26:1452–7.
20. Mandon-Pepin B, Touraine P, Kuttenn F, Derbois C, Rouxel A, Matsuda F, et al. Genetic investigation of four meiotic genes in women with premature ovarian failure. Eur J Endocrinol. 2008;158:107–15.
21. Caburet S, Arboleda VA, Llano E, Overbeek PA, Barbero JL, Oka K, et al. Mutant cohesin in premature ovarian failure. N. Engl J Med. 2014;370:943–9.
22. Carlosama C, Elzaiat M, Patino LC, Mateus HE, Veitia RA, Laissue P. A homozygous donor splice-site mutation in the meiotic gene MSH4 causes primary ovarian insufficiency. Hum Mol Genet. 2017;26:3161–6.
23. Franca MM, Funari MFA, Lerario AM, Santos MG, Nishi MY, Domenice S, et al. Screening of targeted panel genes in Brazilian patients with primary ovarian insufficiency. PLoS One. 2020;15:e0240795.
24. Felipe-Medina N, Caburet S, Sanchez-Saez F, Condezo YB, de Rooij DG, Gomez HL, et al. A missense in HSF2BP causing primary ovarian insufficiency affects meiotic recombination by its novel interactor C19ORF57/BRME1. Elife. 2020;9:e56996.
25. Naslavsky MS, Yamamoto GL, de Almeida TF, Ezquina SAM, Sunaga DY, Pho N, et al. Exomic variants of an elderly cohort of Brazilians in the ABraOM database. Hum Mutat. 2017;38:751–63.
26. Lerario AM, Mohan DR, Montenegro LR, Funari MFA, Nishi MY, Narcizo AM, et al. SELAdb: A database of exonic variants in a Brazilian population referred to a quaternary medical center in Sao Paulo. Clinics. 2020;75:e1913.
27. Franca MM, Mendonca BB. Genetics of ovarian insufficiency and defects of folliculogenesis. Best Pr Res Clin Endocrinol Metab. 2022;36:101594.
28. Wiese C, Hinz JM, Tebbs RS, Nham PB, Urbin SS, Collins DW, et al. Disparate requirements for the Walker A and B ATPase motifs of human RAD51D in homologous recombination. Nucleic Acids Res. 2006;34:2833–43.
29. Niu W, Spradling AC. Two distinct pathways of pregranulosa cell differentiation support follicle formation in the mouse ovary. Proc Natl Acad Sci USA. 2020;117:20015–26.
30. da Cruz I, Rodriguez-Casuriaga R, Santinaque FF, Farias J, Curti G, Capoano CA, et al. Transcriptome analysis of highly purified mouse spermatogenic cell populations: gene expression signatures switch from meiotic-to postmeiotic-related processes at pachytene stage. BMC Genomics. 2016;17:294.
31. Brandsma I, Sato K, van Rossum-Fikkert SE, van Vliet N, Sleddens E, Reuter M, et al. HSF2BP Interacts with a Conserved Domain of BRCA2 and Is Required for Mouse Spermatogenesis. Cell Rep. 2019;27:3790–8. e7
32. Enguita-Marruedo A, Martin-Ruiz M, Garcia E, Gil-Fernandez A, Parra MT, Viera A, et al. Transition from a meiotic to a somatic-like DNA damage response during the pachytene stage in mouse meiosis. PLoS Genet. 2019;15:e1007439.
33. Zhang J, Fujiwara Y, Yamamoto S, Shibuya H. A meiosis-specific BRCA2 binding protein recruits recombinases to DNA double-strand breaks to ensure homologous recombination. Nat Commun. 2019;10:722.
34. Miller KA, Sawicka D, Barsky D, Albala JS. Domain mapping of the Rad51 paralog protein complexes. Nucleic Acids Res. 2004;32:169–78.
35. Kuznetsov S, Pellegrini M, Shuda K, Fernandez-Capetillo O, Liu Y, Martin BK, et al. RAD51C deficiency in mice results in early prophase I arrest in males and sister chromatid separation at metaphase II in females. J Cell Biol. 2007;176:581–92.
36. Howlett NG, Taniguchi T, Durkin SG, D'Andrea AD, Glover TW. The Fanconi anemia pathway is required for the DNA replication stress response and for the regulation of common fragile site stability. Hum Mol Genet. 2005;14:693–701.
37. Somyajit K, Saxena S, Babu S, Mishra A, Nagaraju G. Mammalian RAD51 paralogs protect nascent DNA at stalled forks and mediate replication restart. Nucleic Acids Res. 2015;43:9835–55.
38. Berti M, Teloni F, Mijic S, Ursich S, Fuchs J, Palumbieri MD, et al. Sequential role of RAD51 paralog complexes in replication fork remodeling and restart. Nat Commun. 2020;11:3531.
39. Mouron S, Rodriguez-Acebes S, Martinez-Jimenez MI, Garcia-Gomez S, Chocron S, Blanco L, et al. Repriming of DNA synthesis at stalled replication forks by human PrimPol. Nat Struct Mol Biol. 2013;20:1383–9.
40. Takata M, Sasaki MS, Tachiiri S, Fukushima T, Sonoda E, Schild D, et al. Chromosome instability and defective recombinational repair in knockout mutants of the five Rad51 paralogs. Mol Cell Biol. 2001;21:2858–66.
41. Takahashi K, Yamanaka S. Induction of pluripotent stem cells from mouse embryonic and adult fibroblast cultures by defined factors. Cell. 2006;126:663–76.
42. Gonzalez F, Georgieva D, Vanoli F, Shi ZD, Stadtfeld M, Ludwig T, et al. Homologous recombination DNA repair genes play a critical role in reprogramming to a pluripotent state. Cell Rep. 2013;3:651–60.
43. Ruiz S, Lopez-Contreras AJ, Gabut M, Marion RM, Gutierrez-Martinez P, Bua S, et al. Limiting replication stress during somatic cell reprogramming reduces genomic instability in induced pluripotent stem cells. Nat Commun. 2015;6:8036.
44. Juknyt EG, Laurinaityt EI, VilkeviCiUt EA, Gedvilait EG, Glebauskien EB, KriauCiUnien EL, et al. TBX15 rs98422, DNM3 rs1011731, RAD51B rs8017304, and rs2588809 Gene Polymorphisms and Associations With Pituitary Adenoma. Vivo. 2021;35:815–26.
45. Havre PA, Rice M, Ramos R, Kmiec EB. HsRec2/Rad51L1, a protein influencing cell cycle progression, has protein kinase activity. Exp Cell Res. 2000;254:33–44.
46. Orr N, Lemnrau A, Cooke R, Fletcher O, Tomczyk K, Jones M, et al. Genome-wide association study identifies a common variant in RAD51B associated with male breast cancer risk. Nat Genet. 2012;44:1182–4.
47. Song H, Dicks E, Ramus SJ, Tyrer JP, Intermaggio MP, Hayward J, et al. Contribution of Germline Mutations in the RAD51B, RAD51C, and RAD51D Genes to Ovarian Cancer in the Population. J Clin Oncol. 2015;33:2901–7.
48. Thermann R, Neu-Yilik G, Deters A, Frede U, Wehr K, Hagemeier C, et al. Binary specification of nonsense codons by splicing and cytoplasmic translation. EMBO J. 1998;17:3484–94.
49. Lindeboom RG, Supek F, Lehner B. The rules and impact of nonsense-mediated mRNA decay in human cancers. Nat Genet. 2016;48:1112–8.
50. Adelman CA, Lolo RL, Birkbak NJ, Murina O, Matsuzaki K, Horejsi Z, et al. HELQ promotes RAD51 paralogue-dependent repair to avert germ cell loss and tumorigenesis. Nature. 2013;502:381–4.
51. Ward JD, Muzzini DM, Petalcorin MI, Martinez-Perez E, Martin JS, Plevani P, et al. Overlapping mechanisms promote postsynaptic RAD-51 filament disassembly during meiotic double-strand break repair. Mol Cell. 2010;37:259–72.
52. Vaz F, Hanenberg H, Schuster B, Barker K, Wiek C, Erven V, et al. Mutation of the RAD51C gene in a Fanconi anemia-like disorder. Nat Genet. 2010;42:406–9.
53. Thomas G, Jacobs KB, Kraft P, Yeager M, Wacholder S, Cox DG, et al. A multistage genome-wide association study in breast cancer identifies two new risk alleles at 1p11.2 and 14q24.1 (RAD51L1). Nat Genet. 2009;41:579–84.
54. Date O, Katsura M, Ishida M, Yoshihara T, Kinomura A, Sueda T, et al. Haploinsufficiency of RAD51B causes centrosome fragmentation and aneuploidy in human cells. Cancer Res. 2006;66:6018–24.
55. Qin HD, Shugart YY, Bei JX, Pan QH, Chen L, Feng QS, et al. Comprehensive pathway-based association study of DNA repair gene variants and the risk of nasopharyngeal carcinoma. Cancer Res. 2011;71:3000–8.
56. Schoenmakers EF, Huysmans C, Van de Ven WJ. Allelic knockout of novel splice variants of human recombination repair gene RAD51B in t(12;14) uterine leiomyomas. Cancer Res. 1999;59:19–23.
57. Nowacka-Zawisza M, Wisnik E, Wasilewski A, Skowronska M, Forma E, Brys M, et al. Polymorphisms of homologous recombination RAD51, RAD51B, XRCC2, and XRCC3 genes and the risk of prostate cancer. Anal Cell Pathol. 2015;2015:828646.
58. Cortez D. Replication-Coupled DNA Repair. Mol Cell. 2019;74:866–76.
59. Franca MM, Lerario AM, Funari MFA, Nishi MY, Narcizo AM, de Mello MP, et al. A Novel Homozygous Missense FSHR Variant Associated with Hypergonadotropic Hypogonadism in Two Siblings from a Brazilian Family. Sex Dev. 2017;11:137–42.
60. Li H, Durbin R. Fast and accurate long-read alignment with Burrows-Wheeler transform. Bioinformatics. 2010;26:589–95.
61. Singh P, Schimenti JC, Bolcun-Filas E. A mouse geneticist's practical guide to CRISPR applications. Genetics. 2015;199:1–15.
62. Schwanhausser B, Busse D, Li N, Dittmar G, Schuchhardt J, Wolf J, et al. Global quantification of mammalian gene expression control. Nature. 2011;473:337–42.

63. Akeson EC, Davisson MT. Mitotic chromosome preparations from mouse cells for karyotyping. Curr Protoc Hum Genet. 2001;Chapter 4:Unit4 10.
64. Li N, Ding L, Li B, Wang J, D'Andrea AD, Chen J. Functional analysis of Fanconi anemia mutations in China. Exp Hematol. 2018;66:32–41.
65. Rodriguez-Acebes S, Mouron S, Mendez J. Uncoupling fork speed and origin activity to identify the primary cause of replicative stress phenotypes. J Biol Chem. 2018;293:12855–61.
66. Jackson DA, Pombo A. Replicon clusters are stable units of chromosome structure: evidence that nuclear organization contributes to the efficient activation and propagation of S phase in human cells. J Cell Biol. 1998;140:1285–95.

ACKNOWLEDGEMENTS

The authors thank the patients and their family for participating in this study. The authors are grateful to LIM42 and SELA teams for providing technical assistance. We thank also to Dr. Alex N. Zelensky for his useful comments and to Isabel Ramos and Marina Jiménez-Ruiz (Molecular Mechanisms Program, Centro de Investigación del Cáncer) for their help in genotyping and intraperitoneal injections of the mice used in this study. We also are indebted to Maria Daniela Corte Torres (Biobanco of the Principado de Asturias/Instituto de Investigación Sanitaria del Principado de Asturias) for her technical assistance. This work was supported by the Fundação de Amparo à Pesquisa do Estado de São Paulo (FAPESP) Grant 2014/14231-0 (to MMF); FAPESP Grant 2013/02162-8, Nucleo de Estudos e Terapia Celular e Molecular (NETCEM), Conselho Nacional de Desenvolvimento Científico e Tecnológico Grant 303002/2016-6 (to BBM); and FAPESP Grant 2014/50137-5 (to SELA). This work was supported by MINECO (PID2020-120326RB-I00) and by Junta de Castilla y León (CSI239P18 and CSI148P20). NFM, FSS, and MRMH are supported by European Social Fund/JCyLe grants (EDU/310/2015, EDU/556/2019 and EDU/1992/2020). YBC and RSU are funded by a grant from MINECO (BS-2015–073993 and BFU2017-89408-R). Experiments performed at CNIO were supported by grant PID2019-106707-RB to JM, co-sponsored by EU ERDF funds. SM was supported by an international postdoctoral contract "CNIO Friends". The proteomic analysis was performed in the Proteomics Facility of Centro de Investigación del Cáncer, Salamanca, Grant PRB3(IPT17/0019 -ISCIII-SGEFI/ERDF). CIC-IBMCC is supported by the Programa de Apoyo a Planes Estratégicos de Investigación de Estructuras de Investigación de Excelencia cofunded by the Castilla–León autonomous government and the European Regional Development Fund (CLC–2017–01). Veitia's Lab is supported by the University of Paris and the Centre National de la Recherche Scientifique.

AUTHOR CONTRIBUTIONS

MMF and ME contributed with the identification of the human variant of RAD51B. YBC, performed the validation of the truncating variant in vitro and characterization of the mutant mice including the cytological and biochemical analysis with the help of NFM, FSS, RSU, and MRMH, which contributed also with the formal analysis. SM and JM performed the stretched DNA fiber experiments. RGV contributed with the MS data analysis. MSM carried out the Cas9 injections. AA performed pituitary immunohistochemistry. EL, RV, BBM and AMP designed the experiments and wrote the paper with the input of the remaining authors.

COMPETING INTERESTS

The authors declare no competing interests.

ETHICS STATEMENT

Mice were housed in a temperature-controlled facility (specific pathogen free, spf) using individually ventilated cages, standard diet and a 12 h light/dark cycle, according to EU laws at the "Servicio de Experimentación Animal, SEA". Mouse protocols have been approved by the Ethics Committee for Animal Experimentation of the University of Salamanca (USAL). We made every effort to minimize suffering and to improve animal welfare. Blinded experiments were applied when possible. No randomization methods were applied since the animals were not divided in groups/treatments. The minimum size used for each analysis was two animals/genotype. The mice analyzed were between 2 and 4 months of age, except in those experiments where it is indicated.

ADDITIONAL INFORMATION

Supplementary information The online version contains supplementary material available at https://doi.org/10.1038/s41418-022-01021-z.

Correspondence and requests for materials should be addressed to Reiner A. Veitia, Berenice B. Mendonca or Alberto M. Pendás.

Reprints and permission information is available at http://www.nature.com/reprints

Publisher's note Springer Nature remains neutral with regard to jurisdictional claims in published maps and institutional affiliations.

Chromosoma (2019) 128:237–247
https://doi.org/10.1007/s00412-019-00697-6

ORIGINAL ARTICLE

Ubiquitin-specific protease 26 (USP26) is not essential for mouse gametogenesis and fertility

Natalia Felipe-Medina[1] · Laura Gómez-H[1] · Yazmine B. Condezo[1] · Manuel Sanchez-Martín[2,3] · José Luis Barbero[4] · Isabel Ramos[1] · Elena Llano[1,5] · Alberto M. Pendás[1]

Received: 24 October 2018 / Revised: 18 February 2019 / Accepted: 22 February 2019 / Published online: 18 March 2019

Abstract

Ubiquitin-specific protease 26 (USP26) is a deubiquitylating enzyme belonging to the USPs family with a transcription pattern restricted to the male germline. Since protein ubiquitination is an essential regulatory mechanism during meiosis, many efforts have been focused on elucidating the function of USP26 and its relationship with fertility. During the last decade, several studies have reported the presence of different polymorphisms in *USP26* in patients with non-obstructive azoospermia (NOA) or severe oligozoospermia suggesting that this gene may be associated with human infertility. However, other studies have revealed the presence of these and novel polymorphisms, including nonsense mutations, in men with normal spermatogenesis as well. Thus, the results remain controversial and its function is unknown. In the present study, we describe the in vivo functional analysis of mice lacking USP26. The phenotypic analysis of two different *Usp26*-null mutants showed no overt-phenotype with both males and females being fertile. Cytological analysis of spermatocytes showed no defects in synapsis, chromosome dynamics, DNA repair, or recombination. Histopathological analysis revealed a normal distribution and number of the different cell types in both male and female mice. Finally, normal counts were observed in fertility assessments. These results represent the first in vivo evidence showing that USP26 is not essential for mouse gametogenesis.

Keywords Fertility · Spermatogenesis · Ubiquitination · Meiosis · Ubiquitin-specific protease

Introduction

Infertility is a major health issue with an estimated 8–12% of couples affected worldwide (Ombelet et al. 2008; Prieto et al. 2004). Men contribute to 50% and are solely responsible for 20–30% of reported cases (Sharlip et al. 2002). Many factors have been associated with male infertility such as environmental or occupational exposures and genetic abnormalities. Genetic causes are thought to underlie 15–30% of male infertilities being non-obstructive azoospermia (NOA), the complete absence of spermatozoa in the ejaculate due to a testicular failure, the most common outcome associated (Ferlin et al. 2007). Although chromosomal aberrations and microdeletions of the Y chromosome have been largely considered to be the main cause of genetic male infertility (Matzuk and Lamb 2008; Reijo et al. 1996), in the past decades, a large number of fertility-related genes have been identified through the analysis of mouse models, clinical cases, and genome-wide association studies (Caburet et al. 2014; Gomez et al. 2016; Hu et al. 2011). However, much work remains to be done as idiopathic azoospermia is still the most

This article is part of a Special Issue on Recent advances in meiosis from DNA replication to chromosome segregation" edited by Valérie Borde and Francesca Cole, co-edited by Paula Cohen and Scott Keeney".

Electronic supplementary material The online version of this article (https://doi.org/10.1007/s00412-019-00697-6) contains supplementary material, which is available to authorized users.

✉ Alberto M. Pendás
amp@usal.es

[1] Molecular Mechanisms Program, Centro de Investigación del Cáncer and Instituto de Biología Molecular y Celular del Cáncer (CSIC-Universidad de Salamanca), 37007 Salamanca, Spain

[2] Departamento de Medicina, Universidad de Salamanca, Salamanca 37007, Spain

[3] Transgenic Facility, Nucleus platform, Universidad de Salamanca, Salamanca 37007, Spain

[4] Departamento de Biología Celular y Molecular, Centro de Investigaciones Biológicas (CSIC), Madrid 28040, Spain

[5] Departamento de Fisiología y Farmacología, Universidad de Salamanca, Salamanca 37007, Spain

frequent diagnosis among infertile males, and it is currently believed that a high proportion is related with genetic causes (Hamada et al. 2013).

Spermatogenesis, the process through which spermatogonial stem cells generate mature spermatozoa, represents one of the most complex differentiation programs in developmental biology and requires an accurate spatio-temporal regulation of gene transcription, translation, and protein turnover. In this sense, ubiquitination becomes essential for the correct completion of spermatogenesis as it targets substrates for proteasomal degradation but also can modify their biological activity, stability, or subcellular localization (He et al. 2016). Moreover, the importance of ubiquitination in the regulation of protein turnover during spermatogenesis as well as in mammalian fertilization and sperm quality has been reported (Baarends et al. 2000; Muratori et al. 2005; Yi et al. 2007).

The ubiquitin-specific protease 26 (*Usp26*) is a single-exon gene firstly identified by Wang et al. (2001) from a screen for genes expressed in mouse spermatogonia. USP26 belongs to a family of cysteine-proteases that disassemble polymeric ubiquitin chains from substrates and is responsible for maintaining ubiquitin homeostasis in cells (Komander et al. 2009). *USP26* has attracted increased attention as a candidate infertility gene due to its restricted expression pattern to testis and because of its genetic linkage with X-chromosome (male are hemizygous) which is enriched for testis-specific genes (Nishimune and Tanaka 2006). More specifically, *USP26* expression has been described in spermatogonia (types A and B), preleptotene and leptotene-zygotene spermatocytes, round spermatids, and at the blood-testis barrier from both mouse and human testes (Lin et al. 2011; Wang et al. 2005). Additionally, in humans, it is also expressed in Sertoli and Leydig cells (Wosnitzer et al. 2014).

Genetic polymorphisms identified in the *USP26* locus have been causally associated with male infertility from Sertoli cell only-syndrome to non-obstructive azoospermia or asthenozoospermia (Asadpor et al. 2013; Lee et al. 2008; Li et al. 2015; Ma et al. 2016; Paduch et al. 2005; Stouffs et al. 2005; Xia et al. 2014; Zhang et al. 2007). By contrast, other studies have found the same frequency of *USP26* polymorphisms in fertile and infertile men (Christensen et al. 2008; Luddi et al. 2016; Ravel et al. 2006; Ribarski et al. 2009; Shi et al. 2011; Stouffs et al. 2006; Zhang et al. 2015). In addition, it has been reported that most of the described polymorphisms do not abolish USP26 enzymatic activity (Liu et al. 2018; Zhang et al. 2015).

Given the absence of functional studies, we have addressed the in vivo functional analysis of mice lacking USP26. The analysis of USP26-deficient mice showed no overt-phenotype with both males and females being fertile. The histopathological analysis of testis and ovaries showed a normal number and distribution of cell types, and accordingly, the results obtained in the fertility assessment were similar to the wild-type ones. Finally, spermatogenesis in the absence of USP26 proceeded without any defect neither in synapsis nor in DNA repair or meiotic recombination. These results represent the first in vivo evidence showing that USP26 is not essential for mouse gametogenesis.

Methods

Production of CRISPR/Cas9-edited mice *Usp26*-sgRNAs were predicted at crispr.mit.edu. *Usp26*-sgRNAs were produced by cloning annealed complementary oligos (Table S1) at the BbsI site of pX330 (#42230, Addgene), generating PCR products containing a T7 promoter sequence, and then performing in vitro transcription using the MEGAshortscript™ T7 Transcription Kit (Life Technologies). The plasmid pST1374-NLS-flag-linker-Cas9 (#44758; Addgene) was used for generating CAS9 mRNA after linearization with AgeI. In vitro transcription and capping were performed using the mMESSAGE mMACHINE T7 Transcription Kit (AM1345; Life Technologies). Products were purified using the RNeasy® Mini Kit (Qiagen). RNA (100 ng/ul Cas9 and 50 ng/ul each guide RNA) was microinjected into zygotes (F1 hybrids between strains C57BL6/J and CBA/J also known as B6CBAF1/J) as described previously (Singh et al. 2015). Edited founders were identified by PCR amplification with primers flanking the targeted regions (Table S2) and subcloned into pBlueScript (Stratagene) followed by standard Sanger sequencing. The lengths of the corresponding wild-type and mutant alleles were 307 bp and 411 bp respectively, in the 21 mutants and 259 bp vs 173 bp in the catalytic mutants. The selected founder was crossed with a wild type (B6CBAF1/J) to eliminate possible unwanted off-targets. $Usp26^{(WT/edited)}$ heterozygous mice were sequenced again by Sanger and crossed to give rise to $Usp26^{(edited/edited)}$ homozygous. Genotyping was performed by agarose gel electrophoresis analysis of PCR products from DNA isolated from tail biopsies.

Fertility assessment $Usp26^{WT/Y}$, $Usp26^{21/Y}$, and $Usp26^{Cat/Y}$ males and $Usp26^{WT/WT}$, $Usp26^{21/21}$, and $Usp26^{Cat/Cat}$ females (8 weeks old) were mated with wild-type females and males, respectively during 3 months. Six mice per genotype were crossed. The presence of copulatory plug was examined daily, and the number of pups per litter was recorded.

Histology For histological analysis, adult testes/ovaries were fixed in Bouin's fixative, processed into serial paraffin sections, and stained with Periodic acid–Schiff (PAS) and Hematoxylin (testes) or hematoxylin-eosin (ovaries).

Immunocytology and antibodies Testes were detunicated and processed for spreading using the "dry-down" technique and incubated with the indicated antibodies for

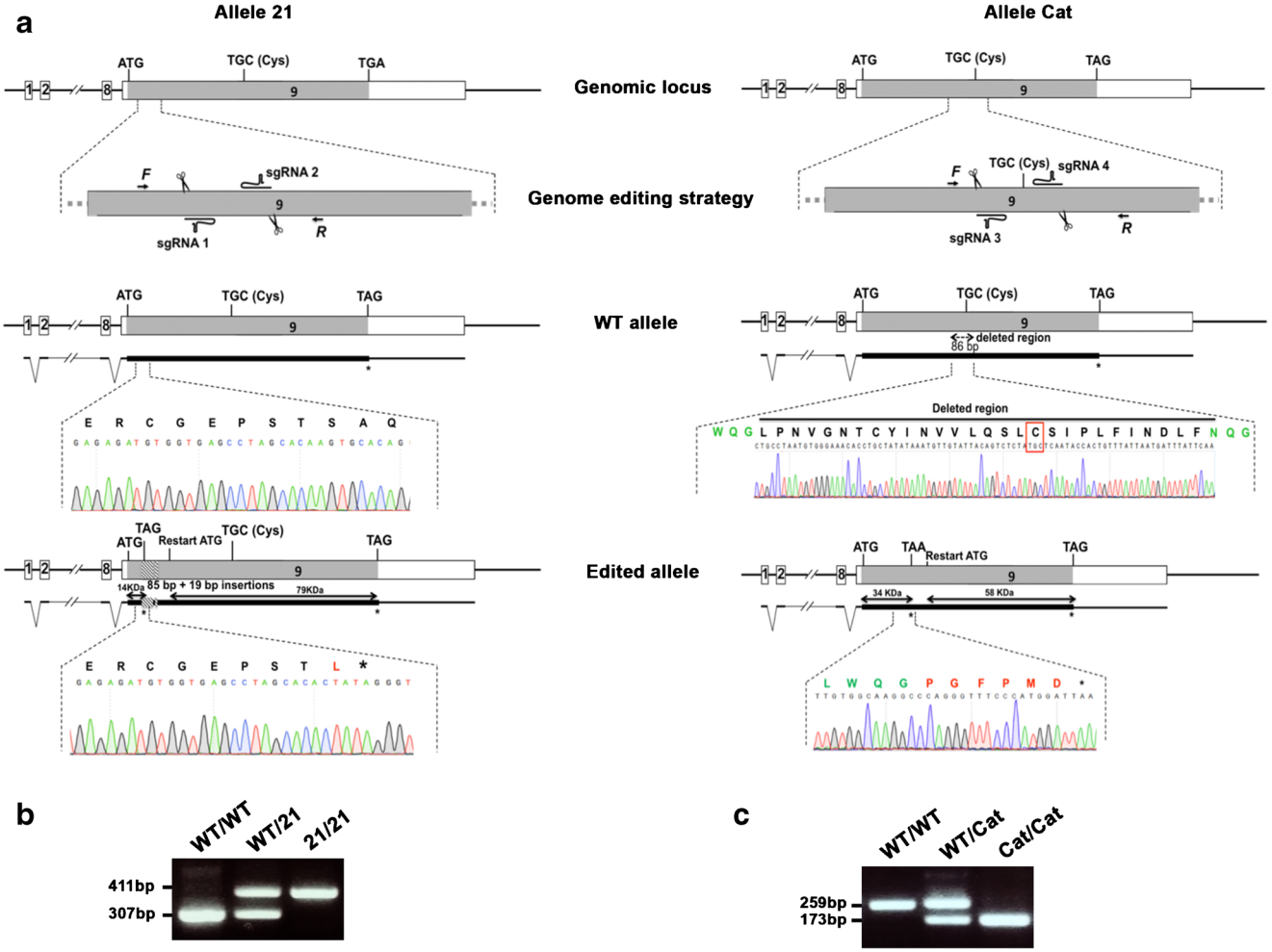

Fig. 1 *Usp26* knockout generation by CRISPR-Cas9 genome editing. **a** Schematic representation of the wild-type locus (WT) and the two genome editing strategies at the *Usp26* locus (left: knockout 21, right: catalytic knockout Cat). The sgRNAs, the single-coding exon of *Usp26* (gray) and the corresponding non-coding region (open box) are represented. Thin (non-coding) and thick (coding sequences) lines under the exon represent the expected transcripts derived from WT and *Usp26* edited alleles. ATG, start codon; TAG/TAA, stop codons; TGC, codon encoding the catalytic Cys295; Restart ATG, codons encoding the Met147(21) and Met331(Cat). Nucleotide sequence of the WT and the edited allele derived from PCR amplification of DNA from the *Usp26* edited mice is shown. In the allele^{Cat}, the catalytic cysteine (Cys) is highlighted (red rectangle). The insertion (left panel) and deletion (right panel) generate a frameshift (amino acids in red) and a premature STOP codon. Double-headed arrows represent the predicted size (KDa) of the peptides that could be expressed in both alleles (from the canonical ATG to the generated STOP codon and from the first ATG after the mutation - restart ATG- to the canonical STOP codon). Arrows represent genotyping primers. **b** PCR analysis of genomic DNA from three pups from *Usp26*$^{WT/21}$ heterozygous crosses. The PCR amplification with primers F and R (arrows) revealed a fragment of 307 bp in the case of the allele^{WT} and 411 bp in the allele^{21} (WT/WT), (WT/21), and (21/21) designate wild-type, heterozygous, and homozygous knockout animals, respectively. **c** PCR analysis of genomic DNA from three pups from Usp26$^{WT/Cat}$ heterozygous crosses. The PCR amplification with primers F and R (arrows) revealed a fragment of 259 bp in the case of the allele^{WT} and 173 bp in the allele^{Cat} (WT/WT), (WT/Cat), and (Cat/Cat) designate wild-type, heterozygous, and homozygous knockout females, respectively

immunofluorescence. The primary antibodies used for immunofluorescence were goat αUSP26 (W-12) sc-51013 (Santa Cruz, 1:5), rabbit αUSP26-M (1:5, provided by Dr. Yi-Wen Lin Institute of Biomedical Sciences, Taipei, Taiwan), mouse αSYCP3 IgG sc-74569 (Santa Cruz, 1:60), rabbit αSYCP3 serum K921 (Prieto et al. 2004), rabbit αSYCP1 IgG ab15090 (Abcam, 1:200), rabbit anti-γH2AX (ser139) IgG #07–164 (Millipore, 1:150), and mouse αMLH1 51-1327GR (BD Biosciences; 1:5). The secondary antibodies used were TRITC α-mouse 115-095-146/α-rabbit 111-025-144 and FITC α-mouse 115-095-146/α-rabbit 111-095-045 (Jackson ImmunoResearch, all 1:100). Slides were visualized at room temperature using a microscope (Axioplan 2; Carl Zeiss, Inc.) with 63 × objectives with an aperture of 1.4 (Carl Zeiss, Inc.). Images were taken with a digital camera (ORCA-ER; Hamamatsu) and processed with OPENLAB 4.0.3 and Photoshop (Adobe). Quantification of γH2AX fluorescence signal was measured by ImageJ software.

Protein extraction and western blotting Whole testis extracts were prepared in RIPA buffer (50 mM Tris Hcl (pH 7,5), 150 mM NaCl, 1% NP40, 0.1% SDS, 0.5% sodium deoxycholate). Fifteen micrograms of total protein was loaded onto 10% reducing polyacrylamide SDS gels and transferred to 0.45 μm Hybond ECL nitrocellulose membranes (RPN303D; GE Healthcare, Life Sciences). The membranes were blocked with 5% nonfat dried milk diluted in TBS-Tween. The proteins were detected by western blotting with the indicated antibodies. Primary antibodies used for western blotting were rabbit goat αUSP26 (W-12) sc-51013 (Santa Cruz, 1:2000), rabbit αUSP26-M (1:2000, provided by Dr. Yi-Wen Lin, Institute of Biomedical Sciences, Taipei, Taiwan), mouse anti-α-Tubulin (T9026, Sigma, 1:40000), and mouse anti-β-Actin (A5441, Sigma, 1:40000). Secondary horseradish peroxidase–conjugated α-mouse (715-035-150, Jackson ImmunoResearch), α-rabbit (711-035-152, Jackson ImmunoResearch), or α-goat (705-035-147, Jackson ImmunoResearch) antibodies were used at 1:5000 dilution. Antibodies were detected by using ImmobilonTM Western Chemiluminescent HRP Substrate from Millipore.

Bioinformatic analysis of RNAseq datasets Gene expression data were obtained from each article repository and processed to extract the relevant information of the genes of interest (*USP* genes) into a dataframe using regular expressions in R language. Colors have been included to represent a gradient of expression for each individual gene. Red and green represent the lower and upper endpoints (stages with lower and higher expression level) and between them an intermediate color gradient has been established.

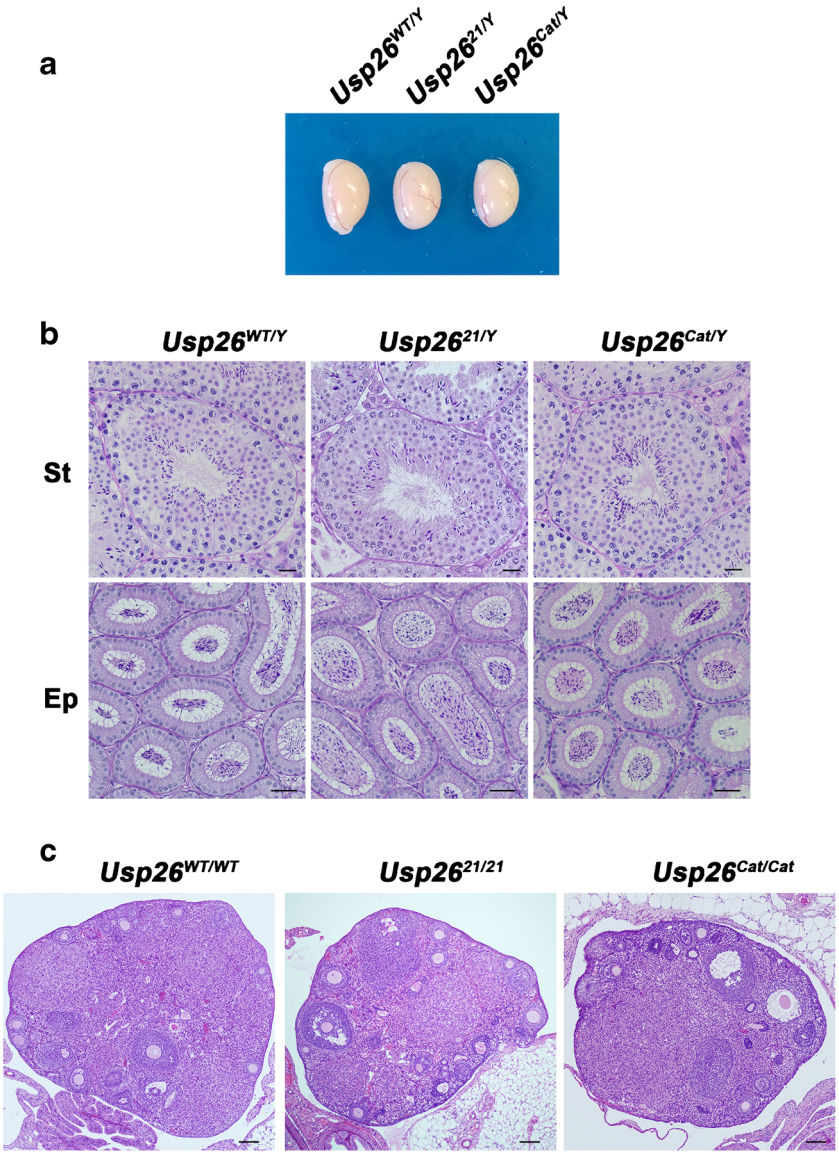

Fig. 2 Histopathological analysis does not show defects in USP26-deficient mice. **a** Testis size was not affected by the absence of USP26. **b** PAS + hematoxylin–stained testis sections show a normal number and distribution of germ cells in the seminiferous tubules (St) and normal counts of spermatozoa in the epididymides (Ep) of *USP26*$^{21/Y}$ and *USP26*$^{Cat/Y}$ mice in comparison with *USP26*$^{WT/Y}$ mice. Bar in upper panels (St), 10 μm, and in lower panels (Ep), 20 μm. **c** Comparative histopathological analysis (hematoxylin + eosin staining) of ovaries from *USP26*$^{21/21}$, *USP26*$^{Cat/Cat}$, and *USP26*$^{WT/WT}$ females at 4 months of age showing the presence of follicles and corpora lutea and a normal appearance of the stroma in the absence of USP26. Bars represent 50 μm

Table 1 USP26 deficiency has no impact on fertility

		Mean (offspring)	SD	*n*
Males	$USP26^{WTY}$	7.0	1.47	15
	$USP26^{21/Y}$	6.9	2.31	18
	$USP26^{Cat/Y}$	6.4	2.32	16
Females	$USP26^{WT/WT}$	7.4	2.33	14
	$USP26^{21/21}$	7.2	1.89	16
	$USP26^{Cat/Cat}$	7.9	2.28	16

Numeric data (mean of pups per litter) obtained from the mating of $USP26^{WT/Y}$, $USP26^{21/Y}$, and $USP26^{Cat/Y}$ males and $USP26^{WT/W}$, $USP26^{21/21}$, and $USP26^{Cat/Cat}$ females with $USP26^{WT/WT}$ females and $USP26^{WT/Y}$ males, respectively. 8-week-old mice were mated for 3 months (6 mice/genotype)

Results

Usp26 CRISPR-Cas9 knockout lines

To gain further insight into USP26 function, we generated a mouse model by targeting the single-coding exon of *Usp26* through CRISPR-Cas9 genome editing. The selected founder carried two consecutive insertions of 85 and 19 base pairs (bp) separated by 5 bp. The first insertion changes the frame and generates a premature STOP codon at position 123 (14KDa) resulting in a predicted null-allele (herein allele^{21}; Fig. 1a, left). This founder was crossed with wild-type (WT) C57BL/6J mice, and the heterozygous offspring was crossed to obtain the homozygous mutant mice, which were identified by PCR (Fig. 1b).

To test whether the generated mutation was a null-allele, we analyzed the expression of USP26 in mouse testis with two different antibodies, the commercial anti-USP26 (W-12) and the anti-USP26-M kindly provided by Dr. Yi-Wen Lin (Lin et al. 2011). We first carried out an immunofluorescence (IF) analysis in spermatocyte spreads from both $Usp26^{21/Y}$ and $Usp26^{WT/Y}$ mice. None of the antibodies showed detectable signal in spermatocytes (leptonema, zygonema, pachynema, diplonema, or diakinesis), spermatogonia, or round spermatid (Fig. S1a-b and S2a-b), where the expression of USP26 has been previously reported (Lin et al. 2011; Wang et al. 2005). We also performed a western blot (WB) analysis of whole testis extracts from wild-type and mutant mice. We did not observe any signal in the blot using the anti-USP26 (W-12) antibody (Fig. S1c) whereas the anti-USP26-M generated similar bands in $Usp26^{21/Y}$ and $Usp26^{WT/Y}$ extracts (Fig. S2c). No shift in the migration of any detected band was observed in the mutant extracts in comparison with the wild type (USP26 size: WT, 95 KDa vs 14 KDa, allele^{21}). These results strongly suggest that the available antibodies are not able to recognize the endogenous protein and, consequently, the detected bands do not correspond to USP26.

Nonsense mutations close to the 5′ of open reading frames (ORF) can lead to a translation restart from downstream AUG codons using the same original frame (Makino et al. 2016). The genomic locus of murine *Usp26* encodes an in-frame methionine at the position 147 which could be used as a downstream AUG initiation codon in our initial mutant (allele^{21}) and could potentially lead to the generation of an N-terminal truncated protein (79 KDa, Fig. 1a, left) with an intact catalytic domain. We did not detect the predicted truncated proteins of 14 KDa (premature STOP codon) or 79 KDa (Restart ATG) in the Usp26$^{21/Y}$ extracts by western blot (Fig. S1c and S2c). Consequently, the absence of working antibodies against USP26 that allowed us to ensure that the allele^{21} was a null mutant led us to generate a second mutant with a deletion in the proteolytic domain of USP26 (dead mutant). This domain is formed by two short motifs known as Cys and His boxes that contain the catalytic triad, one catalytic cysteine, and an histidine and asparagine/aspartate that facilitate the cysteine nucleophilic attack (Davis and Simeonov 2015; Nijman et al. 2005). To abolish the protease activity of USP26, we targeted the CRISPR-Cas9 to the catalytic cysteine (Cys295) generating an 86 bp deletion (including the cysteine) that produces a frameshift and consequently a premature STOP codon at position 293 (34KDa; Fig. 1a, right). Once the founder transmitted the allele, the heterozygous was crossed to obtain the homozygous mutants (herein, $Usp26^{Cat/Cat}$ or $Usp26^{Cat/Y}$), which were identified by PCR (Fig. 1c). Immunofluorescence and western blot analysis were performed for the new catalytic mutant, and the results were identical to those obtained in the $Usp26^{21/Y}$ mutant (Fig.S1a–c and S2a–c). The western blot analysis did not reveal any shift on band migration nor identify the truncated proteins of 34 and/or 56 KDa that could be expressed from the allele^{Cat} (See Fig. 1a right and S1c and S2c). Thus, although we cannot demonstrate the absence of USP26 in our mutants due to the lack of working antibodies that recognize the endogenous protein, the genetic strategy predicts that both of them are null. Especially, the resultant catalytic mutant lacks the genomic information to encode an active catalytic domain (Cys) and, consequently, represents a dead mutant without ubiquitin-specific protease activity.

USP26-deficient mice are fertile

$Usp26^{21/Y}$ and $Usp26^{Cat/Y}$ mice developed normally and showed no overt-phenotype including testis size and weight (Fig. 2a). To determine the potential effect of USP26 absence on mouse fertility, we performed a fertility test. Adult males from $Usp26^{WT/Y}$, $Usp26^{21/Y}$, and $Usp26^{Cat/Y}$ lines were mated with $Usp26^{WT/WT}$ females. The presence of copulatory plug was monitored daily to discard behavioral defects, and the number of pups per litter was recorded. USP26 mutants behaved similar to their wild-type counterparts, and no

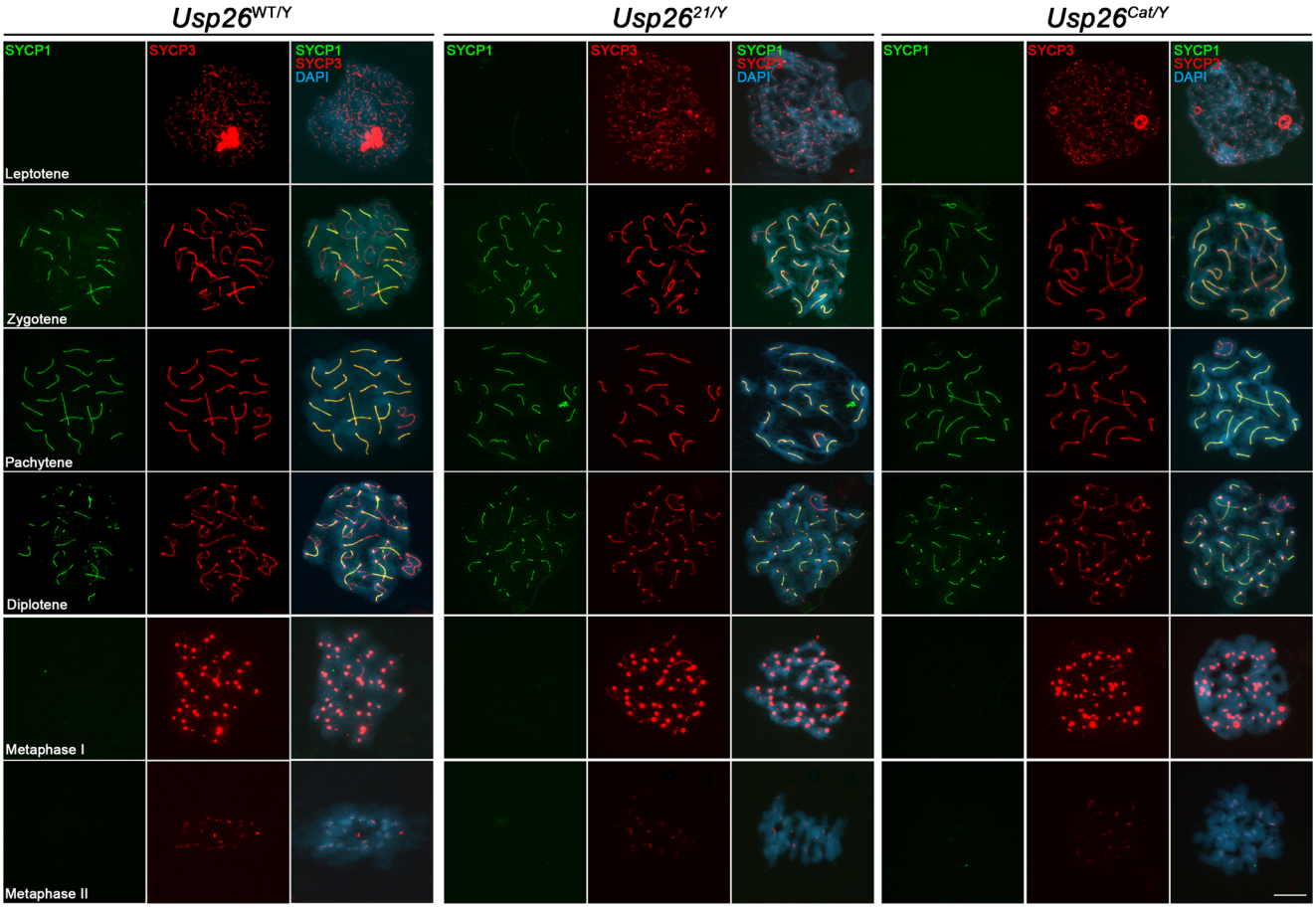

Fig. 3 Chromosome behavior and synapsis proceed properly in spermatocytes lacking USP26. Double immunolabeling of SYCP3 (red) and SYCP1 (green) on spermatocyte spreads from *USP26*$^{21/Y}$, *USP26*$^{Cat/Y}$, and *USP26*$^{WT/Y}$ mice. DNA was stained with DAPI (blue). No differences were observed on synapsis/desynapsis processes between USP26-deficient and WT spermatocytes. Bar in panels, 10 μm

significant differences in litter size between the three groups were observed (Table 1). The histopathological analysis of seminiferous tubules from *Usp26*$^{21/Y}$ and *Usp26*$^{Cat/Y}$ mice showed a normal progression through the 12 stages of epithelial cycle with an organization and number of germ cells similar to the wild-type ones (Fig. 2b). Moreover, a normal amount of spermatozoa were able to reach the epididymides of USP26 mutants (Fig. 2b). Taken together, our findings demonstrate that USP26 seems to have a minimal if any role in mouse male fertility.

Usp26 is not expressed in human whole ovary and mutations associated with female infertility have not been reported. Accordingly, the fertility assessment and histological analysis of *Usp26*$^{21/21}$ and *Usp26*$^{Cat/Cat}$ females did not reveal any defect (Table 1 and Fig. 2c).

USP26-deficient spermatocytes showed normal synapsis, DSBs dynamics, and recombination

Although *Usp26* transcription starts in spermatogonia, it is transcribed at maximum levels during the early stages of meiosis (leptotene and zygotene, Tables S5 and S6 (da Cruz et al. 2016; Margolin et al. 2014)). Moreover, the ubiquitin–proteasome system (UPS) has been involved in the regulation of meiotic prophase in mouse (Rao et al. 2017) and USP26 has been associated with double-strand breaks (DSBs) repair and homologous recombination in somatic cells (Typas et al. 2016). These data prompted us to analyze in more detail chromosome synapsis, double-strand breaks (DSBs) generation/resolution, and meiotic recombination during the meiotic prophase I of USP26-deficient spermatocytes.

Chromosome synapsis is mediated by a proteinaceous scaffold known as synaptonemal complex (SC). The SC is composed of two axial elements (AEs) connected by transverse filaments (TFs) through the assembly of the central element (CE), generating a tripartite zipper-like structure. In mammals, the components of AEs are SYCP2 and SYCP3, TFs consist of SYCP1, and five CE components have been identified as follow: SYCE1-3, TEX12, and the recently described SIX6OS1 (Bolcun-Filas and Schimenti 2012; Gomez et al. 2016). To evaluate the synaptic process, we analyzed the distribution of SYCP3 and SYCP1 in

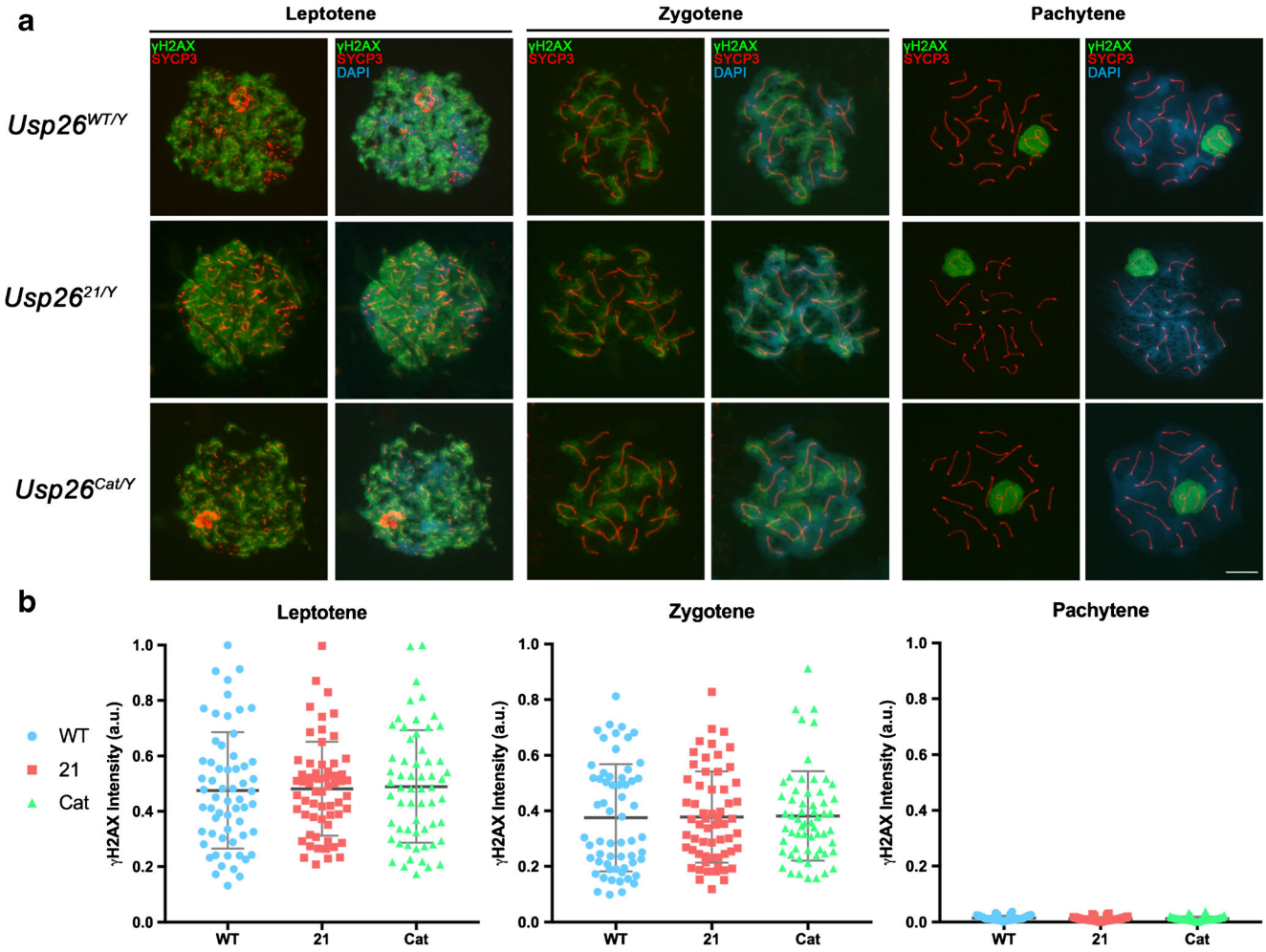

Fig. 4 DSB dynamics is not affected in the absence of USP26. **a** Double immunofluorescence of γ-H2AX (green) with SYCP3 (red) in wild-type and *USP26* mutant spermatocytes showing no differences in the formation and repair of DSBs. DNA was stained with DAPI (blue). DSB formation occurs at leptotene, and they are processed during zygotene and early pachytene. Consequently, γ-H2AX labels intensely the whole nucleus at leptotene and declines until mid-pachytene where the staining is restricted to the unsynapsed sex bivalent. **b** Plots under each panel represent the quantification of fluorescence intensity at the different stages and shows no significant differences ($n = 60$ cells from 2 different mice for each genotype). See Table S3 for numeric data; bars represent standard deviation (SD). Welch's t test analysis: $*p < 0.01$; $**p < 0.001$; $***p < 0.0001$. Bar in panels, 10 μm

spermatocyte spreads from *Usp26*$^{21/Y}$, *Usp26*$^{Cat/Y}$, and *Usp26*$^{WT/Y}$ mice (Fig. 3). We did not observe defects on AEs formation, starting as short patches in leptotene that got longer as zygotene proceeded. Full synapsis was achieved at pachytene, and no defects were observed as desynapsis progressed from diplotene to diakinesis. Additionally, USP26-deficient metaphase I and II plates showed normal morphology (Fig. 3). Altogether, these observations suggest that USP26 has no function on chromosome behavior and synapsis.

Meiotic recombination establishes the physical tethering between homologous chromosomes essential to ensure the correct chromosome segregation during the first meiotic division. Meiotic recombination is initiated at leptotene with the formation of programmed DSBs by SPO11 which are repaired during the prophase I by the homologous recombination (HR) machinery (Bolcun-Filas and Schimenti 2012). Given the involvement of protein ubiquitination and SUMOylation in DSBs repair (Bekker-Jensen and Mailand 2011), we analyzed USP26-deficient spermatocytes for the labeling of phosphorylated H2AX (γ-H2AX), the first appearing modification after DSBs induction (Rogakou et al. 1998). The γ-H2AX distribution in USP26-deficient spermatocytes resembled that of wild-type cells from leptotene, showing whole nucleus labeling, to pachytene where the γ-H2AX signal was restricted to the sex body. These data indicate that DSBs formation and repair are not compromised by the absence of USP26 (Fig. 4).

During early prophase I, DSBs are frequently resolved as non-crossovers (NCO) and only a reduced fraction of the

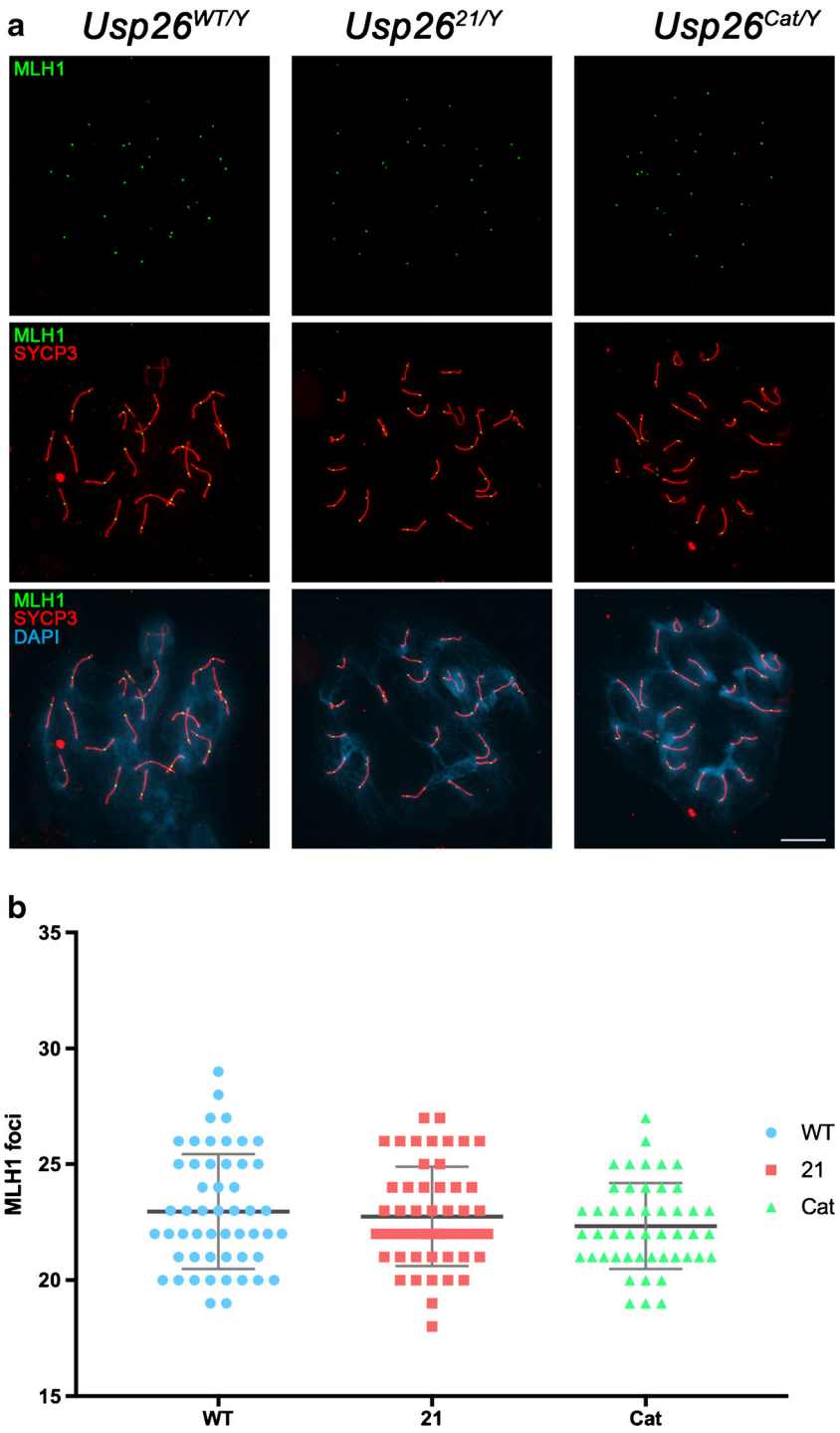

Fig. 5 USP26-deficient mice do not show meiotic recombination defects. **a** Immunostaining of MLH1 (green) and SYCP3 (red). DNA was stained with DAPI (blue). The number of MLH1 foci (corresponding to future chiasmata) in mutant spermatocytes resembles that observed in the wild type. Bar in panels, 10 μm. **b** Quantification of MLH1 foci in *USP26*$^{WT/Y}$, *USP26*$^{21/Y}$, and *USP26*$^{Cat/Y}$ pachytene spermatocytes showing no significant differences ($n = 52$, 52, and 48 cells respectively from 2 different mice for each genotype). See Table S4 for numeric data; bars represent standard deviation (SD). Welch's *t*-test analysis: $*p < 0.01$; $**p < 0.001$; $***p < 0.0001$

DSBs are processed as crossovers (CO), which will give rise to chiasmata. Owing to the association of the UPS to the AEs and its role in regulating meiotic recombination (Rao et al. 2017), we evaluated USP26-deficient spermatocytes for CO formation by MLH1 staining, a mismatch repair protein that marks CO sites (Guillon et al. 2005). No differences were observed in the number of MLH1 foci between *Usp26*$^{21/Y}$, *Usp26*$^{Cat/Y}$, and *Usp26*$^{WT/Y}$ spermatocytes (Fig. 5).

Discussion

In the present study, we have generated two *Usp26* knockout models, one carrying two insertions (allele^{21}) and a second one lacking the catalytic Cys of the protein (dead mutant, allele^{Cat}). Although the in silico analysis predicts that both alleles generate truncated proteins, we have not been able to demonstrate the absence of USP26 in the mutants, likely due

to the lack of sensitivity of the antibodies which failed to detect the endogenous protein. Even though we could not demonstrate the absence of protein, the generated deletion in the catalytic domain of USP26 (allele^{Cat}) ensures that the protein, if present, will not be functional as ubiquitin-specific protease leading to a reliable loss-of-function mutant.

The testis-specific USP26 belongs to the superfamily of deubiquitinating enzymes (DUBs) that remove ubiquitin (Ub) peptides from substrates, process Ub precursors, and disassemble polymeric Ub chains hence being responsible for maintaining ubiquitin homeostasis in cells (Komander et al. 2009). Ubiquitination plays essential roles during spermatogenesis from the establishment and differentiation of spermatogonial stem cells to spermiogenesis (Bose et al. 2014) and to date several deubiquitinating enzymes (i.e., USP2 (Bedard et al. 2011), USP7 (Luo et al. 2015), USP9X (Kishi et al. 2017), Uchl-1(Kwon et al. 2005)) have been associated with defects at different stages of spermatogenesis and fertility impairment. However, here we show that mice lacking the deubiquitinating enzyme USP26 are fertile showing litters of the same size than those from wild-type mice and a normal number and distribution of all the testis cell types.

The maximum transcription levels of *Usp26* are reached during the first stages of meiotic prophase (Tables S5 and S6 (da Cruz et al. 2016; Margolin et al. 2014)). This expression pattern along with the involvement of the UPS in the regulation of meiotic prophase in mouse (Rao et al. 2017) and the association of USP26 with DNA repair and homologous recombination in somatic cells (Typas et al. 2016) strongly suggest a potential role of USP26 on these processes. However, our cytological analysis of mutant spermatocytes did not reveal any obvious defect in synapsis, DSBs repair, and meiotic recombination. These results suggest a very specific function of USP26 that seems unrelated to the regulation of the meiotic prophase I.

The association of this testis-specific protein with male infertility has focused many efforts during the last decades though with controversial conclusions. Several studies have linked *USP26* mutations with male infertility (Asadpor et al. 2013; Lee et al. 2008; Li et al. 2015; Ma et al. 2016; Paduch et al. 2005; Stouffs et al. 2005; Xia et al. 2014; Zhang et al. 2007). However, our functional studies showing that USP26 is dispensable for mouse fertility are in agreement with previous works reporting a lack of association between *USP26* genetic polymorphisms and male infertility (Christensen et al. 2008; Luddi et al. 2016; Ravel et al. 2006; Ribarski et al. 2009; Shi et al. 2011; Stouffs et al. 2006; Zhang et al. 2015). Supporting our observations, it has been described a normozoospermic man carrying a nonsense mutation in USP26 (c.882 C>A) that generates a premature STOP codon (Luddi et al. 2016). This mutation produces a truncated USP26 protein at the position 293 that consequently lacks the catalytic Cys (Cys305). Our results provide new evidences that could shed light on the existing controversy about the relationship between *USP26* mutations and human male infertility. However, although the mouse is the most commonly used organism model in human disease research (Rosenthal and Brown 2007), we cannot exclude the idea that the functional relevance of this protein could differ between both species, showing a critical role in human that does not recapitulate in the mouse where the genetic background can also drastically modulate the observed phenotypes. Nevertheless, our working models have been developed in an outbred background (B6CBAF1/J) that more closely resembles the greater genetic variability of humans.

Given the *Usp26* restricted expression pattern to testis and the importance of the maintenance of ubiquitin homeostasis in cells, the absence of phenotype in the USP26-deficient mice is counterintuitive. Genetic redundancy or biological robustness can be responsible for this lack of deviation in the reproductive phenotype. The in silico analysis of mRNA expression of different USPs during mouse spermatogenesis showed several USPs with an expression pattern highly similar to that of USP26 (i.e., USP9X, USP37, USP14, USP53, USP33, USP28, and USP3. See Tables S5 and S6 (da Cruz et al. 2016; Margolin et al. 2014)). It would be interesting to analyze which of these putative candidates (if any) are upregulated in the absence of USP26 that would provide an indication for compensation. To prove it, a double loss-of-function analysis should be carried out in future studies.

In conclusion, this work reports for the first time a loss-of-function analysis of USP26 in mice and represents in vivo evidence that USP26 is not essential for mouse gametogenesis and fertility.

Acknowledgements We wish to express our sincere thanks to Dr. Yi-Wen Lin (Institute of Biomedical Sciences, Taipei, Taiwan) for providing the anti-USP26-M antibody. We appreciate to Rodrigo García-Valiente for his help with bioinformatic analysis of RNAseq datasets.

Author contributions NFM with the help of LGH and YBC performed the characterization of the mutant mice including the cytological and histological analysis. MSM carried out the Cas9 injections. JLB provided the αSYCP3 serum K921 and reviewed the manuscript. IR carried out infertility phenotyping of mutant mice. AMP and ELC designed the experiments and helped NFM to write the manuscript with the input of the remaining authors.

Funding information This work was supported by BFU2017-89408-R. NFM and LGH are supported by European Social Fund/JCyLe grants (EDU/310/2015 and EDU/1083/2013) and YBC by a FPI grant from the MINECO. IBMCC is supported by the Programa de Apoyo a Planes Estratégicos de Investigación de Estructuras de Investigación de Excelencia cofunded by the Castilla–León autonomous government and the European Regional Development Fund (CLC–2017–01). The IBMCC is supported by the Programa de Apoyo a Planes Estratégicos de Investigación de Estructuras de Investigación de Excelencia cofunded by the Castilla–León autonomous government and the European Regional Development Fund (CLC–2017–01).

References

Asadpor U, Totonchi M, Sabbaghian M, Hoseinifar H, Akhound MR, Zari Moradi S, Haratian K, Sadighi Gilani MA, Gourabi H, Mohseni Meybodi A (2013) Ubiquitin-specific protease (USP26) gene alterations associated with male infertility and recurrent pregnancy loss (RPL) in Iranian infertile patients. J Assist Reprod Genet 30:923–931. https://doi.org/10.1007/s10815-013-0027-9

Baarends WM, van der Laan R, Grootegoed JA (2000) Specific aspects of the ubiquitin system in spermatogenesis. J Endocrinol Investig 23:597–604. https://doi.org/10.1007/BF03343782

Bedard N, Yang Y, Gregory M, Cyr DG, Suzuki J, Yu X, Chian RC, Hermo L, O'Flaherty C, Smith CE, Clarke HJ, Wing SS (2011) Mice lacking the USP2 deubiquitinating enzyme have severe male subfertility associated with defects in fertilization and sperm motility. Biol Reprod 85:594–604. https://doi.org/10.1095/biolreprod.110.088542

Bekker-Jensen S, Mailand N (2011) The ubiquitin- and SUMO-dependent signaling response to DNA double-strand breaks. FEBS Lett 585:2914–2919. https://doi.org/10.1016/j.febslet.2011.05.056

Bolcun-Filas E, Schimenti JC (2012) Genetics of meiosis and recombination in mice. Int Rev Cell Mol Biol 298:179–227. https://doi.org/10.1016/B978-0-12-394309-5.00005-5

Bose R, Manku G, Culty M, Wing SS (2014) Ubiquitin-proteasome system in spermatogenesis. Adv Exp Med Biol 759:181–213. https://doi.org/10.1007/978-1-4939-0817-2_9

Caburet S, Arboleda VA, Llano E, Overbeek PA, Barbero JL, Oka K, Harrison W, Vaiman D, Ben-Neriah Z, García-Tuñón I, Fellous M, Pendás AM, Veitia RA, Vilain E (2014) Mutant cohesin in premature ovarian failure. N Engl J Med 370:943–949. https://doi.org/10.1056/NEJMoa1309635

Christensen GL, Griffin J, Carrell DT (2008) Sequence analysis of the X-linked USP26 gene in severe male factor infertility patients and fertile controls. Fertil Steril 90:851–852. https://doi.org/10.1016/j.fertnstert.2007.06.096

da Cruz I, Rodríguez-Casuriaga R, Santiñaque FF, Farías J, Curti G, Capoano CA, Folle GA, Benavente R, Sotelo-Silveira JR, Geisinger A (2016) Transcriptome analysis of highly purified mouse spermatogenic cell populations: gene expression signatures switch from meiotic-to postmeiotic-related processes at pachytene stage. BMC Genomics 17:294. https://doi.org/10.1186/s12864-016-2618-1

Davis MI, Simeonov A (2015) Ubiquitin-specific proteases as druggable targets. Drug Target Rev 2:60–64

Ferlin A, Raicu F, Gatta V, Zuccarello D, Palka G, Foresta C (2007) Male infertility: role of genetic background. Reprod BioMed Online 14:734–745

Gomez HL et al (2016) C14ORF39/SIX6OS1 is a constituent of the synaptonemal complex and is essential for mouse fertility. Nat Commun 7:13298. https://doi.org/10.1038/ncomms13298

Guillon H, Baudat F, Grey C, Liskay RM, de Massy B (2005) Crossover and noncrossover pathways in mouse meiosis. Mol Cell 20:563–573. https://doi.org/10.1016/j.molcel.2005.09.021

Hamada AJ, Esteves SC, Agarwal A (2013) A comprehensive review of genetics and genetic testing in azoospermia. Clinics (Sao Paulo) 68(Suppl 1):39–60

He M, Zhou Z, Shah AA, Zou H, Tao J, Chen Q, Wan Y (2016) The emerging role of deubiquitinating enzymes in genomic integrity, diseases, and therapeutics. Cell Biosci 6:62. https://doi.org/10.1186/s13578-016-0127-1

Hu Z, Xia Y, Guo X, Dai J, Li HG, Hu H, Jiang Y, Lu F, Wu Y, Yang X, Li H, Yao B, Lu C, Xiong C, Li Z, Gui Y, Liu J, Zhou Z, Shen H, Wang X, Sha J (2011) A genome-wide association study in Chinese men identifies three risk loci for non-obstructive azoospermia. Nat Genet 44:183–186. https://doi.org/10.1038/ng.1040

Kishi K, Uchida A, Takase HM, Suzuki H, Kurohmaru M, Tsunekawa N, Kanai-Azuma M, Wood SA, Kanai Y (2017) Spermatogonial deubiquitinase USP9X is essential for proper spermatogenesis in mice. Reproduction 154:135–143. https://doi.org/10.1530/REP-17-0184

Komander D, Clague MJ, Urbe S (2009) Breaking the chains: structure and function of the deubiquitinases. Nat Rev Mol Cell Biol 10:550–563. https://doi.org/10.1038/nrm2731

Kwon J, Mochida K, Wang YL, Sekiguchi S, Sankai T, Aoki S, Ogura A, Yoshikawa Y, Wada K (2005) Ubiquitin C-terminal hydrolase L-1 is essential for the early apoptotic wave of germinal cells and for sperm quality control during spermatogenesis. Biol Reprod 73:29–35. https://doi.org/10.1095/biolreprod.104.037077

Lee IW, Kuan LC, Lin CH, Pan HA, Hsu CC, Tsai YC, Kuo PL, Teng YN (2008) Association of USP26 haplotypes in men in Taiwan, China with severe spermatogenic defect. Asian J Androl 10:896–904. https://doi.org/10.1111/j.1745-7262.2008.00439.x

Li Z, Huang Y, Li H, Hu J, Liu X, Jiang T, Sun G, Tang A, Sun X, Qian W, Zeng Y, Xie J, Zhao W, Xu Y, He T, Dong C, Liu Q, Mou L, Lu J, Lin Z, Wu S, Gao S, Guo G, Feng Q, Li Y, Zhang X, Wang J, Yang H, Wang J, Xiong C, Cai Z, Gui Y (2015) Excess of rare variants in genes that are key epigenetic regulators of spermatogenesis in the patients with non-obstructive azoospermia. Sci Rep 5:8785. https://doi.org/10.1038/srep08785

Lin YW, Hsu TH, Yen PH (2011) Localization of ubiquitin specific protease 26 at blood-testis barrier and near Sertoli cell-germ cell interface in mouse testes. Int J Androl 34:e368–e377. https://doi.org/10.1111/j.1365-2605.2010.01130.x

Liu YL, Zheng J, Mi YJ, Zhao J, Tian QB (2018) The impacts of nineteen mutations on the enzymatic activity of USP26. Gene 641:292–296. https://doi.org/10.1016/j.gene.2017.10.074

Luddi A, Crifasi L, Quagliarello A, Governini L, De Leo V, Piomboni P (2016) Single nucleotide polymorphisms of USP26 in azoospermic men. Syst Biol Reprod Med 62:372–378. https://doi.org/10.1080/19396368.2016.1238116

Luo M, Zhou J, Leu NA, Abreu CM, Wang J, Anguera MC, de Rooij DG, Jasin M, Wang PJ (2015) Polycomb protein SCML2 associates with USP7 and counteracts histone H2A ubiquitination in the XY chromatin during male meiosis. PLoS Genet 11:e1004954. https://doi.org/10.1371/journal.pgen.1004954

Ma Q, Li Y, Guo H, Li C, Chen J, Luo M, Jiang Z, Li H, Gui Y (2016) A novel missense mutation in USP26 gene is associated with nonobstructive azoospermia. Reprod Sci 23:1434–1441. https://doi.org/10.1177/1933719116641758

Makino S, Fukumura R, Gondo Y (2016) Illegitimate translation causes unexpected gene expression from on-target out-of-frame alleles created by CRISPR-Cas9. Sci Rep 6:39608. https://doi.org/10.1038/srep39608

Margolin G, Khil PP, Kim J, Bellani MA, Camerini-Otero RD (2014) Integrated transcriptome analysis of mouse spermatogenesis. BMC Genomics 15:39. https://doi.org/10.1186/1471-2164-15-39

Matzuk MM, Lamb DJ (2008) The biology of infertility: research advances and clinical challenges. Nat Med 14:1197–1213. https://doi.org/10.1038/nm.f.1895

Muratori M, Marchiani S, Forti G, Baldi E (2005) Sperm ubiquitination positively correlates to normal morphology in human semen. Hum Reprod 20:1035–1043. https://doi.org/10.1093/humrep/deh678

Nijman SM, Luna-Vargas MP, Velds A, Brummelkamp TR, Dirac AM, Sixma TK, Bernards R (2005) A genomic and functional inventory of deubiquitinating enzymes. Cell 123:773–786. https://doi.org/10.1016/j.cell.2005.11.007

Nishimune Y, Tanaka H (2006) Infertility caused by polymorphisms or mutations in spermatogenesis-specific genes. J Androl 27:326–334. https://doi.org/10.2164/jandrol.05162

Ombelet W, Cooke I, Dyer S, Serour G, Devroey P (2008) Infertility and the provision of infertility medical services in developing countries.

Hum Reprod Update 14:605–621. https://doi.org/10.1093/humupd/dmn042

Paduch DA, Mielnik A, Schlegel PN (2005) Novel mutations in testis-specific ubiquitin protease 26 gene may cause male infertility and hypogonadism. Reprod BioMed Online 10:747–754

Prieto I, Tease C, Pezzi N, Buesa JM, Ortega S, Kremer L, Martínez A, Martínez-A C, Hultén MA, Barbero JL (2004) Cohesin component dynamics during meiotic prophase I in mammalian oocytes. Chromosom Res 12:197–213

Rao HB et al (2017) A SUMO-ubiquitin relay recruits proteasomes to chromosome axes to regulate meiotic recombination. Science 355:403–407. https://doi.org/10.1126/science.aaf6407

Ravel C, el Houate B, Chantot S, Lourenço D, Dumaine A, Rouba H, Bandyopadahyay A, Radhakrishna U, Das B, Sengupta S, Mandelbaum J, Siffroi JP, McElreavey K (2006) Haplotypes, mutations and male fertility: the story of the testis-specific ubiquitin protease USP26. Mol Hum Reprod 12:643–646. https://doi.org/10.1093/molehr/gal063

Reijo R, Alagappan RK, Patrizio P, Page DC (1996) Severe oligozoospermia resulting from deletions of azoospermia factor gene on Y chromosome. Lancet 347:1290–1293

Ribarski I, Lehavi O, Yogev L, Hauser R, Bar-Shira Maymon B, Botchan A, Paz G, Yavetz H, Kleiman SE (2009) USP26 gene variations in fertile and infertile men. Hum Reprod 24:477–484. https://doi.org/10.1093/humrep/den374

Rogakou EP, Pilch DR, Orr AH, Ivanova VS, Bonner WM (1998) DNA double-stranded breaks induce histone H2AX phosphorylation on serine 139. J Biol Chem 273:5858–5868

Rosenthal N, Brown S (2007) The mouse ascending: perspectives for human-disease models. Nat Cell Biol 9:993–999. https://doi.org/10.1038/ncb437

Sharlip ID, Jarow JP, Belker AM, Lipshultz LI, Sigman M, Thomas AJ, Schlegel PN, Howards SS, Nehra A, Damewood MD, Overstreet JW, Sadovsky R (2002) Best practice policies for male infertility. Fertil Steril 77:873–882

Shi YC, Wei L, Cui YX, Shang XJ, Wang HY, Xia XY, Zhou YC, Li H, Jiang HT, Zhu WM, Huang YF (2011) Association between ubiquitin-specific protease USP26 polymorphism and male infertility in Chinese men. Clin Chim Acta 412:545–549. https://doi.org/10.1016/j.cca.2010.12.005

Singh P, Schimenti JC, Bolcun-Filas E (2015) A mouse geneticist's practical guide to CRISPR applications. Genetics 199:1–15. https://doi.org/10.1534/genetics.114.169771

Stouffs K, Lissens W, Tournaye H, Van Steirteghem A, Liebaers I (2005) Possible role of USP26 in patients with severely impaired spermatogenesis. Eur J Hum Genet 13:336–340. https://doi.org/10.1038/sj.ejhg.5201335

Stouffs K, Lissens W, Tournaye H, Van Steirteghem A, Liebaers I (2006) Alterations of the USP26 gene in Caucasian men. Int J Androl 29:614–617. https://doi.org/10.1111/j.1365-2605.2006.00708.x

Typas D, Luijsterburg MS, Wiegant WW, Diakatou M, Helfricht A, Thijssen PE, van den Broek B, Mullenders LH, van Attikum H (2016) The de-ubiquitylating enzymes USP26 and USP37 regulate homologous recombination by counteracting RAP80. Nucleic Acids Res 44:2976. https://doi.org/10.1093/nar/gkv1480

Wang PJ, McCarrey JR, Yang F, Page DC (2001) An abundance of X-linked genes expressed in spermatogonia. Nat Genet 27:422–426. https://doi.org/10.1038/86927

Wang PJ, Page DC, McCarrey JR (2005) Differential expression of sex-linked and autosomal germ-cell-specific genes during spermatogenesis in the mouse. Hum Mol Genet 14:2911–2918. https://doi.org/10.1093/hmg/ddi322

Wosnitzer MS, Mielnik A, Dabaja A, Robinson B, Schlegel PN, Paduch DA (2014) Ubiquitin specific protease 26 (USP26) expression analysis in human testicular and extragonadal tissues indicates diverse action of USP26 in cell differentiation and tumorigenesis. PLoS One 9:e98638. https://doi.org/10.1371/journal.pone.0098638

Xia JD, Chen J, Han YF, Chen H, Yu W, Chen Y, Dai YT (2014) Association of 370-371insACA, 494T>C, and 1423C>T haplotype in ubiquitin-specific protease 26 gene and male infertility: a meta-analysis. Asian J Androl 16:720–724. https://doi.org/10.4103/1008-682X.129134

Yi YJ, Manandhar G, Oko RJ, Breed WG, Sutovsky P (2007) Mechanism of sperm-zona pellucida penetration during mammalian fertilization: 26S proteasome as a candidate egg coat lysin. Soc Reprod Fertil Suppl 63:385–408

Zhang J, Qiu SD, Li SB, Zhou DX, Tian H, Huo YW, Ge L, Zhang QY (2007) Novel mutations in ubiquitin-specific protease 26 gene might cause spermatogenesis impairment and male infertility. Asian J Androl 9:809–814. https://doi.org/10.1111/j.1745-7262.2007.00305.x

Zhang W, Liu T, Mi YJ, Yue LD, Wang JM, Liu DW, Yan J, Tian QB (2015) Evidence from enzymatic and meta-analyses does not support a direct association between USP26 gene variants and male infertility. Andrology 3:271–279. https://doi.org/10.1111/andr.295

PLOS GENETICS

RESEARCH ARTICLE

The PSMA8 subunit of the spermatoproteasome is essential for proper meiotic exit and mouse fertility

Laura Gómez-H[1], Natalia Felipe-Medina[1], Yazmine B. Condezo[1], Rodrigo Garcia-Valiente[1], Isabel Ramos[1], José Angel Suja[2], José Luis Barbero[3], Ignasi Roig[4], Manuel Sánchez-Martín[5], Dirk G. de Rooij[6,7], Elena Llano[1,8]*, Alberto M. Pendas[1]*

1 Molecular Mechanisms Program, Centro de Investigación del Cáncer and Instituto de Biología Molecular y Celular del Cáncer (CSIC-Universidad de Salamanca), Salamanca, Spain, **2** Unidad de Biología Celular, Universidad Autónoma de Madrid, Madrid, Spain, **3** Centro de Investigaciones Biológicas (CSIC), Madrid, Spain, **4** Genome Integrity and Instability Group, Institut de Biotecnologia i Biomedicina, Universitat Autònoma de Barcelona, Cerdanyola del Vallès, Spain, **5** Departamento de Medicina, Universidad de Salamanca, Salamanca, Spain, **6** Reproductive Biology Group, Division of Developmental Biology, Department of Biology, Faculty of Science, Utrecht University, Utrecht, The Netherlands, **7** Center for Reproductive Medicine, Academic Medical Center, University of Amsterdam, Amsterdam, The Netherlands, **8** Departamento de Fisiología y Farmacología, Universidad de Salamanca, Salamanca, Spain

* ellano@usal.es (EL); amp@usal.es (AMP)

Citation: Gómez-H L, Felipe-Medina N, Condezo YB, Garcia-Valiente R, Ramos I, Suja JA, et al. (2019) The PSMA8 subunit of the spermatoproteasome is essential for proper meiotic exit and mouse fertility. PLoS Genet 15(8): e1008316. https://doi.org/10.1371/journal.pgen.1008316

Editor: Mary Ann Handel, The Jackson Laboratory, USA, UNITED STATES

Received: February 21, 2019

Accepted: July 17, 2019

Published: August 22, 2019

Data Availability Statement: Amino acid sequences of PSMA8 from H. sapiens (Q8TAA3) and M. musculus (Q9CWH6) and PSMA7 from H. sapiens (O14818) and from M. musculus (Q9Z2U0) were obtained from the UniProt database (http://www.uniprot.org/). Searches were generated versus the Mus musculus proteome (UP000000589, May 2017 release) and Maxquant contaminants. PSMA8 expression was obtained at https://gtexportal.org/home/gene/PSMA8. All

Abstract

The ubiquitin proteasome system regulates meiotic recombination in yeast through its association with the synaptonemal complex, a 'zipper'-like structure that holds homologous chromosome pairs in synapsis during meiotic prophase I. In mammals, the proteasome activator subunit PA200 targets acetylated histones for degradation during somatic DNA double strand break repair and during histone replacement during spermiogenesis. We investigated the role of the testis-specific proteasomal subunit α4s (PSMA8) during spermatogenesis, and found that PSMA8 was localized to and dependent on the central region of the synaptonemal complex. Accordingly, synapsis-deficient mice show delocalization of PSMA8. Moreover, though *Psma8*-deficient mice are proficient in meiotic homologous recombination, there are alterations in the proteostasis of several key meiotic players that, in addition to the known substrate acetylated histones, have been shown by a proteomic approach to interact with PSMA8, such as SYCP3, SYCP1, CDK1 and TRIP13. These alterations lead to an accumulation of spermatocytes in metaphase I and II which either enter massively into apoptosis or give rise to a low number of aberrant round spermatids that apoptose before histone replacement takes place.

Author summary

Proteins within the cells that are unnecessary or damaged are degraded by a large protein complex named the proteasome. The proteins to be degraded are marked by a small protein called ubiquitin. The addition of a small modification (acetyl group) to some proteins also promotes their degradation by the proteasome. Proteasomal degradation of proteins

remaining data generated in this study are available in the Article and the Supporting Information files.

Funding: This work was supported by MINECO (BFU2017-89408-R) and by Junta de Castilla y Leon (CSI239P18). LGH and NFM are supported by European Social Fund/JCyLe grants (EDU/1083/2013 and EDU/310/2015) and YBC by a FPI grant from the MINECO (BS-2015-073993). IR was supported by MINECO (BFU2016-80370-P). JAS was supported by MINECO (BFU2014-53681-P). We appreciate the help of Mª Luz Sánchez García for the FACs analysis. The proteomic analysis was performed in the Proteomics Facility of Centro de Investigación del Cáncer, Salamanca, Grant PRB3 (IPT17/0019 - ISCIII-SGEFI / ERDF). CIC-IBMCC is supported by the Programa de Apoyo a Planes Estratégicos de Investigación de Estructuras de Investigación de Excelencia cofunded by the Castilla–León autonomous government and the European Regional Development Fund (CLC–2017–01). The funders had no role in study design, data collection and analysis, decision to publish, or preparation of the manuscript.

Competing interests: The authors have declared that no competing interests exist.

is an essential mechanism for many developmental programs including gametogenesis, a process whereby a diploid cell produces a haploid cell or gamete (sperm or egg). The mechanism by which this genome reduction occurs is called meiosis. Here, we report the study of a protein, named PSMA8 that is specific for the testis proteasome in vertebrates. Using the mouse as a model, we show that loss of PSMA8 leads to infertility in males. By co-immunoprecipitation-coupled mass spectroscopy we identified a large list of novel PSMA8 interacting proteins. We focused our functional analysis on several key meiotic proteins which were accumulated such as SYCP3, SYCP1, CDK1 and TRIP13 in addition to the known substrate of the spermatoproteasome, the acetylated histones. We suggest that the altered accumulation of these important proteins causes a disequilibrium of the meiotic division that produces apoptotic spermatocytes in metaphase I and II and also early spermatids that die soon after reaching this stage.

Introduction

Intracellular protein content is controlled through the balance between the rates of their synthesis and degradation. In eukaryotic cells, the bulk of the degradation is carried out by the ubiquitin-proteasome system (UPS). The proteasome is a multi-subunit complex that eliminates proteins, typically labeled with ubiquitin, by ATP-driven proteolysis [1]. Proteasome complexes comprise a cylindrical catalytic core particle (CP, 20S) and different regulatory particles (RPs, 19S) that regulate the access to the CP by capping it at either end [2]. The CP is composed of seven α-type subunits and seven β-type subunits arranged as a cylinder of four rings (α1–7, β1–7, β1–7, α1–7) [1, 3]. RPs are composed of 20 subunits and their association with the CP is ATP-dependent. There are four additional activators, the 11S regulator PA28α/β/γ and the ubiquitous PA200 (*Psme4*) regulator that stimulates protein degradation independently of ubiquitin [4] and plays a main role in acetylation-dependent degradation of somatic core histones during DNA repair and spermiogenesis [5, 6]. Hybrid proteasomes enclosing a RP at one end and an activator at the other end are also possible [7]. In addition, there are paralogs for three β-genes that are expressed only in the immunological system, which constitutes the immunoproteasome [8], and one β5t gene expressed exclusively in the thymus, which constitutes the thymoproteasome [9]. Finally, there is a meiotic paralog of the α4 subunit (*Psma7*), named α4s (*Psma8)* [10], which might provide substrate specificity and heterogeneity to the α4s-cotaning proteasome.

The proteolytic activity of the proteasome is regulated by the rate of protein ubiquitylation, but also by its association with E3 ubiquitin ligases and deubiquitinating enzymes that edit their potential substrates [11, 12]. The classical targets of the UPS are misfolded or damaged proteins and/or short-lived regulatory proteins, whose concentration is regulated by fine-tuning of their synthesis and degradation kinetics [13, 14]. Typical examples of the latter proteins are cyclins [15, 16]. More recently, it has been hypothesized but not proven that the ZMM complex (also known as the synapsis initiation complex) involved in meiotic homologous recombination is similarly regulated in the mouse [17, 18].

Meiosis is a fundamental process in sexually reproducing species that ensures the production of genetic diversity and the generation of haploid gametes from diploid progenitors [19]. This reduction in genome content is achieved by the physical connections between homologs by chiasmata [20], which are mediated by the repair of self-induced DNA double-strand breaks (DSBs) as crossing-overs (COs). Meiotic recombination takes place on proteinaceous core structures or axial elements (AEs) that scaffold the chromosomal DNA content and

physically connect (synapse) homologs through the assembly of the synaptonemal complex (SC) during prophase I [21].

The UPS regulates meiotic recombination in yeast and mouse *via* its physical association to AEs [17, 22]. Given the unknown function that the α4s-containing proteasome plays during spermatogenesis, we explored its function in the mouse. In this study, we show that PSMA8 is localized to and dependent on the central element of the SC, and promotes the assembly of the proteasome activator PA200. Accordingly, synapsis-deficient mice show delocalization of PSMA8. Also, *Psma8*-deficient mice are proficient in meiotic homologous recombination, but show alterations in the proteostasis of several key meiotic players including acetylated histones, SYCP3, SYCP1, CDK1 and TRIP13, which in turn leads to an aberrant meiotic exit, accumulation of apoptotic spermatocytes in metaphase I and II, and finally early spermatid arrest long before histone replacement takes place.

Results

PSMA8 is expressed in spermatocytes and its localization to the SC is dependent on synapsis

Psma8 mRNA expression in mouse tissues is almost exclusively restricted to the testis (GTEx database [23] and previous studies [10]). To elucidate the cell type in which PSMA8 is expressed, we examined by western blotting testis extracts at various postnatal ages during the first wave of spermatogenesis, which progresses more synchronously than in adult mice. PSMA8 expression (using a specific antibody against the PSMA8 C-terminus [10], see Fig 1A) was first detected at P12 and increased from P14 to P20. We also used a PSMA8-R2 antibody raised against the entire recombinant PSMA8 protein, which detected the expression of both PSMA7 (already apparent at P8, before meiosis has started) and PSMA8 (Fig 1A and S1 Fig). Analysis of testis cell lines (including spermatogonium GC1-spg, Leydig cell TM3, and Sertoli cell TM4 lines), revealed the expression of PSMA7 but not PSMA8 (Fig 1A). These results indicate that its expression is restricted to cells undergoing meiosis.

To explore the subcellular localization of PSMA8, we employed the R2 antibody (PSMA7/8) since the PSMA8 C-terminus antibody did not produce any specific labeling. Double immunolabeling of PSMA8 with the AE protein SYCP3 or with SYCP1, the transverse filament protein essential for synapsis (Fig 1B and S2 Fig), revealed PSMA7/8 presence at the central region of the synaptonemal complex (super resolution imaging, Fig 1B). We validated this localization by *in vivo* electroporating [24] an expression plasmid encoding GFP-PSMA8 in the testis (Fig 1C). These results agree with the recent localization of the proteasome to the chromosome axes [17].

To investigate the possible dependence of PSMA8 localization on synapsis, we analyzed synaptic mutants with mild (*Rec8*$^{-/-}$ [25]) and severe (*Six6os1*$^{-/-}$ [24]) phenotypes. Mutants for the meiotic cohesin REC8 show pseudo-synapsis between sister chromatids [25], and PSMA8 was detected at these atypical synapsed-like regions (Fig 1D). In mice lacking the novel central element protein SIX6OS1, in which AEs are physically separated and unsynapsed at pachynema [24], PSMA8 signal was not restricted to their AEs and showed a broader and more disperse labeling (Fig 1D). These results indicate that PSMA8 localization to the SC central region is consequently dependent on the assembly of the SC.

Male mice lacking PSMA8 are infertile

To study the role of PSMA8, we generated a targeted mutation in exon 1-intron 1 of the murine *Psma8* gene by CRISPR/Cas9 genome editing (S3A and S3B Fig). Homozygous mutant

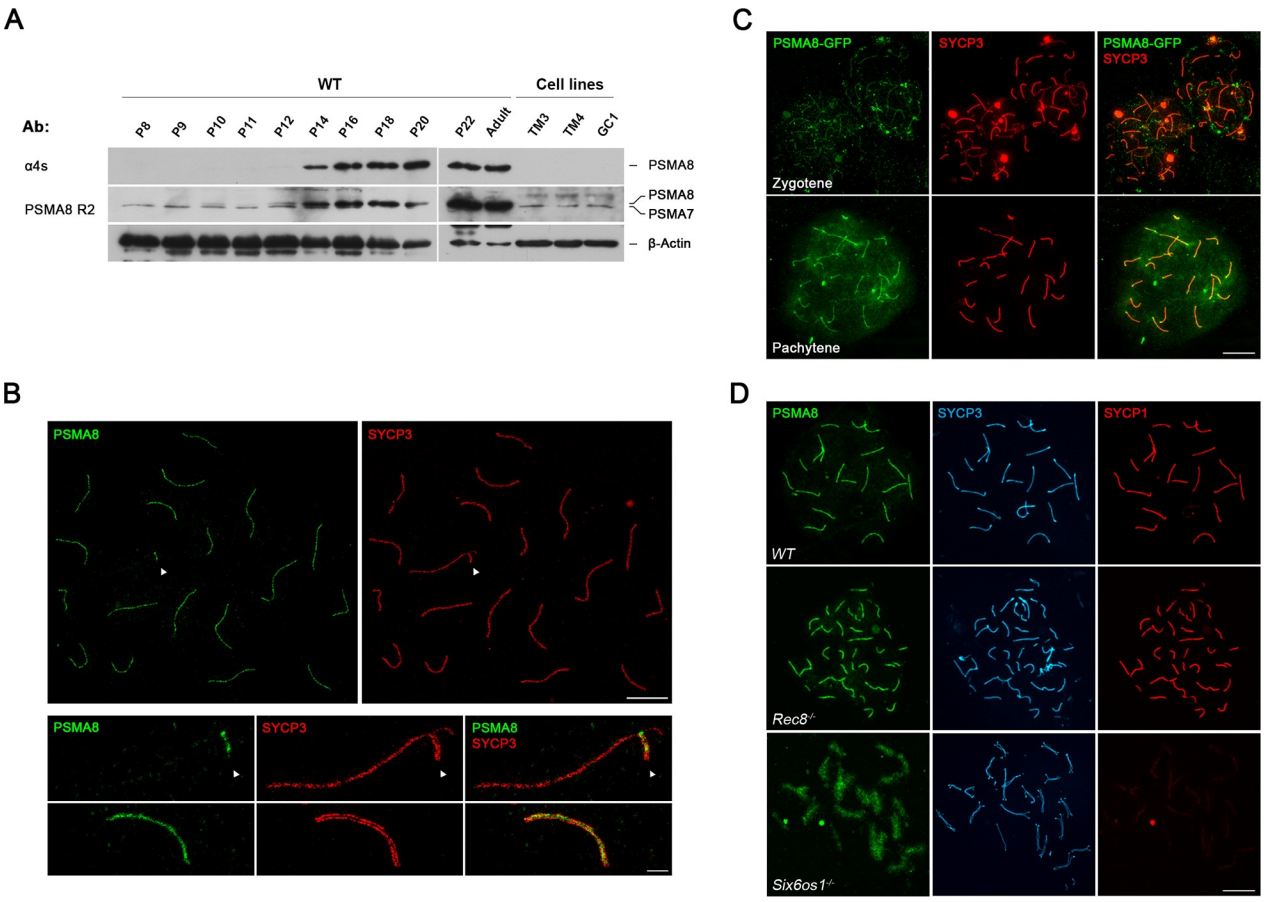

Fig 1. Expression analysis and localization of PSMA8 in the mouse. (A) Western blot analysis of protein extracts from mouse testis (from P8 to adult) and cell lines (TM3, TM4 and GC1) with a specific antibody against the C-terminal (α4S) and whole recombinant PSMA8 protein (PSMA8-R2). β-Actin was used as loading control. The corresponding bands to PSMA8 and PSMA7 are indicated in the right of the panel. Note that from P16 to adult the intensity of both PSMA8 and PSMA7 bands impedes its independent observation. (B) Double immunolabeling of spermatocyte spread preparations with PSMA8 (green) and SYCP3 (red) by Stimulated emission depletion (STED) microscopy, showing that PSMA8 localizes to the central region of the SC. PAR (pseudo-autosomal region) of the XY bivalent is indicated with an arrow. (C) Immunolocalization of PSMA8 in mouse testis after *in vivo* electroporation of a plasmid encoding a protein fusion of PSMA8 with GFP (GFP-PSMA8). PSMA8 was detected with anti-GFP antibody (green) and endogenous SYCP3 was detected using mouse anti-SYCP3 (red). (D) Triple labeling of PSMA8 (green), SYCP3 (blue) and SYCP1 (red) in *Rec8*$^{-/-}$ and *Six6os1*$^{-/-}$. PSMA8 is detected in the pseudosynapsed AEs of the meiotic *Rec8* cohesin mutant but is absent from the unsynapsed AEs in *Six6os1*$^{-/-}$ spermatocytes. Bar in panels, 5 μm (B, upper panel), 1 μm (B, lower panel) and 10 μm (C, D).

https://doi.org/10.1371/journal.pgen.1008316.g001

testes showed no PSMA8 protein expression by western blotting when analyzed using two independent polyclonal antibodies (S3C Fig). Immunofluorescence analysis of PSMA8 expression (R2 antibody, S3D Fig) revealed a weaker signal in the SC of the mutant spermatocytes than in WT spermatocytes (51% less; 4.22±1.9 WT vs 2.05±1.7 KO), likely representing PSMA7 detected by the R2 antibody (also observed in the western blot; S3C Fig). These results indicate that the generated mutation is a null allele of the *Psma8* gene (herein termed *Psma8*$^{-/-}$).

Mice lacking PSMA8 did not display any somatic abnormalities; however, male but not female mice were sterile (S1 Table). Indeed, *Psma8* mutation resulted in a reduction of the testis weight (63.09% decrease; N = 6) and the absence of spermatozoa in the epididymides (Fig 2A and 2B). Histological analysis of adult *Psma8*$^{-/-}$ testes revealed the presence of apparently normal numbers of spermatogonia, spermatocytes, Sertoli cells and Leydig cells (Fig 2B).

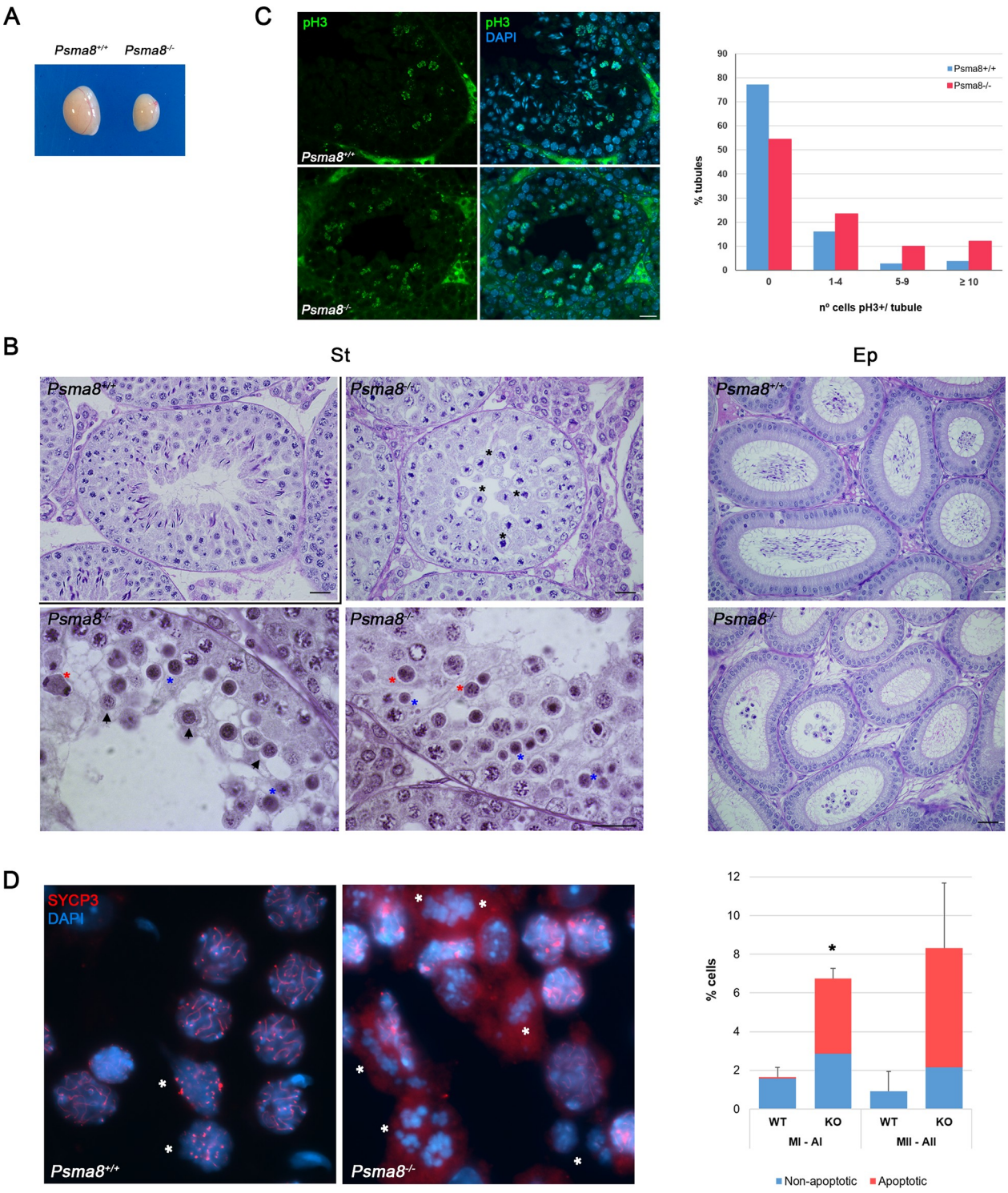

Fig 2. PSMA8 deficiency leads to azoospermia. (A-B) Genetic ablation of *Psma8* leads to a reduction of the testis size (A) (n = 6, WT and KO; Welch´s *t*-test analysis: $p<0.0001$), and (B) the accumulation of metaphase I (black asterisks), apoptotic meiotic division (red asterisks), round spermatids entering apoptosis (arrowheads), and apoptotic round spermatids (blue asterisks) in PAS stained testis sections. The spermatogenic arrest leads to empty epididymides and azoospermia. Bar in upper panels 100 μm, lower panels 200 μm and in right panels, 5 μm. (**St**) Seminiferous tubules and (**Ep**) Epididymides. (C) Immunofluorescence analysis of p-ser10-H3 (green) of paraffin sections of *Psma8*$^{+/+}$ and *Psma8*$^{-/-}$ tubules. Nuclei were counterstained with DAPI. Bar represents 10 μm. The diagram represents the quantification of the fraction of tubules showing the indicated number of metaphase I/II. Number of tubules counted for each genotype is expressed in S2B Table. (D) Low magnification view of a

representative squash preparation of seminiferous tubules showing the accumulation of metaphases I and metaphases II in knock-out *Psma8* in comparison with a representative wild-type view. The identity of metaphases I /metaphases II (asterisks) was confirmed by the immunolabeling of SYCP3 (red) in squash preparations. Chromosomes were counterstained with DAPI (blue). The diagram represents the percentage of spermatocytes at metaphase I and II (normal and apoptotic) in relation with the total number of spermatocytes from *Psma8*$^{+/+}$ and *Psma8*$^{-/-}$ tubules (right). Quantification and number of cells analyzed are described in S2C Table. Welch´s *t*-test analysis: * $p<0.01$; ** $p<0.001$; *** $p<0.0001$.

https://doi.org/10.1371/journal.pgen.1008316.g002

Mouse seminiferous tubules can be classified from epithelial stage I to XII by determining the groups of associated germ cell types in histological sections. Following these criteria, we found that spermatogenesis in the mutant testes proceeded normally up to diplotene in epithelial stage XI. However, the proportion of tubules at stage XII was more than 2-fold increased in the mutant sections (12.5% in mutants versus 5.4% in WT, S2A Table). Given that spermatocytes in meiotic divisions were seen to occur at epithelial stage XII, we used p-ser10-H3 (pH3) staining to analyze the number of metaphase I and II cells present in these tubules, finding an increase in the mutant (Fig 2C and S2B Table). Quantitative analysis of seminiferous tubules in squashed preparations confirmed the increase in the number of metaphase I and metaphase II cells as compared with WT testes (77% and 89% respectively, Fig 2D and S2C Table). Moreover, a large proportion of these metaphases were positive for Caspase-3 and TUNEL indicating apoptosis (Figs 2D, 3A and 3B and S2C Table).

Together with the accumulation of apoptotic meiotic divisions, other apoptotic cells could be also observed that, from their size and molecular markers of the acrosome and chromatoid body, were round spermatids (Fig 3C and S4 Fig). Indeed, seminiferous tubules in PSMA8-deficient testes sometimes contained a few surviving round spermatids. However, these round spermatids were unable to form a proper acrosome but did accumulate some PAS positive material. Apoptotic round spermatids were also seen and no elongating spermatids were observed (Fig 2B). We corroborated that round spermatids were arrested at early stages by immunolabeling for H2AL2. H2AL2 is a transition histone essential for the first replacement of histones by TNP1 and TNP2 before protamine incorporation [26]. H2AL2 was absent from mutant spermatids (S5A Fig). We also used FACs analysis of whole cells from seminiferous tubules to verify this analysis. The results obtained confirmed the presence of a small haploid compartment in *Psma8*$^{-/-}$ testes (Fig 3D and S5B Fig). We conclude from these results that PSMA8 deficiency causes the accumulation of spermatocytes in metaphase I and II which either enter massively into apoptosis or give rise to a low number of aberrant round spermatids that finally apoptose long before histone replacement takes place.

Psma8-deficient spermatocytes show normal synapsis/desynapsis and DSB repair but have abnormal metaphases I and II

Metaphase I accumulation can occur either because of a failure to enter anaphase or because of some event taking place during prophase (SC formation, DBSs repair or chromosome recombination) that aberrantly triggers a checkpoint-mediated delay.

To test this, we first analyzed the assembly/disassembly of the SC by monitoring the distribution of SYCP1, as co-labeling of SYCP3 and SYCP1 highlights regions of synapsis in spermatocytes. We did not observe any differences in this process from zygonema to diakinesis (S6 Fig).

We next studied the kinetics of DSB repair during meiosis. Meiotic DSBs are generated by the nuclease SPO11 and are then resected to form ssDNA ends that invade into the homologous chromosome. DSBs are marked by the presence of phosphorylated H2AX (γ-H2AX) [27]. The distribution of γ-H2AX in mutant spermatocytes was similar to that found in WT cells at prophase I (S7A Fig and S3 Table). We also did not observe any differences in the

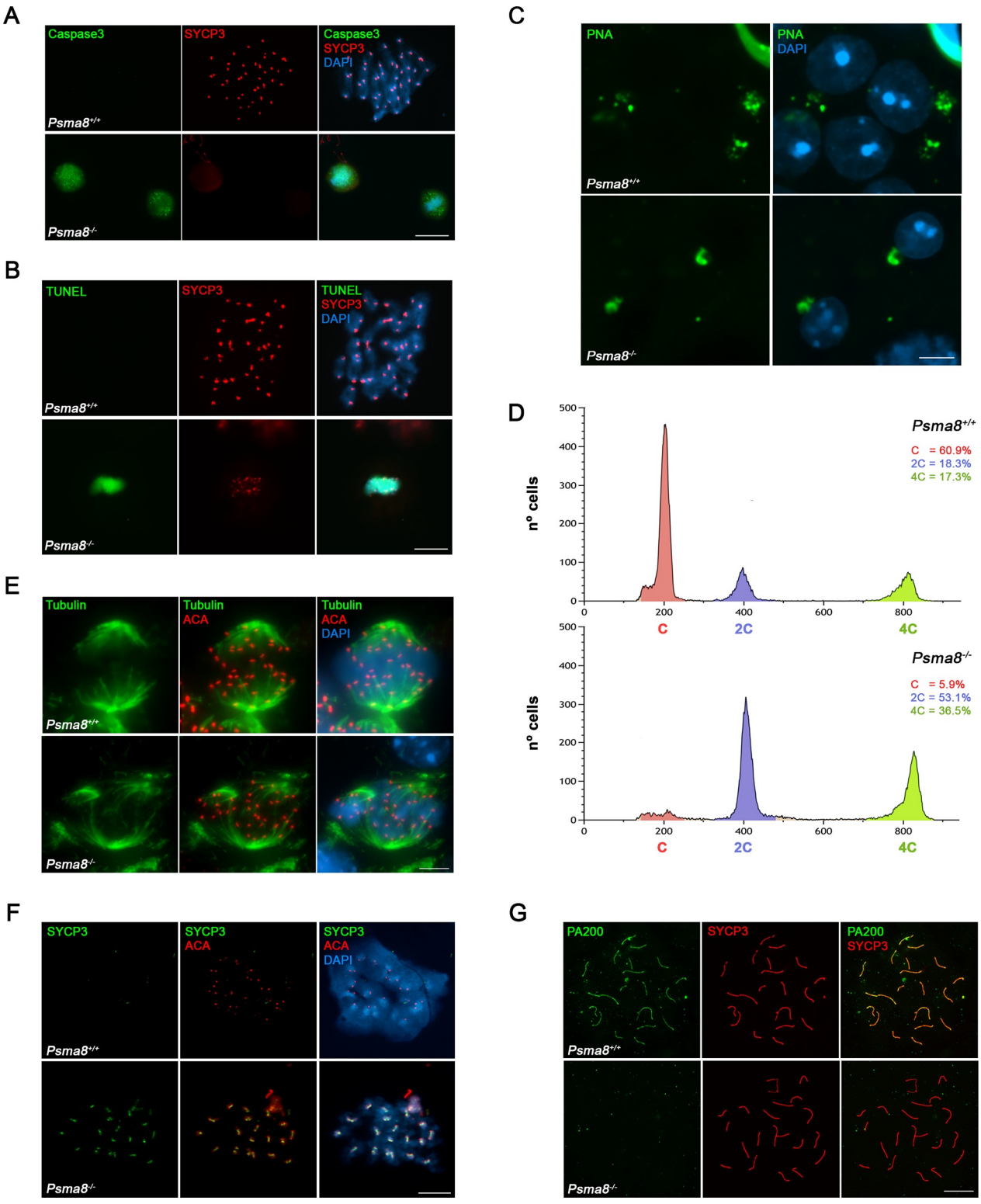

Fig 3. Apoptosis, FACs and aberrant metaphase II and spermatid cells in *Psma8*-deficient mice. (A) Double immunolabeling of Caspase3 (green) and (B) TUNEL (green) with SYCP3 (red). Non-apoptotic metaphase I cells from *Psma8*$^{+/+}$ show absence of green staining whereas apoptotic metaphases I from *Psma8*$^{-/-}$ show intense Caspase-3 and TUNEL labeling. Chromatin was counterstained with DAPI. (C) Acrosome positive labeling of round spermatids by PNA staining (green). (D) FACs analysis of cells from whole seminiferous tubules from wild type and *Psma8*$^{-/-}$ showing in both genotypes (N = 2) the presence of 4C, 2C and 1C compartment as a result of the early spermatid arrest. Source data

describing the gating strategy is shown in S5B Fig. (E) Double immunolabeling of metaphase I cells with tubulin (green) and ACA (red) showing normal (*Psma8*$^{+/+}$) and abnormal spindles (*Psma8*$^{-/-}$). (F) Double immunolabeling of SYCP3 (green) with ACA (red) in wild-type and *Psma8*$^{-/-}$ spermatocytes at metaphase II which shows aberrant accumulation of SYCP3 at the centromeres. (G) Double immunolabeling of PA200 (green) and SYCP3 (red) in chromosome spreads. PA200 is detected at the chromosome axes of the autosomal and XY bivalents during pachytene in wild type spermatocytes in contrast to the absence of labeling in *Psma8*$^{-/-}$ spermatocytes. Bar in panels (C, E) 5 μm and 10 μm (A, B, F and G).

https://doi.org/10.1371/journal.pgen.1008316.g003

distribution of RAD51, a recombinase that promotes homologous strand invasion [28], (S7B Fig and S3 Table). Because defective DNA repair ultimately abrogates CO formation [29] and because of the involvement of ubiquitylation / sumoylation in CO designation [30], we analyzed the distribution of MLH1 foci [31], a mismatch repair protein (marker of crossover sites) that functions in the resolution of joint molecules at the end of crossover formation [32]. We found a similar value between the KO (24.9±0.9 foci) and the WT (24.3±1.1 foci; S7C Fig and S3 Table). These results indicate that the repair of meiotic DSBs and synapsis/desynapsis proceed normally during prophase I in the absence of PSMA8, and is not responsible for the observed metaphase I accumulation.

We also analyzed the morphology of the metaphase I / II cells by staining for tubulin (spindle) and SYCP3. The results showed an aberrant morphology, the presence of multipolar spindles (Fig 3E), and also a striking aberrant labeling of SYCP3 at the centromeres of metaphase II chromosomes (SYCP3 labeling is barely visible in metaphase II sister kinetochores in WT cells, Fig 3F). Finally, the arrested round spermatids showed the presence of multiple patches of heterochromatin after DAPI staining (Fig 3C and S4 Fig, chromocenter fragmentation), suggesting abnormal chromosome segregation or cytokinesis.

PSMA8 deficiency abolishes H4ac turnover from late prophase to round spermatids

During spermiogenesis, most of the histones are replaced by basic transition proteins, and ultimately by protamines, facilitating chromatin compaction. Hyperacetylation of core histones during this process, and especially the acetylation of H4K16, is assumed to play a pivotal role in the initiation of histone displacement and chromatin ultracondensation [33, 34]. The proteasome activator subunit PA200 targets acetylated histones for degradation during histone replacement [5].

The core subunit PSMA8 co-immunoprecipitated PA200 (S4 Table). Given the stoichiometric relationship between the CP and RP, we analyzed the expression of PA200 by immunofluorescence in the absence of PSMA8. Whilst PA200 decorated the AEs of WT spermatocytes, we failed to observe any signal in the AEs of mutants (Fig 3G and S8 Fig). In addition, we were not able to detect PA200 by mass spectrometry analysis of PSMA7/8 immunoprecipitation of *Psma8*-deficient testis extracts (see section Purification of PSMA8-interacting proteins, S4 Table). These results indicate that PSMA8 is necessary or promotes the assembly of PA200 to the CP. Thus, within the limits of detection, the deficiency of *Psma8* leads to a drastic decrease of PA200.

To understand the acetylated-dependent degradation of histones by the proteasome [5], we measured the acetylation status of three core histones, H2AK5ac, H3ac and H4ac (pan-H4ac and H4K16ac) in chromosome spreads by double immunolabeling for SYCP3 and the corresponding acetylated histone (Fig 4A–4D and S9–S12 Figs). This procedure enables a more precise staging of the spermatocytes and is a more efficient mean to quantitate signals than peroxidase immunostaining of testis sections [5]. The loss of PSMA8 led to the accumulation of H2AK5ac, H3ac, H4ac and H4K16ac, albeit to different degrees. Results showed that the levels of H2AK5ac, H3ac, H4ac and H4K16ac were moderately higher in *Psma8*$^{-/-}$ cells, with a

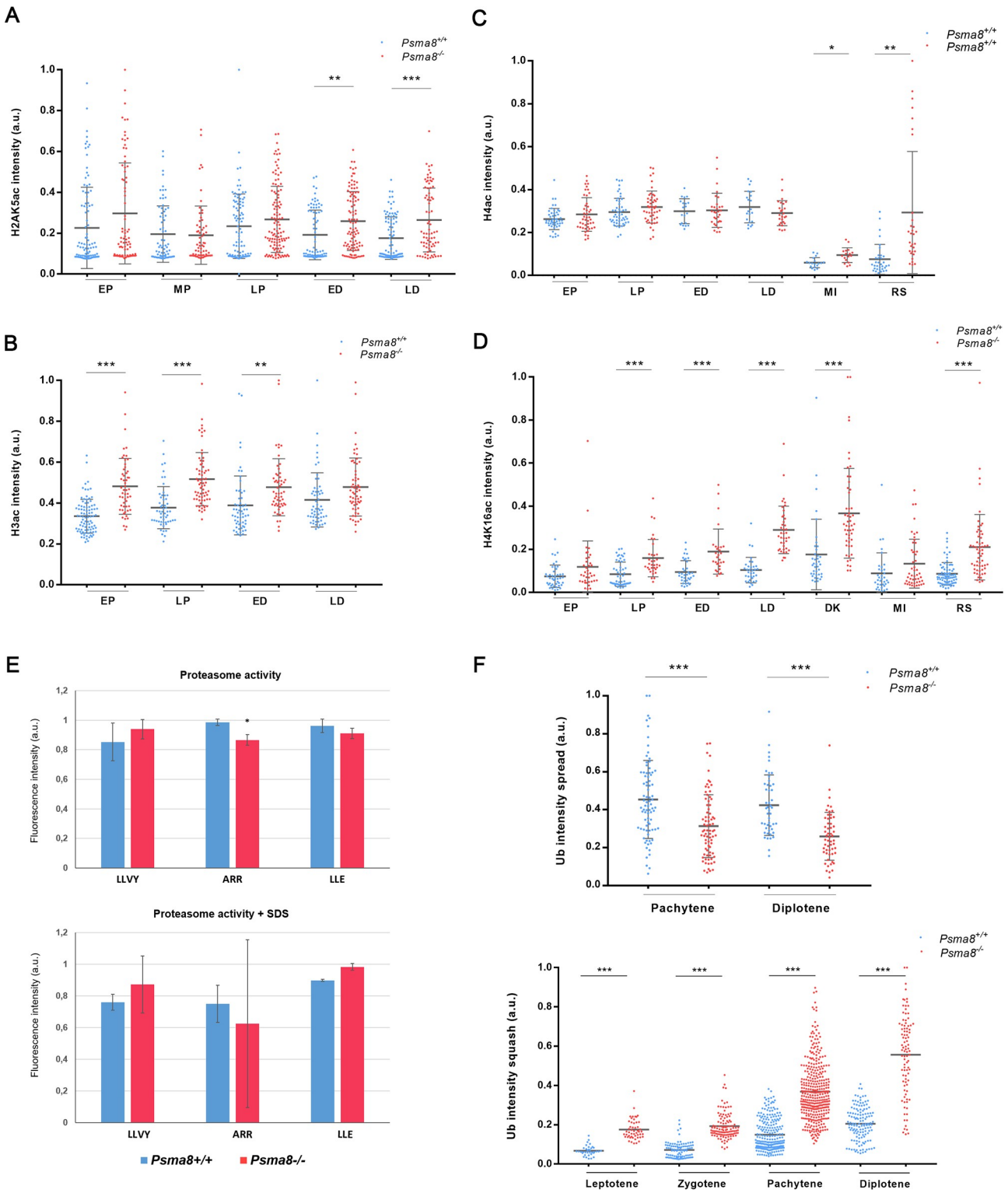

Fig 4. Histone acetylation, nuclei ubiquitylation and proteasome activity in PSMA8-deficient mice. (A-D) Plots represent the quantification of the fluorescence intensity from *Psma8*$^{+/+}$ and *Psma8*$^{-/-}$ spermatocytes at early pachytene (EP), mid pachytene (MP), late pachytene (LP), early diplotene (ED), late diplotene (LD), diakinesis (DK), metaphase I (MI) and round spermatid (RS) corresponding to the immunolabeling of (A) H2AK5ac, (B) H3ac, (C) H4ac, and (D) H4K16ac. Representative figures for each immunofluorescence are presented in S9–S12 Figs. (E) Proteasome activity of *Psma8*-deficient testis. 100 μg of protein from whole testis extracts of *Psma8*$^{+/+}$and *Psma8*$^{-/-}$ mice were inoculated into 96-well plate and the proteasome peptidases activities were measured. The enzymatic activities relative to WT are shown. (F) Plots represent the quantification of the

fluorescence intensity from *Psma8*$^{+/+}$ and *Psma8*$^{-/-}$ spread (upper) and squashed (lower) spermatocytes. Welch´s *t*-test analysis: * $p<0.01$; ** $p<0.001$; *** $p<0.0001$.

https://doi.org/10.1371/journal.pgen.1008316.g004

relative increase at late prophase I (Fig 4A–4D and S9–S12 Figs). We failed to detect staining for H2AK5ac and H3ac in spermatocytes in late diakinesis and round/arrested spermatids. In contrast, pan-H4ac and H4K16ac also labeled metaphase I chromosomes, interkinesis nuclei and round/arrested spermatids, with greater intensity in mutant than in WT cells (Fig 4C and 4D and S11 and S12 Figs). The accumulation of acetylated histones during prophase I and particularly of H4ac and H4K16ac in the arrested round spermatids suggests that the PSMA8--containing proteasomes are involved in the acetylation-dependent degradation of histones.

Proteasomal activity in *Psma8*-deficient mice

We next investigated the biochemical activity of testis extracts lacking PSMA8-containing proteasomes by measuring chymotrypsin-like activity (corresponding to the catalytic subunit β1), caspase-like activity (corresponding to β5) and trypsin-like activity (β3) by a standard fluorogenic assay [35] in the presence and absence of SDS (activated proteasome). Results showed that proteasomal activity in *Psma8*-deficient testis extracts was not noticeably different from that in WT extracts. Indeed, the trypsin-like activity was the only proteolytic function with a modest reduction in the KO (Fig 4E). Overall, these results show that the general proteasome activity of the *Psma8*-deficient testis is not radically changed, which is likely due to the presence of PSMA7-dependent CPs (see dataset 1 in [36]).

To ascertain the degree of activity *in vivo*, we first investigated the steady-state levels of protein ubiquitylation in testis during mouse meiosis. Using immunofluorescence, we analyzed spermatocytes obtained from spreads and squashed preparations with ubiquitin antibodies (Fig 4F and S13 Fig). The results showed a slight decrease of chromatin bound ubiquitylated proteins but an increase in the soluble fraction of ubiquitylated proteins during prophase I (Fig 4F and S13 Fig). These results are partially in agreement with the observed increase in the ubiquitylation state of cultured spermatocytes treated with the proteasome inhibitor MG132 (18), and suggest a specific function of the PSMA8-containing proteasomes in the controlled degradation of ubiquitylated proteins during spermatogenesis.

Purification of PSMA8-interacting proteins

The composition of the CP and its RPs has previously been established by mass-spectrometric analysis of crude preparation of proteasomes from whole testes [37]. To better understand the molecular mechanism underlying the mutant phenotype, we purified PSMA7/8-interacting proteins by single-step affinity chromatography (see Material and methods for a detailed description). Most of the canonical subunits of the CP and RP were present within the more than 596 proteins of the PSMA8 proteome (S5 Table, using a conservative cut-off, see methods). In agreement with previous results, among the two activators of the testis-specific proteasome detected (PA200 and Pa28γ) [5], PA200 was the most abundant. In contrast to previous observations, we were unable to detect Pa28α and Pa28β or the inducible catalytic subunits of the immunoproteasome (β1i, β2i and β5i) [5], suggesting a very low abundance or absence. We could not detect PA200 as an interacting protein of PSMA7/8 in testis extracts from *Psma8*-deficient testes (S4 Table).

Among the novel proteasome-interacting proteins (PIPs) detected were chaperones including CCT6b and CCT2, ubiquitin ligases (TRIP12, NEDD4, TRIM36 and RAD18), and novel ubiquitin specific proteases (USPs) such as USP9X, USP34, USP5 and USP47 (S6 Table). We

studied the proteins enriched in the immunoprecipitation through functional (gene ontology, GO) and pathway analysis (KEGG). The top GO and KEGG results were related to the proteasome and to ribonucleoproteins. Pathway analysis showed links to spermatogenesis, cell cycle, and meiosis (see S1 Text), in accordance with the observed mutant phenotype.

Interestingly, we identified meiotic proteins *a priori* unrelated to the UPS such as DAZL (deleted in azoospermia), SPAG1 (Sperm-associated antigen 1), SPATA5/20 (Spermatogenesis-associated protein 5/20), the tudor domain proteins TDRD1/6/9, MAEL (repressor of transposable elements), and RNF17. These PIPs could represent proteins captured during ubiquitin-dependent targeted degradation [38] and/or proteins interacting *via* ubiquitin-independent proteasomal degradation, as has been shown for the related subunit α4/PSMA7 [39]. Altogether, the list of novel PIPs included novel potential readers, erasers and writers of the ubiquitin code [40] of the testis-specific proteasome, reflecting its complexity. Among these PIPs, we focused our attention on the following candidates for their role in chromosome segregation and synapsis: SYCP1, TRIP13, TEX30, PIWIL1, PIWIL2 and CDK1 (S6 Table).

Among the possible interactors, we first evaluated the transverse filament protein SYCP1. Because *Sycp1* mutant mice are infertile but otherwise healthy [41], we analyzed the interaction of SYCP1 with PSMA8 and its localization in mutant meiosis. We co-transfected *Sycp1* with *Psma8* in HEK293T cells and we detected co-immunoprecipitation between SYCP1 and PSMA8 (Fig 5A). Despite the observation that SYCP1 is properly loaded to the SC and removed from desynapsed regions (S6 Fig), we observed an abnormal accumulation of SYCP1 in *Psma8*-deficient metaphase I cells, (Fig 5B). These results suggest defective degradation of SYCP1 with very likely detrimental functional consequences in the exit of meiosis.

We next extended the validation analysis of the remaining candidate interactors by co-immunoprecipitation with PSMA8, making use of the same heterologous system of HEK293T cells. These included TEX30, PIWIL1, PIWIL2, CDK1 and TRIP13. All protein-protein interaction assays carried out were negative (S14A Fig) with the exceptions of the cyclin dependent kinase CDK1 and the AAA-ATPase TRIP13 (AAA-ATPases associated with diverse cellular activities; see Figs 6A and 7A). Because of the relevance of CDK1 in metaphase transition, we first determined the expression levels of CDK1 by immunofluorescence. The results showed that more CDK1 but not the related kinase CDK2 [42] could be detected in the centromeres of metaphase I chromosome from mutant cells (Fig 6B and S15A Fig; KO 0.31±0.2 vs 0.19±0.1 WT; an increase of ~ 40%). To determine whether the increased level of CDK1 corresponded to its active or inactive phosphorylated form, we used an antibody against CDK1-Tyr15-p (inactive form, Fig 6C). The results showed no differences in the labeling at the centromeres of the metaphase I chromosomes, and therefore a decrease in phospho-CDK1/total CDK1 ratio in mutant cells. Given that CDK1 must be complexed with cyclin B1 to be active, we reasoned that if higher levels of active CDK1 are present, cyclin B1 would be similarly increased. Results showed an increase of cyclin B1 at the centromeres of metaphase I chromosomes (Fig 6D). This result was congruent with the increased amount of CDK1 and CyclinB1 observed by western blot and in squashed seminiferous tubules (Fig 6E and S15B and S15C Fig). Overall, these findings suggest that loss of PSMA8 causes an increase of CDK1 / CyclinB1 which would cooperate in the accumulation of metaphase I / metaphase II that ultimately results in apoptotic metaphase plates.

We also analyzed the distribution of TRIP13, a pleiotropic ATPase that participates in meiotic DNA repair and chromosome synapsis through HORMAD interaction and somatic spindle assembly checkpoint (SAC) proficiency through MAD2 interaction [43–46]. We first performed immunofluorescence analysis of TRIP13 in *Psma8*-deficient and WT spermatocytes. Results using two independent antibodies showed robust labeling of the telomeres from zygonema (two dots) to pachynema (fused to a single dot) in WT cells, which declined from

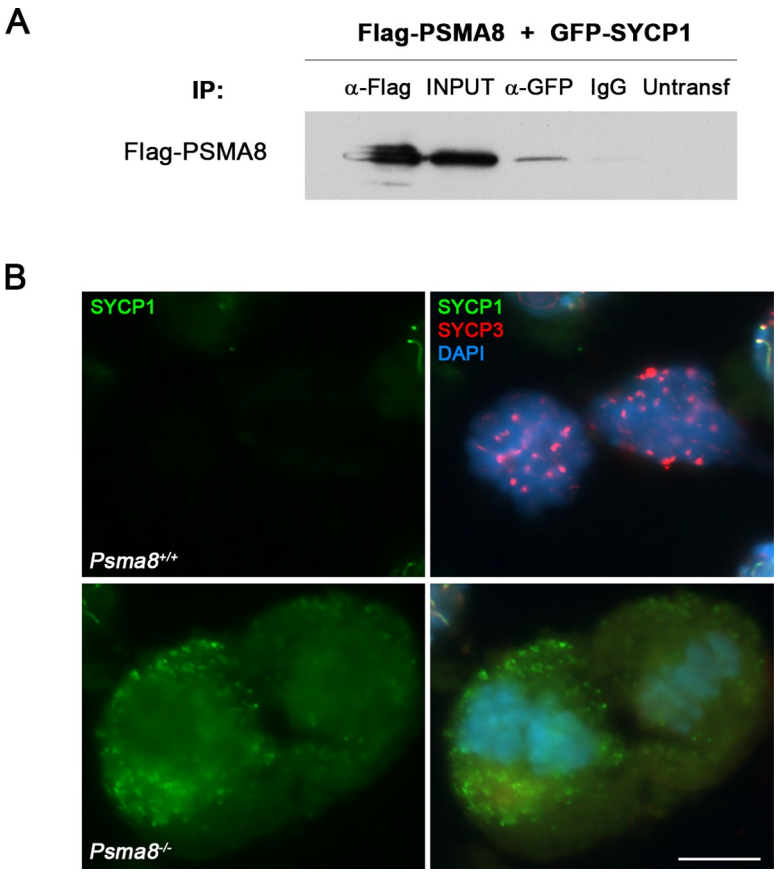

Fig 5. SYCP1 interacts with PSMA8 and is accumulated in *Psma8*-deficient metaphase I cells. (A) HEK293T cells were transfected with Flag-PSMA8 and GFP-SYCP1. Protein complexes were immunoprecipitated overnight with either an anti-Flag or anti-EGFP or IgGs (negative control), and were analyzed by immunoblotting with the indicated antibody. PSMA8 co-immunoprecipitates with SYCP1. (B) Double immunolabeling of squashed tubules with SYCP1 (green) and SYCP3 (red) in wild-type and *Psma8*$^{-/-}$ spermatocytes at metaphase I. Chromatin was stained with DAPI (blue). Bar in panel, 10 μm.

https://doi.org/10.1371/journal.pgen.1008316.g005

diplonema to diakinesis. The staining pattern was similar but enhanced in mutant spermatocytes (Fig 7B). However, the staining pattern of TRIP13 at metaphase I differed between WT and mutant cells. Specifically, it was detected at the kinetochores of *Psma8*$^{-/-}$ spermatocytes but was absent in WT cells (Fig 7B). This labeling pattern at the metaphase I kinetochores resembles TRIP13 staining in somatic cells [47]. These results thus suggest that TRIP13 accumulates in the absence of a functional PSMA8-containing proteasome.

We next analyzed several downstream effectors of TRIP13, HORMAD1, HORMAD2, and the mitotic checkpoint protein MAD2 [48–50]. No differences were observed in the HORMAD1/2 labeling pattern between WT and mutant cells (S16 Fig). It has been shown in *C. elegans* that in the absence of TRIP13, MAD2 recruitment to kinetochores is delayed and that in addition to its role in checkpoint silencing, TRIP13 also contributes to spindle checkpoint activation [50]. It could thus be argued that an excess of TRIP13 would increase MAD2 loading to kinetochores thereby delaying mitotic exit. We confirmed this prediction and found that MAD2 expression at the kinetochores was enhanced in *Psma8*$^{-/-}$ spermatocytes (Fig 7C), further validating a functional consequence of TRIP13 accumulation at the kinetochores.

In order to validate the substrate specificity of the PSMA8-containing proteasome in protein degradation, we analyzed the expression levels of the separase inhibitor securin (PTTG1),

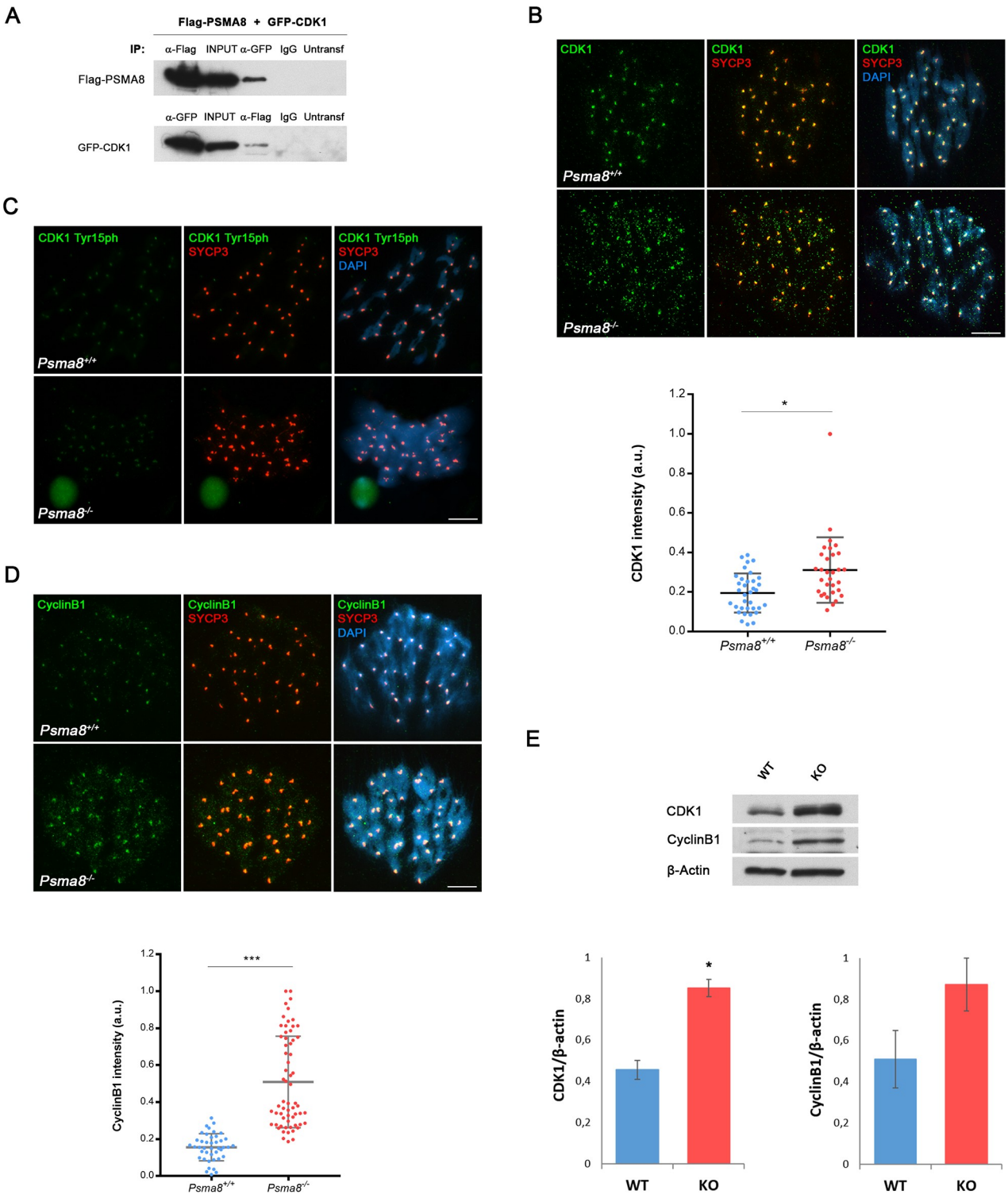

Fig 6. PSMA8 deficiency causes an accumulation of CDK1 and Cyclin B1 in spermatocytes. (A) HEK293T cells were transfected with Flag-PSMA8 and GFP-CDK1. Protein complexes were immunoprecipitated with either an anti-Flag or anti-EGFP or IgGs (negative control) and were analyzed by immunoblotting with the indicated antibody. PSMA8 co-immunoprecipitates with CDK1 (as well as reciprocally). (B) Double labeling of endogenous CDK1 (green) and SYCP3 (red) in mouse spermatocytes at metaphase I. Chromatin was stained with DAPI (blue). During metaphase I, CDK1 labels in a slight and disperse way the chromosomes and in a more intensely fashion the centromeres of bivalents. This labeling pattern is enhanced in a normal *Psma8*-deficient metaphase I. Plot under the panel represents the quantification of the fluorescence intensity from *Psma8*$^{+/+}$ and *Psma8*$^{-/-}$ metaphase I cells. (C) Double labeling of endogenous CDK1-Tyr15phosphorylated (green) and SYCP3 (red) in mouse spermatocytes at

metaphase I showing similar expression levels in *Psma8*$^{+/+}$ and *Psma8*$^{-/-}$. Chromatin was stained with DAPI (blue). (D) Double labeling of endogenous cyclin B1 (green) and SYCP3 (red) in mouse spermatocytes at metaphase I showing higher expression levels in *Psma8*$^{-/-}$. Plot under the panel represents the quantification of the fluorescence intensity from *Psma8*$^{+/+}$ and *Psma8*$^{-/-}$ metaphase I cells. Welch´s *t*-test analysis: * $p<0.01$; ** $p<0.001$; *** $p<0.0001$. (E) CDK1 and CyclinB1 were measured by western blot analysis of protein extracts from whole testis of *Psma8*$^{+/+}$ (WT) and *Psma8*$^{-/-}$ (KO) (n = 2 mice). Bar in panels, 10 μm. Welch´s *t*-test analysis: * $p<0.05$; ** $p<0.001$; *** $p<0.0001$.

https://doi.org/10.1371/journal.pgen.1008316.g006

a well-known substrate of the somatic proteasome. Immunofluorescence analysis showed similar levels of PTTG1 in *Psma8*$^{-/-}$ and WT spermatocytes (S17 Fig). This result suggests that PSMA8-containing proteasomes are not involved in the degradation of classical ubiquitylated substrates degraded by the somatic proteasome.

PSMA8 interacts with proteins of the synaptonemal complex

To investigate the molecular basis of PSMA8 localization in the SC, and considering the alteration of SYCP3 and SYCP1 in *Psma8*$^{-/-}$ spermatocytes (Fig 3F and Fig 5B), we used a candidate gene approach to identify additional putative interactors of PSMA8. We co-transfected *Psma8* with cDNAs encoding each of the known central element proteins (SIX6OS1, SYCE1, SYCE2, SYCE3, and TEX12), and the AE protein SYCP3. As positive controls, we exploited the well-known interaction between SYCE2 and TEX12 [51] (S14C Fig). Surprisingly, we detected specific co-immunoprecipitation of PSMA8 with SIX6OS1 and SYCE3 (Fig 8A and S14B Fig). We were unable to immunoprecipitate transfected SYCP3 (using several tags or antibodies against SYCP3), likely due to the highly complex structures of transfected SYCP3, which prevented to perform co-immunoprecipitation experiments. Because SYCP3 forms filamentous structures in the cytoplasm of transfected cells, termed polycomplexes [52], co-expression of an interacting protein with SYCP3 may lead to its recruitment to polycomplexes [24], an indication of protein interaction. Indeed, we obtained self assembled higher structures when *Psma8* was co-transfected with *Sycp3* (Fig 8B). This SYCP3-dependent cytological interaction was not observed when *Psma7* was co-transfected (Fig 8B), further validating the specificity of the interaction given the extensive protein similarity between both PSMA8 and PSMA7 (92%). To validate this interaction *in vivo*, we performed a detailed analysis of SYCP3 in mouse mutant squashed spermatocytes, a procedure in which no solubilization or protein extraction is performed. We observed SYCP3 aggregates/polycomplexes in the *Psma8*-deficient spermatocytes during prophase I and metaphase I / II (Fig 8C and 8D and S7 Table). SYCP3 accumulated in metaphase II chromosomes as abnormal SYCP3 labeling at the centromeres between sister kinetochores and as aggregates in the cytosol (Fig 3F and Fig 8D). Global accumulation of SYCP3 was also observed by western blot of whole testis under high denaturing conditions (Fig 8E) [53]. Interestingly, it has been previously shown that cultured spermatocytes chemically treated with the proteasome inhibitor MG132 form SYCP3 aggregates [17]. Overall, our results suggest that SYCP3 is targeted for degradation by the PSMA8-containing proteasome and that in the absence of PSMA8 its accumulation could mediate, at least in part, the arrest and apoptosis of spermatocytes.

Discussion

The testis-specific proteasome is one of the three tissue-specific proteasomes identified in mammals (together with the immunoproteasome and the thymoproteasome); however, little is known about its biochemical and physiological function. The groundbreaking work of Xiao-Bo Qiu and colleagues showing the acetyl-histone preference of the PA200 subunit of the proteasome [5] has provided novel insights into the proteasome-dependent degradation of non-ubiquitylated proteins and led to the designation of spermatoproteasome to the

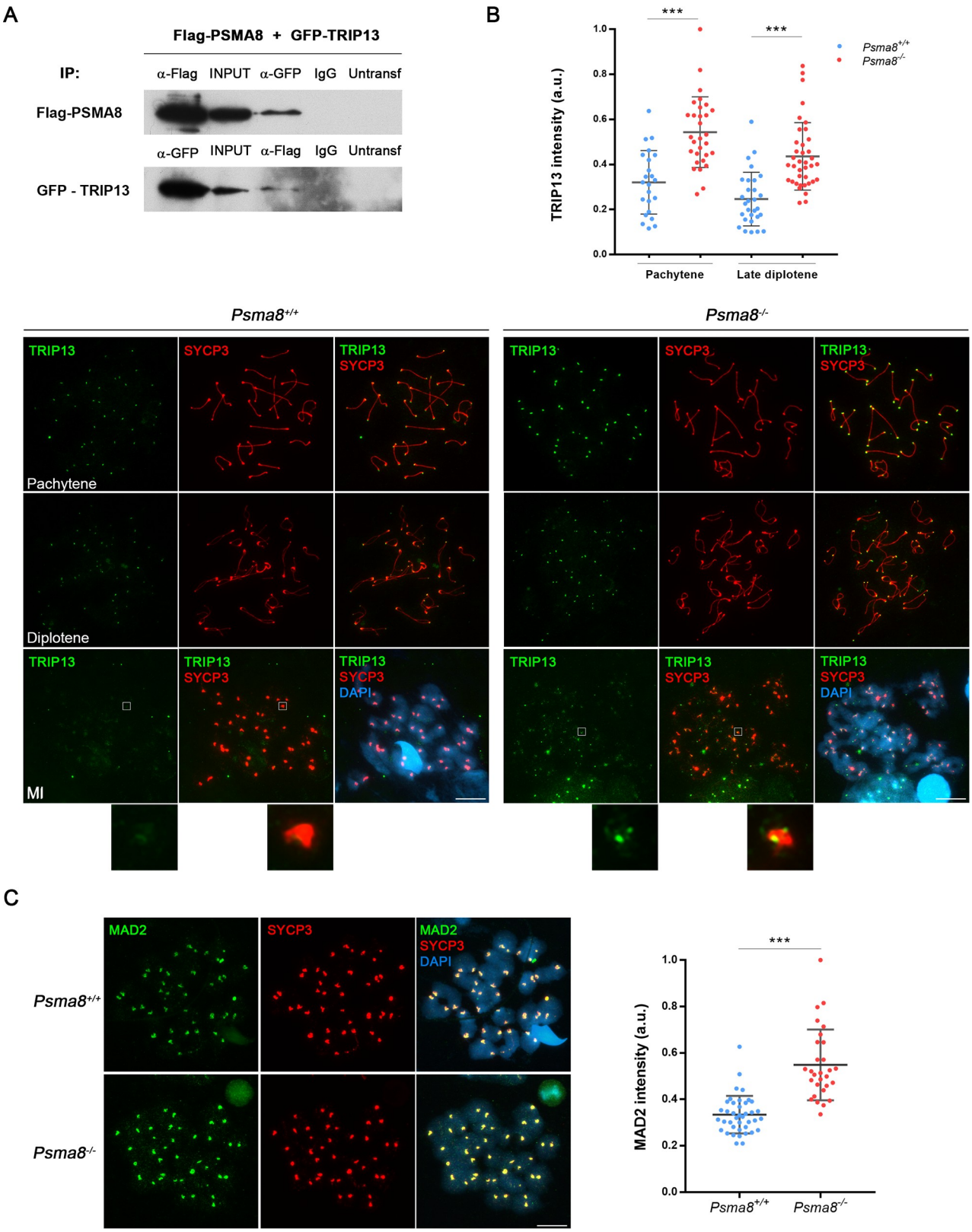

Fig 7. TRIP13 and MAD2 levels are increased in *Psma8*-deficient spermatocytes. (A) HEK293T cells were transfected with a plasmid encoding GFP-TRIP13 and Flag-PSMA8. Protein complexes were immunoprecipitated with either an anti-Flag or anti-EGFP or IgGs (negative control), and

immunoblotted with the indicated antibody. (B) Double immunolabeling of TRIP13 (green) and SYCP3 (red). TRIP13 labels the telomeres at pachytene and the intensity of the labeling decreases through desynapsis at diplotene and diakinesis. This labeling is enhanced during prophase I in the *Psma8* mutants but its main pattern is not altered. At metaphase I, a faint labeling of sister kinetochores is observed in the *Psma8*$^{-/-}$ spermatocytes that is absent in the wild type. Plot over the panel represents the quantification of the fluorescence intensity from *Psma8*$^{+/+}$ and *Psma8*$^{-/-}$ spermatocytes at pachytene and late diplotene. (C) MAD2 (green) labels with enhanced intensity the centromeres of the chromosomes from *Psma8*$^{-/-}$ metaphase I cells in comparison with the WT controls. Plot right to the panel represents the quantification of the fluorescence intensity from *Psma8*$^{+/+}$ and *Psma8*$^{-/-}$ spermatocytes at metaphase I spermatocytes. Bar in panels, 10 μm. Welch´s *t*-test analysis: * $p<0.01$; ** $p<0.001$; *** $p<0.0001$.

https://doi.org/10.1371/journal.pgen.1008316.g007

PA200-containing proteasome. However, following the criteria employed for the designation of the thymoproteasome, which were devised based on the restricted expression of its β5t subunit in the thymus [9] (GTEx portal), we suggest that the term spermatoproteasome be restricted exclusively to the PSMA8-containing proteasome instead of the widely expressed PA200 subunit [5].

We have shown that genetic depletion of *Psma8* causes the delocalization and the drastic decrease (loss of detection) of the proteasome activator PA200 in spermatocytes. Accordingly, *Psma8*-deficient spermatocytes accumulate acetylated histones. PSMA8 deficiency is comparatively more severe than that of the PA200 single mutant (subfertile) and of the PA200 and PA28γ double mutant, which do not show an arrest in spermatogenesis despite being infertile *in vivo* but not *in vitro* (spermatozoa are not motile but can fertilize *in vitro* [54]). From a genetic analysis perspective, this result would suggest that PSMA8 has additional functions that are independent of the activators PA200 and PA28γ. Our proteomic analysis, together with other data [10], supports this notion and indicates that PSMA8-containing proteasomes can be associated with other regulators such as the 19S subunit, expanding its targets.

Beyond its role in initiation of histone replacement [34], H4K16ac is involved in the three waves of H2AX phosphorylation during prophase I [55]. We have shown that *Psma8* deficiency causes the accumulation of H4ac and H4K16ac during prophase I. However, we did not observe defects in this process in the form of a different staining pattern for γ-H2AX (leptonema and zygonema), including the expansion of γ-H2AX staining to the chromatin of the sex body (in pachynema). However, the observed premature accumulation of H4K16ac at early round spermatid might cause a defect in histone removal later on in spermiogenesis if the *Psma8*$^{-/-}$ mutants spermatids would not have entered apoptosis before this event.

We have shown that spermatoproteasome deficiency causes severe defects in protein turnover of key meiotic players that affect metaphase I/II exit, but not the complex process of meiotic recombination that occurs during prophase I (CO). By using a candidate approach of PIPs, we have identified CDK1 and TRIP13 as likely crucial proteins that have an abnormal expression pattern during meiotic metaphase in mutant mice. Given the key roles of these proteins in all aspects of mitotic/meiotic division (including SAC activation), the accumulation of aberrant metaphase I/II spermatocytes in *Psma8*-deficient mice is to be expected.

The role of CDK1 in the metaphase-anaphase transition is complex and is multifaceted. CDK1 inhibits and activates APC/C by promoting the SAC and also by a SAC-independent mechanism [56]. The balance between these opposing functions determines cyclin B1 destruction and separase activation, giving rise to cohesin cleavage and anaphase onset [57]. Based on the normal expression levels of PTTG1 in *Psma8*$^{-/-}$ metaphase I cells, it can be argued that there is no precocious APC activation in *Psma8*-deficient cells (S17 Fig). Given that CDK1 activation of the SAC is dominant over the activation of APC^{Cdc20} [58] in oocytes, we suggest that the former effect is acting on *Psma8*-deficient spermatocytes. The question how CDK1 promotes the SAC is still unresolved in oocytes and even less is known about this in spermatocytes

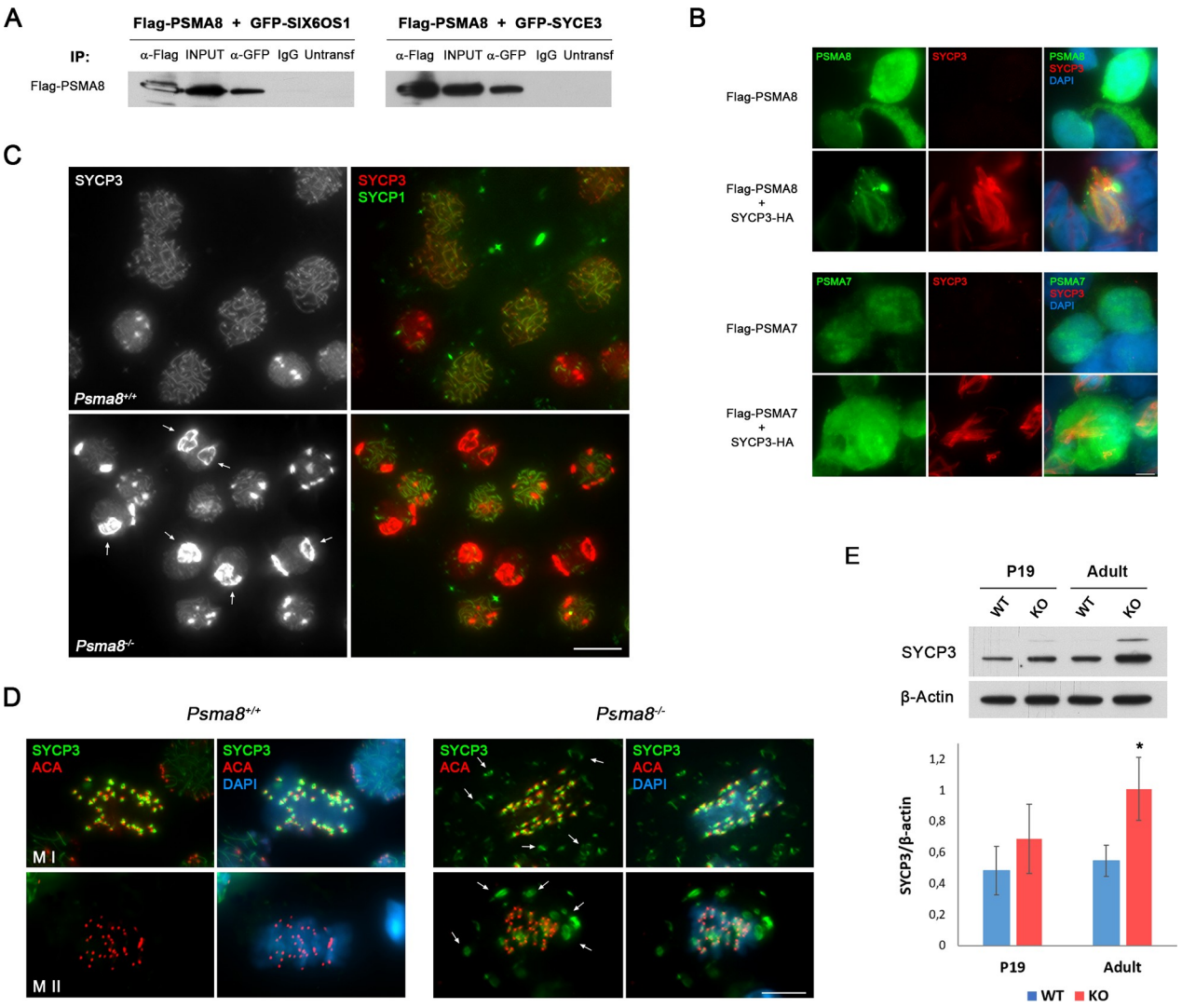

Fig 8. PSMA8 interacts with proteins of the SC. (A) PSMA8 co-immunoprecipitates with SIX6OS1 and SYCE3. HEK293T cells were transfected with plasmids encoding Flag-PSMA8 and GFP-SIX6OS1 or GFP-SYCE3. Protein complexes were immunoprecipitated overnight with either an anti-Flag or anti-EGFP or IgGs (negative control), and were analyzed by immunoblotting with the indicated antibody. (B) Double immunofluorescence of transfected HEK293T cells with plasmids encoding Flag-PSMA8 and Flag-PSMA7 alone or together with plasmid encoding SYCP3-HA and immuno-detected with antibodies against Flag (green) or HA (red). Transfected PSMA8 alone is delocalized and occupies the whole cell whereas when co-transfected with SYCP3-HA is recruited to form polycomplexes. PSMA7 do not form polycomplexes when co-transfected with SYCP3-HA. (C-D) SYCP3 is accumulated *in vivo* in *Psma8*$^{-/-}$ spermatocytes. (C) Double immunolabeling of squashed tubules with SYCP3 (red) and SYCP1 (green) in wild-type and *Psma8*$^{-/-}$ spermatocytes at prophase I showing large SYCP3 aggregates surrounding the nuclei (arrows). (D) Double immunolabeling of squashed tubules with SYCP3 (green) and ACA (red) in wild-type and *Psma8*$^{-/-}$ spermatocytes at metaphase I and II. *Psma8*$^{-/-}$ metaphases I show labeling of SYCP3 in aggregates (arrows, absent in the WT) in addition to its typical labeling at the centromeres. Metaphases II from *Psma8*$^{-/-}$ show labeling for SYCP3 at the centromeres between the sister kinetochores and as aggregates in the cytosol (arrows) whereas wild type metaphases II show barely visible SYCP3 labeling. (E) SYCP3 was measured by western blot analysis of protein extracts from whole testis of *Psma8*$^{+/+}$ (WT) and *Psma8*$^{-/-}$ (KO) (n = 2 mice). Bar in panels, 10 μm. Welch´s *t*-test analysis: * $p<0.05$; ** $p<0.001$; *** $p<0.0001$.

https://doi.org/10.1371/journal.pgen.1008316.g008

Another group of proteins found to be deregulated in spermatoproteasome-deficient mice are the SC structural proteins SYCP1 and SYCP3. The precise effect of the accumulated SYCP1 in the cytoplasm of *Psma8*$^{-/-}$ spermatocytes cannot be experimentally analyzed. However, the coiled-coil structure and self-assemblance abilities of SYCP1 strongly suggest a functionally detrimental consequence. Similarly, the presence of SYCP3 aggregates during pachynema and metaphase I mutant spermatocytes and its persistence at metaphase II

centromeres, where SYCP3 is barely visible in WT cells, also suggest a detrimental effect on these cells causing their entrance into apoptosis.

We have also shown that PSMA8 is delocalized in the severe synapsis *Six6os1* mutant, which is consistent with the observed co-immunoprecipitation of PSMA8 with SYCP1, SIX6OS1 and SYCE3. All the synapsis-less mutants of CE proteins failed to load properly or lacked SYCP1 and the remaining CE proteins [24, 59–61]. Thus, we would predict delocalization of the spermatoproteasome from the SC in the remaining mouse mutants of the CE proteins. Overall, our results support the idea of a physical anchorage or recruitment of the spermatoproteasome to the SC especially through SYCP3, possibly facilitated or mediated by SYCP1, SIX6OS1 and SYCE3 as their most relevant structural partners. Supporting this notion, the Zip1 transverse filament protein of the yeast SC participates in the recruitment of the proteasome to the SC [22], suggesting an evolutionary conservation of the mechanism.

Yeast mutated for a nonessential subunit of the proteasome (pre9) showed abnormal meiotic recombination, pairing and synapsis [22]. Similar but milder defects were also observed in spermatocytes cultured with a proteasome inhibitor [17]. It has been proposed that the UPS regulates the proteostatic turnover of the ZMM which is required for efficient synapsis and CO [17], through the RNF212 (E3 sumo ligase)-Hei10 (E3 ubiquitin ligase) pathway [31]. Given this, the lack of a meiotic recombination phenotype (DSBs are generated and repaired and COs are generated normally) in our *Psma8*-deficient mouse is surprising. It can be argued that PSMA7-containing proteasomes are still present and at the early stages of meiosis are compensating for the loss of function of *Psma8*. Another possible but not mutually exclusive explanation is that the main targets of the PSMA8-containing proteasome are proteins from mid-prophase I onwards.

The spermatoproteasome through its complex interactome would serve as a hub for the fine tuning of several fundamental key molecules of the spermatogenic process such as those analyzed during the present work (SYCP1, SYCP3, TRIP13, CDK1 and acetyl-histones). Our data suggest that deregulation of proteostasis of key meiotic proteins promoting cell division leads to the presence of multipolar spindles and aberrant meiotic exit. Thus, we favor an explanation in which the joint contribution of several pathways is responsible for the observed infertility.

In relation to human disease, protein degradation was one of the top cellular functions found in an unbiased differential proteomic profiling of spermatozoa proteins from infertile men with a varicocele [62]. More specifically, PSMA8 is among the top 7 in this list of proteins that are differentially expressed, suggesting a causal role in the severity of the disease. From an organismal perspective, *Psma8* transcription is mainly restricted to the human testis and to some tumors like Burkit lymphoma and melanoma (TCGC database). Altogether, and considering the PSMA8 dependency of the mouse male germline, we suggest that the spermatoproteasome may be an effective target for male contraception and for the treatment of some human malignancies.

Material and methods

In vivo electroporation of testes

Testes were freed from the abdominal cavity and 10 μl of DNA solution (50 μg) mixed with 1μl of 10×FastGreen (Sigma Aldrich F7258) was injected into the rete testis with a DNA embryo microinjection tip. After a period of 1 h following the injection, testes were held between electrodes and four electric pulses were applied (35 V for 50 ms each pulse) using a CUY21 BEX electroporator.

Production of CRISPR/Cas9-Edited mice

Psma8-sgRNAs G71 5'- GGGCATACT CCACTTGGAAA -3' G84 5'-ACCGCGGTAAGCTG CTCCCC-3' targeting exon 1 and intron 1 were predicted at crispr.mit.edu. Psma8-sgRNAs were produced by cloning annealed complementary oligos at the BbsI site of pX330 (#42230, Addgene), generating PCR products containing a T7 promoter sequence that were purified (NZYtech), and then *in vitro* transcribed with the MEGAshortscrip T7 Transcription Kit (Life Technologies). The plasmid pST1374-NLS-flag-linker-Cas9 (#44758; Addgene) was used for generating Cas9 mRNA. After linearization with AgeI, it was transcribed and capped with the mMESSAGE mMACHINE T7 Transcription Kit (AM1345; Life Technologies). RNAs were purified using the RNeasy Mini Kit (Qiagen). RNAs (100 ng/μl Cas9 and 50ng/μl each guide RNA) were microinjected into B6/CBA F2 zygotes (hybrids between strains C57BL/6J and CBA/J) [63] at the Transgenic Facility of the University of Salamanca. Edited founders were identified by PCR amplification (Taq polymerase, NZYtech) with primers flanking exons 1 and intron 1 (Primer F 5'-CTTCTCGGTATGACAGGGCAATC-3' and R 5'- ACTCTACCTC CACTGCCAAC CTG-3') and either direct sequenced or subcloned into pBlueScript (Stratagene) followed by Sanger sequencing. The predicted best null mutation was selected by PCR sequencing of the targeted region of *Psma8* (S3B Fig). The selected mutant allele was 166 bp long versus 222bp of the wild-type. The founder was crossed with wild-type C57BL/6J to eliminate possible unwanted off-targets. *Psma8*$^{+/-}$ heterozygous mice were re-sequenced and crossed to give rise to *Psma8*$^{-/-}$ homozygous. Genotyping was performed by analysis of the PCR products of genomic DNA with primers F and R. Mouse mutants for Rec8 and Six6os1 have been previously developed [24, 25].

Histology

For histological analysis of adult testes, mice were perfused and their testes were processed into serial paraffin sections and stained with hematoxylin-eosin or were fixed in Bouin´s fixative and stained with Periodic acid–Schiff (PAS) and hematoxylin.

Microscopy

Slides were visualized at room temperature using a microscope (Axioplan 2; Carl Zeiss, Inc.) with 63 × objectives with an aperture of 1.4 (Carl Zeiss, Inc.). Images were taken with a digital camera (ORCA-ER; Hamamatsu) and processed with OPENLAB 4.0.3 and Photoshop (Adobe). Quantification of fluorescence signals was performed using Image J software. Squashed preparations were visualized with a Delta vision microscopy station. Stimulated emission depletion (STED) microscopy (SP8, Leica) was used to generate the super-resolution images. Secondary antibodies for STED imaging were conjugated to Alexa 555 and 488 (Invitrogen). Slides were mounted in Prolong Antifade Gold without DAPI.

Immunocytology

Testes were detunicated and processed for spreading using a conventional "dry-down" technique or squashing [64]. Antibody against the C-term of PSMA8 was a gift from Dr. Murata (Univ of Tokyo, Japan) and has been previously described [10]. Rabbit polyclonal antibodies against PSMA8 were developed by Proteintech (R1 and R2) against a fusion protein of poly-His with full length PSMA8 (pET vector) of mouse origin (see S1 Fig for validation) and was used to validate the immunofluorescence and western results. The primary antibodies used for immunofluorescence were rabbit αSYCP1 IgG ab15090 (1:200) (Abcam), rabbit anti-γH2AX (ser139) IgG #07–164 (1:200) (Millipore), ACA or purified human α-centromere proteins IgG

15–235 (1:5, Antibodies Incorporated), mouse αMLH1 51-1327GR (1:5, BD Biosciences), mouse αSYCP3 IgG sc-74569 (1:100), rabbit αRAD51 PC130 (1:50, Calbiochem), Mouse αCDK1 sc-54 (1:20 IF; 1:1000 wb, Santa Cruz), rabbit αCDK1 Tyr15p #4539 (1:10, Cell Signaling), rabbit αCDK2 sc-6248 (1:20, Santa Cruz), rabbit αPTTG1 serum K783 (1:20 IF, 1:1000 wb), rabbit αTRIP13 19602-1-AP (1:20, Proteintech), rabbit αH2AL2 (1:100, from Dr. Saadi Khochbin), rabbit αPA200 (1:20, Bethyl A303-880A), rabbit α-Caspase3 #9661 (1:30, Cell Signaling), rabbit αH2AK5ac ab45152 (1:20, Abcam), Rabbit αH4K16ac #07–329 (1:50 Millipore), Rabbit αH3ac (K9 and K14) #06–599 (1:20, Millipore), Rabbit αH4ac (K5, K8, K12 and K16) #06–598 (1:20, Millipore), Mouse αUbiquitin 11023 (1:20 IF, 1:1000 wb, QED Bioscience), Rabbit αHORMAD1 and αHORMAD2 and chicken anti SYCP1 (1:50, from Dr. Attila Toth; [65]), Rabbit anti p-ser10-H3 06–570 (1:100, Millipore), Mouse anti α-tubulin T9026 (1:100, Sigma), Rabbit αCyclin B1 ab72 (1:20, Abcam), Rabbit αMAD2 (1:30 provided by Dr. Stemmann), Peanut agglutinin lectin L7381 (15μg/ml, Sigma), SMC6 ab18039 (1:50, Abcam), Human αVASA 560189 (1:100, BD), Rabbit αINCENP 1186 (1:50, provided by Dr. Earnshaw). TUNEL staining of chromosome spreads was performed with the *in situ* cell death detection kit (Roche).

FACs analysis

Psma8$^{+/+}$ and *Psma8*$^{-/-}$ testicular cells preparation and measurement of their DNA content were performed by a standard procedure [66]. Briefly, the testes were detunicated and the seminiferous tubules were kept in 5 ml of ice-cold separation medium (DMEM supplemented with 10% FCS, 0.1 mM NEAA, 1.5 mM sodium pyruvate, 4 mM L-glutamine and 75 μg/ml ampicillin). They were treated with 0.1 mg/ml collagenase at 37˚C for 10 min under mild shaking. The sedimented seminiferous tubules were washed twice with separation medium and treated for 2 min at 37˚C with 2.5 μg/ml trypsin and 1 U/ml DNAse I in separation medium and transferred to ice. Afterwards, single cells were extracted from the seminiferous cords with a Pasteur pipette and filtered through a 40 μm nylon mesh. The cell suspension (2×10^6 cells/ml) was diluted 1:1 with a solution containing 0.05 mg/ml propidium iodide and 0.1 mg/ml RNAse for 15 min. Finally, the cells were analyzed through flow cytometry in a cytometer FACSCalibur and the BD Cell-Quest software. The cell cycle distribution was analyzed with the Kaluza Analysis software (Beckman Coulter).

Proteasome assay

The 26S proteasome assay was carried out in a total volume of 250 μl in 96 well plates with 2 mM ATP in 26S buffer using 100 μg of protein supernatants from whole extracts of mouse testis. Fluorescently labeled substrates employed were: succinyl-Leu-Leu-Val-Tyr-7-amino-4-methylcoumarin (Suc-LLVY-AMC), Z-Ala-Arg-Arg-AMC (Z-ARR-AMC, Bachem), and Z-Leu-Leu-Glu-AMC (Z-LLE-AMC) for the detection of the chymotrypsin- (β5 catalytic subunit), trypsin- (β2 catalytic subunit) and caspase- (β1 catalytic) like activity measurements respectively. The final substrate concentration in each assay was 100 μM.

Cell lines

The HEK293T, GC1-spg, Leydig TM3, and Sertoli TM4 cell lines were directly purchased at the ATCC and cultured in standard cell media. HEK293T cell line was transfected with Lipofectamine (Invitrogen) or Jetpei (PolyPlus). Cell lines were tested for mycoplasma contamination (Mycoplasma PCR ELISA, Sigma).

Generation of plasmids

Full-length cDNAs encoding PSMA8, PSMA7, CDK1, SYCP1 and SIX6OS1, SYCP3, SYCE2, TEX12, TEX30, PIWIL1 and PIWIL2 were RT-PCR amplified from murine testis RNA. Full-length cDNAs were cloned into the EcoRV pcDNA3-2XFlag or SmaI pEGFP-C1 expression vectors under the CMV promoter. In frame cloning was verified by Sanger sequencing.

Immunoprecipitation and western blotting

200 μg of antibody R1 and R2 were bound to 100 μl of sepharose beads slurry (GE Healthcare). Testis extracts were prepared in 50mM Tris HCl (pH8), 500mM NaCl, 1mM EDTA 1% tritonX-100. 20 mg of proteins extracts were incubated o/n with the Sepharose beads. Protein-bound beads were packed into columns and washed in extracting buffer for three times. Protein were eluted in 100 mM glycine pH3. The whole immunoprecipitation of PSMA8 was performed in a buffer lacking ATP and glycerol to increase the stringency of the interactors and regulators/activators subunits. HEK293T cells were transiently transfected and whole cell extracts were prepared and cleared with protein G Sepharose beads (GE Healthcare) for 1 h. The antibody was added for 2 h and immunocomplexes were isolated by adsorption to protein G-Sepharose beads o/n. After washing, the proteins were eluted from the beads with 2xSDS gel-loading buffer 100mM Tris-Hcl (pH 7), 4% SDS, 0.2% bromophenol blue, 200mM β-mercaptoethanol and 20% glycerol, and loaded onto reducing polyacrylamide SDS gels. The proteins were detected by western blotting with the indicated antibodies. Immunoprecipitations were performed using mouse αFlag IgG (5μg; F1804, Sigma-Aldrich), mouse αGFP IgG (4 μg; CSB-MA000051M0m, Cusabio), rabbit αMyc Tag IgG (4μg; #06–549, Millipore), mouse αHA.11 IgG MMS- (5μL, aprox. 10μg/1mg prot; 101R, Covance), ChromPure mouse IgG (5μg/1mg prot; 015-000-003), ChomPure rabbit IgG (5μg/1mg prot.; 011-000-003, Jackson ImmunoResearch), ChomPure goat IgG (5μg/1mg prot.; 005-000-003, Jackson ImmunoResearch). Primary antibodies used for western blotting were rabbit αFlag IgG (1:2000; F7425 Sigma-Aldrich), goat αGFP IgG (sc-5385, Santa Cruz) (1:3000), rabbit αHA IgG (H6908, Sigma-Aldrich) (1:1.000), mouse αMyc obtained from hybridoma cell myc-1-9E10.2 ATCC (1:5). Secondary horseradish peroxidase-conjugated α-mouse (715-035-150, Jackson ImmunoResearch), α-rabbit (711-035-152, Jackson ImmunoResearch), or α-goat (705-035-147, Jackson ImmunoResearch) antibodies were used at 1:5000 dilution. Antibodies were detected by using Immobilon Western Chemiluminescent HRP Substrate from Millipore. Protein extracts for the analysis of SYCP3, CDK1 and CyclinB1 were extracted in Tris-HCl 250mM, SDS10%, Glycerol 50% (denaturing buffer).

MS/MS data analysis

Raw MS data were analized using MaxQuant (v. 1.5.7.4) and Perseus (v. 1.5.6.0) programmes 71. Searches were generated versus the *Mus musculus* proteome (UP000000589, May 2017 release) and Maxquant contaminants. All FDRs were of 1%. Variable modifications taken into account were oxidation of M, acetylation of the N-term and ubiquitylation remnants di-Gly and LRGG, while fixed modifications included considered only carbamidomethylation of C. The maximum number of modifications allowed per peptide was 5. For the case of the protein group of CDK1 to 3, experimental results showed that the protein detected was CDK1. For the PSMA8 antibodies R1 and R2, ratios of their respective iBAQ intensity versus the correspondent iBAQ intensity in the control sample were calculated. Proteins with ratio higher or equal to 5 and two or more unique peptides for at least one RP antibody were selected for ulterior analysis. Additionally, in order to avoid filtering rare proteins, those with at least one unique

peptide and one peptide for both Rabbit antibodies (R1 and R2) and none for anti-IgG were also selected for further analysis.

Functional and pathway analysis

GO and KEGG over-representation tests were performed using the R package *clusterProfiler* [67] using standard parameters except for a FDR cutoff of 0.01. KEGG pathways where some key genes (TRIP13, CDK1, SYCP1, DDX4, SYCP3, SYCE3, SIX6OS1) operate and the role of the co-immunoprecipitated proteins were studied using the R package *pathview* [68].

Statistics

In order to compare counts between genotypes at different stages, we used the Welch´s t-test (unequal variances t-test), which was appropriate as the count data were not highly skewed (i.e., were reasonably approximated by a normal distribution) and in most cases showed unequal variance. We applied a two-sided test in all the cases. Asterisks denote statistical significance: *p-value <0.01, **p-value <0.001 and ***p-value<0.0001.

Ethics statement

Mice were housed in a temperature-controlled facility (specific pathogen free, spf) using individually ventilated cages, standard diet and a 12 h light/dark cycle, according to EU laws at the "Servicio de Experimentación Animal, SEA". Mouse protocols were approved by the Ethics Committee for Animal Experimentation of the University of Salamanca (USAL). We made every effort to minimize suffering and to improve animal welfare. Blinded experiments were not possible since the phenotype was obvious between wild type and *Psma8*-deficient mouse for all of the experimental procedures used. No randomization methods were applied since the animals were not divided in groups/treatments. The minimum size used for each analysis was two animals/genotype.

Supporting information

S1 Fig. Validation of the antibodies raised against PSMA8. (A) HEK293T cells were transfected with a plasmid encoding PSMA8-GFP, PSMA7-GFP or GFP and the whole extracts were analyzed by western blot using rabbit α-PSMA8 C-terminal (left panel, α4S), rabbit α-PSMA8 (central panel, R2) and α-GFP (right panel, GFP). Immunodetection of β-actin was used as loading control. The rabbit α-α4S antibody detected exclusively the 60 kDa band representing PSMA8-GFP. The rabbit α-PSMA8 R2 antibody detected both bands representing PSMA8-GFP and PSMA7-GFP. The bands of 60 kDa (PSMA7 and PSMA8) and 30 kDa (GFP) were all detected with the goat α-GFP validating the experiments. (B) Immunofluorescence of HEK293T cells transfected with plasmids encoding PSMA8-GFP, PSMA7-GFP or GFP. Both PSMA8 and PSMA7 were detected with rabbit α-PSMA8-R2 (red) and GFP by direct fluorescence signal (green). Green and red signals co-localize in the cytoplasm of the transfected HEK293T cells. The experiments were reproduced three times. Bar represents 10 μm.
(TIF)

S2 Fig. Localization of PSMA8 in mouse spermatocytes. (A) Double immunolabeling of endogenous PSMA8 (R2 antibody, green) and SYCP3 (red) in mouse spermatocytes. From the leptotene to zygotene stage, PSMA8 is detected at the synapsed autosomal LEs. At pachytene, PSMA8 is located at the totally synapsed axes and at the PAR of the sex XY bivalent. In diplotene, PSMA8 localizes at the still synapsed AEs and disappears at diakinesis. (B) Double

immunolabeling of spermatocytes spread preparations with PSMA8 (green) and SYCP1 (red), showing that PSMA8 localizes to the synapsed LEs but do not perfectly co-localize with SYCP1 (upper panel). Magnification of the XY bivalent (lower panel) showing the PAR (arrow). Bars represent 10 μm (A and B, upper panel) and 1.5 μm (B, lower panel).
(TIF)

S3 Fig. Generation and genetic characterization of *Psma8*-deficient mice. (A) Diagrammatic representation of the mouse *Psma8* locus (WT) and the genome editing strategy showing the sgRNAs located on exon 1 and intron 1 (see methods), the corresponding coding exons (light grey) and non-coding exons (open boxes). Thin (non-coding) and thick (coding sequences) lines under exons represent the expected transcript derived from wild-type (black) and *Psma8* edited allele (blue). ATG, initiation codon; TGA and *, stop codon. The nucleotide sequence of the 56 base pair deletion derived from PCR amplification of DNA from the *Psma8* $^{edited/edited}$ is indicated (Δ). Primers (F and R) are represented by arrows. (B) PCR analysis of genomic DNA from three littermate progeny of *Psma8*$^{+/-}$ heterozygote crosses. The PCR amplification with primers F and R revealed 222 and 166 bp fragments for wild-type and disrupted alleles respectively. Wild-type (WT, +/+), heterozygous (Het, +/-), and homozygous knock-out (KO, -/-) animals. (C) Western blot analysis of protein extracts from wild type testis (P22 and adult), KO testis (P16, P22 and adult) with a specific antibody against the C-terminal (α4S) and whole recombinant PSMA8 protein (PSMA8-R2). β-actin was used as loading control. The corresponding bands to PSMA8 and PSMA7 are indicated in the right of the panel. Note that at the P22 and in adult stages the intensity of both bands abolishes its independent observation. (D) Double immunofluorescence of spermatocytes at pachytene stage obtained from *Psma8*$^{+/+}$ and *Psma8*$^{-/-}$ mice using SYCP3 (red) and PSMA8 (R2 antibody, green). Green labeling in *Psma8*$^{-/-}$ spermatocytes (49% of the wild type) represents cross-reactivity of the antiserum with PSMA7. Plot under the image panel represents the quantification of intensity from *Psma8*$^{+/+}$ and *Psma8*$^{-/-}$ spermatocytes. Welch´s *t*-test analysis: * $p<0.01$. Bar in panel, 10 μm.
(TIF)

S4 Fig. Validation of the identity of round spermatids with molecular markers. (A) PNA staining (green) of acrosome in spread preparations from wild type and *Psma8*$^{-/-}$ cells. Double labeling of squash tubules of VASA (chromatoid body), INCENP [1], SMC6 [2] (green) with SYCP3 (red) from wild type and *Psma8*$^{-/-}$ mice. The combined labeling of INCENP (labels both interkinesis and round spermatids, [1]) and SYCP3 (mainly labels interkinesis with a typical barr patterning at the chromocenters, see below S4B Fig) is compatible with round spermatids. The combined double immunolabeling of SMC6 (labels both interkinesis and round spermatids, [2]) and SYCP3 (mainly labels interkinesis with a typical barr patterns at the chromocenters, see below S4B Fig) is also compatible being round spermatids. (B) Double labeling of SYCP3 (green) and ACA (red) showing the different pattern of secondary spermatocytes at interkinesis and round spermatids. Bars in panels represent 10 μm (A, PNA panel) and 5 μm (rest of panels).
(TIF)

S5 Fig. Early arrest of *Psma8*$^{-/-}$ spermatids and gating strategy of the FACs analysis. (A) Immunolabeling of H2AL2 (green) show positive staining in elongating spermatids from wild type mice but lack of staining in *Psma8*$^{-/-}$ mice. Chromatin was stained with DAPI. Bar represents 10 μm. (B) Gating strategy employed in the FACs analysis of Fig 3D. Grey dots represent cells that were excluded from the analysis whilst dots included in the polygon represent cells that were employed for the analysis. Red dots enclose 1C cells, blue dots represent 2C cells and

green dots enclose 4C cells.
(TIF)

S6 Fig. Normal synapsis and desynapsis in spermatocytes lacking PSMA8. Double immunolabeling of SYCP3 (red) and SYCP1 (green) showing normal synapsis and desynapsis from early zygotene to diakinesis in *Psma8*$^{-/-}$ in comparison with *Psma8*$^{+/+}$. Bar represents 10 μm.
(TIF)

S7 Fig. DSBs are generated and repaired as COs in spermatocytes lacking PSMA8. (A) Double immunolabeling of γ-H2AX (green) with SYCP3 (red) in wild-type and *Psma8*$^{-/-}$ spermatocytes from leptotene to diplotene (upper panel). In WT and KO leptonemas, γ-H2AX labels intensely the chromatin. After repair, γ-H2AX labeling remains only in the chromatin of the sex body of the pachynemas. Plot right to the panel represent the quantification of the fluorescence intensity from *Psma8*$^{+/+}$ and *Psma8*$^{-/-}$ spermatocytes at leptotene and pachytene. Late round spermatids (LR) but not early round spermatids (ER) from wild type mice show positive staining for γ-H2AX but these highly differentiated cells are lacking in the *Psma8*$^{-/-}$ tubules which are arrested at early round spermatids without γ-H2AX staining (bottom panel). (B) Double immunolabeling of SYCP3 (red) and RAD51 (green). RAD51 foci associates to the AEs in leptonema spermatocytes of both genotypes (similar number of foci) and dissociate towards pachytene with a similar kinetics. Plot right to the image panel represents the quantification of the number of foci from *Psma8*$^{+/+}$ and *Psma8*$^{-/-}$ spermatocytes. (C) Double immunolabeling of SYCP3 (red) with MLH1 (green). MLH1 foci are present along each autosomal SC in wild-type and *Psma8*$^{-/-}$ pachynema meiocytes in a similar way. Plot right to the panel represents the quantification of the values of the MLH1 foci from *Psma8*$^{+/+}$ and *Psma8*$^{-/-}$ spermatocytes. Bars represent 10 μm. Welch´s *t*-test analysis: * $p<0.01$; ** $p<0.001$; *** $p<0.0001$. Quantification data is indicated in S3 Table.
(TIF)

S8 Fig. PA200 localization in prophase I from *Psma8*$^{+/+}$ and *Psma8*$^{-/-}$ spermatocytes. Double immunolabeling of PA200 (green) and SYCP3 (red) in chromosome spreads from zygotene to diakinesis. PA200 is detected at the chromosome axes in wild type spermatocytes in contrast to the absence of labeling in *Psma8*$^{-/-}$ spermatocytes. Bar in panels, 10 μm.
(TIF)

S9 Fig. PSMA8 deficiency provokes an slight increase of H2AK5ac at prophase I. Double immunolabeling of H2AK5ac (green) with SYCP3 (red) in wild-type (left panel) and *Psma8*$^{-/-}$ spermatocytes (right panel). In WT and KO spermatocytes chromatin start to be labelled at early pachytene around chromosomes axes. Plots from each panel representing the quantification of fluorescence intensity from *Psma8*$^{+/+}$ and *Psma8*$^{-/-}$ spermatocytes are depicted in Fig 4A. Bar represents 10 μm.
(TIF)

S10 Fig. PSMA8 deficiency provokes an slight increase of H3ac at prophase I. Double immunolabeling of H3ac (green) with SYCP3 (red) in wild-type (left panel) and *Psma8*$^{-/-}$ spermatocytes (right panel). Spermatocytes from *Psma8*$^{+/+}$ and *Psma8*$^{-/-}$ show labeling for H3ac at early pachytene in a very diffuse manner surrounding chromosomes axes. Plots from each panel representing the quantification of fluorescence intensity from *Psma8*$^{+/+}$ and *Psma8*$^{-/-}$ spermatocytes are in Fig 4B. Bar represents 10 μm.
(TIF)

S11 Fig. PSMA8 deficiency provokes an slight increase of H4ac at prophase I and in round spermatids. Double immunolabeling of H4ac (green) with SYCP3 (red) in wild-type and

Psma8$^{-/-}$ spermatocytes. Spermatocytes from *Psma8*$^{+/+}$ and *Psma8*$^{-/-}$ show labeling for H4ac in a very diffuse manner surrounding chromosomes from pachytene to metaphase I (right panel). In wild type metaphase I, H4ac labeling appears weakly painting the chromosomes and on some of the centromeres. However, *Psma8*-deficient cells show a more intense labeling specially at the centromeres (lower panel). Round spermatid from *Psma8*$^{-/-}$ accumulates H4ac labeling at the chromatin in comparison with the WT. Plots from each panel representing the quantification of fluorescence intensity from *Psma8*$^{+/+}$ and *Psma8*$^{-/-}$ spermatocytes are in Fig 4C. Bars represent 10 μm.
(TIF)

S12 Fig. PSMA8 deficiency provokes an increase of H4K16ac at prophase I and in metaphase I / round spermatids. Double immunolabeling of H4K16ac (green) with SYCP3 (red) in wild-type and *Psma8*$^{-/-}$ spermatocytes. Spermatocytes from *Psma8*$^{+/+}$ and *Psma8*$^{-/-}$ show labeling for H4K16ac in a very diffuse manner surrounding chromosomes from pachytene to metaphase I (right panel). In wild type metaphase I, H4K16ac labeling appears weakly painting the chromosomes. However, *Psma8*-deficient cells show enhance labeling in the chromosomes of metaphase I cells (lower panel). Round spermatid from *Psma8*$^{-/-}$ accumulates H4K16ac labeling at the chromatin in comparison with the WT. Plots from each panel representing the quantification of fluorescence intensity from *Psma8*$^{+/+}$ and *Psma8*$^{-/-}$ spermatocytes are in Fig 4D. Bars represent 10 μm.
(TIF)

S13 Fig. PSMA8 deficiency alters Ubiquitylation of mouse spermatocytes. (A) Double immunolabeling of Ubiquitin (green) and SYCP3 (red) in mouse chromosome spreads at pachytene stage from *Psma8*$^{+/+}$ and *Psma8*$^{-/-}$mice. (B) Double immunolabeling of Ubiquitin (green) and SYCP3 (red) in mouse squashed tubules from *Psma8*$^{+/+}$ and *Psma8*$^{-/-}$ mice. Chromatin was stained with DAPI. Bars represent 10 μm (A) and 5 μm (B).
(TIF)

S14 Fig. Lack of co-immunoprecipitation of PSMA8 with candidate interactors. (A-B) HEK293T cells were co-transfected with GFP-TEX30, GFP-PIWIL1, GFP-PIWIL2, GFP-SYCE1, GFP-SYCE2, and GFP-TEX12, and with Flag-PSMA8. PSMA8 does not co-immunoprecipitates (co-IP) with any of them. (C) Positive control was generated by transfecting HEK293T cells with Flag-SYCE2 and GFP-TEX12. Protein complexes were immunoprecipitated overnight with either an anti-Flag or anti-EGFP or IgGs (negative control) and were analyzed by immunoblotting with the indicated antibody.
(TIF)

S15 Fig. CDK1 / Cyclin B1, but not CDK2, are accumulated in *Psma8* mutant spermatocytes. (A) Double immunolabeling of endogenous CDK2 (green) and SYCP3 (red) in WT and KO mouse chromosome spreads at pachytene and metaphase I showing similar labeling at the telomeres and centromeres, respectively. (B) Double immunolabeling of CDK1 (green) and SYCP3 (red) in mouse squashed metaphases I from *Psma8*$^{+/+}$ and *Psma8*$^{-/-}$mice showing CDK1 accumulation. Plot right to the panel represents the quantification of total CDK1 fluorescence intensity from *Psma8*$^{+/+}$ and *Psma8*$^{-/-}$ metaphase I cells. (C) Double immunolabeling of Cyclin B1 (green) and SYCP3 (red) in mouse squashed tubules from *Psma8*$^{+/+}$ and *Psma8*$^{-/-}$ mice showing CyclinB1 accumulation. Plot right to the panel represents the quantification of total CyclinB1 fluorescence intensity in metaphase I cells. Bars represent 10 μm (A), and 5 μm (B,C). Welch´s *t*-test analysis: * $p<0.01$; ** $p<0.001$; *** $p<0.0001$.
(TIF)

S16 Fig. HORMADs are not affected by the increased expression of TRIP13 in the *Psma8*$^{-/-}$ spermatocytes. (A-B) Double immunolabeling of HORMAD1 (A) and HORMAD2 (B) (green) with SYCP3 (red) in *Psma8*$^{+/+}$ and *Psma8*$^{-/-}$ spermatocytes at zygotene and pachytene stages. As synapsis progresses HORMAD1 and HORMAD2 are released from the AEs and maintained at the AE of the sex body similarly in the wild type and in the mutant spermatocytes. Bars represent 10 μm.
(TIF)

S17 Fig. PTTG1 expression is not altered in the absence of PSMA8. Double immunofluorescence of PTTG1 (green) and SYCP3 (red) in metaphase I cells showing similar expression levels of PTTG1. Plot under the panel represents the quantification of the fluorescence intensity from *Psma8*$^{+/+}$ and *Psma8*$^{-/-}$ metaphase I cells. Bar in panels, 10 μm. Welch´s *t*-test analysis: * $p<0.01$; ** $p<0.001$; *** $p<0.0001$.
(TIF)

S1 Table. Fertility assessment of *Psma8*$^{+/+}$, *Psma8*$^{+/-}$ and *Psma8*$^{-/-}$ mice.
(PDF)

S2 Table. Quantification of metaphases I/II in Psma8-/- testis. (A) Quantification of the proportion of tubules with metaphase I/II in PAS stained tubule sections from the histology example shown in Fig 2B. (B) Quantification of the number of metaphase I and II cells present in p-Ser10-H3 stained tubules that show meiotic divisions (Fig 2C). (C) Quantification of the percentage of metaphases-anaphases I and metaphases-anaphases II in squash preparations (double immunolabeled with ACA and SYCP3) measured as the N° of Metaphase-Anaphase I/II divided by the N° of cells (prophase I + Metaphase-Anaphase I + Interkinesis +-Metaphase-Anaphase II) (Fig 2D). Apoptotic Metaphase-Anaphase I and Metaphase-Anaphase II within each genotype are indicated.
(PDF)

S3 Table. Quantification of γH2AX levels, RAD51 foci, and MLH1 foci (S7 Fig).
(PDF)

S4 Table. Proteasome subunits and proteasome regulators co-immunoprecipitated with PSMA8 from *Psma8*$^{+/+}$and *Psma8*$^{-/-}$ testis protein extracts using anti-PSMA8 R2 antibody.
(PDF)

S5 Table. Proteasome subunits and proteasome regulators co-immunoprecipitated with PSMA8 selected after analysis and filtering of the data.
(PDF)

S6 Table. Selection of some of the proteasome-related proteins co-immunoprecipitated with PSMA8 selected after analysis and filtering of the data.
(PDF)

S7 Table. Quantification of the percentage of spermatocytes showing SYCP3 aggregates during prophase I stages in squash of seminiferous tubules of *Psma8*$^{+/+}$ and *Psma8*$^{-/-}$ testis. They have been classified in cells with small or large aggregates (n = 2 mice).
(PDF)

S1 Text. Exploratory representation of representative KEGG pathways. (A) Cell cycle (mmu04110). (B) Progesterone-mediated oocyte maduration (mmu04914). (C) Oocyte meiosis (mmu04114). In red, proteins detected in the co-IP experiment over the established cut-off.
(HTM)

S2 Text. Supporting information references.
(DOCX)

Acknowledgments

We wish to express our sincere thanks to Drs. Liu (Univ. of Toledo, USA), Dr Schimenti (Cornell Univ, USA), A. Toth (Dresden Univ. Germany), S. Khochbin (Univ. of Grenoble, France), Dr. Stemmann (Bayreuth Univ., Germany), Dr. Earnshaw, Dr. Murata (Univ of Tokyo, Japan) and Dr M. Sacristan for providing antibodies (TRIP13, Hormad1, Hormad2, SYCP1, H2AL2, MAD2, INCENP, PSMA8, and CDK1) and reagents (plasmid and REC8 mutant mice).

Author Contributions

Conceptualization: Elena Llano, Alberto M. Pendas.

Data curation: Laura Gómez-H.

Formal analysis: Laura Gómez-H, Dirk G. de Rooij, Alberto M. Pendas.

Funding acquisition: Alberto M. Pendas.

Investigation: Laura Gómez-H, Alberto M. Pendas.

Methodology: Laura Gómez-H, Natalia Felipe-Medina, Yazmine B. Condezo, Isabel Ramos, Manuel Sánchez-Martín, Dirk G. de Rooij.

Project administration: Alberto M. Pendas.

Resources: Natalia Felipe-Medina, José Luis Barbero, Ignasi Roig, Manuel Sánchez-Martín, Alberto M. Pendas.

Software: Rodrigo Garcia-Valiente.

Supervision: Alberto M. Pendas.

Validation: Laura Gómez-H, José Angel Suja.

Visualization: Laura Gómez-H, José Angel Suja.

Writing – original draft: Laura Gómez-H, Alberto M. Pendas.

Writing – review & editing: Laura Gómez-H, Dirk G. de Rooij, Elena Llano, Alberto M. Pendas.

References

1. Collins GA, Goldberg AL. The Logic of the 26S Proteasome. Cell. 2017; 169(5):792–806. https://doi.org/10.1016/j.cell.2017.04.023 PMID: 28525752
2. Schmidt M, Haas W, Crosas B, Santamaria PG, Gygi SP, Walz T, et al. The HEAT repeat protein Blm10 regulates the yeast proteasome by capping the core particle. Nature structural & molecular biology. 2005; 12(4):294–303.
3. Murata S, Yashiroda H, Tanaka K. Molecular mechanisms of proteasome assembly. Nature reviews Molecular cell biology. 2009; 10(2):104–15. https://doi.org/10.1038/nrm2630 PMID: 19165213
4. Finley D. Recognition and processing of ubiquitin-protein conjugates by the proteasome. Annual review of biochemistry. 2009; 78:477–513. https://doi.org/10.1146/annurev.biochem.78.081507.101607 PMID: 19489727
5. Qian MX, Pang Y, Liu CH, Haratake K, Du BY, Ji DY, et al. Acetylation-mediated proteasomal degradation of core histones during DNA repair and spermatogenesis. Cell. 2013; 153(5):1012–24. https://doi.org/10.1016/j.cell.2013.04.032 PMID: 23706739

6. Khor B, Bredemeyer AL, Huang CY, Turnbull IR, Evans R, Maggi LB Jr., et al. Proteasome activator PA200 is required for normal spermatogenesis. Molecular and cellular biology. 2006; 26(8):2999–3007. https://doi.org/10.1128/MCB.26.8.2999-3007.2006 PMID: 16581775
7. Cascio P, Hilton C, Kisselev AF, Rock KL, Goldberg AL. 26S proteasomes and immunoproteasomes produce mainly N-extended versions of an antigenic peptide. The EMBO journal. 2001; 20(10):2357–66. https://doi.org/10.1093/emboj/20.10.2357 PMID: 11350924
8. Griffin TA, Nandi D, Cruz M, Fehling HJ, Kaer LV, Monaco JJ, et al. Immunoproteasome assembly: cooperative incorporation of interferon gamma (IFN-gamma)-inducible subunits. The Journal of experimental medicine. 1998; 187(1):97–104. https://doi.org/10.1084/jem.187.1.97 PMID: 9419215
9. Murata S, Sasaki K, Kishimoto T, Niwa S, Hayashi H, Takahama Y, et al. Regulation of CD8+ T cell development by thymus-specific proteasomes. Science. 2007; 316(5829):1349–53. https://doi.org/10.1126/science.1141915 PMID: 17540904
10. Uechi H, Hamazaki J, Murata S. Characterization of the testis-specific proteasome subunit alpha4s in mammals. The Journal of biological chemistry. 2014; 289(18):12365–74. https://doi.org/10.1074/jbc.M114.558866 PMID: 24668818
11. Kisselev AF, Akopian TN, Castillo V, Goldberg AL. Proteasome active sites allosterically regulate each other, suggesting a cyclical bite-chew mechanism for protein breakdown. Molecular cell. 1999; 4 (3):395–402. PMID: 10518220
12. Inobe T, Matouschek A. Paradigms of protein degradation by the proteasome. Current opinion in structural biology. 2014; 24:156–64. https://doi.org/10.1016/j.sbi.2014.02.002 PMID: 24632559
13. Guo X, Wang X, Wang Z, Banerjee S, Yang J, Huang L, et al. Site-specific proteasome phosphorylation controls cell proliferation and tumorigenesis. Nature cell biology. 2016; 18(2):202–12. https://doi.org/10.1038/ncb3289 PMID: 26655835
14. Belle A, Tanay A, Bitincka L, Shamir R, O'Shea EK. Quantification of protein half-lives in the budding yeast proteome. Proceedings of the National Academy of Sciences of the United States of America. 2006; 103(35):13004–9. https://doi.org/10.1073/pnas.0605420103 PMID: 16916930
15. Glotzer M, Murray AW, Kirschner MW. Cyclin is degraded by the ubiquitin pathway. Nature. 1991; 349 (6305):132–8. https://doi.org/10.1038/349132a0 PMID: 1846030
16. Meyer HJ, Rape M. Enhanced protein degradation by branched ubiquitin chains. Cell. 2014; 157 (4):910–21. https://doi.org/10.1016/j.cell.2014.03.037 PMID: 24813613
17. Rao HB, Qiao H, Bhatt SK, Bailey LR, Tran HD, Bourne SL, et al. A SUMO-ubiquitin relay recruits proteasomes to chromosome axes to regulate meiotic recombination. Science. 2017; 355(6323):403–7. https://doi.org/10.1126/science.aaf6407 PMID: 28059716
18. Lake CM, Hawley RS. Becoming a crossover-competent DSB. Seminars in cell & developmental biology. 2016; 54:117–25.
19. Zickler D, Kleckner N. Recombination, Pairing, and Synapsis of Homologs during Meiosis. Cold Spring Harbor perspectives in biology. 2015; 7(6).
20. Kim J, Ishiguro K, Nambu A, Akiyoshi B, Yokobayashi S, Kagami A, et al. Meikin is a conserved regulator of meiosis-I-specific kinetochore function. Nature. 2015; 517(7535):466–71. https://doi.org/10.1038/nature14097 PMID: 25533956
21. Baudat F, Imai Y, de Massy B. Meiotic recombination in mammals: localization and regulation. Nature reviews Genetics. 2013; 14(11):794–806. https://doi.org/10.1038/nrg3573 PMID: 24136506
22. Ahuja JS, Sandhu R, Mainpal R, Lawson C, Henley H, Hunt PA, et al. Control of meiotic pairing and recombination by chromosomally tethered 26S proteasome. Science. 2017; 355(6323):408–11. https://doi.org/10.1126/science.aaf4778 PMID: 28059715
23. Consortium GT. Human genomics. The Genotype-Tissue Expression (GTEx) pilot analysis: multitissue gene regulation in humans. Science. 2015; 348(6235):648–60. https://doi.org/10.1126/science.1262110 PMID: 25954001
24. Gomez HL, Felipe-Medina N, Sanchez-Martin M, Davies OR, Ramos I, Garcia-Tunon I, et al. C14ORF39/SIX6OS1 is a constituent of the synaptonemal complex and is essential for mouse fertility. Nature communications. 2016; 7:13298. https://doi.org/10.1038/ncomms13298 PMID: 27796301
25. Bannister LA, Reinholdt LG, Munroe RJ, Schimenti JC. Positional cloning and characterization of mouse mei8, a disrupted allelle of the meiotic cohesin Rec8. Genesis. 2004; 40(3):184–94. https://doi.org/10.1002/gene.20085 PMID: 15515002
26. Barral S, Morozumi Y, Tanaka H, Montellier E, Govin J, de Dieuleveult M, et al. Histone Variant H2A.L.2 Guides Transition Protein-Dependent Protamine Assembly in Male Germ Cells. Molecular cell. 2017; 66(1):89–101 e8. https://doi.org/10.1016/j.molcel.2017.02.025 PMID: 28366643

27. Rogakou EP, Pilch DR, Orr AH, Ivanova VS, Bonner WM. DNA double-stranded breaks induce histone H2AX phosphorylation on serine 139. The Journal of biological chemistry. 1998; 273(10):5858–68. https://doi.org/10.1074/jbc.273.10.5858 PMID: 9488723

28. Mimitou EP, Symington LS. Nucleases and helicases take center stage in homologous recombination. Trends in biochemical sciences. 2009; 34(5):264–72. https://doi.org/10.1016/j.tibs.2009.01.010 PMID: 19375328

29. Dai J, Voloshin O, Potapova S, Camerini-Otero RD. Meiotic Knockdown and Complementation Reveals Essential Role of RAD51 in Mouse Spermatogenesis. Cell reports. 2017; 18(6):1383–94. https://doi.org/10.1016/j.celrep.2017.01.024 PMID: 28178517

30. Qiao H, Prasada Rao HB, Yang Y, Fong JH, Cloutier JM, Deacon DC, et al. Antagonistic roles of ubiquitin ligase HEI10 and SUMO ligase RNF212 regulate meiotic recombination. Nature genetics. 2014; 46 (2):194–9. https://doi.org/10.1038/ng.2858 PMID: 24390283

31. Shinohara M, Oh SD, Hunter N, Shinohara A. Crossover assurance and crossover interference are distinctly regulated by the ZMM proteins during yeast meiosis. Nature genetics. 2008; 40(3):299–309. https://doi.org/10.1038/ng.83 PMID: 18297071

32. Moens PB, Marcon E, Shore JS, Kochakpour N, Spyropoulos B. Initiation and resolution of interhomolog connections: crossover and non-crossover sites along mouse synaptonemal complexes. Journal of cell science. 2007; 120(Pt 6):1017–27. https://doi.org/10.1242/jcs.03394 PMID: 17344431

33. Gaucher J, Boussouar F, Montellier E, Curtet S, Buchou T, Bertrand S, et al. Bromodomain-dependent stage-specific male genome programming by Brdt. The EMBO journal. 2012; 31(19):3809–20. https://doi.org/10.1038/emboj.2012.233 PMID: 22922464

34. Lu LY, Wu J, Ye L, Gavrilina GB, Saunders TL, Yu X. RNF8-dependent histone modifications regulate nucleosome removal during spermatogenesis. Developmental cell. 2010; 18(3):371–84. https://doi.org/10.1016/j.devcel.2010.01.010 PMID: 20153262

35. Gomes AV, Young GW, Wang Y, Zong C, Eghbali M, Drews O, et al. Contrasting proteome biology and functional heterogeneity of the 20 S proteasome complexes in mammalian tissues. Molecular & cellular proteomics: MCP. 2009; 8(2):302–15.

36. da Cruz I, Rodriguez-Casuriaga R, Santinaque FF, Farias J, Curti G, Capoano CA, et al. Transcriptome analysis of highly purified mouse spermatogenic cell populations: gene expression signatures switch from meiotic-to postmeiotic-related processes at pachytene stage. BMC genomics. 2016; 17:294. https://doi.org/10.1186/s12864-016-2618-1 PMID: 27094866

37. Bousquet-Dubouch MP, Baudelet E, Guerin F, Matondo M, Uttenweiler-Joseph S, Burlet-Schiltz O, et al. Affinity purification strategy to capture human endogenous proteasome complexes diversity and to identify proteasome-interacting proteins. Molecular & cellular proteomics: MCP. 2009; 8(5):1150–64.

38. Verma R, Chen S, Feldman R, Schieltz D, Yates J, Dohmen J, et al. Proteasomal proteomics: identification of nucleotide-sensitive proteasome-interacting proteins by mass spectrometric analysis of affinity-purified proteasomes. Molecular biology of the cell. 2000; 11(10):3425–39. https://doi.org/10.1091/mbc.11.10.3425 PMID: 11029046

39. Sanchez-Lanzas R, Castano JG. Proteins directly interacting with mammalian 20S proteasomal subunits and ubiquitin-independent proteasomal degradation. Biomolecules. 2014; 4(4):1140–54. https://doi.org/10.3390/biom4041140 PMID: 25534281

40. Dittmar G, Selbach M. Deciphering the Ubiquitin Code. Molecular cell. 2017; 65(5):779–80. https://doi.org/10.1016/j.molcel.2017.02.011 PMID: 28257698

41. de Vries FA, de Boer E, van den Bosch M, Baarends WM, Ooms M, Yuan L, et al. Mouse Sycp1 functions in synaptonemal complex assembly, meiotic recombination, and XY body formation. Genes & development. 2005; 19(11):1376–89.

42. Mikolcevic P, Isoda M, Shibuya H, del Barco Barrantes I, Igea A, Suja JA, et al. Essential role of the Cdk2 activator RingoA in meiotic telomere tethering to the nuclear envelope. Nature communications. 2016; 7:11084. https://doi.org/10.1038/ncomms11084 PMID: 27025256

43. Roig I, Dowdle JA, Toth A, de Rooij DG, Jasin M, Keeney S. Mouse TRIP13/PCH2 is required for recombination and normal higher-order chromosome structure during meiosis. PLoS genetics. 2010; 6 (8).

44. Yost S, de Wolf B, Hanks S, Zachariou A, Marcozzi C, Clarke M, et al. Biallelic TRIP13 mutations predispose to Wilms tumor and chromosome missegregation. Nature genetics. 2017; 49(7):1148–51. https://doi.org/10.1038/ng.3883 PMID: 28553959

45. Bolcun-Filas E, Rinaldi VD, White ME, Schimenti JC. Reversal of female infertility by Chk2 ablation reveals the oocyte DNA damage checkpoint pathway. Science. 2014; 343(6170):533–6. https://doi.org/10.1126/science.1247671 PMID: 24482479

46. Wojtasz L, Daniel K, Roig I, Bolcun-Filas E, Xu H, Boonsanay V, et al. Mouse HORMAD1 and HORMAD2, two conserved meiotic chromosomal proteins, are depleted from synapsed chromosome axes with the help of TRIP13 AAA-ATPase. PLoS genetics. 2009; 5(10):e1000702. https://doi.org/10.1371/journal.pgen.1000702 PMID: 19851446

47. Wang K, Sturt-Gillespie B, Hittle JC, Macdonald D, Chan GK, Yen TJ, et al. Thyroid hormone receptor interacting protein 13 (TRIP13) AAA-ATPase is a novel mitotic checkpoint-silencing protein. The Journal of biological chemistry. 2014; 289(34):23928–37. https://doi.org/10.1074/jbc.M114.585315 PMID: 25012665

48. Wojtasz L, Cloutier JM, Baumann M, Daniel K, Varga J, Fu J, et al. Meiotic DNA double-strand breaks and chromosome asynapsis in mice are monitored by distinct HORMAD2-independent and -dependent mechanisms. Genes & development. 2012; 26(9):958–73.

49. Daniel K, Lange J, Hached K, Fu J, Anastassiadis K, Roig I, et al. Meiotic homologue alignment and its quality surveillance are controlled by mouse HORMAD1. Nature cell biology. 2011; 13(5):599–610. https://doi.org/10.1038/ncb2213 PMID: 21478856

50. Nelson CR, Hwang T, Chen PH, Bhalla N. TRIP13PCH-2 promotes Mad2 localization to unattached kinetochores in the spindle checkpoint response. The Journal of cell biology. 2015; 211(3):503–16. https://doi.org/10.1083/jcb.201505114 PMID: 26527744

51. Davies OR, Maman JD, Pellegrini L. Structural analysis of the human SYCE2-TEX12 complex provides molecular insights into synaptonemal complex assembly. Open biology. 2012; 2(7):120099. https://doi.org/10.1098/rsob.120099 PMID: 22870393

52. Winkel K, Alsheimer M, Ollinger R, Benavente R. Protein SYCP2 provides a link between transverse filaments and lateral elements of mammalian synaptonemal complexes. Chromosoma. 2009; 118 (2):259–67. https://doi.org/10.1007/s00412-008-0194-0 PMID: 19034475

53. Miake H, Mizusawa H, Iwatsubo T, Hasegawa M. Biochemical characterization of the core structure of alpha-synuclein filaments. The Journal of biological chemistry. 2002; 277(21):19213–9. https://doi.org/10.1074/jbc.M110551200 PMID: 11893734

54. Huang L, Haratake K, Miyahara H, Chiba T. Proteasome activators, PA28gamma and PA200, play indispensable roles in male fertility. Scientific reports. 2016; 6:23171. https://doi.org/10.1038/srep23171 PMID: 27003159

55. Jiang H, Gao Q, Zheng W, Yin S, Wang L, Zhong L, et al. MOF influences meiotic expansion of H2AX phosphorylation and spermatogenesis in mice. PLoS genetics. 2018; 14(5):e1007300. https://doi.org/10.1371/journal.pgen.1007300 PMID: 29795555

56. Yang Q, Ferrell JE Jr. The Cdk1-APC/C cell cycle oscillator circuit functions as a time-delayed, ultrasensitive switch. Nature cell biology. 2013; 15(5):519–25. https://doi.org/10.1038/ncb2737 PMID: 23624406

57. Hellmuth S, Pohlmann C, Brown A, Bottger F, Sprinzl M, Stemmann O. Positive and negative regulation of vertebrate separase by Cdk1-cyclin B1 may explain why securin is dispensable. The Journal of biological chemistry. 2015; 290(12):8002–10. https://doi.org/10.1074/jbc.M114.615310 PMID: 25659430

58. Rattani A, Vinod PK, Godwin J, Tachibana-Konwalski K, Wolna M, Malumbres M, et al. Dependency of the spindle assembly checkpoint on Cdk1 renders the anaphase transition irreversible. Current biology: CB. 2014; 24(6):630–7. https://doi.org/10.1016/j.cub.2014.01.033 PMID: 24583015

59. Bolcun-Filas E, Hall E, Speed R, Taggart M, Grey C, de Massy B, et al. Mutation of the mouse Syce1 gene disrupts synapsis and suggests a link between synaptonemal complex structural components and DNA repair. PLoS genetics. 2009; 5(2):e1000393. https://doi.org/10.1371/journal.pgen.1000393 PMID: 19247432

60. Bolcun-Filas E, Costa Y, Speed R, Taggart M, Benavente R, De Rooij DG, et al. SYCE2 is required for synaptonemal complex assembly, double strand break repair, and homologous recombination. The Journal of cell biology. 2007; 176(6):741–7. https://doi.org/10.1083/jcb.200610027 PMID: 17339376

61. Schramm S, Fraune J, Naumann R, Hernandez-Hernandez A, Hoog C, Cooke HJ, et al. A novel mouse synaptonemal complex protein is essential for loading of central element proteins, recombination, and fertility. PLoS genetics. 2011; 7(5):e1002088. https://doi.org/10.1371/journal.pgen.1002088 PMID: 21637789

62. Agarwal A, Sharma R, Durairajanayagam D, Cui Z, Ayaz A, Gupta S, et al. Differential proteomic profiling of spermatozoal proteins of infertile men with unilateral or bilateral varicocele. Urology. 2015; 85 (3):580–8. https://doi.org/10.1016/j.urology.2014.11.030 PMID: 25733269

63. Singh P, Schimenti JC, Bolcun-Filas E. A mouse geneticist's practical guide to CRISPR applications. Genetics. 2015; 199(1):1–15. https://doi.org/10.1534/genetics.114.169771 PMID: 25271304

64. Page J, Suja JA, Santos JL, Rufas JS. Squash procedure for protein immunolocalization in meiotic cells. Chromosome research: an international journal on the molecular, supramolecular and evolutionary aspects of chromosome biology. 1998; 6(8):639–42.

65. Papanikos F, Clement JAJ, Testa E, Ravindranathan R, Grey C, Dereli I, et al. Mouse ANKRD31 Regulates Spatiotemporal Patterning of Meiotic Recombination Initiation and Ensures Recombination between X and Y Sex Chromosomes. Molecular cell. 2019.

66. Malkov M, Fisher Y, Don J. Developmental schedule of the postnatal rat testis determined by flow cytometry. Biol Reprod. 1998; 59(1):84–92. https://doi.org/10.1095/biolreprod59.1.84 PMID: 9674997

67. Yu G, Wang LG, Han Y, He QY. clusterProfiler: an R package for comparing biological themes among gene clusters. Omics: a journal of integrative biology. 2012; 16(5):284–7. https://doi.org/10.1089/omi.2011.0118 PMID: 22455463

68. Brouwer CA, Postma A, Hooimeijer HL, Smit AJ, Vonk JM, van Roon AM, et al. Endothelial damage in long-term survivors of childhood cancer. Journal of clinical oncology: official journal of the American Society of Clinical Oncology. 2013; 31(31):3906–13.

RESEARCH ARTICLE

A missense in HSF2BP causing primary ovarian insufficiency affects meiotic recombination by its novel interactor C19ORF57/BRME1

Natalia Felipe-Medina[1†], Sandrine Caburet[2,3†], Fernando Sánchez-Sáez[1], Yazmine B Condezo[1], Dirk G de Rooij[4], Laura Gómez-H[1], Rodrigo Garcia-Valiente[1], Anne Laure Todeschini[2,3], Paloma Duque[1], Manuel Adolfo Sánchez-Martin[5,6], Stavit A Shalev[7,8], Elena Llano[1,9], Reiner A Veitia[2,3,10]*, Alberto M Pendás[1]*

[1]Molecular Mechanisms Program, Centro de Investigación del Cáncer and Instituto de Biología Molecular y Celular del Cáncer (CSIC-Universidad de Salamanca), Salamanca, Spain; [2]Universite´ de Paris, Paris Cedex, France; [3]Institut Jacques Monod, Universite´ de Paris, Paris, France; [4]Reproductive Biology Group, Division of Developmental Biology, Department of Biology, Faculty of Science, Utrecht University, Utrecht, Netherlands; [5]Transgenic Facility, Nucleus platform, Universidad de Salamanca, Salamanca, Spain; [6]Departamento de Medicina, Universidad de Salamanca, Salamanca, Spain; [7]The Genetic Institute, "Emek" Medical Center, Afula, Israel; [8]Bruce and Ruth Rappaport Faculty of Medicine, Technion, Haifa, Israel; [9]Departamento de Fisiología y Farmacología, Universidad de Salamanca, Salamanca, Spain; [10]Université Paris-Saclay, Institut de Biologie F. Jacob, Commissariat à l'Energie Atomique, Fontenay aux Roses, France

***For correspondence:** reiner.veitia@ijm.fr (RAV); amp@usal.es (AMP)

[†]These authors contributed equally to this work

Competing interests: The authors declare that no competing interests exist.

Funding: See page 26

Received: 17 March 2020
Accepted: 26 August 2020
Published: 26 August 2020

Reviewing editor: Bernard de Massy, CNRS UM, France

Abstract Primary Ovarian Insufficiency (POI) is a major cause of infertility, but its etiology remains poorly understood. Using whole-exome sequencing in a family with three cases of POI, we identified the candidate missense variant S167L in *HSF2BP*, an essential meiotic gene. Functional analysis of the HSF2BP-S167L variant in mouse showed that it behaves as a hypomorphic allele compared to a new loss-of-function (knock-out) mouse model. *Hsf2bp*$^{S167L/S167L}$ females show reduced fertility with smaller litter sizes. To obtain mechanistic insights, we identified C19ORF57/BRME1 as a strong interactor and stabilizer of HSF2BP and showed that the BRME1/HSF2BP protein complex co-immunoprecipitates with BRCA2, RAD51, RPA and PALB2. Meiocytes bearing the HSF2BP-S167L variant showed a strongly decreased staining of both HSF2BP and BRME1 at the recombination nodules and a reduced number of the foci formed by the recombinases RAD51/DMC1, thus leading to a lower frequency of crossovers. Our results provide insights into the molecular mechanism of HSF2BP-S167L in human ovarian insufficiency and sub(in)fertility.

Introduction

The process of gametogenesis is one of the most complex and highly regulated differentiation programs. It involves a unique reductional cell division, known as meiosis, to generate highly specialized cells: the gametes. Indeed, the outcome of meiosis is the production of oocytes and spermatozoa, which are the most distinctive cells of an adult organism and are essential for the faithful transmission of the genome across generations.

The meiotic division is an orderly process that results in the pairing and synapsis of homologous chromosomes and crossover (CO) formation, which ultimately enable homologous chromosomes segregation (**Hunter, 2015**; **Loidl, 2016**; **Zickler and Kleckner, 2015**). In mammals, pairing of homologs is dependent on the repair of self-induced double-strand breaks (DSBs) during prophase I by homologous recombination (**Handel and Schimenti, 2010**) and it leads to the intimate alignment of homologous chromosomes (synapsis) through the zipper-like synaptonemal complex (SC) (**Cahoon and Hawley, 2016**). The SC is a proteinaceous tripartite structure that provides the structural framework for DSBs repair (**Baudat et al., 2013**), as epitomized by the tight association of the recombination nodules (RNs, multicomponent recombinogenic factories) and the axial elements of the SC (**Zickler and Kleckner, 2015**).

Meiotic DSBs repair is an evolutionarily conserved pathway that is highly regulated to promote the formation of at least one CO per bivalent. This chromosome connection between bivalents through chiasmata is required for a correct reductional division. As other DNA repair processes, proper meiotic recombination is essential for genome stability and alterations can result in infertility, miscarriage and birth defects (**Geisinger and Benavente, 2017**; **Handel and Schimenti, 2010**; **Webster and Schuh, 2017**).

Infertility refers to failure of a couple to reproduce and affects 10–15% of couples (**Isaksson and Tiitinen, 2004**). Infertility can be due to female factors, male factors, a combination of both or to unknown causes, each category representing approximately 25% of cases (**Isaksson and Tiitinen, 2004**; **Matzuk and Lamb, 2008**). There are several underlying causes and physiological, genetic and even environmental and social factors can play a role. Forward and reverse genetic analyses in model organisms have identified multiple molecular pathways that regulate fertility and have allowed to infer reasonable estimates of the number of protein-coding genes essential for fertility (**de Rooij and de Boer, 2003**; **Schimenti and Handel, 2018**).

Primary ovarian insufficiency (POI) is a major cause of female infertility and affects about 1–3% of women under 40 years of age. It is characterized by cessation of ovarian function before the age of 40 years. POI results from a depletion of the ovarian follicle pool and can be isolated or syndromic. Genetic causes of POI account for approximately 20% of cases (**Rossetti et al., 2017**). Although infertility-causing pathogenic variants are inherently unlikely to spread in a population, they can be observed within families, especially when there is consanguinity. Such cases provide crucial insights into the function of the genes and molecular mechanisms that they disrupt. Over the last decade, causative variants in several genes have been found using whole exome sequencing in 'POI pedigrees'. In particular, pathogenic variants in genes involved in DNA replication, recombination or repair, such as *STAG3, SYCE1, HFM1, MSH5* and *MEIOB* have been formally implicated in this condition by ourselves and others (**Caburet et al., 2014**; **Caburet et al., 2019a**; **de Vries et al., 2014**; **Guo et al., 2017**; **Primary Ovarian Insufficiency Collaboration et al., 2014**).

In this study, we have identified in a consanguineous family with POI the candidate S167L missense variant in *HSF2BP*, an essential yet poorly studied meiotic gene. *HSF2BP* encodes an interactor of the heat-shock response transcription factor HSF2 (**Yoshima et al., 1998**). During the course of this work and, in agreement with our results, two independent groups showed that HSF2BP is essential for meiotic recombination through its ability to interact with BRCA2 (**Brandsma et al., 2019**; **Zhang et al., 2019**). Here, we report that the introduction of the missense variant HSF2BP-S167L in mouse leads to subfertility and DNA repair defects during prophase I. In addition, we identified a protein complex composed of BRCA2, HSF2BP, and the as yet unexplored C19ORF57/BRME1 (meiotic double-stranded break BRCA2/HSF2BP complex associated protein) as a key component of the meiotic recombination machinery. Our studies show that a single substitution (S167L) in HSF2BP leads to a reduced loading of both BRME1 and HSF2BP at the RNs. Furthermore, our results suggest that meiotic progression requires a critical threshold level of HSF2BP/BRME1 for the ulterior loading of the recombinases to the RNs.

Results

Clinical cases

The parents are first-degree cousins of Israeli Arab origin. Of the five daughters, three are affected with POI and presented with early secondary amenorrhea. They had menarche at normal age (at 13–

14) but with irregular menses that stopped around 25. Only one of the patients affected by POI could have a child with the help of a fertility treatment (see pedigree in ***Figure 1***). In order to identify the genetic basis of this familial POI case, we performed whole exome sequencing on genomic DNA from two POI patients, III-2 and III-3, and their fertile sister III-10 (***Supplementary file 1a***). Variants were filtered on the basis of (i) their homozygosity in the patients, (ii) their heterozygosity or absence in the fertile sister, (iii) their absence in unrelated fertile in-house controls and (iv) a minor allele frequency (MAF) below 0.01 in all available databases (***Supplementary file 1b***). This filtering process led to the identification of a missense substitution located in the *HSF2BP* gene: rs200655253 (21:43630396 G > A, GRCh38). The variant lies within the sixth exon of the reference transcript ENST00000291560.7 (NM_007031.2:c.500C > T) and changes a TCG codon into a TTG (NP_008962.1:p.Ser167Leu). It is very rare (Variant Allele Frequency/VAF 0.0001845 in the GnomAD database and 0.0005 in the GME Variome dedicated to Middle-East populations) and absent in a

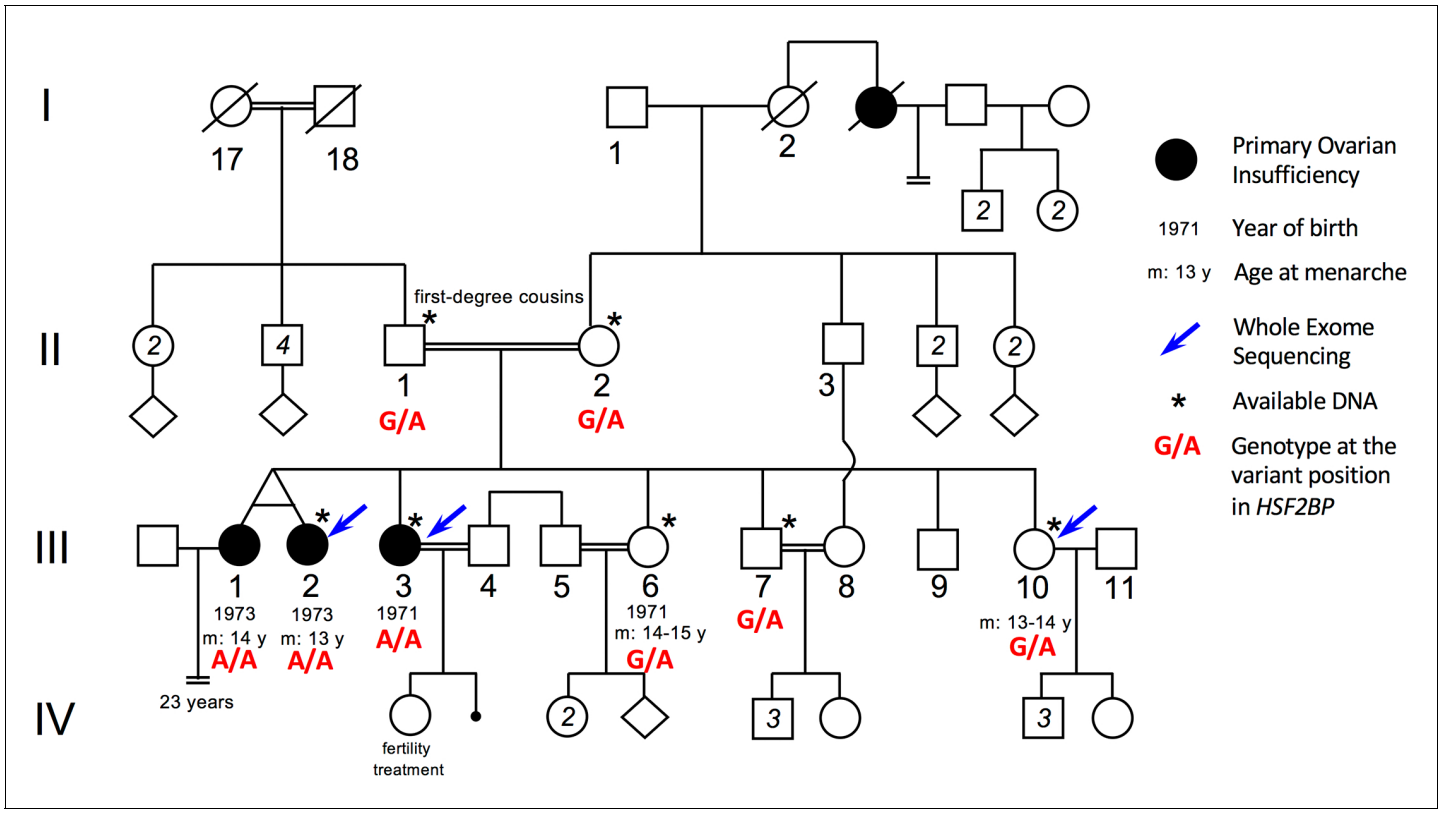

Figure 1. Pedigree of the consanguineous family with the variant HSF2BP-S167L. III-1 and III-2 are monozygotic twins, who appear phenotypically dizygotic. Clinical investigation confirmed POI, with normal 46, XX karyotype (500 bands and SKY spectral karyotyping). Year of birth and age of menarche are indicated when known. III-1 became amenorrheic at age 24 and III-2 at age 25, both after irregular menstruations since menarche. III-1 presents with a short stature (152 cm, within the 3–5 percentile), a normal neck, cubitus valgus and metacarpal shortening of 4–5. Ultrasound investigation showed normal uterus and ovaries. Her g-banding karyotyping was normal 46, XX (500 bands) and variants in FMR1 gene were ruled out. III-2 displays a normal secondary sexual development with no dysmorphic sign. Clinical investigation confirmed POI, with normal 46, XX karyotype (500 bands and SKY spectral karyotyping). The elder sister III-3 was also diagnosed with POI, with no further clinical information. She is 160.5 cm. She had one normal pregnancy with the help of 'fertility treatment', and a second unsuccessful attempt. The two fertile sisters, III-6 and III-10 had their menarche at 14–15 and 13–14 respectively, with regular menstruations ever since. They are respectively 150 cm and 151 cm, with no clinical sign, and each one had several children without difficulties. The fertile brother III-7 is 171 cm and shows no health or fertility problem. He developed frontal baldness since the age of 30. The genotype of each individual at the variant genomic position in *HSF2BP* is shown in red, as determined by Sanger sequencing for available DNAs (See ***Figure 1—figure supplement 1***).

The online version of this article includes the following figure supplement(s) for figure 1:

Figure supplement 1. Segregation of the S167L Variant in HSF2BP in the consanguineous family shows the chromatograms obtained by Sanger sequencing of the HSF2BP-S167L variant in the family.

Figure supplement 2. Strong conservation of the Ser167 residue in HSF2BP protein in 99 mammals.

Figure supplement 3. Strong conservation of the Ser167 residue in HSF2BP in 48 birds and reptiles and 64 fish species.

homozygous state from all available databases. The variant was verified by Sanger sequencing and was found to segregate in a Mendelian fashion within the family: the affected twin III-1 was homozygous for the variant and both parents and fertile siblings were heterozygous carriers (***Figure 1—figure supplement 1***). Therefore, there was no homozygous males identified in this family, preventing the analysis of the impact of this variant on male fertility. Serine 167 is a highly conserved position and the S167L variant is predicted to be pathogenic or deleterious by 11 out of the 18 pathogenicity predictors available in dbNSFP 3.5. (***Supplementary file 1c***, ***Figure 1—figure supplement 2*** and ***Figure 1—figure supplement 3***).

Mice with the HSF2BP S167L variant show a partial reduction of fertility

During the course of this work, two independent groups showed that HSF2BP is essential for meiotic recombination through its ability to interact with the armadillo repeats of BRCA2 (***Zhang et al., 2019***). Both groups showed that genetic disruption of *Hsf2bp* in mouse leads to the accumulation in the chromosomes axes of DNA repair proteins such as γH2AX (ATR-dependent phosphorylation of H2AX marks DSBs) and the single stranded-DNA binding protein RPA, a strong reduction of the recombinases DMC1 and RAD51 at the RNs and a lack of COs as labelled by MLH1 (***Baker et al., 1996***). The end result is male sterility (***Brandsma, 2006***; ***Brandsma et al., 2019***; ***Zhang et al., 2019***). However, loss of HSF2BP in female mice showed a milder meiotic phenotype (***Zhang et al., 2019*** and our own data, see below) and a weak albeit non-statistical significant reduction of fertility (***Brandsma et al., 2019***) despite all of the mutants are nulls though in different genetic backgrounds.

In order to confirm the causality of the S167L variant in this POI family, we generated a knock-in mouse *Hsf2bp*$^{S167L/S167L}$ by genome editing (***Figure 2—figure supplement 1a***). We also generated a loss-of-function model (*Hsf2bp*$^{-/-}$) for direct comparison (***Figure 2—figure supplement 1b–d***). *Hsf2bp*$^{S167L/S167L}$ male and female mice were able to reproduce but females showed a significant reduction in the number of litters (***Figure 2a***), whilst males only showed a slight non-significant reduction in fertility (***Figure 2a***), suggesting that the S167L variant impacts murine fertility.

Histological analysis of *Hsf2bp*$^{S167L/S167L}$ ovaries revealed no apparent differences in the number of follicles in comparison to wild-type (WT) animals (***Figure 2b–c*** and ***Figure 2—figure supplement 2a***), in contrast with the drastic reduction of the follicle pool in *Hsf2bp*$^{-/-}$ ovaries (***Figure 2b–c***). Testes from *Hsf2bp*$^{S167L/S167L}$ mice displayed a reduced size (21% reduction compared to WT mice; testis/body weight ratio: S167L 0.26% ± 0.07 (n = 12) vs 0.33% ± 0.05 for WT controls (n = 14), **p<0,01, ***Figure 2d*** and ***Figure 2—figure supplement 2b***) and this reduction was stronger in *Hsf2bp*$^{-/-}$ testes (70% reduction compared to WT, testis/body weight ratio: *Hsf2bp*$^{-/-}$ 0.10% ± 0.005 (n = 6) vs 0.33% ± 0.05 for WT controls (n = 14) ****p<0,001, ***Figure 2d*** and ***Figure 2—figure supplement 2b***). Histological analysis of adult *Hsf2bp*$^{S167L/S167L}$ testes revealed seminiferous tubules with a partial arrest with apoptotic spermatocytes (meiotic divisions) and their epididymis exhibited scarcer spermatozoa (***Figure 2e***). Consistent with these results, *Hsf2bp*$^{S167L/S167L}$ males showed increased numbers of meiotic divisions positive for TUNEL staining (***Figure 2f***) and a reduction in the number of spermatozoa in the epididymis (3.3×10^6 in the *Hsf2bp*$^{S167L/S167L}$ mutant vs 4.3×10^6 in the WT; ***Figure 2g***). During mouse spermatogenesis, the 12 stages of the epithelial cycle can be distinguished in seminiferous tubule sections by identifying groups of associated germ cell types (***Ahmed and de Rooij, 2009***). Following these criteria, the seminiferous epithelium of *Hsf2bp*$^{-/-}$ mice showed a stage IV arrest, characterized by a massive apoptosis of zygotene-like spermatocytes occurring at the same time that In spermatogonia divide into B spermatogonia (***Figure 2e***). The presence of spermatogonia, spermatocytes, Sertoli and Leydig cells was not altered in any of the mutants (***Figure 2e***). These results suggest that mice bearing the POI-causing variant only partially phenocopy the human disease.

Hsf2bp$^{S167L/S167L}$ meiocytes show an altered meiotic homologous recombination

To further characterize meiotic defects, *Hsf2bp*$^{S167L/S167L}$ meiocytes were first analyzed for the assembly/disassembly of the SC by monitoring the distribution of SYCP1 and SYCP3. We did not observe any difference in synapsis and desynapsis from leptotene to diplotene in both oocytes and

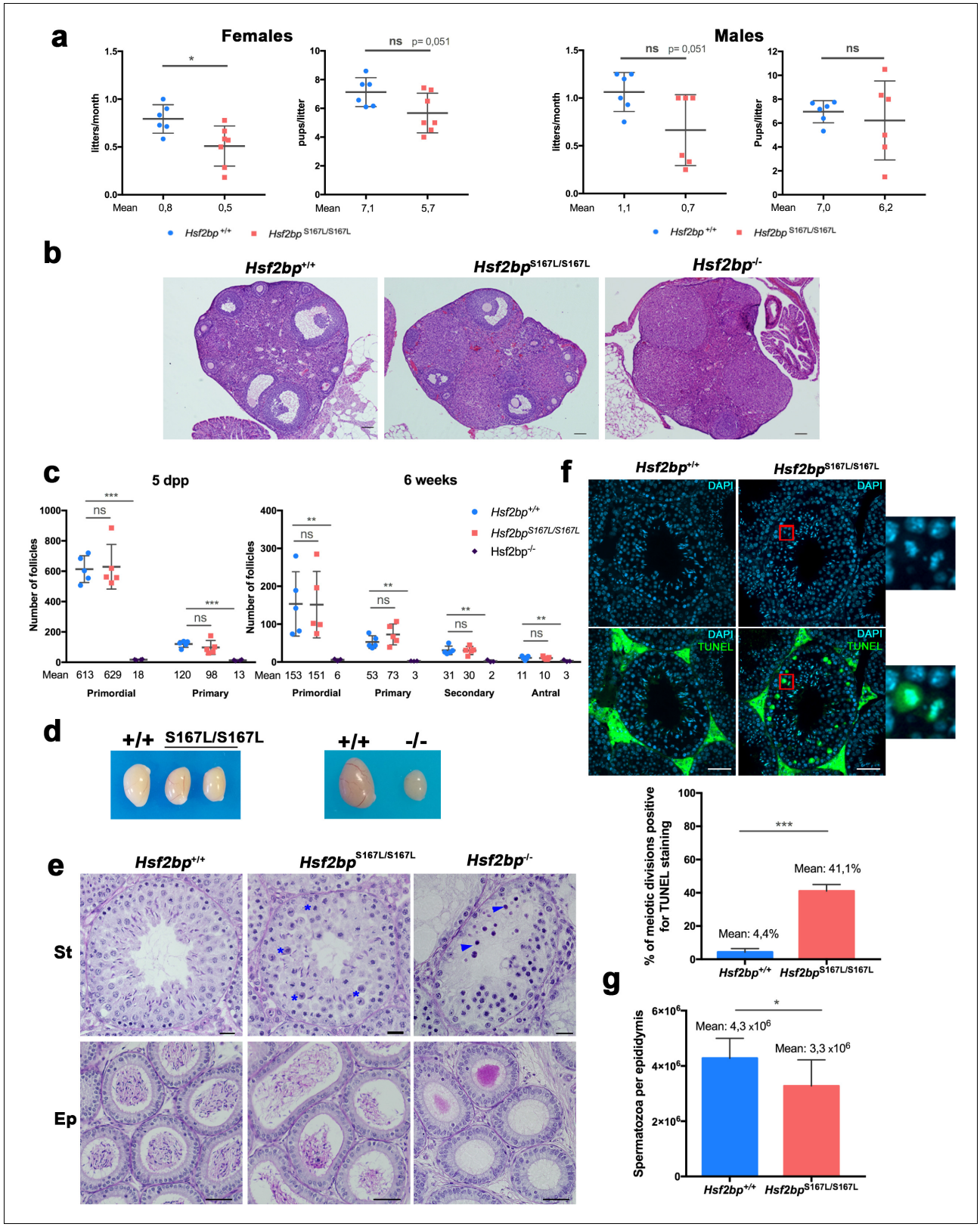

Figure 2. Mice carrying the HSF2BP S167L variant show a partial reduction of fertility. (**a**) Fertility assessment of males and female *Hsf2bp*$^{S167L/S167L}$ and WT mice showing the number of litters per month and the number of pups per litter (see Materials and methods). Mice: *Hsf2bp*$^{+/+}$n = 6 females/6 males, *Hsf2bp*$^{S167L/S167L}$n = 7 females/6 males. Two-tailed Welch's t-test analysis: *p<0.05. (**b**) Hematoxylin and eosin stained sections of ovaries from adult (8 weeks) *Hsf2bp*$^{+/+}$, *Hsf2bp*$^{S167L/S167L}$ and *Hsf2bp*$^{-/-}$ females. *Hsf2bp*$^{-/-}$ ovaries but not *Hsf2bp*$^{+/+}$ and *Hsf2bp*$^{S167L/S167L}$ showed a strong depletion

Figure 2 continued on next page

Figure 2 continued

of follicles. Bar in panels 100 μm. (**c**) Quantification of the number of follicles (primordial, primary, secondary and antral follicles) per ovary in *Hsf2bp*$^{+/+}$, *Hsf2bp*$^{S167L/S167L}$ and *Hsf2bp*$^{-/-}$ females at 5 dpp and 6 weeks of age showing no differences between *Hsf2bp*$^{+/+}$ and *Hsf2bp*$^{S167L/S167L}$ but a strong reduction in the oocyte pool in *Hsf2bp*$^{-/-}$ females. Ovaries: five dpp/6 weeks = 5/5 ovaries from *Hsf2bp*$^{+/+}$ and *Hsf2bp*$^{S167L/S167L}$ and 4/3 from *Hsf2bp*$^{-/-}$. Two-tailed Welch's t-test analysis: ns, no significant differences, **p<0.01, ***p<0.001. (**d**) Testis size of *Hsf2bp*$^{S167L/S167L}$ (left, 21% reduction) and *Hsf2bp*$^{-/-}$ mice (right, 70% reduction) in comparison with their WT counterparts. See ***Figure 2—figure supplement 2b*** for the quantification. (**e**) PAS and Hematoxylin stained testis sections. The S167L variant leads to a partial spermatogenic arrest with an elevated number of apoptotic meiotic divisions (blue asterisks) and a reduction of the number of spermatozoa in the epididymides in comparison with the WT control (*Hsf2bp*$^{+/+}$). The null allele (*Hsf2bp*$^{-/-}$) showed a complete spermatogenic arrest at epithelial stage IV and absence of spermatozoa. Massive apoptosis of spermatocytes is indicated (blue arrowheads). Bar: upper panels 10 μm, lower panels 20 μm. (St) Seminiferous tubules, (Ep) Epididymides. (**f**) Immunohistochemical detection of apoptotic cells by TUNEL staining showing an increase of apoptotic meiotic divisions in stage XII tubules from *Hsf2bp*$^{S167L/S167L}$ males (magnified panel). Plot under the panel represents the quantification. Mice: n = 3 adult mice for each genotype. Two-tailed Welch's t-test analysis: ***p<0.001. Bar in panel, 25 μm. (**g**) Quantification of epididymal sperm in *Hsf2bp*$^{+/+}$ and *Hsf2bp*$^{S167L/S167L}$ adult mice. Epididymides: n = 8 for each genotype. Two-tailed Welch's t-test analysis: *p<0.05.

The online version of this article includes the following figure supplement(s) for figure 2:

Figure supplement 1. Generation and genetic characterization of *Hsf2bp* S167L and *Hsf2bp*-deficient mice.

Figure supplement 2. Fertility defects in *Hsf2bp*$^{S167L/S167L}$ mice.

spermatocytes (***Figure 3—figure supplement 1a–b***). However, we observed an elevated number of apoptotic meiotic divisions in *Hsf2bp*$^{S167L/S167L}$ males (***Figure 2—figure supplement 2c***). These results are consistent with the partial arrest observed in the histological analysis (***Figure 2e***). As expected, this phenotype was exacerbated in *Hsf2bp*$^{-/-}$ spermatocytes that were arrested at a zygotene-like stage (***Figure 3—figure supplement 1c***). *Hsf2bp*$^{-/-}$ oocytes showed a delay in prophase I progression with the majority of cells at zygotene stage in 17.5 days post-coitum (dpc) females, whilst the WT oocytes were mainly at pachytene stage. Additionally, we observed increased numbers of oocytes showing synapsis defects in the *Hsf2bp*$^{-/-}$ oocytes (*Hsf2bp*$^{-/-}$: 45,5% ± 1,5 vs WT: 7,5% ± 1,5; n = 2 (both genotypes), **p<0,01, ***Figure 3—figure supplement 1d***). These results strongly suggest that the POI variant S167L is a hypomorphic allele.

Next, we analyzed whether the POI-inducing variant affects the loading/stability of HSF2BP by immunolabeling meiocytes from *Hsf2bp*$^{S167L/S167L}$ mice. We observed a striking reduction of HSF2BP staining at the axes during prophase I in both spermatocytes and oocytes (***Figure 3a–b***). Western blot analysis of WT, *Hsf2bp*$^{S167L/S167L}$ and *Hsf2bp*$^{-/-}$ in whole testis extracts from 13 days post-partum (dpp) animals (***Figure 3c***) revealed that the reduced labeling observed by immunofluorescence correlated with a reduced protein expression level, suggesting that the mutation leads to a reduced expression and/or stability.

Given that HSF2BP is essential for DNA repair, we carried out a comparative staining analysis of γH2AX, the ssDNA-binding protein RPA, the recombinases RAD51 and DMC1, the ssDNA-binding protein SPATA22 (complexed to RPA during resection) and CO formation in meiocytes from *Hsf2bp*$^{S167L/S167L}$, *Hsf2bp*$^{-/-}$ and WT animals (***Figures 4***, ***5*** and ***6***, ***Figure 4—figure supplement 1***, ***Figure 5—figure supplement 1*** and ***Figure 6—figure supplement 1***). Our results revealed that *Hsf2bp*$^{S167L/S167L}$ spermatocytes showed an increased labeling of γH2AX at pachytene (***Figure 4a***), an accumulation of RPA at the chromosome axis (***Figure 4b*** and ***Figure 4—figure supplement 1a***), a reduction of the recombinases DMC1 and RAD51 staining (***Figure 5a–b*** and ***Figure 5—figure supplement 1a–b***), an accumulation of SPATA22 (***Figure 6a*** and ***Figure 6—figure supplement 1a***), and a decreased number of COs (measured as MLH1, ***Figure 6b*** and ***Figure 6—figure supplement 1b***). In accordance with the reduction of COs, we observed the presence of univalents in the XY pair at pachynema as well as univalents in metaphase I spermatocytes from *Hsf2bp*$^{S167L/S167L}$ mice (***Figure 6d*** and ***Figure 6—figure supplement 1c***). These results would explain the elevated number of apoptotic metaphases observed (***Figure 2e–f*** and ***Figure 2—figure supplement 2c***).

Our analysis in females showed accumulation of γH2AX staining (***Figure 4c***) but no accumulation in RPA labeling in *Hsf2bp*$^{S167L/S167L}$ and *Hsf2bp*$^{-/-}$ oocytes (***Figure 4d*** and ***Figure 4—figure supplement 1b***). Similar to the spermatocytes, DMC1 and RAD51 staining showed a reduction in both *Hsf2bp*$^{S167L/S167L}$ and *Hsf2bp*$^{-/-}$ oocytes (***Figure 5c–d*** and ***Figure 5—figure supplement 1c–d***). SPATA22 labeling in females showed a clear accumulation in *Hsf2bp*$^{-/-}$ but only a trend towards accumulation in *Hsf2bp*$^{S167L/S167L}$ oocytes (***Figure 6a*** and ***Figure 6—figure supplement 1a***). In

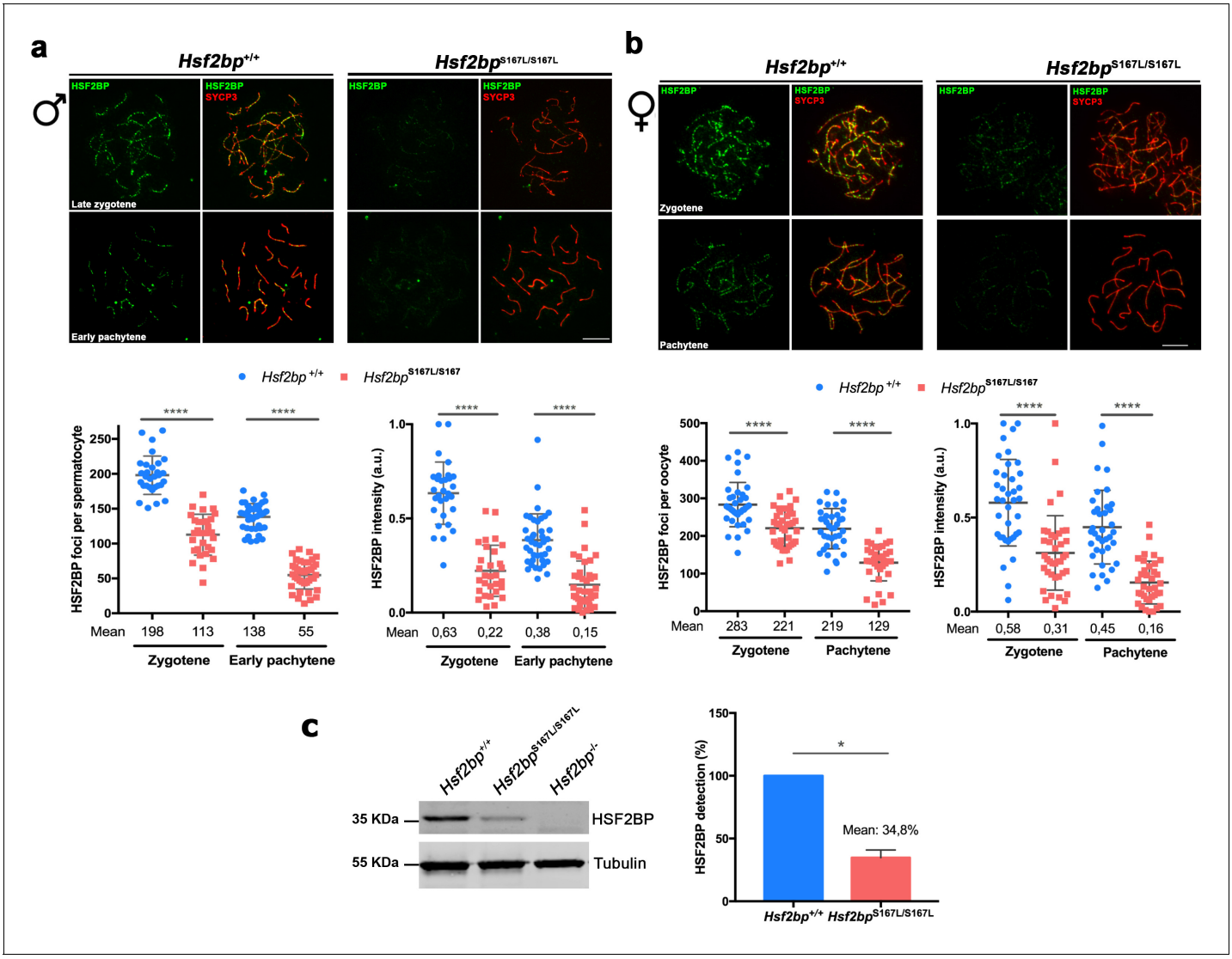

Figure 3. Meiocytes from *Hsf2bp*$^{S167L/S167L}$ mice show a decrease in the expression of HSF2BP. (**a–b**) Double immunofluorescence of HSF2BP (green) and SYCP3 (red) in *Hsf2bp*$^{+/+}$and *Hsf2bp*$^{S167L/S167L}$ (**a**) spermatocyte and (**b**) oocyte spreads showing a strong reduction in the labeling of HSF2BP at the chromosome axis. Plots under the panels show the quantification. Nuclei analyzed: 30 zygonemas and 40 pachynemas from two adult male mice of each genotype. In females 38/39 zygonemas and 37/35 pachynemas from two 17.5 dpc embryos of *Hsf2bp*$^{+/+}$ and *Hsf2bp*$^{S167L/S167L}$, respectively. Two-tailed Welch's t-test analysis: ****p<0.0001. (**c**) Western blot analysis of protein extracts from 13 dpp WT, *Hsf2bp*$^{S167L/S167L}$ and *Hsf2bp*$^{-/-}$ testes using polyclonal antibodies against HSF2BP. Tubulin was used as loading control. Graph on the right represents the relative quantification of the immunoblotting. Mice: n = 2 *Hsf2bp*$^{+/+}$, *Hsf2bp*$^{S167L/S167L}$ and *Hsf2bp*$^{-/-}$. Two-tailed Welch's t-test analysis: *p<0.05. Bar in panels a-c, 10 μm.
The online version of this article includes the following figure supplement(s) for figure 3:

Figure supplement 1. *Hsf2bp*$^{S167L/S167L}$ mice do not show synapsis defects.

agreement with the lower presence of recombinases, the number of COs (measured as interstitial CDK2 foci) was also reduced in *Hsf2bp*$^{S167L/S167L}$ oocytes, and a stronger reduction was observed in *Hsf2bp*$^{-/-}$ oocytes (***Figure 6c*** and ***Figure 6—figure supplement 1d***). Overall, male and female *Hsf2bp*$^{S167L/S167L}$ mice share alterations in the meiotic recombination pathway although with different reproductive outcome.

We next sought to understand how the *HSF2BP* pathogenic variant was mediating the observed meiotic alteration. HSF2BP has been shown to bind BRCA2, an essential protein for meiotic homologous recombination (***Martinez et al., 2016***; ***Sharan et al., 2004***), by a direct interaction that involves Arg200 in HSF2BP and the Gly2270-Thr2337 region within the C-terminal fragment of BRCA2

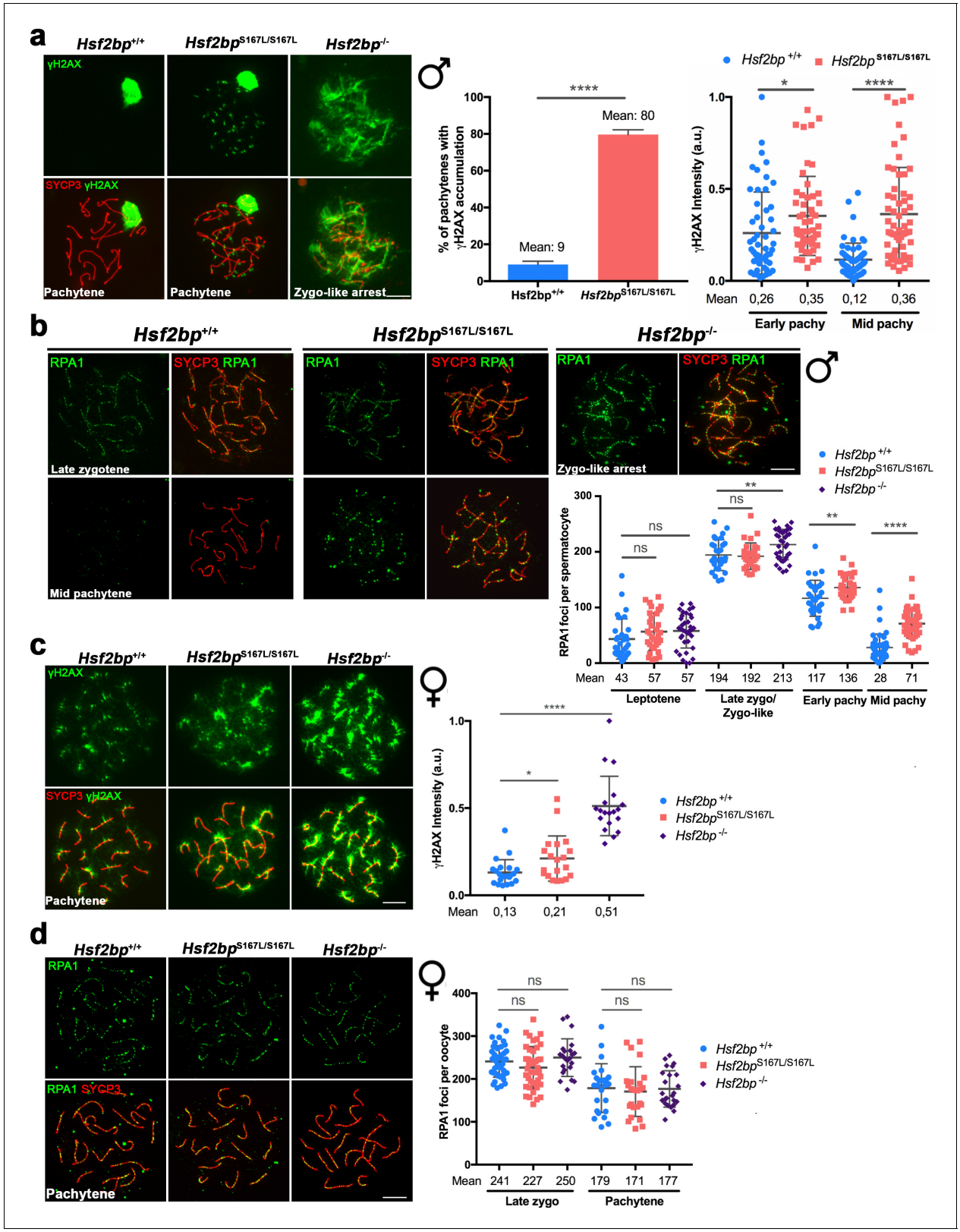

Figure 4. DNA repair in *Hsf2bp*$^{S167L/S167L}$ mice. (**a**, **c**) Double labeling of γH2AX (green) and SYCP3 (red) in (**a**) spermatocyte and (**c**) oocyte spreads from WT, *Hsf2bp*$^{S167L/S167L}$ and *Hsf2bp*$^{-/-}$ mice. (**a**) Males display an accumulation of γH2AX patches in *Hsf2bp*$^{S167L/S167L}$ pachynemas and a strong accumulation in the whole nucleus in *Hsf2bp*$^{-/-}$ zygotene-like arrested cells. Plots on the right of the panel represent the percentage of pachynemas with γH2AX labeling (Nuclei: 364 *Hsf2bp*$^{+/+}$ and 376 *Hsf2bp*$^{S167L/S167L}$ from three adult mice) and the quantification of γH2AX intensity on autosomes at

Figure 4 continued on next page

Figure 4 continued

early and mid-pachytene stages (Nuclei: 53 early and 60 mid pachynemas from three adult mice of each genotype). Two-tailed Welch's t-test analysis: *p<0.05, ****p<0.0001. (**c**) In females there is an accumulation of γH2AX in *Hsf2bp*$^{S167L/S167L}$ pachynemas that is stronger in those from *Hsf2bp*$^{-/-}$ females. Nuclei: n = 21/20/19 pachynemas from 2 *Hsf2bp*$^{+/+}$/*Hsf2bp*$^{S167L/S167L}$/*Hsf2bp*$^{-/-}$ embryos (17.5 dpc). Two-tailed Welch's t-test analysis: *p<0.05, ****p<0.0001. (**b, d**) Double immunolabeling of RPA1 (green) and SYCP3 (red) in (**b**) spermatocyte and (**d**) oocyte spreads from *Hsf2bp*$^{+/+}$, *Hsf2bp* $^{S167L/S167L}$ and *Hsf2bp*$^{-/-}$. (**b**) In males, RPA1 accumulates at early and mid-pachytene in S167L spermatocytes and in the zygotene-like arrested cells from *Hsf2bp*$^{-/-}$. Plot on the right of the panel represents the quantification. Nuclei: n = 31/34/37 leptonemas, n = 29/29/37 zygonemas/zygonemas-like from three adult *Hsf2bp*$^{+/+}$, *Hsf2bp* $^{S167L/S167L}$ and *Hsf2bp*$^{-/-}$ mice respectively, n = 33 early and 46 mid pachynemas from three adult *Hsf2bp*$^{+/+}$ and *Hsf2bp* $^{S167L/S167L}$ mice. Two-tailed Welch's t-test analysis: ns, no significant differences; **p<0.01, ****p<0.0001. (**d**) In females, RPA1 labeling is similar in *Hsf2bp*$^{+/+}$, *Hsf2bp* $^{S167L/S167L}$ and *Hsf2bp*$^{-/-}$ oocytes at zygotene and pachytene. Plot on the right of the panel represents the quantification. Nuclei: *Hsf2bp*$^{+/+}$/*Hsf2bp* $^{S167L/S167L}$/ *Hsf2bp*$^{-/-}$ n = 42/41/23 zygonemas from two embryos (16.5 dpc) and n = 25/25/24 pachynemas from two embryos (17.5 dpc). Two-tailed Welch's t-test analysis: ns, no significant differences. Bar in all panels, 10 μm. Extended panels for RPA1 figures in ***Figure 4—figure supplement 1***.

The online version of this article includes the following figure supplement(s) for figure 4:

Figure supplement 1. RPA localization in *Hsf2bp* mutants.

(***Brandsma et al., 2019***). Given the impossibility to detect endogenous BRCA2 by immunofluorescence in mouse spermatocytes, we carried out co-localization/interaction assays in a heterologous system by transfecting BRCA2-C (i.e. its C-term) and HSF2BP in U2OS/HEK293T. Our results showed that BRCA2-C co-immunoprecipitates with both HSF2BP-WT and HSF2BP-S167L in similar ways (***Figure 6—figure supplement 2a***). In single transfections, HSF2BP localized in the nucleus and cytoplasm whereas BRCA2-C showed nuclear localization. This pattern changed drastically to a nuclear dotted pattern when co-transfected (***Figure 6—figure supplement 2b***). This re-localization was independent of the HSF2BP variant, suggesting that the HSF2BP variant effects are not directly mediated by BRCA2 delocalization.

BRME1, a novel interactor of HSF2BP

In order to further understand the mechanism underlying the pathogenicity of the HSF2BP-S167L variant, we searched for proteins that interact with the murine HSF2BP through a yeast two hybrid (Y2H) screening. The analysis of the clones with putative interactors revealed that 19 out of 98 analyzed clones matched the uncharacterized gene 4930432K21Rik, which corresponds to human C19ORF57, hereby dubbed BRME1 for Break Repair Meiotic recombinase recruitment factor 1. This HSF2BP interactor consists of 600 amino acids with a high content of acidic residues, has no recognizable functional domains and is intrinsically disordered. The interaction was validated by transiently transfecting plasmids driving the expression of HSF2BP and BRME1. Both HSF2BP-S167L and WT interacted with BRME1 (***Figure 7a***). We further validated this interaction in vivo by co-immunoprecipitation (co-IP) of both proteins from mouse whole testis extracts (***Figure 7b***). To identify the regions required for this interaction, we split the BRME1 protein into three fragments (N-terminal, central region and C-terminal). We mapped the HSF2BP/BRME1-interacting domain to the C-term fragment of BRME1 (spanning residues 475–600 of the murine protein, ***Figure 7c***). In line with this, the *Brme1*$^{\Delta 142\text{-}472/\Delta 142\text{-}472}$ mutant mice, expressing the BRME1 protein devoid of its central part, were fertile and did not show defects in chromosome synapsis or an alteration of HSF2BP loading to axes, further indicating that a large fraction of the coding protein of BRME1 is not essential for BRME1/HSF2BP function in vivo (***Figure 7—figure supplement 1***).

We also sought to characterize the involvement of BRME1 in meiosis through immunofluorescence. BRME1 localized to the chromosome axes of WT meiocytes from zygotene to pachytene with a pattern of discrete foci that mimics the RNs (***Figure 7—figure supplement 2a–b***). In agreement with the yeast two hybrid and co-IP results, BRME1 perfectly co-localized with HSF2BP on the chromosome axes (***Figure 7d*** and ***Supplementary file 1d*** for quantification). This co-localization was verified by super-resolution microscopy (***Figure 7e***). In accordance with the tight association of BRME1 with HSF2BP and with a role in DSB repair, both HSF2BP and BRME1 colocalized with RPA and DMC1 foci. During prophase I, HSF2BP and BRME1 showed higher levels of spatio-temporal colocalization at the RNs with RPA than with DMC1 (***Figure 7—figure supplement 3a–b*** and ***Supplementary files 1d-e*** for quantification). We also analyzed the HSF2BP-dependent localization of BRME1 in *Hsf2bp*$^{-/-}$ and *Hsf2bp*$^{S167L/S167L}$ mutants. Immunofluorescence analysis of meiocytes

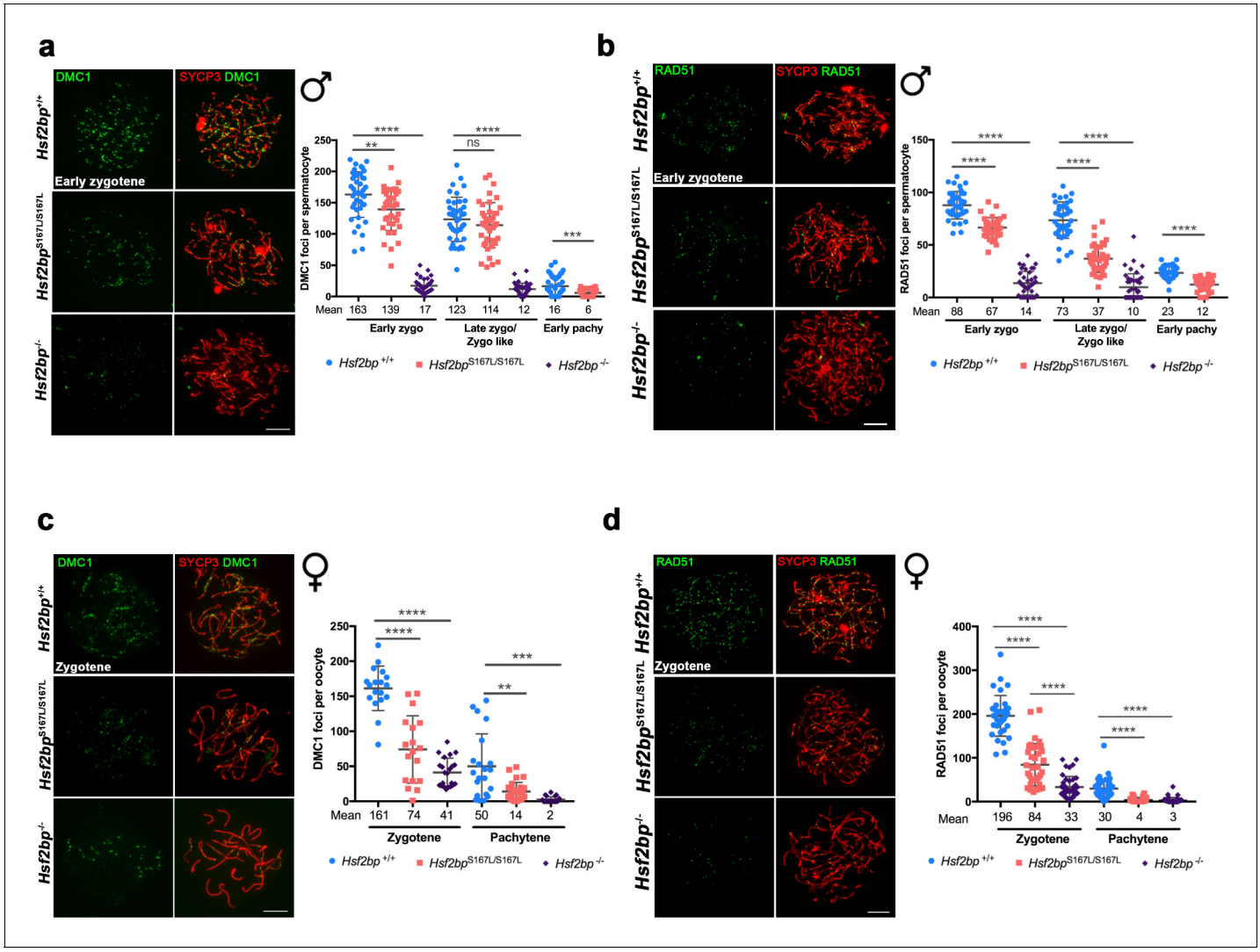

Figure 5. The loading of recombinases is compromised in *Hsf2bp*$^{S167L/S167L}$ mice. Double immunolabeling of (**a, c**) DMC1 or (**b, d**) RAD51 (green) and SYCP3 (red) in *Hsf2bp*$^{+/+}$, *Hsf2bp* $^{S167L/S167L}$ and *Hsf2bp*$^{-/-}$ (**a, b**) spermatocytes and (**c, d**) oocytes showing a strong reduction (*Hsf2bp*$^{-/-}$) and mild reduction (*Hsf2bp* $^{S167L/S167L}$) in the number of foci in comparison with their WT counterparts. Plots on the right of the panels represent the quantification of foci on each genotype and stage. Male nuclei DMC1: *Hsf2bp*$^{+/+}$/*Hsf2bp* $^{S167L/S167L}$/*Hsf2bp*$^{-/-}$, respectively, n = 43/38/37 early zygonemas, 41/43/37 late zygonemas/zygonemas-like and 44/37 early pachynemas from two adult mice of each genotype. Male nuclei RAD51: *Hsf2bp*$^{+/+}$/*Hsf2bp* $^{S167L/S167L}$/*Hsf2bp*$^{-/-}$ respectively n = 39 early zygonemas from all genotypes, 37/40/43 late zygonemas/zygonema-like and 37/39 early pachynemas from two adult mice of each genotype. Oocyte nuclei DMC1: *Hsf2bp*$^{+/+}$/*Hsf2bp* $^{S167L/S167L}$/*Hsf2bp*$^{-/-}$ n = 18/18/22 zygonemas from two embryos and n = 21/30/23 pachynemas from two embryos (17.5 dpc). Oocyte nuclei RAD51: *Hsf2bp*$^{+/+}$/*Hsf2bp* $^{S167L/S167L}$/*Hsf2bp*$^{-/-}$ n = 35/35/42 zygonemas and n = 42/42/40 pachynemas from two embryos (17.5 dpc). Two-tailed Welch's t-test analysis: ns, no significant differences, **p<0.01, ***p<0.001, ****p<0.0001. Bar in all panels, 10 µm. Extended panels for these figures in ***Figure 5—figure supplement 1***.

The online version of this article includes the following figure supplement(s) for figure 5:

Figure supplement 1. Defective loading of recombinases in *Hsf2bp*$^{S167L/S167L}$ mice.

showed a complete lack of BRME1 staining in the absence of HSF2BP and a significant reduction of foci number in the presence of HSF2BP-S167L variant (35% reduction in males and 72% in females at pachytene; ***Figure 7f–g*** and ***Figure 7—figure supplement 4a***). Western blot analysis also revealed a drastic reduction of BRME1 expression in *Hsf2bp*$^{S167L/S167L}$ and *Hsf2bp*$^{-/-}$ spermatocytes, suggesting an HSF2BP-dependent stabilization of BRME1 (***Figure 7h***).

To assess if HSF2BP and/or BRME1 had DNA-binding activity (targeting to DSBs), we carried out an in vitro binding assay using HSF2BP and BRME1 proteins expressed in a transcription and translation coupled reticulocyte system (TNT; ***Loregian et al., 2004***; ***Souquet et al., 2013***) in which there

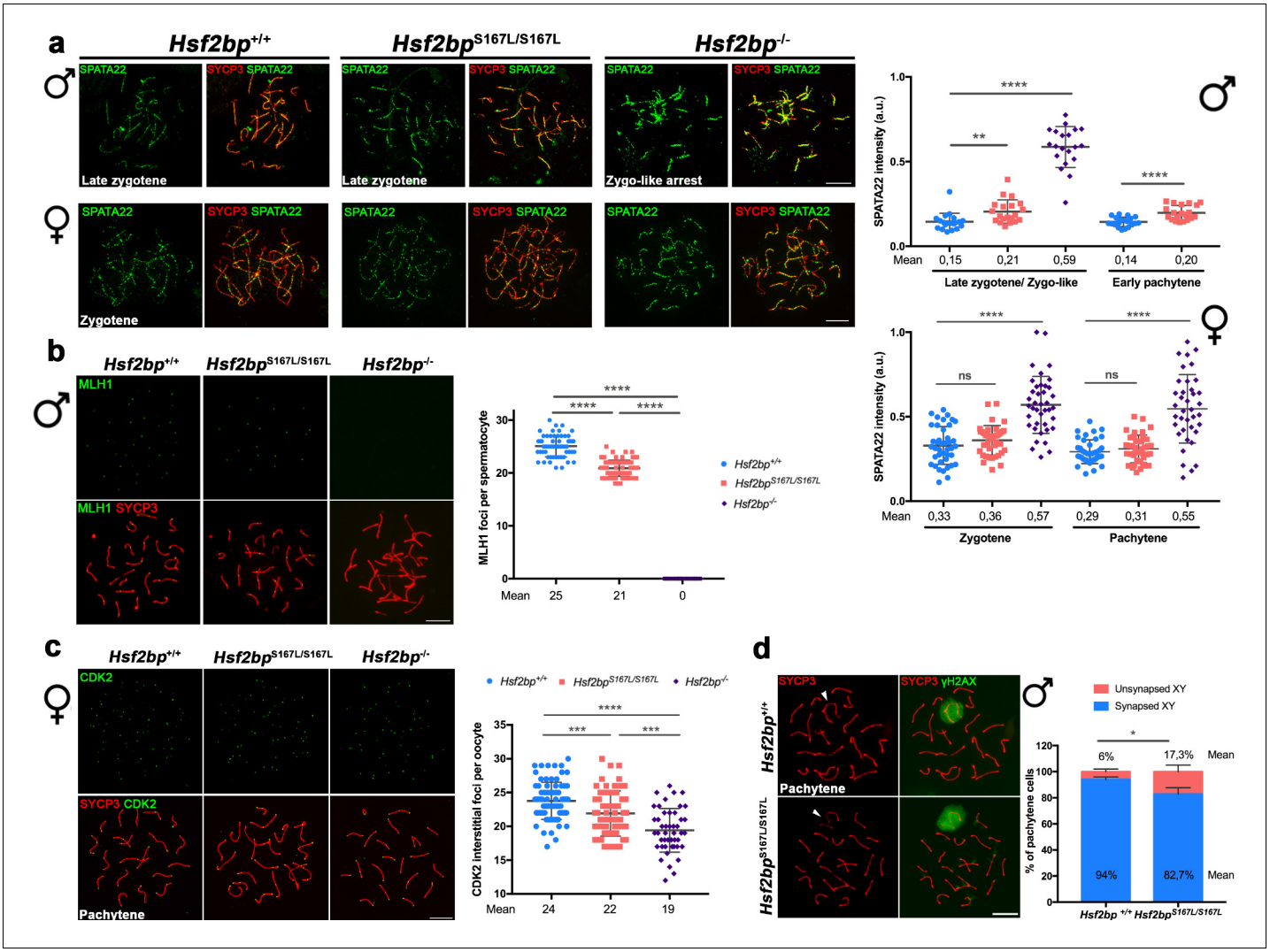

Figure 6. Recombination proficiency is decreased in *Hsf2bp*$^{S167L/S167L}$ mice. (**a**) Double labeling of SPATA22 (green) and SYCP3 (red) in spermatocyte (upper panel) and oocyte (lower panel) spreads from WT, *Hsf2bp*$^{-/-}$ and *Hsf2bp*$^{S167L/S167L}$ mice. SPATA22 is accumulated in knock-out spermatocytes and oocytes and shows a milder accumulation in the *Hsf2bp*$^{S167L/S167L}$ spermatocytes. *Hsf2bp*$^{S167L/S167L}$ oocytes show a slight but not significant accumulation. Plots on the right of the panel represents the quantification of SPATA22 labeling. Males nuclei: n = 20 cells for each stage from two adult mice of each genotype. Females nuclei: *Hsf2bp*$^{+/+}$/*Hsf2bp* $^{S167L/S167L}$/*Hsf2bp*$^{-/-}$ n = 41/40/40 zygonemas from two embryos and n = 40/39/38 pachynemas from two embryos (17.5 dpc). Two-tailed Welch's t-test analysis: ns, no significant differences, **p<0.01, ****p<0.0001. (**b**) Double immunofluorescence of MLH1 (green) and SYCP3 (red) in spermatocyte spreads from WT, *Hsf2bp*$^{S167L/S167L}$ and *Hsf2bp*$^{-/-}$. MLH1 foci are significantly reduced in the *Hsf2bp*$^{S167L/S167L}$ spermatocytes and absent in the knock-out. The plot on the right shows the quantification. See also ***Figure 6—figure supplement 1b*** for the plot showing the percentage of bivalents without CO. Nuclei: n = 61 for *Hsf2bp*$^{+/+}$, 89 for *Hsf2bp*$^{S167L/S167L}$ and 60 for *Hsf2bp*$^{-/-}$ from three adult mice of each genotype. Two-tailed Welch's t-test analysis: ****p<0.0001. (**c**) Double labeling of CDK2 (green) and SYCP3 (red) in oocyte spreads from 17.5 dpc *Hsf2bp*$^{+/+}$, *Hsf2bp*$^{S167L/S167L}$ and *Hsf2bp*$^{-/-}$ embryos. During meiotic prophase I, CDK2 localizes to the telomeres of chromosomes from leptotene to diplotene. However, around mid-pachytene additional interstitial CDK2 signals appear at CO sites, colocalizing with MLH1. As a measure of COs, just interstitial CDK2 foci (non-telomeric) have been counted. *Hsf2bp*$^{-/-}$ and *Hsf2bp*$^{S167L/S167L}$ females show a high and moderate reduction in the number of COs, respectively. Plot on the right of the panel show the quantification. See also ***Figure 6—figure supplement 1d*** for the plot showing the percentage of bivalents without CO. Nuclei: *Hsf2bp*$^{+/+}$/*Hsf2bp* $^{S167L/S167L}$/*Hsf2bp*$^{-/-}$ n = 79/67/46 from three embryos (17.5 dpc). Two-tailed Welch's t-test analysis: ***p<0.0001, ****p<0.0001. (**d**) Double immunofluorescence of γH2AX (green) and SYCP3 (red) in spermatocyte spreads from WT and *Hsf2bp*$^{S167L/S167L}$ mice. At pachytene, γH2AX allows the identification of the XY bivalent. Diagram on the right represents the quantification of the pachynemas with unsynapsed sex chromosomes from *Hsf2bp*$^{S167L/S167L}$ and WT mice. Nuclei: n = 150 pachynemas from three adult mice of each genotype. Two-tailed Welch's t-test analysis: *p<0.05. Bar in all panels, 10 μm.

The online version of this article includes the following figure supplement(s) for figure 6:

Figure supplement 1. Meiotic recombination is affected in *Hsf2bp*$^{S167L/S167L}$ mice.

Figure supplement 2. Comparative interaction of HSF2BP-S167L and HSF2BP-WT with BRCA2.

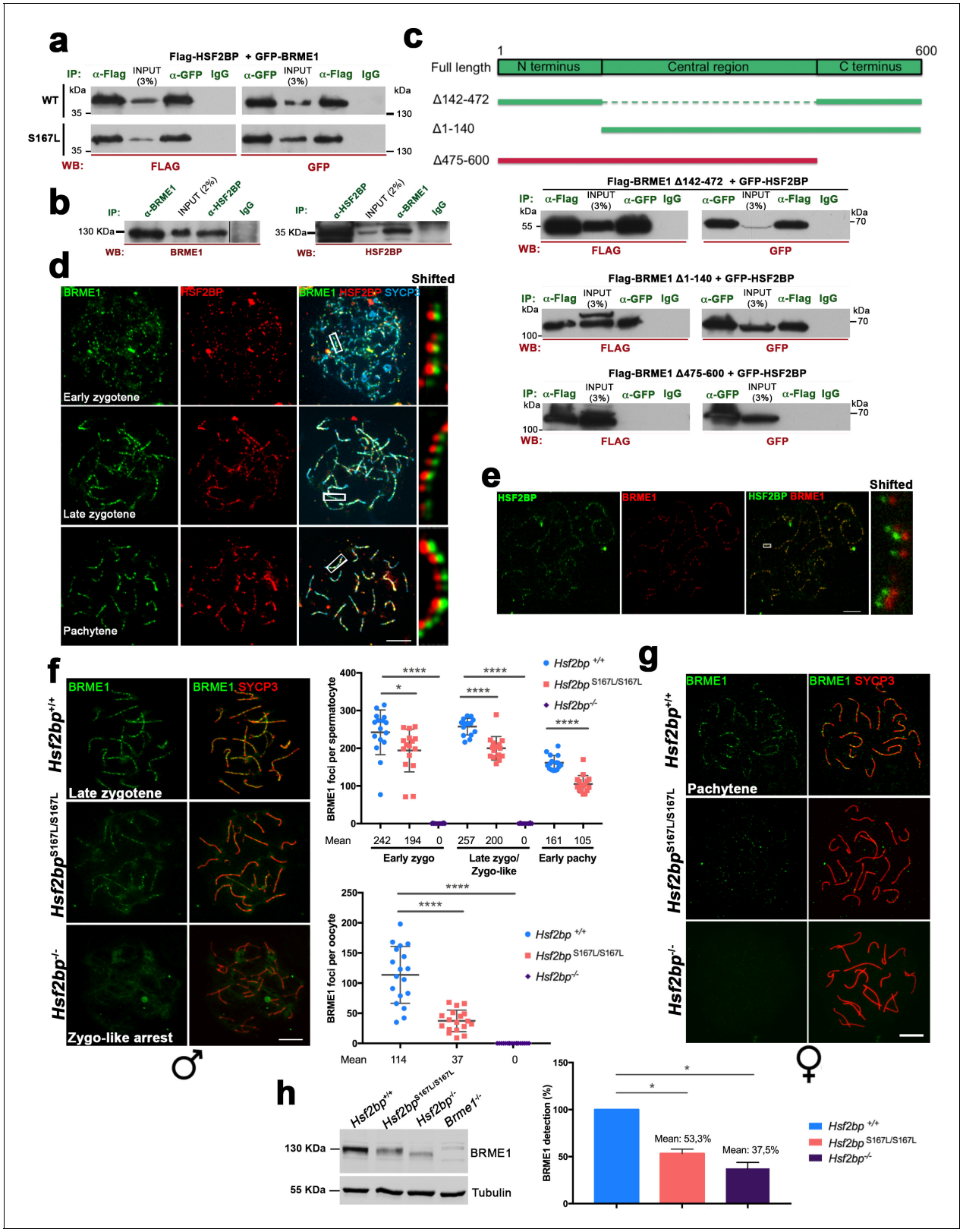

Figure 7. BRME1, a novel HSF2BP interactor that colocalizes to the recombination nodules. (**a**) HEK293T cells were transfected with Flag-HSF2BP (WT, upper panel; S167L, lower panel) and its novel interactor GFP-BRME1. Protein complexes were immunoprecipitated (IP: green text) with either anti-Flag or anti-EGFP or IgGs (negative control) and analysed by immunoblotting with the indicated antibody (WB: red text). Both HSF2BP variants (WT and S167L) co-immunoprecipitated similarly with BRME1. (**b**) IP of testis extracts with antibodies against BRME1, HSF2BP and IgGs as a negative control (IP:

Figure 7 continued on next page

Figure 7 continued

green text) and western blot with the indicated antibodies (WB: red text) (**c**) Schematic representation of full-length BRME1 protein and the corresponding deletion (Δ) constructs (filled boxes) generated to decipher the essential BRME1 region for interacting with HSF2BP (green positive interaction and red no interaction). Western blots under the scheme show the Co-IP experiments. HEK293T cells were transfected with GFP-HSF2BP and the different delta constructs of Flag-BRME1. The Δ475–600 abolishes the interaction, indicating that the C terminus of BRME1 is the essential region of interaction with HSF2BP. (**d**) Triple immunofluorescence of BRME1 (green), HSF2BP (red) and SYCP3 (blue) in WT spermatocyte spreads showing high colocalization between BRME1 and HSF2BP at late zygotene and pachytene (See ***Supplementary file 1d*** for quantification). Bar in panel, 10 μm. (**e**) Double immunolabeling of spermatocyte spread preparations with HSF2BP (green) and BRME1 (red) analyzed by Stimulated emission depletion (STED) microscopy. Bar in panel, 5 μm. (**f–g**) Double immunofluorescence of BRME1 (green) and SYCP3 (red) in (**f**) spermatocytes and (**g**) oocyte spreads from *Hsf2bp*$^{+/+}$, *Hsf2bp*$^{S167L/S167L}$ and *Hsf2bp*$^{-/-}$ showing a strong reduction of BRME1 staining in the S167L mutant and absence in the *Hsf2bp* knock-out. Plots next to the panel represent the quantification. See also extended ***Figure 7—figure supplement 4a***. Male nuclei: *Hsf2bp*$^{+/+}$/*Hsf2bp*$^{S167L/S167L}$/*Hsf2bp*$^{-/-}$: n = 16/16/20 early and 15/15/16 late zygonemas, 16/16 /- pachynemas from two adult mice. Female nuclei: n = 18 pachynemas from two embryos (17.5 dpc) of each genotype. Two-tailed Welch's t-test analysis: *p<0.05, ****p<0.0001. Bar in panels, 10 μm. (**h**) Western blot analysis of protein extracts from 13 dpp WT, *Hsf2bp*$^{S167L/S167L}$ and *Hsf2bp*$^{-/-}$ testes using an antibody against BRME1. Tubulin was used as loading control. Graph on the right represents the relative quantification of the immunoblotting. Mice: n = 2 *Hsf2bp*$^{+/+}$, *Hsf2bp*$^{S167L/S167L}$ and *Hsf2bp*$^{-/-}$. Two-tailed Welch's t-test analysis: *p<0.05.

The online version of this article includes the following figure supplement(s) for figure 7:

Figure supplement 1. *Brme1* Δ142–472 mutants do not show meiotic defects.
Figure supplement 2. C19ORF57/BRME1 localizes at meiotic RNs.
Figure supplement 3. Colocalization analysis of BRME1 and HSF2BP with RPA and DMC1.
Figure supplement 4. BRME1 localization depends on HSF2BP and none of them has DNA-binding abilities.
Figure supplement 5. Generation and genetic characterization of *Rnf212*$^{-/-}$ and *Hei10*$^{-/-}$ mice.
Figure supplement 6. BRME1 loading depends on DSBs generation but not on synapsis.

are no nuclear proteins and chromatin (***Melton et al., 1984***) and used RPA as positive control. Our results show that both proteins lacked direct DNA-binding abilities, in contrast to the strong activity of RPA (***Figure 7—figure supplement 4b–c***).

To determine the role of BRME1 in recombination and DNA repair, we analyzed its cytological distribution pattern in different mutants lacking synapsis/recombination-related proteins. These mutants were the meiotic cohesin REC8 (***Bannister et al., 2004***), the central element protein of the SC SIX6OS1 (***Gómez-H et al., 2016***), the E3 ligases involved in the stabilization of recombinogenic proteins RNF212 and HEI10 (***Qiao et al., 2014***), the spermatoproteasomal subunit PSMA8 (***Gómez-H et al., 2019***), and the nuclease SPO11 required for DSBs generation (*Rnf212*$^{-/-}$, *Hei10*$^{-/-}$ *and Spo11*$^{-/-}$ mouse mutants are described in this work, see Materials and methods and ***Figure 7—figure supplement 5*** and ***Figure 7—figure supplement 6a***, ***Baudat et al., 2000***). HSF2BP staining was also carried out for a direct comparison. We were able to show that none of the recombination-deficient mutants abrogate BRME1 labeling at zygotene (or the corresponding meiotic stage at which the mutant spermatocytes are arrested), in contrast to its absence of loading in SPO11-deficient mice (***Figure 7—figure supplement 6b***, left). These results are very similar to those obtained for HSF2BP in these mutants (***Figure 7—figure supplement 6b***, right) and indicate that SPO11-dependent DSBs are essential for targeting HSF2BP/BRME1 to the RNs, and that the heterocomplex can be positioned at early events soon after DSBs generation.

To functionally analyze the role of BRME1 in mouse fertility, we generated a *Brme1*$^{-/-}$ null mutant by genome editing (***Figure 8—figure supplement 1a–d***). *Brme1*$^{-/-}$ females, despite being fertile, showed a strong reduction of the follicle pool (***Figure 8a***). Male *Brme1*$^{-/-}$ mice were infertile, the average size of their testes was severely reduced (76% reduction compared to WT; testis weight/body weight ratio: *Brme1*$^{-/-}$ 0,08% ± 0004 (n = 6) vs 0,33% ± 0,05 for WT controls (n = 14), ****p<0.0001, ***Figure 8b*** and ***Figure 2—figure supplement 2b***), and lacked spermatozoa (***Figure 8c***). Histological analysis showed a meiotic arrest at epithelial stage IV with apoptotic spermatocytes (***Figure 8c***). Double immunolabeling of SYCP3 and SYCP1 revealed that spermatocytes were partially synapsed and showed a partner-switch phenotype in which synapsis is not restricted to homologous pairs (***Figure 8d***). The arrest corresponds to a zygotene-like stage though a small fraction of cells (3,7% ± 1,9; n = 3) were able to escape this blockage reaching early pachytene. *Brme1*$^{-/-}$ oocyte spread analysis revealed the presence of a subset of fully synapsed pachynemas but an increased number of cells with different degree of asynapsis (47,9% ± 2,2 vs 12% ± 5,7 in the WT; n = 2 (both genotypes), *p<0,05 ***Figure 8e*** and ***Figure 8—figure supplement 1e***). Given the

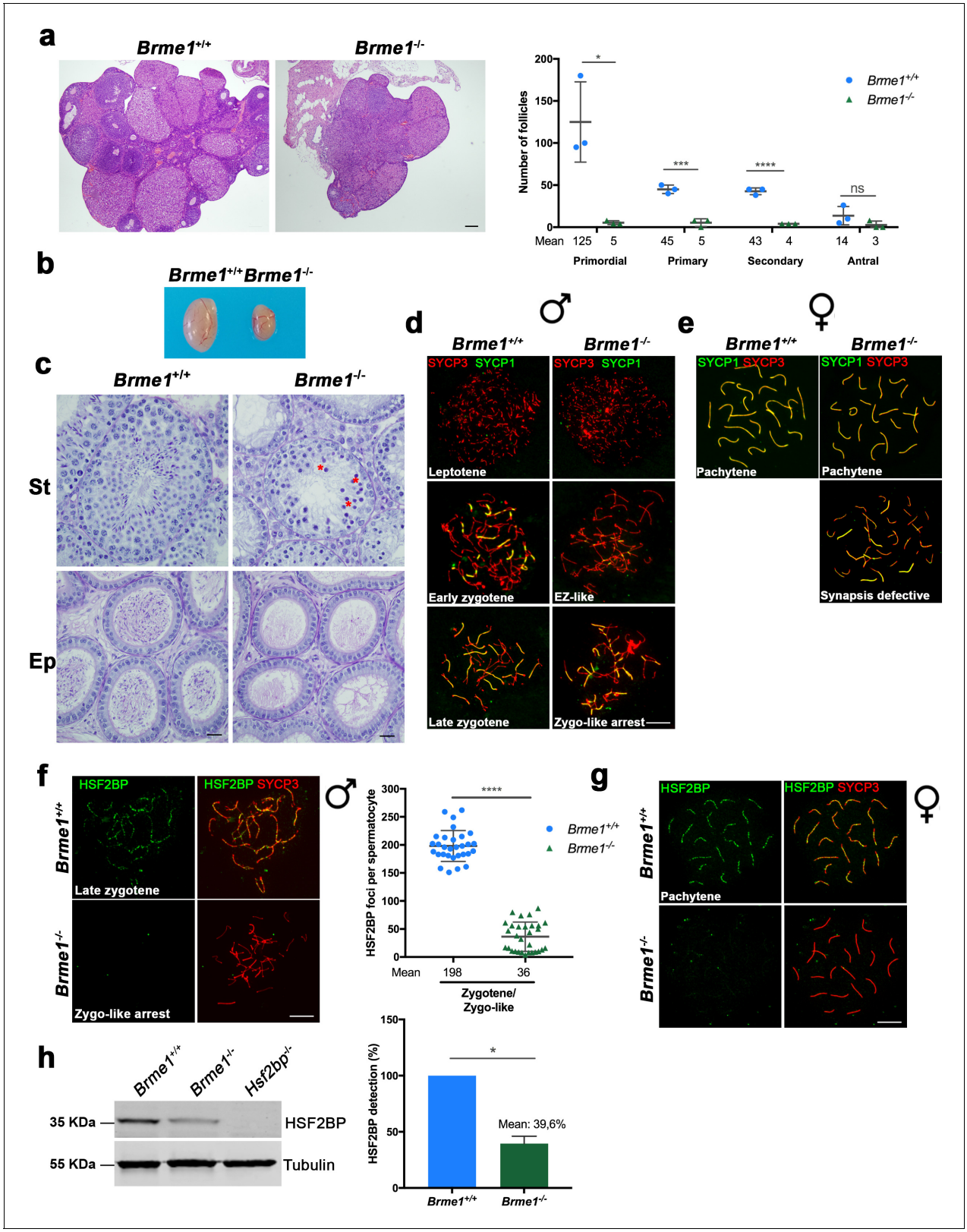

Figure 8. *Brme1*$^{-/-}$ mice show severe fertility defects. (**a**) Hematoxylin+eosin stained sections of ovaries from adult *Brme1*$^{-/-}$ females showing a strong depletion of follicles. Plot on the right represents the quantification in 3 months-old females. Ovaries: n = 3 ovaries for each genotype. Two-tailed Welch's t-test analysis: *p<0.05, ***p<0.001, ****p<0.0001. Bar in panels, 50 µm. (**b**) Testes from adult *Brme1*$^{-/-}$ males show a strong reduction of the testis size. See quantification of testis weight/body weight at ***Figure 2—figure supplement 2b***. (**c**) Spermatogenesis is arrested at epithelial stage IV in

Figure 8 continued on next page

Figure 8 continued

Brme1$^{-/-}$ as shown in PAS+hematoxylin stained testis sections. Massive apoptosis of spermatocytes is indicated (red asterisks). The spermatogenic arrest leads to empty epididymides and non-obstructive azoospermia. (St) Seminiferous tubules. (Ep) Epididymides. Bar in panels, 10 µm. (**d–e**) Double labeling of (**d**) spermatocyte and (**e**) oocyte spreads from WT and *Brme1*$^{-/-}$ mice with SYCP3 (red) and SYCP1 (green). *Brme1*$^{-/-}$ spermatocytes arrest in a zygotene-like stage and show synapsis between non-homologous chromosomes. (**e**) *Brme1*$^{-/-}$ females showed a subset of fully-synapsed pachynemas (18.5 dpc) but increased numbers of synapsis-defective cells. See extended panel for females at ***Figure 8—figure supplement 1e***. Bar in panels, 10 µm. (**f–g**) Double labeling with HSF2BP (green) and SYCP3 (red) of (**f**) spermatocyte and (**g**) oocyte spreads from *Brme1*$^{-/-}$ mice showing faint HSF2BP labeling in spermatocytes and total absence of labeling in oocytes. Plot on the right of (**f**) panel represents de quantification of HSF2BP foci in *Brme1*$^{-/-}$ spermatocytes. Nuclei: n = 30 zygonemas/zygonemas-like from two adult mice of each genotype (*Brme1*$^{+/+}$ values from ***Figure 3a***) Two-tailed Welch's t-test analysis: ****p<0.0001. Bar in panels, 10 µm. (**h**) Western blot analysis of protein extracts from 13 dpp WT, *Brme1*$^{-/-}$ and *Hsf2bp*$^{-/-}$ testes with a specific antibody against HSF2BP. Tubulin was used as loading control. Graph on the right represents the relative quantification of the immunoblotting. Mice: n = 2 *Brme1*$^{+/+}$, *Brme1*$^{-/-}$ and *Hsf2bp*$^{-/-}$. Two-tailed Welch's t-test analysis: *p<0.05.

The online version of this article includes the following figure supplement(s) for figure 8:

Figure supplement 1. Generation and genetic characterization of *Brme1* knock-out mice.

interaction between HSF2BP and BRME1, we tested whether HSF2BP localization depended on BRME1 by immunolabeling of HSF2BP in *Brme1*$^{-/-}$ spermatocytes and oocytes. Our results showed a strong reduction of HSF2BP staining in BRME1-null spermatocytes (***Figure 8f***) and a total absence in oocytes (***Figure 8g***). Western blot analysis of HSF2BP in 13 dpp testis extracts from *Brme1*$^{-/-}$ mice showed a strong reduction in comparison with the WT control (***Figure 8h***), suggesting again that BRME1 is necessary for HSF2BP protein stabilization.

Immunostaining of *Brme1*$^{-/-}$ spermatocytes for γH2AX, RPA, the recombinases RAD51 and DMC1 or SPATA22 revealed an accumulation of γH2AX and RPA on zygonema-like spermatocytes (***Figure 9—figure supplement 1a–b***), a drastic reduction of RAD51/DMC1 foci in early and late zygonema (***Figure 9a and c***, ***Figure 9—figure supplement 2a and c***) and a strong accumulation of SPATA22 (***Figure 9e*** and ***Figure 9—figure supplement 2e***). According to the meiotic arrest at the zygotene-like stage, MLH1 staining revealed a total absence of COs (***Figure 9g***). As in males, *Brme1*$^{-/-}$ oocytes showed an accumulation of γH2AX (***Figure 9—figure supplement 1c***) and SPATA22 (***Figure 9f*** and ***Figure 9—figure supplement 2f***) and a reduced staining of DMC1 and RAD51 leading to a reduced number of COs (measured as interstitial CDK2; ***Figure 9b, d and h***, ***Figure 9—figure supplement 2b and d***). However, *Brme1*$^{-/-}$ oocytes did not show RPA accumulation (***Figure 9—figure supplement 1d***). These results are similar to the phenotypes described for HSF2BP mutants (***Figures 4***, ***5*** and ***6***, ***Figure 4—figure supplement 1***, ***Figure 5—figure supplement 1***, ***Figure 6—figure supplement 1*** and (***Brandsma et al., 2019***) see ***Supplementary file 1f*** for a complete comparison among mutants and their meiotic alterations). Thus, both HSF2BP and BRME1 mutant mice show a highly similar phenotype including sexual dimorphism.

BRME1 and HSF2BP form a multimeric complex with PALB2 and BRCA2

To further delineate the interactome of BRME1, we immuno-precipitated BRME1 from testis extracts coupled to mass-spectrometry. We identified as expected HSF2BP as the main interactor, but also BRCA2, PALB2, RAD51 and RPA, strongly suggesting that they form a large multimeric complex (***Supplementary files 1g-1h***). For validation, we transfected the corresponding expression plasmids in HEK293T cells for co-IP analysis. BRME1 co-immunoprecipitated with BRCA2 and HSF2BP when they were all co-transfected, but importantly BRME1 alone did not co-immunoprecitate with BRCA2 (***Figure 10a–b***). The reciprocal co-IP of BRCA2 with HSF2BP and BRME1 was also positive. We also observed modest but positive co-IP of HSF2BP with RPA, PALB2 and RAD51; and of BRME1 with RAD51 and RPA but not with PALB2 (***Figure 10—figure supplement 1a***). These interactions were further analyzed in a cell-free TNT system coupled to co-immunoprecipitation assays. We observed an absence of direct interaction between any of them, with the exception of BRME1 and HSF2BP, as expected from the Y2H analysis (***Figure 10—figure supplement 1b***). These results suggest that these proteins belong to a complex (or complexes) in vivo (likely through BRCA2) and that the HSF2BP-S167L variant could be altering BRME1 interaction with partners of major BRCA2-containing recombination complexes.

Finally, given the interaction of BRME1 and HSF2BP, we analysed their interdependence in U2OS cells. Transfected HSF2BP was localized diffusely in the cytoplasm and the nucleus (***Figure 10c***).

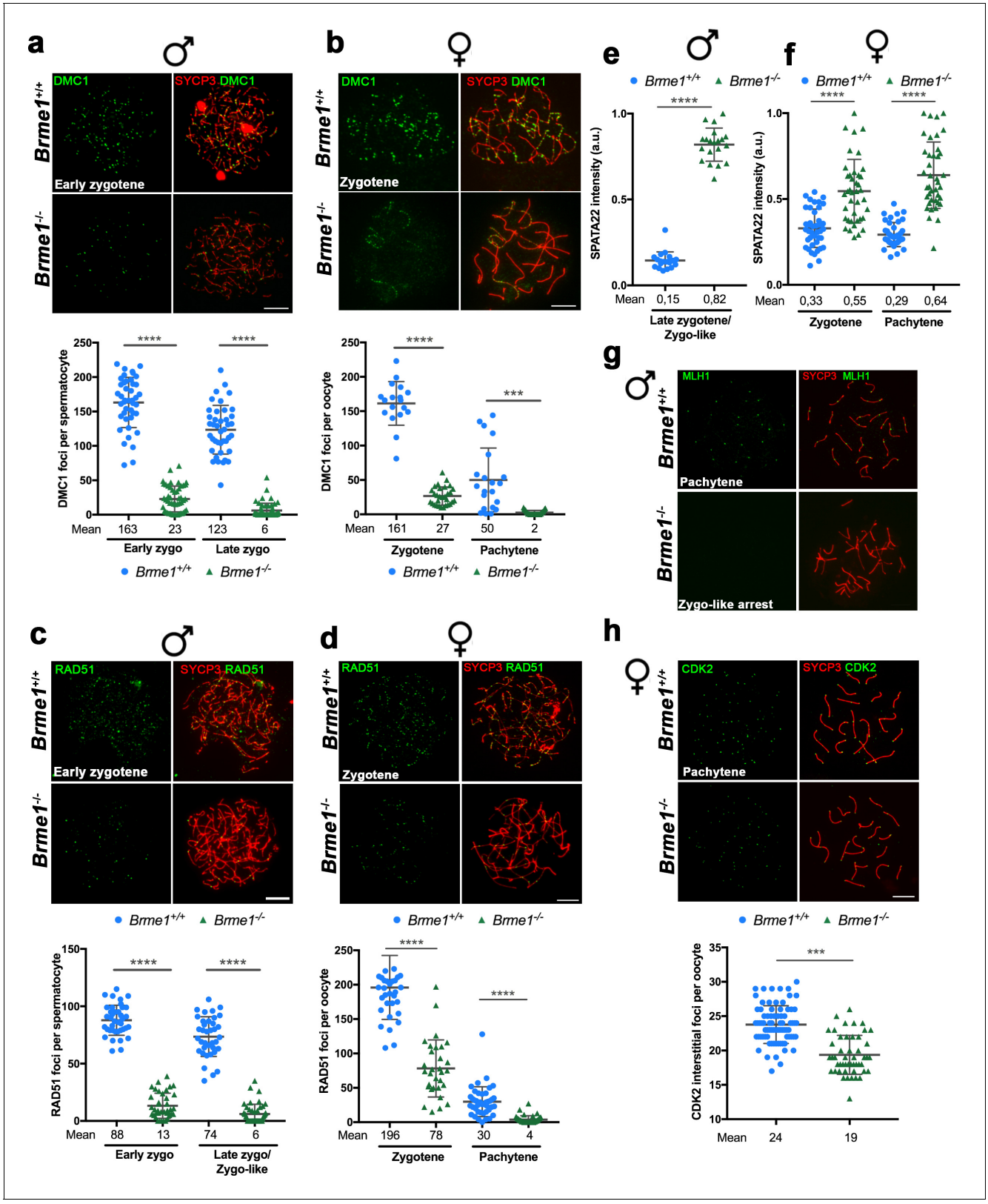

Figure 9. BRME1 is essential for meiotic recombination. (**a–b**) Double immunofluorescence of DMC1(green) and SYCP3 (red) in *Brme1*$^{+/+}$ and *Brme1*$^{-/-}$ (**a**) spermatocytes and (**b**) oocytes showing a reduction in the number of DMC1 foci. Plots under each panel represent the quantification. See also extended panels on ***Figure 9—figure supplement 2a–b***. Male nuclei for DMC1: *Brme1*$^{+/+}$/*Brme1*$^{-/-}$ n = 43/50 early and 41/52 late zygonemas/ zygonemas like from two adult mice of each genotype (*Brme1*$^{+/+}$ values from ***Figure 5a***). Female nuclei for DMC1: *Brme1*$^{+/+}$/*Brme1*$^{-/-}$ n = 18/30

Figure 9 continued on next page

Figure 9 continued

zygonemas and 21/31 pachynemas from two embryos (17.5 dpc) of each genotype (*Brme1*$^{+/+}$ values from ***Figure 5c***). Two-tailed Welch's t-test analysis: ***p<0.001, ****p<0.0001. Bar in panels, 10 μm. (**c–d**) Double immunofluorescence of RAD51 (green) and SYCP3 (red) in *Brme1*$^{+/+}$ and *Brme1*$^{-/-}$ (**c**) spermatocytes and (**d**) oocytes showing a reduction in the number of RAD51 foci in the *Brme1*$^{-/-}$ in comparison to the WT. Plots under each panel represent the quantification. See also extended panels on ***Figure 9—figure supplement 2c–d***. Male nuclei for RAD51: *Brme1*$^{+/+}$/*Brme1*$^{-/-}$ n = 39/39 early and 37/45 late zygonemas/zygonemas like from two adult mice of each genotype (*Brme1*$^{+/+}$ values from ***Figure 5b***). Female nuclei for RAD51: *Brme1*$^{+/+}$/*Brme1*$^{-/-}$ n = 35/31 zygonemas and 42/40 pachynemas from two embryos (17.5 dpc) of each genotype (*Brme1*$^{+/+}$ values from ***Figure 5d***). Two-tailed Welch's t-test analysis: ****p<0.0001. (**e–f**) Quantification of SPATA22 intensity in (**e**) spermatocytes and (**f**) oocyte spreads from *Brme1*$^{+/+}$ and *Brme1*$^{-/-}$. See immunofluorescences in ***Figure 9—figure supplement 2e–f***. Nuclei: Males, n = 20 cells from two adult mice of each genotype (*Brme1*$^{+/+}$ from ***Figure 6a***). Females, *Brme1*$^{+/+}$/*Brme1*$^{-/-}$ n = 41/40 zygonemas and 40/40 pachynemas from two embryos of each genotype (17.5 dpc) (*Brme1*$^{+/+}$ from ***Figure 6a***). Two-tailed Welch's t-test analysis: ****p<0.0001. (**g**) Double immunofluorescence of MLH1 (green) and SYCP3 (red) in *Brme1*$^{+/+}$ and *Brme1*$^{-/-}$ spermatocytes showing the absence of MLH1 labeling in the knock-out. (**h**) Double labeling of CDK2 (green) and SYCP3 (red) in oocyte spreads from 17.5 dpc *Brme1*$^{+/+}$ and *Brme1*$^{-/-}$ embryos. During meiotic prophase I, CDK2 localizes to the telomeres of chromosomes from leptotene to diplotene. However, around mid-pachytene additional interstitial CDK2 signals appear at CO sites, colocalizing with MLH1. As a measure of COs, just interstitial CDK2 foci (non-telomeric) have been counted. *Brme1*$^{-/-}$ females show a strong reduction in the number of COs. Plot under the panel show the quantification. Nuclei: *Brme1*$^{+/+}$/*Brme1*$^{-/-}$ n = 79/49 from three embryos (17.5 dpc) in WT and two embryos in *Brme1*$^{-/-}$ (*Brme1*$^{+/+}$ from ***Figure 6c***). Two-tailed Welch's t-test analysis: ***p<0.0001. Bar in all panels, 10 μm.

The online version of this article includes the following figure supplement(s) for figure 9:

Figure supplement 1. DSBs are formed but not properly repaired in *Brme1*-deficient mice and mimic the phenotype of *Hsf2bp*-deficient mice.

Figure supplement 2. Altered dynamic of recombinational proteins in the absence of BRME1.

However, when HSF2BP was co-overexpressed with BRME1, its pattern changed to an intense nucleoplasm staining with nuclear invaginations that resemble nucleoplasmic reticulum (***Figure 10c***; ***Malhas et al., 2011***). Interestingly, such invaginations were reduced when BRME1 was co-transfected with HSF2BP-S167L (***Figure 10c***). In addition, the intensity of the fluorescence signal of HSF2BP-S167L was lower than for HSF2BP-WT and both intensities increased when HSF2BP was co-expressed with BRME1 (***Figure 10c***). Western blot analysis indicated a reduced protein stability of the S167L variant (***Figure 10d***), in agreement with the results observed in vivo (*Hsf2bp*$^{S167L/S167L}$ mutant, ***Figure 3***). Interestingly, the protein expression level of transfected HSF2BP increased when co-transfected with BRME1 and was partially dependent on proteasome degradation (***Figure 10d***), indicating a role of BRME1 in stabilizing HSF2BP. Taken altogether and given the low protein expression of BRME1 in the *Hsf2bp*$^{S167L/S167L}$, these results suggest a functional interdependence between BRME1 and HSF2BP that leads to their lower protein stability/expression in mutant meiocytes, which might induce recombination defects.

Discussion

Using exome sequencing, we identified the S167L missense variant in *HSF2BP* in a consanguineous family with three cases of POI with secondary amenorrhea. All affected family members are homozygous for the variant, and the healthy relatives are heterozygous carriers. The causality of the HSF2BP-S167L variant is supported by the meiotic phenotype and the subfertility observed in *Hsf2bp*$^{S167L/S167L}$ female mice. Furthermore, the DNA repair defects in murine *Hsf2bp*$^{S167L/S167L}$ meiocytes, displayed by the reduced number of RAD51/DMC1 foci on DSBs and the subsequent reduction in the number of COs, provide evidence that this missense variant alters meiotic recombination. This conclusion was further supported by the comparative analysis of the S167L allele with the *Hsf2bp* null allele, which revealed that the missense variant can be considered as a hypomorphic allele. This is in agreement with the secondary amenorrhea observed in the patients, and the residual (medically-assisted) fertility in one of the affected sisters. Our identification of *HSF2BP* as a gene implicated in POI is in line with recent reports of POI-causing variants in genes that are required for DNA repair and recombination, such as *MCM8, MCM9, SYCE1, MSH4, PSMC3IP, FANCM* or *NBN* (***AlAsiri et al., 2015***; ***Carlosama et al., 2017***; ***de Vries et al., 2014***; ***Fouquet et al., 2017***; ***He et al., 2018***; ***Tenenbaum-Rakover et al., 2015***; ***Tucker et al., 2018***; ***Wood-Trageser et al., 2014***; ***Zangen et al., 2011***).

Meiotic mouse mutants often exhibit sexually dimorphic phenotypes (***Cahoon and Libuda, 2019***). These differences can have a structural basis, given that the organization of the axial elements is known to be different between sexes. This is supported by the difference in length of the axes and

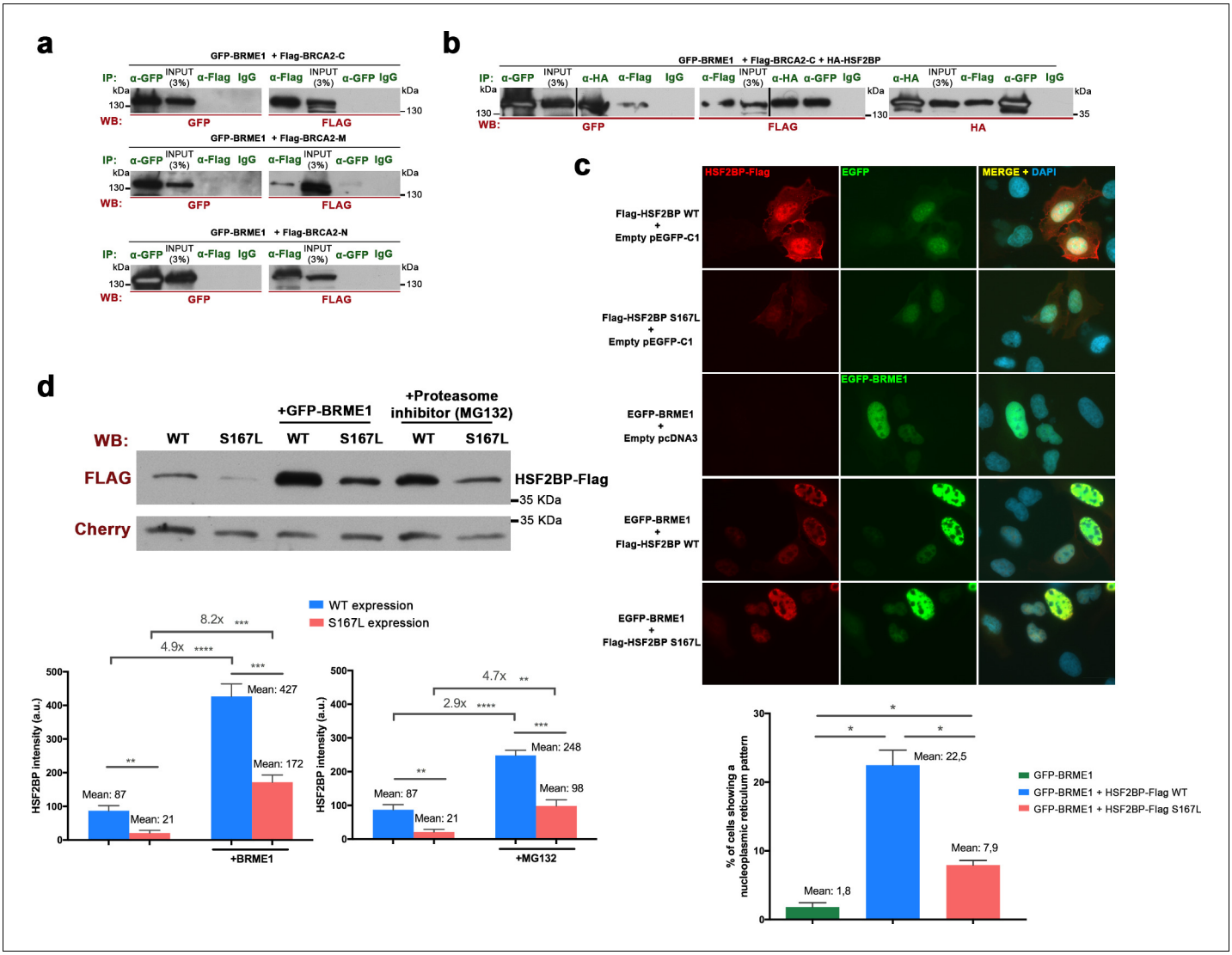

Figure 10. BRME1 forms a complex with BRCA2 and HSF2BP and stabilizes HSF2BP. (**a–b**) HEK293T cells were co-transfected with GFP-BRME1, Flag-BRCA2-C and HA-HSF2BP. Protein complexes were immunoprecipitated (IP: green text) with either an anti-Flag, anti-EGFP, anti-HA or IgGs, and analyzed by western blot with the indicated antibody (WB: red text). (**a**) BRME1 does not co-immunoprecipitate with BRCA2-N, BRCA2-M or BRCA2-C. (**b**) In the presence of HA-HSF2BP (triple co-transfection) BRCA2-C and BRME1 coimmunoprecipitate (co-IPs between HSF2BP and BRCA2-C are shown in ***Figure 6—figure supplement 2a***). (**c**) Transfected U2OS cells with plasmids encoding Flag-HSF2BP (WT or S167L) and EGFP-BRME1 alone or together were immuno-detected with antibodies against Flag (red) and EGFP (green). Transfected HSF2BP (WT and S167L) labels the whole cell (S167L less intense) whereas BRME1 shows nuclear localization. When co-expressed, BRME1 and HSF2BP change their patterns and form nuclear invaginations that resemble nucleoplasmic reticulum. This phenotype is milder in the presence of HSF2BP-S167L than with the WT (graph under the panel: quantification of the number of cells showing a nucleoplasmic reticulum pattern). n > 400 cells from two independent transfections of each condition. Two-tailed Welch's t-test analysis: *p<0.05. Bar in panel, 20 μm. (**d**) HEK293T cells were transfected with Flag-HSF2BP (WT and S167L) alone or with GFP-BRME1. Additionally, cells transfected with Flag-HSF2BP were treated with the proteasome inhibitor (MG132, 10 μM) and analyzed by western blot. Cherry was used as transfection efficiency control. HSF2BP-WT was expressed at higher levels than HSF2BP-S167L and their detection (both the WT and the S167L variant) was increased when co-transfected with BRME1. The increase was greater for the HSF2BP-S167L variant in comparison with the WT. Incubation with MG132 increased the detection levels of transfected HSF2BP mimicking the effect of co-transfecting BRME1. n = 3 independent transfections for each condition. Two-tailed Welch's t-test analysis: **p<0.01, ***p<0.001, ****p<0.0001.

The online version of this article includes the following figure supplement(s) for figure 10:

Figure supplement 1. Co-immunoprecipitations of BRME1, HSF2BP, RPA, RAD51 and PALB2 expressed from transfected HEK293 cells and from TNT assays.

by the essential role that the meiotic cohesin subunit RAD21L plays in males but not in females (**Herrán et al., 2011**). In general, meiotic recombination mutants appear to proceed further in female than in male, because in males the asynapsis of the sex bivalent leads to a loss of silencing of the Y chromosome, and perhaps also because of the presence of less stringent checkpoints in oogenesis (**Hunt and Hassold, 2002**). A sexually dimorphic phenotype is also observed here in our HSF2BP-S167L mutant mice. Both sexes show a significant decrease in the number of COs and consequently an increase in the frequency of meiocytes showing bivalents without CO. This leads to a significant reduction of spermatozoa in the epididymis, while the number of oocytes and their distribution in the follicular pool are not affected in females. Our failure to detect any significant impact of the variant on male fertility could be due to the high variability in litter frequency and size in our study. However, it is known that a strong reduction of the spermatozoa count (up to 60%) does not affect male mouse fertility (**Schürmann et al., 2002**), which would explain the normal fertility of male mice bearing the HSF2BP-S167L variant despite the presence of overt meiotic alterations. By contrast, female mice with the HSF2BP-S167L variant show a mild sub-fertility phenotype with a reduction of litter frequency. This can be due to the very much fewer gametes available for fertilization in females in comparison to males but also to molecular differences in the meiotic recombination process in both sexes (**Cahoon and Libuda, 2019**), as displayed by the absence of RPA accumulation or the more pronounced decrease in DMC1 foci observed in HSF2BP-S167L oocytes.

Although we cannot exclude that a POI-like phenotype would appear over time in HSF2BP-S167L female mice, the sub-fertility observed in HSF2BP-S167L females appears to be milder in comparison to the phenotype of the human patients. This could be explained by a lower sensitivity of mice to hypomorphic alleles compared to humans, in a similar manner to the known lower gene dosage sensitivity of the former in the context of genes that are haploinsufficient in human (**Veitia, 2003**). In addition, the initial events of human female meiosis appear to be more error-prone than in mice, or even than human males, as evidenced by the increased incidence of synaptic defects in the human oocytes or the fact that MLH1 foci appear much earlier in prophase I (**Hassold et al., 2007**). Furthermore, it has recently been shown that human oocytes exhibit a specific CO maturation inefficiency (**Wang et al., 2017**). Indeed, despite a higher total number of COs in women, the frequency of bivalents without CO is paradoxically higher in women than in men. Altogether, these observations could explain the stronger phenotype of the human POI patients compared to the *Hsf2bp*$^{S167L/S167L}$ female mice.

The absence of homozygous male carriers in the consanguineous family studied here prevents the direct comparison of the impact of the HSF2BP-S167L variant on fertility phenotypes between human and mouse males. Although future studies might identify infertile men homozygous for the S167L variant, it is interesting to note that another variant of HSF2BP (G224*) was shown to affect recombination rate in males and that two siblings homozygous for this HSF2BP variant in the analyzed Icelandic population were healthy but without descendants, suggesting they were infertile (**Halldorsson et al., 2019**). This reinforces a conserved function of HSF2BP in human male fertility.

We have shown through a biochemical analysis that BRME1 immunoprecipitates mainly with its partner HSF2BP (constituting or belonging to a complex) but also with PALB2, RAD51, RPA and BRCA2 (in testis extracts). These interactions could possibly be mediated by the multidomain hub protein BRCA2 (**Siaud et al., 2011**) as HSF2BP interacts directly with BRCA2 (**Brandsma et al., 2019**) and with BRME1 (this work). In addition, BRCA2 also directly interacts with the DSBs recruiter PALB2, with the recombinases RAD51 and DMC1 (through different specific domains), and with DNA (**Siaud et al., 2011**). This BRCA2-containing complex participates in the orderly orchestration of events at DSBs such as the initial binding of RPA to the resected DNA, the exchange of RPA by RAD51/DMC1, and the loading of the MEIOB-SPATA22 complex to the RPA complexes (**Martinez et al., 2016**; **Zhao et al., 2015**). Interestingly, genes with recently identified variants in POI patients are implicated in the repair of induced DSBs at the early stages of meiosis and encode BRCA2-interacting factors, such as *MEIOB*, *DMC1* or *BRCA2* itself (**Caburet et al., 2019a**; **Caburet et al., 2020**; **Caburet et al., 2019b**; **He et al., 2018**). This highlights the crucial importance and the high sensitivity of this particular meiotic step, and the hub role of BRCA2 as a tightly regulated platform for correct meiotic recombination.

We have also shown by several complementary approaches that the proteins HSF2BP/BRME1 constitute in vivo a functional complex in which both subunits are essential for meiotic recombination and for their mutual protein expression and/or stability in vivo. Accordingly, the genetic depletion of

BRME1 or HSF2BP leads to similar if not identical phenotypes in which oogenesis is altered with severe defects in chromosome synapsis that promotes premature loss of ovarian follicles and spermatogenesis is arrested at zygotene-like stage resulting in a lack of spermatozoa. These meiocytes are not able to load the recombinases RAD51/DMC1, impairing the proper repair of DSBs leading to the generation of no COs or very few in males and females, respectively. As a consequence, zygonema-like spermatocytes accumulate the single strand binding proteins SPATA22 and RPA, whereas oocytes accumulates only SPATA22. During the course of the reviewing of this work, three *Brme1* knockouts have been described (**Zhang et al., 2020**; **Shang et al., 2020**; **Takemoto et al., 2020**). All the described male mutants show strong fertility defects and similar molecular alterations although with different severity. In females, the two works that address their analysis (Shang et al. and Takemoto et al.), describe normal fertility which is in contrast with the strong reduction in the follicle pool and meiotic defects observed in our *Brme1*$^{-/-}$ females. The higher severity of our male and female mutants could be explained on the basis of the different genetic background of the mice given that all of them are apparently similar.

The S167L human recessive POI variant behave as a hypomorphic allele in mice, which results in a reduction of the protein expression/stability of itself and of its partner BRME1 in vivo and in transfected cells. As a consequence, both male and female *Hsf2bp*$^{S167L/S167}$ mice show a similar but milder phenotype than that of the *Hsf2bp*$^{-/-}$or *Brme1*$^{-/-}$, consisting in a reduction in the spermatozoa count while being fertile and a subtle reduction in female fertility. Molecularly, the reduction observed in the meiocytes of the mutant *Hsf2bp*$^{S167L/S167L}$ mice of RAD51/DMC1, the reduction of COs (both in males and females), the accumulation of RPA (only in males) and SPATA22 (in males and females) are also weaker than in the null mutant. The observed accumulation of RPA in males is likely to occur at the early stages of recombination because SPATA22 loading to the DSBs is also increased in the mutants of HSF2BP and BRME1. RPA, as part of a trimeric replication protein complex (RPA1-RPA2-RPA3), binds and stabilizes ssDNA intermediates that form during DNA repair. In meiosis, RPA is also forming a complex with two other essential meiotic players MEIOB (homologue of RPA) and SPATA22. However, the loading of this complex to DSBs is RPA-independent (**Shi et al., 2019**). It has been postulated that RPA functions in meiosis at two different stages; (i) during the early recombination stages when the DSBs ends are resected by the MRN complex and (ii) during the strand invasion into the homologous duplex that is carried out by RAD51/DMC1 and ssDNA is generated at the displacement loops (**Shi et al., 2019**). The observed lack of DNA-binding ability of HSF2BP/BRME1 points towards a model in which the absence of the complex HSF2BP/BRME1 through a direct interaction with BRCA2 impairs the replacement of RPA by RAD51/DMC1 in the foci that form on the DSBs of the spermatocytes. Similarly, the reduced expression at the protein level of HSF2BP/BRME1 as a consequence of the POI variant, which does not affect their heterodimerization, would make them less proficient in replacing RPA in the spermatocytes by the recombinases RAD51/DMC1 leading to a lower frequency of COs. Given the unknown function that RPA plays in vivo during oogenesis (**Shi et al., 2019**), it is tempting to speculate that the role of RPA in mediating the replacement of RAD51/DMC1 in female meiosis would be carried out by another protein complex such as SPATA22/MEIOB in a HSF2BP/BRME1-dependent manner.

Very recently, a high-resolution genome-wide recombination map revealed novel loci involved in the control of meiotic recombination and highlighted genes involved in the formation of the SC (SYCE2, RAD21L, SYCP3, SIX6OS1) and the meiotic machinery itself as determinants of COs (**Halldorsson et al., 2019**). Within the second category, variants of the SUMO ligase RNF212 and the ubiquitin ligase HEI10 have been largely documented as genetic determinants of the recombination rate in humans and, importantly, so were variants of HSF2BP. Consequently, gene dosage of RNF212 and HEI10 affects CO frequency through their activity in CO designation and maturation (**Lake and Hawley, 2013**; **Reynolds et al., 2013**). We found that both BRME1 and HSF2BP localization are unaffected in the loss-of-function mouse mutants of *Rnf212* and *Hei10 (Ccnb1ip1)*. This observation together with the proper co-localization of BRME1/HSF2BP with RPA allows us to map these proteins upstream in the recombination pathway.

It is worth noting that some of the genes affecting the recombination rate have also been described as 'fertility genes', such as *SYCP3, HFM1* and *HSF2BP* (**Geisinger and Benavente, 2017**; **Primary Ovarian Insufficiency Collaboration et al., 2014** and this work). Altogether, we propose that different variants of the same meiotic gene (alleles responsible for mild or strong phenotypes) can give rise to either an altered genome-wide recombination rate with no detrimental effect, or

cause infertility when the decreased recombination rate falls below the lower limit of one COs per bivalent. In the present POI family, the S167L variant in HSF2BP seems to be below that limit. To our knowledge, HSF2BP is one of the very few human genes with variants known to affect both the genome-wide recombination rate in the human population and meiotic chromosome missegregation (fertility) through a reduction of the recombination rate (***Halldorsson et al., 2019***). Along similar lines, it is conceivable that variants with additive effects (***Schimenti and Handel, 2018***) can lead to a genome-wide reduction of the recombination rate and thus to aneuploidy and infertility. Specifically, variants in genes involved in meiotic recombination and SC constituents could be responsible for a large fraction of genetic infertilities. These variants should be under purifying selection and would be removed or substantially reduced from the population. However, this is not the case for genes with sexual phenotypic dimorphism (***Gershoni and Pietrokovski, 2014***) as is apparent for a wide number of meiotic genes (***Cahoon and Libuda, 2019***), including HSF2BP and BRME1, where individuals of one of the sexes are fertile carriers.

In summary, we describe for the first time a human family where POI co-segregates with a genetic variant in HSF2BP (S167L) in a Mendelian fashion. Humanized mice reveal that the HSF2BP variant is a hypomorphic allele that promotes the lower protein expression and/or stability of the HSF2BP/BRME1 complex and phenocopy in a milder manner the meiotic defects observed in mice lacking either HSF2BP or its direct interactor BRME1.

Materials and methods

Whole exome sequencing

Written informed consent was received from participants prior to inclusion in the study and the institutions involved. Genomic DNA was extracted from blood samples by standards protocols.

For individuals III-3 and III-10, library preparation, exome capture, sequencing and initial data processing were performed by Beckman Coulter Genomics (Danvers, USA). Exon capture was performed using the hsV5UTR kit target enrichment kit. Libraries were sequenced on an Illumina HiSEQ instrument as paired-end 100 bp reads. For individual III-2, library preparation, exome capture, sequencing and data processing were performed by IntegraGen SA (Evry, France) according to their in-house procedures. Target capture, enrichment and elution were performed according to manufacturer's instructions and protocols (SureSelect Human All Exon Kits Version CRE, Agilent). The library was sequenced on an Illumina HiSEQ 2500 as paired-end 75 bp reads. Image analysis and base calling was performed using Illumina Real Time Analysis (RTA 1.18.64) with default parameters.

Bioinformatic analysis

For the three individuals, sequence reads were mapped onto the human genome build (hg38/GRCh38) using the Burrows-Wheeler Aligner (BWA) tool. Duplicated reads were removed using sambamba tools. Whole exome sequencing metrics are provided in ***Supplementary file 1a***. Variant calling, allowing the identification of SNV (Single Nucleotide Variations) and small insertions/deletions (up to 20 bp) was performed via the Broad Institute GATK Haplotype Caller GVCF tool (3.7). Ensembl VEP (Variant Effect Predictor, release 87) program was used for initial variant annotation. This tool considers data available in dbSNP (dbSNP147), the 1000 Genomes Project (1000G_phase3), the Exome Variant Server (ESP6500SI-V2-SSA137), the Exome Aggregation Consortium (ExAC r3.0), and IntegraGen in-house databases. Additional annotation data was retrieved using dbNSFP (version 3.5, https://sites.google.com/site/jpopgen/dbNSFP) and Varsome (https://varsome.com/). Minor allele frequencies were manually verified on GnomAD (http://gnomad.broadinstitute.org), ISB Kaviar (http://db.systemsbiology.net/kaviar/), and Great Middle Eastern variant database GME Variome (http://igm.ucsd.edu/gme/).

Variant filtering was performed on the following criteria:

- minimum depth at variant position of 10,
- correct segregation in the family, on the basis of homozygosity by descent: variants should be homozygous in both affected sisters III-2 and III-3, and heterozygous or homozygous for Reference allele in the fertile sister III-10,
- absence in unrelated in-house fertile controls,

- Minor Allele Frequency (MAF) below 1% in global and in each population in the GnomAD database,
- presence in the coding sequence (i.e not in UTRs, introns, intergenic,.)
- high predicted functional impact on the protein. Impact was evaluated based on the predictors included in dbNSFP3.5 (**Cahoon and Libuda, 2019**; **Carlosama et al., 2017**; **Cox and Mann, 2008**) (considered as pathogenic when the majority of the predictors agreed).

The number of variants fulfilling those criteria is provided in **Supplementary file 1b**. Visual inspection of the variant was performed using the IGV viewer.

Sanger sequencing analysis

To confirm the presence and segregation of the variant, direct genomic Sanger DNA sequencing of *HSF2BP* was performed in the patients, the parents and non-affected siblings using specific primers: HSF2BP-ex6F: 5'-ctagaatcttctgtatcctgca-3' and HSF2BP-ex6R2: 5'-ggtctggaagcaaacaggcaa-3'. The resulting chromatograms are shown in **Figure 1—figure supplement 1**.

Predictions of pathogenicity and sequence conservation

The S167L variant was predicted to be pathogenic or deleterious and highly conserved by 11 out of the 18 pathogenicity predictors available in dbNSFP 3.5 (**Supplementary file 1c**). Upon verification, it appears that the conflicting interpretation of this variant might stem from the single occurrence of a Leu at this position in zebrafish. As the change in zebrafish is the variant that we have in the human family, we checked all the available sequences (Ensembl Release 99, January 2020, removing the one-to-many relationships). Ser167 is very highly conserved in mammals, birds and reptiles and fish and is present in 208 of 212 orthologous sequences (**Figure 1—figure supplement 2** and **Figure 1—figure supplement 3**).

Generation of CRISPR/Cas9-edited mice

For developing all the mutant mice models (*Hsf2bp*$^{-/-}$, *Hsf2bp*$^{S167L/S167L}$, *Brme1*$^{\Delta142\text{-}472/\Delta\ \Delta142\text{-}472}$, *Brme1*$^{-/-}$, *Spo11*$^{-/-}$, *Rnf212*$^{-/-}$ and *Hei10*$^{-/-}$) the different crRNAs were predicted at https://eu.idtdna.com/site/order/ designtool/index/CRISPR_CUSTOM. The crRNAs, the tracrRNA and the ssODNs were produced by chemical synthesis at IDT (crRNAs and ssODNs sequences are listed in **Supplementary files 1i-1j**). For the *Hsf2bp*^{S167L} we introduced a mutation in the mouse counterpart residue (p.Ser171Leu) of the POI mutation found in the clinical case (p.Ser167Leu). However, for the shake of simplicity, on this manuscript we refer to the mutant allele by the acronym of the human mutation (S167L). The ssODN contains the mutation on the corresponding position of the mouse sequence (c.512C > T, p.Ser171Leu, see character in red in **Supplementary file 1j**) and the PAM mutations avoiding amino acid changes (see characters in bold in the **Supplementary file 1j**). For the *Spo11*$^{-/-}$ mice generation, the ssODN contains the mutations in the active site (TACTAC >TTCTTC p.YY137-138FF, see **Supplementary file 1j**) and the PAM mutations (bold characters in **Supplementary file 1j**). In all cases the crRNA and tracrRNA were annealed to obtain the mature sgRNA. A mixture containing the sgRNAs, recombinant Cas9 protein (IDT) and the ssODN (30 ng/µl Cas9, 20 ng/µl of each annealed sgRNA and 10 ng/µl ssODN) were microinjected into B6/CBA F2 zygotes (hybrids between strains C57BL/6J and CBA/J) (**Singh et al., 2015**) at the Transgenic Facility of the University of Salamanca. Edited founders were identified by PCR amplification (Taq polymerase, NZYtech) with primers flanking the edited region (see **Supplementary file 1k** for primer sequences). The PCRs products were direct sequenced or subcloned into pBlueScript (Stratagene) followed by Sanger sequencing, selecting the founders carrying the desired alelles. The selected founders were crossed with wild-type mice to eliminate possible unwanted off-targets. Heterozygous mice were re-sequenced and crossed to give rise to edited homozygous. Genotyping was performed by analysis of the PCR products produced from genomic DNA extracted from tail biopsies. The primers and the expected amplicon sizes are listed in the **Supplementary file 1k**. Mouse mutants for *Rec8, Six6os1* and *Psma8* have been previously described (**Bannister et al., 2004**; **Gómez-H et al., 2019**; **Gómez-H et al., 2016**).

Ethics statement

All the experiments were approved by the Ethics Committee for Animal Experimentation of the University of Salamanca (USAL) and the Ethics committee of the Spanish Research Council (CSIC) under protocol #00–245. Accordingly, all the mouse protocols used in this work have been approved by the Animal Experimentation committees mentioned above. Specifically, mice were always housed in a temperature-controlled facility (specific pathogen free, spf) using individually ventilated cages, standard diet and a 12 hr light/dark cycle, according to EU law (63/2010/UE) and the Spanish royal law (53/2013) at the "Servicio de Experimentación Animal, SEA. In addition, animal suffering was always minimized, and we made every effort to improve animal welfare during the life of the animals. The mice analysed were between 2 and 4 months of age, except in those experiments where the age is indicated.

Histology

For histological analysis, after the necropsy of the mice their testes or ovaries were removed and fixed in Bouin´s fixative or formol 10%, respectively. They were processed into serial paraffin sections and stained with haematoxylin-eosin (ovaries) or Periodic acid–Schiff (PAS) and hematoxylin (testes). The samples were analysed using a microscope OLYMPUS BX51 and images were taken with a digital camera OLYMPUS DP70. For TUNEL assay, sections were deparaffinized and apoptotic cells were detected with the In Situ Cell Death Detection Kit (Roche) and counterstained with DAPI.

Follicle counting

The inner third of each ovary was serially sliced into 5 µm thick sections and follicles were counted every five sections and classified into four stages (primordial, primary, secondary and antral). Only those follicles in which the nucleus of the oocyte was clearly visible were counted.

Epididymal sperm count

The epididymides were removed, minced and incubated in 1,5 ml of KSOM for 30 min at 37˚C to release sperm into the medium. The suspension was incubated for 10 min at 60˚C and the total sperm count was quantified by using a hemacytometer.

Fertility assessment

Hsf2bp$^{+/+}$ and *Hsf2bp*$^{S167L/S167L}$ males and females (8 weeks old) were mated with WT females and males, respectively, over the course of 4–12 months. six mice per genotype (seven mice for *Hsf2bp*$^{S167L/S167L}$ females) were crossed. The presence of copulatory plug was examined daily and the number of pups per litter was recorded.

Immunocytology and antibodies

Testes were detunicated and processed for spreading using a conventional 'dry-down' technique or for squashing (***Gómez-H et al., 2016***). Oocytes from fetal ovaries (E16.5, E17.5 and E19.5 embryos) were digested with collagenase, incubated in hypotonic buffer, disaggregated and fixed in paraformaldehyde. Rabbit polyclonal antibodies against HSF2BP and BRME1 were developed by ProteintechTM against a fusion protein of poly-His with full length HSF2BP or BRME1 (pUC57 vector) of mouse origin. Two antibodies (named R1 and R2) were generated against each protein (HSF2BP or BRME1) by immunization of two different host rabbits. Rabbit polyclonal antibody against DMC1 was developed by ProteintechTM against a DMC1 peptide (EESGFQDDEESLFQDIDLLQKHGINMADIKKLKSVGICTIKG). The primary antibodies used for immunofluorescence were rabbit αHSF2BP R2 (1:30, ProteintechTM), rabbit αBRME1 R2 (1:100, ProteintechTM), mouse αSYCP3 IgG sc-74569 (1:100, Santa Cruz), rabbit α-SYCP3 serum K921 (provided by Dr. José Luis Barbero, Centro de Investigaciones Biológicas, Spain), rabbit αSYCP1 IgG ab15090 (1:200, Abcam), rabbit anti-γH2AX (ser139) IgG #07–164 (1:500, Millipore), mouse αMLH1 51-1327GR (1:20, BD Biosciences), mouse αCDK2 (1:20; Santa Cruz Sc-6248) rabbit αRAD51 PC130 (1:50, Calbiochem), rabbit αRPA1 serum ¨Molly¨ (1:30, provided by Dr. Edyta Marcon, Medical Research University of Toronto, Canada), rat αRPA2 2208S (1:100, Cell Signaling), rabbit αDMC1 (1:500, ProteintechTM), rabbit αSPATA22 16989–1-AP (1:60, Proteintech), mouse αFlag IgG (1:100; F1804, Sigma-Aldrich).

Image acquisition and analysis

Slides were visualized at room temperature using a microscope (Axioplan 2; Carl Zeiss, Inc) with 63 × objectives with an aperture of 1.4 (Carl Zeiss, Inc). Images were taken with a digital camera (ORCA-ER; Hamamatsu) and processed with OPENLAB 4.0.3 and Photoshop (Adobe). The slides from the different genotypes used for comparative analyses were all freshly prepared in parallel and immunofluorescence were also carried out in parallel with the same freshly prepared cocktail of antibodies. Slides were not frozen to avoid differences in the background and antigen reactivity. All the images acquired were taken with constant exposure times for comparison. Quantification of foci and fluorescence intensity were performed using Image J software. Only the axis-associated foci were counted. For colocalization analysis, the same nucleus was quantified without rotation (experiment) and after rotating 90 degrees one of the images. This condition allows to determine non-specific colocalization (random). Background was subtracted for intensity quantification. Squashed preparations were visualized with a Delta vision microscopy station. Stimulated emission depletion (STED) microscopy (SP8, Leica) was used to generate the super-resolution images. Secondary antibodies for STED imaging were conjugated to Alexa 555 and 488 (Invitrogen) and the slides were mounted in Prolong Antifade Gold without DAPI.

Generation of plasmids

Full-length cDNAs encoding HSF2BP, BRME1 (full length and delta constructs), RPA1, BRCA2 (N, M and C constructs), PALB2, RAD51, and PSMA8 were RT-PCR amplified from murine testis RNA. The cDNAs were cloned into the EcoRV pcDNA3-2XFlag, SmaI pcDNA3-2XHA or SmaI pEGFP-C1 expression vectors under the CMV promoter. In frame cloning was verified by Sanger sequencing.

Y2H assay and screening

Y2H assay was performed using the Matchmaker Gold Yeast Two-Hybrid System (Clontech) according to the manufacturers' instructions. Mouse *Hsf2bp* cDNA was subcloned into the vector pGBKT7 and was used as bait to screen a mouse testis Mate and Plate cDNA library (Clontech Laboratories Inc). Positive clones were initially identified on double dropout SD (synthetic dropout)/–Leu /– Trp/X-α-Gal/Aureobasidin A plates before further selection on higher stringency quadruple dropout SD /– Ade /– His /– Leu /– Trp/X-α-Gal/Aureobasidin A plates. Pray plasmids were extracted from the candidate yeast clones and transformed into *Escherichia coli*. The plasmids from two independent bacteria colonies were independently grown, extracted and Sanger sequenced.

DNA pull-down assay

ssDNA/dsDNA pull down assays were performed using the protocol previously described by ***Souquet et al., 2013***. A HPLC-purified biotinylated oligonucleotide was used for the DNA pull down assays: ss60-mer F: 5′-GAT CTG CACGACGCACACCGGACGTATCTGCTATCGCTCATG TCAACCGCTCAAGCTGC/3′BiotinTEG/ (IDT) and ss60-mer R (No biotinylated): 5′- GCAGC TTGAGCGGTTGACATGAGCGATAGCAGATACGTCCGGTGTGCGTCGTGCAGATC-3′. Double-stranded DNA annealing was carried out in 50 mM NaCl, 25 mM Tris-HCl, pH 7.5 buffer with complementary sequences at molecular equivalence by a denaturing step (5 min at 95˚C) and a slow return to room temperature. DNA was immobilized onto Dynabeads M-280 Streptavidin (Dynal) following the manufacturer instructions (0.2 pmol per 1 µg of beads). Protein extracts were obtained from in vitro coupled transcription/translation systems (TNT T7 Coupled Reticulocyte Lysate Systems, Promega) according to manufacturer's protocol. 15 µl of Flag-tagged proteins from TNT assays were pre-incubated on ice for 10 min in modified DBB (DBB: 50 mM Tris HCl, 100 mM NaCl, 10% (w/v) glycerol, Complete Protease inhibitor, 1 mM 2-mercaptoethanol pH 7,4 modified with 25 mM Tris-HCl, 1 mM EDTA plus 5 mg/ml BSA). After this preincubation 500 µg Dynabeads with immobilized ss- or ds-DNA were added and incubated for 1 hr at 4˚C under agitation. Then the beads were washed three times (5 min rotating at RT) in 700 µl of modified DBB without BSA, before being washed once in 700 µl of rinsing buffer (modified DBB with 150 mM NaCl). Finally, DNA-binding proteins were eluted by resuspending the beads in 30 µl of Laemmli buffer boiling the samples for 5 min. The samples were analyzed by western blot.

Cell lines and transfections

HEK293T and U2OS cell lines were obtained from the ATCC and transfected with Jetpei (PolyPlus) according to the manufacturer protocol. Cell lines were tested for mycoplasma contamination using the Mycoplasma PCR ELISA (Sigma).

Immunoprecipitation and western blotting

HEK293T cells were transiently transfected and whole cell extracts were prepared in a 50 mM Tris-HCl pH 7,4, 150 mM NaCl, 1 mM EDTA, 1% Triton X-100 buffer supplemented with protease inhibitors. Those extracts were cleared with protein G Sepharose beads (GE Healthcare) for 1 hr. The corresponding antibodies were incubated with the extracts for 2 hr and immunocomplexes were isolated by adsorption to protein G-Sepharose beads o/n. After washing, the proteins were eluted from the beads with 2xSDS gel-loading buffer 100 mM Tris-Hcl (pH 7), 4% SDS, 0.2% bromophenol blue, 200 mM β-mercaptoethanol and 20% glycerol, and loaded onto reducing polyacrylamide SDS gels. The proteins were detected by western blotting with the indicated antibodies. Immunoprecipitations were performed using mouse αFlag IgG (5 µg; F1804, Sigma-Aldrich), mouse αGFP IgG (4 µg; CSB-MA000051M0m, Cusabio), ChromPure mouse IgG (5 µg/1 mg prot; 015-000-003). Primary antibodies used for western blotting were rabbit αFlag IgG (1:2000; F7425 Sigma-Aldrich), goat αGFP IgG (sc-5385, Santa Cruz) (1:3000), rabbit αMyc Tag IgG (1:3000; #06–549, Millipore), rabbit αHSF2BP R2 (1:2000, ProteintechTM), rabbit αBRME1 R1 (1:3000, ProteintechTM), rat αRPA2 (1:1000, Cell Signaling (Cat 2208S)). Secondary horseradish peroxidase-conjugated α-mouse (715-035-150, Jackson ImmunoResearch), α-rabbit (711-035-152, Jackson ImmunoResearch), α-goat (705-035-147, Jackson ImmunoResearch) or α-rat (712-035-150, Jackson ImmunoResearch) antibodies were used at 1:5000 dilution. Antibodies were detected by using Immobilon Western Chemiluminescent HRP Substrate from Millipore. Secondary DyLight conjugated α-mouse (DyLight 680, 35518 Thermo-Scientific) and α-rabbit (DyLight 800, 35571 Thermo-Scientific) were used at 1:10,000 dilution. Antiboides were detected using a LI-COR Oddysey fluorescent Imager.

Testis immunoprecipitation

Testis extracts were prepared in 50 mM Tris-HCl (pH8), 500 mM NaCl, 1 mM EDTA 1% Triton X100. 4 mg of protein were incubated with 10 µg of the specific antibody against the protein to be immunoprecipitated for 2 hr at 4˚C rotating. Then 50 µl of sepharose beads (GE Healthcare) were added to the protein-Ab mixture and incubated overnight at 4˚C with rotation. After that, the protein-bounded beads were washed four times with 500 µl of the extraction buffer by centrifugating 1 min at 10,000 rpm and 4˚C. Finally, the co-immunoprecipitated proteins were eluted from the beads by resuspending the beads in 50 µl Laemmli buffer and boiling for 5 min. The samples were analyzed by western blot.

Testis immunoprecipitation coupled to mass spectrometry analysis

200 µg of antibodies R1 and R2 against BRME1 (two independent IPs) and IgG from rabbit (negative control) were crosslinked to 100 ul of sepharose beads slurry (GE Healthcare). Testis extracts were prepared in 50 mM Tris-HCl (pH8), 500 mM NaCl, 1 mM EDTA 1% Triton X100. 20 mg of protein extracts were incubated o/n with the sepharose beads. Protein-bound beads were packed into columns and washed in extracting buffer for three times. Proteins were eluted in 100 mM glycine pH3 and analysed by Lc-MS/MS shotgun in LTQ Velos Orbitrap at the Proteomics facility of Centro de Investigación del Cáncer (CSIC/University of Salamanca).

Mass spectrometry data analysis

Raw data were analysed using MaxQuant v 1.6.2.6 (***Cox and Mann, 2008***) against SwissProt Mouse database (UP000000589, Oct, 2019) and MaxQuant contaminants. All FDRs were of 1%. Variable modifications taken into account were oxidation of M and acetylation of the N-term, while fixed modifications included considered only carbamidomethylation of C. The maximum number of modifications allowed per peptide was of 5. Proteins were quantified using iBAQ (***Schwanhäusser et al., 2011***). Potential contaminants, reverse decoy sequences and proteins identified by site were removed. Proteins with less than two unique peptides in the R1 and R2 groups were not considered for ulterior analysis. Proteins with less than two unique peptides in the control group and more than

two in both groups R1 and R2 were selected as high-confidence candidates (group R1 and R2 only). An additional group of putative candidates was selected for those proteins with two or more unique peptides in one of the R1 or R2 groups and no unique peptides in the control sample (groups R1 only and R2 only, respectively).

Statistics

In order to compare counts between genotypes, we used the Two-tailed Welch's t-test (unequal variances t-test), which was appropriate as the count data were not highly skewed (i.e., were reasonably approximated by a normal distribution) and in most cases showed unequal variance. We applied a two-sided test in all the cases. Asterisks denote statistical significance: *p-value<0.05, **p-value<0.01, ***p-value<0.001 and ****p-value<0.0001.

Acknowledgements

We thank Dr. Barbero and Dr. Edyta Marcon, for providing antibodies against SYCP3 and RPA, respectively, Dr. Emmanuelle Martini for helpful advice with the DNA binding assay,Dr. Fabien Fauchereau for the genetic analysis of the family and Dr. Alex N Zelenskyy for helpful discussion. This study was supported by Universite´ Paris Diderot and the Fondation pour la Recherche Me´dicale (Labelisation Equipes DEQ20150331757, SC, A-LT and RAV). This work was supported by MINECO (BFU2017-89408-R) and by Junta de Castilla y León (CSI239P18). NFM, FSS and LGH are supported by European Social Fund/JCyLe grants (EDU/310/2015, EDU/556/2019 and EDU/1083/2013). YBC is funded by a grant from MINECO (BS-2015–073993). The proteomic analysis was performed in the Proteomics Facility of Centro de Investigación del Cáncer, Salamanca, Grant PRB3(IPT17/0019 - ISCIII-SGEFI/ERDF). CIC-IBMCC is supported by the Programa de Apoyo a Planes Estratégicos de Investigación de Estructuras de Investigación de Excelencia cofunded by the Castilla–León autonomous government and the European Regional Development Fund (CLC–2017–01). The funders had no role in study design, data collection and analysis, decision to publish, or preparation of the manuscript.

Additional information

Funding

Funder	Author
Ministerio de Economía y Competitividad	Alberto M Pendás

The funders had no role in study design, data collection and interpretation, or the decision to submit the work for publication.

Author contributions

Natalia Felipe-Medina, Resources, Formal analysis, Supervision, Investigation, Methodology, Writing - review and editing; Sandrine Caburet, Formal analysis, Investigation, Methodology, Writing - original draft, Writing - review and editing; Fernando Sánchez-Sáez, Yazmine B Condezo, Laura Gómez-H, Paloma Duque, Formal analysis, Methodology; Dirk G de Rooij, Anne Laure Todeschini, Formal analysis, Investigation; Rodrigo Garcia-Valiente, Formal analysis; Manuel Adolfo Sánchez-Martin, Resources, Methodology; Stavit A Shalev, Resources; Elena Llano, Conceptualization, Formal analysis, Investigation, Writing - original draft, Writing - review and editing; Reiner A Veitia, Conceptualization, Funding acquisition, Investigation, Writing - original draft, Writing - review and editing; Alberto M Pendás, Conceptualization, Formal analysis, Supervision, Funding acquisition, Investigation, Methodology, Writing - original draft, Writing - review and editing

Author ORCIDs

Natalia Felipe-Medina https://orcid.org/0000-0001-6975-2524
Sandrine Caburet http://orcid.org/0000-0002-7404-8213
Rodrigo Garcia-Valiente http://orcid.org/0000-0003-0444-5587

Reiner A Veitia https://orcid.org/0000-0002-4100-2681
Alberto M Pendás https://orcid.org/0000-0001-9264-3721

Ethics

Animal experimentation: All the experiments were approved by the Ethics Committee for Animal Experimentation of the University of Salamanca (USAL) and the Ethics committee of the Spanish Research Council (CSIC) under protocol #00-245. Accordingly, all the mouse protocols used in this work have been approved by the above mentioned Animal Experimentation committees. Specifically, mice were always housed in a temperature-controlled facility (specific pathogen free, spf) using individually ventilated cages, standard diet and a 12 h light/dark cycle, according to EU law (63/2010/UE) and the Spanish royal law (53/2013) at the "Servicio de Experimentación Animal, SEA. In addition, animal suffering was always minimized and we made every effort to improve animal welfare during the life of the animals.

Decision letter and Author response

Decision letter https://doi.org/10.7554/eLife.56996.sa1
Author response https://doi.org/10.7554/eLife.56996.sa2

Additional files

Supplementary files

- Source data 1. Raw data for all figures and figure supplements.
- Supplementary file 1. Supplementary data and tables including quantification data. Supplementary file 1a. shows the whole exome sequencing and mapping metrics for the three genomic samples. Supplementary file 1b. shows the numbers of variants from the WES analysis and passing the various filters. Supplementary file 1c. shows the predictions of pathogenicity and conservations by 18 computational predictors. Supplementary files 1d and 1e. show the quantification of the colocalization between HSF2BP, BRME1, RPA1 and DMC1. Supplementary file 1f. shows the comparative alterations between all the mutants. Associated to ***Figures 4***, ***5***, ***6*** and ***9***. Supplementary files 1g and 1h. show the putative BRME1 interactors identified by mass spectrometry. Supplementary files 1i and 1j. show respectively the crRNAs and the ssODN employed in the generation of the different mouse models. Supplementary file 1k. shows the primers and expected product sizes for genotyping mouse models. Supplementary file 1l. shows a summary of all the main and supplementary figures and their relationship.
- Transparent reporting form

Data availability

All data generated or analysed during this study are included in the manuscript and supporting files.

References

Ahmed EA, de Rooij DG. 2009. Staging of mouse seminiferous tubule cross-sections. *Methods in Molecular Biology* **558**:263–277. DOI: https://doi.org/10.1007/978-1-60761-103-5_16, PMID: 19685330

AlAsiri S, Basit S, Wood-Trageser MA, Yatsenko SA, Jeffries EP, Surti U, Ketterer DM, Afzal S, Ramzan K, Faiyaz-Ul Haque M, Jiang H, Trakselis MA, Rajkovic A. 2015. Exome sequencing reveals MCM8 mutation underlies ovarian failure and chromosomal instability. *Journal of Clinical Investigation* **125**:258–262. DOI: https://doi.org/10.1172/JCI78473, PMID: 25437880

Baker SM, Plug AW, Prolla TA, Bronner CE, Harris AC, Yao X, Christie DM, Monell C, Arnheim N, Bradley A, Ashley T, Liskay RM. 1996. Involvement of mouse Mlh1 in DNA mismatch repair and meiotic crossing over. *Nature Genetics* **13**:336–342. DOI: https://doi.org/10.1038/ng0796-336, PMID: 8673133

Bannister LA, Reinholdt LG, Munroe RJ, Schimenti JC. 2004. Positional cloning and characterization of mouse mei8, a disrupted allelle of the meiotic cohesin Rec8. *Genesis* **40**:184–194. DOI: https://doi.org/10.1002/gene.20085, PMID: 15515002

Baudat F, Manova K, Yuen JP, Jasin M, Keeney S. 2000. Chromosome Synapsis defects and sexually dimorphic meiotic progression in mice lacking Spo11. *Molecular Cell* **6**:989–998. DOI: https://doi.org/10.1016/S1097-2765(00)00098-8, PMID: 11106739

Baudat F, Imai Y, de Massy B. 2013. Meiotic recombination in mammals: localization and regulation. *Nature Reviews Genetics* **14**:794–806. DOI: https://doi.org/10.1038/nrg3573, PMID: 24136506

Brandsma I. 2006. *Balancing Pathways in DNA Double Strand Break Repair*. Erasmus Rotterdam University.

Brandsma I, Sato K, van Rossum-Fikkert SE, van Vliet N, Sleddens E, Reuter M, Odijk H, van den Tempel N, Dekkers DHW, Bezstarosti K, Demmers JAA, Maas A, Lebbink J, Wyman C, Essers J, van Gent DC, Baarends WM, Knipscheer P, Kanaar R, Zelensky AN. 2019. HSF2BP interacts with a conserved domain of BRCA2 and is required for mouse spermatogenesis. *Cell Reports* **27**:3790–3798. DOI: https://doi.org/10.1016/j.celrep.2019.05.096

Caburet S, Arboleda VA, Llano E, Overbeek PA, Barbero JL, Oka K, Harrison W, Vaiman D, Ben-Neriah Z, García-Tuñón I, Fellous M, Pendás AM, Veitia RA, Vilain E. 2014. Mutant cohesin in premature ovarian failure. *New England Journal of Medicine* **370**:943–949. DOI: https://doi.org/10.1056/NEJMoa1309635, PMID: 24597867

Caburet S, Heddar A, Dardillac E, Creux H, Lambert M, Messiaen S, Misrahi M. 2019a. A homozygous hypomorphic BRCA2 variant causes primary ovarian insufficiency without cancer or Fanconi anemia traits. *bioRxiv*. DOI: https://doi.org/10.1101/751644

Caburet S, Todeschini AL, Petrillo C, Martini E, Farran ND, Legois B, Livera G, Younis JS, Shalev S, Veitia RA. 2019b. A truncating MEIOB mutation responsible for familial primary ovarian insufficiency abolishes its interaction with its partner SPATA22 and their recruitment to DNA double-strand breaks. *EBioMedicine* **42**:524–531. DOI: https://doi.org/10.1016/j.ebiom.2019.03.075, PMID: 31000419

Caburet S, Heddar A, Dardillac E, Creux H, Lambert M, Messiaen S, Misrahi M. 2020. Homozygous hypomorphic. *Journal of Medical Genetics* **43**:909–912. DOI: https://doi.org/10.2337/dc19-1843

Cahoon CK, Hawley RS. 2016. Regulating the construction and demolition of the synaptonemal complex. *Nature Structural & Molecular Biology* **23**:369–377. DOI: https://doi.org/10.1038/nsmb.3208, PMID: 27142324

Cahoon CK, Libuda DE. 2019. Leagues of their own: sexually dimorphic features of meiotic prophase I. *Chromosoma* **131**:199–214. DOI: https://doi.org/10.1007/s00412-019-00692-x

Carlosama C, Elzaiat M, Patiño LC, Mateus HE, Veitia RA, Laissue P. 2017. A homozygous donor splice-site mutation in the meiotic gene MSH4 causes primary ovarian insufficiency. *Human Molecular Genetics* **26**:3161–3166. DOI: https://doi.org/10.1093/hmg/ddx199, PMID: 28541421

Cox J, Mann M. 2008. MaxQuant enables high peptide identification rates, individualized p.p.b.-range mass accuracies and proteome-wide protein quantification. *Nature Biotechnology* **26**:1367–1372. DOI: https://doi.org/10.1038/nbt.1511, PMID: 19029910

de Rooij DG, de Boer P. 2003. Specific arrests of spermatogenesis in genetically modified and mutant mice. *Cytogenetic and Genome Research* **103**:267–276. DOI: https://doi.org/10.1159/000076812, PMID: 15051947

de Vries L, Behar DM, Smirin-Yosef P, Lagovsky I, Tzur S, Basel-Vanagaite L. 2014. Exome sequencing reveals SYCE1 mutation associated with autosomal recessive primary ovarian insufficiency. *The Journal of Clinical Endocrinology & Metabolism* **99**:E2129–E2132. DOI: https://doi.org/10.1210/jc.2014-1268, PMID: 25062452

Fouquet B, Pawlikowska P, Caburet S, Guigon C, Mäkinen M, Tanner L, Hietala M, Urbanska K, Bellutti L, Legois B, Bessieres B, Gougeon A, Benachi A, Livera G, Rosselli F, Veitia RA, Misrahi M. 2017. A homozygous *FANCM* mutation underlies a familial case of non-syndromic primary ovarian insufficiency. *eLife* **6**:e30490. DOI: https://doi.org/10.7554/eLife.30490, PMID: 29231814

Geisinger A, Benavente R. 2017. Mutations in genes coding for synaptonemal complex proteins and their impact on human fertility. *Cytogenetic and Genome Research* **150**:77–85. DOI: https://doi.org/10.1159/000453344

Gershoni M, Pietrokovski S. 2014. Reduced selection and accumulation of deleterious mutations in genes exclusively expressed in men. *Nature Communications* **5**:4438. DOI: https://doi.org/10.1038/ncomms5438, PMID: 25014762

Gómez-H L, Felipe-Medina N, Sánchez-Martín M, Davies OR, Ramos I, García-Tuñón I, de Rooij DG, Dereli I, Tóth A, Barbero JL, Benavente R, Llano E, Pendas AM. 2016. C14ORF39/SIX6OS1 is a constituent of the synaptonemal complex and is essential for mouse fertility. *Nature Communications* **7**:13298. DOI: https://doi.org/10.1038/ncomms13298, PMID: 27796301

Gómez-H L, Felipe-Medina N, Condezo YB, Garcia-Valiente R, Ramos I, Suja JA, Barbero JL, Roig I, Sánchez-Martín M, de Rooij DG, Llano E, Pendas AM. 2019. The PSMA8 subunit of the spermatoproteasome is essential for proper meiotic exit and mouse fertility. *PLOS Genetics* **15**:e1008316. DOI: https://doi.org/10.1371/journal.pgen.1008316, PMID: 31437213

Guo T, Zhao S, Zhao S, Chen M, Li G, Jiao X, Wang Z, Zhao Y, Qin Y, Gao F, Chen ZJ. 2017. Mutations in MSH5 in primary ovarian insufficiency. *Human Molecular Genetics* **26**:1452–1457. DOI: https://doi.org/10.1093/hmg/ddx044, PMID: 28175301

Halldorsson BV, Palsson G, Stefansson OA, Jonsson H, Hardarson MT, Eggertsson HP, Gunnarsson B, Oddsson A, Halldorsson GH, Zink F, Gudjonsson SA, Frigge ML, Thorleifsson G, Sigurdsson A, Stacey SN, Sulem P, Masson G, Helgason A, Gudbjartsson DF, Thorsteinsdottir U, et al. 2019. Characterizing mutagenic effects of recombination through a sequence-level genetic map. *Science* **363**:eaau1043. DOI: https://doi.org/10.1126/science.aau1043, PMID: 30679340

Handel MA, Schimenti JC. 2010. Genetics of mammalian meiosis: regulation, dynamics and impact on fertility. *Nature Reviews Genetics* **11**:124–136. DOI: https://doi.org/10.1038/nrg2723, PMID: 20051984

Hassold T, Hall H, Hunt P. 2007. The origin of human aneuploidy: where we have been, where we are going. *Human Molecular Genetics* **16**:R203–R208. DOI: https://doi.org/10.1093/hmg/ddm243, PMID: 17911163

He WB, Tu CF, Liu Q, Meng LL, Yuan SM, Luo AX, He FS, Shen J, Li W, Du J, Zhong CG, Lu GX, Lin G, Fan LQ, Tan YQ. 2018. *DMC1* mutation that causes human non-obstructive azoospermia and premature ovarian

insufficiency identified by whole-exome sequencing. *Journal of Medical Genetics* **55**:198–204. DOI: https://doi.org/10.1136/jmedgenet-2017-104992, PMID: 29331980

Herrán Y, Gutiérrez-Caballero C, Sánchez-Martín M, Hernández T, Viera A, Barbero JL, de Álava E, de Rooij DG, Suja JÁ, Llano E, Pendás AM. 2011. The cohesin subunit RAD21L functions in meiotic Synapsis and exhibits sexual dimorphism in fertility. *The EMBO Journal* **30**:3091–3105. DOI: https://doi.org/10.1038/emboj.2011.222, PMID: 21743440

Hunt PA, Hassold TJ. 2002. Sex matters in meiosis. *Science* **296**:2181–2183. DOI: https://doi.org/10.1126/science.1071907, PMID: 12077403

Hunter N. 2015. Meiotic recombination: the essence of heredity. *Cold Spring Harbor Perspectives in Biology* **12**: a016618. DOI: https://doi.org/10.1101/cshperspect.a016618

Isaksson R, Tiitinen A. 2004. Present concept of unexplained infertility. *Gynecological Endocrinology* **18**:278–290. DOI: https://doi.org/10.1080/09513590420001998 78, PMID: 15346664

Lake CM, Hawley RS. 2013. RNF212 marks the spot. *Nature Genetics* **45**:228–229. DOI: https://doi.org/10.1038/ng.2559, PMID: 23438588

Loidl J. 2016. Conservation and variability of meiosis across the eukaryotes. *Annual Review of Genetics* **50**:293–316. DOI: https://doi.org/10.1146/annurev-genet-120215-035100, PMID: 27686280

Loregian A, Appleton BA, Hogle JM, Coen DM. 2004. Specific residues in the connector loop of the human Cytomegalovirus DNA polymerase accessory protein UL44 are crucial for interaction with the UL54 catalytic subunit. *Journal of Virology* **78**:9084–9092. DOI: https://doi.org/10.1128/JVI.78.17.9084-9092.2004, PMID: 15308704

Malhas A, Goulbourne C, Vaux DJ. 2011. The nucleoplasmic reticulum: form and function. *Trends in Cell Biology* **21**:362–373. DOI: https://doi.org/10.1016/j.tcb.2011.03.008, PMID: 21514163

Martinez JS, von Nicolai C, Kim T, Ehlén Å, Mazin AV, Kowalczykowski SC, Carreira A. 2016. BRCA2 regulates DMC1-mediated recombination through the BRC repeats. *PNAS* **113**:3515–3520. DOI: https://doi.org/10.1073/pnas.1601691113, PMID: 26976601

Matzuk MM, Lamb DJ. 2008. The biology of infertility: research advances and clinical challenges. *Nature Medicine* **14**:1197–1213. DOI: https://doi.org/10.1038/nm.f.1895, PMID: 18989307

Melton DA, Krieg PA, Rebagliati MR, Maniatis T, Zinn K, Green MR. 1984. Efficient *in vitro* synthesis of biologically active RNA and RNA hybridization probes from plasmids containing a bacteriophage SP6 promoter. *Nucleic Acids Research* **12**:7035–7056. DOI: https://doi.org/10.1093/nar/12.18.7035, PMID: 6091052

Primary Ovarian Insufficiency Collaboration, Wang J, Zhang W, Jiang H, Wu BL. 2014. Mutations in *HFM1* in recessive primary ovarian insufficiency. *The New England Journal of Medicine* **370**:972–974. DOI: https://doi.org/10.1056/NEJMc1310150, PMID: 24597873

Qiao H, Prasada Rao HB, Yang Y, Fong JH, Cloutier JM, Deacon DC, Nagel KE, Swartz RK, Strong E, Holloway JK, Cohen PE, Schimenti J, Ward J, Hunter N. 2014. Antagonistic roles of ubiquitin ligase HEI10 and SUMO ligase RNF212 regulate meiotic recombination. *Nature Genetics* **46**:194–199. DOI: https://doi.org/10.1038/ng.2858, PMID: 24390283

Reynolds A, Qiao H, Yang Y, Chen JK, Jackson N, Biswas K, Holloway JK, Baudat F, de Massy B, Wang J, Höög C, Cohen PE, Hunter N. 2013. RNF212 is a dosage-sensitive regulator of crossing-over during mammalian meiosis. *Nature Genetics* **45**:269–278. DOI: https://doi.org/10.1038/ng.2541, PMID: 23396135

Rossetti R, Ferrari I, Bonomi M, Persani L. 2017. Genetics of primary ovarian insufficiency. *Clinical Genetics* **91**: 183–198. DOI: https://doi.org/10.1111/cge.12921, PMID: 27861765

Schimenti JC, Handel MA. 2018. Unpackaging the genetics of mammalian fertility: strategies to identify the "reproductive genome". *Biology of Reproduction* **99**:1119–1128. DOI: https://doi.org/10.1093/biolre/ioy133, PMID: 29878059

Schürmann A, Koling S, Jacobs S, Saftig P, Krauss S, Wennemuth G, Kluge R, Joost HG. 2002. Reduced sperm count and normal fertility in male mice with targeted disruption of the ADP-ribosylation factor-like 4 (Arl4) gene. *Molecular and Cellular Biology* **22**:2761–2768. DOI: https://doi.org/10.1128/MCB.22.8.2761-2768.2002, PMID: 11909968

Schwanhäusser B, Busse D, Li N, Dittmar G, Schuchhardt J, Wolf J, Chen W, Selbach M. 2011. Global quantification of mammalian gene expression control. *Nature* **473**:337–342. DOI: https://doi.org/10.1038/nature10098, PMID: 21593866

Shang Y, Huang T, Liu H, Liu Y, Liang H, Yu X, Li M, Zhai B, Yang X, Wei Y, Wang G, Chen Z, Wang S, Zhang L. 2020. MEIOK21: a new component of meiotic recombination bridges required for spermatogenesis. *Nucleic Acids Research* **48**:6624–6639. DOI: https://doi.org/10.1093/nar/gkaa406, PMID: 32463460

Sharan SK, Pyle A, Coppola V, Babus J, Swaminathan S, Benedict J, Swing D, Martin BK, Tessarollo L, Evans JP, Flaws JA, Handel MA. 2004. BRCA2 deficiency in mice leads to meiotic impairment and infertility. *Development* **131**:131–142. DOI: https://doi.org/10.1242/dev.00888, PMID: 14660434

Shi B, Xue J, Yin H, Guo R, Luo M, Ye L, Shi Q, Huang X, Liu M, Sha J, Wang PJ. 2019. Dual functions for the ssDNA-binding protein RPA in meiotic recombination. *PLOS Genetics* **15**:e1007952. DOI: https://doi.org/10.1371/journal.pgen.1007952, PMID: 30716097

Siaud N, Barbera MA, Egashira A, Lam I, Christ N, Schlacher K, Xia B, Jasin M. 2011. Plasticity of BRCA2 function in homologous recombination: genetic interactions of the PALB2 and DNA binding domains. *PLOS Genetics* **7**: e1002409. DOI: https://doi.org/10.1371/journal.pgen.1002409, PMID: 22194698

Singh P, Schimenti JC, Bolcun-Filas E. 2015. A mouse geneticist's practical guide to CRISPR applications. *Genetics* **199**:1–15. DOI: https://doi.org/10.1534/genetics.114.169771, PMID: 25271304

Souquet B, Abby E, Hervé R, Finsterbusch F, Tourpin S, Le Bouffant R, Duquenne C, Messiaen S, Martini E, Bernardino-Sgherri J, Toth A, Habert R, Livera G. 2013. MEIOB targets single-strand DNA and is necessary for meiotic recombination. *PLOS Genetics* **9**:e1003784. DOI: https://doi.org/10.1371/journal.pgen.1003784, PMID: 24068956

Takemoto K, Tani N, Takada-Horisawa Y, Fujimura S, Tanno N, Yamane M, Okamura K, Sugimoto M, Araki K, Ishiguro KI. 2020. Meiosis-Specific C19orf57/4930432K21Rik/BRME1 modulates localization of RAD51 and DMC1 to DSBs in mouse meiotic recombination. *Cell Reports* **31**:107686. DOI: https://doi.org/10.1016/j.celrep.2020.107686, PMID: 32460033

Tenenbaum-Rakover Y, Weinberg-Shukron A, Renbaum P, Lobel O, Eideh H, Gulsuner S, Dahary D, Abu-Rayyan A, Kanaan M, Levy-Lahad E, Bercovich D, Zangen D. 2015. Minichromosome maintenance complex component 8 (MCM8) gene mutations result in primary gonadal failure. *Journal of Medical Genetics* **52**:391–399. DOI: https://doi.org/10.1136/jmedgenet-2014-102921, PMID: 25873734

Tucker EJ, Grover SR, Robevska G, van den Bergen J, Hanna C, Sinclair AH. 2018. Identification of variants in pleiotropic genes causing "isolated" premature ovarian insufficiency: implications for medical practice. *European Journal of Human Genetics* **26**:1319–1328. DOI: https://doi.org/10.1038/s41431-018-0140-4, PMID: 29706645

Veitia RA. 2003. A sigmoidal transcriptional response: cooperativity, synergy and dosage effects. *Biological Reviews of the Cambridge Philosophical Society* **78**:149–170. DOI: https://doi.org/10.1017/S1464793102006036, PMID: 12620064

Wang S, Hassold T, Hunt P, White MA, Zickler D, Kleckner N, Zhang L. 2017. Inefficient crossover maturation underlies elevated aneuploidy in human female meiosis. *Cell* **168**:977–989. DOI: https://doi.org/10.1016/j.cell.2017.02.002, PMID: 28262352

Webster A, Schuh M. 2017. Mechanisms of aneuploidy in human eggs. *Trends in Cell Biology* **27**:55–68. DOI: https://doi.org/10.1016/j.tcb.2016.09.002, PMID: 27773484

Wood-Trageser MA, Gurbuz F, Yatsenko SA, Jeffries EP, Kotan LD, Surti U, Ketterer DM, Matic J, Chipkin J, Jiang H, Trakselis MA, Topaloglu AK, Rajkovic A. 2014. MCM9 mutations are associated with ovarian failure, short stature, and chromosomal instability. *The American Journal of Human Genetics* **95**:754–762. DOI: https://doi.org/10.1016/j.ajhg.2014.11.002, PMID: 25480036

Yoshima T, Yura T, Yanagi H. 1998. Novel testis-specific protein that interacts with heat shock factor 2. *Gene* **214**:139–146. DOI: https://doi.org/10.1016/S0378-1119(98)00208-X, PMID: 9651507

Zangen D, Kaufman Y, Zeligson S, Perlberg S, Fridman H, Kanaan M, Abdulhadi-Atwan M, Abu Libdeh A, Gussow A, Kisslov I, Carmel L, Renbaum P, Levy-Lahad E. 2011. XX ovarian dysgenesis is caused by a PSMC3IP/HOP2 mutation that abolishes coactivation of estrogen-driven transcription. *The American Journal of Human Genetics* **89**:572–579. DOI: https://doi.org/10.1016/j.ajhg.2011.09.006, PMID: 21963259

Zhang J, Fujiwara Y, Yamamoto S, Shibuya H. 2019. A meiosis-specific BRCA2 binding protein recruits recombinases to DNA double-strand breaks to ensure homologous recombination. *Nature Communications* **10**:722. DOI: https://doi.org/10.1038/s41467-019-08676-2, PMID: 30760716

Zhang J, Gurusaran M, Fujiwara Y, Zhang K, Echbarthi M, Vorontsov E, Guo R, Pendlebury DF, Alam I, Livera G, Emmanuelle M, Wang PJ, Nandakumar J, Davies OR, Shibuya H. 2020. The BRCA2-MEILB2-BRME1 complex governs meiotic recombination and impairs the mitotic BRCA2-RAD51 function in Cancer cells. *Nature Communications* **11**:2055. DOI: https://doi.org/10.1038/s41467-020-15954-x, PMID: 32345962

Zhao W, Vaithiyalingam S, San Filippo J, Maranon DG, Jimenez-Sainz J, Fontenay GV, Kwon Y, Leung SG, Lu L, Jensen RB, Chazin WJ, Wiese C, Sung P. 2015. Promotion of BRCA2-Dependent homologous recombination by DSS1 via RPA targeting and DNA mimicry. *Molecular Cell* **59**:176–187. DOI: https://doi.org/10.1016/j.molcel.2015.05.032, PMID: 26145171

Zickler D, Kleckner N. 2015. Recombination, pairing, and Synapsis of homologs during meiosis. *Cold Spring Harbor Perspectives in Biology* **7**:a016626. DOI: https://doi.org/10.1101/cshperspect.a016626, PMID: 25986558

Appendix 1

Key resources table

Appendix 1—key resources table

Reagent type (species) or resource	Designation	Source or reference	Identifiers	Additional information
Genetic reagent (*M. musculus*)	*Hsf2bp*$^{-/-}$	This paper		Materials and methods section ***Figure 2—figure supplement 1*** Available from the authors upon request Dr. Alberto M. Pendás (amp@usal.es)
Genetic reagent (*M. musculus*)	*Hsf2bp*$^{S167L/S167L}$	This paper		Materials and methods section ***Figure 2—figure supplement 1*** Available from the authors upon request Dr. Alberto M. Pendás (amp@usal.es)
Genetic reagent (*M. musculus*)	*Brme1*$^{-/-}$	This paper		Materials and methods section ***Figure 8—figure supplement 1*** Available from the authors upon request Dr. Alberto M. Pendás (amp@usal.es)
Genetic reagent (*M. musculus*)	*Brme1*$^{\Delta 142\text{-}472/\Delta 142\text{-}472}$	This paper		Materials and methods section ***Figure 7—figure supplement 1*** Available from the authors upon request Dr. Alberto M. Pendás (amp@usal.es)
Genetic reagent (*M. musculus*)	*Rnf212*$^{-/-}$	This paper		Materials and methods section ***Figure 7—figure supplement 5*** Available from the authors upon request Dr. Alberto M. Pendás (amp@usal.es)
Genetic reagent (*M. musculus*)	*Hei10*$^{-/-}$	This paper		Materials and methods section ***Figure 7—figure supplement 5*** Available from the authors upon request Dr. Alberto M. Pendás (amp@usal.es)
Genetic reagent (*M. musculus*)	*Spo11*$^{-/-}$	This paper		Materials and methods section ***Figure 7—figure supplement 6*** Available from the authors upon request Dr. Alberto M. Pendás (amp@usal.es)
Genetic reagent (*M. musculus*)	*Psma8*$^{-/-}$	PMID:31437213		
Genetic reagent (*M. musculus*)	*Six6os1*$^{-/-}$	PMID:27796301		
Genetic reagent (*M. musculus*)	*Rec8*$^{-/-}$	PMID:15515002		Dr. John C. Schimenti (Cornell university)
Cell line (*H. sapiens*)	U2OS	ATCC	HTB-96	

Continued on next page

Appendix 1—key resources table continued

Reagent type (species) or resource	Designation	Source or reference	Identifiers	Additional information
Cell line (*H. sapiens*)	HEK293T	ATCC	CRL-11268	
Recombinant DNA reagent	pEGFP-C1	Clontech	Catalog: 6084–1	
Recombinant DNA reagent	pcDNA3	Invitrogen	A-150228	
Recombinant DNA reagent	pcDNA3-2xFlag	This paper Generated from pcDNA3		Materials and methods section ***Figure 6—figure supplement 2*** Available from the authors upon request Dr. Alberto M. Pendás (amp@usal.es)
Recombinant DNA reagent	pEGFP-C1 HSF2BP	This paper		Materials and methods section ***Figure 7*** Available from the authors upon request Dr. Alberto M. Pendás (amp@usal.es)
Recombinant DNA reagent	pcDNA3 2xFlag HSF2BP	This paper		Materials and methods section ***Figure 7*** Available from the authors upon request Dr. Alberto M. Pendás (amp@usal.es)
Recombinant DNA reagent	pcDNA3 2xFlag HSF2BP-S167L	This paper		Materials and methods section ***Figure 7*** Available from the authors upon request Dr. Alberto M. Pendás (amp@usal.es)
Recombinant DNA reagent	pcDNA3 2xHA HSF2BP	This paper		Materials and methods section ***Figure 10—figure supplement 1*** Available from the authors upon request Dr. Alberto M. Pendás (amp@usal.es)
Recombinant DNA reagent	pEGFP-C1 BRME1	This paper		Materials and methods section ***Figure 10—figure supplement 1*** Available from the authors upon request Dr. Alberto M. Pendás (amp@usal.es)
Recombinant DNA reagent	pcDNA3 2xFlag BRME1	This paper		Materials and methods section ***Figure 10—figure supplement 1*** Available from the authors upon request Dr. Alberto M. Pendás (amp@usal.es)
Recombinant DNA reagent	pcDNA3 2xFlag BRME1Δ142–472	This paper		Materials and methods section ***Figure 7*** Available from the authors upon request Dr. Alberto M. Pendás (amp@usal.es)

Continued on next page

Appendix 1—key resources table continued

Reagent type (species) or resource	Designation	Source or reference	Identifiers	Additional information
Recombinant DNA reagent	pEGFP-C1 HSF2BP	This paper		Materials and methods section ***Figure 10*** Available from the authors upon request Dr. Alberto M. Pendás (amp@usal.es)
Recombinant DNA reagent	pEGFP-C1 HSF2BP-S167L	This paper		Materials and methods section ***Figure 10*** Available from the authors upon request Dr. Alberto M. Pendás (amp@usal.es)
Recombinant DNA reagent	pEGFP-C1 BRCA2-C	This paper		Materials and methods section ***Figure 6—figure supplement 2*** Available from the authors upon request Dr. Alberto M. Pendás (amp@usal.es)
Recombinant DNA reagent	pcDNA3 2xFlag BRCA2-C	This paper		Materials and methods section ***Figure 10*** Available from the authors upon request Dr. Alberto M. Pendás (amp@usal.es)
Recombinant DNA reagent	pcDNA3 2xFlag BRCA2-M	This paper		Materials and methods section Available from the authors upon request Dr. Alberto M. Pendás (amp@usal.es)
Recombinant DNA reagent	pcDNA3 2xFlag BRCA2-N	This paper		Materials and methods section Available from the authors upon request Dr. Alberto M. Pendás (amp@usal.es)
Recombinant DNA reagent	pcDNA3 2xFlag RPA1	This paper		Materials and methods section ***Figure 10—figure supplement 1*** Available from the authors upon request Dr. Alberto M. Pendás (amp@usal.es)
Recombinant DNA reagent	pcDNA3 2xFlag RAD51	This paper		Materials and methods section ***Figure 10—figure supplement 1*** Available from the authors upon request Dr. Alberto M. Pendás (amp@usal.es)
Recombinant DNA reagent	pEGFP-C1 PALB2	This paper		Materials and methods section ***Figure 10—figure supplement 1*** Available from the authors upon request Dr. Alberto M. Pendás (amp@usal.es)
Recombinant DNA reagent	pcDNA 2xHA PALB2	This paper		Materials and methods section ***Figure 10—figure supplement 1*** Available from the authors upon request Dr. Alberto M. Pendás (amp@usal.es)

Continued on next page

Appendix 1—key resources table continued

Reagent type (species) or resource	Designation	Source or reference	Identifiers	Additional information
Antibody	Anti-HSF2BP-R2 (rabbit polyclonal)	This paper (ProteintechTM)		Materials and methods section IF (1:30) WB (1:2000) Available from the authors upon request Dr. Alberto M. Pendás (amp@usal.es)
Antibody	Anti-BRME1-R1 (rabbit polyclonal)	This paper (ProteintechTM)		Materials and methods section WB (1:3000) Available from the authors upon request Dr. Alberto M. Pendás (amp@usal.es)
Antibody	Anti-BRME1-R2 (rabbit polyclonal)	This paper (ProteintechTM)		Materials and methods section IF (1:100) Available from the authors upon request Dr. Alberto M. Pendás (amp@usal.es)
Antibody	Anti-DMC1 (rabbit polyclonal)	This paper (ProteintechTM)		Materials and methods section IF (1:500) Available from the authors upon request Dr. Alberto M. Pendás (amp@usal.es)
Antibody	Anti-SYCP3 (mouse monoclonal)	Santa cruz	sc-74569	IF (1:100)
Antibody	Anti-SYCP3 (rabbit polyclonal)	PMID:27796301	K921	Dr. José Luis Barbero (Centro de Investigaciones Biologicas) IF (1:60)
Antibody	Anti-SYCP1 (rabbit polyclonal)	Abcam	ab15090	IF (1:200)
Antibody	anti-γH2AX (ser139) (rabbit polyclonal)	Millipore	#07–164	IF (1:500)
Antibody	Anti-MLH1 (mouse monoclonal)	BD Biosciences	51-1327GR	IF (1:20)
Antibody	Anti-CDK2 (mouse monoclonal)	Santa Cruz	sc-6248	IF (1:20)
Antibody	αRAD51 (rabbit polyclonal)	Calbiochem	PC130	IF (1:50)
Antibody	αRPA1 serum (rabbit polyclonal)		¨Molly¨	Dr. Edyta Marcon (Medical Research University of Toronto) IF (1:30)
Antibody	αRPA2 (rat monoclonal)	Cell Signalling	2208S	IF (1:100) WB (1:1000)
Antibody	Anti-SPATA22 (rabbit polyclonal)	Proteintech Europe	16989–1-AP	IF (1:60)
Antibody	Anti-Flag (mouse monoclonal)	Sigma-Aldrich	F1804	IF (1:100) IP (5 µg)
Antibody	Anti-GFP (mouse monoclonal)	Cusabio	CSB-MA000051M0m	IP (5 µg)
Antibody	Anti-HA (mouse monoclonal)	BioLegend	MMS-101P	IP (5 µg)

Continued on next page

Appendix 1—key resources table continued

Reagent type (species) or resource	Designation	Source or reference	Identifiers	Additional information
Antibody	Mouse IgGs (mouse polyclonal)	Jackson Immunoresearch	015-000-003	IP (5 µg)
Antibody	Anti-Flag (rabbit polyclonal)	Sigma-Aldrich	F7425	WB (1:2000)
Antibody	Anti-GFP (goat polyclonal)	Santa Cruz	sc-5385	WB (1:3000)
Antibody	Anti-GFP (rabbit polyclonal)	Life technologies	A-11122	WB (1:3000)
Antibody	Anti-HA (rabbit polyclonal)	Sigma-Aldrich	H6908	WB (1:3000)
Antibody	Goat α-mouse Alexa555 (goat polyclonal)	ThermoFisher	A-32727	IF (1:200)
Antibody	Goat α-mouse Alexa488 (goat polyclonal)	ThermoFisher	A-11001	IF (1:200)
Antibody	Donkey α-rabbit Alexa555 (donkey polyclonal)	ThermoFisher	A-31572	IF (1:200)
Antibody	Goat α-rabbit Alexa488 (goat polyclonal)	ThermoFisher	A-32731	IF (1:200)
Antibody	Goat α-rabbit Alexa488 Fab (goat polyclonal)	Jackson Immunoresearch	111-547-003	IF (1:100)
Antibody	Goat α-mouse AMCA (goat polyclonal)	Jackson Immunoresearch	115-155-146	IF (1:100)
Antibody	Donkey α-rabbit AMCA (donkey polyclonal)	Jackson Immunoresearch	711-155-152	IF (1:100)
Antibody	Goat α-rat Alexa488 (goat polyclonal)	ThermoFisher	A-11006	IF (1:200)
Antibody	Secondary horseradish peroxidase-conjugated α-mouse (donkey polyclonal)	Jackson Immunoresearch	715-035-150	WB (1:5000)
Antibody	Secondary horseradish peroxidase-conjugated α-rabbit (donkey polyclonal)	Jackson Immunoresearch	711-035-152	WB (1:5000)
Antibody	Secondary horseradish peroxidase-conjugated α-goat (donkey polyclonal)	Jackson Immunoresearch	705-035-147	WB (1:5000)
Antibody	Secondary horseradish peroxidase-conjugated α-rat (donkey polyclonal)	Jackson Immunoresearch	712-035-150	WB (1:5000)

Continued on next page

Appendix 1—key resources table continued

Reagent type (species) or resource	Designation	Source or reference	Identifiers	Additional information
Antibody	Secondary DyLightTM 680 conjugated α-mouse (goat polyclonal)	Thermo Scientific	35518	WB (1:10000)
Antibody	Secondary DyLightTM 800 conjugated α-rabbit (goat polyclonal)	Thermo Scientific	35571	WB (1:10000)
Sequence-based reagent	sgRNA1 *Hsf2bp*	This paper (IDT)	CRISPR-Cas9 crRNA	Materials and methods section ***Supplementary file 1i*** ***Figure 2—figure supplement 1*** 5′-TCACAAAACTCTCCATCGTC-3′
Sequence-based reagent	sgRNA2 *Hsf2bp*	This paper (IDT)	CRISPR-Cas9 crRNA	Materials and methods section ***Supplementary file 1i*** ***Figure 2—figure supplement 1*** 5′-ATTGGATGGGGATGTCAAGG-3′
Sequence-based reagent	sgRNA3 *Brme1*	This paper (IDT)	CRISPR-Cas9 crRNA	Materials and methods section ***Supplementary file 1i*** ***Figure 7—figure supplement 1*** 5′-AACCTCAGGGACTCTCTCTG-3′
Sequence-based reagent	sgRNA4 *Brme1*	This paper (IDT)	CRISPR-Cas9 crRNA	Materials and methods section ***Supplementary file 1i*** ***Figure 7—figure supplement 1*** 5′-GAAGTCTAGTTCCATTGCTG-3′
Sequence-based reagent	sgRNA5 *Spo11*	This paper (IDT)	CRISPR-Cas9 crRNA	Materials and methods section ***Supplementary file 1i*** ***Figure 7—figure supplement 6*** 5′-TATGTCTCTATGCAGATGCA-3′
Sequence-based reagent	sgRNA6 *Spo11*	This paper (IDT)	CRISPR-Cas9 crRNA	Materials and methods section ***Supplementary file 1i*** ***Figure 7—figure supplement 6*** 5′- ACACTGACAGCCAGCTCTTT-3′
Sequence-based reagent	sgRNA7 *Rnf212*	This paper (IDT)	CRISPR-Cas9 crRNA	Materials and methods section ***Supplementary file 1i*** ***Figure 7—figure supplement 5*** 5′- ACCCACGTGAGACTCGCGCG-3′
Sequence-based reagent	sgRNA8 *Rnf212*	This paper (IDT)	CRISPR-Cas9 crRNA	Materials and methods section ***Supplementary file 1i*** ***Figure 7—figure supplement 5*** 5′- CCTCAAAGGTCCGCGTATTC-3′
Sequence-based reagent	sgRNA9 *Hei10*	This paper (IDT)	CRISPR-Cas9 crRNA	Materials and methods section ***Supplementary file 1i*** ***Figure 7—figure supplement 5*** 5′- GAAAGGGTACTGTTGCAAGC-3′

Continued on next page

Appendix 1—key resources table continued

Reagent type (species) or resource	Designation	Source or reference	Identifiers	Additional information
Sequence-based reagent	ssODN *Hsf2bp*$^{S167L/S167L}$	This paper (IDT)		Materials and methods section ***Supplementary file 1j*** ***Figure 2—figure supplement 1*** 5′CTTTGGAAAGATGTGACAG TTCTATCTTTTTTATCTTTCA GGACAAAGCATTGAAGTTTT TCAACATAACTGGACAGACGA TGGAGAGTTTTGTGAAGTTA TTGGATGGGGATGTCAAGGAAG TTGATTCTGATGAAAATCAATTTGTC TTTGCACTGGCTGGAATTGTAAC AAGTAGGTAACTTTT CAGATACAGCGCT3′
Sequence-based reagent	ssODN *Brme1*$^{\Delta 142\text{-}472/\Delta 142\text{-}472}$	This paper (IDT)		Materials and methods section ***Supplementary file 1j*** ***Figure 7—figure supplement 1*** 5′CTTCAGAGTGCTTGCTTAT TGAAGGCCAGGACTGAATCT TCTTTTTCCACAGGAAACAA GGCCAGAGCTGGGAGCCCTC AAAGCAGCCAGCCAGCCACA GGCAATGGAACTAGACTTCC TGCCTGACAGCCAGATACAG GATGCCCTGGATGCCACTAA CATGGAGCAGGTAAGAGCT TTCTGTACTCAAATGTACACCC3′
Sequence-based reagent	ssODN *Spo11*$^{-/-}$	This paper (IDT)		Materials and methods section ***Supplementary file 1j*** ***Figure 7—figure supplement 6*** 5′GTTTCCTGCGGTATGTGT TCTCTGCCGTGGTCTGTGTT TGTCACCGTCCAGGAGCAA TGCTCATTCTGTGTTGAGCT TGCATCTGCATAGAGACAT ATTCTTCACTGACAGCCAGCT CTTTGGCAACCAGGCTGCG GTGGACAGCGCCATCGATG ACATTTCCTGTATGCTGA AAGTGCCCAGGAGGAG TCTGCACGTGG-3′
Sequence-based reagent	HSF2BP-F1	This paper	PCR primer	Materials and methods section ***Supplementary file 1j*** ***Figure 2—figure supplement 1*** 5′-TTCTTTGGAAAGATGTGACAGTTC-3′
Sequence-based reagent	HSF2BP-R1	This paper	PCR primer	Materials and methods section ***Supplementary file 1j*** ***Figure 2—figure supplement 1*** 5′-ACCTGGGTTTCCTTTAGATCAGTTA-3′
Sequence-based reagent	BRME1- F2	This paper	PCR primer	Materials and methods section ***Supplementary file 1j*** ***Figure 7—figure supplement 1*** 5′-GAAAGTTCTTCAGAGTGCTTGCT-3′

Continued on next page

Appendix 1—key resources table continued

Reagent type (species) or resource	Designation	Source or reference	Identifiers	Additional information
Sequence-based reagent	BRME1- R2	This paper	PCR primer	Materials and methods section ***Supplementary file 1j*** ***Figure 7—figure supplement 1*** 5′-AGCCCTATCTTGTCACCTAAAG-3′
Sequence-based reagent	BRME1- F3	This paper	PCR primer	Materials and methods section ***Supplementary file 1j*** ***Figure 7—figure supplement 1*** 5′-CCCAGCAGATGCCTCTCTTAT-3′
Sequence-based reagent	BRME1- R3	This paper	PCR primer	Materials and methods section ***Supplementary file 1j*** ***Figure 7—figure supplement 1*** 5′-CTCAGCAGAGTTCCAATGCAG-3′
Sequence-based reagent	SPO11-F4	This paper	PCR primer	Materials and methods section ***Supplementary file 1j*** ***Figure 7—figure supplement 6*** 5′- AGAGCCCCCAGTGCTCTTAAC-3′
Sequence-based reagent	SPO11-R4	This paper	PCR primer	Materials and methods section ***Supplementary file 1j*** ***Figure 7—figure supplement 6*** 5′- GGCAGACCCCTCTACCTCTGT-3′
Sequence-based reagent	RNF212-F5	This paper	PCR primer	Materials and methods section ***Supplementary file 1j*** ***Figure 7—figure supplement 5*** 5′- TTTCTTTGCCTCCGTACTTTTGG-3′
Sequence-based reagent	RNF212-R5	This paper	PCR primer	Materials and methods section ***Supplementary file 1j*** ***Figure 7—figure supplement 5*** 5′- CCCAGGCTTTACTTCAACAACAA −3′
Sequence-based reagent	HEI10-F6	This paper	PCR primer	Materials and methods section ***Supplementary file 1j*** ***Figure 7—figure supplement 5*** 5′- CTGCCTGTTCTCACATCTTC-3′
Sequence-based reagent	HEI10-R6	This paper	PCR primer	Materials and methods section ***Supplementary file 1j*** ***Figure 7—figure supplement 5*** 5′- AGCTTTCCAGAAAGGGTACTG −3′
Sequence-based reagent	ss60-mer F	PMID:24068956	DNA Binding assay primer	Materials and methods section ***Figure 7—figure supplement 4*** 5′-GAT CTG CACGACGC ACACCGGACGTATCTGCTATC GCTCATGTCAACCGCT CAAGCTGC/3′BiotinTEG/
Sequence-based reagent	ss60-mer R	PMID:24068956	DNA Binding assay primer	Materials and methods section ***Figure 7—figure supplement 4*** 5′- GCAGCTTGAGCGGTTGACAT GAGCGATAGCAGATACGTCCG GTGTGCGTCGTGCAGATC-3′

Continued on next page

Appendix 1—key resources table continued

Reagent type (species) or resource	Designation	Source or reference	Identifiers	Additional information
Sequence-based reagent	HSF2BP-EX6F	This Paper	Sanger sequencing primer	Material and methods section ***Figure 1—figure supplement 1*** 5′-CTAGAATCTTCTGTATCCTGCA-3′
Sequence-based reagent	HSF2BP-EX6R2	This Paper	Sanger sequencing primer	Material and methods section ***Figure 1—figure supplement 1*** 5′-GGTCTGGAAGCAAACAGGCAA-3′
Commercial assay or kit	TNT T7 Coupled Reticulocyte Lysate Systems	Promega	L4610	***Figure 7—figure supplement 4***
Commercial assay or kit	In Situ Cell Death Detection Kit	Roche	11684795910	***Figure 2***
Commercial assay or kit	Matchmaker Gold Yeast Two-Hybrid System	Clontech	630489	Materials and methods section
Commercial assay or kit	Mouse testis Mate and Plate cDNA library	Clontech	638852	Materials and methods section
Commercial assay or kit	Jetpei	PolyPlus	101–40N	Materials and methods section
Commercial assay or kit	GammaBind G Sepharose	GE Healthcare	17-0885-02	Materials and methods section
Commercial assay or kit	Dynabeads M-280 Streptavidin	Thermo Fisher	11205D	Materials and methods section ***Figure 7—figure supplement 4***
Chemical compound, drug	MG132	Sigma-Aldrich PMDI:28059716	M8699	***Figure 10***
Other	DAPI stain	Invitrogen	D1306	Materials and methods section
Other	Vectashield Mounting Medium	Vector Laboratories	H1000	Materials and methods section
Other	ProLong Gold antifade reagent	Invitrogen	P10144	Materials and methods section